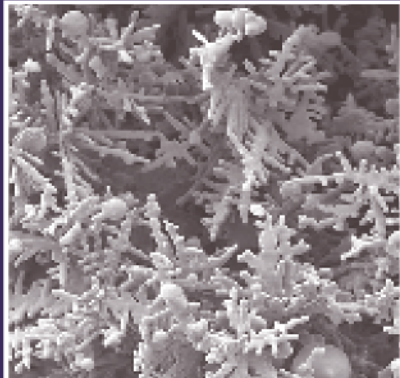


WOODHEAD PUBLISHING IN MATERIALS



Fundamentals of metallurgy

Edited by Seshadri Seetharaman



WP

Fundamentals of metallurgy

Related titles:

New developments in advanced welding

(ISBN-13: 978-1-85573-970-3; ISBN-10: 1-85573-970-4)

Recent developments in high-technology areas have significantly transformed the welding industry. Automation, computers, process control, sophisticated scientific instruments and advanced processing methods are all common in today's modern industry. Today's engineers and technologists have to support complex systems and apply sophisticated welding technologies. This comprehensive new book discusses the changes in advanced welding technologies preparing the reader for the modern industry.

Welding residual stress and distortion

(ISBN-13: 978-1-85573-771-6; ISBN-10: 1-85573-771-X)

Measurement techniques for characterisation of residual stress and distortion have improved significantly. More importantly the development and application of computational welding mechanics have been phenomenal. Through the collaboration of experts, this book provides a comprehensive treatment of the subject. It develops sufficient theoretical treatments on heat transfer, solid mechanics and materials behaviour that are essential for understanding and determining welding residual stress and distortion. It will outline the approach for computational analysis that engineers with sufficient background can follow and apply. The book will be useful for advanced analysis of the subject and provide examples and practical solutions for welding engineers.

The science and technology of materials in automotive engines

(ISBN-13: 978-1-85573-742-6; ISBN-10: 1-85573-742-6)

This new book provides an introductory text on the science and technology of materials used in automotive engines. It focuses on reciprocating engines, both four and two-stroke, with particular emphasis on their characteristics and the types of materials used in their construction. The book considers the engine in terms of each specific part: the cylinder, piston, camshaft, valves, crankshaft, connecting rod and catalytic converter. The materials used in automotive engines are required to fulfill a multitude of functions. It is a subtle balance between material properties, essential design and high performance characteristics. The intention here is to describe the metallurgy, surface modification, wear resistance, and chemical composition of these materials. It also includes supplementary notes that support the core text. The book will be essential reading for engineers and designers of engines, as well as lecturers and graduate students in the fields of combustion engineering, machine design and materials science looking for a concise, expert analysis of automotive materials.

Details of these and other Woodhead Publishing materials books and journals, as well as materials books from Maney Publishing, can be obtained by:

- visiting our web site at www.woodheadpublishing.com
- contacting Customer Services (e-mail: sales@woodhead-publishing.com; fax: +44 (0) 1223 893694; tel.: +44 (0) 1223 891358 ext. 30; address: Woodhead Publishing Limited, Abington Hall, Abington, Cambridge CB1 6AH, England)

If you would like to receive information on forthcoming titles, please send your address details to: Francis Dodds (address, tel. and fax as above; email: francisd@woodhead-publishing.com). Please confirm which subject areas you are interested in.

Maney currently publishes 16 peer-reviewed materials science and engineering journals. For further information visit www.maney.co.uk/journals.

Fundamentals of metallurgy

Edited by
Seshadri Seetharaman

**Woodhead Publishing and Maney Publishing
on behalf of
The Institute of Materials, Minerals & Mining**

**CRC Press
Boca Raton Boston New York Washington, DC**

WOODHEAD PUBLISHING LIMITED
Cambridge England

Woodhead Publishing Limited and Maney Publishing Limited on behalf of
The Institute of Materials, Minerals & Mining

Published by Woodhead Publishing Limited, Abington Hall, Abington,
Cambridge CB1 6AH, England
www.woodheadpublishing.com

Published in North America by CRC Press LLC, 6000 Broken Sound Parkway, NW,
Suite 300, Boca Raton, FL 33487, USA

First published 2005, Woodhead Publishing Limited and CRC Press LLC
© Woodhead Publishing Limited, 2005
The authors have asserted their moral rights.

This book contains information obtained from authentic and highly regarded sources.
Reprinted material is quoted with permission, and sources are indicated. Reasonable
efforts have been made to publish reliable data and information, but the authors and
the publishers cannot assume responsibility for the validity of all materials. Neither the
authors nor the publishers, nor anyone else associated with this publication, shall be
liable for any loss, damage or liability directly or indirectly caused or alleged to be
caused by this book.

Neither this book nor any part may be reproduced or transmitted in any form or by
any means, electronic or mechanical, including photocopying, microfilming and
recording, or by any information storage or retrieval system, without permission in
writing from Woodhead Publishing Limited.

The consent of Woodhead Publishing Limited does not extend to copying for general
distribution, for promotion, for creating new works, or for resale. Specific permission
must be obtained in writing from Woodhead Publishing Limited for such copying.

Trademark notice: Product or corporate names may be trademarks or registered
trademarks, and are used only for identification and explanation, without intent to
infringe.

British Library Cataloguing in Publication Data

A catalogue record for this book is available from the British Library.

Library of Congress Cataloging in Publication Data

A catalog record for this book is available from the Library of Congress.

Woodhead Publishing Limited ISBN-13: 978-1-85573-927-7 (book)

Woodhead Publishing Limited ISBN-10: 1-85573-927-5 (book)

Woodhead Publishing Limited ISBN-13: 978-1-84569-094-6 (e-book)

Woodhead Publishing Limited ISBN-10: 1-84569-094-X (e-book)

CRC Press ISBN-10: 0-8493-3443-8

CRC Press order number: WP3443

The publishers' policy is to use permanent paper from mills that operate a sustainable
forestry policy, and which has been manufactured from pulp which is processed using
acid-free and elementary chlorine-free practices. Furthermore, the publishers ensure
that the text paper and cover board used have met acceptable environmental
accreditation standards.

Project managed by Macfarlane Production Services, Dunstable, Bedfordshire
(macfarl@aol.com)

Typeset by Godiva Publishing Services Ltd, Coventry, West Midlands

Printed by TJ International Limited, Padstow, Cornwall, England

Contents

<i>Contributor contact details</i>	xi
<i>Preface</i>	xiii
Part I Understanding the effects of processing on the properties of metals	
1 Descriptions of high-temperature metallurgical processes	3
H Y SOHN, University of Utah and S SRIDHAR, Carnegie Mellon University, USA	
1.1 Introduction	3
1.2 Reactions involving gases and solids	4
1.3 Reactions involving liquid phases	17
1.4 Casting processes	27
1.5 Thermomechanical processes	31
1.6 References	34
1.7 Appendix: notation	37
2 Thermodynamic aspects of metals processing	38
R E AUNE and S SEETHARAMAN, Royal Institute of Technology, Sweden	
2.1 Introduction	38
2.2 Basic concepts in thermodynamics	39
2.3 Chemical equilibrium	44
2.4 Unary and multicomponent equilibria	49
2.5 Thermodynamics of solutions	57
2.6 Thermodynamics of multicomponent dilute solutions	66
2.7 Modelling of metallic systems	70

vi	Contents	
2.8	Thermodynamics of ionic melts	72
2.9	Basics of electrochemical thermodynamics	79
2.10	Conclusions	79
2.11	Further reading	80
2.12	References	80
3	Phase diagrams, phase transformations, and the prediction of metal properties	82
K MORITA, The University of Tokyo and N SANO, Nippon Steel Corporation, Japan		
3.1	Introduction	82
3.2	Phase diagrams and potential diagrams	83
3.3	Ternary phase diagrams	87
3.4	Solidification in ternary systems and four-phase equilibria	95
3.5	Examples of solidification behaviour from a phase diagram perspective	102
3.6	Conclusions	107
3.7	References	108
4	Measurement and estimation of physical properties of metals at high temperatures	109
K C MILLS, Imperial College London, UK		
4.1	Introduction	109
4.2	Factors affecting physical properties and their measurement	113
4.3	Measurements and problems	120
4.4	Fluid flow properties	122
4.5	Properties related to heat transfer	136
4.6	Properties related to mass transfer	146
4.7	Estimating metal properties	148
4.8	Acknowledgements	169
4.9	References	169
4.10	Appendix A: calculation of structural parameters NBO/T and optical basicity	175
4.11	Appendix B: notation	176
5	Transport phenomena and metals properties	178
A K LAHIRI, Indian Institute of Science, India		
5.1	Introduction	178
5.2	Mass transfer	178
5.3	Heat transfer	200

5.4	Fluid flow	217
5.5	Further reading	235
5.6	References	236
6	Interfacial phenomena, metals processing and properties	237
K MUKAI, Kyushu Institute of Technology, Japan		
6.1	Introduction	237
6.2	Fundamentals of the interface	238
6.3	Interfacial properties of a metallurgical melts system	257
6.4	Interfacial phenomena in relation to metallurgical processing	260
6.5	Further reading	267
6.6	References	267
7	The kinetics of metallurgical reactions	270
S SRIDHAR, Carnegie Mellon University, USA and H Y SOHN, University of Utah		
7.1	Introduction	270
7.2	Fundamentals of heterogeneous kinetics	270
7.3	Solid-state reactions	278
7.4	Gas–solid reactions	290
7.5	Liquid–liquid reactions	311
7.6	Solid–liquid reactions	313
7.7	Gas–liquid reactions	318
7.8	Comprehensive process modeling	321
7.9	References	341
7.10	Appendix: notation	346
8	Thermoanalytical methods in metals processing	350
O N MOHANTY, The Tata Iron and Steel Company, India		
8.1	Introduction	350
8.2	Thermogravimetry (TG)	356
8.3	Differential thermal analysis (DTA) and differential scanning calorimetry (DSC)	358
8.4	Evolved gas analysis (EGA) and detection (EGD)	363
8.5	References	365

Part II Improving process and product quality

9	Improving process design in steelmaking	369
	D SICHEN, Royal Institute of Technology, Sweden	
9.1	Introduction	369
9.2	Overview of process design	369
9.3	Thermodynamics and mass balance	375
9.4	Kinetics – mass transfer and heat transfer	385
9.5	Optimization of interfacial reactions	387
9.6	Micro-modelling	393
9.7	Conclusions	396
9.8	References	396
10	Solidification and steel casting	399
	A W CRAMB, Carnegie Mellon University, USA	
10.1	Introduction	399
10.2	Solidification fundamentals	400
10.3	The growth of solids	413
10.4	The casting of steels	428
10.5	Conclusions	449
10.6	Acknowledgements	450
10.7	References	450
11	Analysing metal working processes	453
	G ENGBERG, SSAB Tunnplåt AB and MIK Research AB (MIKRAB) and L KARLSSON, Dalarna University, Sweden	
11.1	Introduction	453
11.2	Work hardening	454
11.3	Rate effects	457
11.4	Interaction with phase transformations	462
11.5	Examples of material behaviour during processing	463
11.6	Development trends	468
11.7	References	469
12	Understanding and improving powder metallurgical processes	471
	F LEMOISSON and L FROYEN, Katholieke Universiteit Leuven, Belgium	
12.1	Introduction	471
12.2	Production processes for powders	471
12.3	Forming processes towards near-net shape	486

12.4	Conclusions	500
12.5	References	500
13	Improving steelmaking and steel properties	503
	T E M I, Royal Institute of Technology, Sweden	
13.1	Introduction	503
13.2	Developing processes and properties with reference to market, energy, and environment	506
13.3	Optimization of processes to meet properties and productivity	523
13.4	Economic optimization	537
13.5	Environmental optimization	546
13.6	Future trends	550
13.7	Further reading	553
13.8	References	553
	<i>Index</i>	555

Contributor contact details

(* = main contact)

Chapters 1 and 7

Professor H. Y. Sohn*

Department of Metallurgical
Engineering
University of Utah
135 S 1460 E
Salt Lake City
UT 84112-0114
USA

E-mail: hysohn@mines.utah.edu

Professor S. Sridhar

Department of Materials Science
Carnegie Mellon University
Pittsburgh
PA 15213-3890
USA

E-mail: sridhars@andrew.cmu.edu

Chapter 2

Dr R. E. Aune* and Professor S.
Seetharaman

Division of Materials Process
Science
Department of Materials Science and
Engineering
Royal Institute of Technology
SE-100 44 Stockholm

Sweden

E-mail: aune@mse.kth.se

E-mail: raman@kth.se

Chapter 3

Professor K. Morita*

Department of Metallurgy
The University of Tokyo
Bunkyo-ku
Tokyo 113-8656
Japan

E-mail: morita@wood2.mm.t.u-tokyo.ac.jp

Professor N. Sano

Executive Advisor
Nippon Steel Corporation

E-mail: sano@re.nsc.co.jp

Chapter 4

Professor K. C. Mills

Department of Materials
Imperial College of Science,
Technology and Medicine
Prince Consort Road
South Kensington
London SW7 2BP
UK

E-mail: kenmills@tesco.net

Chapter 5

Professor A. K. Lahiri
Department of Metallurgy
Indian Institute of Science
Bangalore 560012
India

E-mail: metakl@metalrg.iisc.ernet.in

Carnegie Mellon University

Pittsburgh
PA 15213
USA

E-mail: cramb@andrew.cmu.edu

Chapter 6

Professor Emeritus K. Mukai
Department of Materials Science and
Engineering
Kyushu Institute of Technology
Sensui-Cho
Tobata-ku
Kitakyushu 804 8550
Japan

E-mail: hiro_mukai@nifty.com

Chapter 11

Dr G. Engberg*
MIK Research AB (MIKRAB)
Teknikdalen
Forskargatan 3
SE-781 27 Borlange
Sweden

E-mail: goran.engberg@mikrab.se

Dr L. Karlsson
Dalarna University

Chapter 8

Professor O. N. Mohanty
Research and Development Services
The Tata Iron and Steel Company Ltd
11T Kharagpur-721302
India

E-mail: onmohanty@lot.tatasteel.com
onm@metal.iitkgp.ernet.in

Chapter 12

Dr F. Lemoisson* and Professor L.
Froyen
Physical Metallurgy and Materials
Engineering Section
Katholieke Universiteit Leuven
Kasteelpark Arenberg 44
BE 3001 Heverlee
Belgium

E-mail: fabienne.lemoisson
@mtm.kuleuven.ac.be

E-mail:
ludo.froyen@mtm.kuleuven.ac.be

Chapter 9

Professor Du Sichen
Department of Materials Science and
Engineering
Royal Institute of Technology
SE-100 44 Stockholm
Sweden

E-mail: du@mse.kth.se

Chapter 13

Professor T. Emi
Takasu 5-1
B1905
Urayasu-shi
Chiba 279-0023
Japan

E-mail: t-emi@yb3.so-net.ne.jp

Chapter 10

Professor A. W. Cramb
Department of Materials Science and
Engineering

Preface

Metallurgy refers to the science and technology of metals. The subject area can be considered as a combination of chemistry, physics and mechanics with special reference to metals. In later years, metallurgy has expanded into materials science and engineering encompassing metallic, ceramic and polymeric materials.

Metallurgy is an ancient subject linked to the history of mankind. The development of civilisations from stone age, bronze age and iron age can be thought of as the ages of naturally available ceramic materials, followed by the discovery of copper that can be produced relatively easily and iron that needs higher temperatures to produce. These follow the pattern of the Ellingham diagram known to all metallurgists. Faraday introduced the concept of electrolysis which revolutionised metal production. Today, we are able to produce highly reactive metals by electrolysis.

The prime objective to produce metals and alloys is to have materials with optimised properties. These properties are related to structure and thus, physical as well as mechanical properties form essential parts of metallurgy. Properties of metals and alloys enable the choice of materials in production engineering.

The book, *Fundamentals of Metallurgy* is a compilation of various aspects of metallurgy in different chapters, written by the most eminent scientists in the world today. These participants, despite their other commitments, have devoted a great deal of time and energy for their contributions to make this book a success. Their dedication to the subject is admirable. I thank them sincerely for their efforts.

I also thank Woodhead Publishing Company for this initiative which brings the subject of metallurgy into limelight.

Seshadri Seetharaman
Stockholm

Part I

Understanding the effects of processing
on the properties of metals

Descriptions of high-temperature metallurgical processes

H Y S O H N , University of Utah and
S S R I D H A R , Carnegie Mellon University, USA

1.1 Introduction

Metallurgical reactions take place either at high temperatures or in aqueous solutions. Reactions take place more rapidly at a higher temperature, and thus large-scale metal production is mostly done through high-temperature processes. Most metallurgical reactions occurring at high temperatures involve an interaction between a gas phase and condensed phases, which may be molten liquids or solids. In some cases, interactions between immiscible molten phases are important.

High-temperature metallurgical reactions involving molten phases are often carried out under the conditions of near equilibria among all the phases; other such reactions proceed under the control of interphase mass transfer with equilibria at interphase boundaries. Reactions involving gas–solid contact also often take place under the rate control of mass transfer with chemical equilibrium at the interface, but the chemical kinetics of the heterogeneous reactions are more often important in this case than those involving molten phases. Even in this case, mass transfer becomes increasingly dominant as temperature increases. The solid phases undergo undesirable structural changes, such as fusion, sintering, and excessive reduction of internal porosity and surface area, as temperature becomes too high. Thus, gas–solid interactions are carried out in practice at the highest possible temperatures before these undesirable changes in the solid structure become damaging. In the case of high temperature oxidation, the structure of the product oxide determines the mass transport of gases and ions.

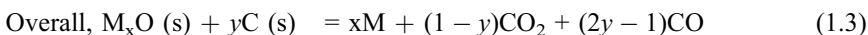
The treatment of metals in their molten state, e.g. refining and alloying, involves reactions between the melt and a gas phase or a molten slag. Interfacial reaction kinetics, mass transport in the molten or gaseous phase becomes important. The production of metals and alloys almost always involves solidification, the rate of which is often controlled by the rate of heat transfer through the mold.

1.2 Reactions involving gases and solids

Since metals occur in nature mostly as compounds (minerals), the first step in the utilization of the naturally occurring sources is their chemical separation into elemental forms. More often than not, the first reaction in this chemical separation step involves an interaction between the solid-phase minerals and a reactant gas.

1.2.1 Reduction of metal oxides by carbon monoxide, carbon, or hydrogen

Metal oxides are most often reduced by carbon or hydrogen. The reason why reduction by carbon is treated in this section on gas–solid reaction is because the actual reduction is largely effected by carbon monoxide gas generated by the reaction of carbon dioxide with carbon, when carbon is used to reduce metal oxides in solid state. These reactions can in general be expressed as follows:



The amount y , which is determined by the p_{CO_2}/p_{CO} ratio in the product gas mixture, depends on the kinetics and thermodynamics of the two gas–solid reactions (1.1) and (1.2). In many systems of practical importance, reaction (1.1) is much faster than reaction (1.2), and thus the p_{CO_2}/p_{CO} ratio approaches the equilibrium value for reaction (1.1). The overall rate of reaction (1.3) is then controlled by the rate of reaction (1.2) taking place under this p_{CO_2}/p_{CO} ratio (Padilla and Sohn, 1979).

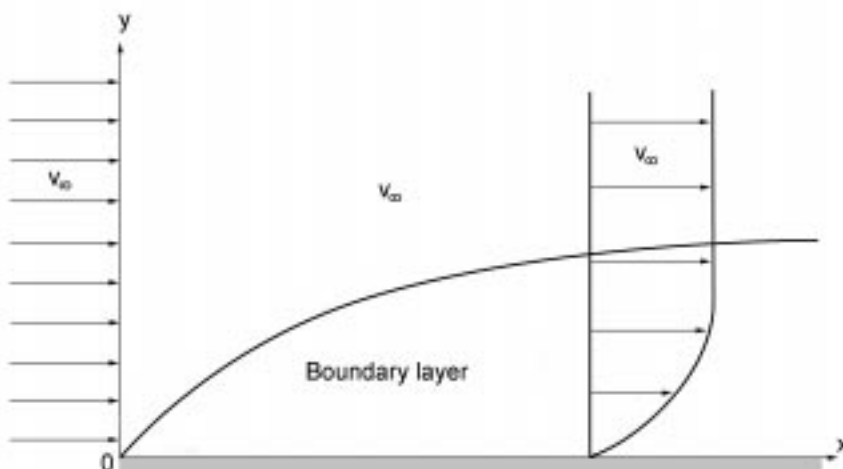
The reduction of iron oxide is the most important reaction in metal production, because iron is the most widely used metal and it occurs in nature predominantly as hematite (Fe_2O_3). The production of iron occupies more than 90% of the tonnage of all metals produced. The most important reactor for iron oxide is the blast furnace, in the shaft region of which hematite undergoes sequential reduction reactions by carbon monoxide (Table 1.1).

Table 1.1

Reaction	Equil. CO/CO ₂ ratio at 900 °C	Heat generation (900 °C)	
$3Fe_2O_3 + CO = 2Fe_3O_4 + CO_2$	0	10.3 kcal	(1.4)
$Fe_3O_4 + CO = 3FeO + CO_2$	0.25	-8.8 kcal	(1.5)
$FeO + CO = Fe + CO_2$	2.3	4.0 kcal	(1.6)

In the blast furnace, the solid charge flows downward, and the tuyere gas with a high CO/CO₂ ratio flows upward. Thus, the tuyere gas first comes into contact with wustite (FeO), the reduction of which requires a high CO/CO₂ ratio, as seen above. The resulting gas reduces magnetite (Fe₃O₄) and hematite (Fe₂O₃) on its way to the exit at the top of the furnace.

The equilibrium percentage of CO in a mixture with CO₂ is shown in Fig. 1.1 as a function of temperature. Again, it is seen that the equilibrium concentration of CO for the reduction of hematite to magnetite is essentially zero; i.e., CO is completely utilized for the reduction. The equilibrium content of CO for the reduction of Fe₃O₄ to FeO and that of FeO to Fe depend on temperature. It is also noted that wustite is a non-stoichiometric compound Fe_xO with an average value of x equal to 0.95 in the temperature range (approximately 600 °C–1400 °C) of its stability. The actual value of x and thus oxygen content depend on temperature and CO/CO₂ ratio, as illustrated by the curves drawn within the wustite region in Fig. 1.1. Furthermore, the CO/CO₂ ratio is limited by the Boudouard reaction given by eqn (1.2) and shown as a sigmoidal curve in Fig. 1.1 (for 1 atm total pressure without any inert gas). Thus, the reduction reactions indicated by the dashed lines to the left of this curve are thermodynamically not feasible. (In practice, however, reduction by CO to the left of the Boudouard curve is possible because the carbon deposition reaction (the decomposition of CO) to produce solid carbon is slow.)



1.1 Equilibrium gas compositions for the reduction of iron oxides by carbon monoxide. (Adapted from Evans and Koo, 1979.)

6 Fundamentals of metallurgy

The reduction of iron oxide by hydrogen is important in the production of direct reduced iron. This method of iron production is gaining increasing significance as an alternative route to the blast furnace technology with the many difficult issues facing the latter, the most important being the problems related to environmental pollution and the sheer size of the blast furnace. Direct reduction technology for iron encompasses the processes that convert iron oxides into metallic iron in solid state without going through a molten phase. In this technology, iron-bearing materials are reduced by reacting with reducing substances, mainly natural gas or a coal, at high temperatures but below the melting point of iron. The product, direct reduced iron (DRI), is a porous solid, also known as sponge iron. It consists primarily of metallic iron with some unreduced iron oxides, carbon and gangue. Carbon is present in the range of 1–4%. The gangue, which is the undesirable material present in the ore, is not removed during reduction as no melting and refining take place during the reduction process. The main usage of DRI products is in the electric arc furnace (EAF). However, due to its superior characteristics, DRI products have found their way into other processes such as blast furnaces, basic oxygen furnaces and foundries. Globally, DRI comprises about 13% of the charge to the EAF (Kopfle *et al.*, 2001). Nowadays, the percentage of crude steel produced by BOF is approximately 63%, while that of EAF is about 33%, and the balance 4% is made up of the open hearth (OH) steel (International Iron and Steel Institute, 2004). However, the contribution of EAF to the world crude steel output is expected to increase to reach 40% in 2010 (Gupta, 1999) and 50% in 2020 (Bates and Muir, 2000).

Direct reduction technology has grown considerably during the last decade. The main reasons that make this technology of interest to iron and steel makers are as follows:

1. Shortage, unpredictability and high price of scrap.
2. The movement of EAF producers into high quality products (flat products).
3. High capital cost of a coke plant for the blast furnace operation.
4. Desire of developing countries to develop small steel industries and capabilities.
5. Availability of ores that are not suitable for blast furnace operation.
6. Necessity for increasing iron production within a shorter time frame.

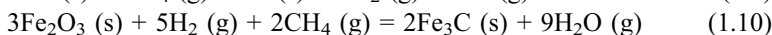
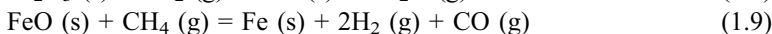
There have been major developments in direct reduction processes to cope with the increasing demand of DRI. DRI production has increased rapidly from 0.80 million tons per year in 1970 to 18 million tons in 1990, 44 million tons in 2000, and 49 million tons in 2003 (MIDREX, 2004). The worldwide DRI production is expected to increase by 3 Mt/y for the period 2000–2010 (Kopfle *et al.*, 2001).

Reduction of iron bearing materials can be achieved with either a solid or gaseous reductant. Hydrogen and carbon monoxide are the main reducing gases used in the ‘direct reduction’ (DR) technology. These gases are largely

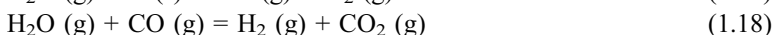
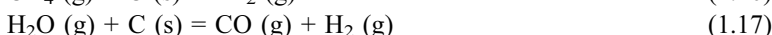
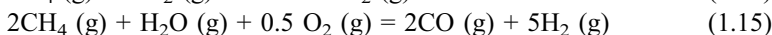
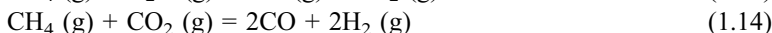
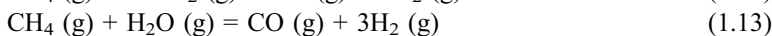
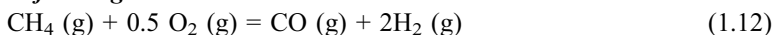
generated by the reforming of natural gas or the gasification of coke/coal. In reforming, natural gas is reacted with carbon dioxide and/or steam. The product of reforming is mainly H₂ and CO, whereas CO is the main product from coal gasification. Reduction reactions by reducing gases take place at temperatures in the range of 850 °C–1100 °C, whereas those by solid carbon occur at relatively higher temperatures of 1300 °C–1500 °C. Carburization reactions, on the other hand, take place at relatively lower temperatures below 750 °C. For reforming reactions, the reformed gas temperature may reach 950 °C for the stoichiometric reformer, and 780 °C in the case of a steam reformer.

Various reactions important in direct reduction processes are listed below.

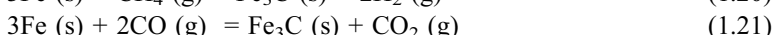
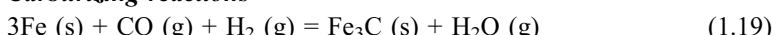
Reduction reactions



Reforming reactions



Carburizing reactions

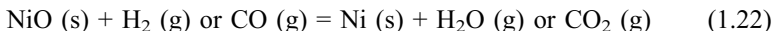


Direct reduction (DR) processes have been in existence for several decades. The evolution of direct reduction technology to its present status has included more than 100 different DR process concepts, many of which have only been operated experimentally. Most were found to be economically or technically unfavorable and abandoned. However, several were successful and subsequently improved to develop into full-scale commercial operations. In some instances, the best features from different processes were combined to develop improved processes to eventually supplant the older ones.

Direct reduction processes may be classified, according to the type of the reducing agent used, to gas-based and coal-based processes. In 2000, DRI produced from the gas-based processes accounted for 93%, while the coal-based

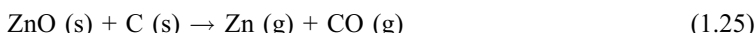
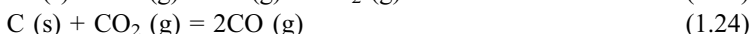
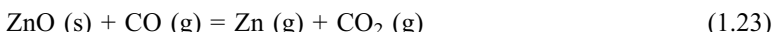
processes produced 7%. Gas-based processes have shaft furnaces for reducing. These furnaces can be either a moving bed or a fluidized bed. The two most dominant gas-based processes are MIDREX and HYL III, which combined to produce approximately 91% of the world's DRI production. Fluid-bed processes, by contrast, have recently received attention, because of its ability to process fine iron ores. These processes are based either on natural gas or coal. A list of the processes together with their relevant characteristics is given in Table 1.2 (MIDREX, 2001).

The gaseous (or carbothermic) reduction of nickel oxide, obtained by dead roasting of nickel sulfide matte or concentrate, is an important intermediate step for nickel production. In the Mond process, crude nickel is obtained this way before undergoing refining by carbonylation. Crude nickel has sometimes been cast into anodes and electrolytically refined. Nickel laterite ores are reduced by carbon monoxide before an ammoniacal leach. Nickel oxide reduction reactions are simple one-step reactions, as follows:



Both reactions have negative Gibbs free energy values. For hydrogen reduction it is -7.2 and -10.3 kcal/mol, respectively, at 600K and 1000K . For reduction by CO, the free energy values are -11.1 kcal/mol at both 600K and 1000K . The thermodynamic data used here as well as below were obtained from Pankratz *et al.* (1984). The corresponding equilibrium ratio $p_{\text{H}_2}/p_{\text{H}_2\text{O}}$ is 2.4×10^{-3} and 5.6×10^{-3} , respectively, at 600K and 1000K , and the equilibrium ratio $p_{\text{CO}_2}/p_{\text{CO}}$ is 9.5×10^{-5} and 3.7×10^{-3} , respectively, at the same temperatures. Therefore, the reactant gases are essentially completely consumed at equilibrium in both cases. These reduction reactions are mildly exothermic, the standard enthalpy of reaction (ΔH_r°) being -2 to -3 kcal/mol for hydrogen reduction and -11.2 to -11.4 kcal/mol for reduction by carbon monoxide.

Zinc occurs in nature predominantly as sphalerite (ZnS). The ZnS concentrate is typically roasted to zinc oxide (ZnO), before the latter is reduced to produce zinc metal by the following reactions (Hong *et al.*, 2003):



The overall reaction is essentially irreversible ($\Delta G^\circ = -12.2$ kcal/mol at 1400K) and highly endothermic ($\Delta H^\circ = +84.2$ kcal/mol at 1400K) and the gaseous product contains a very small amount of CO_2 at temperatures above 1200K (Hong *et al.*, 2003). It is also noted that this reaction is carried out above the boiling point of zinc (1180K), and thus zinc is produced as a vapor mixed with CO and the small amount of CO_2 from the reaction. Zinc is recovered by condensation. Zinc vapor is readily oxidized by CO_2 or H_2O (produced when

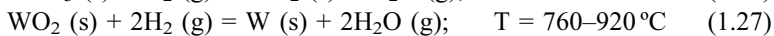
Table 1.2 Characteristics of some DR processes

Process	Builder	Charge	Product	Reactor	Fuel/ Reducant	Capacity, kt/y
MIDREX	MIDREX	Lump/pellet	DRI/HBI	Shaft furnace	Natural gas	Up to 1600
HYL	HYLSA	Lump/pellet	DRI/HBI	Shaft furnace	Natural gas	Up to 700
FINMET	VAI	Fines	HBI	4 fluidized beds	Natural gas	2200–2500
CIRCORED	Lurgi	Fines	HBI	2 fluidized beds	Natural gas	500
IRON CARBIDE	Nucor	Fines	Iron carbide	1 fluidized bed	Natural gas	300
	Qualitech			2 fluidized beds		660
CIRCOFER	Lurgi	Fines	HBI	2 fluidized beds	Coal	5t/d
REDSMELT	SMS Demag	Green pellets	Liquid iron	Rotary hearth furnace	Coal	50–600
IRON DYNAMICS	Mitsubishi	Dried pellets	Liquid iron	Rotary hearth furnace	Coal	520
	Demag					
FASTMET	MIDREX	Dried briquettes and pellets	DRI/HBI Liquid iron	Rotary hearth furnace	Coal	150–650
COMET ITmk3	CRM	Fines	Low carbon slab	Rotary hearth furnace	Coal	100 kg/h
	MIDREX	Dried briquettes and pellets	Iron nuggets	Rotary hearth furnace	Coal	100 kg/h

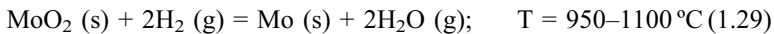
coal is used as the reducing agent) at lower temperatures. Thus, zinc condensation should be done as rapidly as possible, and the CO/CO₂ ratio in the product gas must be kept as high as possible by the use of excess carbon in the reactor.

Small amounts of copper have been produced by the reduction of oxides that occur naturally, obtained by the dead roasting of sulfide, or produced by precipitation from aqueous solution.

The final process in tungsten production is the hydrogen reduction of the intermediate tungsten oxide (WO₃ or W₄O₁₁) obtained through the various processes for treating tungsten ores. Because of the substantial volatility of the higher oxide, its reduction is carried out at a low temperature to obtain non-volatile WO₂. WO₂ is then reduced to tungsten metal at a higher temperature (Habashi, 1986), as indicated below:



Molybdenum is also produced by the hydrogen reduction of its oxide MoO₃. This process is also carried out in two stages for the same reason as in the case of tungsten oxide reduction:



Limited amounts of magnesium are produced by the carbothermic reduction of MgO, according to



The reduction reaction is carried out at about 2200 °C and thus magnesium is produced as a vapor (B.P. = 1090 °C). Much like zinc vapor mentioned earlier, magnesium vapor is susceptible to oxidation and requires similar measures for its condensation and collection.

For other aspects of gaseous reduction of metal oxides, including reduction by carbon involving gaseous intermediates, the reader is referred to the literature (Alcock, 1976; Evans and Koo, 1979; Habashi, 1986).

1.2.2 High temperature oxidation

High temperature oxidation (tarnishing) is a form of environmental degradation of metals and alloys as a result of the following chemical reaction:



Due to the high temperatures involved, these reactions are generally rapid and thus are a concern for high temperature application of structural parts such as turbines, jet propulsion systems and reactors. While the electro-negative gaseous

oxidant (X) could be sulfur, chlorine, etc., the discussion here will mainly be limited to oxidation by oxygen. Thermodynamically, a reaction will be favorable when the free energy is negative. The free energy is decreased by a lower nobility of the metal (or a higher activity of a metallic alloying element), a lower temperature and a higher partial pressure of the oxidizing gas. In the case of alloy oxidation where temperatures are high enough to form oxide slag mixtures, the activities of the oxide species need to be considered too.

In general, oxidation occurs according to the following steps: (i) First, oxygen adsorbs on the surface of the metal, which is usually not a rate-limiting step. (ii) Second, oxide forms and covers the surface, forming an oxide scale. (iii) Finally, the oxide scale thickens at the expense of the metal. From an engineering point of view, it is the rate of the third stage that is of interest since this stage constitutes the major loss of metal. Also, from a mechanistic point of view, surface coverage is generally fast and not rate determining. The thickening rate of the oxide scale is known empirically to occur through one or a combination of distinct time dependent behaviors of weight gain *vs* time, linear, parabolic, logarithmic and cubic. The type of relation observed depends largely on the micro-structural properties of the scale formed.

If the resulting oxide layer is porous enough, pore diffusion is very fast and thus access of the oxidizing gas to the metal is easy. Chemical reaction at the interface controls the rate of oxidation. The rate of mass gain (dm/dt) per unit area (A) will then follow first order heterogeneous reaction kinetics, expressed by

$$\frac{1}{A} \frac{dm}{dt} = k_{rxn} \cdot [a_{Me}] [p_{O_2}] \quad (1.32)$$

If the oxide-scale–metal contact area remains constant and the bulk oxygen partial pressure is kept unchanged with time, the above expression becomes

$$\frac{dm}{dt} = k' \quad (1.33)$$

and after integrating, this results in a linear dependence of weight gain *vs* time:

$$\Delta m = k' \cdot \Delta t \quad (1.34)$$

The parabolic time dependency is the most commonly observed type in metal oxidation and occurs when a dense oxide scale does not allow for gaseous diffusion through the product layer, necessitating ionic diffusion through the oxide layer and an electrochemical reaction process. The surface of the oxide-scale that is exposed to air serves as a cathode where reduction takes place according to,



The oxide-scale–metal interface serves as an anode where oxidation takes place:



The oxide scale itself serves as both electrolyte and electron lead. In this case, the growth of the oxide will occur either at the surface or at the oxide-scale–metal interface depending on the point defect types that dominate the oxide structure. In the case where the defects allow for a rapid transport of metal ions, due to the abundance of metal ion interstitials or vacancies, the oxide growth will take place on the outer surface of the oxide scale, according to



This is the case for Zn oxidation where the product ZnO has an excess of Zn. On the other hand, if defects in the scale promote oxygen transport, i.e. in Zr oxidation where ZrO_2 has a high oxygen vacancy concentration, oxide growth will occur internally at the oxide-scale–metal interface.

Whichever is the case, we can view the process, as a first approximation, as a steady state diffusion across a growing scale, where the flux of the reactant (through ionic diffusion) controls the rate of oxide growth.

$$\frac{dm}{dt} = -kD \frac{C_1 - C_2}{\Delta x} \quad (1.38)$$

C corresponds to the ion (metal or oxygen) that is most mobile as a result of oxide-scale defect chemistry. Its concentration at the surface is C_1 and that at the interface C_2 , and the thickness of the oxide layer is $\Delta x = f(t)$. Since the mass is related to the thickness by $\Delta x(t) \cdot A(\rho_{oxide} - \rho_{metal}) = m(t)$, we can rewrite the last expression as:

$$\frac{dm}{dt} = k'' \frac{1}{m(t)} \quad (1.39)$$

Integrating, we get:

$$\Delta m = \sqrt{k''} \cdot \Delta t^{1/2} \quad (1.40)$$

which results in a parabolic time dependence. A logarithmic rate of oxidation,

$$\Delta m = k_{\log} * \log(at + 1) \quad (1.41)$$

where k_{\log} and a are constants is observed for thin oxide-scales at low temperatures where electronic conductivity is expected to be low.

To a large extent, the resulting oxide film structure determines the rate of oxidation, i.e. whether the oxide forms a dense, compact, continuous scale that acts as a barrier towards gas diffusion or not. In general, the scale offers increased protection with increasing oxide-film adherence, increasing oxide melting point, decreasing oxide vapor pressure, similar thermal expansion of metal and oxide, increasing oxide plasticity and low mobilities of ions and electrons in the oxide. An empirical relation that is called the Pilling–Bedworth ratio (Pilling and Bedworth, 1923) is based on the fact that if the growing oxide

is under compression, it is more likely to be protective. This suggests that when the ratio

$$\text{PB ratio} = \frac{\text{Oxide Volume}}{\text{Metal Volume}} \quad (1.42)$$

is moderately greater than 1, the oxide is likely to be protective. Too high ratios are undesired since excessive compressive stress will be detrimental to adherence. As examples of PB values, the Al-Al₂O₃ system, which is protective, has a ratio of 1.28, whereas the Ca-CaO system, which is non-protective, has a ratio of 0.64.

It is noted that a protective oxide-scale that results in a parabolic oxidation rate may transition into a linear rapid oxidation rate when a failure of the protective layer occurs. This can be caused by fracturing of the film or liquefaction due to slag formation.

Most commercial metals used in high temperature applications are alloys and the oxidation of alloys is an important topic. The oxidation process in a multicomponent metallic system is extremely complex due to the fact that (i) different oxidation products can be formed and oxidation rates are determined by (ii) thermodynamics of the reaction (1.31) of individual alloying elements and transport properties of alloying elements and ions. A detailed discussion on alloy oxidation is beyond the scope of this chapter, but a few common alloying additions that lead to improved oxidation resistance should be mentioned. Chromium is commonly added to ferrous alloys to form Cr-rich protective scales. Beyond 20 wt% Cr in Fe–Cr alloys, the parabolic rate constant drops drastically (Jones, 1992). Nickel in conjunction with Cr enhances the oxidation resistance, primarily in applications involving thermal cycling.

For an in-depth study on oxidation and tarnishing, a text by Kofstad (1988) may be consulted.

1.2.3 Coking

Coal is constituted of partially decomposed organic matter in the presence of moisture. The term ‘coking’ is used for a process in which all the volatile constituents in coal are eliminated. This is carried out by heating coal in the absence of air in retort ovens that consist of vertically oriented chambers that are heated from the outside (Rosenqvist, 1983). The chambers are about 5 m in height but relatively narrow in width (0.5 m) in order to allow for appreciable heat flux through thermal conduction from the outside into the chamber. The heat from the evolved gases is used to help heat the retorts. In the case of coke for metallurgical applications, it is carbonized at a high temperature range (between 900 °C and 1096 °C) (Wakelin, 1999) and it is important that the product remains structurally stable and does not break into powder during the process. The coking process can be separated into the following three stages

(Wakelin, 1999): first, the primary coal breaks down below 700 °C and water, oxides of C, H₂S, aromatic hydrocarbon compounds, paraffins, olefins, phenolic and nitrogen-containing compounds are released. Second, above 700 °C, large amounts of hydrogen are released along with aromatic hydrocarbons and methane. Nitrogen-containing compounds react to form ammonia, HCN, pyridine bases and nitrogen. Finally, in the third stage, hydrogen is removed and hard coke is produced. During the process, 20–35% by weight of the original coal is released as volatiles. Inorganic non-volatile constituents in the coal remain in the coke as ash.

1.2.4 Decomposition reactions

A number of decomposition reactions are important in metallurgy. Examples include the decomposition of alkali earth carbonates (especially calcium carbonate in limestone and dolomite) to oxides; sulfates to oxides, oxysulfates and metals; carbonyls and iodides in the refining, respectively, of nickel and of titanium and zirconium; and sulfides to lower sulfides. Decomposition reactions are endothermic and thus consume large amounts of energy with the associated cost and environmental implications. The most important decomposition reaction relevant to metal production is the decomposition of limestone to lime according to

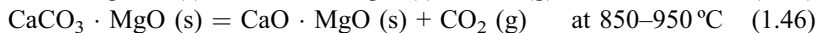
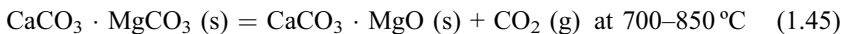


The thermodynamic decomposition temperature of CaCO₃ is 907 °C. This reaction occurs in the blast furnace and other smelting furnace operations in which limestone is charged to produce lime as a flux. The calcination of limestone is also performed separately for the specific purpose of producing lime to be used as a flux in such processes as oxygen steelmaking as well as a neutralizing agent for acid pickling and leaching solutions. Limestone calcination is carried out in rotary kilns, shaft kilns and rotary hearth reactors.

Magnesite (magnesium carbonate) is calcined to obtain magnesia (MgO), which is used to make refractory bricks. The decomposition reaction occurs according to (Hong *et al.*, 2003),



This reaction also occurs in the calcinations of dolomite, which proceeds according to the following reactions:



According to the results of differential thermal analysis (Habashi, 1986), the decomposition of the MgCO₃ component in dolomite takes place at 100 °C higher than pure MgCO₃. This is because dolomite contains calcium and

magnesium atoms forming a complex crystal structure, rather than being a physical mixture of CaCO_3 and MgCO_3 .

Strontium carbonate is decomposed to SrO according to the following reaction (Arvanitidis *et al.* 1997),



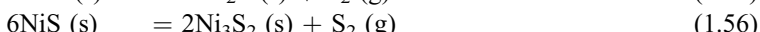
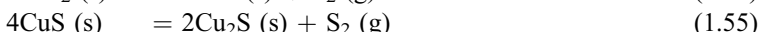
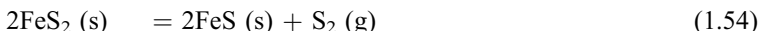
Examples of sulfate decomposition are listed below (Habashi, 1986):



Nickel carbonyl, which is obtained by reacting crude nickel with carbon monoxide, is decomposed at about $180 \text{ }^\circ\text{C}$ to obtain pure nickel according to



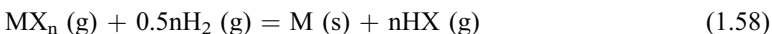
Some sulfides decompose to lower sulfides upon heating and release sulfur. Examples are:



1.2.5 Chemical vapor synthesis of metallic and intermetallic powders

Many metals in the form of powder, especially ultrafine powder (UFP), display useful physical properties. With a large specific surface area, they are the raw materials for powder metallurgical processing. They also possess other exceptional properties involving light absorption (Nikkilason, 1987), magnetism (Okamoto *et al.*, 1987), and superconductivity (Parr and Feder, 1973). For much the same reasons, the powders of intermetallic compounds are also expected to offer promising possibilities. Several methods have been practiced in the production of metallic and intermetallic powders. Here, we will summarize developments in the synthesis of such powders by the vapor-phase reduction of metal chlorides, with an emphasis on the synthesis of intermetallic powders.

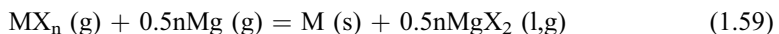
A reaction between a metal halide and hydrogen can in general be written as follows:



where M and X represent the metal and the halogen, respectively. The hydrogen reduction of single-metal chlorides for the preparation of metallic UFP has been studied for tungsten and molybdenum (Lamprey and Ripley, 1962), cobalt (Saeki *et al.*, 1978), and nickel, cobalt, and iron (Otsuka *et al.*, 1984). By reducing vaporized FeCl_2 , CoCl_2 , and NiCl_2 by hydrogen at 1200K to 1300K, Otsuka *et al.* (1984) were able to prepare corresponding metal particles in the size range 52 to 140 nm with up to 99.7% metal chloride conversion. The synthesis of metal carbide UFP has been practiced by the vapor-phase hydrogen reduction (Zhao *et al.*, 1990; Hojo *et al.*, 1978). Hojo *et al.* (1978) produced the UFP of tungsten carbide (WC , W_2C) of 40 to 110 nm size by vapor-phase reaction of the $\text{WCl}_6\text{-CH}_4\text{-H}_2$ system at 1000 °C to 1400 °C.

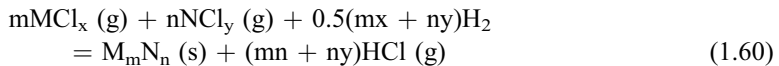
Magnesium is a much stronger reducing agent for chlorides than hydrogen. Thus, the reduction of titanium and aluminum chlorides by magnesium is feasible, whereas the reduction of these chlorides by hydrogen is not feasible up to 2500K. Titanium sponge is prepared by the chlorination of rutile, followed by the reduction of the resulting titanium chloride by liquid or gaseous magnesium (Barksdale, 1966).

A reaction between a metal halide and magnesium vapor can be written as follows:



where M and X are metal and halogen, respectively.

In recent years, Sohn and co-workers (Sohn and PalDey, 1998a; 1998b; 1998c; 1998d; Sohn *et al.*, 2004) applied the basic concepts of the above chloride reduction methods to the ‘chemical vapor synthesis’ of intermetallic and metal alloy powders. These reactions can in general be written as follows, when hydrogen is used:



where M and N represent two different metals, with x and y being the valences, and M_mN_n the intermetallic compound formed.

Sohn and PalDey (1998a) synthesized fine powder (100–200 nm) of Ni_4Mo at 900 °C to 1100 °C using hydrogen as the reducing gas. These authors also prepared a coating of Ni_4Mo of 0.7 μm thickness on a nickel substrate. Sohn and PalDey (1998b) also synthesized nickel aluminide (Ni_3Al) particles (50–100 nm) at 900 °C to 1150 °C using hydrogen as the reducing agent. The fact that aluminum chloride is reduced by this reaction scheme is very significant, because the reduction of AlCl_3 alone by hydrogen is thermodynamically unfavorable at moderate temperatures. The negative free energy of formation of the intermetallic compound makes the overall reaction feasible. Using the same chemical vapor synthesis process, Sohn *et al.* (2004) prepared ultrafine particles of Fe-CO alloys by the hydrogen reduction of $\text{FeCl}_2\text{-CoCl}_2$ mixtures. Sohn and

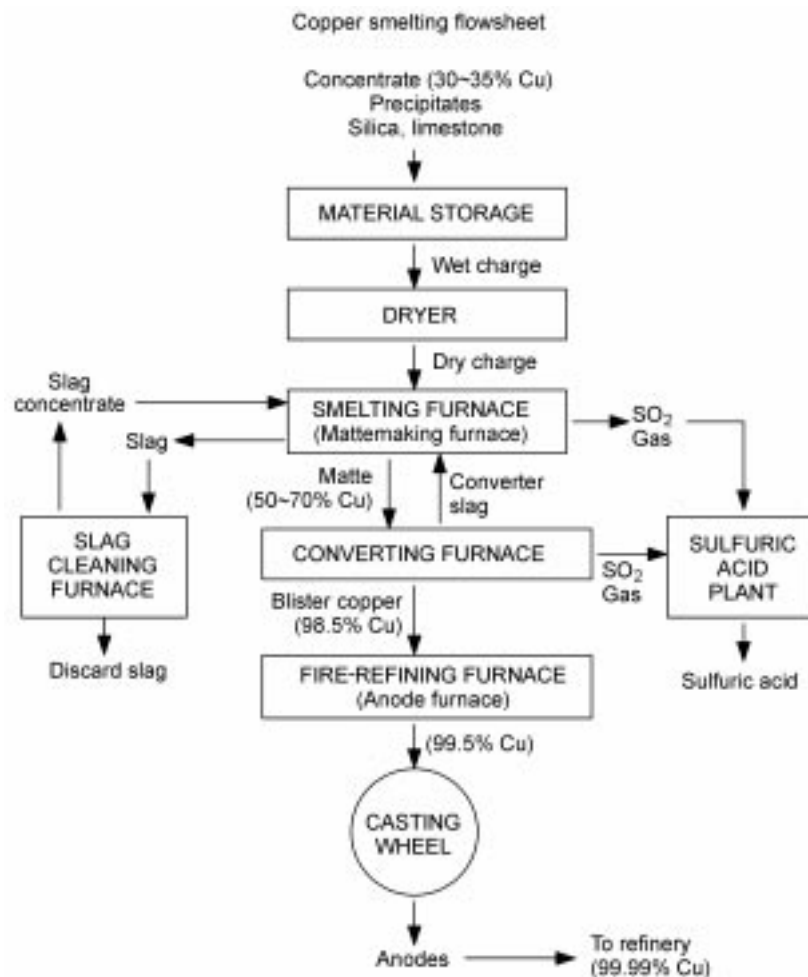
PalDey (1998c; 1998d) also synthesized ultrafine powders of the aluminides of titanium and nickel using magnesium as the reducing agent.

1.3 Reactions involving liquid phases

1.3.1 Smelting and converting

The term ‘smelting’ has broad and narrow definitions. In the broadest sense, any metal production process that involves a *molten stage* is called ‘smelting’, the word having its origin in the German word ‘*schmelzen*’ – to melt. Thus, aluminum smelting and iron smelting in addition to sulfide smelting would be included in this category. The next level of definition is the *overall process* of producing primary metals from *sulfide* minerals by going through a molten stage. The narrowest definition is the *first step* of the two-step oxidation of sulfur and iron from sulfide minerals, mainly Cu and Ni, i.e., *matte smelting* or ‘mattemaking’ as opposed to ‘converting’ in which the matte is further oxidized, in the case of coppermaking, to produce metal. Thus, especially in coppermaking, we talk about a ‘smelting’ step and a ‘converting’ step. The reason for doing it in two stages has largely to do with oxygen potentials in the two stages as well as heat production, the former in turn affecting the slag chemistry (magnetite formation, for example) and impurity behavior. If one goes all the way to metal in one step, much more of the impurities go into the metal, rather than the slag, and too much heat is produced. Thus, in the first stage – the ‘smelting step’, as much iron, sulfur and harmful impurities as possible are removed into the large amount of slag formed in that stage, and the matte is separated and treated in a subsequent step, usually the converting step.

Figure 1.2 presents a simplified flowsheet of a typical copper production operation. The copper contents at various stages are indicated in the flowsheet. The major chemical reactions that occur in the smelting and the converting steps are shown in Figs 1.3 and 1.4. In the smelting (mattemaking) step, which takes place in a molten state, large portions of sulfur and iron contained in the copper mineral (typically chalcopyrite, CuFeS_2 , mixed with some pyrite, FeS_2) are oxidized by oxygen supplied in the form of oxygen-enriched air of various oxygen contents. The sulfur dioxide is sent to the acid plant to be fixed as sulfuric acid. The oxidized iron combines with silica, contained in the concentrate and added as a flux, to form a fayalite slag. The remaining metal sulfides Cu_2S and FeS , which are mutually soluble, form a copper matte of a certain copper content, which varies from smelter to smelter (50–70%). The matte and the slag form an immiscible phase, enabling their separation, with the lighter slag floating above the matte. Another important aspect of the mattemaking step, in addition to the removal of iron and sulfur, is that large portions of undesirable impurities in the concentrate such as As, Bi, Sb, and Pb are absorbed into the slag and thus removed from copper. Valuable metals such

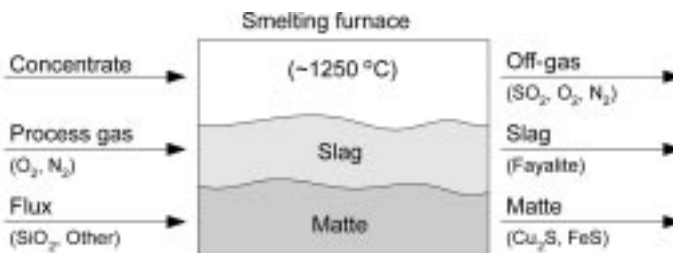


1.2 A typical copper production operation.

as gold, silver, and other precious metals present in the concentrate largely remain in the copper.

The matte, consisting of Cu_2S and FeS , is separated from the slag and fed to the converting step. In the converting step, the FeS in the matte is first oxidized into FeO and sulfur dioxide. Silica or limestone is added to absorb the FeO by forming a slag. The remaining Cu_2S is then further oxidized to form metallic copper, called the blister or crude copper, which still contains small amounts of undesirable impurities as well as valuable minor elements plus residual amounts of sulfur and iron.

The sulfur and iron in the blister copper are removed by further oxidation in a fire-refining furnace. To remove iron completely, the oxygen potential must be

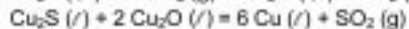
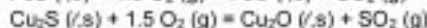
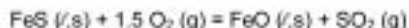
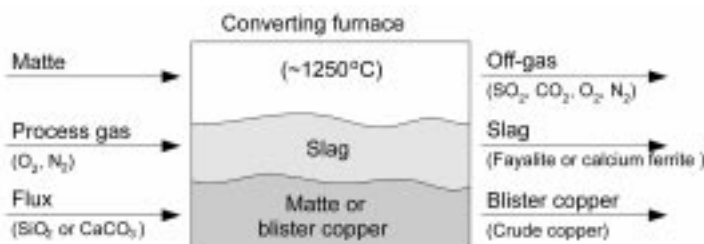


Concentrate: CuFeS₂ (chalcopyrite), FeS₂ (pyrite), FeS (pyrrhotite), other minerals

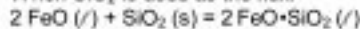


$2 \text{ FeO} (\text{l}) + \text{SiO}_2 (\text{s}) = 2 \text{ FeO} \cdot \text{SiO}_2 (\text{l}) = \text{Fe}_2\text{SiO}_4 (\text{l})$: fayalite slag (absorbs impurities)

1.3 Major chemical reactions in copper smelting.



When SiO₂ is used as the flux:



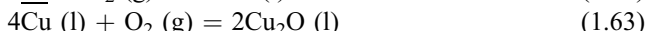
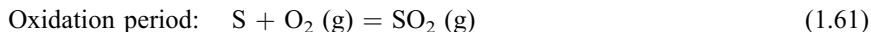
When CaCO₃ is used as the flux:

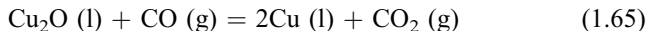
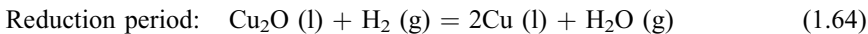


Calcium ferrite slag: solution of FeO, Fe₂O₃, and CaO

1.4 Major chemical reactions in copper matte converting.

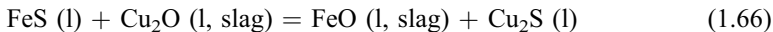
sufficiently high, and thus some copper is oxidized in this step. After iron oxide is removed, therefore, a reducing agent such as reformed natural gas is used to remove oxygen from the copper. The relevant chemical reactions are as follows:





The fire-refined copper is cast into anodes that go to the electrolytic cell to be refined to 99.99 % pure copper cathodes. Thus, the fire-refining furnace is also called the anode furnace.

The equilibrium that is important in the mattemaking (smelting) step as well as for iron removal in the converting step is

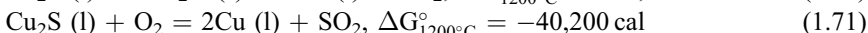
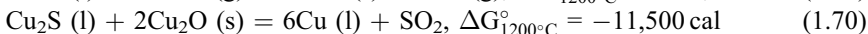


$$\Delta G^\circ = -35,000 - 4.6T, \text{ cal/mol (T in K)} \quad (1.67)$$

$$K = \exp\left(\frac{-\Delta G^\circ}{RT}\right) = \frac{a_{\text{Cu}_2\text{S}} \cdot a_{\text{FeO}}}{a_{\text{Cu}_2\text{O}} \cdot a_{\text{FeS}}} \quad (1.68)$$

$K(1200^\circ\text{C}) \approx 10^4$, assuming $a_{\text{Cu}_2\text{S}}/a_{\text{FeS}} \approx 1$; $a_{\text{FeO}} \approx 0.3$, and $a_{\text{Cu}_2\text{O}} \approx 3 \times 10^{-5}$ at 1200°C (Biswas and Davenport, 1976). This indicates that FeS will be oxidized long before Cu_2S .

The thermodynamic relations of coppermaking reactions in the converting step are as follows:



These reactions indicate that the oxidation of Cu_2S (l) to Cu (l) is highly favorable.

The removal of sulfur in the fire-refining step is represented by

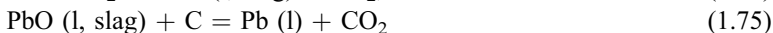
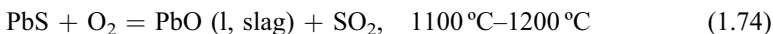


for which

$$K' = \frac{P_{\text{SO}_2}}{[\% \text{S}][\% \text{O}]} \approx (90 \text{ at } 1100^\circ\text{C}; 20 \text{ at } 1300^\circ\text{C}) \quad (1.73)$$

The smelting of nickel sulfide concentrates is similar to that of copper sulfide concentrates, except that the converting step in this case produces high-grade, low-iron matte for further treatment, rather than crude nickel metal.

The smelting of lead sulfide (galena) concentrate is somewhat different in that lead sulfide is easily oxidized to PbO. Thus, the reactions for producing lead from the sulfide concentrate are as follows:



In this process, the slag is typically composed of CaO, FeO, and SiO₂.

1.3.2 Slag refining

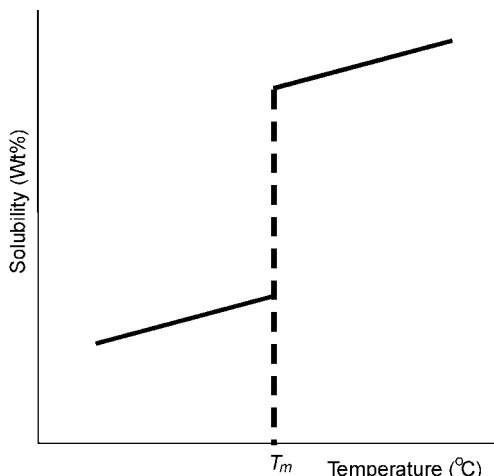
After producing a metal from its ore or from recycled scrap, it will contain impurities. Some of these may be acceptable but many are not and therefore have to be removed. This depends on the elements constituting the impurity. The impurity elements can be classified as:

- Economically valuable elements, e.g. Ag, Au in Cu.
- Elements that are harmful for the final metal properties, e.g. P, S, Sb, Sn, H, O, N.

During product formation, the metal will be cast into one form or another. This means that the metal undergoes a physical conversion from liquid into solid state.



The amount of an impurity element (or any other element for that matter) that can be contained in the metal lattice is always greater in the liquid metal than in the solid. In other words, the solubility of an element is greater in a liquid than in a solid. Generally the solubility of an impurity in a metal follows the trend shown in Fig. 1.5 (at constant total pressure) during cooling and solidification that occurs in casting. From the solubility change with temperature shown in this figure, it can be seen that a substantial drop in solubility happens at the melting point. Hence during casting, if the impurity level is higher in the liquid than what the solid can incorporate, there is a rejection of the impurity solute from the solidifying front into the remaining liquid. Thus, the remaining liquid continuously gets enriched by the impurity. At some point the amount of impurity in the liquid will be high enough that one of the following happens:



1.5 Solubility change during solidification.

- The impurity forms a gas: e.g. 2H (dissolved in the liquid) \Rightarrow H₂ (g)
- The impurity forms a solid or liquid compound: e.g. Mn + S \Rightarrow MnS or Fe + O \Rightarrow FeO

Both pores and inclusions form in-between the grains and end up at dendrite boundaries since that is where the last liquid existed and where the concentration of the impurities were highest. The gaseous species can be entrapped during casting and result in pores which degrade the fatigue and fracture strength of the metal. The inclusion compounds form second phase inclusions inside the metal that also degrade the fatigue and fracture strength and ductility. Furthermore, they cause a loss in metals since the metal reacts with the impurity to form a second phase. In the steelmaking process the primary method of removing sulfur, phosphorous and oxygen is to separate them into a second phase, namely a slag.

Generally, industrial slags and fluxes contain SiO₂, Me_xO (metal oxides) and, depending on the slag, additional compounds like Al₂O₃, CaF₂ and P₂O₅. The ratio SiO₂/Me_xO is an indication of the degree of polymerization. This is because each Me_xO is considered to break a bond of the three dimensional network of tetrahedral units of SiO₄⁴⁻ or (:Si-O⁻) by supplying an additional oxygen and charge, compensating the electron at the broken bond with the cation. When the ratio of SiO₂/Me_xO is 2, each tetrahedral unit has one unshared corner and the structure is expected to resemble that of an endless sheet (Richardson, 1974) and at a ratio of 1, endless chains. At higher Me_xO contents the network breaks down further to form rings and then to discrete units of silica compounds. While P₂O₅ can easily accommodate itself by substituting P for Si in the silica network (PO₄⁴⁻), Al₂O₃ is amphoteric and accommodates itself in the silica network in silica rich melts as AlO₄⁵⁻ but acts as a network breaker in melts with low silica contents. Fluorides are generally thought to break the network (Kozakevitch, 1954; Mills and Sridhar, 1999) according to the reaction: (:Si-O-Si:) + (F⁻) = (:Si-O⁻) + (F-Si:). There still is uncertainty, however, concerning (i) the individual effect of the cation, (ii) whether fluorine acts as a network breaker also at basic compositions and (iii) whether a unit of (F-Si:) is equivalent to a unit of (:Si-O⁻) with respect to physical properties such as viscosity and thermal conductivity.

Unlike most other elements, sulfur does not need to form a compound before partitioning to the slag phase. Molten slags are able to absorb sulfur from either molten pig iron or steel through a reduction process:



In the equation above, the underline denotes dissolved state in the steel melt. The distribution ratio of sulfur in the slag to that in the metal can then be written as:

$$\frac{(S)}{[S]} = \frac{C_S f_S^*}{K \sqrt{p_{CO_2}}} \quad (1.78)$$

where (S) and $[S]$ denote sulfur concentrations in weight percent in the slag and metal, respectively. K is the equilibrium constant for the reaction $\frac{1}{2}S_2 = \underline{S}$ and C_S is the sulfide capacity of the slag, defined as:

$$C_S = (S) \sqrt{\frac{p_{O_2}}{p_{S_2}}} \quad (1.79)$$

From the equation above, it is clear that de-sulfurization is favored by a high sulfide capacity, an increased sulfur activity coefficient in the metal melt and a low oxygen potential. The activity coefficient of sulfur (f_S^*) is increased by carbon and silicon, and thus de-sulfurization is best achieved prior to the oxygen steelmaking (de-carburization) process.

The removal of silicon, phosphorous and manganese are carried out through oxidation, and are therefore favored during oxygen steelmaking, but since they are all highly exothermic, they are favored at lower temperatures. In the cases of Si and Mn,



$$\Delta G^\circ = -594,000 + 230.1 * T, J \quad (1.81)$$



$$\Delta G^\circ = -291,000 + 129.79 * T, J \quad (1.83)$$

In the case of phosphorous,



The phosphate capacity of a slag can be defined (Wakelin, 1999):

$$\log K_{PO} = \log \left(\frac{(\%P)}{[\%P]} [\%O]^{-5/2} \right) = \frac{21,740}{T} - 9.87 + 0.071 * BO \quad (1.85)$$

where $BO = \%CaO + 0.3 * (\%MgO)$.

Slags and their properties play a crucial role in the removal of non-metallic inclusions during clean steel manufacturing. Non-metallic inclusions are generally removed in the ladle, tundish and continuous casting mold. In all these three vessels, the molten metal is covered by a molten slag in order to provide thermal and chemical protection and, in the case of the caster, also to lubricate the mold-strand interface. Inclusions are removed by (i) transporting the inclusion to the steel-slag interface, (ii) separating across the interface and (iii) dissolving into the slag phase.

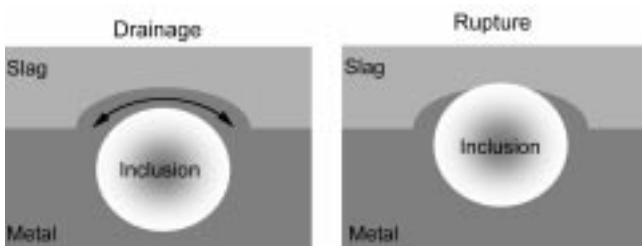
Among the three steps for inclusion removal, the second step involving separation across the interface is probably the least understood and is strongly influenced by interfacial properties. The thermodynamics of inclusion removal has been studied in a number of papers (Kozakevitch *et al.*, 1968; Kozakevitch and Olette, 1970, 1971; Riboud and Olette, 1982; Cramb and Jimbo, 1988).

Consider an inclusion at the slag–metal interface. For an inclusion to be removed it is necessary for it to travel through the slag–metal interface and on into the slag phase. In terms of interfacial energies, a favorable separation will be achieved when the free energy change given by the following relationship is negative:

$$\Delta G = \gamma_{\text{inclusion-slag}} - \gamma_{\text{inclusion-metal}} - \gamma_{\text{metal-slag}} \quad (1.86)$$

While the above-mentioned model for separation of inclusions across a metal–slag interface is based on thermodynamics, it is a rather simplified view and thus its applicability limited since the kinetics may be slow. As a spherical particle approaches the interface, the film between the particle and the other phase must be drained and the hydrodynamic forces determine the speed. At closer distances to the interface, the assumption of a continuous medium is no longer valid and the thin liquid film ahead of the particle is removed slowly. The final rupture of the interface is probably rapid, as this has been found in the case of droplet separation. The residence time of particles at a fluid–fluid interface may thus be long although it is energetically favorable to separate it from one phase to another. The steps of drainage and rupture are schematically shown in Fig. 1.6.

The separation time would likely depend strongly on whether the inclusion is solid or liquid. In the case of solid inclusions, it is primarily a hydrodynamic problem. Shannon and Sridhar (2004), Bouris and Bergeles (1998), Nakajima and Okamura (1992) and Cleaver and Yates (1973) have all studied the mechanism of solid particle separation across steel–slag interfaces. First, the existence of a film (that needs to be drained) was contingent upon the Reynolds number, i.e. if $\text{Re} < 1$, no film formation was assumed. The drainage step was computed based on (i) a force balance between the buoyancy on one hand and the drag, gravity and a so-called *rebound force* on the other and (ii) fluid flow past a sphere. The rebound force resulting from a normal interfacial stress is a function of the steel–melt–slag interfacial energy ($\gamma_{\text{melt-slag}}$). It should be mentioned that the presence of Marangoni forces might delay the drainage due to differences along the droplet surface as explained for the case of drainage around gas bubbles by Lahiri *et al.* (2002). Upon reaching a critical separation



1.6 Schematics of kinetic/transport issues in inclusion separation across metal–slag interfaces.

from the interface, the interface was assumed to be ruptured and continued separation occurred based on the balance between the drag, buoyancy and the dynamically changing interfacial forces. Here, as long as the inclusions were not wetted by the melt, i.e. $\gamma_{\text{inclusion-melt}} > \gamma_{\text{inclusion-slag}}$, the inclusions would initially be pushed towards the slag. According to calculations (Bouris and Bergeles, 1998), an Al_2O_3 inclusion of $20\ \mu\text{m}$, would separate completely into a $\text{SiO}_2\text{-Al}_2\text{O}_3\text{-CaF}_2\text{-MgO-CaO}$ (mold flux type) slag within roughly 0.5×10^{-5} seconds. Incomplete separation occurred when the steel wetted the inclusions and TiO_2 in the inclusions had a profound effect on this.

1.3.3 Processes for reactive/high requirement alloys

Vacuum degassing

Impurities can be removed by forcing them to form gases and float out (e.g. $\text{C} + \text{O} = \text{CO}$ in the oxygen steelmaking furnace). For certain applications, extremely low impurity levels must be obtained. This can be achieved through vacuum degassing. The principle is as follows, taking as an example the degassing of hydrogen:



At equilibrium, assuming Henry's law applies in the dilute solution standard state, we get:

$$a_{\text{H}} \approx \text{wt\%}H = \left(p_{\text{H}_2} \cdot e^{\left(\frac{\Delta G^\circ}{RT} \right)} \right)^{1/2} \quad (1.88)$$

By reducing the partial pressure of hydrogen we can lower the thermodynamic limit hydrogen solubility in the liquid metal. By maintaining a vacuum, the partial pressure of the gas, corresponding to the impurity that is to be removed, is minimized and the thermodynamic conditions for refining are improved. The kinetic mechanisms by which impurities are removed are diffusion of the dissolved impurity species through a boundary layer in the melt to the melt surface and evaporation from the surface. If boundary layer diffusion is assumed to be the slower of the two steps (Pehlke, 1973), a simple model can be used to describe the degassing kinetics. Using Fick's first law and assuming steady state diffusion across the liquid-side boundary layer, setting the impurity concentration at the surface to C_o , and assuming that the bulk of the melt is stirred enough to maintain a constant concentration, the change in the melt impurity concentration (C) with time is given by:

$$\frac{dC}{dt} = -D \frac{A}{\delta V} (C - C_o) \quad (1.89)$$

Here, A is the gas–melt interfacial area, V is the melt volume, and δ is the boundary layer thickness. C_o is the concentration of the impurity at the surface

(established by equilibrium with the partial pressure in the gas). D is the diffusion coefficient of the dissolved impurity element in the melt.

When a boundary layer is absent, a model has been developed (Danckwerts, 1951; Machlin, 1960; Darken and Gurry, 1952) that assumes that rigid body elements of fluid move parallel to the melt–gas interface, and during their time of contact with the interface, they get degassed. The streamline flow of the elements is assumed to be free of convective currents and within the elements, semi-infinite diffusion is assumed to be valid. The rate of degassing, is then:

$$\frac{dC}{dt} = \frac{dM}{dA} \frac{dA}{dt} \frac{1}{V} \quad (1.90)$$

Here dA/dt is the rate at which gas–melt interface is created and V is the volume of the melt. dM/dt is the change in solute per unit area of gas–metal interface, and can be expressed (Darken and Gurry, 1952) as:

$$\frac{dM}{dA} = 1.1284(C_o - C)(Dt')^{1/2} \quad (1.91)$$

where t' is the time interval during which solute is lost from the fluid element.

Due to the dependence upon diffusion, vacuum degassing is a very slow and expensive method and is therefore primarily used for applications where high purity is needed.

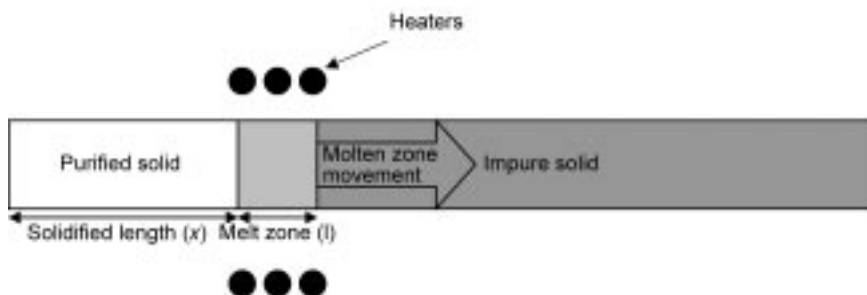
Electro slag remelting

In this refining method, an impure ingot is used as an electrode that is immersed into a molten, ion-conducting slag consisting of CaO, Al₂O₃ and CaF₂. A high current is passed through the ingot, whereupon the ingot melts. During this process, inclusions dissolve in the slag. The molten metal, now purified from inclusions, drops through the slag, and resolidifies as an ingot in the bottom in a water-cooled mold. The water-cooled mold allows for a skull to be formed and thus enables the refining of reactive molten alloys that cannot be easily contained.

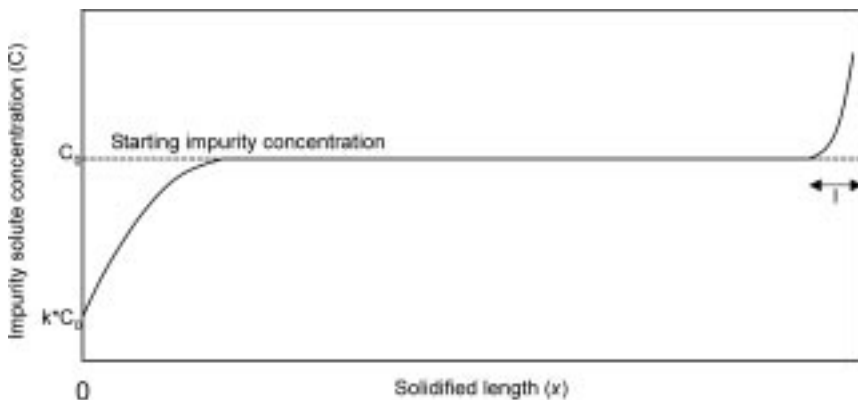
Zone-refining

Zone refining is used to produce primarily materials for electronic components such as Si or Ge. The principle is to utilize the fact that most impurities have a higher solubility in the melt than the solid metal (Fig. 1.5) and thus partition into the melt ahead of the solidification front during solidification. During zone refining, an impure bar is passed slowly through a hot zone that melts a small section of the bar as shown in Fig. 1.7. As the melt zone is moved along the bar, impurity successively builds up in the melt as shown in Fig. 1.8.

A model developed by Pfann (1958) describes the concentration in a bar, with initially a uniform impurity concentration of C_o during a single pass.



1.7 Purification by zone melting (Pfann, 1952).



1.8 Schematic of concentration change during zone melting.

$$\frac{C}{C_o} = 1 - (1 - k)e^{-kx/l} \quad (1.92)$$

Here, C is the impurity concentration, k is the partition coefficient of the impurity between the solid and liquid metal, x is the length solidified and l is the length of the molten zone. Several passes are carried out to reach extreme levels of cleanliness.

1.4 Casting processes

In order to convert a liquid metal into a solid it is necessary to remove heat to (i) cool the liquid below its melting point and (ii) remove the latent heat (exothermic enthalpy release) during the transformation from liquid to solid. This is carried out in a container called a mold.

In general, the transformation of an element of liquid into solid follows a heat balance given by:

$$\rho c_p \frac{\partial T}{\partial t} = L \frac{\partial f_s}{\partial t} - Q \frac{S}{V} \quad (1.93)$$

where ρ , c_p and L are the density, specific heat capacity and volumetric latent heat of the metal, respectively. S and V are the surface area and volume of the element, and f_s is the fraction solid. Q is the net heat flux to/from the volume element.

This equation can be closed by specifying an f_s-t-T relationship if Q and f_s can be identified. Q is dependent upon the thermal field caused by the structure around the element and the mold characteristics. The fraction solid, f_s , depends on the solidification kinetics, which is governed by the rates of nucleation and growth. The specific conditions of the alloy chemistry and mold will govern nucleation and growth rates and thermal fields, and this in turn will determine solidification structure in terms of solid crystal size and shape, micro and macro segregation and porosity.

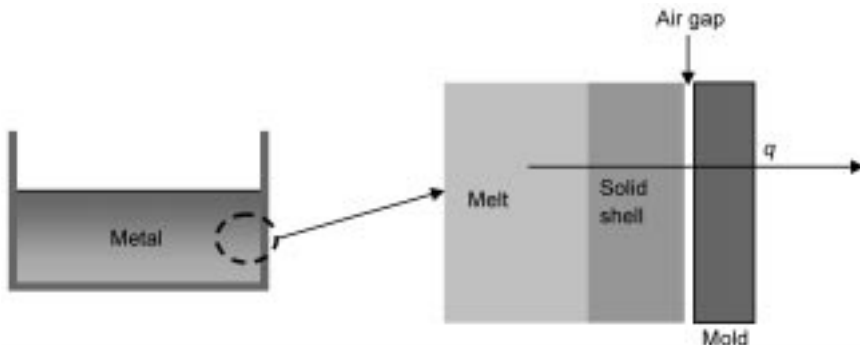
Casting processes are carried out in a wide variety of mold types and processes. They includes continuous processes such as:

1. Oscillating molds to cast profiles with uniform cross-sections such as billet, blooms, slabs, thin slabs or rails. This is by far the dominant process for producing steel bars and sheets. In this process, molten metal is continuously poured through a submerged entry nozzle from a tundish into an oscillating, water-cooled mold. A mold slag is used to cover the surface of the melt meniscus and also to fill the gap between the mold and the solidifying shell. The roles of the mold flux are to control heat transfer, lubricate the mold-strand interface and to refine and protect the melt from impurities.
2. Moving molds using two large rotating wheels in between which thin sections can be cast have resulted in the strip casting process that reduces to a large extent the need for rolling in the production of sheet steels.
3. Atomization is a process by which metal powder is produced by intercepting melt pouring from a tundish with a high velocity gas. By controlling gas velocity and angle of intercept different shapes and sizes of powders can be produced. Atomized powder is a major source for the powder metallurgy industry.

Casting is also carried out in batch processes such as:

1. Large permanent ingot molds. This is used to caste large parts that are to be later machined into specific shapes and sizes. In the case of steels, this has largely given way to continuous casting.
2. Permanent or expendable molds. This is used to shape-cast various structural parts of complex geometry, e.g. in the automotive and aerospace industries. Expendable molds include those made from sand or ceramics.

As mentioned before, the solidified microstructure depends on the cooling rate. The cooling rate is determined by how fast heat is removed from the melt (heat transfer). In casting processes, the heat transfer is thus the most pertinent variable that needs to be controlled. During solidification, the melt adjacent to the mold wall usually solidifies first since this is where it is coolest. The heat



1.9 Schematic of the heat transfer resistances during solidification.

from the melt must thus be transported through (as shown in Fig. 1.9):

- the liquid metal;
- the solid metal shell that forms at the mold wall;
- across the interface between the solid shell and the mold; and
- the mold.

The rate of heat transfer depends on the design of the mold and thus the mold is designed according to the desired microstructure and production rates in various industrial casting processes. Heat is transferred by conduction, convection and radiation. Usually the heat transfer through the liquid metal is fast due to the high degree of convection in the melt.

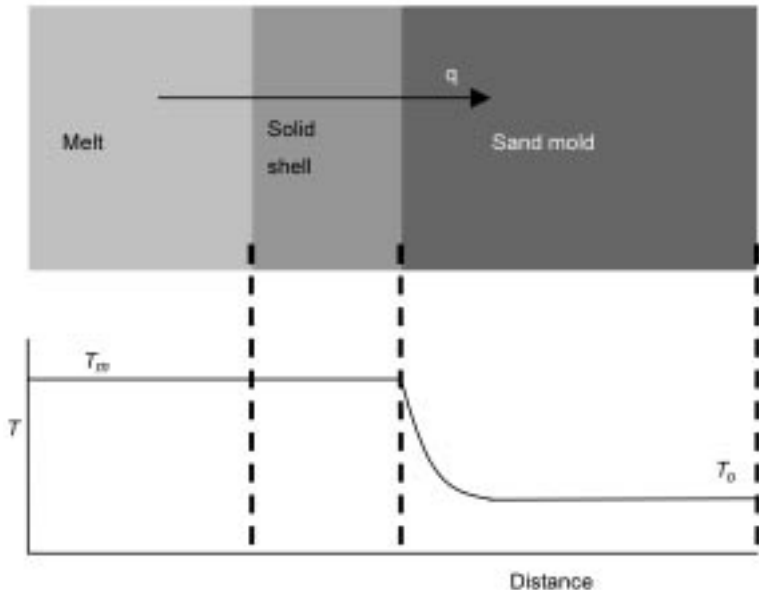
The temperature profile and corresponding heat flux is calculated by simultaneously solving the multi-scale problem of heat transfer and solidification kinetics. Solving a general coupled problem of solidification and heat transfer is complicated and beyond the scope of this chapter. Two simplified cases, each having some practical importance in the casting industry, are discussed below.

1.4.1 Heat conduction in the mold controls the heat transfer: expendable ceramic molds (sand casting, investment casting) used for shape casting

Molds made out of ceramics conduct heat so slowly that the entire temperature drop occurs across the mold (i.e. temperature in solid and liquid metal and mold–metal interface are equal and thus at thermal equilibrium). Furthermore, the mold can often be assumed to be infinitely thick in such a batchwise casting process. The situation is schematically shown in Fig. 1.10.

The Fourier's law solution to this problem yields the following expression for the heat flux:

$$\text{Heat flux } q = \frac{\sqrt{k_{mold} \rho_{mold} C_{p,mold}}}{\sqrt{\pi t}} (T_m - T_o) \quad (1.94)$$



1.10 Schematic temperature profile across a sand mold.

The heat generated per unit area during the growth of the solid is given by the latent heat:

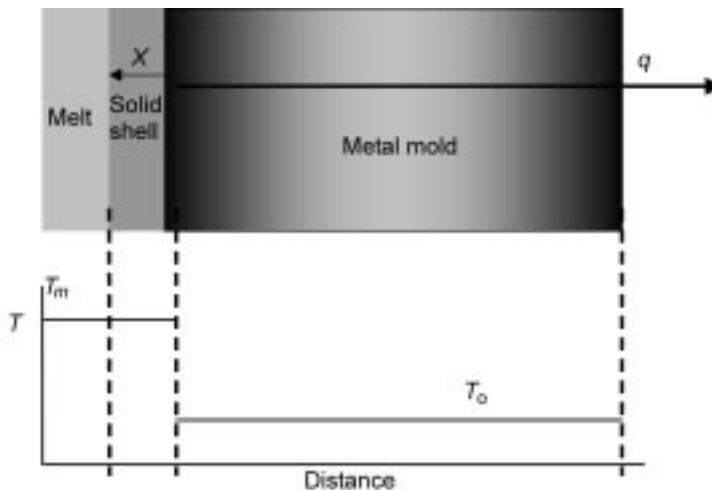
$$\text{Released heat} = \Delta H_m \cdot \frac{dx}{dt} \cdot \frac{\rho_{\text{metal}}}{M_{W,\text{metal}}} \quad (1.95)$$

The released heat is the heat that is to be transported in the heat flux and thus we can equate the two: released heat = heat flux. After integrating (with $x = 0$ at $t = 0$) we end up with an expression for the solid thickness:

$$x = \frac{2(T_m - T_0) \cdot M_{W,\text{metal}}}{\rho_{\text{metal}} \cdot \Delta H_m \cdot \sqrt{\pi}} \cdot \sqrt{k_{\text{mold}} \cdot \rho_{\text{mold}} \cdot C_{p,\text{mold}}} \cdot \sqrt{t} \quad (1.96)$$

1.4.2 Heat transport across the mold–solid metal controls the heat transfer: strip casting, thin slab casting, wire casting, die casting and atomization

This is often the case when casting thin cross-sections in short times using metal molds. Mold thickness is usually large compared to the cross-section of cast metal. This situation is shown in Fig. 1.11. In this case heat transfer in the ingot and mold are so fast that it is the interfacial heat transfer that controls how fast heat is transported. The heat transfer equations yield the following expressions for the heat flux and shell thickness in this case:



1.11 Schematic temperature profile across a metal mold and metal strip.

$$q = h(T_m - T_o) \quad (1.97)$$

$$x = \frac{h(T_m - T_o)}{\rho_{\text{metal}} \cdot \Delta H_m} \cdot M_{W,\text{metal}} \cdot t \quad (1.98)$$

In the first equation, h is the interfacial heat transfer coefficient [$\text{J}/(\text{m}^2 \cdot \text{K})$]. Its value depends on both the contact between the solid shell and the mold as well as the surface properties of both and whether or not a gas fills the gap. Due to its complexity, it must usually be determined experimentally for each type of mold.

1.5 Thermomechanical processes

There are two basic goals in thermomechanical processing of metals:

1. Plastic deformation at ambient or elevated temperature of a cast metal into a desired shape. This is necessary for metals that have not been cast into their final shape such as continuously cast metal or ingots from electroslag refining or vacuum arc re-melting. Alternative methods to achieve this are shape casting (die or investment molds) or powder compaction.
2. Use of deformation and heat treatment to obtain micro-structural changes in order to improve properties. This applies not only to mechanical properties but also to others, e.g. electrical, magnetic and ferroelectric properties.

1.5.1 Deformation processing to obtain shape changes

The principle of deformation processing is to apply a mechanical force resulting in stresses that exceed the metal's yield stress. For example, for the case of uniaxial

tension, we can define a yield stress at the end of the Hooke's law regime. The condition for reaching the yield stress is approximated through a suitable yield criterion, e.g. Tresca or Von Mises. The metal flows due to the creation and movement of dislocations. The yield stress increases as the deformation increases, because more dislocations are created as they get entangled more into one another. This causes an increase in the yield stress and is called work hardening:

$$\sigma = \sigma_o \text{ (no work hardening)} + k^* (\rho_d)^{1/2} \quad (1.99)$$

Here, ρ_d = dislocation density.

Most deformation processes can be described by the following characteristics (shown in Fig. 1.12):

- The metal has an initial shape and initial properties.
- It goes through a plastic deformation zone.
- The metal has a final shape and final properties.
- The process is affected by the friction condition at the interface.

A few examples of deformation processes are listed below:

Rolling

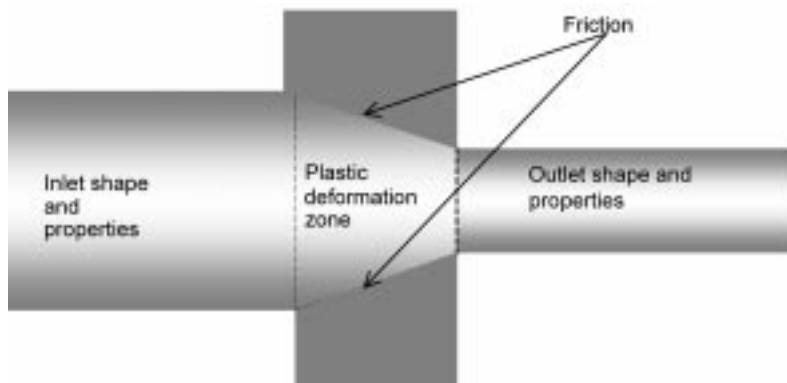
Material is passed between two rolls of equal radius. This is used for reducing the thickness of the plates and sheets (see Fig. 1.13).

Forging

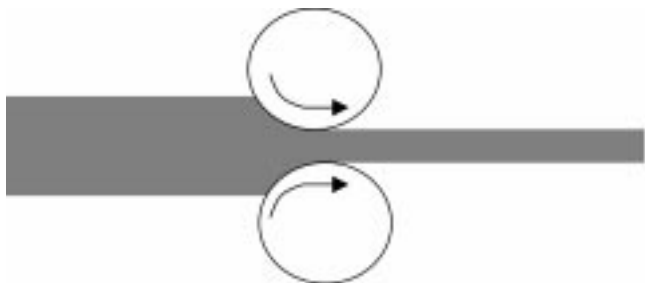
A die is used to apply a force and change the shape of the metal sample. The material is in compression during deformation (see Fig. 1.14).

Wire drawing

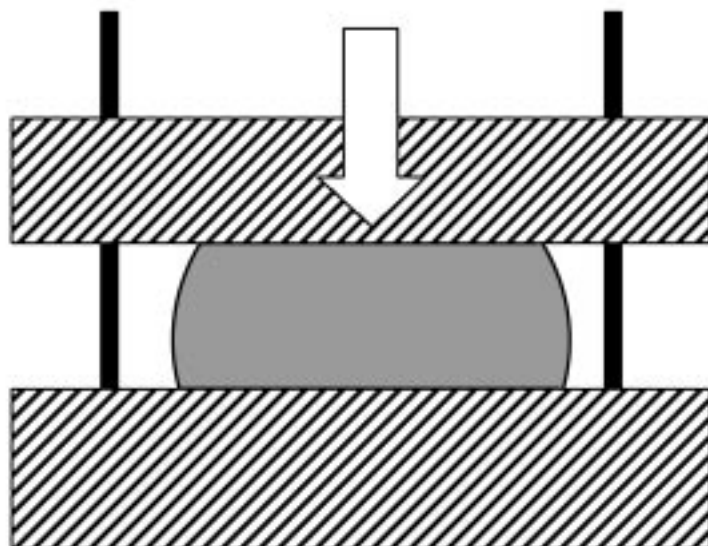
The material is drawn through a die and is in tension during the deformation (see Fig. 1.15).



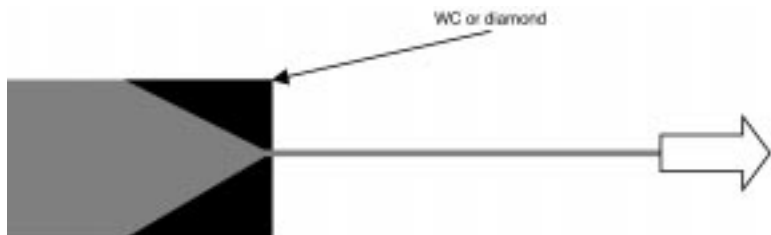
1.12 A generic schematic of a deformation process.



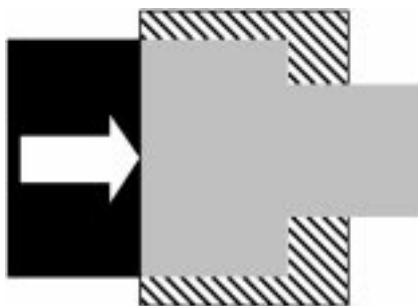
1.13 Rolling.



1.14 Forging.



1.15 Wire drawing.



1.16 Extrusion.

Extrusion

Similar to wire drawing but material is in compression (see Fig. 1.16).

1.6 References

- Alcock C.B. (1976) *Principles of Pyrometallurgy*, London, Academic Press, 180–226.
- Arvanitidis I., Sichen D., Sohn H.Y. and Seetharaman S. (1997) ‘The Intrinsic Thermal Decomposition Kinetics of SrCO₃ by a Nonisothermal Technique’, *Metall Mater Trans B*, 28B, 1063–68.
- Barksdale J. (1966) *Titanium Its Occurrence, Chemistry and Technology*, New York, Ronald Press Co., 213–23, 400–79.
- Bates P. and Muir A. (2000) ‘HIs melt – Low Cost Iron Making’, *Gorham Conference, Commercializing New Hot Metal Processes – Beyond The Blast Furnace*, June 2000.
- Biswas A.K. and Davenport W.G. (1976) *Extractive Metallurgy of Copper*, Oxford, Pergamon, 81–82.
- Bouris D. and Bergeles G. (1998) ‘Investigation of inclusion re-entrainment from the steel–slag interface’, *Metall Mater Trans B*, 29B, 641–649.
- Cleaver J.W. and Yates B. (1973) ‘Mechanism of detachment of colloidal particles from a flat substrate in a turbulent flow’, *J Coll Interface Sci*, 44(3), 464–74.
- Cramb A.W. and Jimbo I. (1988) ‘Interfacial considerations in continuous casting’, W.O. Philbrook memorial symposium, Toronto, Ontario Canada, 17–20 April 1988, Warrendale, PA, USA, ISS, 259–71.
- Danckwerts P.V. (1951) ‘Significance of liquid-film coefficient in gas adsorption’, *Ind Eng Chem*, 43, 1460–67.
- Darken L.S. and Gurry R.W. (1952) *Physical Chemistry of Metals*, New York, McGraw-Hill.
- Evans J.W. and Koo C-H. (1979) ‘The Reduction of Metal Oxides’, in Sohn H.Y. and Wadsworth M.E., *Rate Processes of Extractive Metallurgy*, New York, Plenum, 285–321.
- Gupta S. (1999) ‘Steelmaking-Technological Options’, in *International Conference on Alternative Routes of Iron and Steelmaking (ICARISM '99)*, 15–17 September 1999, Perth, WA, Australia, 81–84.
- Habashi F. (1986) *Principles of Extractive Metallurgy, Vol. 3 Pyrometallurgy*, New York, Gordon and Beach, 326.

- Hojo J., Oku T. and Kato A. (1978) 'Tungsten Carbide Powder Produced by the Vapor Phase Reaction of the WCl₆-CH₄-H₂ System', *J Less Common Metals*, 59(1), 85–95.
- Hong L., Sohn H.Y. and Sano M. (2003) 'Kinetics of Carbothermic Reduction of Magnesia and Zinc Oxide by Thermogravimetric Analysis Technique', *Scandinavian J. Metallurgy*, 32, 171–76.
- International Iron and Steel Institute (2004) 'World Steel in Figures', from website, <http://www.worldsteel.org/wsif.php>.
- Jones D. (1992) *Principles and Prevention of Corrosion*, 2nd edn, New Jersey, Prentice Hall.
- Kofstad P. (1988) *High Temperature Corrosion*, 2nd edn, New York, Elsevier.
- Kopfle J., Anderson S.H. and Hunter R. (2001) 'Scrap, DRI and Pig Iron: Whassup?' *ISRI Ferrous Conference*, Chicago, IL, 2001; <http://www.midrex.com/uploadedfiles/Whassup.pdf>.
- Kozakevitch P. (1954) 'Viscosity of blast-furnace slags', *Revue Metall*, 51, 569–87.
- Kozakevitch P., Lucas L. and Louis D. (1968) 'Part placed by surface phenomena in the elimination of solid inclusions in a metal bath', *Revue Metall*, 65, 589–98.
- Kozakevitch P. and Olette M. (1970) 'Role of surface phenomena in the mechanism of removal of solid inclusions', *Production and application of clean steel*, Intl. Conference, 1970, Balatonfured, Hungary, London, The Iron and Steel Institute, 42–49.
- Kozakevitch P. and Olette M. (1971) 'Role of surface phenomena in the mechanism used for eliminating solid inclusions', *Revue Metall*, 68, 636–46.
- Lahiri A.K., Yogambha R., Dayal P. and Seetharaman S. (2002) 'Foam in Iron and Steelmaking', in Aune R.E. and Sridhar S., *Proceedings of the Mills Symposium, Metals, Slags, Glasses: High Temperature Properties and Phenomena*, 22–23 August 2002, London, vol. 2, London, The Institute of Materials.
- Lamprey H. and Ripley R.L. (1962) 'Ultrafine Tungsten and Molybdenum Powders', *J. Electrochem Soc*, 109(8), 713–15.
- Machlin E.S. (1960) 'Kinetics of vacuum induction refining: theory', *Trans AIME*, 218, 314–26.
- MIDREX Technologies Inc. (2001) '2000 World Direct Reduction Statistics', <http://www.midrex.com/info/world.asp>.
- MIDREX Technologies Inc. (2004) '2003 World Direct Reduction Statistics', <http://www.midrex.com/info/world.asp>.
- Mills K.C. and Sridhar S. (1999) 'Viscosities of iron and steelmaking slags', *Ironmaking Steelmaking*, 26, 262–68.
- Nakajima K. and Okamura K. (1992) 'Inclusion transfer behavior across molten steel–slag interfaces', 4th Intl. Conf. on Molten Slags and Fluxes, ISIJ, Sendai, 1992, 505–10.
- Nikklason G.A. (1987) 'Optical Properties of Gas-Evaporated Metal Particles: Effects of a Fractal Structure', *J Appl Phys*, 62, 258–65.
- Okamoto Y., Koyano T. and Takasaki A. (1987) 'A Magnetic Study of Sintering of Ultrafine Particles', *Japan J Appl Phys*, 26, 1943–45.
- Otsuka K-I., Yamamoto H. and Yoshizawa A. (1984) 'Preparation of Ultrafine Particles of Nickel, Cobalt and Iron by Hydrogen Reduction of Chloride Vapors', *J Chem Soc Japan*, 6, 869–78.
- Padilla R. and Sohn H.Y. (1979) 'Reduction of Stannic Oxide with Carbon', *Metall Trans*

- B, 10B, 109–15.
- Pankratz L.B., Stuve J.M. and Gokcen N.A. (1984) *Thermodynamic Data for Mineral Technology, U.S. Bureau of Mines Bull.* 677, Washington DC, US Government Printing Office.
- Parr H. and Feder J. (1973) ‘Superconductivity in β -Phase Gallium’, *Phys Rev*, 7, 166–81.
- Pehlke D. (1973), *Unit Processes of Extractive Metallurgy*, New York, Elsevier.
- Pfann W.G. (1958) *Zone Melting*, New York, Wiley.
- Pilling N.N. and Bedworth R.E. (1923) ‘Oxidation of metals at high temperatures’, *J Inst Met*, 29, 529–83.
- Riboud P.V. and Olette M. (1982) ‘Mechanisms of some of the reactions involved in secondary refining’, *Proc 7th International conference on vacuum metallurgy*, Tokyo, Japan, 879–89.
- Richardson, F.D. (1974) *Physical Chemistry of Melts in Metallurgy*, Volume 1, London, Academic Press, 81.
- Rosenqvist T. (1983) *Principles of Extractive Metallurgy*, 2nd edn, New York, McGraw-Hill, 202.
- Saeki Y., Zaki R.M., Nishikara H. and Ayoama N. (1978) ‘Preparation of Cobalt Powder by Hydrogen Reduction of Cobalt Dichloride’, *Denki Kagaku*, 46(12), 613–17.
- Shannon G.S. and Sridhar S. (2004) ‘Separation of Al_2O_3 Inclusions Across Interfaces between Molten Steel and Ladle-, Tundish- and Mold-Slags’, *METAL SEPARATION TECHNOLOGIES III*, Symposium in Honor of Professor Lauri E. Holappa, Copper Mountain Colorado, June 20–24, 2004, Engineering Foundation Conferences.
- Sohn H.Y. and PalDey S. (1998a) ‘Synthesis of Ultrafine Particles and Thin Films of Ni_4Mo by the Vapor-Phase Hydrogen Coreduction of the Constituent Metal Chlorides’, *Mater Sci Eng A*, 247, 165–72.
- Sohn H.Y. and PalDey S. (1998b) ‘Synthesis of Ultrafine Nickel Aluminide Particles by the Hydrogen Reduction of Vapor-Phase Mixtures of NiCl_2 and AlCl_3 ’, *J Mater Res*, 13, 3060–69.
- Sohn H.Y. and PalDey S. (1998c) ‘Synthesis of Ultrafine Particles of Intermetallic Compounds by the Vapor-Phase Magnesium Reduction of Chloride Mixtures: Part I. Titanium Aluminides’, *Metall Mater Trans B*, 29B, 457–64.
- Sohn H.Y. and PalDey S. (1998d) ‘Synthesis of Ultrafine Particles of Intermetallic Compounds by the Vapor-Phase Magnesium Reduction of Chloride Mixtures: Part II. Nickel Aluminides’, *Metall Mater Trans B*, 29B, 465–69.
- Sohn H.Y., Zhang Z., Deevi S. and PalDey S. (2004) ‘Chemical Vapor Synthesis of Ultrafine Fe-Co Powder’, *High Temperature Materials and Processes*, 23, 329–33.
- Wakelin D. (ed.) (1999) *The Making, Shaping and Treating of Steel*, 11th edn, Pittsburgh, PA, The AISI Steel Foundation, 403–567.
- Zhao G.Y., Revenkar V.V.S. and Hlavacek V. (1990) ‘Preparation of Tungsten and Tungsten Carbide Submicron Powders in a Chlorine-Hydrogen Flame by Chemical Vapor Phase Reaction’, *J Less Common Metals*, 163(2), 269–80.

1.7 Appendix: notation

Nomenclature

Italics

A	effective area or interface where reaction takes place
a	chemical activity or constant in eqn 1.41
C	concentration per unit volume
C_p	heat capacity
C_s	sulfide capacity
D	diffusion coefficient
f_i	activity coefficient of specie ‘i’ in the infinite dilution standard state
f_s	fraction solid
G	Gibbs free energy
H	heat transfer coefficient
H	enthalpy
k	reaction rate constant, partition coefficient or thermal conductivity
K	chemical equilibrium constant
l	melt zone length
m	mass of product formed or reactants consumed
M	solute per unit area
M_W	molar weight
p	partial pressure
PB	Pilling–Bedworth ratio
Q	net heat flux
R	ideal gas constant
S	surface area
t	time
T	temperature in K
V	volume
x	distance or thickness

Greek symbols

δ	boundary layer thickness in a fluid phase
ρ	density
σ	stress

Subscripts

o	reference state
m	mold

Superscript

o	starting value
$'$	interval or defines intermediate constant

2.1 Introduction

According to Albert Einstein,¹ thermodynamics is marked by its simplicity, the different kinds of things it relates to and the wide area of its applicability. Thermodynamics is by definition a subject that describes the link between heat and motion. With the development of physics and chemistry and the application of mathematical principles, the subject area today covers all forms of energy including, thermal, electrical, mechanical energies and the impact of the same in the change of the states of the systems we are interested in. The area of thermodynamics stretches from the atomistics to macro systems including huge metallurgical reactors. The applications of the concepts of thermodynamics to metallurgy reached significant advancements during the past four decades with stalwarts like Wagner from Germany, Darken, Chipman and Elliott from the US, Richardson in UK as well as Hillert from Sweden. The present chapter is intended to cover the areas of thermodynamics that are of relevance to metallurgy, particularly, the processing of metals and the properties of metals and alloys. For further reading, the readers are requested to resort to the classical textbooks in this area presented in the bibliography at the end of this chapter. The present chapter is also to an extent inspired by the course literature in thermodynamics at the Royal Institute of Technology by the present authors and their predecessors.

Since thermodynamics is a subject that can be almost philosophical, it is imperative to have clear definitions of the various terms involved in order to apply its concepts in metallurgical applications. As mentioned earlier, we are concerned with the changes of state of a system due to energy impact. Thermodynamics does not provide any information as to the rate of this change.

2.2 Basic concepts in thermodynamics

2.2.1 State and state functions

System

A system in thermodynamics is a limited but well-defined part of the universe focused on presently. The rest of the universe can be considered as the surrounding. The aim is to examine the interaction between the system and the universe in a simple but well-specified way. An *open system* can exchange with its surroundings both matter and energy. A *closed system* on the other hand can exchange only energy with the surroundings, but not matter. An *isolated system* can neither exchange matter nor energy with the surroundings. A *homogeneous system* is identical in physical and chemical properties in all parts of the system, as for example, liquid steel at 1600 °C. A system that has differences in physical and chemical properties within the system is referred to as a *heterogeneous system*, as for example, water and ice at 0 °C.

A system is composed of different types of molecules. For example, air, as a system consists of nitrogen, oxygen and other minor gas molecules. These are referred to as *components* of a system. Considering a gas system consisting of three molecular types, H₂, O₂ and H₂O, there is mutual reaction between these molecular types, namely:



The number of these molecular types in the system can be altered by introducing some of these molecules from the surroundings or change, for example, the total pressure of the system. Thus, it is enough to define two of the three types of molecules, *viz.* the system has two components.

A heterogeneous system that may have different physical properties with the same components throughout may have different phases. For example, water at its freezing point contains a solid (ice) and a liquid, and thus, two phases. Within each phase, the molar properties have the same value at every point. Generally, the three phases, solid, liquid and gas are considered in a heterogeneous system. In metallurgy, it is often necessary to consider different allotropic modifications in the solid state, as for example, α , γ or δ iron with different crystal structures. Water at the triple point will have three phases, *viz.* ice, water and steam.

State

The macroscopic definition of ‘state’, which is relevant to metallurgy, is defined by its macroscopic properties like temperature, pressure, volume, vapour pressure, viscosity, surface tension, etc. With a focus on the chemical properties, surface energy is also related to the state of the system. For example, in defining

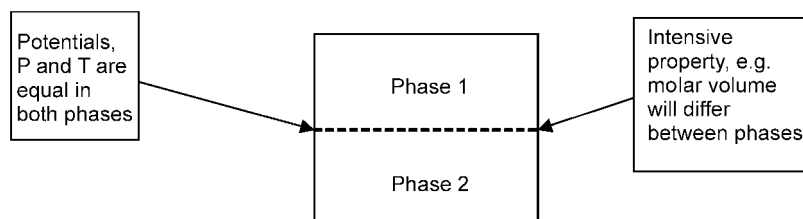
10 moles of nitrogen, it is important to define the temperature and pressure, as the other properties get defined implicitly.

State properties

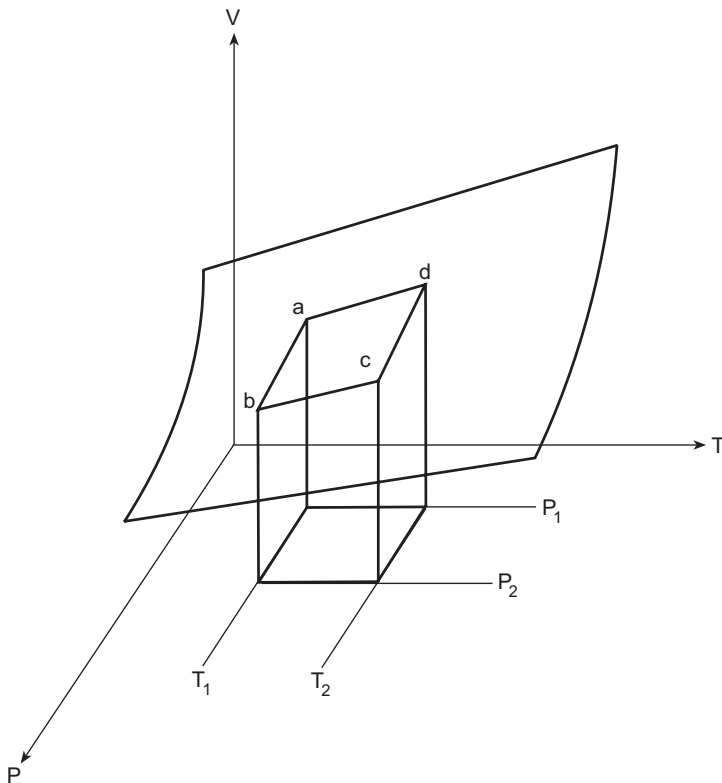
The properties stated above along with others being defined in the following chapters that define the state of the system are the state properties. The properties that are additive are called the *extensive properties*, as for example mass, volume and energy and, in the case of a homogeneous system, are proportional to the total mass. On the other hand, properties, to which a value could be assigned at each point in the system are *intensive properties*. Some of the common intensive properties are temperature, pressure, density etc. Since the ratio of two extensive properties is independent of total mass, and may be assigned a value at a point, these ratios fall under intensive properties. Examples of such properties are molar properties like volume per mole. In order to differentiate these from intensive properties like temperature and pressure, the latter are often classified as *potentials*. It is useful to introduce, at this point, the concept of *chemical potential*, represented usually as μ , which is the potential corresponding to the chemical energy in the system. The equality of the potentials and the inequality in molar properties between phases is illustrated in Fig. 2.1.

A system is in a state of *mechanical equilibrium* if the pressure at all points in the system is the same. If the system has no thermal gradients, it is supposed to be in *thermal equilibrium*. The system is in chemical equilibrium if the chemical potential is uniform throughout the system. The system is in *complete thermodynamic equilibrium* if it is having mechanical, thermal as well as chemical equilibria. The properties of the system can be varied by interaction between the system and the surrounding. Mass transfer could change the material content of the system while heat transfer could alter the energy content.

In order to define the macroscopic state of the system unequivocally, all the properties of the system need be known. On the other hand, due to the interdependency of the properties, it is sufficient to define only a few. For example, in the case of a gas in a container, it is only necessary to define the temperature and pressure. The volume of the system, V in $\text{m}^3 \cdot \text{mol}^{-1}$ gets



2.1 Two phases in thermodynamic equilibrium.

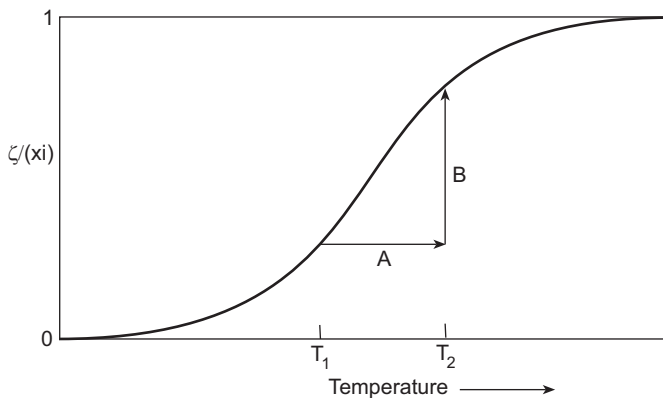


2.2 The states of a defined amount of gas—schematic diagram.² The letters 'a', 'b', 'c' and 'd' refer to different states of the system. P_1 and P_2 refer to two different pressures where $P_1 > P_2$. T_1 and T_2 are the two temperatures, $T_1 < T_2$.

implicitly defined by the gas law. Thus, in this case, we can define pressure, P , N.m^{-2} and temperature, T , K are the *independent variables* and volume is the dependent variable. The gas law

$$V = NRT/P \quad (2.2)$$

where N is the number of moles in a system is an equation of state. A schematic representation of the various states of a system, where the variables are T , P and V , is presented in Fig. 2.2. In some cases, especially in the case of phase transformations, it is sometimes advantageous to define a new term 'inner state variable'³ as, for example, the degree of change due to conditions imposed on the system, as represented by the symbol ξ . Since thermodynamics is concerned with the changes associated with the interactions between the system and the surroundings, the degree of change could be a useful parameter in following the path of a reaction. This is illustrated in Fig. 2.3.



2.3 Gradual change of an inner state variable caused by a quick change in temperature.³

2.2.2 The first law of thermodynamics

Energy change between the system and its surroundings is defined by the first law of thermodynamics. It is also variously considered as a definition of energy or a law of conservation of energy.

$$dU = \delta Q + \delta W \quad (2.3)$$

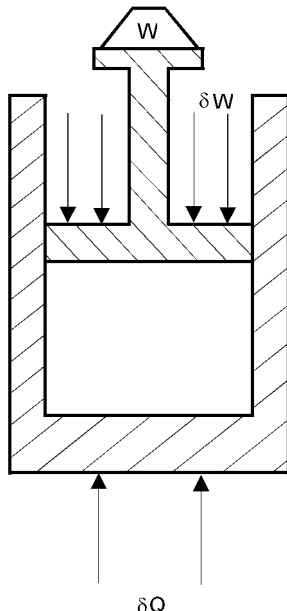
where dU is the change in the internal energy of the system (without defining the microscopic state), δQ is the energy added to the system and δW is the work imposed on the system. (Please note that the symbol ‘ d ’ is used for infinitesimal, defined change in the state property of a system while, ‘ δ ’ is used for an infinitesimal, undefined amount of energy or work coming in from the surroundings). It is to be noted that the term ‘energy’ includes all forms of energy including thermal, electrical, chemical and other known forms. Similarly, the term ‘W’ covers all forms of work: chemical, mechanical, etc. The essence of the first law of thermodynamics is the *law of conservation of energy*. Further, the first law of thermodynamics does not contradict the Einstein’s mass–energy relationship, *viz.*

$$E = m.c^2 \quad (2.4)$$

where E is the energy, m is the mass and c is the velocity of light in the sense that mass could be considered a form of energy. Q and W could be expressed in a suitable energy unit, Joule.

The above figure illustrates the energy–work relationship considering mechanical energy. In the case of a chemical reaction, a negative value of Q refers to exothermic reaction while a positive Q would mean an endothermic one.

One of the direct consequences of the first law of thermodynamics is *Hess’s law of constant heat summation* which states the the heat change in a chemical reaction is the same whether it takes place in one or several steps. In other



2.4 A schematic illustration of the first law of thermodynamics.

words, the heat of a reaction is dependent only on the initial final states of the chemical system.

Using the cylinder–piston analogy in Fig. 2.4, it is possible to express the Q and W terms as system variables. With an external pressure, P, acting on the piston, the change in volume of the system, dV will be PdV (the ‘minus’ sign indicating the decrease in volume). Thus, equation (1.3) can be rewritten as:

$$dU = \delta Q - P.dV \quad (2.5)$$

Between two states of the system 1 and 2, equation (2.6) can be integrated as

$$\int_{U_1}^{U_2} dU = Q - P \int_{V_1}^{V_2} dV$$

$$U_2 - U_1 = Q - P(V_2 - V_1) \quad (2.6)$$

$$(U_2 + PV_2) - (U_1 + PV_1) = Q \quad (2.7)$$

The system properties U and PV terms for the two states can be combined to get an expression for Q, *viz.*

$$H_2 - H_1 = Q \quad (2.8)$$

The term H, which is a system property, includes the internal energy of the system and the mechanical work and is known as *enthalpy*. The internal energy and enthalpy terms can be expressed in terms of the molar heat capacities.

The molar heat capacity at constant volume, C_V , represents the change in the internal energy between the states 1 and 2 and thus,

$$U_2 - U_1 = \int_1^2 C_V dT \quad (2.9)$$

Correspondingly, the molar heat capacity at constant pressure C_P can be expressed as

$$H_2 - H_1 = \int_1^2 C_P dT \quad (2.10)$$

In the case of ideal gases, it can be very easily shown that $C_P - C_V = N.R$, where N is the Avogadro no. and R is the gas constant.

2.3 Chemical equilibrium

2.3.1 The second law of thermodynamics

In thermodynamics, in order to arrive at the maximum work done for a given supply of energy, the concepts of *reversible and irreversible processes* are often used. The term reversibility is applied to a process which takes the system only infinitesimally away from the equilibrium state. The direction of a reversible process can be changed by an infinitesimal change of the parameters of the process, as, for example, changing the voltage in a galvanic cell. Other processes like the flow of heat from a hotter to a colder body are irreversible.

Among the reversible processes, an *isothermal process* is one where there is an exchange of energy between the system and the surroundings (see definition of ‘closed systems’, page 39) during the process. An *adiabatic process* is one where the system is insulated from the surroundings (see definition of ‘isolated systems’, page 39) and there is no exchange in energy. In calculating the energy absorbed for isothermal as well as adiabatic expansions, it can be shown as:

$$\text{Isothermal expansion: external energy required} = RT \ln(V_2/V_1) \quad (2.11)$$

where the subscripts 1 and 2 refer to the initial final states of the system. Similarly,

$$\text{Adiabatic expansion: external energy required} = 0 \quad (2.12)$$

But, in the latter case, the internal energy of the used will be expended for the work done, which is given by the relationship:

$$C_V \ln(T_2/T_1) = R \ln(V_2/V_1) \quad (2.13)$$

Equations (2.11), (2.12) and (2.13) represent the change of state of the system.

Considering a cylinder–piston system, as shown in Fig. 2.4, and a series of reversible processes, *viz.* adiabatic expansion, isothermal expansion, adiabatic

compression and isothermal compression, an exercise termed *Carnot cycle* can be performed. By this, it can be shown that

$$\Sigma(\delta Q/T) = 0 \quad (2.14)$$

for reversible processes. If a state function, *entropy* can be defined as Q/T ,

$$dS = \delta Q_{\text{Rev}}/T \text{ and } dS > \delta Q_{\text{Irrev}}/T \quad (2.15)$$

is a statement of the *second law of thermodynamics*. Q_{Rev} and Q_{Irrev} are the energies associated with reversible and irreversible processes.

2.3.2 Concept of entropy

An irreversible process in a system together with its surroundings is accompanied by an increase in entropy. If the enthalpy change associated with the process is ΔH , the entropy change of the surroundings is $-\Delta H_{\text{system}}/T$. The total entropy change of the system plus surroundings is

$$\Delta S = \Delta S_{\text{System}} = \Delta S_{\text{Surroundings}} = \Delta S_{\text{System}} - \Delta H_{\text{System}}/T \quad (2.16)$$

Thus, for a process at constant pressure,

$$\Delta H - T.\Delta S = 0 \text{ for reversible processes} \quad (2.17)$$

$$\Delta H - T.\Delta S < 0 \text{ for irreversible processes} \quad (2.18)$$

2.3.3 Concepts of Gibbs and Helmholtz energies

When $\Delta H - T.\Delta S > 0$, the reaction would be impossible. Thus, the driving force of a chemical reaction can be expressed in terms of $\Delta H - T.\Delta S$. A new term, *Gibbs energy*, is defined as

$$G = H - TS \quad (2.19)$$

The change in Gibbs energy, ΔG can be expressed as

$$\Delta G = \Delta H - T.\Delta S \quad (2.20)$$

All spontaneous reactions occur with a decrease in the Gibbs energy, while at equilibrium, the Gibbs energy change is zero. The products and reactants have the same Gibbs energy and the reaction lacks a driving force in any direction.

In an analogous way, a corresponding expression for the driving force for a process with constant volume can be derived. The expression, $U - T.S$ is termed *Helmholtz energy*, A .

Thus, at constant volume, for a spontaneous reaction, $dA < 0$. At equilibrium, $dA = 0$ and when $dA > 0$, the reaction is impossible.

2.3.4 Maxwell's relations

Combination of first and second laws yields the following expressions:

$$dU = TdS - PdV \quad (\partial T / \partial V)_S = -(\partial P / \partial S)_V \quad (2.21a)$$

$$dH = TdS + VdP \quad (\partial T / \partial P)_S = (\partial V / \partial S)_P \quad (2.21b)$$

$$dG = VdP - SdT \quad (\partial S / \partial V)_T = (\partial P / \partial T)_V \quad (2.21c)$$

$$dA = -PdV - SdT \quad (\partial V / \partial T)_P = -(\partial S / \partial P)_T \quad (2.21d)$$

These four equations are termed *Maxwell's relations*.

2.3.5 Gibbs energy variation with pressure and temperature

From Maxwell's relations, it is quite easy to derive the pressure and temperature dependencies of Gibbs energy. Equation (2.21c) leads to the relationship:

$$(\partial G / \partial P)_T = V \text{ and } (\partial G / \partial T)_P = -S \quad (2.22)$$

Further, according to equation (2.20),

$$\begin{aligned} \Delta G &= \Delta H - T \cdot \Delta S \\ &= \Delta H + T \cdot (\partial \Delta G / \partial T)_P \end{aligned} \quad (2.23)$$

$$[\partial(\Delta G / T) / \partial T]_P = -\Delta H / T^2 \quad (2.24)$$

and

$$[\partial(\Delta G / T) / \partial(1/T)]_P = \Delta H \quad (2.25)$$

Equations (2.24) and (2.25) are referred to as two different forms of *Gibbs–Helmholtz equation*.

2.3.6 The third law of thermodynamics

Nernst postulated that, for chemical reactions between pure solids, the Gibbs energy and enthalpy functions, $[\partial(\Delta G / T) / \partial T]_P$ as well as $[\partial \Delta H / \partial T]_P$ approach zero as the temperature approaches absolute zero. This further led to the theorem that, for all reactions involving condensed phases, ΔS is zero at absolute zero. This was further developed by Planck to the third law of thermodynamics in a new form, *viz.* ‘the entropy of any homogeneous substance in complete internal equilibrium may be taken as zero at 0 K’.

Glasses, solid solutions or other systems (for example, asymmetric molecules like CO) that do not have internal equilibrium will obviously deviate from third law. The same is true for systems with different isotopes.

2.3.7 Entropy and disorder

The second law of thermodynamics states that the total entropy is increasing for spontaneous processes. In the atomistic level, entropy is considered to be a degree of disorder arising due to randomness in configuration as well as energy contents. The latter can manifest itself as vibrational, magnetic or rotational disorders. From a statistical mechanics treatment of disorder, Boltzman arrived at the equation for configurational entropy as

$$S = k \ln \omega \quad (2.26)$$

where k is the Boltzman constant and ω number of arrangements within the most probable distribution.

Richard's and Trouton's rules

The degree of disorder increases as a substance melts. As a stronger bonding energy between atoms need a higher temperature to cause disorder, Richard's rule states that

$$\Delta S_f = L_f/T_f = \text{ca } 8.4 \text{ J. K}^{-1} \quad (2.27)$$

where ΔS_f is the entropy of fusion, L_f is the latent heat of fusion and T_f is the melting point. In reality, Richard's rule, which is empirical, holds approximately for metals, the values tend to be higher for metalloids and salts.

Another useful empirical rule for the heat of vaporization at the boiling point is given by Trouton's rule, *viz.*

$$\Delta S_v = L_v/T_v = \text{ca } 88 \text{ J. K}^{-1} \quad (2.28)$$

where ΔS_v is the entropy of vaporization, L_v is the latent heat of vaporization and T_v is the boiling point.

2.3.8 Reference states for thermodynamic properties

The absolute values of enthalpy are not known; but only changes can be measured. In order to facilitate the computation of enthalpies, especially as a function of temperature, the accepted convention is to assign a value of zero to all pure elements in their stable modifications at 10^5 Pa and 298.15K, which are the *reference points*. The enthalpies at other temperatures can be calculated by using the expression

$$(\partial H/\partial T)_P = C_P \Rightarrow \Delta H = \int_{T_{\text{Ref}}}^{T_{22}} C_P dT = H(T_2, P) - {}^o H_{\text{Ref}} \quad (2.29)$$

The enthalpies of compounds can be calculated by adding the enthalpy of the reaction between the elements. The superscript 'o' stands for pure substance.

In the case of entropies, the computation of entropies at temperatures other than the reference temperatures is carried out using the equation:

$${}^{\circ}\!S^T = {}^{\circ}\!S^{\text{REF}} + \int_{T_{\text{REF}}}^{T_1} C_p d \ln T \quad (2.30)$$

Newmann–Kopp rule

In the estimation of enthalpies and entropies of compounds from elements, the Newmann–Kopp rule can be applied with reasonable success, even though it is claimed that this rule lacks a theoretical basis. According to this rule

$$C_p(\text{compound}) = \sum C_p(\text{components}) \quad (2.31)$$

2.3.9 Some thermodynamic compilations

It is important that a metallurgist has access to thermodynamic data of the systems of interest at temperatures of relevance. Some of the classical compilations are listed below:

Thermochemical tables

1. *Materials Thermochemistry*, O. Kubaschewski, C.B. Alcock and P.J. Spencer, Pergamon Press (1993).
2. *Thermochemical Properties of Inorganic Substances*, I. Barin and O. Knacke, Springer-Verlag, Berlin (1973, Supplement 1977).
3. *JANAF Thermochemical Tables*, N.B.S., Michigan (1965–68, Supplement 1974–75).
4. *Selected Values of Thermochemical Properties of Metals and Alloys*, R. Hultgren, R.L. Orr, P.D. Anderson and K.K. Kelley, John Wiley & Sons, NY (1963).
5. *Thermochemistry for Steelmaking*, Vol. I & II, J.F. Elliott, M. Gleiser, J.F. Elliott, M. Gleiser and V. Ramakrishna, Addison-Wesley, London (1963).

Thermochemical databases

1. HSC databas – Finland
2. Thermo-Calc – Sweden
3. Chemsage/F.A.C.T. – Canada, Germany, Australia
4. MT Data – England
5. THERMODATA – France

2.4 Unary and multicomponent equilibria

2.4.1 Unary systems

As stated previously, the condition for chemical equilibrium is that the Gibbs energy of the products and reactants are equal and that there is no net driving force for the reaction in either direction. This can be easily understood in the case of systems consisting of a single component. At the melting point of ice, the equilibrium condition is:

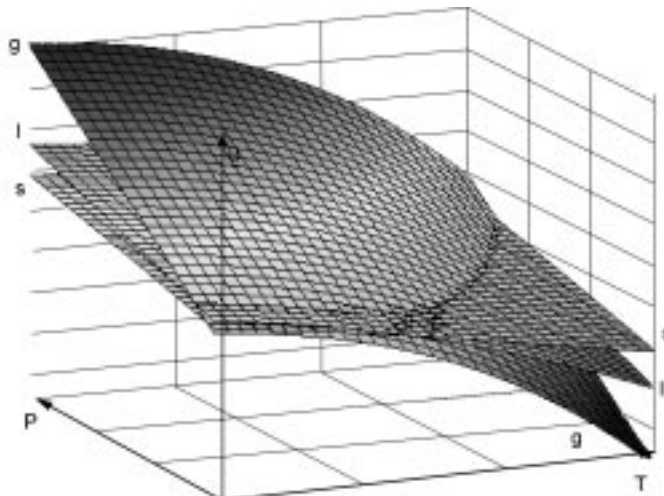
$${}^sG_{H_2O} = {}^lG_{H_2O} \quad (2.32)$$

The Gibbs energy of the solid, liquid and gas phases in a G–P–T diagram, where the intersections of the Gibbs energy planes represent equality in the Gibbs energy values at given temperatures and pressures is presented in Fig. 2.5. Solid and liquid planes cross at the melting point, while the liquid and gas phase intersect at the boiling point. The three planes meet at a unique temperature and pressure when all the three phases have the same Gibbs energy. This point is known as the triple point.

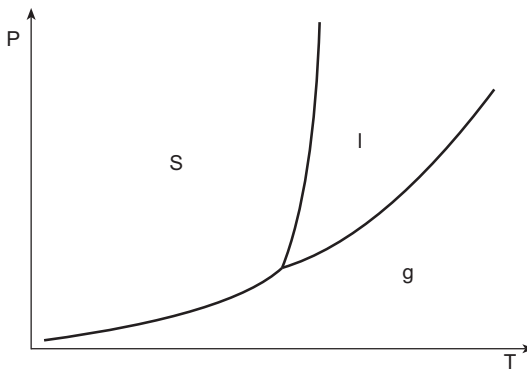
The projection of the Gibbs energy planes in Fig. 2.5 on to the P–T base plane would provide an understanding of the stability areas of various phases as functions of temperature and pressure. Such a projection is presented in Fig. 2.6.

2.4.2 Clapeyron and Clausius–Clapeyron equations

An imaginary line in Fig. 2.5 from the triple point along the intersection of the solid and liquid planes represents the variation of melting point as a function of



2.5 Gibbs energy–temperature–pressure diagram in the case of a one-component system.



2.6 Projection of the Gibbs energy planes in Fig. 2.5 on the P-T base plane.

pressure. The mathematical relationship can easily be derived from equation (2.21c) of the Maxwell relationship, *viz.*

$$dG = VdP - SdT \quad (\partial S / \partial V)_T = (\partial P / \partial T)_V \quad (2.21c)$$

For a phase transformation reaction, the S and V terms could be replaced by ΔS and ΔV , the entropy and volume changes accompanying the transformations respectively. Equation (2.21c) can then be rewritten as

$$-S^S dT + V^S dP = -S^l dT + V^l dT \quad (2.33)$$

$$(S^l - S^S)dT = (V^l - V^S)dP \quad (2.34)$$

$$\frac{dP}{dT} = \frac{\Delta S_f}{\Delta V_f} = \frac{\Delta H_f}{T_f} \cdot \frac{1}{\Delta V_f} \quad (2.35)$$

where ΔS_f , ΔV_f and ΔH_f are the entropy, volume and enthalpy changes respectively accompanying melting at the fusion temperature, T_f . The above equation holds for any phase transformation in a single component system and is referred to as the *Clapeyron equation*. This equation is extremely useful in estimating the variation of the melting point as the ambient pressure changes and finds applications in high pressure synthesis of materials.

When the Clapeyron equation is applied to the vaporization of a liquid or solid, the ΔV term reduces to V , which is much larger compared to the condensed phases. Thus equation (2.33) is rewritten, combining with the ideal gas law, as

$$\frac{dP}{dT} = \frac{\Delta H_V}{T \Delta V_V} = \frac{\Delta H_V}{R \cdot T^2} \cdot P \quad (2.36)$$

$$\frac{dP}{P \cdot dT} = \frac{\Delta H_V}{R \cdot T^2} \quad (2.37)$$

$$\frac{d \ln P}{dT} = \frac{\Delta H_V}{R \cdot T^2} \quad (2.38)$$

where the subscript ‘V’ refers to vaporization.

The Clausius–Clapeyron equation is very useful in determining the latent heat of vaporization or the vapour pressure of a substance at a temperature with a knowledge of the same at another temperature and the latent heat.

2.4.3 Multicomponent systems

Maxwell’s relationship for a single component system is expressed by equation (2.21c). In the case of systems with more than one component, the Gibbs energy of the component should be added to the equation. Hillert³ suggests that the inner driving force, ξ could be added with great advantage in describing reactions like, for example, nucleation. Thus, the integrated driving force can be rewritten for multicomponent systems as

$$dG = V.dP - S.dT + \sum \mu_i dn_i - D.d\xi \quad (2.39)$$

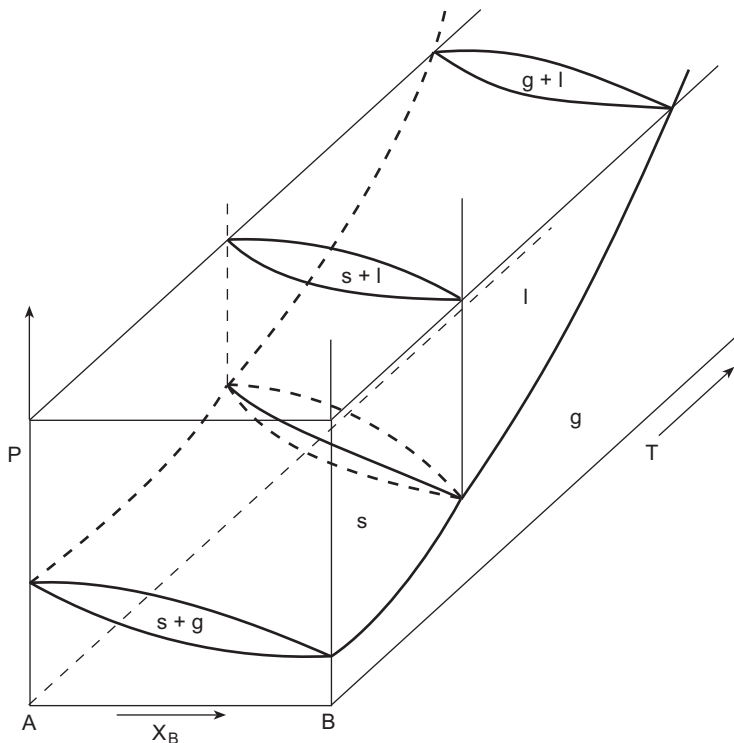
where μ_i is the chemical potential of component ‘i’ per mole of ‘i’, n_i is the number of moles of ‘i’, D is defined as $-(\partial U / \partial \xi)_{S,V,n_i}$. The common practice is to express equation (2.39) without the last term on the right-hand side. It is important to realize that the different phases in the system have thermal, mechanical and chemical equilibria prevailing.

In the case of a binary system, it is illustrative to add a third composition axis to Fig. 2.6 on the basis of equation (2.39) without the last term on the right-hand side. This is shown in Fig. 2.7. While vertical planes corresponding to the pure substances are identical with Fig. 2.6, the region in between has three dimensional regions of stability of single phases as well as those with two phases. The two phase regions are shaped as convex lenses. A section of the diagram in Fig. 2.7 corresponding to 1 bar (10^5 Pa) plane will yield a diagram as shown in Fig. 2.8. Figure 2.8 is a simple binary phase diagram showing the stabilities of solid and liquid phases as a function of temperature. Among the phase diagram types commonly used in metallurgy, eutectic and peritectic types of diagrams are important. These are presented in Fig. 2.9.

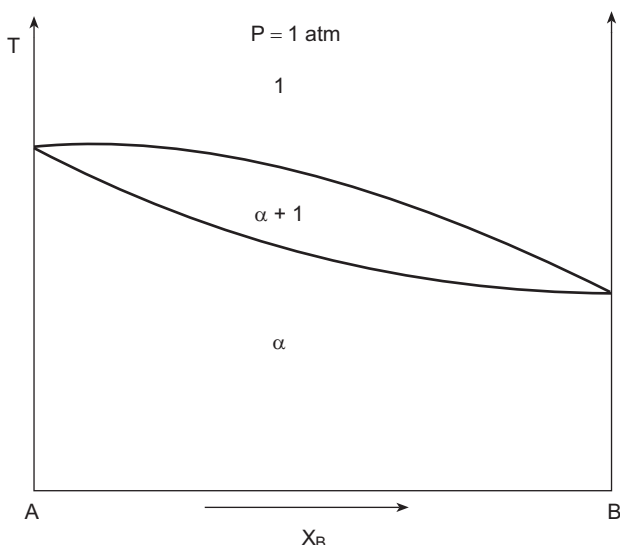
In Fig. 2.8, the two components are chemically similar and thus exhibit complete solubilities in solid and liquid phases. The repulsive or attractive forces between the components in a binary system can result in partial solubilities or compound formation in the solid state respectively. In the former case, the liquid formation is favoured at lower temperatures. The contrary is true in the case of compound formation. Figure 2.10 presents some examples of how attractive and repulsive forces influence the phase diagrams for binary systems.

2.4.4 Gibbs phase rule

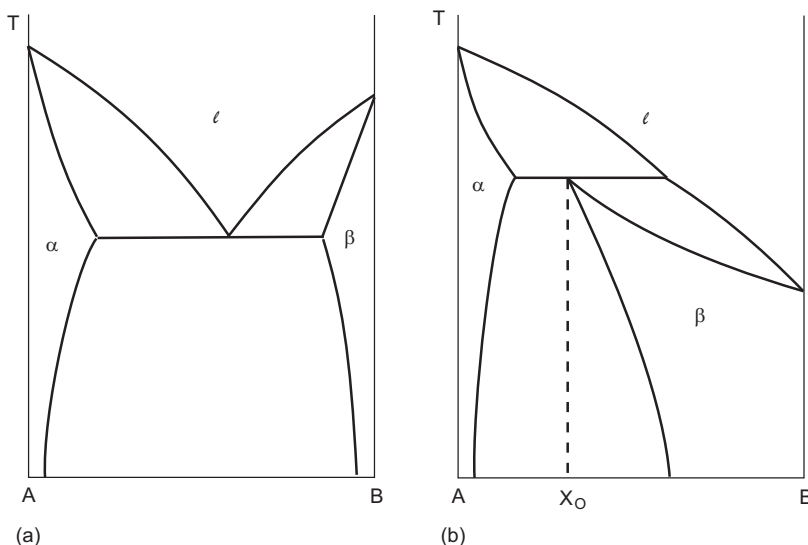
In accordance with the requirements for equilibrium, different phases in a system have the same temperature and pressure. Further, each of the components



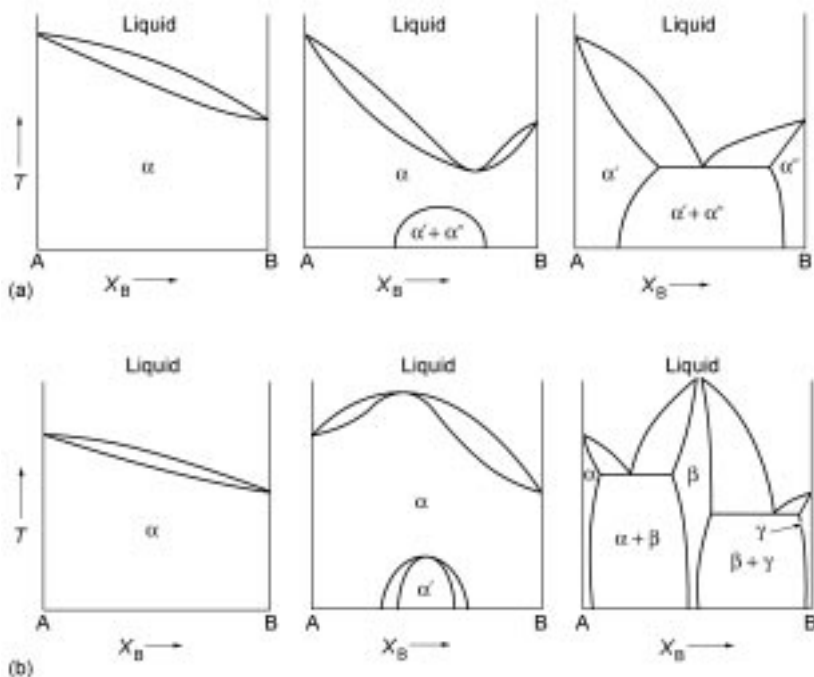
2.7 Composition–temperature–pressure diagram for a binary system.⁴



2.8 A simple binary phase diagram showing the complete mutual solubilities of the two components A and B in solid as well as liquid state.



2.9 Some common types of binary phase diagrams (a) eutectic diagram (b) peritectic diagram.



2.10 (a) Binary phase diagrams where the repulsive forces between the components are manifested.⁵ (b) Binary phase diagrams where the attractive forces between the components are manifested.⁵

has the same chemical potential in all the phases in equilibrium. This led to the derivation of the Gibbs phase rule, which states that

$$F = C - P + 2 \quad (2.40)$$

where ‘F’ is the minimum number of degrees of freedom required to reproduce the system, ‘C’ represents the number of independent components in the system and ‘P’ refers to the number of phases. The Gibbs phase rule is applicable to multicomponent macro systems in determining the number of phases at a given temperature and pressure.

2.4.5 Gas mixtures

Maxwell’s relationship (equation 2.21c) gets reduced at constant temperature to the form

$$dG = VdP = R \cdot T d \ln P \quad (2.41)$$

$$\int_{P_1}^{P_2} dG = R \cdot T \int_{P_1}^{P_2} d \ln P = R \cdot T \cdot \left(\frac{P_2}{P_1} \right) \quad (2.42)$$

$$= G(P_2, T) - G(P_1, T) \quad (2.43)$$

If $P_1 = 1 \text{ bar}$ (10^5 Pa), $G(P_1, T)$ is the Gibbs energy in the standard state at temperature T and can be denoted as ${}^\circ G$, thus equation (2.43) can be rewritten as

$$G(P_2, T) = {}^\circ G + R \cdot T \cdot \ln(P_2/1) = {}^\circ G + R \cdot T \cdot \ln(P_2) \quad (2.44)$$

In chemistry literature, it is common to refer to a term ‘fugacity’ in the case of non-ideal gases. At high temperatures as it is common in metallurgy, gases are near ideal and the term fugacity is considered superfluous.

Dalton’s law of Partial pressures states that the partial pressure of a gas ‘A’, p_A , in a mixture of gases ‘A’, ‘B’, ‘C’, etc., is given by

$$P_A = X_A \cdot P \quad (2.45)$$

where P is the total pressure of the gas mixture ($P = p_A + p_B + p_C \dots$) and X_A is the mole fraction of gas species A.

2.4.6 Ellingham diagrams

Consider the reaction between metal M (s) and oxygen to form oxide MO_2 (s):



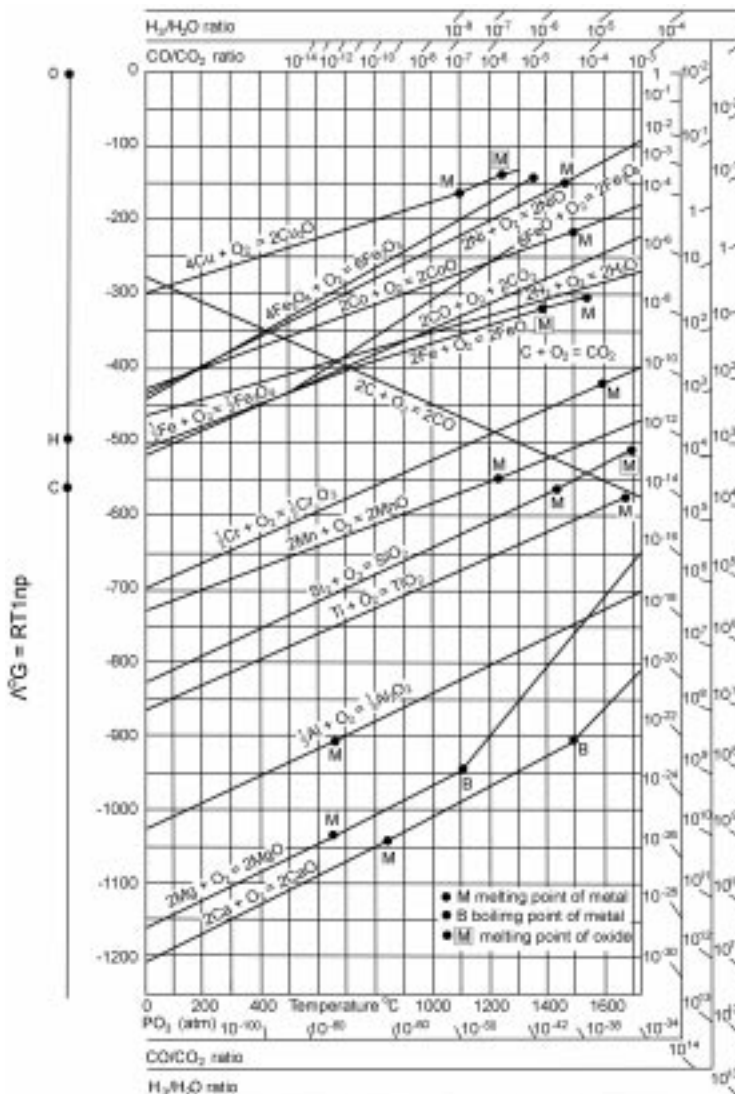
At equilibrium

$$\Delta G = (G_{\text{products}} - \Sigma G_{\text{reactants}}) = 0 \quad (2.47)$$

Assuming that the metal and the oxide phases are mutually insoluble and that they are in their standard state, and, further remembering from equation (2.44), that $G_{O_2} = {}^oG_{O_2} + RT \ln p_{O_2}$, equation (2.47) can be rewritten as

$${}^oG_{MO_{2-x}} ({}^oG_M + {}^oG_{O_2}) = \Delta^oG = RT \ln p_{O_2} \quad (2.48)$$

Figure 2.11 shows a plot of Δ^oG as a function of temperature for a number of metal–metal oxide systems. The stability of the oxide increases as we go down

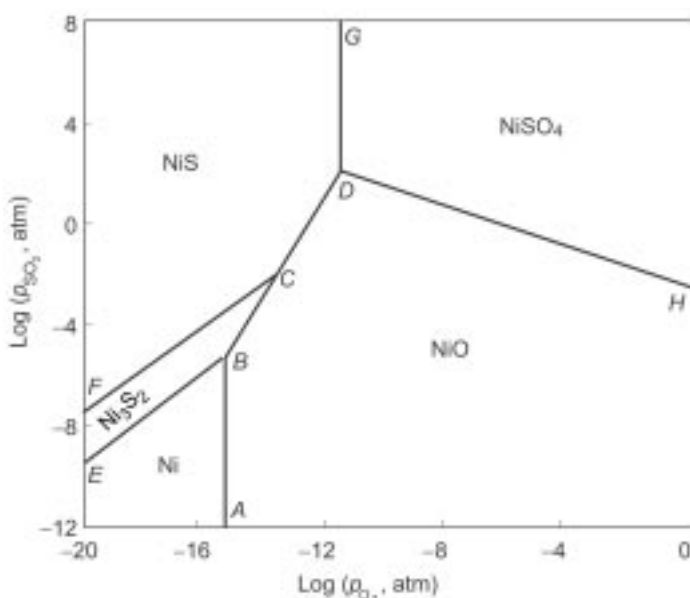


2.11 Ellingham diagram for oxides.⁶

the diagram. The slope of the lines are indications of $-\Delta^\circ S$ for reaction (2.45). The intercept at 0K corresponds to $\Delta^\circ H$ at 0K. The diagram assumes that the enthalpy and entropy changes are constant if there is no phase transformation for the metal or oxide phase. The increase in the $\Delta^\circ G$ with increasing temperature is indicative of the decreasing stability of the oxide. With melting of the metal or the oxide, there are accompanying changes in $\Delta^\circ S$ and correspondingly, in the slope of the lines, marked by sharp break points. The line for CO formation has a negative slope indicating the increase in entropy due to the formation of two gas molecules from one oxygen molecule. As crossing of the lines marks the relative stabilities of the oxides, the diagram indicates the reducibility of a number of oxides by carbon if the temperature is sufficiently raised.

Logarithmic scales corresponding to p_{O_2} as well as CO/CO₂ and H₂/H₂O ratios, introduced in the Ellingham diagram by Richardson and Jeffes, enable the direct reading of the equilibrium partial pressures of oxygen or the corresponding CO/CO₂ and H₂/H₂O ratios directly from the diagram. The diagram is extremely useful in metallurgical processes, as, for example, the choice of reductants, the temperature of reduction as well as the partial pressure ratios.

Similar diagrams have been worked out for sulphides, chlorides, nitrides and other compounds of interest in high temperature reactions.



2.12 The phase stability diagram for Ni-S-O system at 1000K.⁷

2.4.7 Phase stability diagrams (predominance area diagrams)

Another extremely useful set of diagrams representing the stabilities of pure phases is the phase stability diagram or predominance area diagrams. These are generally isothermal diagrams wherein the chemical potential of one component in a ternary system is plotted as a function of another. These diagrams have been found useful in the case of M-S-O system, where M is a metal like Cu, Ni, Fe or Pb (occurring as sulphide). A typical such diagram used for studying the roasting of nickel sulphide is presented in Fig. 2.12. The usefulness of the diagram is well demonstrated in the case of mixed sulphides, where it is possible to superimpose two stability diagrams.

2.5 Thermodynamics of solutions

The concept of pure substances is mainly of theoretical interest. In reality, the systems that are encountered are often multicomponent systems when the components dissolve in each other forming solutions. Even the so-called ultra pure substances have dissolved impurities, albeit in extremely small amounts. Thus, it is an important part of thermodynamics to deal with solutions.

The concept of solution is essentially two components forming a single phase in the macroscopic sense. In the micro level, this refers to an intimate mixing of atoms or molecules. The process of solution is often referred to as ‘mixing’, which is somewhat misleading. Gases ‘mix’ completely. In liquid phase, there are many cases where two liquids do not mix with each other, as, for example, oil and water at room temperature or silver and iron at 1600 °C. In the case of solids, those of similar crystal structure often form ‘mixed crystals’ or solid solutions, which are of single phase, as can be seen by X-ray diffraction measurements.

2.5.1 Integral and partial molar properties

In dealing with extensive thermodynamic properties like enthalpy, entropy or Gibbs energy, it is common to refer to one mole of the substance. Exemplifying this in the case of Gibbs energy, 0G_A refers to one mole of substance ‘A’ in pure state. On the other hand, in a solution containing ‘i’ different species, the molar Gibbs energy, G_m is given by

$$G_m = G(\text{total})/(n_A + n_B + n_C \dots n_i) \quad (2.49)$$

where the ‘n’ terms refer to the number of moles of the different species in solution and G_m is the *integral molar Gibbs energy* of the solution. If the increment in G , caused by the addition of dn_A moles of component A to a very large amount of the solution is dG , this increment per mole of A, denoted as \bar{G}_A will be

$$\bar{G}_A = (\partial G / \partial n_A)_{P,T,n_B,n_C\dots} \quad (2.50)$$

\bar{G}_A is referred to as the *partial molar Gibbs energy* of A in the solution of defined pressure, temperature and composition.

This leads to the relationship for the total change in the Gibbs energy due to the addition of the various components as

$$dG = \bar{G}_A \cdot dn_A + \bar{G}_B \cdot dn_B \dots \quad (2.51)$$

By the addition and removal of $n_A + n_B + n_C \dots n_i$ moles of the components, and considering the Gibbs energy of the solution per mole, it can be shown that

$$G_m = X_A \cdot \bar{G}_A + X_B \cdot \bar{G}_B \dots \quad (2.52)$$

By considering the Gibbs energy for $n_A + n_B + n_C \dots n_i$ moles of solution followed by complete differentiation, it can be shown that

$$X_A \cdot d\bar{G}_A + X_B \cdot d\bar{G}_B \dots = 0 \quad (2.53)$$

The above expression is referred to as *Gibbs-Duhem equation* and is used to compute the partial molar quantity of a second species with a knowledge of that of the first one. The above relationships hold for even other thermodynamic properties like enthalpy and entropy. It is to be noted that \bar{G}_B is identical with the chemical potential of component B in the solution, represented usually as μ_B .

From a knowledge of the integral molar property, the partial molar properties can be arrived at. In the case of a binary solution A-B, the relationship is given by

$$\bar{G}_B = G_m + (1 - X_B) \frac{dG_m}{dX_B} \quad (2.54)$$

This equation can be used graphically to get the partial molar quantities by drawing a tangent to the integral molar Gibbs energy curve with respect to composition (drawn with composition on the x-axis) at a desired composition and reading of the intersection of the tangent on the y-axes (both sides) corresponding to the pure components.

Similar relationships can be derived for ternary and multicomponent systems as well.

2.5.2 Relative integral and relative partial molar properties

Except in the case of molar volumes, it is not possible to determine the absolute values of integral molar properties of solutions experimentally. On the other hand, the difference in the integral molar property of the solution and those corresponding to a ‘mechanical’ mixture of components is experimentally determined. This difference, referred to as the *relative integral molar Gibbs energy*, ΔG^M represented by the equation:

$$\Delta G^M = G_m - (X_A \cdot {}^oG_A + X_B \cdot {}^oG_B) \quad (2.55)$$

Similarly, the relative partial molar Gibbs energy of component A, ΔG_A^M , can be described as corresponding to one mole of each component in solution. The mathematical relationships between relative integral and partial molar properties are analogous to those of the integral and partial molar properties presented earlier in equations (2.52) to (2.54). The relative partial molar Gibbs energy of A, ΔG_A^M is related to the partial molar Gibbs energy of A by means of the relationship

$$\Delta G_A^M = \bar{G}_B - {}^oG_B \quad (2.56)$$

The relative integral molar enthalpies, ΔH^M are negative for solutions with exothermicity while they are positive in the case of endothermic solution formation. On the other hand, the relative integral molar entropies are always positive as the configurational entropy increases by the solution of one component in another. Consequently, the relative integral molar Gibbs energies are always negative in the case of spontaneous solutions as otherwise, the driving force is in the opposite direction. The extent of the negative value is dependent on the relative magnitudes and signs of the enthalpy and entropy terms.

2.5.3 The concept of activity

Activity of a component in a solution, introduced by G.N. Lewis in 1907, is often referred to as the concentration corrected for the intercomponent interactions. It is represented mathematically as

$$\Delta G_B^M = (\bar{G}_B - {}^oG_B) = RT \ln a_B \quad (2.57)$$

where a_B refers to the activity of component B in solution. Equation (2.57) can be graphically represented in Fig. 2.13 along with the partial and integral molar properties.

2.5.4 Chemical potentials and equilibrium constant

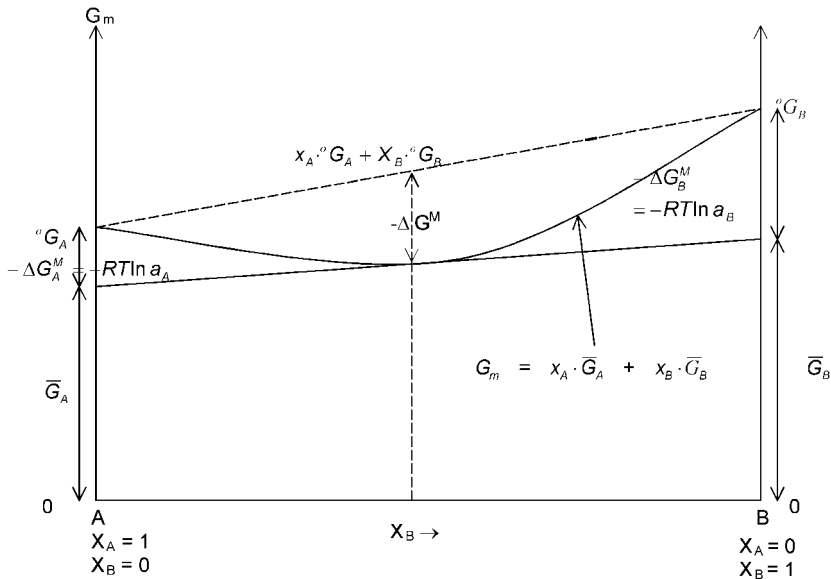
For a chemical reaction in chemical equilibrium, the sum of the Gibbs energies of the reactants will be equal to that of products. as shown in equation (2.47). This provides a basis for an expression for equilibrium constant on the basis of Gibbs energies. For example, for a reaction



where underlines signify solutions. Equation (2.47) can be formulated as

$$\bar{G}_{\text{Fe}} + \bar{G}_{\text{O}_2} = \bar{G}_{\text{FeO}} \quad (2.59)$$

By incorporating equations (2.47) and (2.57), equation (2.59) can be rewritten as



2.13 Graphical representation of the integral and partial molar properties of the system A-B. The line $x_A \cdot {}^oG_A + x_B \cdot {}^oG_B$ corresponds to the 'mechanical' mixture of the components A and B.

$$2^oG_{Fe} + RT \ln a^2_{Fe} + {}^oG_{O_2} + RT \ln p_{O_2} = 2^oG_{FeO} + RT \ln a^2_{FeO} \quad (2.60)$$

And this equation can be rewritten as

$$\begin{aligned} (2^oG_{FeO} - 2^oG_{Fe} - {}^oG_{O_2}) &= \Delta^oG = -RT \ln (a^2_{FeO}/a^2_{Fe} \cdot p_{O_2}) \\ &= -RT \ln K_R \end{aligned} \quad (2.61)$$

where ' K_R ' is the equilibrium constant. The temperature coefficient for the equilibrium constant can be derived as

$$\begin{aligned} \frac{d \ln K_R}{dT} &= \frac{1}{R} \left(\frac{\Delta^oG_R}{T^2} - \frac{\left(\frac{\partial \Delta G_R}{\partial T} \right)_P}{T} \right) \\ &= \frac{1}{R \cdot T^2} (\Delta^oH_R + T \Delta^oS_R) = \frac{\Delta^oH_R}{R \cdot T^2} \end{aligned} \quad (2.62)$$

Δ^oH_R corresponding to the enthalpy of the reaction.

2.5.5 Ideal solutions – Raoult's law

Examining the vapour pressures of components in solution in condensed state, Raoult postulated that

$$P_B = {}^o p_B \cdot X_B \quad (2.63)$$

where P_B and ${}^o p_B$ are the partial pressures of B in solution and pure state respectively. This would lead to the relationship for an *ideal solution* as

$$a_B = X_B \quad (2.64)$$

which is often termed as *Raoult's law*. In reality, many solutions deviate from equation (2.59). Solutions wherein there is repulsive interaction between the components show a positive deviation ($a_B > X_B$) while, in the case of the components exhibiting attractive interactions with each other, the solution would show a negative deviation ($a_B < X_B$).

For non-ideal solutions, the deviation from Raoult's law is denoted by the ratio between the activity and the mole fraction, a_B/X_B , referred to as the *activity coefficient*, γ_B . In the case of ideal solutions, the value of the activity coefficient is unity, while values less than unity are indicative of attractive forces between the components in solution and negative deviation from Raoult's law. Activity coefficient values more than unity mark repulsive forces between the components and positive deviation from Raoult's law.

The relative integral molar enthalpy of mixing for ideal solutions is zero as there are no attractive or repulsive interactions between the components. For the same reason, the different component atoms have no preferential sites and the mixing will be random. Thus, ΔS^M will have a maximum value. From statistical mechanics considerations, an expression for relative integral molar entropy for ideal solutions could be derived, which is presented in equation (2.65).

$$\Delta S^M = -R \sum X_i \ln X_i \quad (2.65)$$

The relative molar Gibbs energy for ideal solutions will thus be the combined effect of the enthalpy and entropy terms, *viz.*

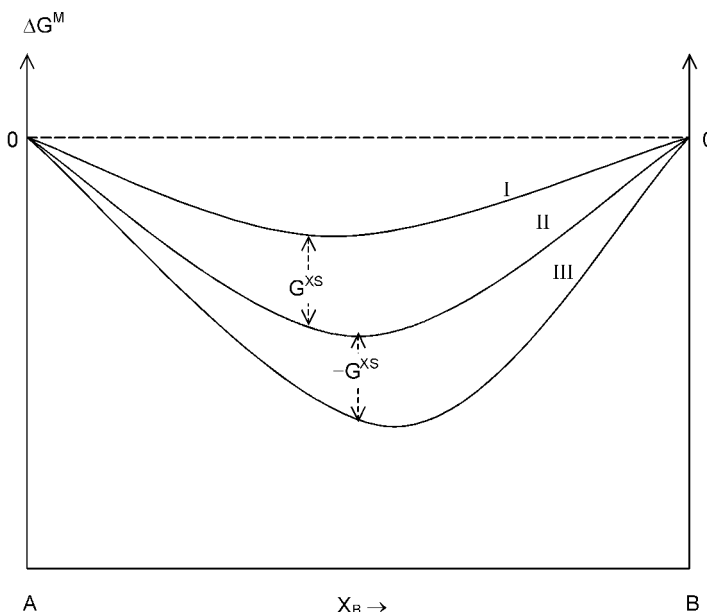
$$\Delta G^M = RT \sum X_i \ln X_i \quad (2.66)$$

2.5.6 Excess properties

The excess property is defined as the difference between the actual value that would be expected if the solution were ideal. For example, in the case of Gibbs energy, the integral molar excess Gibbs energy, G^{XS} , can be expressed as

$$G^{XS} = \Delta G^M - \Delta G^{M, \text{ideal}} \quad (2.67)$$

The relationship between ΔG^M and G^{XS} in the case of a binary solution A-B is presented in Fig. 2.14.



2.14 Excess Gibbs energies in the case of a binary system A-B.

I Repulsive interactions between A and B.

II Ideal solution.

III Attractive interactions between A and B.

2.5.7 Ideality and bond energies

The enthalpies and entropies of reactions as well as the concept of ideality can be illustrated by considering the changes in the bond energies involved in the reaction



The energy change associated with the above reaction can be denoted as ΔE .

$$\Delta E = 2E_{A-B} (E_{A-A} + E_{B-B}) \quad (2.69)$$

where E_{A-B} , E_{A-A} and E_{B-B} are the energies associated with the atom pairs in the subscript. If the probability of forming a A-B bond is denoted as P_{A-B} , the enthalpy of reaction (2.63) can be derived as

$$\Delta H^M = P_{A-B} \cdot \Delta E = P_{A-B} \cdot [2E_{A-B} - (E_{A-A} + E_{B-B})] \quad (2.70)$$

If the energy associated with an A-B bond is the average of the energies of A-A and B-B bonds, the solution process does not involve any net energy change. Consequently, ΔE and ΔH^M will be zero. Formation of ideal solutions require that the components involved are chemically similar.

2.5.8 Regular solutions

The concept of regular solutions was first proposed by Hildebrand in 1950. According to this, a regular solution can have non-ideal enthalpies, while the entropies of mixing are considered ideal. The entropy term has been restricted, by later workers, to configurational entropy and does not include thermal entropy. Thus, the relative molar entropy of mixing for a regular solution would be given by equation (2.60). ΔH^M can be shown to be a symmetrical function with respect to composition in the case of a binary solution A-B and is given by the equation

$$\Delta H^M = \Omega \cdot X_A \cdot X_B \quad (2.71)$$

where Ω is a constant independent of temperature and composition. From bond energy considerations, the constant Ω can be shown to be

$$\Omega = Z \cdot N \cdot \Delta E \quad (2.72)$$

where Z is the coordination number of the atoms in solution, N is the Avogadro's number and ΔE has the same significance as in equation (2.64). Assuming that these terms are constant with respect to temperature and composition, the relative integral molar enthalpy of mixing is given by the relationship

$$\Delta H^M = (Z \cdot N \cdot \Delta E) \cdot X_A \cdot X_B \quad (2.73)$$

which is identical with equation (2.66). The concept of regular solutions has an inbuilt inconsistency as solutions with non-zero enthalpies of mixing can not have ideal entropies of mixing. But the concept is found very helpful in the case of high temperature systems.

2.5.9 Henry's and Sievert's laws

In the case of dilute solutions, the activity coefficient of the solute is found to vary linearly with composition. This behaviour is referred to as *Henry's law* which is normally designated as

$$a_B/X_B = \gamma^\infty_B \quad (2.74)$$

where γ^∞_B is referred to as Henry's constant.

It is observed that when the solute obeys Henry's law, the solvent obeys Raoult's law in the same concentration range. This could be explained on the basis of the interatomic interactions between the solute and the solvent.

In the case of diatomic gases dissolving in metals in low amounts in atomic form, the amount of the gas dissolved was found by Sievert to be proportional to the square root of the partial pressure of the diatomic gas. Thus, the solubility of nitrogen in liquid iron can be represented as

$$X_N = k \cdot \sqrt{p_{N_2}} \quad (2.75)$$

Sievert's law is a corollary of Henry's law.

2.5.10 Standard states

In most of the industrial production of base metals, the choice of pure metal as the standard, *viz.*

$$\gamma_i \rightarrow 1 \text{ when } X_i \rightarrow 1 \quad (2.76)$$

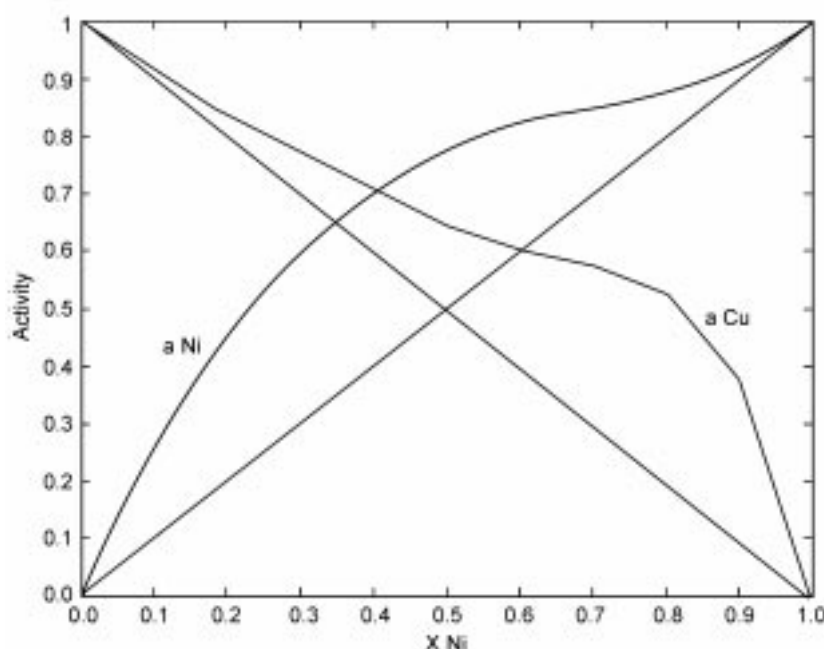
is often impractical as the impurity elements are in low concentrations. Hence, standard states corresponding to Henry's law, *viz.*

$$f_i \rightarrow 0 \text{ when } X_i \rightarrow 0 \quad (2.77)$$

$$f_i \rightarrow 0 \text{ when atom \% } i \rightarrow 0 \quad (2.78)$$

$$f_i \text{ (wt \%)} \rightarrow 0 \text{ when wt. \% } i \rightarrow 0 \quad (2.79)$$

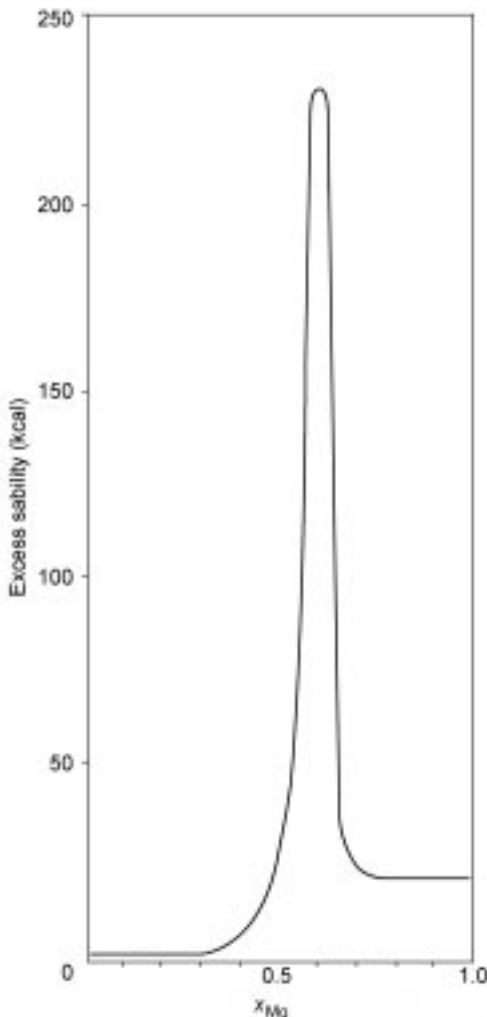
where the 'f'-terms refer to the activity coefficients corresponding to Henrian standard states.



2.15 Activity of tin and gold in the binary Ni-Cu system at 600 °C.

2.5.11 Stabilities and excess stabilities

From a consideration of the thermodynamics of a number of binary metallic molten systems, Darken⁸ suggested that the thermodynamic behaviour of the components in the terminal regions of the solution with respect to composition is expressed by simple expressions and that the solvent and solute have slightly differing behaviours. For a solution A-B, in the region where A is the solvent and B, the solute, the activity coefficients are given by the expressions



2.16 Excess stability as a function of composition in the system Mg-Bi at 700°C.⁸

$$\ln \gamma_A = \alpha_{AB} (1 - X_A)^2 \quad \text{and} \quad \ln \gamma_B = \alpha_{AB} (1 - X_B)^2 + I \quad (2.80)$$

where α_{AB} is a constant independent of composition in the range where A is the solvent and I is an integration constant. Hillert suggests that the difference between the solvent and the solute can be considered as being due to different standard states and the integration constant may be considered as factor for the change of standard state. Darken further evolved the concept of *excess stability*, which is the second derivative of the excess Gibbs energy. The mathematical expression for excess stability in the case of the binary system A-B, as shown by Darken, is

$$(d^2G^{XS}/dX_B^2) = -2RT[d \ln \gamma_B/d(1 - X_B)^2] \quad (2.81)$$

With the occurrence of strong interactions in the system as, for example, formation of the intermetallic compound Mg₂Bi in the Mg-Bi binary, the excess stability function showed a sharp peak corresponding to this composition. This is shown in Fig. 2.16. Darken further showed that the concept of excess stability can be applied, with advantage to even molten oxides as well as aqueous systems.

2.6 Thermodynamics of multicomponent dilute solutions

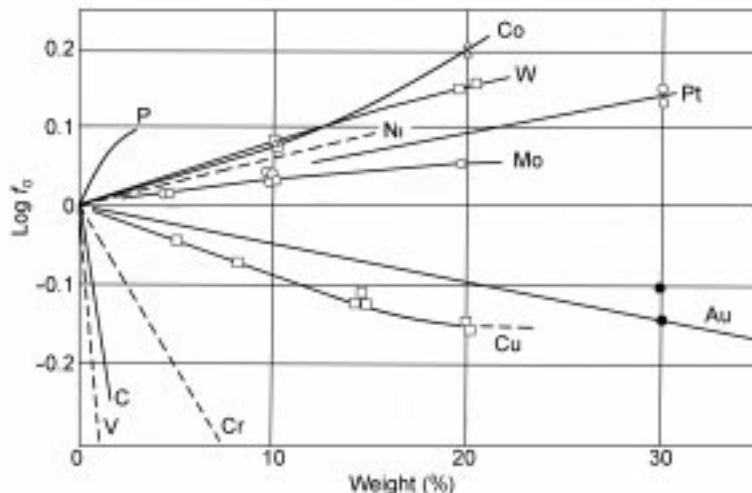
In industrial production of base metals like iron or copper, often dilute solutions are encountered with a number of solute elements dissolved in the same. An understanding of the thermodynamic behaviour of solutes in such solutions is imperative when optimizing these processes.

The thermodynamic behaviour of a solute in a binary solution is described by Henry's law. In ternary solutions with two solutes, it can be assumed that Henry's law holds when the concentrations of the solutes are extremely low, as solute-solute interactions are negligible. With increasing concentrations, the solute-solute interactions affect the thermodynamics of the system and deviations from Henry's law occur. Such deviations in the case of the activity coefficient of oxygen in liquid iron at 1600 °C for a number of solutes are presented in Fig. 2.17.

2.6.1 Wagner's equation

The deviation from Henry's law by solute-solute interactions has been expressed mathematically by means of a MacLaurin type of equation shown below:

$$\begin{aligned} \ln \gamma_B &= \ln \gamma_B^\infty + X_B \cdot (\partial \ln \gamma_B / \partial X_B) + X_C \cdot (\partial \ln \gamma_B / \partial X_C) \dots \\ &\quad + (X_B/2)^2 (\partial^2 \ln \gamma_B / \partial X_B^2) + (X_C/2)^2 (\partial^2 \ln \gamma_B / \partial X_C^2) \dots \\ &\quad + (X_B X_C) (\partial^2 \ln \gamma_B / \partial X_B \cdot \partial X_C) + (X_B X_D) (\partial^2 \ln \gamma_B / \partial X_B \cdot \partial X_D) \dots \end{aligned} \quad (2.82)$$



2.17 The variation of the activity coefficient of oxygen in liquid iron at 1600°C for a number of solutes. Henrian standard state is used for oxygen activity coefficient.⁹

Wagner suggested that, at low concentrations, the second order terms can be neglected and equation (2.82) may be reduced to

$$\ln \gamma_B = \ln \gamma_B^\infty + X_B \cdot \epsilon^{(B)}_B + X_C \cdot \epsilon^{(C)}_B \dots \quad (2.83)$$

where

$$\epsilon^{(C)}_B = [\partial \ln \gamma_B / \partial X_C]_{X_A \rightarrow 1; X_B, X_C \dots \rightarrow 0}$$

(Standard state: $\gamma_i \rightarrow 1$ when $X_i \rightarrow 1$)

If the standard state is changed to $f_B(\text{wt \%}) \rightarrow 1$ when $\text{wt \%}B \rightarrow 0$, the above expression becomes

$$\log_{10} f_B = \log_{10} \gamma_B^\infty + \text{wt \%}B \cdot \epsilon^{(B)}_B + \text{wt \%}C \cdot \epsilon^{(C)}_B \quad (2.84)$$

where $\epsilon^{(C)}_B = [\partial \log \gamma_B / \partial \text{wt \%}C]_{\text{wt \%}A \rightarrow 1; \text{wt \%}B, \text{wt \%}C \rightarrow 0}$. The ‘ ϵ ’ and ‘ e ’ terms are termed interaction parameters.

At higher concentrations of the solute, the second order terms in the MacLaurin expression in equation (2.77) may have to be taken into account.

$$\begin{aligned} \ln \gamma_B &= \ln \gamma_B^\infty + X_B \cdot \epsilon^{(B)}_B + X_C \cdot \epsilon^{(C)}_B \dots + (X_B/2)^2 \rho_B^{(B)} \\ &\quad + (X_C/2)^2 \rho_B^{(C)} + (X_B X_C) \cdot \rho_B^{(B,C)} + (X_B X_D) \cdot \rho_B^{(B,D)} \end{aligned} \quad (2.85)$$

where the ‘ ρ ’-terms correspond to the second order terms in the MacLaurin expression in equation (2.77).

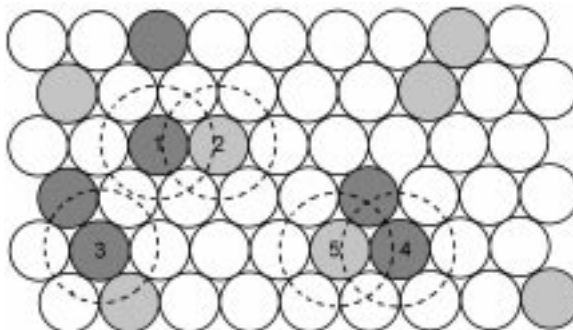
2.6.2 The central atom description¹⁰

The solute–solute interactions can be elegantly described by the central atom model by Lupis and the illustration reproduced from *Chemical Thermodynamics of Materials* by Lupis¹⁰ is presented in Fig. 2.18. The circle filled with lines is solute atom B and the one with dots is solute atom C are solute atoms and blank circles are solvent atoms.

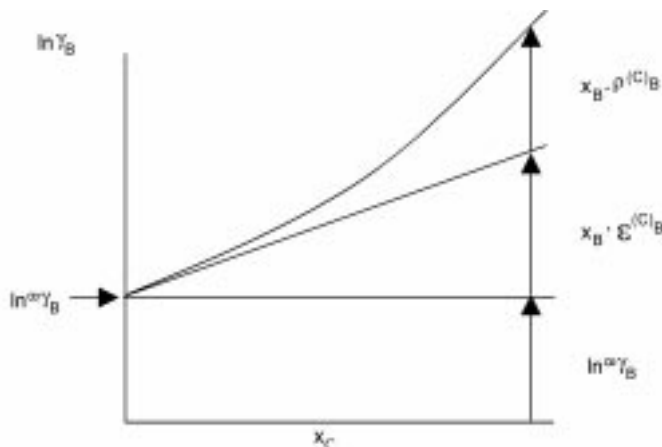
$$\text{Configuration 1} = \epsilon^{(C)}_B, 2 = \epsilon^{(B)}_C, 3, 4 = \rho_B^{(B,C)}, 5 = \rho_C^{(B)}$$

The deviation from Henry's law and the application of the MacLaurin expression is illustrated in Fig. 2.19.

Equations (2.78) and (2.80) are commonly used to calculate the interaction parameters. It should be remembered that these are valid only when the solute



2.18 Solute–solute interactions according to the central atom model by Lupis.¹⁰



2.19 Application of MacLaurin expression for describing the deviation from Henry's law.¹¹

concentrations approach zero. Darken has shown, by applying the Gibbs–Duhem equation, that, if these equations are used for solutes at finite concentrations, it would lead to erroneous results. Equation (2.78) has been modified by Pelton and Bale as

$$\ln \gamma_B = \ln \gamma_B^\infty + \ln \gamma_A + X_B \cdot \epsilon^{(B)}_B + X_C \cdot \epsilon^{(C)}_B \dots \quad (2.86)$$

This equation is compatible with Gibbs–Duhem equation and can be used for finite concentrations of solutes.

2.6.3 Estimations of interaction parameters

Extrapolation of interaction parameters from one temperature to another can be carried out by introducing enthalpy interaction parameter, $\eta^{(C)}_B$ and entropy interaction parameter, $\sigma^{(C)}_B$.¹² These terms are related to the interaction parameter, $\epsilon^{(C)}_B$ by the relationship:

$$RT \epsilon^{(C)}_B \cdot X_C = \eta^{(C)}_B \cdot X_C + T \cdot \sigma^{(C)}_B \cdot X_C \quad (2.87)$$

In analogy with the Gibbs–Helmholtz equation, it can be written

$$(\partial \epsilon^{(C)}_B / \partial (1/T)) = \eta^{(C)}_B / R \quad (2.88)$$

and the ratio between $\epsilon^{(C)}_B$ and $\eta^{(C)}_B$ is given by

$$(\epsilon^{(C)}_B / \eta^{(C)}_B) = 1/R ((1/T) - (1/\tau)) \quad (2.89)$$

The term ‘ τ ’ is a correction term having the unit of temperature. τ is related to the enthalpy and entropy interaction parameters by the equation

$$\eta^{(C)}_B = \tau \cdot \sigma^{(C)}_B \quad (2.90)$$

The value of τ has been estimated in the case of a number of non-ferrous systems as 1800K and in the case of ferrous systems as *circa* 2100K. This enables the prediction of $\eta^{(C)}_B$ from a known value of $\epsilon^{(C)}_B$ as well as estimation of $\epsilon^{(C)}_B$ at the temperatures using equation (2.85).

In the case of systems where there is no data on interaction parameters, the empirical equation proposed by Jacob and Alcock can be used with some success. This is given here:

$$\epsilon^{(C)}_B = -n[(\gamma_{B(A)} / \gamma_{B(C)})]^{1/n} \cdot \gamma_{C(A)}^\alpha - 1 \quad (2.91)$$

where the ‘ γ ’ terms are binary Henry’s coefficients and n and α are empirical constants, with the values $n = 4$ and $\alpha = \frac{1}{2}$. While equation (2.87) is reasonably successful in the case of non-ferrous solutes, it has been shown that caution should be exercised in applying the same to transition metal solutes.

2.6.4 Interaction parameters and solubility of oxides in metallic melts

The concept of interaction parameters has been applied to predict the minima in the solubility curves in a number of metallic melts by St Pierre.¹³ Successful prediction of the minimum in the case of the precipitation of alumina in the case of Fe-O-Al system is a classical case that has applications in the calculations of precipitation of alumina inclusions from steel melts.

2.7 Modelling of metallic systems

Thermodynamic modelling is essential in the case of systems, where there is lack of experimental data or where experimental measurements are extremely difficult. This is particularly true in the case of multicomponent systems. In modelling the thermodynamic properties, attention has been focused on two properties, *viz.* the enthalpies and Gibbs energies of mixing.

In order to extrapolate thermodynamic data from known to unknown composition and temperature ranges, it is generally felt necessary to express enthalpies and Gibbs energies by means of a suitable mathematical expression. In view of the rapid developments in metallurgy and materials, it is necessary to handle the thermodynamics of systems with many components over a wide range of temperatures, necessitating computerized calculations. Thus, the need for models for computer calculations has been felt during the past three decades. One of the earliest expressions for integral molar excess Gibbs energy was due to Margules.¹⁴ Hillert¹⁵ has proposed the use of the Redlich–Kister polynomial to express excess Gibbs energy. It is noteworthy that, as Darken suggests, in the case of binary systems, that series expressions may be unnecessary as the thermodynamic behaviour of these systems is fairly simple except in the central composition region.

Today, based on various empirical or semi-empirical models, thermodynamic databases have been developed that can perform a variety of operations in the case of multicomponent systems. FACT-Sage, MT-data and Thermo-Calc are a few to be named and which have been widely used. In this chapter, only the sublattice model, which is the basis for the Thermo-Calc software will be presented.

2.7.1 The two sublattice model¹⁶

The above model places the substitutional and interstitial sites in a metallic lattice as two distinct sublattices. The entropy of mixing is restricted in each sublattice and the total entropy would be the sum of the entropies of the sublattices. A similar description for ionic melts, with anionic and cationic groupings has been presented by Temkin¹⁷ earlier.

In the two sublattice model, the composition is described in terms of lattice

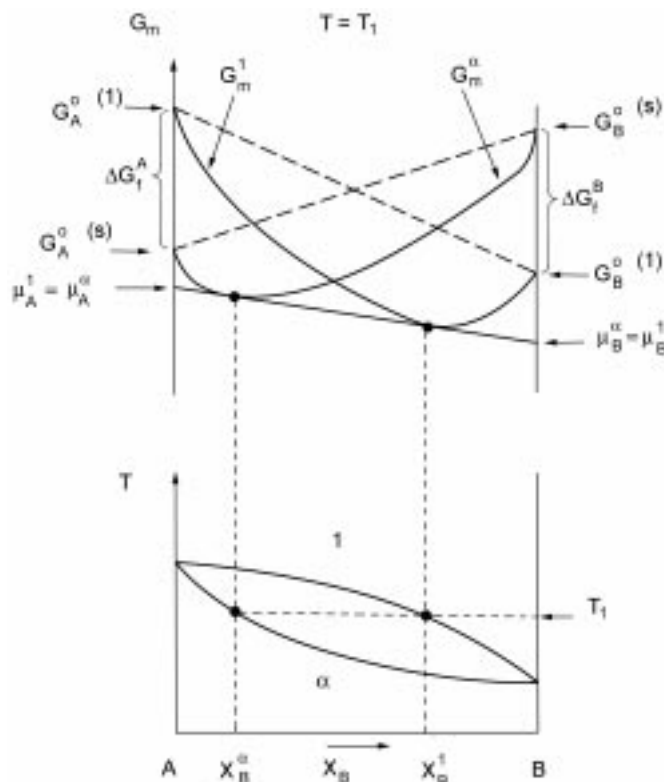
fraction, Y_i . The basic description of the integral molar Gibbs energy is given by the expression

$$G_m = \sum Y_i \cdot {}^o G_i - T \cdot \Delta S^{M, \text{ideal}} + G^{xs} \quad (2.92)$$

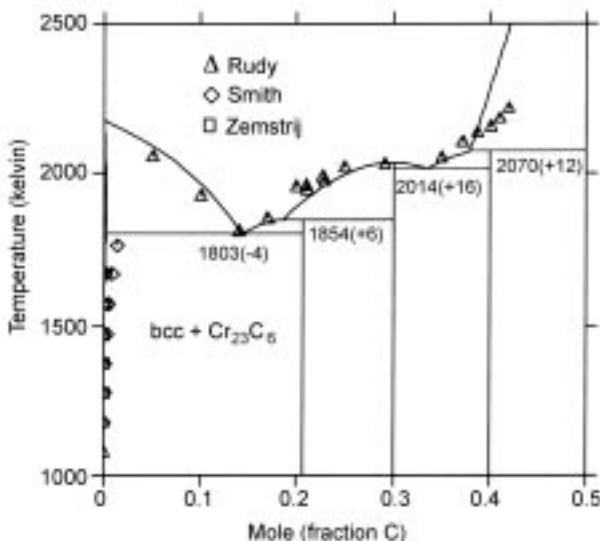
The model is extremely suitable for multicomponent systems with both substitutional and interstitial elements, especially in the solid state. With suitable modifications, the same type of description can be applied to ionic melts as well. The model is extremely suited for computerized applications for multi-component systems. The Thermo-Calc system¹⁸ is based on this model, with more sublattices when needed. The system has a variety of administrative programmes and is used worldwide.

2.7.2 CALPHAD approach

CALPHAD is an abbreviation for CALculation of PHAse Diagrams. In Section 2.4, the link between thermodynamics and phase diagrams has been presented. A



2.20 A schematic representation of Gibbs energy curves corresponding to the phase diagram shown in Fig. 2.8 with complete solubility in solid and liquid states corresponding to temperature T_1 .



2.21 The Cr-C phase diagram calculated using the evaluated parameters.¹⁹ The temperatures of the three-phase equilibrium shown in the figure are those calculated. The values in parentheses show the difference from the selected experimental values.

schematic representation of Gibbs energy curves corresponding to the phase diagram shown in Fig. 2.8 is illustrated in Fig. 2.20. Since phase diagrams are essentially thermodynamic descriptions of the phases in the system, it is necessary that the thermodynamic descriptions are compatible with the phase diagram information available. It should be possible to generate thermodynamic information by combining phase diagram data available with the results of thermodynamic experimental studies. Such efforts have progressed extremely well and the thermodynamic assessments of various systems available are based on CALPHAD approach. The Thermo-Calc system has been extremely valuable in this regard.

A typical phase diagram for Cr-C binary system,¹⁹ developed recently on the basis of the available thermodynamic and phase diagram information is presented in Fig. 2.21.

2.8 Thermodynamics of ionic melts

Salts as well as oxide melts are ionic in nature. An understanding of the thermodynamics of these materials is of importance in fused salt metals extraction as well as slag practice in pyrometallurgy.

The thermodynamic description of ionic liquid is complicated as the entropy of mixing is caused by the mixing of cations among themselves and anions in a

similar fashion. The analogy with the two sublattice model described in Section 2.7.1 is seen clearly here. In addition, in the case of silicate melts, the polymerization as SiO_2 content increases the complexity of the system. Pure SiO_2 has a three dimensional network of SiO_4 tetrahedra which are linked to each other by sharing of the corners, edges and sides.

Depolymerization is effected by the addition of basic oxides like CaO , which break the silicate network. This leads to the existence of a variety of silicate polymers as functions of composition and also with respect to temperature, the latter contributing to the entropy by the destabilization of the silicate polymers.

2.8.1 Temkin's¹⁷ and Flood *et al.*'s²⁰ description of ionic melts

It was long realized that the Raoultian description of ideal systems was not compatible with the experimental results of ionic melts. Temkin realized that this is due to the entropy of mixing in these melts and proposed that anions and cations should be grouped separately and the entropies of mixing should be calculated separately for each subgrouping. On this basis, Temkin suggested that the activity of a component, MA_2 , in a salt melt, is given by

$$a_{\text{MA}_2} = N_{\text{M}_{2+}} \cdot N^2_{\text{A}^-} \quad (2.93)$$

where $N_{\text{M}_{2+}}$ is the cation fraction of M^{2+} ions and A^- the anion fraction of A^- ions. Later on Flood, Førland and Grjotheim²⁰ introduced the concept of equivalent ion fractions. For example, in this case of a salt melt $\text{NaCl}-\text{CaCl}_2$, the activity of NaCl is given by component MA_2 in turn given by

$$a_{\text{NaCl}} = N'_{\text{Na}^+} \cdot N'_{\text{Cl}^-} \quad (2.94)$$

where N' terms are the equivalent ionic fractions. N_{Na^+} can be defined as

$$N'_{\text{Na}^+} = (n_{\text{Na}^+}/(n_{\text{Na}^+} + n_V + n_{\text{Ca}^{2+}})) = (n_{\text{Na}^+}/(n_{\text{Na}^+} + 2n_{\text{Ca}^{2+}})) \quad (2.95)$$

The choice of Temkin's or Flood *et al.*'s ion activity concept, according to Sridhar and Jeffes,²¹ is to be based on the extent of deviation of the system from ideality. For low values of ΔH^M , Temkin activities can be used while, for systems with high values of ΔH^M , it is more appropriate to use to concept of Flood *et al.*

Another word of caution is with respect to ion activities. Since the standard state becomes ambiguous, it is recommended to use Henrian standard states when ion activities are referred to.

In the case of systems with common ions, the bond energy descriptions (equation 2.70) can be used to describe the enthalpies of mixing. But the interactions are between the next-nearest neighbouring ions; for example, in the case of the system $\text{NaCl}-\text{CaCl}_2$, the interactions are between Na^+ and Ca^{2+} ions, while O^{2-} are the nearest neighbours to the cations.

2.8.2 Richardson's theory of ideal mixing of silicates²²

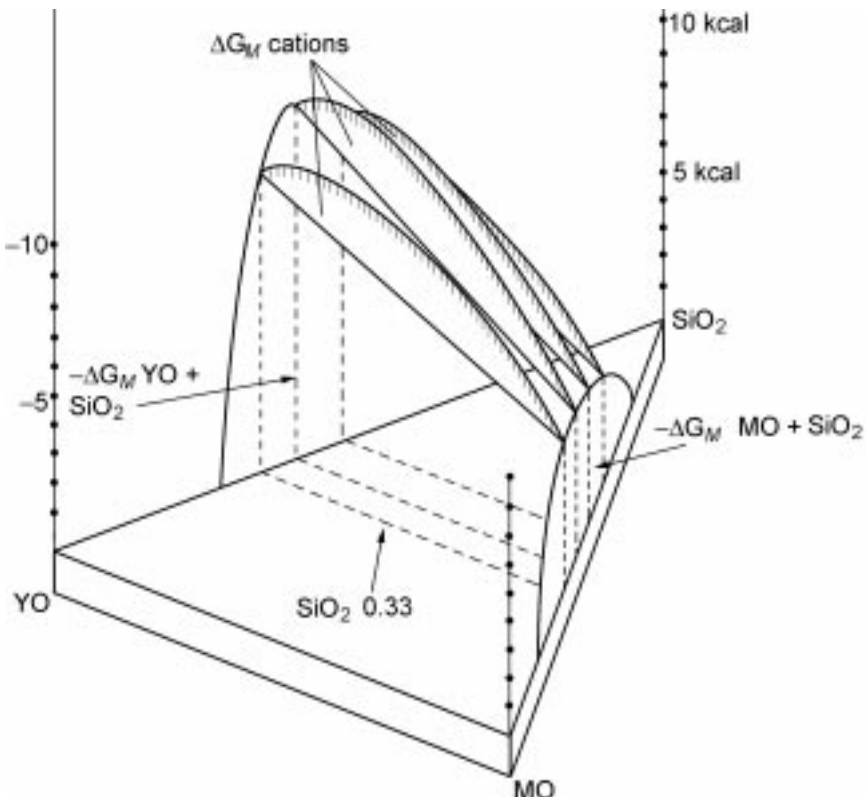
Richardson proposed that binary silicates of equal silica molfraction (such as $\text{FeSiO}_3 + \text{CaSiO}_3$) mix ideally with one another. This would mean that the enthalpy of mixing is zero and the entropy of mixing, which is the same as the configurational entropy arising from the mixing of cations only will be ideal. This is given by

$$\Delta S^M = -R[(X_{\text{MO}} \ln (X_{\text{MO}}/(X_{\text{MO}} + X_{\text{YO}})) + (X_{\text{YO}} \ln (X_{\text{YO}}/(X_{\text{MO}} + X_{\text{YO}})))]$$
(2.96)

The Gibbs energy of mixing is

$$\Delta G^M = -T \cdot \Delta S^M$$
(2.97)

The Gibbs energy surface for the formation of solutions $\text{MO} + \text{YO} + \text{SiO}_2$ is presented in Fig. 2.22. The theory of ideal mixing is very useful in estimating the ternary activities from the binary values. The validity of the theory is somewhat uncertain when the cation sizes differ widely.



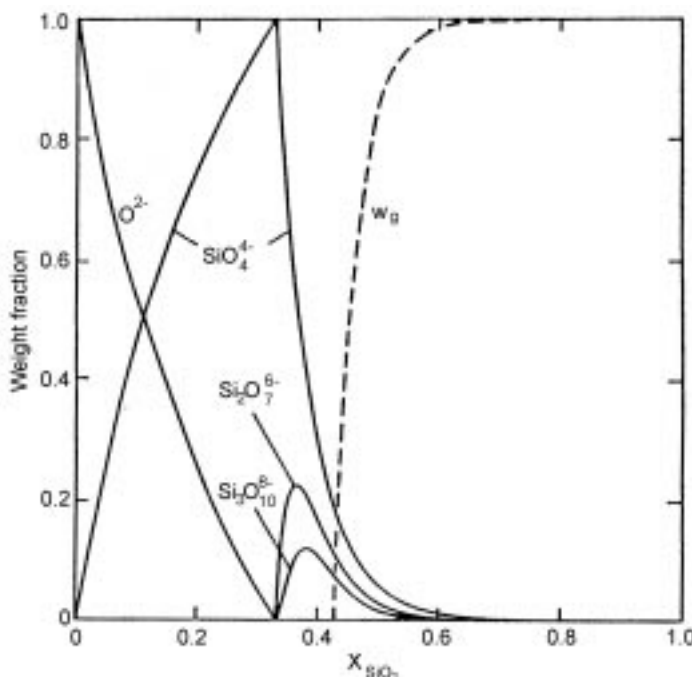
2.22 The Gibbs energy surface of $\text{MO} + \text{YO} + \text{SiO}_2$ solutions.²²

2.8.3 Lumsden's description of silicates⁵

Lumsden proposed that the silicate melts can be considered as melts consisting of O^{2-} ions and cations like Ca^{2+} , Fe^{2+} and even Si^{4+} , the latter by considering the SiO_4^{4-} tetrahedral as dissociating into Si^{4+} and O^{2-} ions. Lumsden's consideration demanded the visualization of pure covalent liquid silica in contrast to the fully ionized silica in the silicate. Lumsden introduced a change of the standard state in order to account for this. While the Lumsden description is contrary to the structure of silicates, it is found to be a very useful tool in empirical modelling of slags.

2.8.4 Slag models

A number of models have been developed for providing an adequate thermodynamic description of slags. These can be classified into structural models and semi-empirical models. Structural models are based on the polymer theory as applied to silicate melts, the pioneering work being that of Masson.²³ The calculated weight fractions of the various anionic species by the polymeric model is presented in Fig. 2.23. While these are successful for simple silicates, a



2.23 Calculated weight fractions of the anions in a silicate system. W_g refers to infinite chain.

great deal of further work is necessary to apply to multicomponent slags. Among the semi-empirical models, a few are briefly mentioned here.

Kapoor and Frohberg²⁴ presented a statistical thermodynamic treatment of silicate melts where units of one oxygen and two cations are visualized. The model was later expanded to more complex systems and is referred to as the IRSID model. Models based on silicate structure and quasichemical approach²⁵ have been developed by Pelton and his group, which form the basis for silicate descriptions for the Chemsage/F.A.C.T. system. Hillert and co-workers have extended their sublattice model to silicate systems.

A simple, empirical description of silicates could be achieved by combining the Temkin description with Lumsden description and describe the complex silicates as consisting of cations including Si^{4+} and O^{2-} ions. This was developed at the Royal Institute of Technology, Stockholm, and is often referred to as the KTH model.²⁶

The ionic solution can be represented as

$$(\text{A}^{2+}, \text{B}^{2+}, \text{Si}^{4+}\dots)_P (\text{O}^{2-})_Q \quad (2.98)$$

where P and Q are stoichiometric constants. The Gibbs energy of mixing in the melt is expressed as

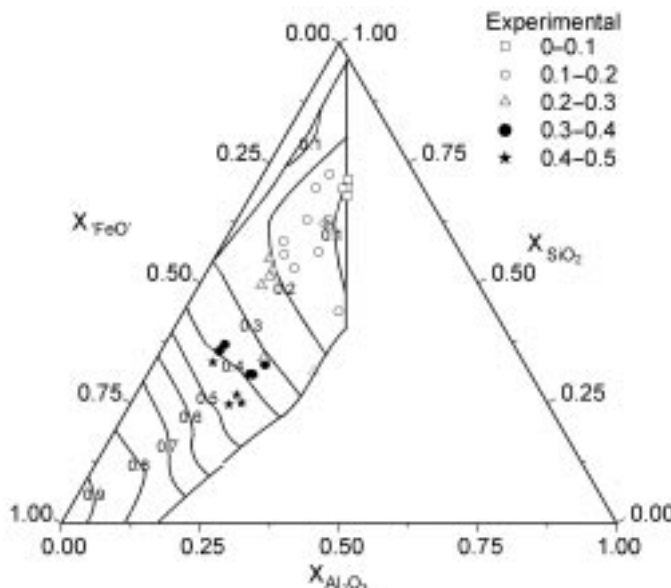
$$G_m = \sum X_{\text{C}_{i,\text{ci}}\text{O}_{ai}} G_{\text{C}_{i,\text{ci}}\text{O}_{ai}}^o + RT_p \sum y_{\text{C}_i} \ln y_{\text{C}_i} + G^{\text{XS}} \quad (2.99)$$

where $\text{C}_{i,\text{ci}}\text{O}_{ai}$ is the oxide component and ‘y’ terms refer to ion fractions. The excess Gibbs energy could be expressed by Redlich–Kister polynomial and the parameters could be derived from the available experimental data. The iso-activity lines of FeO, computed by the above model in the case of a ladle slag are presented in Fig. 2.24. The computation is enabled by a software, THERMOSLAG® developed by the present group.

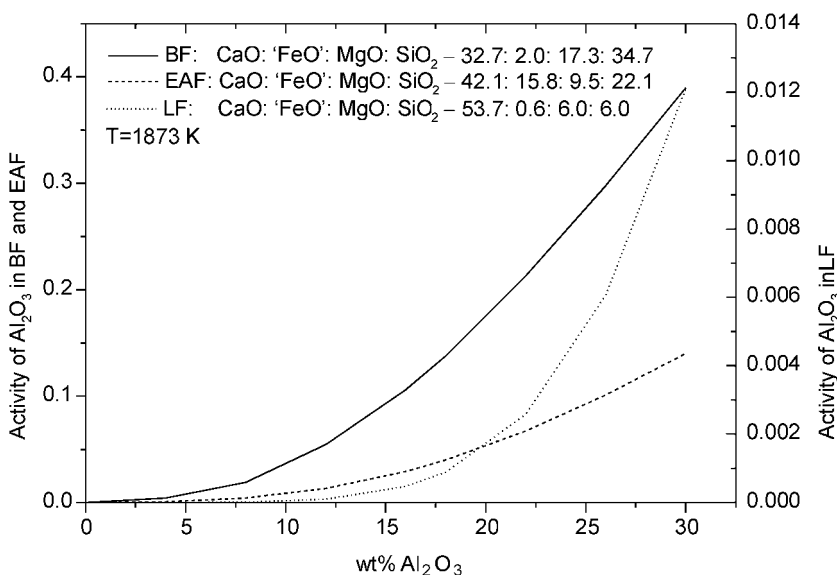
The activities of Al_2O_3 in the $\text{Al}_2\text{O}_3\text{-CaO}\text{-FeO}\text{-MgO-SiO}_2$ system at 1873K corresponding to blast furnace (BF), electric arc furnace (EAF) and ladle furnace (LF) processes computed by the KTH model using the THERMOSLAG® software is presented in Fig. 2.25. Model developments need accurate experimental data, which in many cases is lacking today.

2.8.5 Slag capacities

In refining of metals, it is important to know the ability of a slag to absorb impurities like sulphur or phosphorus. In order to enable this, in the case of sulphur, Fredriksson and Seetharaman²⁷ introduced the sulphide capacities, on the basis of equilibrium between slags and a gas phase with defined oxygen and sulphur potentials. The expression for sulphide capacity, C_s , as defined by Fincham and Richardson,²⁸ is



2.24 Calculated and experimentally determined activities of 'FeO' in the Al_2O_3 - $'\text{FeO}'$ - SiO_2 system at 1873K.²⁷



2.25 The activity of Al_2O_3 in the Al_2O_3 - CaO - $'\text{FeO}'$ - MgO - SiO_2 system at 1873K for the BF, EAF and LF process.²⁷

Table 2.1 Standard electrode potentials²⁹

Electrode reaction	ϵ_H^0
Acid solutions	
$\text{Li} = \text{Li}^+ + e$	3.045
$\text{K} = \text{K}^+ + e$	2.925
$\text{Cs} = \text{Cs}^+ + e$	2.923
$\text{Ba} = \text{Ba}^{++} + 2e$	2.90
$\text{Ca} = \text{Ca}^{++} + 2e$	2.87
$\text{Na} = \text{Na}^+ + e$	2.714
$\text{Mg} = \text{Mg}^{++} + 2e$	2.37
$\text{H}^- = \frac{1}{2}\text{H}_2 + e$	2.25
$\text{Al} = \text{Al}^{+++} + 3e$	1.66
$\text{Zn} = \text{Zn}^{++} + 2e$	0.763
$\text{Fe} = \text{Fe}^{++} + 2e$	0.440
$\text{Cr}^{++} = \text{Cr}^{+++} + e$	0.41
$\text{Cd} = \text{Cd}^{++} + 2e$	0.403
$\text{Sn} = \text{Sn}^{++} + 2e$	0.136
$\text{Pb} = \text{Pb}^{++} + 2e$	0.126
$\text{Fe} = \text{Fe}^{+++} + 3e$	0.036
$\text{D}_2 = 2\text{D}^+ + 2e$	0.0034
$\text{H}_2 = 2\text{H}^+ + 2e$	0.000
$\text{H}_2\text{S} = \text{S} + 2\text{H}^+ + 2e$	-0.141
$\text{Sn}^{++} = \text{Sn}^{+4} + 2e$	-0.15
$\text{Cu}^+ = \text{Cu}^{++} + e$	-0.153
$2\text{S}_2\text{O}_3^= = \text{S}_4\text{O}_6^= + 2e$	-0.17
$\text{Fe}(\text{CN})_6^{-4} = \text{Fe}(\text{CN})_6^{-3} + e$	-0.36
$\text{Cu} = \text{Cu}^{++} + 2e$	-0.337
$2\text{I}^- = \text{I}_2 + 2e$	-0.5355
$\text{Fe}^{++} = \text{Fe}^{+++} + e$	-0.771
$\text{Ag} = \text{Ag}^+ + e$	-0.7991
$\text{Hg} = \text{Hg}^{++} + 2e$	-0.854
$\text{Hg}_2^{++} = 2\text{Hg}^{++} + 2e$	-0.92
$2\text{Br}^- = \text{Br}_2 (\text{l}) + 2e$	-1.0652
$\text{Mn}^{++} + 2\text{H}_2\text{O} = \text{MnO}_2 + 4\text{H}^+ + 2e$	-1.23
$2\text{Cr}^{+3} + 7\text{H}_2\text{O} = \text{Cr}_2\text{O}_7^= + 14\text{H}^+ + 6e$	-1.33
$\text{Cl}^- = \frac{1}{2}\text{Cl}_2 + e$	-1.3595
$\text{Ce}^{+3} = \text{Ce}^{+4} + e$	-1.61
$\text{Co}^{++} = \text{Co}^{+++} + e$	-1.82
$2\text{SO}_4^= = \text{S}_2\text{O}_8^= + 2e$	-1.98
$2\text{F}^- = \text{F}_2 + 2e$	-2.65
Basic solutions	
$2\text{OH}^- + \text{Ca} = \text{Ca}(\text{OH})_2 + 2e$	3.03
$3\text{OH}^- + \text{Cr} = \text{Cr}(\text{OH})_3 + 3e$	1.3
$4\text{OH}^- + \text{Zn} = \text{ZnO}_2^= + 2\text{H}_2\text{O} + 2e$	1.216
$2\text{OH}^- + \text{Cn}^- = \text{CNO}^- + \text{H}_2\text{O} + 2e$	0.97
$2\text{OH}^- + \text{SO}_3^= = \text{SO}_4^= + \text{H}_2\text{O} + 2e$	0.93
$\text{H}_2 + 2\text{OH}^- = 2\text{H}_2\text{O} + 2e$	0.828
$2\text{OH}^- + \text{Ni} = \text{Ni}(\text{OH})_2 + 2e$	0.72
$\text{OH}^- + \text{Fe}(\text{OH})_3 = \text{Fe}(\text{OH})_3 + e$	0.56
$\text{O}_2 + 2\text{OH}^- = \text{O}_3 + \text{H}_2\text{O} + 2e$	-1.24

* W.M. Latimer, *The Oxidation States of the Elements and Their Potentials in Aqueous Solutions* (New York: Prentice-Hall, 2nd edn, 1952).

$$C_S = (\text{wt \% S}) \cdot [p_{O_2}/p_{S_2}]^{1/2} \quad (2.100)$$

Similar expressions for other impurities taken up by the slag phase can be defined. The slag capacities are largely experimentally determined. Extrapolation of the data with respect to composition and temperature is enabled by suitable models. The THERMOSLAG® software can be used to compute the iso-Cs lines in the case of multicomponent slag systems.

2.9 Basics of electrochemical thermodynamics

The application of thermodynamic principles to electrochemical concepts has long since been known. This is a very important field in metallurgy, specifically electrometallurgy in aqueous phase as well as through the molten salt route. The latter is an important process route towards the production of reactive and refractory metals, with great significance to strategic materials.

In the case of a reversible galvanic cell, chemical driving force of the cell reaction, $\Delta G_{\text{Cell reaction}}$ is equal and opposite to the electrical potential generated and is expressed by the Nernst equation as

$$\Delta G_{\text{Cell reaction}} = -nEF \quad (2.101)$$

where ‘n’ refers to the number of electrons participating in the reaction, ‘E’ is the cell EMF and ‘F’ is the Faraday constant. The validity of equation (2.101) implies the absence of electronic conduction in the cell. In the case of aqueous systems, the situation is complicated by the formation of hydrated ions and the electrolysis of H_2O forming H_2 and O_2 . A table of standard oxidation potentials could be established in the case of aqueous electrolysis by assuming that the potential for the reaction

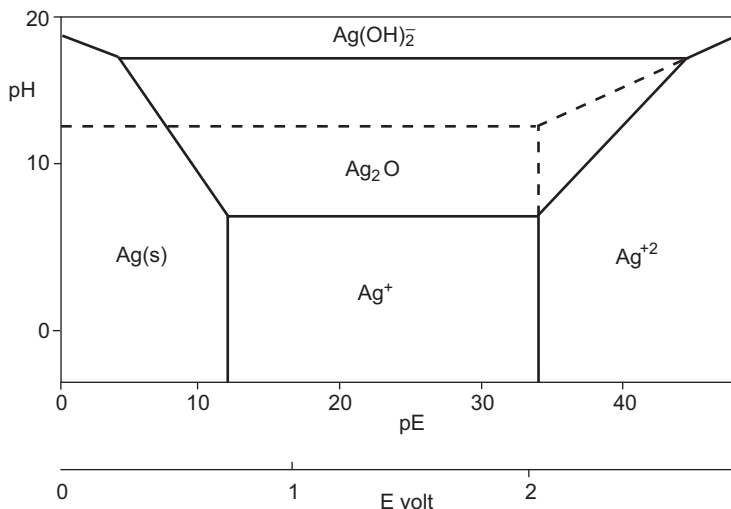


as zero. This table is presented as Table 2.1.

Stability diagrams similar to Fig. 2.12 for aqueous systems could be constructed in order to define the stabilities of various species. The diagram for Ag-O-H system is presented in Fig. 2.26.³⁰

2.10 Conclusions

As mentioned in the beginning of this chapter, thermodynamics has a wide variety of applications and is a fascinating subject. It is very ambitious to condense the subject into a small chapter, without losing the essentialities. The authors have made an attempt to present the important aspects of the subject for an understanding of metallurgical processes and properties, being fully aware of the limitations. For the convenience of more interested readers, a bibliography is presented at the end of this chapter, apart from the reference list. The readers



2.26 The stability diagram for Ag-O-H system (0.1 c mol Ag per litre at 25 °C).³⁰

are advised to consult these classical textbooks for a deeper understanding of the subject and enjoying the beauty of the logic in the same.

2.11 Further reading

- Chemical Thermodynamics of Materials*, C.H.P. Lupis, North-Holland, Elsevier Science Publ. Co., NY, US (1983).
- Introduction to Metallurgical Thermodynamics*, D.R. Gaskell, Hemisphere Publ. Corp., NY (1981).
- Physical Chemistry of Melts in Metallurgy*, F.D. Richardson, Academic Press, London, UK (1974).
- Physical Chemistry of Metals*, L.S. Darken and R.W. Gurry, McGraw-Hill Book Co. Inc., NY, US (1953).
- Thermodynamics of Alloys*, C. Wagner, Addison-Wesley, Reading, MA (1952).
- Thermodynamics of Solids*, R.A. Swalin, John Wiley & Sons, Toronto, Canada (1972).

2.12 References

1. A. Einstein, in *Albert Einstein: Philosopher-Scientist*, Tudor Publishing Co., NY (1949).
2. *Introduction to Metallurgical Thermodynamics*, D.R. Gaskell, Hemisphere Publ. Corp., NY (1981) 2.
3. *Grundläggande thermodynamik*, M. Hillert, Royal Institute of Technology (1991) I:9.
4. *Metallurgisk kemi*, L.I. Staffansson, Royal Institute of Technology (1976).
5. *Thermodynamics of Solids*, R.A. Swalin, John Wiley & Sons, Toronto, Canada (1972) 214, 215.

6. *Introduction to Metallurgical Thermodynamics*, D.R. Gaskell, Hemisphere Publ. Corp., NY (1981) 287.
7. H.H. Kellogg and S.K. Basu, *Trans. AIME* (1960) vol 70, 218.
8. L.S. Darken, *Trans. AIME* (1967) vol. 239, 80.
9. *Physical Chemistry of Melts in Metallurgy*, F.D. Richardson, Academic Press, London, UK (1974) 182.
10. *Chemical Thermodynamics of Materials*, C.H.P. Lupis, North-Holland, Elsevier Science Publ. Co., NY, US (1983) 242.
11. *Chemical Thermodynamics of Materials*, C.H.P. Lupis, North-Holland, Elsevier Science Publ. Co., NY, US (1983) 248.
12. *Physical Chemistry of Melts in Metallurgy*, F.D. Richardson, Academic Press, London, UK (1974) 185.
13. G.R. St Pierre, *Trans. AIME*
14. M. Margules, Sitzungber, Kaiser Akadem. Wissenschaft, Wien, *Mathematisch-Naturwiss. Class.* (1895) vol. 104, 1243.
15. M. Hillert, in *Phase Transformations*, ASM, Metals Park, Ohio (1970) 181.
16. M. Hillert and L.I. Staffansson, *Acta Chem. Scand.* (1970) vol. 24, 3618.
17. M. Temkin, *Acta Phys. Chim URSS* (1945), vol. 20, 411.
18. Thermocalc Software, version P on WinNT (2000) <http://www.thermocalc.com>.
19. L.D. Teng, X.G. Lu, R.E. Aune and S. Seetharaman, accepted for publication in *Metall. Mater. Trans.* (2005).
20. H. Flood, T. Førland and K. Grjotheim, *Inst. Min. Metall.*, London (1953) 47.
21. R. Sridhar and J.H.E. Jeffes, *Trans. Inst. Min. Metall.* (1967), vol. 76, C44.
22. F.D. Richardson, *Trans. Faraday* (1956) vol. 52, 1312.
23. C.R. Masson, *Proc. R. Soc.* (1965) vol. A287, 201.
24. M.L. Kapoor, Mehrotra and M.G. Frohberg, *Archiv. Eisenhüttenw.* (1974), vol. 45, 213 and 663.
25. M. Blander and A. Pelton, *Metall. Trans. B* (1986), vol. 17B, 805.
26. J. Björkvall, D. Sichen and S. Seetharaman, *Ironmaking and Steelmaking*, vol. 28, no. 3 (2001) 250–257.
27. P. Fredriksson and S. Seetharaman, Presented in the VII International Conference on Molten Slags, Fluxes and Salts, Cape Town, South Africa, January 2004.
28. C.J.B. Fincham and F.D. Richardson, *Proc. Roy. Soc.* (1954), vol. A223, 40.
29. *Introduction to Metallurgical Thermodynamics*, D.R. Gaskell, Hemisphere Publ. Corp., NY (1981) 551.
30. *Grundläggande Thermodynamik*, M. Hillert, Royal Institute of Technology (1991) VI:19.

Phase diagrams, phase transformations, and the prediction of metal properties

K M O R I T A , The University of Tokyo and
N S A N O , Nippon Steel Corporation, Japan

3.1 Introduction

Phase diagrams provide a variety of thermodynamic information through equilibria among multiple phases as well as quantitative data on phase distribution in a specific system. Phase relations demonstrate that any chemical potentials of all coexisting phases are identical, imposing significant restrictions in the thermodynamic properties of the probable phases. By solving these restrictions, with simultaneous equations, the variables of compositions can be determined as a function of temperature. Nowadays, a number of phase diagrams are drawn by thermodynamic calculations by commercial PC programs using empirical parameters within some constraint. Although phase diagrams show the phase relations quantitatively by lever rules, an average composition in a multi-phase region shows no difference in chemical potentials, while sometimes there is uncertainty in the chemical potential of a single stoichiometric compound. For instance, an intermetallic compound AB has two different chemical potentials at A deficient side and B deficient side. Strictly speaking, an abrupt gap of each chemical potential should be considered at that composition. In the present chapter, phase diagrams are discussed from the aspect of thermodynamic stability. By further investigation of chemical potential diagrams, their conversion to phase diagrams is used to compare the difference in the physical meanings.

On the other hand, it is important to understand the behaviour of phase transformation as well as phase relations and their phase stability in any metallurgical process. As a primary step, expression and interpretation of ternary phase diagrams are introduced, and then the fundamental features of the diagrams are discussed from thermodynamic aspects. As the easiest way in viewing a three-dimensional phase diagram, just a number of compiled isothermal sections representing various phase relations are shown. Finally, solidification behaviour is described as an example of practical application of the ternary phase diagrams.

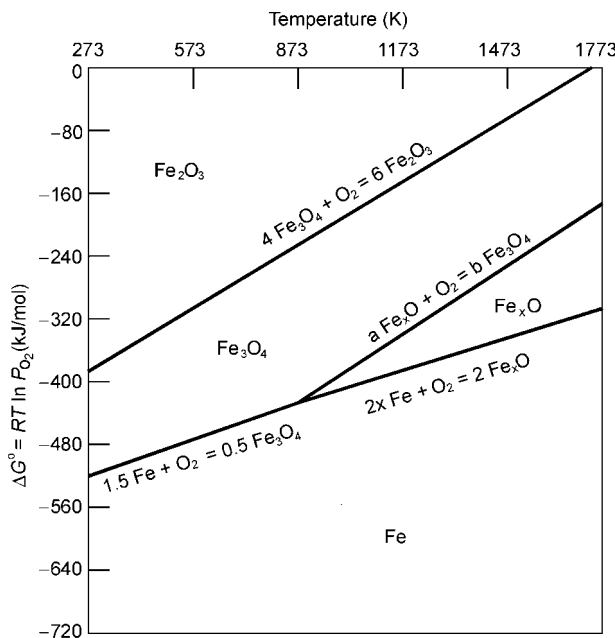
3.2 Phase diagrams and potential diagrams

As introduced in the previous chapter, the Ellingham diagram clearly shows the most stable formulae of substances in terms of their red-ox equilibria, where the standard Gibbs energies of formation of oxides per one mole of oxygen gas are demonstrated as a function of temperature for various materials. Let us consider the oxidation of iron. There are three kinds of oxides, Fe_xO , Fe_3O_4 and Fe_2O_3 , and the following equilibria, (i)–(iv), can be considered. Here, the value of x in the non-stoichiometric compound Fe_xO is assumed to be 0.95 when equilibrated with metallic Fe, and $0.83 < x < 0.95$ when equilibrated with Fe_3O_4 .

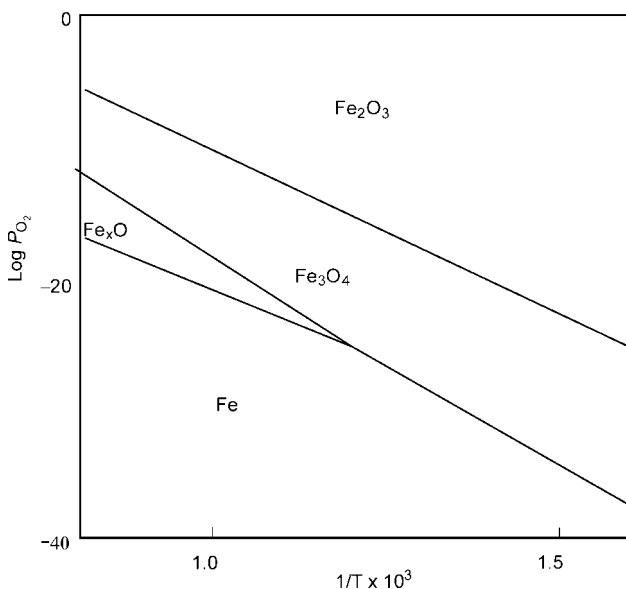
- (i) $2x \text{Fe} + \text{O}_2 = 2\text{Fe}_x\text{O}$ $\Delta G^\circ = -502960 - 36.2 \text{T} + 63.818 \text{T} \log \text{T}$
 $\quad \quad \quad (\text{J/mol})^1$
 $\quad \quad \quad (x = 0.95)$
- (ii) $1.5 \text{Fe} + \text{O}_2 = 0.5 \text{Fe}_3\text{O}_4$ $\Delta G^\circ = -551100 + 153.7 \text{T} (\text{J/mol})^2$
- (iii) $a \text{Fe}_x\text{O} + \text{O}_2 = b \text{Fe}_3\text{O}_4$ $\Delta G^\circ = -543110 - 344.1 \text{T} + 169.893 \text{T} \log \text{T}$
 $\quad \quad \quad (\text{J/mol})^1$
 $\quad \quad \quad (0.83 < x < 0.95)$
- (iv) $4 \text{Fe}_3\text{O}_4 + \text{O}_2 = 6 \text{Fe}_2\text{O}_3$ $\Delta G^\circ = -405040 - 277.4 \text{T} + 158.081 \text{T} \log \text{T}$
 $\quad \quad \quad (\text{J/mol})^1$

According to the above equilibria, each standard Gibbs energy change per one mole of oxygen, ΔG° , can be drawn as a function of temperature as shown in Fig. 3.1. Strictly speaking, however, the standard Gibbs energy changes for (iii) and (iv) are not for ‘formation’, because the reactant Fe cannot coexist with Fe_3O_4 at higher temperatures than 850K or Fe_2O_3 at all temperatures. Since the line shows the coexistence of two compounds with the relationship between temperature, T, and oxygen potential, $RT \ln p_{\text{O}_2}$, the area in between represents the most stable substance at a given temperature and oxygen potential. When the figure is redrawn as the relationship between $\log p_{\text{O}_2}$ and $1/T$, the diagram shows the most stable phase as functions of temperature and oxygen partial pressure more clearly as shown in Fig. 3.2. The stable areas are also represented in the same manner. This typical chemical potential diagram may also be referred as a phase diagram. Compared with the Fe-O binary phase diagram (Fig. 3.3¹), you may notice that each line in the former, which demonstrates a two-phase boundary, corresponds to the dotted area of the latter, and vice versa. This is because oxygen partial pressures of two phases with different oxygen contents in an equilibrium state are identical, while there is a wide range of oxygen partial pressure in a stoichiometric compound. However, as is the case with Fe_xO , non-stoichiometric oxides have their unique oxygen partial pressure as a function of composition.

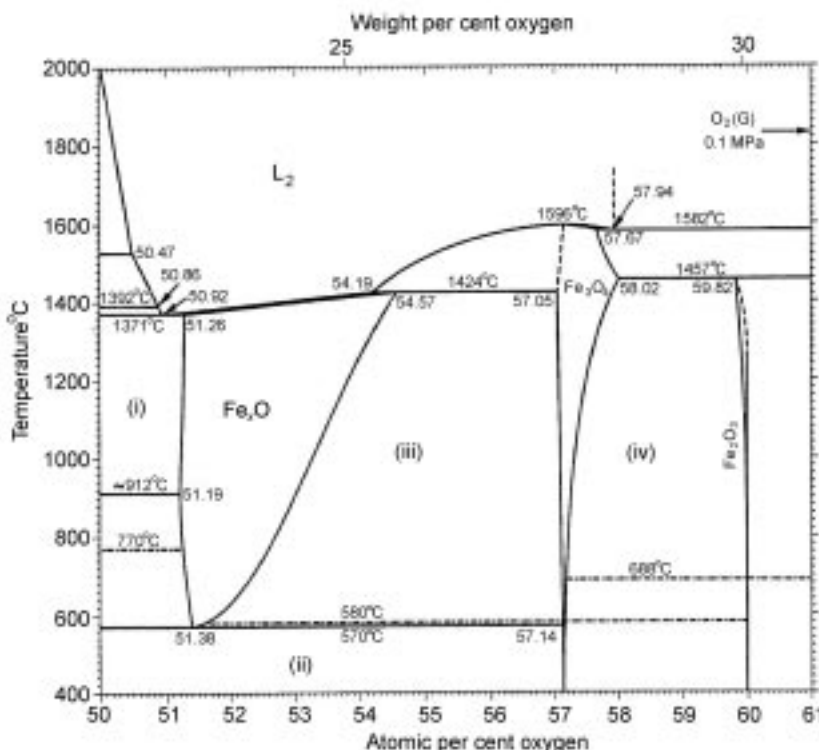
When another component beside oxygen is added, the chemical potential diagram becomes three dimensional. At a constant temperature, however, we can draw such a diagram in a plane, showing the most stable phase as a function



3.1 Standard Gibbs energy changes for the reactions (i)–(iv) as a function of temperature.



3.2 Phase stability regions for various iron oxides as a function of temperature and oxygen partial pressure.



3.3 Phase diagram for the Fe-O system.

of two chemical potentials. As an example, let us consider the Ca-S-O system at 1000K. Probable phases in the present system are considered to be Ca, CaO, CaS and CaSO₄. Stabilities of such substances are controlled by the chemical potentials of oxygen and sulfur, namely their partial pressures at a certain temperature. Hence, there must be six boundaries among four substances, e.g. (i) Ca-CaO, (ii) Ca-CaS, (iii) Ca-CaSO₄, (iv) CaO-CaS, (v) CaO-CaSO₄ and (vi) CaS-CaSO₄. Each boundary can be determined by equilibria between the two compounds as follows.

(i) Ca-CaO



$$\log P_{\text{O}_2} = 55.48$$

(ii) Ca-CaS

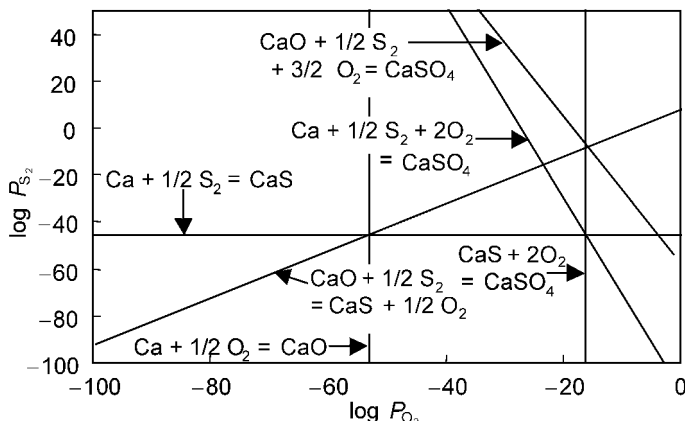


$$\log P_{\text{S}_2} = 46.04$$

(iii) Ca-CaSO₄

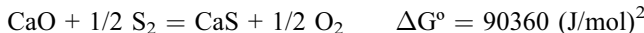


$$4 \log P_{\text{O}_2} + \log P_{\text{S}_2} = 109.11$$



3.4 Boundaries between stable phases for the Ca-O-S system at 1000K.

(iv) CaO-CaS



$$\log P_{\text{O}_2} \log P_{\text{S}_2} = 9.44$$

(v) CaO-CaSO₄



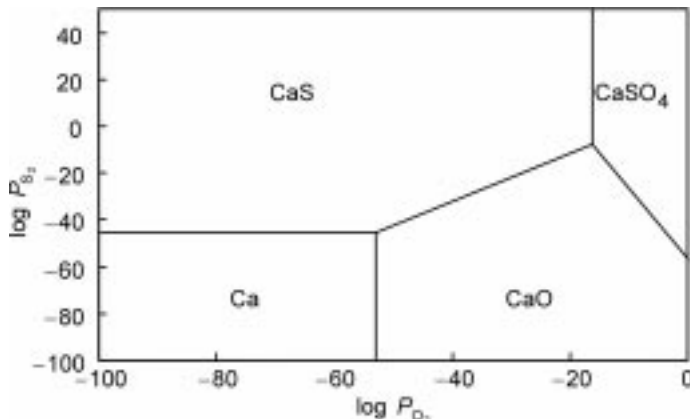
$$3 \log P_{\text{O}_2} + \log P_{\text{S}_2} = 53.63$$

(vi) CaS-CaSO₄



$$\log P_{\text{O}_2} = 15.77$$

From all the relations between $\log P_{\text{O}_2}$ and $\log P_{\text{S}_2}$, six boundaries can be drawn as shown in Fig. 3.4. Each boundary separates the diagram into two regions and shows more stable substance among the two. For example, boundary (i)



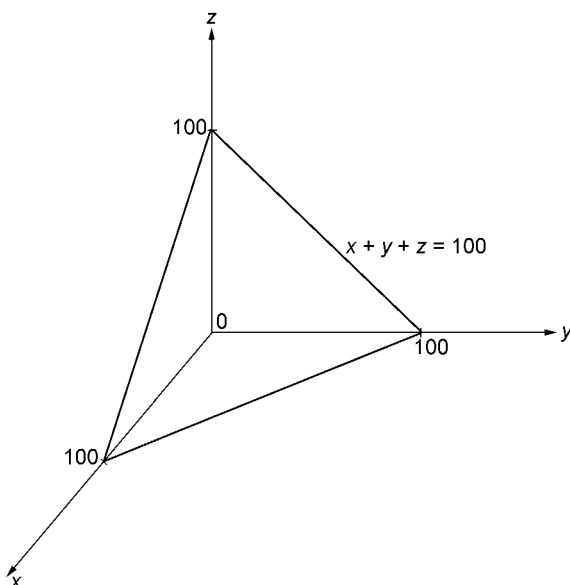
3.5 Chemical potential diagram for the Ca-O-S system at 1000K.

indicates that Ca is more stable than CaO in the left-hand area of the boundary, while CaO is more stable in the other side. From the six restrictions in the figure, one can finally draw the most stable phase as is shown in Fig. 3.5, the so-called chemical potential diagram. As a result, the line (iii) was not used in the determination of the diagram because Ca and CaSO₄ cannot coexist at 1000K, but the line still demonstrates the difference in the order of relative stability.

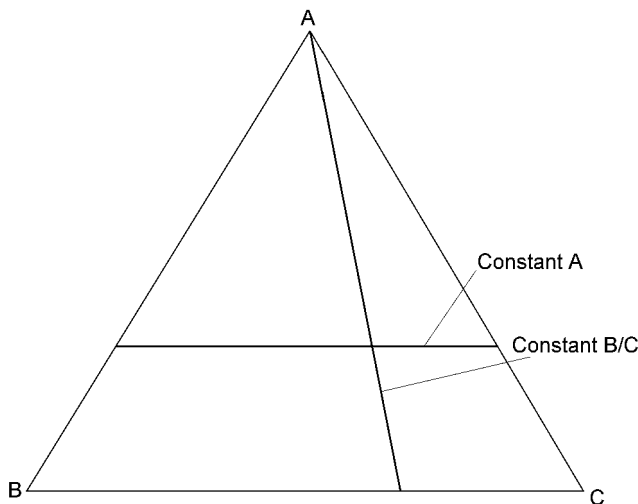
3.3 Ternary phase diagrams

3.3.1 Representation of composition and Gibbs triangle

While a composition can be represented by an axis, which is one dimensional, in binary phase diagrams, one more dimension must be added in order to show a composition for ternary systems. Accordingly, the composition is represented in a plane and that of $x + y + z = 100\%$ can be the simplest representation as shown in Fig. 3.6. In the space of $x, y, z \geq 0$, the plane becomes a regular triangle and any composition (x, y, z) can be represented. This is called Gibbs triangle. Let's consider compositions for the A-B-C ternary system in Fig. 3.7. When a line is parallel to the base, line BC, concentration of A is constant, while the ratio of B/C is constant on any lines drawn through the apex A. When two of the solutes, x and y, are dilute compared to the other solvent, z, rectangular coordinates may be useful by plotting the composition with (x, y) .



3.6 The plane $x + y + z = 100$ ($x, y, z > 0$).

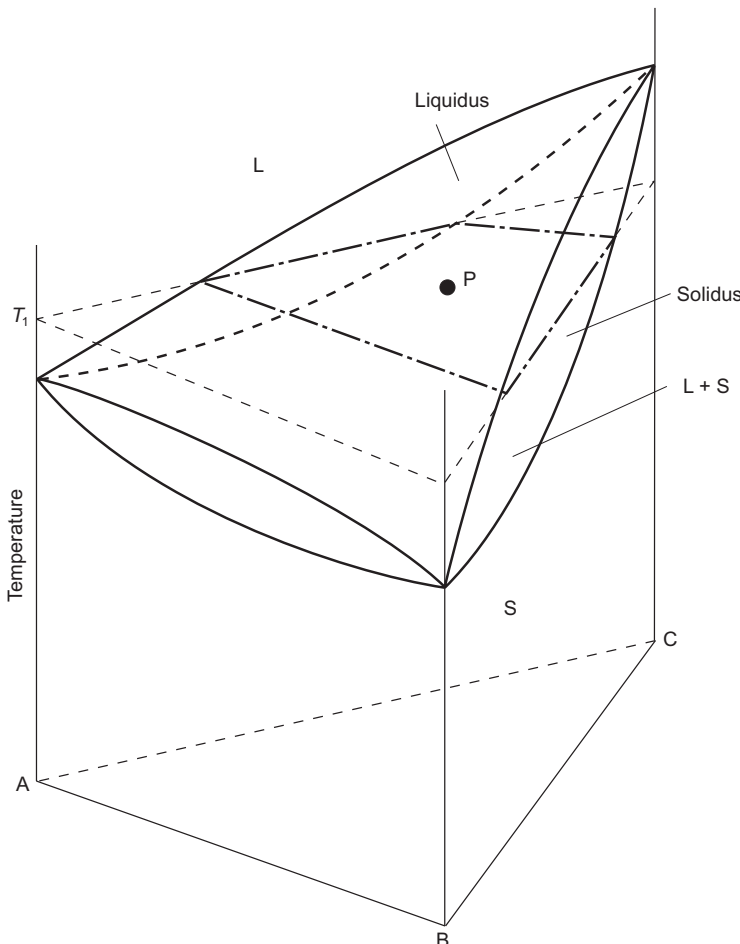


3.7 Representation of compositions in the A-B-C ternary system.

Then another coordinate, temperature, should be added to demonstrate a three-dimensional ternary phase diagram. For simplicity, a ternary system in which all constituents are entirely miscible can be shown in Fig. 3.8. As is the case with a binary system, the triangular prism can be divided into three spaces, a liquid region (L), a solid region (S) and the mixture of both (L + S), and they are separated by liquidus and solidus planes. It is important that how you can figure out the composition locating in the mixture region. Accordingly, an isothermal cross-section would be helpful to understand the phase relations quantitatively.

3.3.2 Isothermal cross section and tie-line

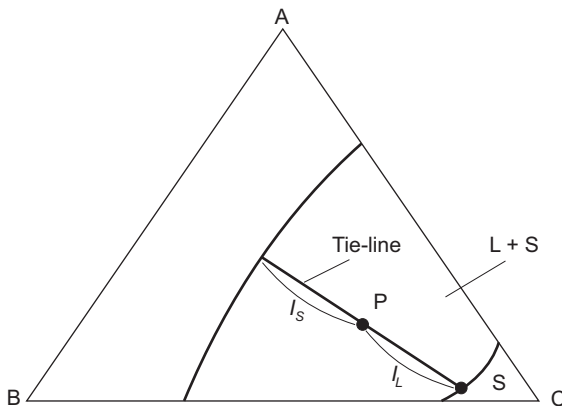
Here, in order to consider the phase relation of point P locating in an L + S region, an isothermal cross-section at the temperature concerned, T_1 , can be demonstrated in Fig. 3.9. The isothermal plane obviously intersects with liquidus and solidus planes at two intersection lines, liquidus and solidus curves. There is a set of the coexisting liquid and solid compositions on respective curves and the straight line between them must go through the point P. The lever rule also applies to the line as well as in binary systems, and this line is called a tie-line or a conjugation line. This is a typical example of two phase equilibria at the average composition of point P, and the amount ratio of liquid at L_1 to solid at S_1 can be identified as l_L/l_S as shown in Fig. 3.9. However, the position of the tie-line, which will not always go through an apex, cannot be recognized just by liquidus and solidus curves and it must be represented in phase diagrams in order to show the relationship of the two phases in exact equilibrium.



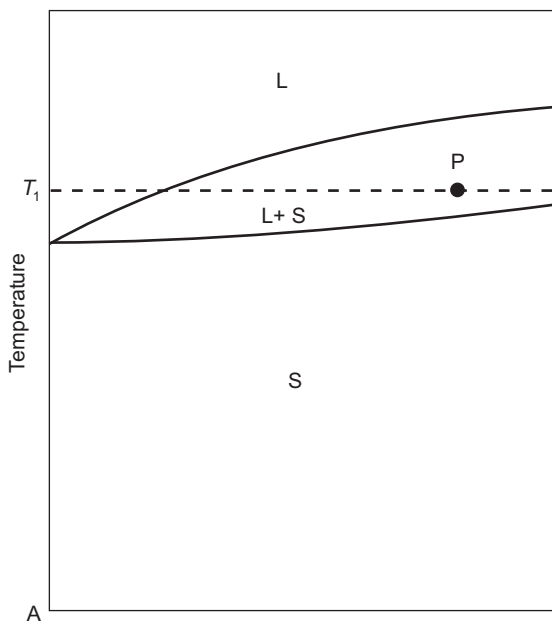
3.8 Phase diagram for the A-B-C ternary system entirely miscible in both liquid and solid phases.

When the triangle prism is cut perpendicularly through the apex A in Fig. 3.8, the cross-section which is shown in Fig. 3.10 looks weird since the lens is not closed at one end. This clearly shows the stability region does not represent phase relations in the two-phase region at all, because such perpendicular cross-sections usually exclude tie-lines. As a special case, when stable congruent compounds exist in binaries, the cross-section through these extremes appears as a pseudo-binary phase diagram as is shown in Fig. 3.11, the system Mg_2SiO_4 - Fe_2SiO_4 .

In ternary systems, sometimes three phases coexist, where degree of freedom is zero at a certain temperature. Wherever two-phase regions come across, the intersection point of two boundaries and those of the other two compositions of

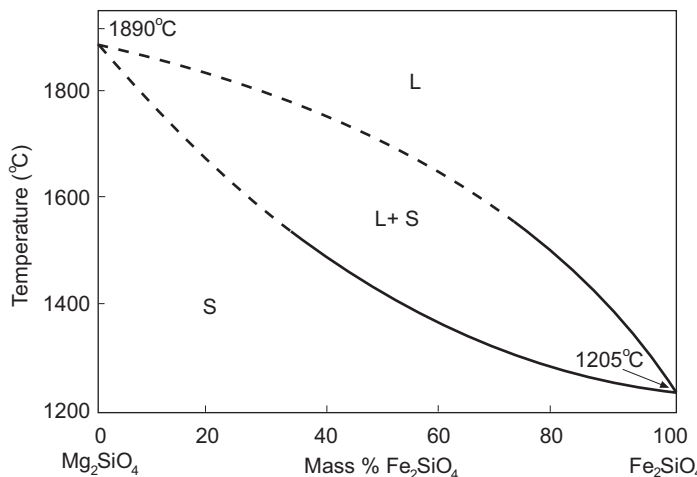


3.9 Isothermal cross-section of the A-B-C ternary system and a tie-line of average composition P between liquid and solid phases at T_1 .



3.10 Perpendicular cross-section of the A-B-C ternary system through A axis and point P.

the coexisting phases make a triangle surrounded by the three tie-lines. This is the so-called three-phase triangle and each phase has a certain composition throughout the region regardless of the mixing ratio. This will be illustrated in isothermal phase relations as shown in the following section. When a liquid phase exists as one of these extremes, its locus with temperature is a boundary



3.11 Pseudo-binary phase diagram for the Mg_2SiO_4 - Fe_2SiO_4 system.³

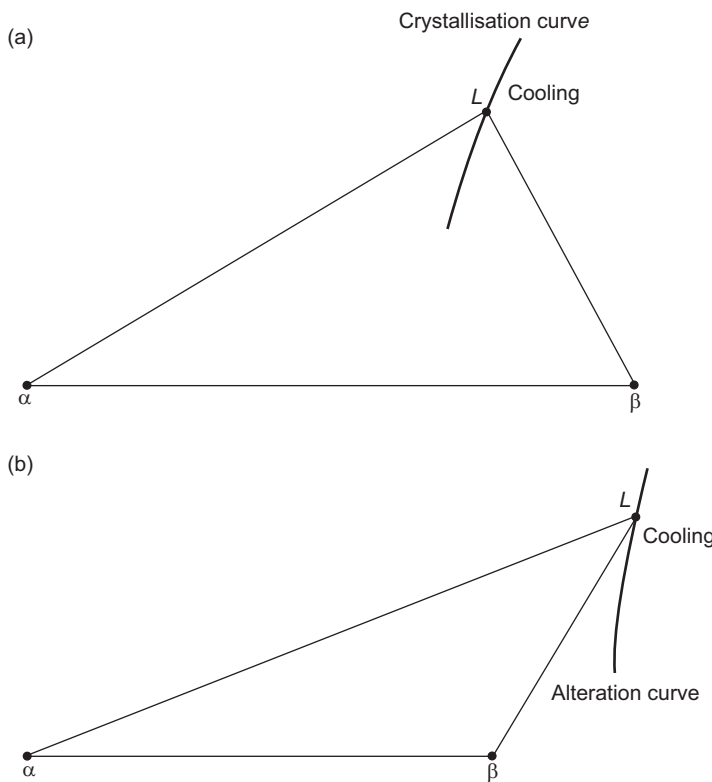
line dividing the primary crystals on the reflected perspective of the diagram. In most cases, the appearance of liquid phase L is related to the other two solid phases, α and β , by either of the following reactions, (i) and (ii).

- (i) $\text{L} \leftrightarrow \alpha + \beta$
- (ii) $\alpha + \text{L} \leftrightarrow \beta$

When the liquid at the extreme follows reaction (i), its composition is called a eutectic point and the boundary line is named as a crystallization curve. On the other hand, the composition is called a peritectic point and the boundary line is named an alteration curve in case of reaction (ii). A crystallization curve ends at the eutectic point of the binary system, hence it must penetrate the three-phase triangle composed of L, α and β as shown in Fig. 3.12(a). In contrast, an alteration curve ends at the peritectic point of the binary system, and it passes outside of the triangle. See Fig. 3.12(b). Accordingly, one can tell if a boundary line is a crystallization curve or an alteration one by graphical investigation.

3.3.3 Representation of ternary oxide systems

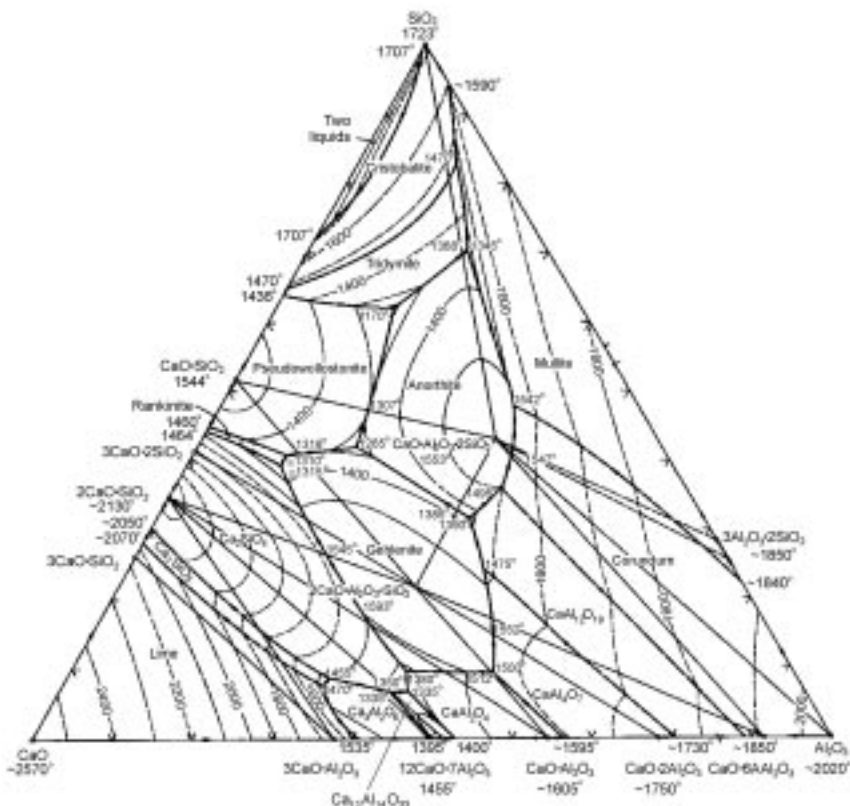
For the metallic systems, which form solid solutions, tie-lines cannot be uniquely determined because the solubility changes with temperature. On the other hand, it is not necessary to show such lines for many oxide systems, since the solubility of a solid solution may be disregarded and you may project every isothermal phase relations on one figure with ease. Herewith, the phase diagram for the CaO - A_2O_3 - SiO_2 system is shown in Fig. 3.13³ as an example.



3.12 Location of (a) crystallization curve and (b) alteration curve.

Liquidus lines for various temperatures are shown by the contours like those of altitude in a map. It turns out that these lines show where the coastline will be made if water is filled to the height when a certain geographical feature is seen from above, and the domain filled with water corresponds to that of liquid phase at a certain temperature. In most cases inter-compounds exist and they appear like mountains or islands. When you can discern which portion of liquidus (coast line) the compounds are in equilibrium with, ternary phase diagrams are already comprehended. In the present system at 1873K, each liquidus curve can easily be followed up and the corresponding solid oxide in equilibrium is recognized as shown in Fig. 3.14. In addition, a break point appears when the liquid is connected to two different solids with respective tie-lines. One should notice that these three points form a three-phase triangle surrounded by three tie-lines. Thus, since there is no width in solid composition, an arbitrary composition of 1873K is specified even in the two-phase domain.

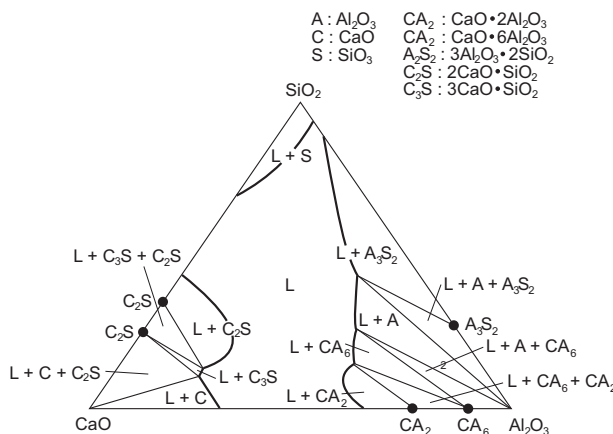
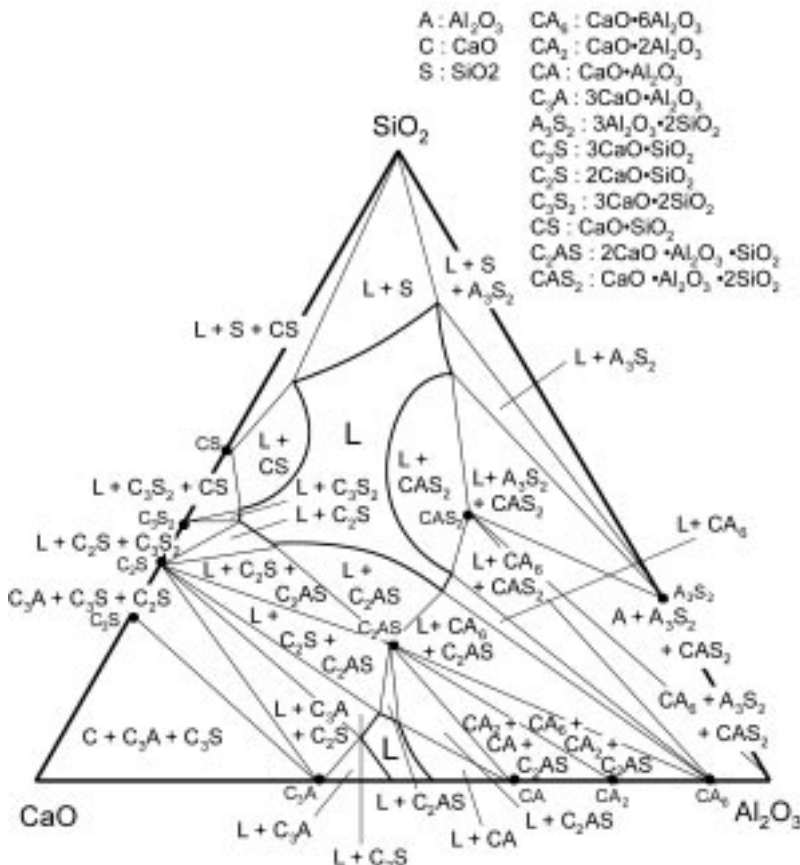
When temperature is lowered, new islands, namely congruent compounds such as $\text{CaO}\cdot\text{Al}_2\text{O}_3$, $2\text{CaO}\cdot\text{Al}_2\text{O}_3\text{SiO}_2$, $\text{CaO}\cdot\text{Al}_2\text{O}_3\cdot 2\text{SiO}_2$, $\text{CaO}\cdot\text{SiO}_2$,



3.13 Phase diagram for the CaO-Al₂O₃-SiO₂ system.³

$12\text{CaO}\cdot7\text{Al}_2\text{O}_3$, appear above sea level and the ocean is separated into several lakes. Such a complicated situation was snappet at 1673K and shown in Fig. 3.15. At 1443K, the final lake will be dried up at the eutectic composition of the $\text{CaO}\cdot\text{SiO}_2\text{-CaO}\cdot\text{Al}_2\text{O}_3\cdot2\text{SiO}_2\text{-SiO}_2$ ternary system. Regarding the incongruent compounds, such as $3\text{CaO}\cdot\text{SiO}_2$ and $\text{CaO}\cdot6\text{Al}_2\text{O}_3$, etc., their summits are not visible, because these compounds do not have their own melting points but decompose into liquid and other solid phases at peritectic temperature as will be explained in the following section. The evidences of such compounds can be seen as strata appearing at slanting surfaces divided by the alteration curves as specified in Fig. 3.13.

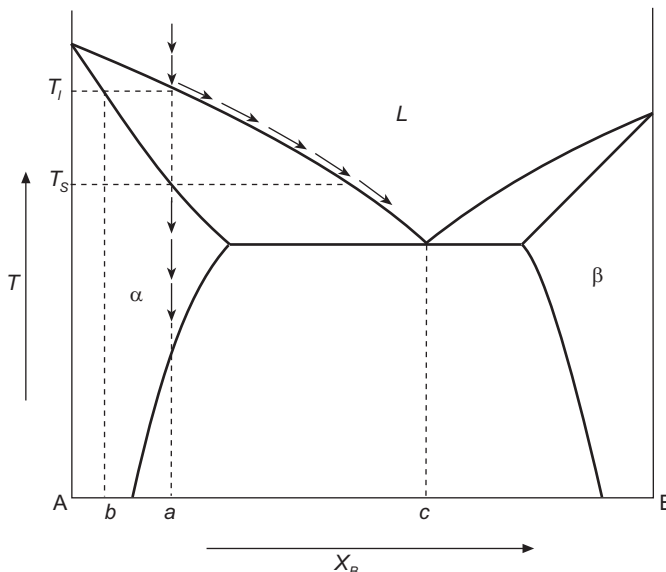
When you glance at a map, you can figure out how creeks run and summits continue. Similarly, one may imagine a diagram to be a map of bird's-eye view, and some general rules of the ternary phase diagrams can be naturally recognized.

3.14 Liquidus and phase relations for the $\text{CaO}-\text{Al}_2\text{O}_3-\text{SiO}_2$ system at 1873K.3.15 Liquidus and phase relations for the $\text{CaO}-\text{Al}_2\text{O}_3-\text{SiO}_2$ system at 1673K.

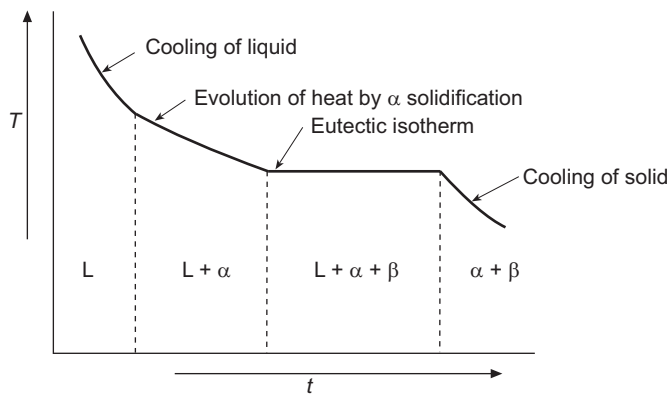
3.4 Solidification in ternary systems and four-phase equilibria

Solidification of binary alloys can be easily understood. Congruent solidification, which is characterized by isothermal freezing point and formation of solid from liquid of the same composition, occurs mainly for pure metals and intermetallic compounds. Also, a system with maxima or minima in the solidus and liquidus shows congruent solidification at that composition. On the other hand, incongruent solidification occurs over a wide temperature range, forming solid of a different composition from liquid, which is typical for binary alloys. As shown in Fig. 3.16, liquid of composition a starts to freeze in forming a solid phase α with composition b richer in component A. Then, liquid becomes enriched in component B and the liquidus temperature will be lowered. Thus the solidification can be followed as a simultaneous progress of equilibrium solid and liquid compositions along the solidus and liquidus lines. The relative amount of liquid phase, determined from the tie-line by the lever rule, decreases with temperature. At the eutectic temperature, congruent solidification, simultaneous precipitation of α and β phases, occurs until the liquid phase with composition c diminishes. A representative cooling curve is shown in Fig. 3.17.

Solidification of ternary alloys can be understood in the same manner as that of binary alloys. The complexity is only due to the possible appearance of another solid phase during cooling, and, as mentioned in the previous section, the tie-lines do not generally lie on an arbitral vertical plane. Let's consider an example of a ternary eutectic system as shown in Fig. 3.18, where some points



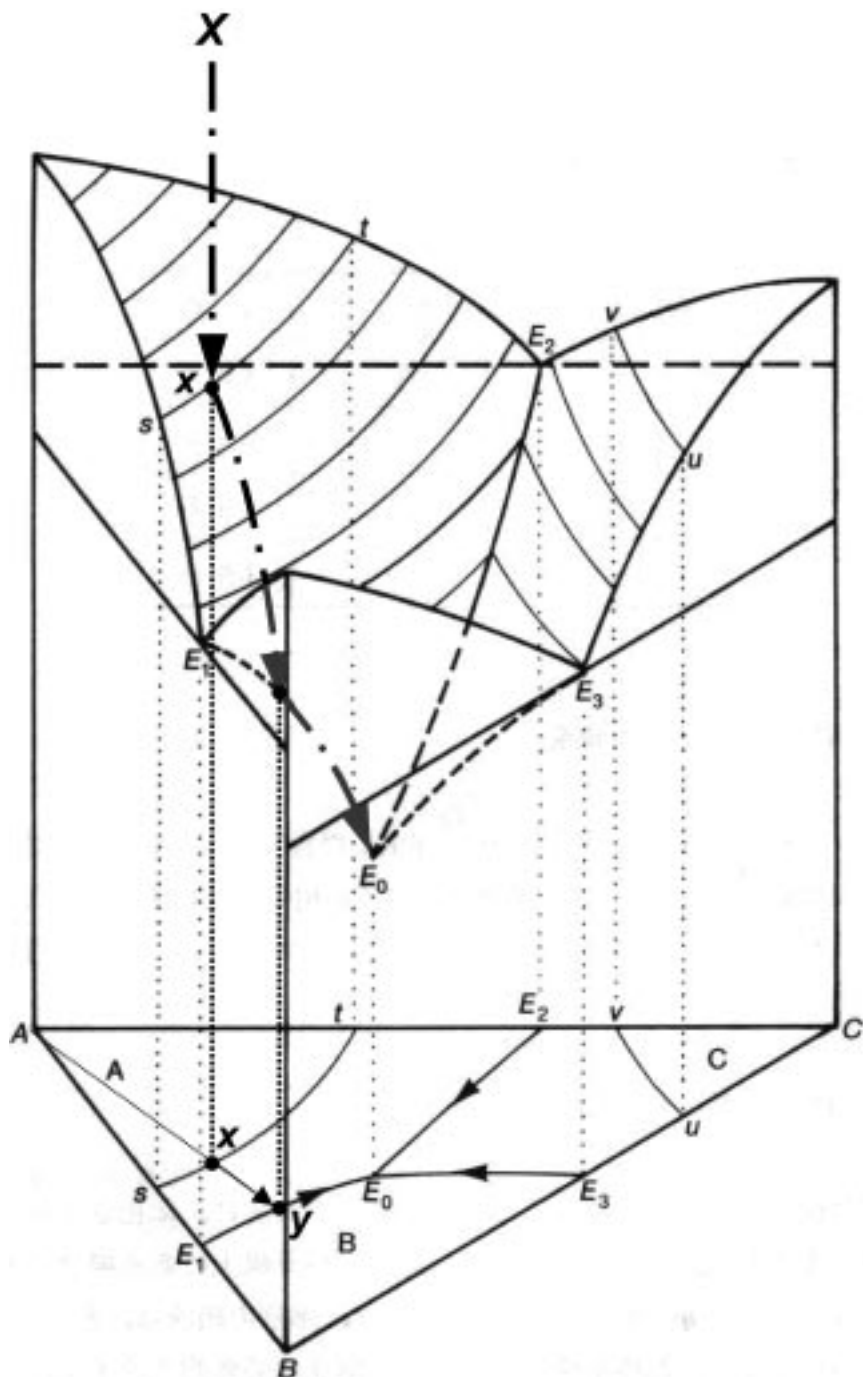
3.16 Phase diagram for the binary A-B system.



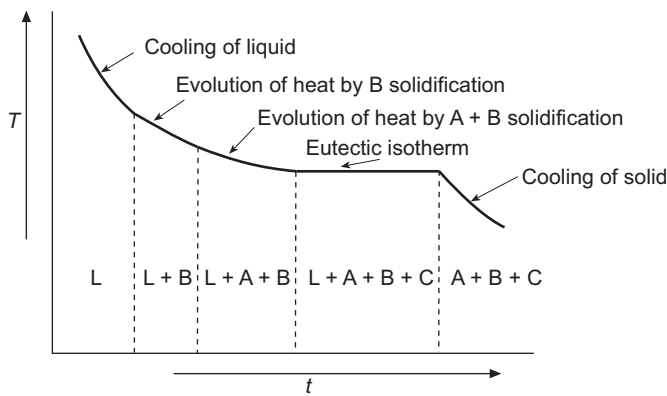
3.17 Cooling curve for the alloy shown in Fig. 3.16.

and lines are reflected to the bottom of the prism to show the behaviour more simply. Here, the solubility of each component in a solid phase is assumed to be negligible for simplicity. When the liquid of a certain composition, X, is cooled along path Xx , it reaches the liquidus surface at x , where the solid of composition B starts to precipitate. This precipitated phase is called a primary crystal and the boundaries which separate primary crystal regions are called boundary lines, such as E_1-E_0 , E_2-E_0 and E_3-E_0 in Fig. 3.18. They are obviously the intersections of liquidus surfaces and correspond to the ‘creeks’ in the map described in the Section 3.3.3. The reflected triangle in the figure can be divided into three regions of $AE_1E_0E_2$, $BE_3E_0E_1$ and $CE_2E_0E_3$, which are named the primary phase fields of A, B and C, respectively.

Once the primary crystal starts to precipitate, the liquid composition changes to one with a lowering A concentration at a constant ratio of B and C along path $x-y$ until it reaches another liquidus surface, namely the boundary line E_1-E_0 . While the liquid composition is cooled along path $x-y$, it is (singly) saturated with B and the composition x should be positioned on the tie-line $A-y$ in the reflected plane of the figure. After the liquid composition reached another liquidus surface, it varies along the boundary line E_1-E_0 , increasing C concentration and coprecipitating the solid phases A and B. The secondary precipitate B can be quoted as a secondary crystal, but may precipitate as a two-phase secondary microconstituent composed of A and B. Thus the liquid composition during solidification along E_1-E_0 is doubly saturated with A and B. Also, the composition X must be kept inside the triangle ABy surrounded by three tie-lines. This is called a three-phase triangle indicating that three phases coexist throughout the triangle keeping every chemical potential constant. Finally, it reaches the eutectic composition at a certain temperature, namely eutectic point, E_0 . Here, the liquid is saturated with three solid phases, and the degree of freedom becomes zero. This situation is the so-called four-phase equilibria, and the three-phase tertiary microconstituent composed of A, B and



3.18 Phase diagram for the ternary eutectic system A-B-C.

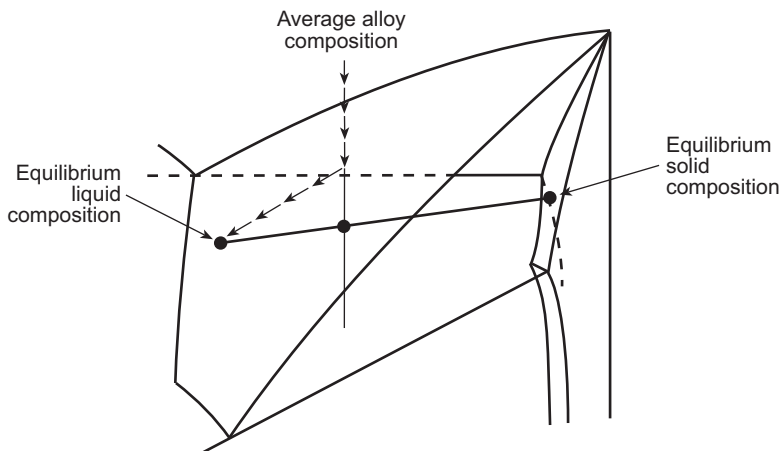


3.19 Cooling curve for the alloy shown in Fig. 3.18.

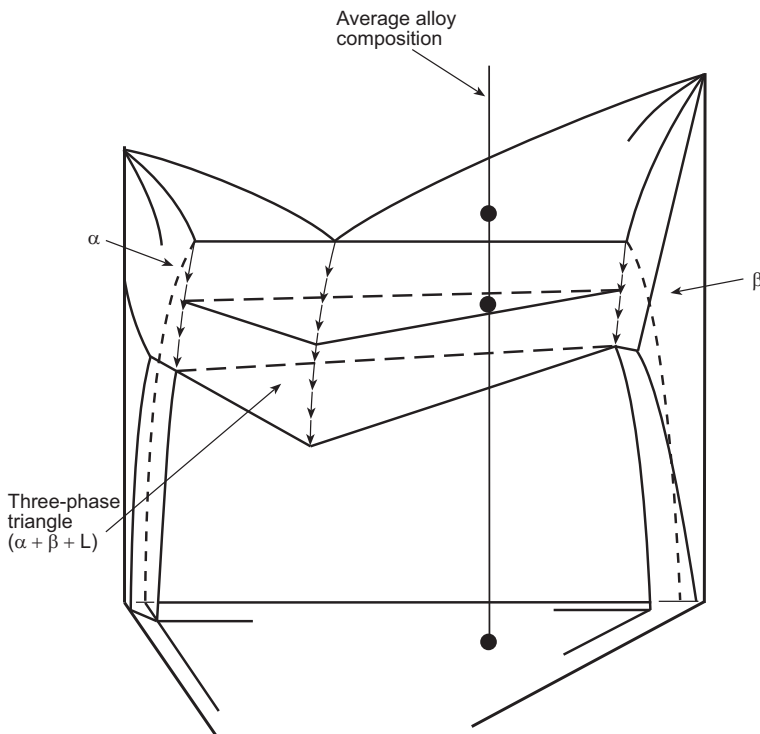
C is precipitated until the liquid phase diminishes. The cooling curve is shown in Fig. 3.19.

For most of the alloys, solid phases have some solubility of the other components. During the precipitation of primary crystals, their composition in equilibrium with the liquid can be given by the tie-line at any temperature. This is demonstrated in Fig. 3.20. After the liquid becomes saturated with primary and secondary crystals, their compositions are determined by the extremities of the three-phase region as shown in Fig. 3.21. The fraction of their amounts can be given by applying the lever rule to the three-phase triangle.

In the practical solidification processes of a system with more than two components, however, equilibrium solidification is exceptional and solidus curves or surfaces will be depressed due to the non-uniformity of the solid



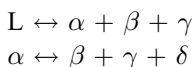
3.20 Solid composition during primary solidification.

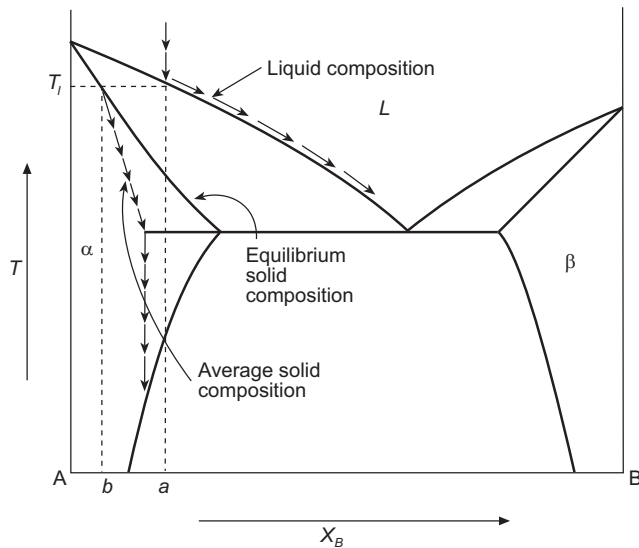


3.21 Solid composition during secondary solidification.

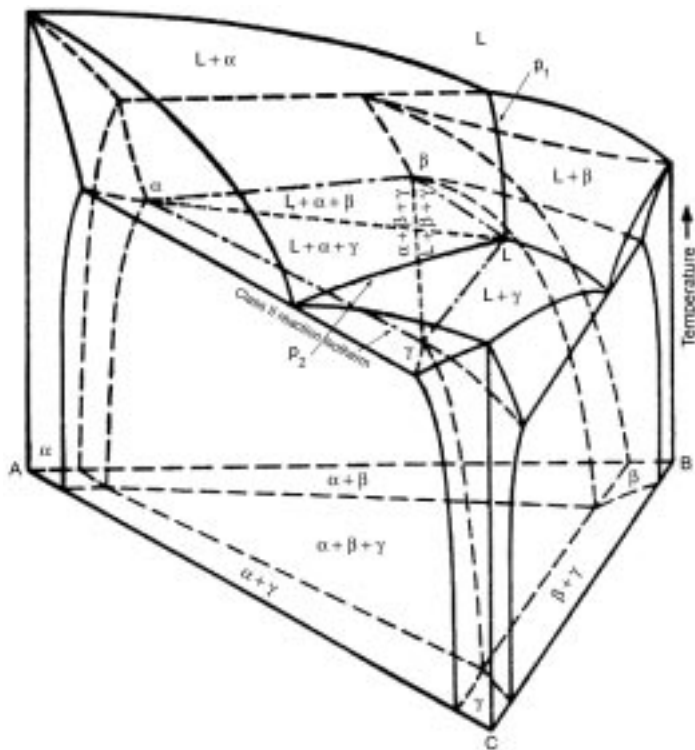
phase. Accordingly, the average composition of the solid inside will lie below the equilibrium curves or surfaces, although the equilibrium solidus lines or curves still demonstrate the composition in equilibrium with the liquid phase (Fig. 3.22). Thus, when considering the average composition of solid phases in ternary systems, apparent solidus surfaces will be depressed and the three-phase regions will also be enlarged. The eutectic temperature will not be affected, but the apparent tie-line will be lengthened showing the average compositions of primary and secondary microconstituents in a non-equilibrium eutectic microstructure.

Although phase relations in practical systems may not follow equilibria as mentioned, such alloys can be treated as in the equilibrium state, and a number of phase transformations can be described in ternary systems. Four-phase equilibrium is one of the distinctive cases. The first representative case is a decomposition of a single phase upon cooling to form three new phases, which was already pointed out in Fig. 3.18, such eutectic and eutectoid reactions.

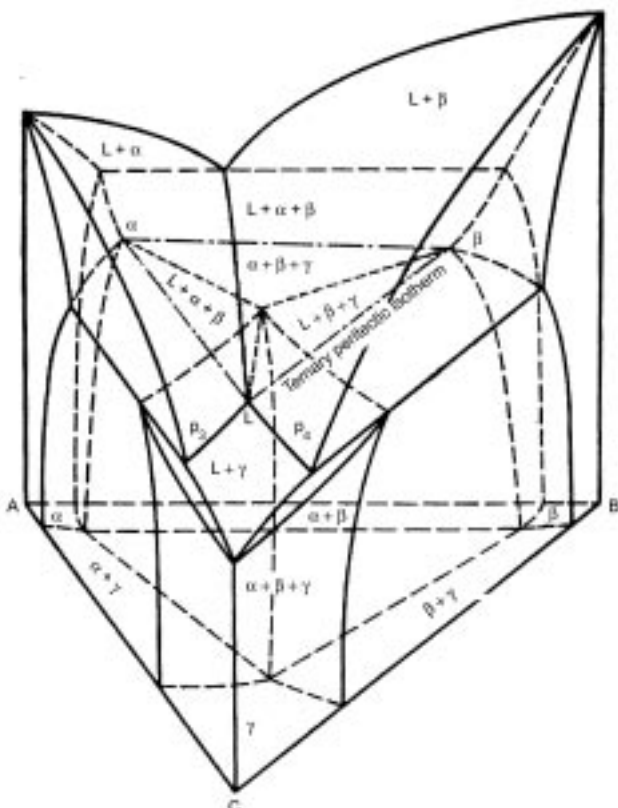




3.22 Non-equilibrium solidification for the binary eutectic system A-B.



3.23 Phase diagram for the ternary system A-B-C based on two eutectic and one peritectic binaries.⁴



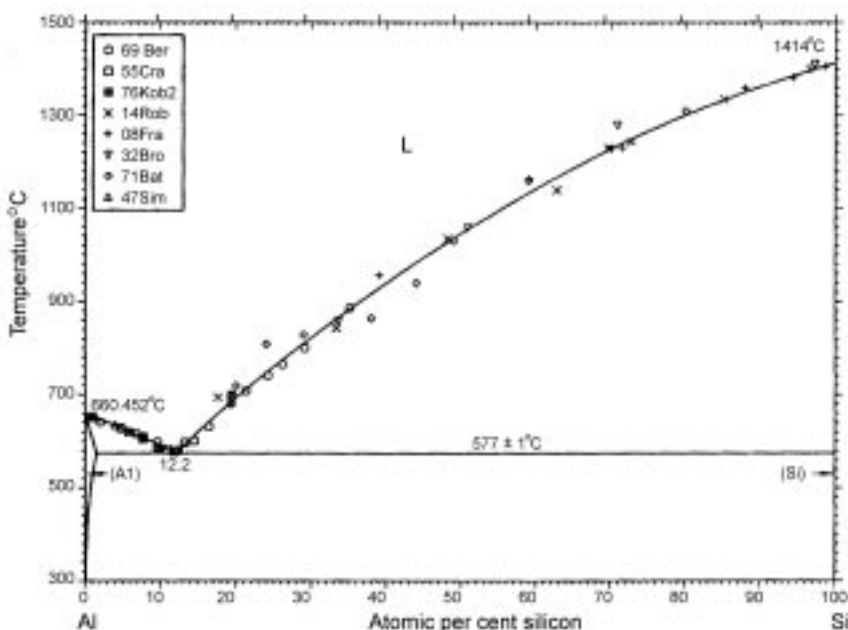
3.24 Phase diagram for the ideal ternary peritectic system A-B-C.⁴

Another type of four-phase equilibrium is a decomposition of two phases on cooling to form two new phases, which can be explained by a typical phase diagram shown in Fig. 3.23.⁴ The system is composed of one peritectic and two eutectic binaries. Two boundary lines (alterative and crystallization curves of $L + \alpha \rightarrow \beta$ and $L \rightarrow \alpha + \gamma$), p_1 and p_2 , descend from each binary with increasing amount of the third component and meet somewhere in the middle, where the reaction, $L + \alpha \rightarrow \beta + \gamma$, occurs at a constant temperature until the α phase diminishes. During this stage, four-phase equilibria are attained. Thereafter, three-phase equilibria among L , β and γ will be kept on cooling.

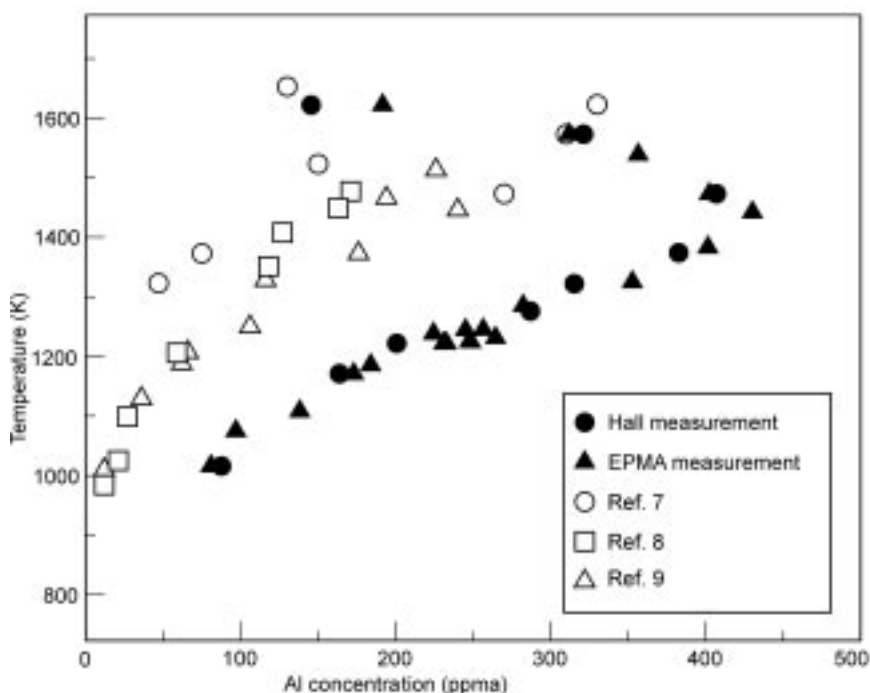
One more case is shown in Fig. 3.24.⁴ When two alterative curves forming γ phase, p_3 and p_4 ($L + \alpha \rightarrow \gamma$ and $L + \beta \rightarrow \gamma$), ascend from binaries with increasing amounts of the third component and meet as shown in the figure, where the reaction, $L + \alpha + \beta \rightarrow \gamma$, occurs at a constant temperature.

3.5 Examples of solidification behaviour from a phase diagram perspective

Various metals are often refined by oxidation of impurities followed by their removal into slag phases. In steel refining treatments, several impurities, such as phosphorus, silicon, carbon, etc., are removed during oxygen blowing processes. As can be seen in the Ellingham diagram, oxidation refining of silicon is hopeless because it will be preferentially oxidized to most of the impurity elements, such as iron, titanium, etc. On the other hand, the solubilities of most impurity elements in solid silicon are extremely low. Figure 3.25 shows the Al-Si binary phase diagram⁵ and the solubility curve of aluminum in solid silicon is reported as shown in Fig. 3.26.⁶ Although there are discrepancies among the reported data, the solubility of aluminium in solid silicon can be found to be lower than 100 ppmw at 1000K. For example, when 74 mass% Al-Si molten alloy was cooled from above liquidus temperature, solid silicon with only 100 ppmw Al starts to precipitate at 1000K, which means that 99.995% of aluminium was excluded by solidification at the initial stage. This principle of solidification refining makes the ultra high purification of silicon for semiconductors easier. Although some elements, such as phosphorus and boron, have high solubility in solid silicon, most impurities can



3.25 Phase diagram for the Al-Si binary system.



3.26 Solubility of aluminium in solid silicon reported by several researchers.

be removed by the one-directional solidification refining due to their small segregation coefficients, which are tabulated in Table 3.1.

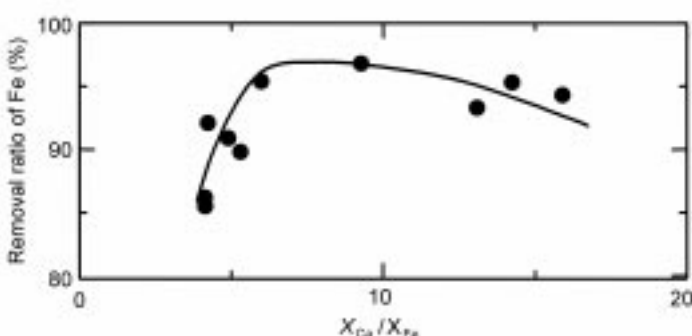
Herewith, an example of solidification behaviour of a ternary silicon-based alloy is considered. Since solubilities of most impurities in solid silicon are negligibly small, they tend to concentrate at the grain boundaries of primary crystals of silicon almost free from such impurities. By making use of this tendency, a new refining process¹⁰ has been proposed, combined with the acid leaching procedure. Although efficiency of impurity removal strongly depends on its segregation coefficient, pure silicon grains remain after condensed impurities at the grain boundary are washed away by acid dissolution. In order to promote the selective dissolution of the grain boundaries by leaching process, a

Table 3.1 Segregation coefficients of impurities in silicon

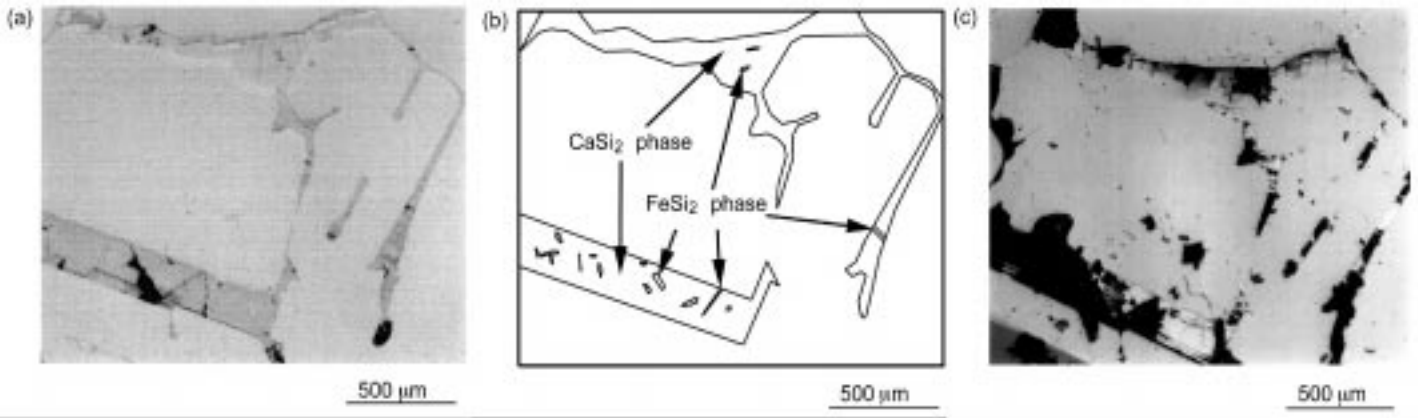
Impurity	Segregation coefficient	Impurity	Segregation coefficient
B	8.00×10^{-1}	Fe	6.40×10^{-6}
P	3.50×10^{-1}	Ti	2.00×10^{-6}
C	5.00×10^{-2}	Cu	8.00×10^{-4}
Al	2.80×10^{-3}		

leachate must corrode the boundary phase, but its amount may not be enough in the case of silicon. Hence, the addition of an acid soluble element which forms intermetallic compounds or eutectic microstructure with silicon might be effective. One of the promising elements to form such phases is calcium as shown in the following paragraph.

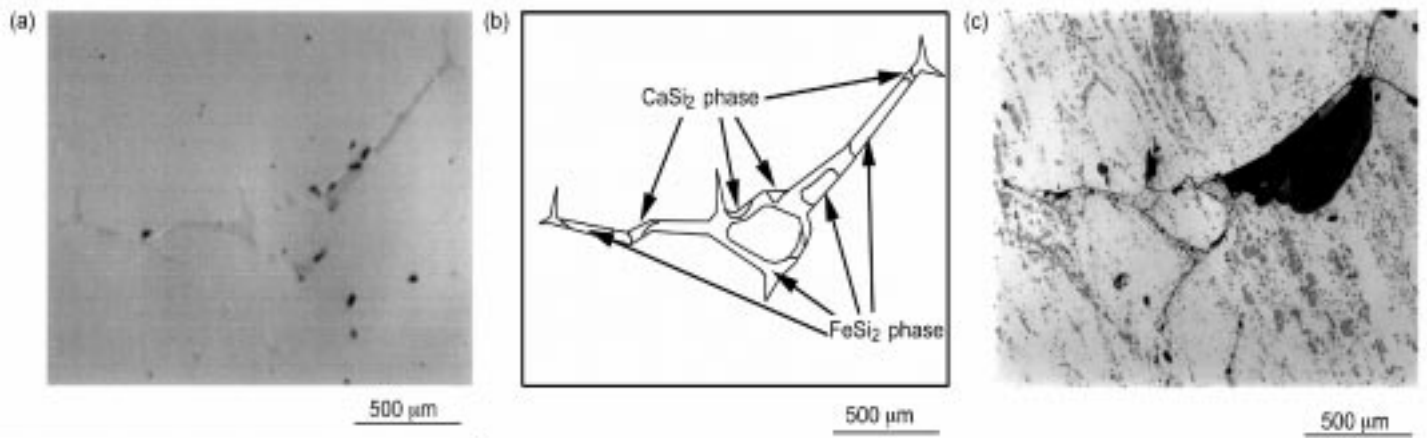
Recently, a new mass production process of solar grade silicon has been developed in order to solve the rapidly increasing demand of solar cells. Metallurgical grade silicon (>98%) is selected as a starting material and the final purity of solar grade silicon should be higher than 6N through some metallurgical refining treatments. Among others, iron is one of the most harmful elements for the solar grade silicon since it shortens the lifetime and drastically lowers the efficiency of solar cells. As mentioned previously, however, iron is less favourable to be oxidized than silicon, and oxidation refining is not suitable as well as vacuum refining for high vapour pressure species. Hence, the only effective way is solidification refining using a segregation coefficient as low as 10^{-6} .¹¹ However, another pretreatment at the stage of metallurgical grade silicon may be helpful for reducing the solidification refining cost. Accordingly, iron removal from metallurgical grade silicon by acid leaching was investigated.¹² Figure 3.27 shows the experimental results in which Si-Ca-Fe alloys with various compositions were subjected to acid leaching procedure using aqua regia. Calcium was added to form an acid soluble grain boundary. As seen in the figure, there seems to be an optimum ratio of calcium to iron content. Optical images of Si-Ca-Fe alloys of two different compositions before and after acid leaching are shown in Figs 3.28(a), (c) and 3.29(a), (c). The sample shown in Figs 3.28(a), (b) and (c) has higher calcium to iron ratio and calcium silicide, CaSi_2 , seems to have precipitated as a secondary phase during cooling, after silicon precipitated as a primary phase. Iron silicide phase, FeSi_2 , was considered to exist as a part of the microstructure



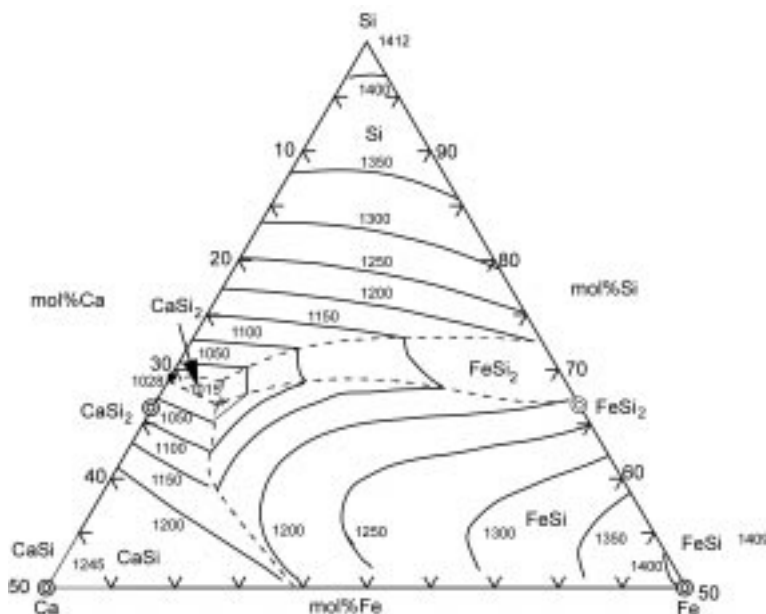
3.27 The relationship between ratio of calcium to iron content and removal ratio of iron.



3.28 (a) Optical image of Si-Ca-Fe alloy (Si-8.64%Ca-0.756%Fe, before acid leaching). (b) Microstructure of Si-Ca-Fe alloy. (c) Optical image of Si-Ca-Fe alloy (Si-8.64%Ca-0.756%Fe, 5 min. in aqua regia).



3.29 (a) Optical image of Si-Ca-Fe alloy (Si-0.929%Ca-1.21%Fe, before acid leaching). (b) Microstructure of Si-Ca-Fe alloy. (c) Optical image of Si-Ca-Fe alloy (Si-0.929%Ca-1.21%Fe, 5 min. in aqua regia).



3.30 Phase diagram for the Ca-Si-Fe system.

of the ternary eutectic of $\text{Si}-\text{CaSi}_2-\text{FeSi}_2$ which is easily soluble in aqua regia. On the other hand, when the ratio of calcium to iron is lower, FeSi_2 precipitates as a secondary phase and most of the FeSi_2 precipitates remained after acid leaching procedure. Figure 3.29(c) shows the optical image after acid leaching, where a large piece of undissolved FeSi_2 was observed on the grain boundary.

These phenomena can be confirmed by following the solidification behaviour from phase diagram viewpoint. Since reliable data for the $\text{Si}-\text{Ca}-\text{Fe}$ system were not available, the ternary phase diagram was drawn as shown in Fig. 3.30 using ‘Thermo-Calc’, a thermodynamic database and software. From the diagram, the secondary phase should be CaSi_2 when $X_{\text{Ca}}/X_{\text{Fe}} > 6.5$ and FeSi_2 when $X_{\text{Ca}}/X_{\text{Fe}} < 6.5$. This coincides with the experimental results that the optimum composition for iron removal is $X_{\text{Ca}}/X_{\text{Fe}} \approx 6-9$ as shown in Fig. 3.27. Accordingly, controlling the alloy composition to ensure the precipitation of CaSi_2 secondary phase during cooling becomes the key for the removal of iron from silicon by acid leaching procedure. As can be seen in the present example, comprehension of phase diagram in view of solidification behaviour is helpful in developing a new technology in materials science.

3.6 Conclusions

In this chapter, fundamentals of chemical potential diagrams and phase diagrams were briefly reviewed and solidification behaviour was discussed through phase

diagram perspective by showing simplified examples together with recent experimental work. Both diagrams are helpful in predicting a final product and in verifying the processing conditions.

We often treat the systems in non-equilibrium states, such as supercooling, appearance of metastable phases, non-uniformity due to slow diffusion or slow reaction processes, etc. Such conditions are preferable or artificially created in producing various new materials, such as low T_C superconductors, semiconductor compounds, new glasses and ceramics, etc. They are developed with profound consideration on relations among the phases whether they are stable or metastable. Henceforth, fundamental studies on phase diagrams should be continued for the future development of materials science and engineering.

3.7 References

1. *Phase Diagram of Binary Iron Alloys*, H. Okamoto (ed.) (1993), ASM International, Materials Park, OH.
2. *Physical Chemistry of High Temperature Technology*, E.T. Turkdogan (1980), Academic Press, New York, NY.
3. *Phase Diagram for Ceramists*, vol. I, E.M. Levin, C.R. Robbins and H.F. McMurdie (eds) (1964), American Ceramic Society, Westerville, OH.
4. *Phase Diagrams in Metallurgy*, F.N. Rhines (1956), McGraw-Hill Book Co., Columbus, OH.
5. *Binary Alloy Phase Diagrams*, T.B. Massalski and H. Okamoto (eds) (1990), ASM International, Materials Park, OH.
6. T. Yoshikawa and K. Morita (2003), *J. Electrochem. Soc.*, **150**, G465.
7. R.C. Miller and A. Savage (1956), *J. Appl. Phys.*, **27**, 1430.
8. D. Navon and V. Chernyshov (1957), *J. Appl. Phys.*, **28**, 823.
9. V.N. Lozovskii and A.I. Udyanskaya (1968), *Izv. Akad. Nauk SSSR, Neorg. Mater.*, **4**, 1174.
10. T.L. Chu and S.S. Chu (1983), *J. Electrochem. Soc.*, **130**, 455.
11. R.H. Hopkins and J. Rothatgi (1986), *J. Cryst. Growth*, **73**, 67.
12. T. Sakata, T. Miki and K. Morita (2002), *J. Japan Inst. Metals*, **66**, 459.

Measurement and estimation of physical properties of metals at high temperatures

K C M I L L S , Imperial College, London, UK

4.1 Introduction

4.1.1 The need for thermo-physical property data

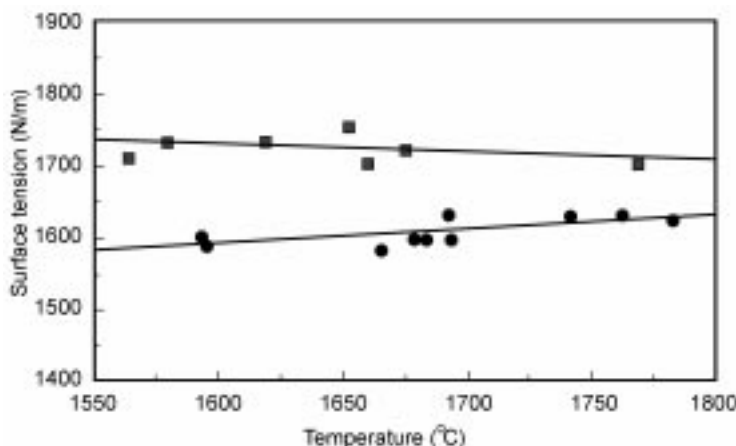
Surveys of the requirements of industry show that there is an urgent need for reliable data for the thermo-physical properties of the materials involved in high-temperature processes (metals, slags and refractories). This need arises from the fact that thermo-physical property data have proved extremely useful in improving both process control and product quality. Physical property data are beneficial in two ways:

1. In the direct solution of industrial problems.
2. As input data in the mathematical modelling of processes.

One example of the direct use of physical property data is in the case of ‘Variable weld penetration’ in gas tungsten arc (GTA sometimes known as TIG) welding of steels. Some applications require a large number of welds (e.g. heat exchangers). In these cases the welding conditions providing good weld penetration are established in preliminary trials. However, sometimes another batch of the materials (fully matching the materials specification) had to be used and the resulting welds were very shallow and consequently, weak. Compositional differences between the two batches were very small. Subsequent work^{1–3} showed that:

- (i) good weld penetration was associated with lower surface tensions (γ) and a positive temperature dependence ($d\gamma/dT$) and a sulphur content of >50 ppm of the steel; and
- (ii) shallow weld penetration was associated with a high surface tension, a negative ($d\gamma/dT$) and a sulphur content of <30 ppm (Fig. 4.1).

The effect of sulphur on the surface tension (γ) and its temperature dependence ($d\gamma/dT$) of steel is shown in Fig. 4.2.⁴ The heat transfer in the weld pool is determined by the fluid flow and there are several forces affecting the fluid flow,



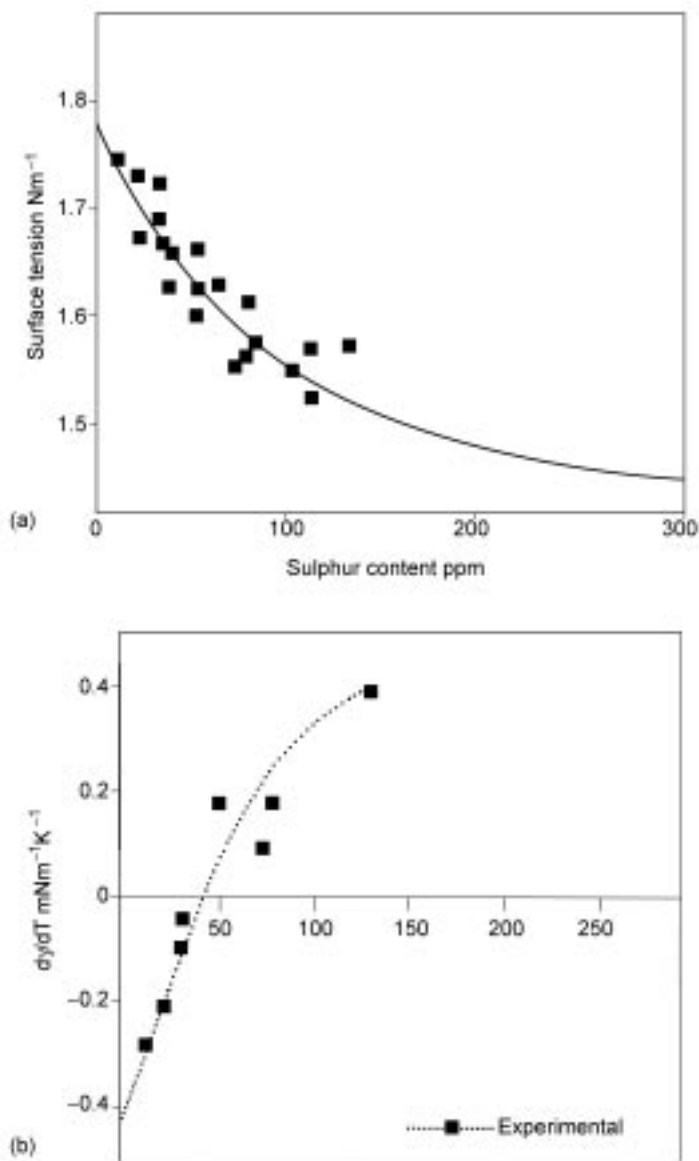
4.1 Surface tension–temperature relations for two stainless steels exhibiting good penetration (lower curve, S content > 50 ppm) and poor penetration (upper curve, S content < 30 ppm).

namely, buoyancy, Lorenz, aerodynamic drag and thermo-capillary (Marangoni) forces.^{1–3} However, the Marangoni forces are dominant because of the huge temperature gradients across the surface of the weld pool. In steels with S < 30 ppm ($d\gamma/dT$) is negative (Fig. 4.2) and thermo-capillary flow (high γ to low γ) is radially-outward taking hot liquid to the periphery of the weld where melt-back produces a shallow weld (Fig. 4.3). For steels containing more than 50 ppm S the thermo-capillary forces are inward and the hot liquid is forced down the weld and melt-back occurs in the bottom of the pool giving a deep weld. Surface tension measurements played an important part in solving this problem.

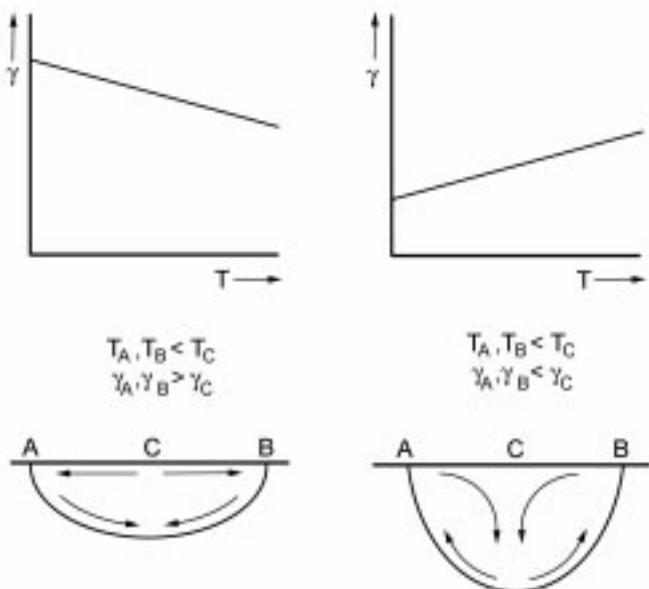
Mathematical modelling has proved a valuable tool in improving process control and product quality. There are several types of mathematical models, e.g. those based on thermodynamics, kinetics and heat and fluid flow of the process. In this review we are mainly concerned in the modelling of the heat and fluid flow in the process.

Defects in a casting can result in the scrapping of a casting. The cost of scrapping has been estimated to be greater than 2 billion US\$ per annum. Mathematical models of the heat and fluid flow have been developed to predict the locations of defects. It has been shown that the accurate prediction of defects requires accurate thermo-physical data for the alloy being cast.⁵ Similar models have been developed for the prediction of micro-structure (e.g. dendrite arm spacing) and Fig. 4.4 shows the sensitivity of local solidification time to changes in the various properties⁶ of aluminium alloys. It can be seen that it is particularly sensitive to the thermal conductivity value used.

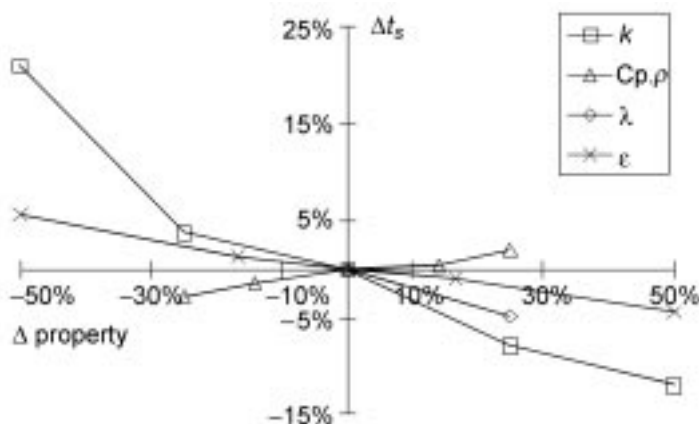
The properties needed for modelling fluid flow and heat and mass transfer are as follows.



4.2 The effect of sulphur content on (a) surface tension (γ) at 1923K and (b) its temperature dependence ($d\gamma/dT$).⁴



4.3 Schematic diagram illustrating the mechanism for variable weld penetration showing fluid flow in the weld pool for a steel with $S < 30$ ppm on the left and for a steel with S content > 50 ppm on the right.^{1,2,3}



4.4 Sensitivity of local solidification time to thermal conductivity, (k) the parameter (density \times heat capacity, ($Cp.\rho$)) latent heat (denoted λ)⁶ and emissivity (ϵ).

Heat flow	Fluid flow	Mass transfer
Heat capacity, enthalpy	Density	Diffusion coefficient
Thermal conductivity/diffusivity (Electrical conductivity)	Viscosity	
Emissivity	Surface/Interfacial tension	
Optical properties (slags and glasses)		

These data are needed for alloys, slags, glasses and fluxes. The measurements are time-consuming and require considerable expertise. Consequently, it is an enormous task to provide all the thermo-physical data for all materials involved in the various industrial processes. Thus, considerable effort has been devoted to the estimation of physical properties. Usually these estimations are based on the chemical composition since this is usually available on a routine basis.

4.2 Factors affecting physical properties and their measurement

4.2.1 Structure

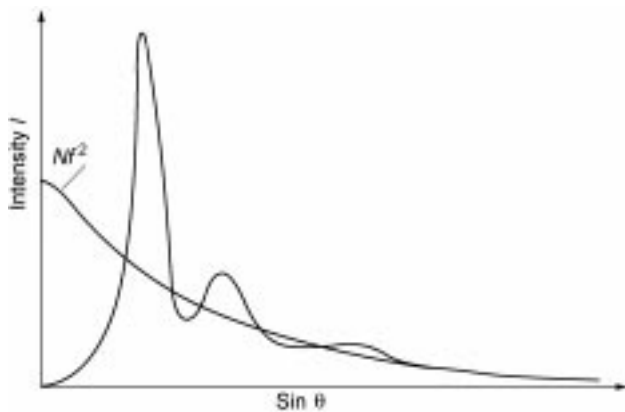
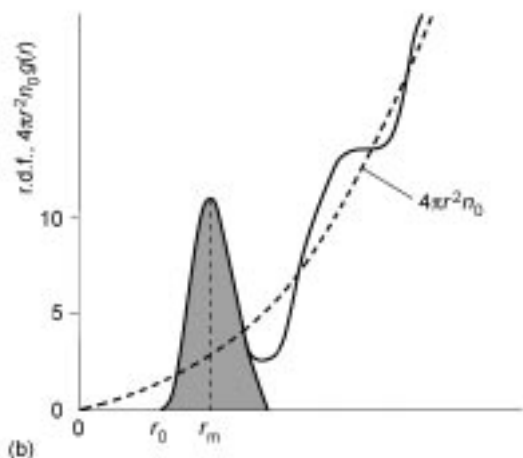
Some physical properties are very dependent upon the structure of the sample. The effect of structure is greatest in the case of viscosity and, in fact, viscosity measurements have been used in conjunction with other data to determine the structure of melts. The effect of structure on property values is in the following hierarchy: viscosity > thermal conductivity > electrical conductivity > density (small) > enthalpy (usually has little effect). Structural effects tend to be much larger for slags and glasses than for metals.

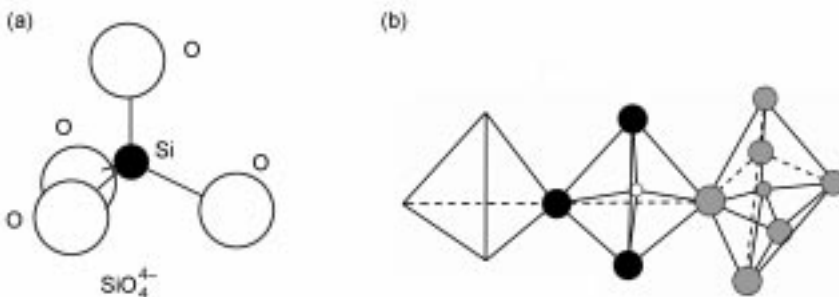
Both X-ray and neutron diffraction have proved very useful in determining the structure of solids. In crystalline solids the atoms have well-defined positions. The array of atoms interferes with the passage of X-rays which are scattered in all directions except those predicted from Braggs law:

$$\lambda = 2d \sin \theta \quad (4.1)$$

where λ is the wavelength, d is the distance between two layers of crystals and θ is the angle of diffraction. X-ray diffraction patterns for a gas show a constant scattering intensity with no maxima due to the random distribution of atoms. However, X-ray diffraction patterns for liquids exhibit a few maxima and minima (Fig. 4.5) indicating that atoms are randomly distributed in an approximately close-packed array (short range order) but have little long range order due to the thermal excitation and motion.⁷ The principal parameters used to describe structure are derived from X-ray and neutron diffraction data, namely:

- **Pair distribution factor ($g(r)$)** where r is the radius and $g(r)$ is the probability of finding another atom at a certain position (Fig. 4.6a); in real liquids $g(r)$ is

4.5 X-ray diffraction pattern for a liquid.⁷4.6 (a) Pair distribution function ($g(r)$) of a metal near its melting point and (b) radial distribution function (rdf): the number of nearest neighbours can be determined from the area of the hatched region.



4.7 Schematic drawings of (a) tetrahedral arrangement of Si-O bonds and (b) silicate chain with bridging O (O°) shown in black, non-bridging O (O^-) as hatched and tetrahedrally-coordinated cations as open.

affected by attraction and repulsion forces (of other atoms).

- **Radial distribution factor** (rdf) can be calculated from $g(r)$; the hatched area in Fig. 4.6b is a measure of the number of nearest neighbours (i.e. coordination number).

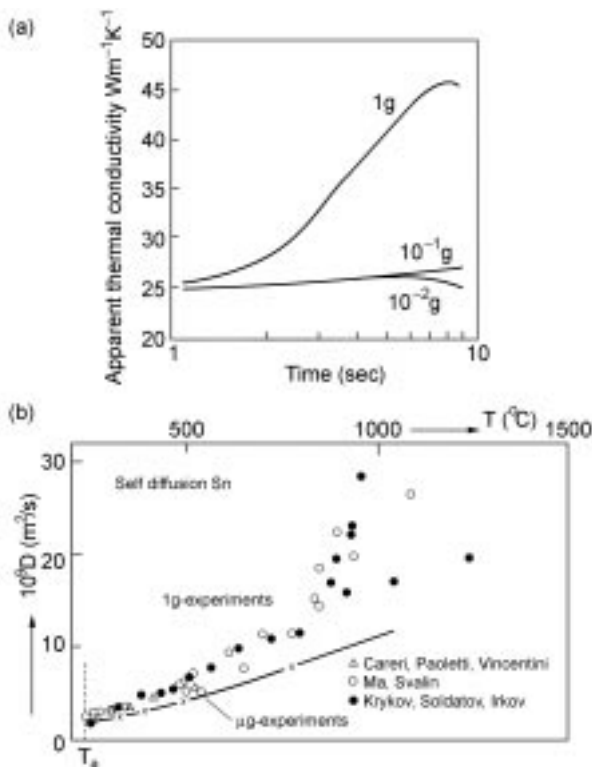
Other parameters used to describe the structure are summarised by Iida and Guthrie.⁷ The situation is much more complicated in alloys since for a binary alloy three distribution factors are needed, namely, $(g(r))_{11}$, $(g(r))_{22}$ and $(g(r))_{12}$.

Structure of slags and glasses

Slags and glasses are polymers in the form of chains, rings etc made up of SiO_4^{4-} tetrahedral units. They have the following characteristics:⁸⁻¹¹

- Each Si (with a valence of 4) is surrounded (tetrahedrally) by 4 O ions (with a valence of 2) each connecting to 2Si ions (Fig. 4.7).
- In SiO_2 these SiO_4^{4-} tetrahedra are connected in a three-dimensional polymerised structure (Fig. 4.8) and the oxygens are predominantly *bridging oxygens* (denoted O°).
- Cations such as Ca^{2+} , Mg^{2+} etc. tend to break up the Si-O bonds and depolymerise the melt by forming *non-bridging oxygens* (NBO denoted O^-) and *free oxygens* (denoted O^{2-}), i.e. not bound to Si.
- Other cations such as Al^{3+} , P^{5+} , Ti^{4+} can fit into the Si polymeric chain but need to maintain charge balance, e.g. if an Al^{3+} is incorporated into a Si^{4+} chain it must have a Na^+ (or half* of a Ca^{2+}) sitting near the Al^{3+} to maintain local charge balance.
- Smaller cations such as Mg^{2+} tend to give a wider distribution of chain lengths than larger cations such as Ba^{2+} .

* The Ca^{2+} would charge balance two neighbouring Al^{3+} ions.



4.8 The effect of convective flows (shown by differences between values obtained in micro-gravity (0g) and on earth (1g)) for (a) thermal conductivity¹⁹ and (b) diffusion coefficient.²⁰

- Cations such as Fe^{3+} in small concentrations can act as network breakers but in higher concentrations can be incorporated into the chain in a similar way to Al^{3+} .
- The degree of polymerisation can be expressed in terms of the numbers of bridging (N^{Oo}) non-bridging (N^{O^-}) and free-oxygens ($\text{N}^{\text{O}_2^-}$). However, the degree of de-polymerisation is frequently represented by parameters such as the ratio of {NBO/(the number of O atoms in tetragonal coordination)} which is denoted (NBO/T)⁸⁻¹¹ or the optical basicity¹¹ (see Appendix A).
- The structure of melts (both slags and metals) can be represented using thermodynamic quantities (e.g. excess free energy^{12,13}) since thermodynamics provides a description of bond strengths.
- B^{3+} has threefold coordination in borosilicates but the structure of borosilicates (used as enamels) is a complex mixture of 3- and 4-coordination.^{14,15}
- The structure of glasses are very similar to those of liquid slags.¹⁶

- Many metallurgical slags have a high basicity (e.g. $\text{CaO}/\text{SiO}_2 > 2$) and consequently the Si ions are predominantly in the form of monomers, i.e. completely de-polymerised.

Methods of determining structure

The various methods of determining structure are summarised in Table 4.1. For further details the reader should consult other sources.^{7,8,9,17}

4.2.2 Surface and interfacial properties

It should be noted that surface and interfacial tensions are *interfacial* properties and not *bulk* properties. Consequently, they are dependent upon the composition and structure of the interface. Certain materials are *surface active* and have a dramatic effect on the surface tension and its temperature dependence as can be seen in Fig. 4.2. These surface-active materials have low surface tensions and have much larger concentrations in the surface layer than in the bulk. For instance, sulphur concentrations in the surface layers of steels were found to be 100x that in the bulk. Thus ppm levels of strongly surface active components can have a dramatic effect on surface and interfacial tensions. In metals the hierarchy of surface activity is Group VI > Group V > Group IV and within any group surface activity increases with increasing molecular weight, e.g. Te > Se > S = O. In slags and glasses it has been reported that B_2O_3 , P_2O_5 , Fe_2O_3 , Cr_2O_3 , Na_2O and CaF_2 are surface-active.¹⁸

4.2.3 Convection

Measurements of both thermal conductivity and diffusivity and diffusion coefficients for liquids are greatly affected by convection.^{19,20} In practice it is difficult to eliminate convection. The following techniques have been used to eradicate (or minimise) convection:

- Use of *transient* techniques where the measurements are made very rapidly such that the experiment is completed (in usually <1s) before the convective flow has been established.
- Creating a slightly higher temperature at the free surface of the liquid than at the bottom.
- Carrying out measurements in micro-gravity (0g) to eliminate buoyancy-driven convection.¹⁹
- Suppressing convection by using electro-magnetic fields.²¹

It should be noted that thermo-capillary convection can also arise from temperature gradients along the free surface but Nagata *et al.*²² placed a solid lid on the free surface to eliminate these forces.

Table 4.1 Methods used to obtain structural information on melts

Method	Measurement	Structural information obtained
Diffraction		
X-ray, neutron, electron	rdf	1. Bond lengths 2. Coordination numbers 3. Inter-tetrahedral angles T-O-T 4. Overall intermediate structure 5. Local O coordination around large cations
Spectroscopy		
Raman, infra-red ultra-violet		1. Bond lengths 2. Bond angles 3. Identification and concentrations of various anionic units
Nuclear magnetic resonance (NMR)	Chemical shift	1. Bond lengths 2. Bond angles 3. Identification and concentrations of various anionic units
Mossbauer	Isomer shift	1. Valence state 2. Coordination of environment; identification and concentration of Fe^{3+} with fourfold and sixfold coordination 1. Distortion of O polyhedron 2. Oxidation state Fe^{2+} or Fe^{3+} 3. Coordination of Fe^{3+} (fourfold or sixfold)
	Quadrupole splitting	
X-ray absorption spectroscopy	EXAFS	1. Bond lengths 2. Bond angles
	XANES	3. Coordination of specific atoms or ions
X-ray emission (ESCA or XPS) ESR spectroscopy	$K_\alpha: K_\beta$	1. Coordination of specific atoms or ions 2. Changes in valence state
Luminescence spectroscopy		Coordination of Mn^{2+} , Fe^{3+} , Ti^{3+} or S (S^{2-} or SO_4^{2-})
Chromatography		Distribution of chain lengths of different polymeric units
Property measurement		
	Density, molar volume	Packing and coordination
	Molar refractivity	Concentrations of $\text{N}^{0\circ}$, N^{0-} ; N^{02-}
	Viscosity	1. Activation energies related to bond strength 2. Effect of cations on structure
	Enthalpy of mixing, or solution	1. Measure of bond strength 2. Effect of different cations including structural ordering
	Electrical/ Thermal conductivity	1. Indication of amount of ionic and electronic conduction 2. Information on whether fluorides form Si-F bonds
Molecular dynamics (MD)	Calculations	1. Bond strengths 2. T-O-T angles 3. Coordination (e.g. Al is fourfold in $\text{Na}_2\text{O} + \text{Al}_2\text{O}_3 + \text{SiO}_2$ slags)
Thermo-dynamic modelling	Calculations	Concentration of various anionic polymeric units in melt

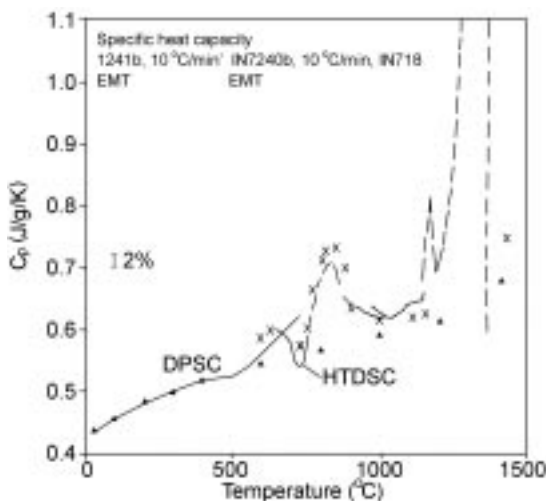
The effect of buoyancy-driven convection on thermal conductivity and diffusion coefficient measurements can be clearly seen in Fig. 4.8.

4.2.4 Dynamic methods

In some techniques (e.g. DTA or DSC) a set heating rate is used (e.g. 10 Kmin^{-1}). The property measurements (e.g. heat capacity) derived with these *dynamic* techniques are in general agreement with *equilibrium* values when the sample contains no phase transitions. However, solid state transitions tend to be sluggish. Consequently, when using dynamic techniques the sample reaches the transition temperature and the transition does not have time to disorder completely and come to equilibrium. This leads to erroneous values of the property being studied (e.g. C_p) for this temperature. However, at some higher temperature the phase transition will occur and there will be a re-organization of the atoms and this will result in a readjustment of the property value.²³ In the exploding wire technique^{24–28} the heating rates are exceedingly high ($>10^6\text{ Kmin}^{-1}$) and thus any changes in enthalpy arising from solid state transitions will tend to be ‘smeared’ over a temperature range.

In nickel-based superalloys the coarsening of the γ phase is followed closely by the dissolution of the γ' phase (Fig. 4.9). Under these circumstances it is difficult to determine to obtain an equilibrium value for the C_p of the γ' phase.²³

In dynamic methods (DSC) the enthalpy of fusion is manifested as an *apparent* enhanced C_p value (C_p^{app}) (Fig. 4.9) The enthalpy of fusion can be obtained by integrating the C_p -T curve and the fraction solid at any specific temperature can be derived from the area up to that temperature divided by the



4.9 Heat capacity values for Ni-based superalloy IN 718 as a function of temperature: the dotted sections should be regarded as apparent C_p values.²³

area corresponding to the enthalpy of fusion. However, these C_p^{app} values are not the true values of the heat capacity and should not be used for calculating, for instance, thermal conductivity (k) values from thermal diffusivity (α) measurements by the relation, $k = \alpha \cdot C_p \cdot \rho$.²³ Estimated values (see Section 4.7.1) can be used for this purpose without much loss of accuracy. This would also apply to first order solid state transformations.

4.2.5 Measurements in the mushy zone

Transient techniques are the most reliable way of minimising convective contributions to thermal conductivity (k) measurements on liquids. In these techniques a short pulse of energy is delivered and the change in temperature as a function of time is monitored. However, when these techniques are applied to samples containing both solid and liquid ('mushy') some of the energy is not conducted but is used to convert solid into liquid. This leads to erroneous values of the conductivity in the mushy range. It has been shown that the Wiedemann–Franz–Lorenz (WFL) rule ($k = 2.445 \times 10^{-8} (T/R) \text{ W m}^{-1} \text{ K}^{-1}$ where T is in K) linking thermal conductivity (k) and electrical resistivity (R) works well around the melting range and consequently the best way of deriving thermal conductivities is via electrical resistivity measurements in the mushy zone. Alternatively, the following formula can be used: $k_T = f_s k_{s\text{Tsol}} + (1 - f_s) k_{l\text{Tliq}}$ where f_s = fraction solid in the sample, $k_{s\text{Tsol}}$ is the thermal conductivity of the solid phase at the solidus temperature and $k_{l\text{Tliq}}$ is the thermal conductivity of the liquid at the liquidus temperature.²³

4.2.6 Commercial materials

Measurements on commercial materials are more difficult and are subject to greater uncertainty than those carried out on pure metals or synthetic slags for the following reasons:

- Commercial materials are sometimes inhomogeneous and the compositional differences may be significant when small specimens are used.
- Commercial materials frequently contain reactive elements (such as Al in alloys) which can react with containers, the atmosphere or soluble elements (e.g. oxygen) to form Al_2O_3 inclusions (which increase the viscosity), or surface films or oxide skins which affect the experiment.

4.3 Measurements and problems

4.3.1 Reactivity of sample

The paucity of reliable values of thermo-physical properties at high temperatures is a reflection of the measurement difficulties experienced at high temperatures.

These difficulties can be expressed in terms of the unofficial laws of high temperatures, namely:

1. '*At high temperatures everything reacts with everything else.*'
2. '*They react very quickly and the situation gets worse (quicker) the higher the temperature.*'
3. '*At high temperatures there are no electrical insulators.*'

Consequently, in recent years there has been a rapid development of *containerless* methods and techniques since these minimise the contact between the sample and the container. These containerless methods encompass:^{29,30}

- *Levitation*, including electro-magnetic (EML), electro-static (ESL), aerodynamic (ADL) and ultra-sonic (USL) levitation.
- *Measurements carried out in micro-gravity (0 g)* using space flights, parabolic flights and drop towers.
- *Pendent drop* where the tip of a sample rod is melted with an electron beam or other source of energy (consequently the liquid is only in contact with the remainder of the sample).
- *Exploding wire* techniques where measurements are carried out between room temperature and up to 5000K in a period of ms and values are obtained for both the solid and liquid phases before the sample explodes.

Other techniques used for high temperature measurements should be (i) robust; (ii) involve minimum contact between sample and container; and (iii) have a minimum of moving parts. Typical examples are:

- *Laser pulse method* for measuring the thermal diffusivity of solid and liquid samples.
- *Surface laser light scattering (SLLS)* where measurements of viscosity and surface tension have been derived from the reflected beam hitting the surface of a liquid.
- The *draining crucible method* where the viscosity, surface tension and density have been derived from the drainage rates through an orifice in the base of a crucible.

When using a technique which involves some contact between sample and container, the selection of container materials is an important issue in high temperature measurements. It is customary to fabricate containers and probes from oxides when making measurements on metals. Similarly, metals are used as containers when making measurements on liquid oxides (slags, glasses and fluxes).

- The usual oxides used for containing molten metals are those with high thermodynamic stability, namely Al₂O₃, MgO, ZrO₂ and CaO.
- The usual metals used for containing molten slags and glasses are Pt (for

oxidising or neutral atmospheres) Mo, W, Ta and Fe or Ni (with reducing or neutral atmospheres).

- Graphite (carbon) and carbide (e.g. SiC) containers are sometimes used where metals have a low solubility for carbon (e.g. copper and aluminium) but should not be used for metals with a high solubility for carbon (e.g. Fe, Co and Ni). Carbon has also been used for containing slags and glasses but may react with some components (e.g. PbO) of the sample.
- Boron nitride has also been used for holding metals but tends to oxidise to form an oxy-nitride at high temperatures and should only be considered for use where low partial pressures of oxygen in the apparatus can be guaranteed. Other nitrides have also been used where an oxide has been thought unsuitable.

4.3.2 Different methods for metals and slags and glasses

Property values for slags are sometimes very different from those for alloys. Consequently, different methods are needed for measurements on metals and alloys to those used for slags. For instance, the viscosities of slags lies in the range 100– 10^4 mPas and the rotating cylinder method is frequently used for measurements. In contrast, the viscosities of metals and alloys lie in the range 1–5 mPas where capillary and oscillating viscometers are the most suitable techniques.

4.4 Fluid flow properties

The principal properties involved in fluid flow are density (ρ), viscosity (η) and surface tension (γ). It should be noted that their temperature coefficients are equally important since $(d\rho/dT)$ determines the buoyancy-driven convection and $(d\gamma/dT)$ determines the strength of thermo-capillary flow.

4.4.1 Density (ρ) and thermal expansion coefficient (α, β)

The density (ρ) and molar volume (V) are linked through the relation:

$$(\rho V) = M \quad (4.2)$$

where M is the molecular mass.

The linear (α) and volume (β) thermal expansion coefficients are defined through equations (4.3) and (4.4), respectively, where L and V are the length and volume.

$$\alpha (K^{-1}) = (1/L)(dL/dT) \quad (4.3)$$

$$\beta (K^{-1}) = (1/V)(dV/dT) \quad (4.4)$$

Methods

There are several well-established methods for measuring density; these are listed below and further details are given elsewhere.^{7,30–34} The experimental uncertainty is usually $\pm 2\%$ or less.

- **Dilatometry** is the established method for determining the thermal expansion coefficient from length changes in the sample; the ‘piston method’ has recently been used to determine the densities of liquid metals and is particularly successful where the metal readily forms an oxide which tends to seal the apparatus.³⁵
- **Sessile and large drop** methods³⁶ have provided more accurate values in recent years as a result of the introduction of software to fit the profile of the drop or the free surface. Some errors may arise from asymmetry of the drop if it is viewed from one direction only.
- **Pycnometry** involves filling and weighing a vessel with known volume containing a liquid sample after cooling to room temperature.^{7,34,36}
- The **Archimedean** method provides reliable results but corrections have to be made for the effect of the surface tension of the sample on the suspension wire; there are several ways of compensating for this effect.⁷
- The **hydrostatic probe** works on similar principles and records the apparent weight of a probe at different immersion depths in the melt.³⁷
- The **maximum bubble pressure** method is principally used for measuring surface tension but densities can be obtained by measuring maximum bubble pressures at different immersion depths.⁷

Several new techniques have been introduced recently.

- The **exploding wire method**^{24,25} has been used to determine densities and thermal expansion coefficients for both solid and liquid states. Its principal drawbacks are (i) when studying materials exhibiting solid state transitions (see Section 4.2.4) and (ii) in the measurement of temperature. However, it is capable of obtaining measurements up to 5000K though experimental uncertainties for the thermal expansion values of $\pm 10\%$ have been reported.²⁵
- The **levitated drop** method views a drop horizontally and vertically and spherical images of the drop are selected and the volume of a drop (of known mass) determined; since the drops are only a few mm in diameter errors in edge detection can lead to experimental uncertainty but this is usually overcome by processing a large number of images.³⁸
- In the **draining crucible** method the rate of draining through an orifice is determined and the density is determined from a hydrodynamic analysis of the data.³⁹

In general, density measurements have sufficient accuracy for their subsequent use in mathematical models. The worst problems seem to be those caused by the

formation of tenacious oxide films or ‘skins’ such as those encountered in measurements on molten alloys containing significant amounts of Al and Mg.

Density data for metals, alloys slags, glasses

Sources of density data are given in Table 4.2 and density data for metallic elements are given in Table 4.3.

4.4.2 Viscosity (η)

There is a considerable difference between the viscosities of slags and glasses ($\eta = 100$ to 10000 mPas) and those for metals and alloys ($\eta = 0.5$ to 10 mPas). Consequently, different techniques are required to measure the viscosities of metals⁷ to those used for slags and glasses.

Slags

Methods

Several established methods are available:

- The **concentric cylinder** method exists in two forms in which the torque is measured when (i) the outer cylinder (crucible) is rotated and (ii) the inner cylinder (bob) is rotated. Although the **rotating crucible** method^{7,31–33} is capable of measuring to lower viscosities, the **rotating bob** method^{7,33} is usually preferred because it is easier to align and operate.
- In the **falling ball** method the time for a sphere to either fall or be dragged through the liquid sample is determined.³³ It is difficult to apply at high temperatures due to the limited length of the uniform hot zone under these conditions.

Table 4.2 Sources of property data for metals, alloys, slags and glasses

Property	Metals and alloys	Slags, glasses and fluxes
Density, ρ	7: 111, 112, 113, 114, 32, 34	33: 111, 18: 115
Viscosity, η	7: 111, 116, 112	33: 111, 18: 115
Surface tension, γ	7: 111, 58: 114	33: 111, 18: 115
C_p , ($H_T - H_{298}$)	117: 114, 118	
$\Delta_{\text{fus}}^{\text{H}}$		
Thermal conductivity, k	111, 80, 119, 120	33: 111, 18: 115
diffusivity, a		
Electrical conductivity, R	7, 111, 119, 120	33: 111, 18: 115
Emissivity and optical constants	111, 119, 120	33: 111, 18
Diffusion coefficients, D	7, 111: 121, 122	33: 111

- In the **oscillating plate** method the amplitudes of an oscillating plate are determined in the melt and in air.⁷ The apparatus constants are determined by calibration with liquids of known viscosity. Data for the product ($\eta\rho$) are obtained, so it is necessary to know the density of the melt for the given temperature.

Recently, two methods have been reported which may be suitable for measurements on slags and glasses:

- In the **surface laser light scattering (SLLS)** method ‘riplpons’ are monitored.^{40–42} The surface of a melt may appear smooth but it is being continually deformed by thermal fluctuations of the molecules. Capillary waves (riplpons) have small amplitude (*circa* 1 nm) and a wavelength of *circa* 100 μm which is dependent upon the frequency. Riplpon action depends upon surface tension for restoration and the kinematic viscosity ($\nu = \eta/\rho$) for oscillation damping. The spectrum of the ripples is derived using a Fourier spectrum analyser allowing the surface tension and the viscosity to be determined. The method has been successfully used for measurements on liquid silicon⁴² and LiNbO₃ up to 1750K.⁴¹ It has been estimated that it can be used for liquids with viscosities in the range 0.5–1000 mPas.⁴⁰
- In the **draining crucible** method³⁹ the rate of drainage through an orifice is determined and the viscosity is derived from a hydrodynamic analysis of the data. Although it has been applied to H₂O and liquid Al it would appear that the method is ideal for carrying out measurements on liquid slags and glasses.

Problems in measurements on slags and glasses

The experimental uncertainties associated with viscosity measurements on slags is of the order of $\pm 25\%$ but these uncertainties can be reduced to $\pm < 10\%$ by careful attention to the problems outlined below.

- Changes in chemical composition of the sample during measurements, e.g. the emission of gaseous fluorides (HF, NaF, SiF₃, etc.) or through crucible/sample reactions (e.g. FeO in the slag reacting with a C crucible).
- If the slag is non-wetting to the bob (which is thought to occur with some graphite bobs) there is ‘slip’ of the liquid around the bob which leads to low torque readings and hence low viscosity values.
- Inaccurate measurements of the temperature of the melt.

Metals

Metals have viscosities in the range 0.5 to 10 mPas and require different methods to those listed above for slags and glasses. The following methods are applicable to measurements on metals and alloys.

Table 4.3 The physical properties of metallic elements; the principal source for each property is given below and additional references are shown in parenthesis

Metal	T ^m K	ρ_{298} kg.m ⁻³	$\rho^m(I)$ kgm ⁻³	η^m mPas	γ^m mNm ⁻¹	k ^m (s) Wm ⁻¹ K ⁻¹	k ^m (I) Wm ⁻¹ K ⁻¹	$\epsilon^m(s)$	$\epsilon^m(I)$	$10^8 \cdot R^m$ (s) Ωm	$10^8 \cdot R^m$ (I) Ωm	Cp ₂₉₈ JK ⁻¹ kg ⁻¹	Cp ^m (I) JK ⁻¹ kg ⁻¹	$\Delta^{fus} H$ kJ kg ⁻¹
Ag	1235	10500	9330	3.9	925	363	175	0.037	0.066	8.2	17.2	235	310	105
Al	933	2698	2380	1.1	890 ^a (1024)	211	91			10.9	24.2	896	1180	397
Au	1336	19281	17400	5.0	1145	247	105	0.15	0.24	13.7	31.2	129	157	63.7
Bi	545	9803	10050	1.8	382	7.6	12			291	130			54.1
Cd	594	8647	8020	2.3	637	93	41			17.1	33.7	231	264	55.1
Ce	1072	6711	6690	2.9			22					193	269	39.0
Co	1768	8800	7750	5.4	1882	45	36	0.30	0.33	97	102	424	667	275
Cr	2180	7194	6290	5.7	1642	45	35							312
Cs	302	1900	1840	0.68		36	20			21.7	36			15.8
Cu	1358	8933	8000	4.37	1330	330	163	0.12	0.16	10.3 9.4	21.1 20	384	495	209
Dy		8531										172	308	66.4
Fe	1811	7873	7030	5.6	1870	34	33	0.35	0.38	128 122	139 110	439	824	247
Ga	303	5905	6100	2.0			28					639	695	80.2
Gd	1585	7870				19	19					147	235	62.4
Ge	1211	5323	5490	0.73		15	39			900	60	321	380	509
Hf	2506	13276	11970	5.0	1545	39						143	246	32.8
Hg	234	13546	13350	2.1						18.4	91	140	140	11.4
In	430	7290	7030	1.8	556	76	38			15.2	33.1	233	253	28.6
Ir	2719	22550			2264	95	76					130	305	214
K	337	862	830	0.5		98	56			8.3	13	760	800	59.3
La	1193	6174	5960	2.45			17					176	246	44.6
Li	454	533	518	0.57		71	43					3560	4200	432
Mg	923	1738	1590	1.25	577	145	79			15.4	27.4	1030	1410	349

Mn	1519	7473	5760	5.0	1152	24	22			66	40	482	874	235
Mo	2896	10222	9000		2083	87	72	[0.21]	[0.29]	6.6	9.6	250	443	375
Na	371	966	9270	0.68		120	88			9.6	1230	1348	113	
Nb	2750	8578	7620		1864	78	62	0.55*	0.35			267	452	323
Nd	1289	7000	6690				18.4					190	340	49.5
Ni	1728	8907	7900		1796	70	60	0.34	0.36	65.4	85	426	750	298
Os		22580	19200		2500							131	263	305
Pb	601	11343	10670	2.6	457	30	15			49	95	130	142	23.0
Pd	1828	11995	10490	4.2	1482	99	87	0.05				237	387	157
Pr	1204	6779	6610	2.8			22					195	305	48.9
Pt	2042	21450	18910		1746	80	53	0.32	0.36			133	187	114
Rb	312	1533	1480	0.6		58	33			13.7	22	363	363	25.6
Re	3459	21023	18000		2610	65	55	0.20*				137	269	325
Rh	2237	12420	10700		1915	110	69		[0.18]			243	491	258
Ru		12360	10750		2215							242	512	382
Sc	1814	2992				24.5	22.5					567	983	313
Si	1687	2329	2530	0.8	775 (859)	25	56	0.49	0.27 [0.17]			711	969	84.7
Sn	505	7285	6980	1.85	561	67	27			22.8	48	187	240	59.2
Ta	3290	16670	14600		2016	70	58	0.55*	0.37			141	232	202
Tc		11496			2200							255	480	340
Ti	1941	4508	4130	2.2	1525	31	31	0.45*		35.5	73.1	522	965	295
Tl	576	11871	11350	2.6	459							127	147	20.3
U	1406	19050	17270	6.5				0.26	0.34			110	126	38.4
V	2183	6090	5360	2.4	1855	51	44	0.18				490	929	422
W	3695	19254	16200		2210	95	63	0.50*	0.40			135	294	285
Zn	693	7135	6580	3.5	789	90	50	0.05		16.7	37.4	388	480	112
Zr	2128	6507	6240	3.5	1500	38	36.5	0.52*	0.36 [0.30]			279	460	230

Notes: ^a = O-saturated; * = may be affected by oxidation; [] = ϵ_{TH} ; () = indicates pure metal; Density (ρ) 7 (114); ρ_{298} 123 Viscosity (η) 116 (111, 112) Thermal conductivity (k) 80 $\epsilon_{\lambda N}$ (650–700 nm) 98, 99, 100 ϵ_{TH} Si = 54 Mo, Rh, Zr = 124–126 Electrical resistivity (R) = 7 Cp, Δf^{fus} H; 117

Methods

1. **Capillary viscometers** have been used for metals with melting points below <1400K. Full details of the method are given by Iida and Guthrie.⁷ Capillaries (80 mm long) and with small diameter (e.g. 0.3 mm) are required to maintain laminar flow. At high temperatures it is difficult to obtain a sufficiently large hot zone with uniform temperature.
2. In **oscillating viscometers** the crucible containing the test sample is given a twist and frictional energy absorption and dissipation occurs within the liquid. The time of oscillation and the log decrement of the amplitude of oscillations are determined.^{7,43,44} The aspect ratio of the crucible (i.e. length/internal radius) should have a value of >6.⁴⁵ Values for (η/ρ) are derived from the data. Several equations have been proposed to derive (η/ρ) from the log decrement data and these can lead to differences of $\pm 20\%$ in the calculated viscosity values. It has been shown^{7,45} that the modified Roscoe equation⁴⁶ provides the best solution but it should be noted that the equation usually used contains a typographical error.⁴⁵ When this is rectified the Roscoe equation gives values in excellent agreement with the Beckwith–Newell model.⁴⁷ Recent measurements for the viscosities of metals and alloys in different laboratories^{43,48,49} indicate that the differences are 10% or less.
3. Measurements of the damping characteristics of a levitated, **oscillating drop** yield values for the viscosity of the liquid.^{50–54} The method has been used with various forms of levitation (space experiments,⁵⁰ parabolic flights,⁵² drop tube,^{53,54} and electro-static levitation⁵¹). At the present time the values obtained have not been compared with viscosity values obtained by oscillation viscometry but the results for Ni-based superalloys are for the most part within $\pm 10\%$ of values obtained with oscillation viscometry.
4. The **surface laser light scattering (SLLS)** method (see above) is suitable for measurements on metals and may be used in the future.
5. The **draining crucible** (see above) has been used for the measurement of molten Al.^{38,55} Although the value obtained is lower than the value obtained (0.65 mPas) is lower than that obtained by oscillation viscometry (*circa* 1.1 mPas); the latter result may have been affected by the presence of a ‘skin’ of Al₂O₃ on the free surface of the melt or Al₂O₃ inclusions.

Problems with viscosity measurements

Most experimental problems lead to an erroneously high value for the viscosity:

- The presence of (i) oxide inclusions (e.g. Al₂O₃) (ii) unmelted phases (iii) the presence of a second immiscible phase in the primary liquid phase would all lead to an increase in the viscosity. Inclusions also tend to block the capillary in capillary viscometers and lead to erroneously high drainage times.
- Reactive metals (e.g. Al, Mg) form oxide films on the free surface of the sample, these oxide films can:

- (i) damp out all oscillations on the free surface and affect the results obtained with the oscillating drop and SLLS methods;
- (ii) affect the results obtained with oscillating viscometry (when the surface of Al was covered with a molten flux the viscosity was found to decrease from 1.2 to 0.7 mPas⁵⁶); and
- (iii) any oxide film drawn into the capillary during drainage would tend to block the capillary.
- Changes in composition can occur during measurements and the filling of the crucible, e.g. fluorine emissions during measurements on oxy-fluoride melts or the reaction of FeO with crucible.
- The use of a non-wetting material for the rotor, container or capillary would lead to ‘slip’ of the liquid and lead ultimately to a low value for the viscosity (unlike the other problems). A correction for non-wetting has been proposed for the oscillating viscometer.⁷ The oscillating drop and SLLS methods should not be affected by non-wetting.

Viscosity data for metals, alloys slags, glasses

Sources of data are given in Table 4.2 and data for the metallic elements are given in Table 4.3.

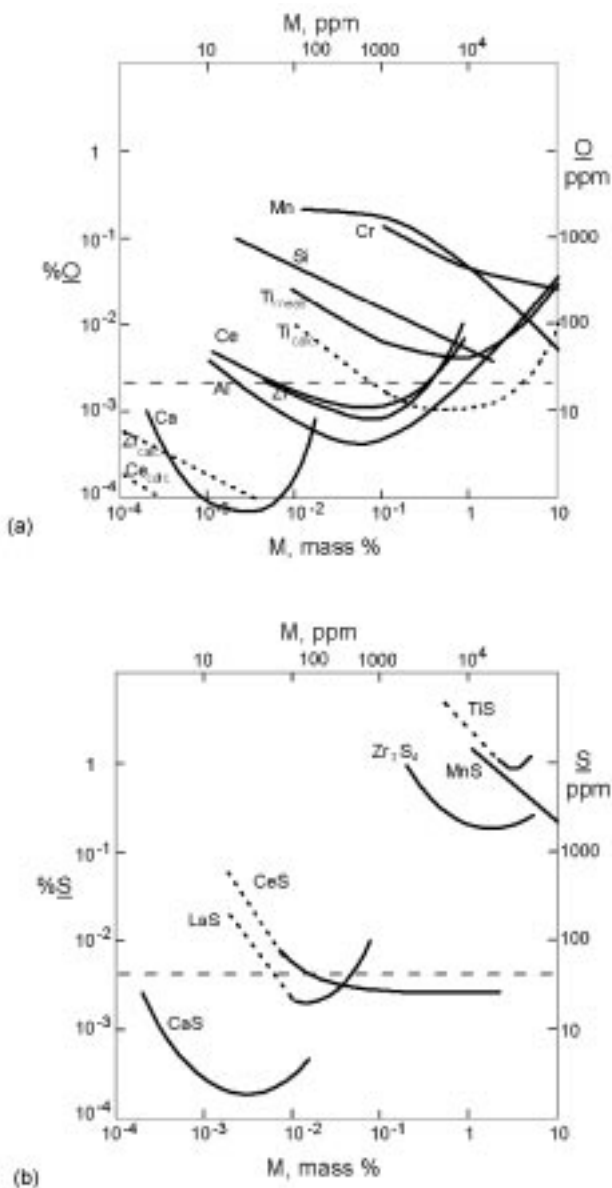
4.4.3 Surface (γ) and interfacial tension (γ_{MS})

In this article *surface tension* refers to a liquid sample in contact with a gas and *interfacial tension* to a liquid sample in contact with another liquid. The methods outlined below can be used to determine surface tensions of both metals and slags and glasses.

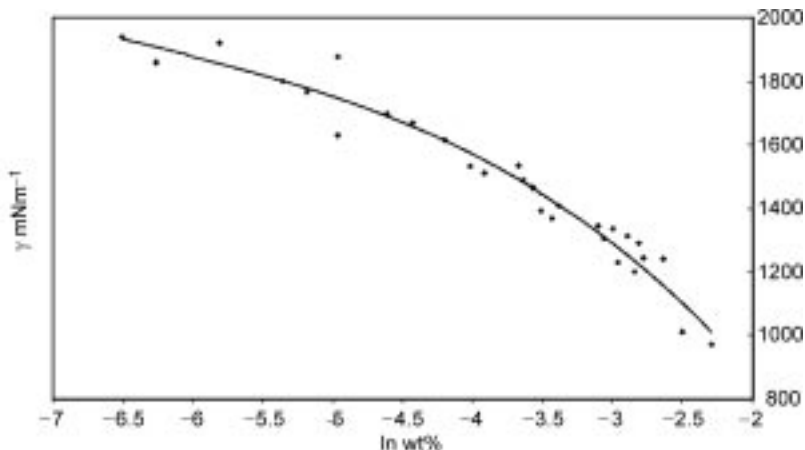
Surface tension – metals and slags

Surface active elements such as Te, Se, S and O have a dramatic effect on (i) the surface tension and (ii) on the temperature coefficient ($d\gamma/dT$) of metals. Inspection of Fig. 4.2 shows that an increase of 50 ppm S causes a decrease in surface tension of *circa* 20% and changes ($d\gamma/dT$) from a negative to a positive value. The biggest problem lies in control of oxygen for it is difficult to exclude all oxygen. It should be noted that it is the *soluble* O concentration (denoted O%) which is important since *combined* O (present in the metal as oxides, e.g. Al_2O_3) has little effect on the surface tension of metals. However, the soluble O (and S, etc.) concentrations are affected by the other elements present in the metal.² It can be seen from Fig. 4.10 that the soluble O for the Fe-Al-O system decreases to about 4 ppm when the Al content is about 60 ppm.

Oxygen contamination can arise from a partial pressure of O_2 in the atmosphere or from reaction of the metal with the container (which are usually oxides). Some metals (e.g. Al, Si) have a limited solubility for oxygen whereas



4.10 The effect of different alloying additions (M) on (a) the soluble O (O%) content in the Fe–M–O system and (b) the soluble S (S%) content in the Fe–M–S system.²



4.11 Surface tension data for Fe-O system at 1823K as a function of \ln (wt % O).

other elements (e.g. Ti, Zr) have a large solubility of oxygen. Consequently, it is my opinion that the only certain way of determining a surface tension for a pure metal is to determine the surface tension at different partial pressures of oxygen (p_{O_2}). The surface tension of Fe is shown as a function of $\log p(\text{O}_2)$ in Fig. 4.11.⁵⁷ It can be seen that the surface tension comes to a constant value at low levels of soluble O .

Unfortunately, few investigators have reported either the soluble oxygen content of their sample or $\log p(\text{O}_2)$ in equilibrium with the sample. If we take the case of molten gold (which is thought to have no oxygen solubility) the reported surface tension values⁵⁸ fall within a band of 2 to 3%, thus the experimental uncertainty associated with the various methods is $\pm 1\text{--}2\%$. However, the uncertainty in the surface tension associated with the soluble O content of the sample could be much larger, especially in the case of elements having a large solubility for oxygen (e.g. Ti or Zr).

Methods

- In the **sessile drop** method there is a balance between surface tension and gravity. The liquid sample is placed on an inert plaque.^{7,31–33} The accuracy of the method has improved significantly in recent years with the introduction of iterative software to determine the best fit for the drop profile. The method also gives values for the contact angle (see below). In some cases reactions between melt and container occur at the triple point. The **large or big drop** method⁵⁹ is a variant of the sessile drop in which the crucible is slightly over-filled to form a free surface (proud of the top of the crucible).
- The **pendent drop** also represents a balance between surface tension and gravity forces. This method^{7,31–33,60} has also benefited from software

providing surface tensions from best fits for the drop profile. In some cases the sample is provided in wire form and is heated by an external source. In these cases, values can only be derived for one temperature (the melting temperature) but the detached drops can be weighed or collected and the surface tension can also be collected by the **drop weight** method.⁶⁰

- In the **maximum bubble pressure** (MBP) the maximum pressure occurs when the bubble formed by a capillary is hemispherical. The Laplace equation is used to derive the surface tension of the melt from the MBP.^{7,31–33} Care must be taken to establish the optimum conditions, e.g. the lifetime of the bubble.
- In the **detachment** method the maximum force is measured to detach a probe from the surface of the liquid.³³ Various shapes have been used for the probe, namely, ring, hollow cylinder, flat plate and rod. This method has mostly been used in measuring the surface tensions of slags and glasses. A correction term is required to account for the shape of the probe and this term can be determined by measurements on liquids of known surface tension.
- In the **oscillating drop** method the frequency of oscillation of a levitated drop of known weight is determined. The following means of levitation have been used to determine the surface tension of metals: electro-magnetic,^{61–63} electro-static^{51,54} aerodynamic^{64,65} micro-gravity.^{66,52} When electro-magnetic (EM) levitation is used the EM pressure causes asymmetry of the drop which, in turn, results in a five-peak frequency spectrum and an enhanced value for the surface tension. It is necessary to apply a correction based on the translation frequency of the drop.^{67–69} Alternatively, a rough correction can be obtained by subtracting $170 \text{ mNm}^{-1} \text{ g (sample)}^{-1}$ from the measured value.
- In the **SLLS method** (see the section ‘Slags’ on p. 128) the surface tension is derived from the frequency of the ripplons.^{40–42} The surface tension of molten Si obtained with this technique was in good agreement with values obtained by other methods.⁵⁴

Problems

- The formation of oxide skins on the free surface (e.g. Al_2O_3 on surface of Al melts) will obviously affect the results obtained with the oscillating drop, detachment and SLLS methods. In fact, surface oscillations of an Al drop are completely eliminated by a solid Al_2O_3 skin. Alumina can also penetrate up the internal diameter of the capillary and reduce the effective area of the capillary in the MBP method.
- All surface tension measurements on metals and alloys should be accompanied by measurements of the partial pressure of oxygen in the system. This is rarely the case. Consequently, most reported measurements refer to samples with an unknown soluble O_2 content. Where appropriate, the sample should be flushed with Ar/H_2 mixtures to reduce the soluble O_2 concentration before the measurements.

- Temperature measurement is a minor problem in levitated drop experiments where pyrometry is used and the emissivity of the sample is not known accurately. Laser heating is used in aerodynamically and electro-statically levitated samples and this may cause steep temperature gradients across the drop, these gradients can be minimised by using several lasers at different angles to heat the sample.

Surface tension data for metals, alloys slags, glasses

Sources of data are given in Table 4.2 and data for the elements are given in Table 4.3.

Contact angle (θ)

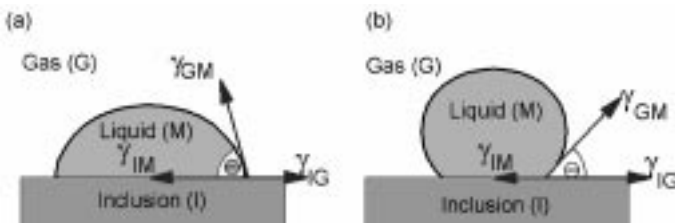
The contact angle determines whether a liquid ‘wets’ a solid (contact angle, $\theta < 90^\circ$, Fig. 4.12a) or is ‘non-wetting’ to a solid (contact angle, $\theta > 90^\circ$, Fig. 4.12b). At high temperatures ‘reactive wetting’ is common. Consequently, in many applications wetting is promoted by reactions between the liquid and the substrate. Some typical applications making use of reactive wetting are highlighted below:

- Good bonding (i.e. wetting) is needed between the fibres and the metal is needed in metal-matrix composites, this is usually achieved through introducing a reactive component (e.g. Mg) into the metal which reacts with the fibre.
- To ensure good wetting in metal–ceramic (e.g. Si_3N_4) joining, Ti is added to the braze to react with the ceramic (to form a silicide).

It is very difficult to measure interfacial tensions involving solid phases. However, Young’s equation, which can be derived from Fig. 4.12, allows us to determine the difference between the surface and interfacial tensions of the solid phase where s, l and g denote the solid, liquid and gas phases, respectively:

$$\gamma_{lg} \cos \theta = (\gamma_{sg} - \gamma_{sl}) \quad (4.5)$$

The following terms are useful in understanding interfacial phenomena affecting



4.12 Schematic diagrams showing (a) a liquid wetting a solid inclusion and (b) non-wetting liquid on a solid inclusion (I = solid in this diagram).

the removal of inclusions (I) from liquid metal (M) by gas bubbling, the spreading of one liquid over another, etc.

- The *work of adhesion* (W_A) is a measure of the energy change (per unit contact area) in separating two media at the solid–liquid interface.

$$W_A = \gamma_{lg} + \gamma_{sg} - \gamma_{ls} = \gamma_{lg}(1 + \cos \theta) \quad (4.6)$$

- The *spreading coefficient* (S^*) is a measure of the tendency of a non-reacting liquid to spread across a solid surface.

$$S^* = \gamma_{sg} - \gamma_{ls} - \gamma_{lg} = \gamma_{lg}(\cos \theta - 1) \quad (4.7)$$

- The *floatation coefficient* (Δ) provides a measure of the ease of removing solid particles (e.g. inclusions) by gas bubbling; the best conditions are obtained when Δ is both positive and has a high value.⁷⁰

$$\Delta = \gamma_{IM} + \gamma_{MG} - \gamma_{IG} = \gamma_{MG}(1 - \cos \theta) \quad (4.8)$$

Interfacial tension (γ_{MS})

Many metal-producing processes use a molten slag to protect the metal from oxidation and to promote the removal of undesirable impurities from the metal (e.g. S, P and non-metallic inclusions). The metal–slag interfacial is important since a low interfacial tension will promote the formation of emulsions and foams which provide very fast refining reactions (because of the huge surface area/mass ratio) and high productivity. However, low interfacial tension also encourages slag entrapment in the metal which is a major problem in the continuous casting of steel.⁷¹

The interfacial tension is linked to the surface tensions of the metal (M) and slag phases (S) through the Good–Girafalco equation, where φ is an interaction parameter.

$$\gamma_{MS} = \gamma_M + \gamma_S - \varphi(\gamma_M, \gamma_S)^{0.5} \quad (4.9)$$

The surface tension of the metal is usually the biggest term in this equation (e.g. for steel $\gamma_M = 1700\text{--}1400\text{ mNm}^{-1}$ depending on S content compared with $\gamma_S = 450 \pm 50\text{ mNm}^{-1}$ for the slag). Thus the S content of the steel has a marked effect on the interfacial tension.

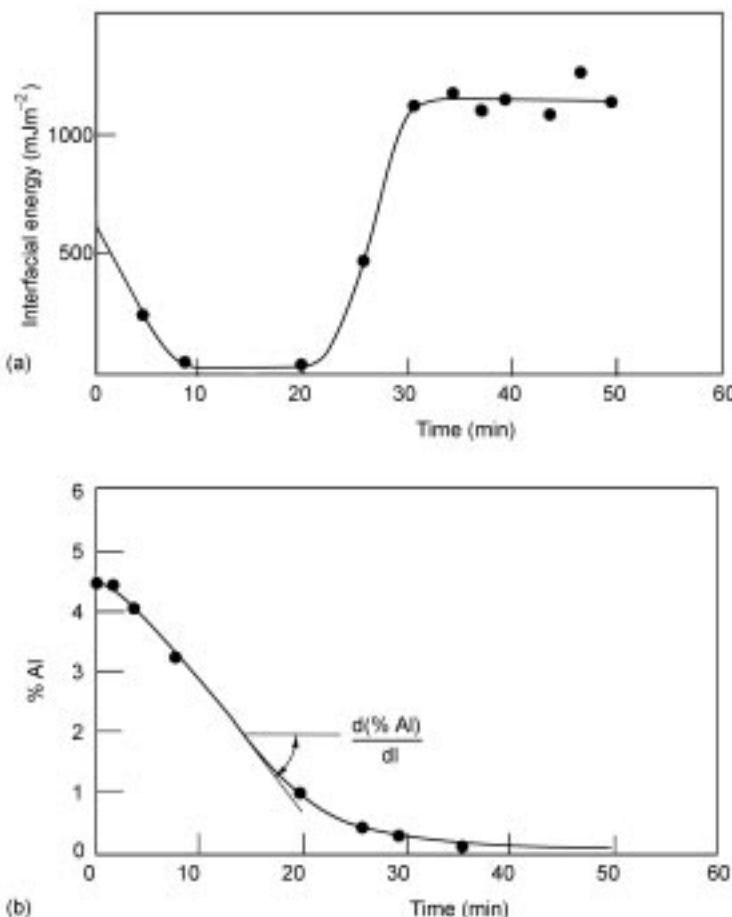
Methods

The following methods have been used to determine the interfacial tensions of metal–slag systems (γ_{MS}):

- The most widely-used method is the **X-ray sessile drop** method^{18,72,73} in which a metal drop is placed in a crucible of molten slag. The crucible must be transparent to X-rays and Al_2O_3 and MgO are frequently used. The interfacial tension is determined using software which derives the parameters

giving the best fit with the measured profile of the drop. The **X-ray pendent drop** could also be used for measurements at high temperatures.

- Another form of the **sessile drop** method (which does not require X-rays) has also been reported.^{18,74,73} A crucible is filled with molten metal and a drop of slag is placed on the surface of the metal and forms a sessile drop. The drop is photographed and the contact angle derived.
- The **maximum drop pressure** method (MDP)⁷³ is similar to the MBP method and consists of a crucible containing one liquid into a second vessel containing the other liquid which is joined to the first liquid via a capillary. The second vessel is evacuated in a controlled manner and the liquid from the crucible rises up the capillary and forms a drop which, subsequently,



4.13 The effects of time (a) on interfacial tension and (b) on the mass transfer of Al from steel (to the slag).^{75,76}

detaches. The maximum pressure is determined and used to calculate the interfacial tension. This method has not been widely used for measurements at high temperatures.

Results

Slag–metal reactions are ionic in nature (e.g. equation 4.10):



Rapid mass transfer between the metal and slag has been found to be associated with low interfacial tension (Fig. 4.13) and when the rate of mass transfer slowed down the interfacial tension was found to increase to a high value once more.^{75,76} It has been suggested that that the decrease in interfacial tension occurs when the rate of oxygen transfer from slag to metal exceeds a critical value. Similar phenomena have been observed in organic systems⁷⁷ and it was found that the decrease in interfacial tension did not occur when the volumes of the two liquids were similar. Consequently, there is a possibility that the observed phenomenon is due to the fact that the volume of the metal is much lower than that of the slag in the X-ray sessile drop method.

4.5 Properties related to heat transfer

4.5.1 Heat capacity (C_p), enthalpy ($H_T - H_{298}$)

The temperature dependence of the heat capacity is usually expressed in the form:

$$C_p = a + bT - c/T^2 \quad (4.11)$$

The enthalpy at a specific temperature, T, relative to 298K, can be derived by integrating C_p between 298 and T.

$$(H_T - H_{298}) = \int_{298}^T C_p dT = a(T - 298) + (b/2)(T^2 - 298^2) + (c/T - c/298) \quad (4.12)$$

which can be expressed as a power series:

$$(H_T - H_{298}) = aT + (b/2)T^2 - (c/T) - d \quad (4.13)$$

where d contains all 298K terms.

Methods

The following methods have been used to measure heat capacities and enthalpies:

- **Calorimetry** is a well-established technique but is difficult and time-consuming at higher temperatures. Detailed descriptions of the methods

adopted have been reported elsewhere.⁷⁸ Enthalpies have been studied extensively by **drop calorimetry**. In this technique a crucible containing the sample (of known mass and temperature) is dropped into a copper or silver block and the temperature rise of the block (typically 1–5K) is measured very accurately. In **levitated drop calorimetry** the sample is levitated by EML, ESL, ADL or USL and in the case of high melting metals (e.g. W) a laser heating can be used to augment the EM heating. The experimental uncertainty in enthalpy measurements is usually around $\pm 1\%$.

- In recent years the development of commercial, **differential scanning calorimeters** (DSC) has resulted in the wide use of these instruments to measure to Cp and enthalpies. There are two types of DSC: (i) in which the temperature difference between the sample and reference pans are monitored (**differential temperature scanning calorimeter** (DTSC)) and (ii) in which the power required to keep the two pans at the same temperature (**differential power scanning calorimeter** (DPSC)). DPSC can be used to temperatures to <1000K and Cp values have an experimental uncertainty of $\pm 1\text{--}2\%$. DTSC is used for temperatures in the range 1000K to 1800K and the experimental uncertainties are probably around $\pm 5\%$. Enthalpies of fusion or transition are manifested as a peak in the apparent Cp–T Curve (see Section 4.2.4 and Fig. 4.9) and are determined by integrating under the curve (experimental uncertainty $<\pm 10\%$). Fraction solid values are usually derived in the cooling cycle by integrating under the curve to a specific temperature and dividing this value by the total area under the curve for the solidification process. One problem with dynamic measurements (DPSC, DTSC) is that in the fusion (or solidification) process the calorimeter must suddenly provide (or remove) a large amount of energy (latent heat). Since the temperature is not static, the apparent Cp is ‘smeared’ over a few degrees. The **single pan calorimeter** avoids this problem. It consists of two concentric crucibles⁷⁹ with thermocouples placed on the walls. The temperature difference between inner and outer crucibles is monitored continuously. The sample is placed in the inner crucible. Measurements are made with the inner crucible (i) empty (ii) filled with a calibrant of known Cp (e.g. Al₂O₃) and (iii) filled with the sample. Accurate results were obtained with Al alloys.⁷⁹
- In the **exploding wire** method the specimen is heated very rapidly^{24,25} and the enthalpy is derived from the known current and potential values and the measured temperature. As mentioned above, solid state transitions tend to be slow and consequently enthalpies tend to get ‘smeared out’ in regions where solid state transitions occur. Experimental uncertainties in the enthalpy are probably around $\pm 5\%$.

Problems

The principal problems encountered are:

- Measurement of temperatures since (i) there can be a considerable gradient between the measurement site and sample temperatures in conventional drop calorimetry and (ii) in levitated drop calorimetry the measurements are made by pyrometry and consequently either the emissivity must be known accurately or the temperature scale should be calibrated.
- When measuring the enthalpy of metallic samples using conventional drop calorimetry, it is necessary to use oxide (e.g. Al_2O_3) crucibles and these have a high heat capacity (cf. metallic crucibles used to hold slags and glasses) and this reduces the accuracy of the results obtained for the metal.
- The rapid quenching of slags and glasses can result in the sample adopting a metastable state (i.e. a non-equilibrium state).
- It is necessary to differentiate enthalpy data to obtain C_p values from $(H_T - H_{298})$ values; more accurate values of C_p can be derived if C_p values are available at low temperatures but the presence of high-temperature, phase transitions (e.g. in steels, Ni-superalloys and Ti-alloys) makes differentiation very difficult.
- Solid state transitions tend to be sluggish and when using dynamic techniques (such as DSC) the sample does not have enough time to disorder when passing through the transition range. This is an especial problem where the transition is followed by a second transition (e.g. in Ni-superalloys (Fig. 4.9) where the coarsening of the γ' phase transition is followed by the dissolution of the γ' phase²³).
- In some slags and glasses a glassy phase converts into a supercooled liquid at the glass transition temperature and then subsequently crystallises at a higher temperature; measured properties in this region where glass and crystal co-exist are in an undefined (non-equilibrium) state and refer solely to that sample for that specific temperature.

4.5.2 Thermal conductivity (k) thermal diffusivity (a) thermal effusivity (e)

The thermal conductivity (k) is related to thermal diffusivity through the equation

$$k = C_p \cdot a \cdot \rho \quad (4.14)$$

Thermal conductivity can be defined as the heat flow (q) across a unit area per second per unit temperature gradient (dT/dx). Thus the units are $\text{W m}^{-1}\text{K}^{-1}$

$$k = (-q/A)(dT/dx) \quad (4.15)$$

The principal conduction mechanism in metals at high temperatures is through the transport of electrons, although, phonon (or lattice) conduction can make a significant contribution at ambient temperatures. Consequently, there is a relation between the electrical and thermal conductivity of metals at high

temperatures since both involve electron transport. This relation is known as the Wiedemann–Franz–Lorenz (WFL) rule

$$k = L_o \cdot T / R \quad (4.16)$$

where L_o is a constant with a value of $2.445 \times 10^{-8} \text{ W}\Omega\text{K}^{-2}$, R is the electrical resistivity and T is in K. The WFL rule has been shown to be valid for a large number of pure metals in both the solid and liquid phases near the melting point.⁸⁰ Consequently, thermal conductivity values can be derived from measurements of the electrical resistivity. This method is particularly useful for measurements in the (solid + liquid) or ‘mushy’ region (see Section 4.2.5). It has been proposed⁸¹ that the temperature dependence takes the form

$$k = (A \cdot L_o \cdot T / R_{el}) + B \quad (4.17)$$

where A and B are constants. However, it has been pointed out⁹⁴ that measured thermal conductivities of molten Ge, Si, Sn and Pb decrease with increasing temperature while the values calculated from electrical resistivity values and Equation 4.16 show the opposite trend. This was attributed to an inelastic scattering of electrons (possibly due to electron–electron scattering) at higher temperatures.⁹⁴

There is a large increase in electrical resistivity when a solid transforms to a liquid; the ratio (R_l^m / R_s^m) has a value of about 2 for most metals but transition metals have much smaller values (Fe, 1.06, Co, 1.15 and Ni, 1.40)⁷ and thermal conductivities of most metals show a marked decrease at the melting point.

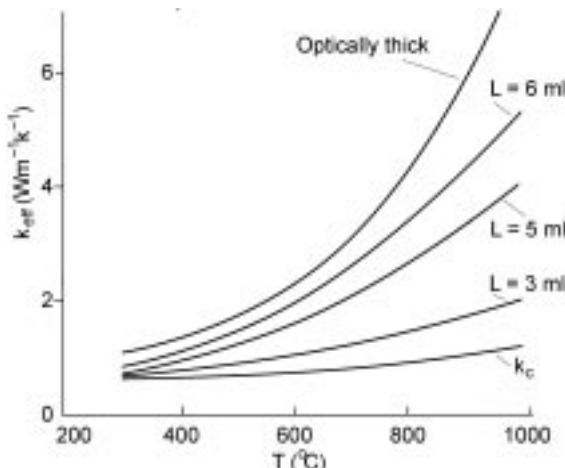
There are two major problems affecting thermal conductivity and diffusivity measurements, namely, convection and radiation conduction in semi-transparent media such as glasses and some slags in both liquid and solid phases.

Convection

As described in Section 4.2.3, convection is difficult to eliminate. Methods used to measure the thermal conductivity or diffusivity fall into two classes, namely, *steady state* and *transient* methods. Convective contributions to the thermal conductivities (or diffusivities) tend to be large in *steady state* measurements. However, in *transient* methods (where the temperature–time curves are determined following a short heat pulse) the convective contributions are much smaller, especially if the measurements can be carried out in a time period shorter than the time required (< 1 sec) for convection to be initiated. Consequently, steady state experiments are not very suitable for measurements on the liquid phase and transient methods are preferred. Convection in transient experiments can be minimised by taking the various measures outlined in Section 4.2.3 into account.

Radiation conductivity

In the 1960s it was noted that measurements of the thermal conductivities of glasses were dependent upon the thickness of the specimen used (Fig. 4.14). In



4.14 Effective thermal conductivity of glass as a function of temperature showing the effect of sample thickness.

order to explain this observation it was proposed⁸² that in addition to the phonon (or lattice) conductivity (k_c) there were also contributions from a heat transfer mechanism known as radiation conductivity (k_R). This radiation conduction arises by a mechanism of absorption and re-emission. Consider a pulse of energy focused onto the surface of a glass specimen. The surface layer will increase in temperature and this will be at a higher temperature than the next layer in the glass and thus heat will be radiated from the surface layer to this second layer. This second layer will absorb the heat and will be, consequently, at a higher temperature than the third layer and thus will radiate heat to the third layer and so on. It was also found that k_R increased with increasing thickness until it came to a certain point where it remained constant. The sample is said to be '*optically thick*' at this point. Optically thick is usually understood to occur when the product of absorption coefficient (α^*) \times thickness is > 3 . For optically thick conditions, k_R can be calculated using equation 4.18 where n is the refractive index and σ is the Stefan Boltzmann constant with a value of $5.67 \times 10^{-8} \text{ Wm}^{-2}\text{K}^{-4}$.

$$k_R = 16\sigma \cdot n^2 \cdot T^3 / 3\alpha^* \quad (4.18)$$

However, it is difficult to calculate k_R if it lies outside the optically thin region. The effective conductivity k_{eff} is given by equation 4.19.

$$k_{\text{eff}} = k_c + k_R \quad (4.19)$$

where k_c is the phonon (or lattice) conductivity.

Radiation conductivity is diminished by the presence of crystallites in the sample which scatter the radiation (i.e. photons). Radiation conductivity is also decreased by the presence of transition metallic oxides such as FeO, NiO or Cr₂O₃ which increase the absorption coefficient significantly. For solids the

absorption coefficient in equation 4.18 should be replaced by the extinction coefficient $E = \alpha^* + s^*$ where s^* is the scattering coefficient.

Although, steady state methods can be used to calculate the effective conductivity of semi-transparent media such as glasses in the solid state it is essential that the sample be optically thick. Furthermore, it is necessary to measure the absorption coefficient and refractive index of the sample if the contributions from k_R and k_c need to be determined. However, transient techniques are preferred for measuring k_{eff} since contributions from k_R tend to be much smaller.

The thermal conductivities of slags and glasses are dependent upon the polymeric structure of the melt. The thermal resistance ($1/k^m$, i.e. reciprocal thermal conductivity at the melting point) has been shown to be a linear function of structural parameters (e.g. (NBO/T) or the corrected optical basicity).^{11,83} The thermal resistance was found to decrease as the polymerisation increased (or the conductivity increases as the chain length of the slag increases (i.e. SiO_2) increases). Susa *et al.*⁸³ showed that the thermal resistance terms were smaller for the Si-O bonds in the chain than those for ionic (NBO) bonds at the end of the chain (denoted as O-O bonds). There is also some evidence that a change in slope in the k-temperature plot for some solid slags may be due to the change of a glass into a supercooled liquid which occurs at the glass transition temperature.

Thermal effusivity (e) is a measure of the ability of a body to exchange thermal energy with its surroundings (thermal impedance) and is given by the following equation and has units of $\text{Js}^{0.5} \text{m}^{-2} \text{K}^{-1}$.⁸⁴⁻⁸⁶

$$e = (k \cdot C_p \cdot \rho)^{0.5} \quad (4.20)$$

It has been reported that thermal effusivity measurements carried out on a drop of liquid at ambient temperatures were free from convection contributions⁸⁴ and this may provide a way in the future of obtaining thermal conductivity/diffusivity values which are free from convective contributions.

Methods for thermal conductivity and diffusivity measurement

1. Steady state techniques

The conventional steady state techniques such as the **concentric cylinder**, **parallel plate** and **axial and radial flow** methods⁷⁸ are all suitable for measuring thermal conductivities of metals in the solid state. However, they are not particularly suitable for measurements (i) in the liquid state because of the difficulties of minimising convection at high temperatures, and (ii) on semi-transparent solid unless the samples are optically thick (see above).

2. Non-steady and transient techniques

The **laser pulse** apparatus is manufactured commercially by several companies and is a very popular technique.⁷⁸ The sample is a disc-shaped specimen 10–12 mm in

diameter and usually 2–3 mm thick with parallel faces. For measurements on solids the sample is placed horizontally and a pulse of energy is directed onto the front face of the specimen. The temperature of the back face is monitored continuously (usually with an infra-red detector). The temperature–time curve goes through a maximum (ΔT_{\max}) because of radiation losses and it is customary to determine the time ($t_{0.5}$) needed for 0.5 (ΔT_{\max}). The thermal diffusivity is derived from the relation $a = 0.1388L^2/t_{0.5}$ where L is the thickness of the specimen.

For measurements on liquids and semi-transparent media a metallic (e.g. Pt or C) disc is usually placed on the upper surface of the sample and the temperature transient can be measured by monitoring the temperature of the disc or by the temperature of the back face.⁸⁷ Liquid samples are usually held in sapphire or silica crucibles^{88,89} and it is desirable to carry out the measurements very rapidly (< 1 sec) to avoid the initiation of convection.

In the **transient hot wire** (THW or line source) method a current is applied to a fine wire (*circa* 0.1 mm diameter) of known length which acts as both a heating element and a resistance thermocouple.^{90,22,33,80} The wire is immersed in the melt and a current is applied then the temperature rise of the wire (ΔT) (or strip) is measured continuously as a function of time. The thermal conductivity is derived from the reciprocal of the slope of the linear portion of the plot of ΔT versus $\ln(t)$ (time). Convective contributions to k_c can be detected as departures from the linear relation. The current should be applied for < 1 sec to avoid the establishment of buoyancy driven convection. Experiments have been carried out in 0 g using a drop tower to minimise convection.²² Thermo-capillary convection can be minimised by floating a lid on top of the test liquid.²² There is some evidence indicating that radiation conduction contributions in semi-transparent liquids (and solids) are smaller in the THW method than in the laser pulse method. This is probably due to the much smaller surface area of the wire compared with that of the metal disc used in the laser pulse. When the method is applied to metals it is necessary to insulate the metallic probe from the melt and coatings of Al_2O_3 or other oxides are applied to the wire or strip. Recent work has shown that thermal conductivity values for liquid metals must be corrected for the thickness of the insulating coating on the probe.⁹¹

In the **radial temperature wave** (RTW) method,^{92,80} a modulated heat flux is applied along the centre of a cylindrical sample. The variations in temperature are monitored on the outside of the specimen. There is a phase lag between the input and output and this is related to the thermal diffusivity. Thermal diffusivities can be calculated from (i) the amplitude of temperature oscillations and (ii) from phase differences. Values calculated by the two methods are usually in good agreement.⁹²

In the **plane temperature wave** (PTW) method^{93,80} the plane temperature waves are generated by bombarding the specimen with a harmonically-modulated electron beam. PTWs are directed onto one face of a disc-shaped sample and the temperature transient is recorded on the other face. The method

can be used either at constant temperature or in a dynamic mode (and heating rates of up to 1000K per second have been used) to derive thermal diffusivity values. For measurements on liquids only the central portion of the disc was allowed to melt and high heating rates ensure that measurements are carried out very quickly thereby avoiding the problem of buoyancy-driven convection.⁹³ With temperature gradients across the free surface some contributions to the thermal diffusivity from thermo-capillary convection might be expected.

Problems

Solids

- In **metallic alloys** phonons can be scattered by grain boundaries, precipitated particles, etc. and consequently, the thermal conductivity or diffusivity value depends on microstructure of the sample and this is dependent upon both the heat and mechanical treatment. Differences in values of k or α of 10–20% can occur when repeating the measurements on the same sample.
- Corrections should be applied to account for the effect of the insulating oxide layer on the wire (or strip) used in the THW method⁹¹ when making measurements on metals.
- The determination of the magnitude of the contribution from radiation conduction (k_R)⁹⁴ is the principal problem with measurements on slags and glasses in the solid state (and there may be considerable difference in the contributions to k_R for the experimental and the industrial conditions). Some indication of the magnitude of k_R in the experiments could possibly be obtained by: (i) doping the slag or glass with FeO which increases the absorption coefficient and decreases k_R for optically thick specimens (but for optically thin specimens it could also have the effect of making the specimen more optically thick), and (ii) by using materials with different emissivities for the wire in the THW method on the disc or the top of melt in the laser pulse method (e.g. Pt, C, W).

Liquids

The principal problems with thermal conductivity and diffusivity measurements lie in eliminating convection and minimising radiation conduction (in the case of molten slags and glasses). These problems and ways of overcoming them have been described above.

4.5.3 Electrical resistivity (R)

Electrical resistivity increases with increasing temperature in both the solid and liquid phases. The resistivity of the liquid metal at the melting point is approximately twice that of the solid for many metals but (R_l^m/R_s^m) ratios for Fe, Co and Ni are between 1 and 1.4.

Methods

Electrical resistivity (R) measurements on melts can be classified as either *direct* or *indirect* measurements.

Direct measurements

The electrical resistivity is determined from measurements of current and potential and the use of Ohm's Law.

Capillary methods have been used for measurements on molten metals. The 4-probe method is usually adopted in which the potential drop across the liquid column is determined with two electrodes and the other two electrodes are used to measure the current.^{7,78} The cell constant is usually determined using a liquid of known resistivity (e.g. Hg). The two principal problems lie in the selection of (i) the capillary material (e.g. glass, quartz) and (ii) the electrode since C, W or Pt may dissolve in (or react with) the metal (one solution is to use a solid electrode of the same material as the sample by cooling the ends of the cell).

The exploding wire method has been used for measurements on the solid state and also for measurements on the liquid phase.^{24,25} Values obtained for the liquid are frequently in good agreement with values obtained with 4-probe studies.²⁵

Capillary methods have been little used for measurements on slags. This is due to the fact that resistance values are much smaller and are also more prone to polarisation and other effects. Two-electrode probes have been used with different geometries:

- central electrode where one electrode is immersed in a crucible and the crucible serves as the other electrode;^{18,33}
- two electrodes are immersed in a cell;^{18,33}
- ring electrode cells where the electrodes are in the form of two concentric cells.^{18,33}

However, **4-electrode** cells are preferred since they largely eliminate the effects of polarisation on the current-carrying electrodes (by measuring the potential drop and the current at different electrodes).

Resistances have been measured on molten slags using (i) AC bridges (ii) potentiometric methods and (iii) phase sensitive techniques.^{18,33}

The effect of frequency on the measured resistance/conductivity has been discussed by several workers.³³

Indirect method

The **rotating magnetic field** method is based on the principle that a torque is developed when a liquid metal is subjected to a rotating magnetic field; the torque is inversely proportional to the electrical resistivity.^{7,96} Values of the liquid density are needed to calculate the resistivity from the torque.

4.5.4 Emissivity (ϵ), absorption coefficient (α^*)

Emissivity (ϵ) is defined as the ratio of radiated energy emitted by a surface to that emitted by a black body. However, the radiated energy is dependent upon the nature of the surface, temperature, wavelength (λ) and the direction.

Spectral emissivity (ϵ_λ) denotes the emissivity of a body at a specific wavelength. **Total emissivity** (ϵ_T) is the ratio of (intensity of radiation emitted at all wavelengths by a body/intensity of radiation emitted at all wavelengths by a black body).

With respect to direction emissivities these can be measured either (i) normal to the plane of the surface (denoted by subscript, N) or (ii) for the hemisphere containing all the radiated energy (denoted by subscript H). Thus ($\epsilon_{\lambda N}$) and (ϵ_{TH}) refer to the normal spectral emissivity and the total hemispherical emissivity, respectively.

The nature of the surface also affects the measured value, and measured values depend upon whether a surface is rough or smooth or whether the surface has been oxidised (or nitrided) by reaction with the atmosphere. Most cited values of emissivity refer to polished surfaces.

Methods

Emissivities are usually measured (using a spectroscope) by determining the ratio of the energies emitted by the surface divided by that emitted by a neighbouring black body. Values have been obtained using both electromagnetic⁹⁷ and cold crucible levitation.⁹⁸ Emissivities for the solid and liquid phases have also been obtained using the exploding wire method using a submicrosecond-resolution laser polarimeter.⁹⁹

However, they can also be determined by measurements of other optical constants (refractive indices, reflectivities, etc.) using rotating analyser ellipsometry to determine the polarisation state of monochromatic light reflected from the surface at various angles.¹⁰⁰

Values of (C_p/ϵ_{TN}) can be derived from the cooling curves of levitated spheres in vacuum.^{54,101} Values of emissivity given in Table 4.2 were obtained from various sources.

Absorption coefficient (α^) and extinction coefficients (E)*

Absorption and extinction coefficients of semi-transparent media are needed for calculations of the magnitude of the radiation conductivity (k_R) in glasses and slags.

Methods

There are two methods of measuring absorption coefficients.

Transmission methods

The absorption coefficient can be determined by using a spectrophotometer to measure the intensities of the incident (I_o) and emerging beams after transmission through a sample of known thickness (d).^{33,102}

$$I = I_o \exp(-\alpha^* d) \quad (4.21)$$

In solids the extinction coefficient (E) is measured since radiation can be scattered by crystallites, grain boundaries, particles, etc.

$$E = \alpha^* + s^* \quad (4.22)$$

where s^* = scattering coefficient.

Reflectance methods

Absorption coefficients have been determined from measurements of transmittance and reflectance.^{33,103}

4.6 Properties related to mass transfer

4.6.1 Diffusion coefficient (D)

There are several types of diffusion coefficient.

Self diffusion involves the movement of various species present in the melt by random motions. There is no net flux of any species and no chemical potential gradients within the melt. It is also customary to quote self-diffusion values for **impurity diffusion** but which is strictly chemical diffusion since a concentration gradient is produced.

Tracer diffusion is essentially the same process as self-diffusion but some of the species are radioactive. Consequently, there is a net flux and chemical potential; but this gradient refers solely to the radioactive species.

Chemical diffusion is the movement of a species in the melt in response to a gradient of chemical potential arising as a result of either concentration or temperature gradients in the melt. Diffusion occurs in a direction that results in a reduction of the concentration gradient. Chemical diffusion in response to a temperature gradient is referred to as **Soret diffusion**.

When diffusion involves the movement of two or more species it is referred to **interdiffusivity**. For example, if the cation is more mobile than the anion an electrical field is established which retards the cation and enhances the anion mobility in order to prevent a space charge being established in the melt.

Fick's first and second laws apply for single component diffusion

$$J = -D (dC/dy) \quad (4.23)$$

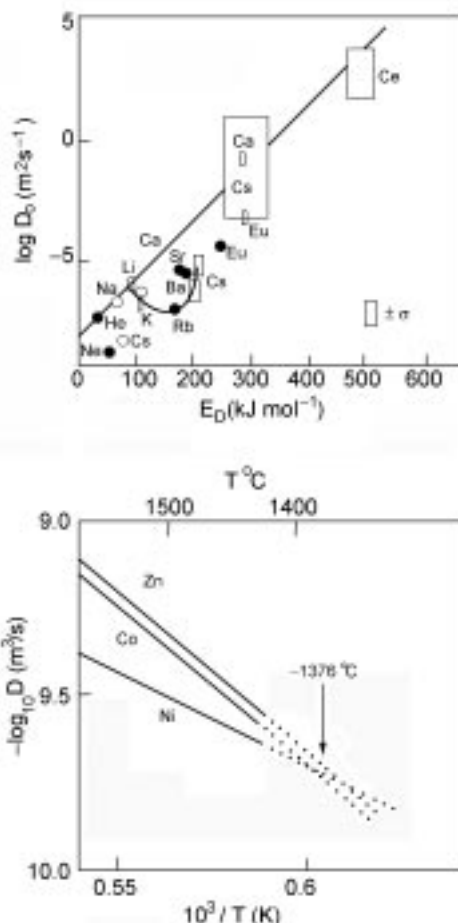
$$dC/dT = D (d^2C/dy^2) \quad (4.24)$$

where J is the flux across a plane, (dC/dy) is the concentration gradient, D is the diffusion coefficient, and t is the time. The average value of the square of linear displacement (d) of a species after time t is given by

$$d^2 = 2Dt \quad (4.25)$$

The temperature dependence of the diffusion coefficient is usually expressed as an Arrhenius relation:

$$D = D_0 \exp(-E_D/R*T) \quad (4.26)$$



4.15 Relation between $\log_{10} D_0$ and (a) activation energy for diffusion of various impurities in solid obsidian¹⁰⁴ and (b) reciprocal temperature for Co, Ni and Zn in CaO.MgO.2SiO_2 ¹⁰⁵

where D_0 is a constant and E_D is the activation energy for diffusion. These parameters D_0 and E_D are inversely proportional to one another (Fig. 4.15a) and this is known as the *compensation effect*. It is the diffusion equivalent to Urbain's assumption regarding the relation between A and E_η for viscosity. One effect of the compensation rule is that diffusion coefficients for different species tend to come to a common value (Fig. 4.15b) at a specific temperature (around 1650K in Fig. 4.15b).

Methods^{7,106–108,33}

In the **capillary reservoir** method the sample containing the solute to be studied is contained in a capillary tube (of uniform diameter and known length) with one end sealed. The capillary is then immersed in a large container holding the solvent sample. The capillary tube is removed after a set time and the concentration in the capillary tube determined. Convection is minimised because of the small diameter of the capillary.

In the **diffusion couple** method a long capillary of known cross-section is half-filled with the solvent and the solute samples. The capillary is then rapidly heated to the required temperature and maintained at this temperature for a specific time and is then quenched. Diffusion coefficients can then be determined by determining solute concentrations at various positions along the specimen. One difficulty is that some diffusion may occur during the heating and cooling periods.

The **shear method** avoids the problems by only aligning the samples at the start of the run and then misaligning the samples at the end of the measurement period. It has not been used for high-temperature measurements.

In the **instantaneous plane** method the solute is in the form of a thin disc and while the solvent consists of a long thin specimen. At the start of the experiment the thin disc disperses into the solvent sample.

The **electrochemical** method has the advantage that time-consuming chemical analysis is replaced by measurements of current and voltage. However, it cannot be applied to some systems.

The **Rayleigh scattering** has been used to measure diffusion coefficients in liquids at room temperatures; this technique has the advantages of being a non-contact method and is very rapid.¹⁰⁹

Electro-magnetic fields have recently been used to minimise contributions from convection to the diffusion coefficient.¹¹⁰

4.7 Estimating metal properties

It is apparent from the above text that the accurate measurement of thermo-physical properties at high temperatures is both time-consuming and requires considerable expertise. Furthermore, process control often requires a rapid input of data for the relevant properties of the materials involved, for instance how

much CaO must be added to a coal slag to obtain a viscosity where the slag can be poured from the reaction vessel. Thus it is not surprising that models or routines have been developed to estimate the properties from the chemical composition, for this is frequently available on a routine basis. Many models have been reported in the literature. This review does not claim to cover all these published models but covers only the models and routines with which the author has used or tested or which have come to his notice.

The partial molar method is a simple method that has proved very useful for estimating some physical properties for alloys and slags. Using the case of a property (P) of an alloy, the value can be calculated from the sum of the product of the (mole fraction \times the property value) for each constituent of the alloy. The partial molar property for each constituent is denoted \bar{P} .

$$P = \sum [(X_1 \bar{P}_1) + (X_2 \bar{P}_2) + (X_3 \bar{P}_3) + (X_4 \bar{P}_4)] \quad (4.27)$$

where X = mole fraction and 1, 2, 3, 4 denote the different components.

However, some properties (such as viscosity) are very dependent upon the structure of the alloy or slag and in these cases the structure has been taken into account. Consequently, the partial molar method is particularly effective in estimating those properties which are least affected by structure (e.g. C_p and density).

4.7.1 Estimation of C_p and $(H_T - H_{298})$

The heat capacity–temperature relation for solid materials (alloys and slags) can be represented in the form:

$$C_p = a + bT - (c/T^2) \quad (4.28)$$

Integration of C_p dT between 298K and the temperature of interest, T gives

$$\int_{298}^T C_p dT = (H_T - H_{298}) = aT + (b/2)T^2 + (c/T) + d \quad (4.29)$$

where d contains all 298K terms. The values of the constant a for the alloy or slag can be calculated by:

$$a = \sum [(X_1 \bar{a}_1) + (X_2 \bar{a}_2) + (X_3 \bar{a}_3) + (X_4 \bar{a}_4) + \dots] \quad (4.30)$$

Thus the constants b and c can be calculated in a similar way so the C_p and enthalpy for the solid can be calculated for any required temperature.

The heat capacity of the liquid is usually assumed to be constant, i.e. independent of temperature and consequently values for C_p of the alloy can be calculated from equation 4.27 where \bar{P}_1, \bar{P}_2 , etc. are the C_p values of liquid for the various components. The only parameter now required is the enthalpy of fusion $\Delta^{fus} H$. This can be calculated in a similar way for the entropy of fusion, $\Delta^{fus} S$ which represents the disorder which occurs when a solid transforms to a liquid.

$$\Delta^{\text{fus}} H = T_{\text{liq}} \cdot \Delta^{\text{fus}} S \quad (4.31)$$

Thus it is necessary to have a value for the liquidus temperature (T_{liq}) or have an estimated value. The enthalpy of fusion can then be calculated by the relation:

$$\Delta^{\text{fus}} S = \sum [(X_1 \Delta^{\text{fus}} \bar{S}_1) + (X_2 \Delta^{\text{fus}} \bar{S}_2) + (X_3 \Delta^{\text{fus}} \bar{S}_3) + \dots] \quad (4.32)$$

The enthalpy for a temperature, T , where the liquid is the equilibrium phase can be calculated from

$$(H_T - H_{298}) = \int_{298}^{T_{\text{liq}}} Cp(s) \cdot dT + T_{\text{liq}} \Delta^{\text{fus}} S + \int_{T_{\text{liq}}}^T Cp(l) \quad (4.33)$$

This method works well for alloys and slags and the estimated values for the most part lie within 2 to 5% of the measured values.

Problems

- The above approach does not take into account any solid state transitions which might occur (such as those occurring in steels, Ni-based superalloys and Ti-alloys). Although the $(H_T - H_{298})$ values will be slightly low in the transition ranges the values of $(H_T - H_{298})$ for the liquid will not be affected since the entropy change can be considered as a small step in the disordering associated with the change from a fcc or cph solid to a liquid.
- With glasses there is a transition from a glass to a supercooled liquid at the glass transition temperature (T_g) and this is accompanied by a step increase (ΔC_p) in C_p of about 30% (and a threefold increase in α). The C_p-T relation can be modelled¹⁸ by assuming that the C_p for the supercooled liquid and liquid region remains constant and that there is no enthalpy of fusion involved.
- Another weakness of the approach outlined above is that it assumes that the fusion process occurs at a discrete temperature (T^{liq}) whereas in practice it occurs over a melting range.
- Another difficulty with the partial molar method lies in the fact that some alloys, (e.g. Ni-based superalloys) contain components such as Al (mp 933K) and W (mp 3695K) with melting points far away from the T^{liq} of the alloy (*circa* 1720K). This raises a question of whether the property values used in the calculation should be (i) the property value at the melting point (\bar{P}^m) or (ii) the property value extrapolated to 1720K. The value at the melting point (\bar{P}^m) can be adopted because it is considered that this was the point when all the atoms (including the Al and W) become disordered. Recent evidence on the densities of superalloys indicates that no serious errors are caused by this assumption.³⁶

The values calculated with the partial molar approach are usually within 2–5% of measured values (which are themselves subject to experimental uncertainties). Commercial thermodynamic packages such as MTDATA, Thermocalc and FACT are available. These packages are capable of predicting

solid state transitions and the melting range and their associated enthalpies.¹²⁵ Furthermore, the fraction liquid can be calculated through the Scheil equation.¹²⁵ Consequently, where a high degree of accuracy is required, Cp and enthalpies should be calculated with these packages

4.7.2 Density (ρ) molar volume (V)

The structure of the melt does not have a large effect on the density of the alloy or slag. The density can be calculated from molar volume:

$$V = M/\rho \quad (4.34)$$

where M = molecular mass of the sample ($= \sum x_i M_i$) and the molar volume can be calculated from the partial molar volumes of the constituents:

$$V = \sum [(X_1 \bar{V}_1) + (X_2 \bar{V}_2) + (X_3 \bar{V}_3) + (X_4 \bar{V}_4) + \dots] \quad (4.35)$$

The substitution of density for molar volume in equation 4.35 results in only a small error. The temperature dependence of the volume is calculated from the partial molar (volume) thermal expansion coefficients (usually $\beta \approx 3\alpha$ where α is the linear thermal expansion coefficient).

$$\beta = \frac{(dV/dT)}{V} = \sum [(X_1 \bar{\beta}_1) + (X_2 \bar{\beta}_2) + (X_3 \bar{\beta}_3) + \dots] \quad (4.36)$$

The linear thermal expansion coefficient (α) of a glass or slag can be calculated with the model due to Priven¹²⁶ or using the relation due to Yan *et al.*¹⁵⁵ $10^6\alpha(K^{-1}) (293-573K) = -18.2 + 48.9\Lambda_{cor}$ where Λ_{cor} is the optical basicity corrected for charge balancing of Al³⁺.

Density–temperature relations for the solid state can then be calculated from the molar volumes (or densities) of the solid at 298K and the thermal expansion coefficients. Similarly, values of density of liquids as a function of temperature can be calculated from \bar{V}^m and $\bar{\beta}$ for the constituents in the liquid states. However, the density is affected slightly by the structure of the melt. As we have seen in the section ‘Methods of determining structure’ on p. 118, one way of accounting for the effect of structure is through the use of thermodynamics. Take, for example, the densities of superalloys, values calculated from partial molar volumes are consistently 2–5% lower than measured values and the shortfall increases with increasing Al content. The chemical activities of the constituents in the Ni-Al system show marked negative departures from Raoult’s law (i.e. the atoms like each other). This results in tighter bonding and decrease in molar volume (ΔV^{xs}) or an increase in density ($\Delta\rho^{xs}$) of the melt. Since the effect of structure on the molar volume is relatively small it can be accounted for by adding (ΔV^{xs}) to equation 4.35. In the case of Ni-superalloys, ΔV^{xs} can be expressed in terms of the Al content (K(% Al), where K is the correction term) without much loss in accuracy.

In a similar manner the activities of the CaO-SiO₂ system show negative departures from Raoult's law. Correction terms in this case were determined by back-calculating the parameter ($X_i \bar{V}_1$) as a function of SiO₂ content from measured molar volumes of melts containing CaO and SiO₂ and could be accounted for by the relation, $\bar{V}_{\text{SiO}_2} = (19.55 + 7.97X_{\text{SiO}_2}) \times 10^6 \text{ m}^3 \text{ mol}^{-1}$. Similar relations are used for determining the effects of Al₂O₃ ($\bar{V}_{\text{Al}_2\text{O}_3} = (28.3 + 32X_{\text{Al}_2\text{O}_3} - 31.45X^2_{\text{Al}_2\text{O}_3}) \times 10^6 \text{ m}^3 \text{ mol}^{-1}$) and P₂O₅ ($65.7 \times 10^6 \text{ m}^3 \text{ mol}^{-1}$).

In most cases the values calculated using these corrections are within $\pm 2\%$ (and nearly always within $\pm 5\%$) of the measured values. If more accuracy is required the use of thermodynamic packages such as MTDATA,¹²⁶ Thermocalc and FACT are recommended.

Details of published models for calculating densities of alloys and slags are given in Table 4.4.

4.7.3 Viscosity (η)

The approaches taken to calculate the viscosities of liquids fall into two classes:¹²⁹

1. by treating the liquid as a dense gas;¹³⁰
2. by assuming the liquid structure is similar to that of the solid except that it contains holes (e.g. Frenkel,^{131,132} Weymann,¹³³ Eyring¹³⁴ and Furth¹³⁵).

In the Weymann–Frenkel approach the atoms are in thermal oscillation but for them to move from their present position into another equilibrium position it is necessary that (i) their energy should be greater than the activation energy required to move from site 1 to 2 and (ii) the next position should be empty (i.e. the site of a hole). Thus viscosity can be calculated from the probabilities that molecule can (i) jump from one position to another and (ii) find a 'hole' in the liquid. Weymann¹³³ derived the following equation:

$$\eta = (kT/\epsilon^*)^{0.5} \left\{ (2kmT)^{0.5}/(v^{0.667} P_v) \right\} \exp(\epsilon^*/kT) \quad (4.37)$$

where k = Stefan Boltzmann constant, ϵ^* is the height of potential barrier (associated with activation energy for viscous flow) m and v are the mass and volume of the structural unit and P_v is the probability of finding the next equilibrium site empty.

The biggest drawback in developing reliable models for the viscosities of molten alloys and slags (and glasses) lies in the experimental uncertainties in the experimental data (see the section 'Slags' on p. 154). For instance, Iida and Guthrie⁷ plotted the reported values for molten Fe and Al and showed that these values varied by $\pm 50\%$ and $\pm 100\%$, respectively, around the mean (although the lower values are more likely to be correct unless the crucible is non-wetting to the melt). Thus with uncertainties of this magnitude it is difficult to determine whether factors such as atom radius or structural effects are influencing the

Table 4.4 Details of models to calculate densities of alloys and slags

Reference	System	Details of Method	Uncertainty
Mills <i>et al.</i> ¹²⁷	Alloys	<p>1. Solids: $\rho_{298} = \sum (X_1\rho_{298})_1 + (X_2\rho_{298})_2 + (X_3\rho_{298})_3 + \dots$ $(d\rho/dT) = X_1(d\rho/dT)_1 + X_2(d\rho/dT)_2 + X_3(d\rho/dT)_3 + \dots$ $\rho_T = \rho_{298} + (T - 298K)(d\rho/dT)$ Correction needed when Al > 1% e.g. Ni-alloys</p> <p>2. Liquids: $V^m = \sum X_1V_1^m + X_2V_2^m + X_3V_3^m + \dots$ $2. V - \Delta V^{xs} \beta = \sum X_1\beta_1 + X_2\beta_2 + X_3\beta_3 + \dots$ where $\beta = (1/V)(dV/dT)$ $V_T = V^m(1 + \beta(T - T^m))$ and $\Delta V^{xs} = V + K(\% \text{Al})$ for Ni alloys with Al</p>	2%
Sung <i>et al.</i> ¹¹³	Ni-based alloys	<p>Numerical analysis of measured data: $\alpha(\%) = b_0 + b_1(T - T_R) + b_2(T - T_R)^2 + b_3(T - T_R)^3$ where b_0, b_1, b_2, b_3 and T_R are constants: values given for various elements</p> <p>2. $V - \Delta V^{xs} = \sum X_1V_1 + X_2V_2 + X_3V_3 + \dots$</p> <p>3. $\Delta V^{xs} = -1.50 + 4.5X_{\text{Al}} + 5.2(X_{\text{Cr}} + X_{\text{Ti}}) + 0.43(X_{\text{W}} + X_{\text{Re}} + X_{\text{Ta}} + X_{\text{Mo}})$</p>	2%
Robinson <i>et al.</i> ¹²⁵	Alloys	<p>1. Use of thermodynamic software to predict, V and β data stored for different phases of alloy: e.g. steels $\rho = \rho_{\text{Fe}} + \sum k_i C_i$ where k is effect of different solutes and C = % 2. Values calculated for different phases</p>	<2%
Bottinga and Weill ¹²⁸	Slags	$V = \sum X_1V_1 + X_2V_2 + X_3V_3$ Values of V given Corrections to V values for compositions of Al_2O_3 , Na_2O , K_2O , CaO , MgO , FeO : equations for β also corrected for chemical compositions of these oxides	2–3%
Mills and Keene ¹⁸	Slags	<p>Method 1: $\rho (\text{kgm}^{-3}) = 2460 + 18(\% \text{FeO} + \% \text{Fe}_2\text{O}_3 + \% \text{MnO} + \% \text{FeO})$ Method 2: $V = \sum X_1V_1 + X_2V_2 + X_3V_3 + \dots$ at 1773K $V (10^{-6}\text{m}^3\text{mol}^{-1})$ values for: $\text{CaO} = 20.7$; $\text{FeO} = 15.8$; $\text{Fe}_2\text{O}_3 = 38.4$; $\text{MnO} = 15.6$; $\text{MgO} = 16.1$; $\text{Na}_2\text{O} = 33$; $\text{K}_2\text{O} = 51.8$; $\text{TiO}_2 = 24$; $\text{P}_2\text{O}_5 = 65.7$; $\text{SiO}_2 = (19.55 + 7.97X_{\text{SiO}_2})$ $\text{Al}_2\text{O}_3 = (28.3 + 32X_{\text{Al}_2\text{O}_3} - 31.45X^2_{\text{Al}_2\text{O}_3})$ $(dV/dT) = 0.01\% \text{K}^{-1}$</p>	5% 2%
Robinson <i>et al.</i> ¹²⁵	Slags	Use of thermodynamic software: Molar volumes stored for oxides and correction based on molar Gibbs energy of system	2%
Hayashi and Seetharaman ¹⁴⁷	Slags	$V/\sum X_1V_1 = (K\Delta^{\text{mix}} H/R^*T)$ where is the relative integral enthalpy of mixing (determined with thermodynamic software) and K = constant	2%
Priven ¹²⁶	Glasses	Solids: $V = \sum X_1V_1 + X_2V_2 + X_3V_3$ Values and range of applicability given. Special procedures for boro-silicates	

viscosity. Similarly, the uncertainties associated with the measurements of slag viscosities are probably around $\pm 25\%$ although these uncertainties can be reduced to $< \pm 10\%$ where best practice is observed. Structure has a marked effect on viscosity. The effect of structure is much more pronounced in glasses and slags than in alloys because of the polymeric nature of the structure of glasses and some slags.

The Arrhenius equation is widely used for expressing the temperature dependence of viscosity:

$$\ln \eta = \ln A_A + B_A/T \quad (4.38)$$

where $B_A = E/R^*$ and A_A is a pre-exponential term, E_A is the activation energy and R^* is the gas constant. Equation 4.39 above reduces to equation 4.40. The Weymann relation is thought to provide a slightly better fit of experimental viscosities than the Arrhenius relation

$$\eta = A_w T \exp (B_w/T) \quad (4.39)$$

or

$$\ln (\eta/T) = \ln A_w + B_w/T \quad (4.40)$$

where $B_w = E_w/R^*$ and A_w is a pre-exponential term, E_w is the activation energy.

Slags, glasses

In glasses the liquid transforms on cooling to a supercooled liquid and the viscosity exhibits a smooth relationship with temperature all the way to the glass transition temperature (T_g , which occurs when $\log_{10} \eta(\text{Pas}) = 12.4$). The Vogel–Fulcher–Tammann (VFT) relation (derived from the free volume theory¹³⁶) is frequently used to express the relation between viscosity and temperature for glasses and has the form:

$$\ln \eta = \ln A_V + B_V/(T - T_o) \quad (4.41)$$

Many models for calculating the viscosities of slags and glasses have been reported;^{137–150} details are given in Tables 4.5 and 4.6; information on another 15 models is given by Kondratiev.¹²⁹ Several approaches have been adopted in the models to take the structure of the melt into account, namely:

1. By carrying out a numerical analysis of experimental data.
2. By relating viscosity to structural parameters (such as NBO/T or optical basicity) which provides a measure of the structure.
3. By using thermodynamic parameters as a measure of structure.
4. By using molecular dynamics to calculate the number of bridging (N_{O_o}) non-bridging (N_{O_c}) and free oxygens (N_{O_2}) and relating these to the viscosity.

The reported models for estimating the viscosities of slags, glasses and alloys are given in Tables 4.5, 4.6 and 4.7, respectively.

Table 4.5 Details of published models for the estimation of slag viscosities

Reference	Slag type	T-dependence	Details of model and comments	Slag flux	$\Delta\%$
Riboud <i>et al.</i> ¹³⁷	Various	Wey	$A_W; B_W$ functions of 5 groups 'CaO' + 'SiO ₂ ' + 'Al ₂ O ₃ ' + 'CaF ₂ ' + 'Na ₂ O' where X_{CaO} contains $X_{\text{CaO}} + X_{\text{MgO}} + X_{\text{FeO}} + X_{\text{MnO}}$ etc. $A = -19.81 + 1.73 X_{\text{CaO}} + 3.58 X_{\text{CaF}_2} + 7.02 X_{\text{Na}_2\text{O}} - 35.76 X_{\text{Al}_2\text{O}_3}$ $B = 31140 - 23896 X_{\text{CaO}} - 46356 X_{\text{CaF}_2} - 39159 X_{\text{Na}_2\text{O}} - 68833 X_{\text{Al}_2\text{O}_3}$ Works well (30%) for variety of slags	Mould flux	30
Urbain ¹³⁸	Various	Wey	$A_W; B_W$ functions of 3 groups Glass formers: $X_G = X_{\text{SiO}_2} + X_{\text{P}_2\text{O}_5}$ Amphoterics $X_A = X_{\text{Al}_2\text{O}_3} + X_{\text{B}_2\text{O}_3} + X_{\text{Fe}_2\text{O}_3}$ Modifiers: $X_M = X_{\text{CaO}} + X_{\text{MgO}} + X_{\text{Na}_2\text{O}} + 3 X_{\text{CaF}_2} + X_{\text{FeO}} + X_{\text{MnO}} + 2X_{\text{TiO}_2}$ $+ B_W = B_0 + B_1 X_G + B_2 X_G^2 + B_3 X_G^3$ and $Bi = \alpha l + b i \alpha + c i \alpha i^2$ $\ln A_W = 0.2693 B_W + 11.6725$ Special B_W values for MnO, MgO	Various	25
Iida <i>et al.</i> ¹³⁹	Many	Arr	$\eta(\text{Pas}) = A \eta_0 \exp(E/Bi)$ where η_0 is viscosity of hypothetical network-forming melt and Bi = basicity index $E = 11.11 - 3.65 \times 10^{-3}T$ and $a = 1.745 - 1.962 \times 10^{-3}T + 7 \times 10^{-7} T^2$ and $Bi = \sum(\alpha_i \%)_B / \sum(\alpha_i \%)_A$ where A = acid oxides and B = basic oxides or fluorides: $\eta = 1.8 \times 10^{-7} (M = iT^m)^{0.5} \exp(H_i/RT^m) / V_m^{0.667} \exp(H_i/RT^m)$ where $H_i = 5.1 T^m$ and values of α given	Mould flux	25
Senior ¹⁴⁰	Coal	Wey	$A = a_0 + a_1 B + a_2 (\text{NBO}/T)$ where $a_0 = 2.816$ $a_1 = 0.4634$: $a_2 = 0.3534$ $(\text{NBO}/T) = X_{\text{CaO}} + X_{\text{MgO}} + X_{\text{Na}_2\text{O}} + X_{\text{FeO}} + X_{\text{MnO}} - X_{\text{Al}_2\text{O}_3} + X_{\text{Fe}_2\text{O}_3} / \{0.5(X_{\text{SiO}_2} + X_{\text{TiO}_2}) + X_{\text{Al}_2\text{O}_3} + X_{\text{Fe}_2\text{O}_3}\}$ Equations also given for low temperatures	BF	19

Table 4.5 *Continued*

Reference	Slag type	T-dependence	Details of model and comments	Slag	$\Delta\%$
Mills <i>et al.</i> ¹⁴¹	Various	Arr	Optical basicity (Λ) – measure of depolymerisation Composition adjusted for Al_2O_3 needed for charge balancing $\rightarrow \Lambda_{\text{corr}}$ $\ln A = -232.7 (\Lambda_{\text{corr}})^2 + 357.3 (\Lambda_{\text{corr}}) - 144.2$ $\ln (B/100) = -1.77 + (2.88/\Lambda_{\text{corr}}) \ln \eta(\text{Pas}) = \ln A + \exp(B/T)$	Mould flux	34
Gupta <i>et al.</i> ¹⁴²	Mould fluxes	Arr	3 groups 'Acidic': $Y_X = (%\text{SiO}_2/60) + \alpha(%\text{Al}_2\text{O}_3/102)$ 'Basic' $Y_O = (%\text{CaO}/56) + (%\text{MgO}/40) + (%\text{Na}_2\text{O}/63) + (%\text{FeO}/72)$ 'Fluorides' $Y_F = (%\text{F}/19)$: $N_F = Y_F/(Y_X + Y_O + Y_F)$: $N_X = Y_X/(Y_X + Y_O + Y_F)$: $N_O = Y_O/(Y_X + Y_O + Y_F)$ $\text{Na}^+/\text{Ca}^{2+}$ affected η : Values of a_0 to a_5 given for 1573 and 1673 K $\eta = a_0 + a_1(M^+/M^{2+}) + a_2N_X + a_3N_X(M^+/M^2) + a_4(M^+/M^2)^2 + a_5N_X^2$	Mould flux	35
Koyama <i>et al.</i> ¹⁴³	Mould fluxes	Arr	$\ln A = -24.2X_{\text{Al}_2\text{O}_3} - 6.1X_{\text{CaO}} - 12.1X_{\text{MgO}} - 19X_{\text{Na}_2\text{O}} + 6.3X_{\text{CaF}_2} - 4.816$ $B = -9259X_{\text{SiO}_2} + 28319X_{\text{Al}_2\text{O}_3} - 16564X_{\text{CaO}} - 41365X_{\text{CaF}_2}$ $- 45510X_{\text{Li}_2\text{O}} + 29012$	Mould flux	76
Kim <i>et al.</i> ¹⁴⁴	Mould fluxes	Arr	$\ln A = -2.307 - 0.046X_{\text{SiO}_2} - 0.07X_{\text{CaO}} - 0.041X_{\text{MgO}} - 0.185X_{\text{Al}_2\text{O}_3}$ $+ 0.035X_{\text{CaF}_2} - 0.095X_{\text{B}_2\text{O}_3}$ $B = 6807 + 70.7X_{\text{SiO}_2} + 32.58X_{\text{CaO}} + 312.7X_{\text{Al}_2\text{O}_3} - 34.8X_{\text{Na}_2\text{O}}$ $- 176.1X_{\text{CaF}_2} - 167.4X_{\text{Li}_2\text{O}} + 59.7X_{\text{B}_2\text{O}_3}$ where X in mole %	Mould flux	45
Utidard <i>et al.</i> ¹⁴⁵	Non-ferrous	Emp	$\log \eta(\text{Pas}) = -0.49 - 5.1(VR)^{0.5} + (-3660 + 12080(VR)^{0.5})/T$ $VR = A/B$ where $A = \text{SiO}_2 + 1.5\text{Cr}_2\text{O}_3 + 1.2\text{ZrO}_2 + 1.8\text{Al}_2\text{O}_3$ $B = 1.2\text{FeO} + 0.5(\text{Fe}_2\text{O}_3 + \text{PbO}) + 0.7(\text{CaO} + \text{Cu}_2\text{O}) + 0.8\text{MgO}$ $+ 2.3(\text{Na}_2\text{O} + \text{K}_2\text{O}) + 1.6\text{CaF}_2$ where in wt %		

Reddy ¹⁴⁶	Binary boro-silicate	Emp	$\eta \text{ (dPas)} = 4.9 \times 10^{-9} N_{O_2} T^{0.5} \exp(E/RT)$ N_{O_2} calculated from atomic pair (thermodynamic) model E related to N_{O_2}			
Du and Seetharaman ^{12,147}	Syn	Arr	$\eta = hN_A \rho / M \exp(\Delta G_\eta / RT)$ where h = Planck constant, N_A = Avogadro no. Structure accounted for thermodynamics: $\Delta G^* = \sum \Delta G^*_\eta$ (oxides) + $\Delta G_\eta^{\text{mix}}$ + $3R^*T X_1 X_2$ $\Delta G_\eta^{\text{mix}}$ for interactions of cations only works well for synthetic slags ($\pm 15\%$)	Syn	<20	
Ling Zhang <i>et al.</i> ¹⁴⁸	Various	Wey	Structure as N_O ; N_{O-} ; N_{O2-} calculated from cell model (thermodynamic) A_W and B_W as functions of N_O ; N_{O2-} Molecular Dynamics calculations Works well (20%) several slags	Coal	22	
Tanaka ¹⁴⁹	Syn	Arr	X_O ; X_{O-} ; X_{O2-} calculated from thermodynamic cell model $N_{MO} = a^*(X_{O-} + X_{O2-})$ where a^* is a measure of free space available and n is the frequency of the step in MO-SiO ₂ system: a^* values: Al ₂ O ₃ = 0.95; MgO = 1.8; CaO = 2.0 and FeO = 3.8 Multicomponent slags: $E_\eta = E_0 / (1 + \sum a^* X_{O-})^{0.5}$ where $E_0 = E_\eta$ for SiO ₂			
Kondratiev, Jak I ¹⁵⁰	Coal Syn	Wey	Modified Urbain method for CaO + FeO + Al ₂ O ₃ + SiO ₂ system Modification 1: $-\ln A = mB + N$; $n = 9.322$ but m is composition dependent $m = m_1 X_1 + m_2 X_2 + m_3 X_3 + m_4 X_4$ and values given for various m values Modification 2: Different B values given for FeO and CaO; constants given to calculate B values	Syn	25	
Robinson ¹²⁵	Syn	Arr	Uses thermodynamic software: data for binaries. Based on Du and Seetharaman model			

Notes: Arr = Arrhenius relation; Wey = Weymann relation; Emp = Empirical relation; Syn = Synthetic slag; BF = Blast furnace slags: $\Delta\% = (\sum \delta_n \%) / N$ where $\delta\% = 100 \{(\eta_{\text{meas}} - \eta_{\text{calc}}) / \eta_{\text{meas}}\}$ and N = number of measurements.

Table 4.6 Details of published models for the estimation of viscosities of glasses

Reference	Type	Temp. dependence	Details of model and comments
Lakatos ¹⁵²	Emp	VFT	$\ln \eta = \ln A_v + (B_v/T - T_o)$: $A_v = 1.46 + 1.48X_{Na_2O} + 0.835X_{K_2O} + 1.6X_{CaO} + 5.5X_{MgO} - 1.52X_{Al_2O_3}$ $10^3B_v = 5736 - 6040X_{Na_2O} - 1440X_{K_2O} - 3920X_{CaO} + 6285X_{MgO} + 2254X_{Al_2O_3}$ $T_o = 198 - 25.1X_{Na_2O} - 321X_{K_2O} + 544X_{CaO} - 384X_{MgO} + 294X_{Al_2O_3}$
Feng ¹⁵³	Emp	VFT	Related bond strengths to enthalpy of formation
Sasaki, Ishii ¹⁵⁴	Tdic	Arr	Based on Adams-Gibbs configurational entropy of relaxation $Cp^{conf} = Cp_l - Cp_{gl} = Cp_l - 3R^*$ where Cp^{conf} is configurational Cp and $Cp_{gl} = Cp$ of glass at T_g , $S^{conf} = S^{conf}_{T_g} + \int_{T_g}^T (Cp^{conf}/T) dT$ and $\eta = A \exp(B/TS^{conf})$ Linear relation between $\log \eta = (TS^{conf})$ for $CaO.Al_2O_3.2SiO_2$
Yan <i>et al.</i> ¹⁵⁵		ARR	Structure related to optical basicity corrected for cations charge-balancing Al_2O_3 (Λ_{cor}) Borates $\log_{10} \eta^m$ (dPas) = $-0.55 + (2.35/\Lambda_{cor})$ Silicates $\log_{10} \eta^m$ (dPas) = $-13.47 + (8.91/\Lambda_{cor})$ Boro-silicates: $\log_{10} \eta^m$ (dPas) = $(1-r)\{13.47 + (8.91/\Lambda_{cor})\} + (1-r)\{-0.55 + (2.35/\Lambda_{cor})\}$ where $r = X_{SiO_2}/(X_{SiO_2} + X_{B_2O_3})$ Supercooled region: Silicates $A_v = 0.20 + 2.35\Lambda_{cor}$ $B_v = 10169 - 10530\Lambda_{cor}$; $T_o = 758 - 369\Lambda_{cor}$
		VFT	

Table 4.7 Details of published models for the estimation of viscosities of alloys

References	Type	Temp. dependence	Details of model and comments
Hirai ¹⁵⁶	Emp	Arr	Hirai gives viscosity in terms of T^m , M , V^m $\eta = A(\text{Pas}) = 1.7 \times 10^{-3} \cdot \rho^{0.667} T_m^{0.5} M^{-1/6} / \exp(B/R T_m)$ $B = 2.65 T_m^{1.27}$
Seetharaman ^{122,157}	Tdic	Arr	Structure represented by thermodynamics $\eta = (hN_A \rho / M) \exp(\Delta G_{\eta}^*/RT)$ M = mol mass, N_A = Avogadro no. $\Delta G_{\eta}^* = x_i \cdot \Delta G_{\eta}^* + \Delta G_{\eta}^{\text{mix}} + 3RT x_1 x_2$
Moelwyn-Hughes ¹⁵⁸	Tdic		$\eta = (X_1 \eta_1 + X_2 \eta_2) (1 - 2X_1 X_2 \Omega R^* T)$ where $\Omega = \Delta^{xs} H$ values/ $X_1 X_2 N_A$ Used on binary systems gives negative deviation in viscosity for systems with positive $\Delta^{xs} H$ values but problems with eutectic systems
Iida ⁷	Tdic		Based on Moelwyn-Hughes model but takes size of atom (Pauling atomic radius) into account and uses activity coefficient rather than $\Delta^{\text{mix}} H$ values
Chhabra ¹⁵⁹	Emp.	Emp.	Extended empirical formula used in chemical engineering approach to liquids $\log(\eta + 1) = 10^a T^b$ where $a = \sum x_i a_i$ and $b = \sum x_i b_i$ for various elements (1,2 etc.)
Kucharski ¹⁶⁰	Tdic		$\eta = \sum (V_i/V) X_i (\tau/\lambda)^2 (f_1^{**}/f_1^*) \eta_1$ where 1,2, 3 are constituents where $\tau = \sum_1 X_1 (V_1/N_A)^{1/3}$ and $\lambda_1 = X_1 (V_1/N_A)^{1/3} + \sum_2 X_2 (V_2/N_A)^{1/3} (V_2/V_1)$ and $(f_1^{**}/f_1^*) =$ ratio of component 1 in activated and initial state $(f_1^{**}/f_1^*) = f_1^\alpha$ and α = is obtained by fitting experimental data Subsequently, $[f_1^{**}]_{2,3} / [f_1^*]_{2,3} = [f_1]^\alpha_{2,3}$ and $\alpha_{2,3} = \alpha_{1,2} t_{2,3} + \alpha_{1,3} t_{3,2}$ where $t_{2,3} = (X_2/(X_2+X_3))$ and $t_{3,2} = (X_3/(X_2+X_3))$

A ‘Round Robin’ project was organised to test the relative performance of various models used to estimate slag viscosities.¹⁵¹ Although some ranking of the various models was made (Table 4.5, last column) it was found that more accurate experimental data were needed to test and improve the better-performing models. The principal sources of error are (i) systematic errors in the measurement method, (ii) changes in chemical composition during measurements (post-measurement chemical analysis is recommended) and (iii) the ‘non-wetting’ of the melt on the crucible.

Metals

The principal difficulty in modelling the viscosities of metals and alloys lies in the uncertainties in the reported values. These experimental uncertainties arise from:

1. Systematic errors in the measurement method.
2. ‘Non-wetting’ of the melt on the crucible.
3. Equations used to derive viscosity from damping characteristics.
4. Formation of oxide films on the free surface of the sample.
5. Formation of oxide particles or high-melting phases which cause the viscosity to increase.

Frequently, the magnitude of effects being studied (e.g. the radius of the atoms) is of the same magnitude as (or smaller than) the experimental uncertainties. The introduction of new techniques with experimental uncertainties ($>\pm 10\%$) should see the development of reliable models for the prediction of the viscosities of alloys. Details of extant models are summarised in Table 4.7.

4.7.4 Electrical resistivity (R)

Metals and alloys

As mentioned in Section 4.7.3 the electrical resistivity (R) of solid alloys is affected by the microstructure of the sample; the model is based on the microstructure resulting in the minimum resistance (or highest conductivity). The electrical resistivity values at 298K of commercial alloys can be calculated from the relations given in Table 4.8.

Approximate values for the liquid alloy can be obtained by assuming the electrical resistivity and its temperature dependence are calculated from partial molar quantities.

$$R_{el}^m = (X_1 \bar{R}_{el}^m)_1 + (X_2 \bar{R}_{el}^m)_2 + (X_3 \bar{R}_{el}^m)_3 + \dots \quad (4.42)$$

$$dR_{el}/dT = X_1 (d\bar{R}_{el}/dT)_1 + X_2 (d\bar{R}_{el}/dT)_2 + X_3 (d\bar{R}_{el}/dT)_3 \quad (4.43)$$

Table 4.8 Coefficients for the calculation of k_{lat} and R_{el} for the calculation of thermal conductivities of solid alloys at 298K by $R_{\text{el}} = \sum (\% \cdot R_{\text{el}})_1$ and $k_{\text{lat}} = \sum (\% \cdot k_{\text{lat}})_1$ and note that terms R_{el} and $(1/k_{\text{lat}})$ for Al are not multiplied by 10^2 due to high conductivity of Al; no values given for k_{lat} of Ti-alloys; Bal = balance. No values reported for k_{lat} for Ti alloys

Alloy	Al	C	Cr	Cu	Fe	Mn	Mo	Nb	Ni	Si	V	W	Others
Steel													
$10^2 R_{\text{el}}$	7.9	8.28	1.92	7.48	0.11	3.53	0.97	0.1	2.1	9.9	3.34	0.6	As = 0.1; S = 2; P = 4.45
$10^2 k_{\text{latt}}$	1.0	246	0.35	347	8.1	0.11	0.39	0.81	-0.28	-96.8	1.14	4.63	As = 1; S = 1; P = 1
Ni-alloy													
$10^2 R_{\text{el}}$	6.2	0.1	1.6	-4.0	0.6	3.8	2.7	0	0.1	10.2	9.4	-38	Co = 0.08; Ti = 3
$10^2 k_{\text{latt}}$	-16	0.1	-36.4	-1.56	8.31	187.5	5.5	0	15.7	181	9.4	-818	Co = -0.2 Ti = 7.5
Ti-alloy													
$10^2 R_{\text{el}}$	12.2	-26.1	200	9.1	-173	-11.4	9.2	10		51	8.3		Sn = 65; Ti = 0.75; Bal = 10
Al-alloy													
R_e	3.08			-8.38	5.4	-7.75	52.7			7.1			Mg = 57.3 Zn = -30.9; Li = 3.4; Bal = 30
$(1/k_{\text{lat}})$	0.046	7.4	0.076	0.39	2.90					0.076			Mg = 0.12; Zn = 0.38; Li = 3.36; Bal = 1.1

The thermal conductivity of the liquid at temperature, T, can be calculated from the electrical resistivity value at that temperature using the WFL rule.

4.7.5 Thermal conductivity (k), diffusivity (a)

Metals and alloys

Liquid alloys

At high temperatures heat transferred in metals is predominantly through the movement of electrons. Consequently, thermal conductivity and diffusivity values are usually calculated via the Wiedemann–Franz–Lorenz (WFL) relation shown in equation 4.44

$$k = 2.45 \cdot 10^{-8} (T/R) \quad (4.44)$$

where R is the electrical resistivity, which must be either measured or calculated. This equation works well for liquids around the melting point⁸⁰ but it has been suggested⁸¹ that the following relation should be applied with measurements over extended ranges of temperature.

$$k = (A \cdot L_o T/R_{el}) + B \quad (4.45)$$

where A, B and L_o are constants and the subscript ‘el’ refers to electronic conduction. However, it has been reported that the thermal conductivities of Ge, Si, Sn and Pb calculated from equation 4.44 show the opposite temperature dependence to the measured values. The absence of reliable thermal conductivity data for liquid alloys has hindered the development of models. One possibility for the calculation of thermal conductivities of commercial alloys is: (i) to derive a value of the thermal conductivity (k_s^m) of the solid alloy* at the liquidus temperature (or alternatively, $0.5(T_{sol} + T_{liq})$) and then (ii) multiply k_s^m by (R_l^m/R_s^m) for the parent metal (for steels (Fe) by 1.05 and Ni-alloys by 1.40).

Alternatively, approximate values for the liquid alloy can be obtained by assuming the electrical resistivity and its temperature dependence (dR_{el}/dT) can be calculated from partial molar quantities.

$$R_{el}^m = (X_1 \bar{R}_{el}^m)_1 + (X_2 \bar{R}_{el}^m)_2 + (X_3 \bar{R}_{el}^m)_3 + \dots \quad (4.46)$$

$$(dR_{el}/dT) = X_1 (d\bar{R}_{el}/dT)_1 + X_2 (d\bar{R}_{el}/dT)_2 + X_3 (d\bar{R}_{el}/dT)_3 \dots \quad (4.47)$$

The thermal conductivity of the liquid at temperature, T, can be calculated from the electrical resistivity value at that temperature using the WFL rule.

* Most families of alloys tend to come to a constant value of K_s at higher temperatures, e.g. for steels K_s at 1673K has a value of $33 \text{ W m}^{-1} \text{ K}^{-1}$ (Table 4.9).

Solid alloys

The resistance to thermal transfer at ambient temperatures can be considered to be made up of two contributions, R_{el} and R_{lat} , the resistances associated with electronic and phonon (or lattice) heat transfer. The overall thermal conductivity (k_{eff}) is dependent upon the microstructure; in modelling the thermal conductivity it is customary to derive values for the microstructure corresponding to the minimum resistance for the alloy (or maximum conductivity). There are few models for alloys and these have mostly been directed to the estimation of thermal conductivities of specific families of commercial alloys, e.g. steels, Ni-based superalloys, etc. It was noted that for individual families of alloys (e.g. steels) the thermal conductivity at higher temperatures (e.g. >1100K in steels) seems to be independent of composition of the alloy (e.g. steels), i.e. the conductivity of all alloys at a certain temperature has an identical value. Details of reported models are given in Table 4.9. The uncertainty in the estimated values is around $\pm 10\%$.

Mushy phase alloys

It has been found that thermal conductivity measurements in the mushy phase are subject to considerable error since some of the heat is not conducted but is used to produce further melting of the alloy. Thus values are best estimated using the relation, $k_{eff} = f_s k_{s\,el} + (1 - f_s) k_{l\,el}$ or $R = f_s R_{s\,el} + (1 - f_s) R_{l\,el}$.

Slags

Since it is difficult to estimate the magnitude of the radiation conductivity (k_R) it follows that it is difficult to calculate the effective conductivity (k_{eff}) of solid and liquid slags. The radiation conductivity contribution increases markedly at higher temperatures. However, a correlation of the thermal conductivity data for liquid slags at the melting point (k^m) obtained using transient methods (where k_R might be expected to be small) led to equation 4.48 which was applicable over the range (NBO/T) = 0.5 to 3.5.¹¹ The (NBO/T) can be calculated from the chemical composition (see Appendix A)

$$(1/k^m) = 0.7 + 0.66 \text{ (NBO/T)} \text{ mK W}^{-1} \quad (4.48)$$

Thus the thermal conductivity increases with increasing polymerisation.

4.7.6 Surface tension

The principal difficulties encountered in modelling surface tensions are:

1. Surface active elements (even when present at ppm levels) can have a dramatic effect on the surface tension (γ) and $(d\gamma/dT)$ (this is an especial problem with O, S, Se, Te in metals and alloys).

Table 4.9 Details of models for calculating the thermal conductivities of solid commercial alloys

Alloy	Reference	Details and comments
Steel	Mills <i>et al.</i> ¹²⁷	<p>1. $R_{298}^{el} = (\%R_{298}^{el})_1 + (\%R_{298}^{el})_2 + (\%R_{298}^{el})_3$ + where 1, 2 etc. = different elements (Table 4.8)</p> <p>2. $k_{298}^{el} = 2.45 \times 10^{-8} (T/R_{298}^{el})$</p> <p>3. $k_{298}^{lat} = (\%k_{298}^{lat})_1 + (\%k_{298}^{lat})_2 + (\%k_{298}^{lat})_3$ + (Table 4.8)</p> <p>4. $k_{298}^{eff} = k_{298}^{el} + k_{298}^{lat}$</p> <p>5. For $298 < T < 1073$ K: Join k_{298}^{eff} to k_{1073}^{eff}: $k_T^{eff} = k_{298}^{eff} + \{(T - 298)/775\}(25 - k_{298}^{eff}) \text{ Wm}^{-1}\text{K}^{-1}$</p> <p>6. For $1073 < T < 1573$ K: $k_T^{eff} = 25 + 0.013(T - 1073) \text{ Wm}^{-1}\text{K}^{-1}$ Usually within $\pm 10\%$</p>
Ni-alloys	Powell and Tye ¹⁶¹	<p>1. $k_{eff} = 6 + 2.2 \times 10^{-6} (T/R)$ where R is resistivity at specific temperature Requires resistivity measurements: works within $\pm 5\%$</p>
	Mills <i>et al.</i> ¹²⁷	<p>Steps 1 to 4 see steel above</p> <p>5. For $298 < T < 1073$ K: Join k_{298}^{eff} to k_{1073}^{eff}: $k_T^{eff} = k_{298}^{eff} + \{(T - 298)/775\}(25 - k_{298}^{eff}) \text{ Wm}^{-1}\text{K}^{-1}$</p> <p>6. For $1073 < T < 1573$ K: $k_T^{eff} = 23 + 0.018(T - 1073) \text{ Wm}^{-1}\text{K}^{-1}$ Usually within $\pm 10\%$</p>
Ti-alloys	Mills <i>et al.</i> ¹²⁷	<p>Steps 1 to 4 similar to steels and Ni-alloys but $\alpha \rightarrow \beta$ transformation occurs $973 - 1273$ K</p> <p>5. $298 < T < 973$ K: $k_T = k_{298} + (23 - k_{298}) \{(T - 298)/675\} \text{ Wm}^{-1}\text{K}^{-1}$</p> <p>6. $298 < T < 973$ K: $k_T = k_{298} + 15.2 + 0.0273(T - 973) \text{ Wm}^{-1}\text{K}^{-1}$</p> <p>7. $1273 < T < 1923$ K: $k_T = k_{298} + 15.2 + 0.0273(T - 1273) \text{ Wm}^{-1}\text{K}^{-1}$</p>
Al alloys	Mills <i>et al.</i> ¹²⁷	<p>As for steps 1 to 4 for steels: k_{298}^{el}:</p> <p>5. Calculate $a_{298} = k_{298}/Cp_{298}, \rho_{298}$:</p> <p>6. Calculate a_T: $298 < T < 573$: $a_T = a_{298} \{1 + 0.02 [(T - 298)/275]\}$</p> <p>7. $573 < T < T_{sol}$: $a_T = a_{298} \{1 - 0.02 [(T - 573)/300]\}$</p>

2. The surface tensions of some ‘pure’ metals are not well-established because of problems with O contamination (e.g. Ti and Zr).
3. For alloys exhibiting marked departures from Raoult’s law there is a marked effect on γ (e.g. Ni-Al shows negative departures which means there is less Al at surface than that calculated assuming ideal solution and hence γ (calc. ideal) < γ (actual)).¹³

Several models have been developed and details are given in Table 4.10.

Slags

Tanaka *et al.*^{166,13} have applied their model (outlined in Table 4.10) to the calculation of the surface tension of slags and molten salts using commercial thermodynamic software to calculate $G^{XS,B}$ where the superscript B and S refer to the bulk and surface, respectively. It was found that it was necessary to allow for the fact that the ionic distances in the surface differ from those in the bulk in order to maintain electrical neutrality. This was taken into account using the parameter, ξ , which was $(G^{XS,S}/G^{XS,B}) = (Z^S/Z^B)/\xi^4 = 0.94/\xi^4$ with ξ having a value of 0.97.

Other models have been reported for the calculation of the surface tension of slags.^{7,18,169,170} The model due to Zhang *et al.*¹⁷⁰ makes use of the excess surface tension ($\gamma^{xs} = \gamma_{meas} - \sum X_1 \gamma_1$) and derives constants to express (γ^{xs}) as a function of composition; good agreement was found for the calculated results with measured values.

Interfacial tension (γ_{MS})

Interfacial tensions can be calculated using the following relation

$$\gamma_{ms} = \gamma_m + \gamma_s + 2\phi (\gamma_M \cdot \gamma_S) \quad (4.49)$$

where ϕ is an interaction coefficient. The parameter ϕ was found to have a value of 0.5 for slags free of FeO but increased with FeO additions.¹⁷¹ Tanaka¹³ proposed the following equation

$$\phi = 0.5 + 0.3X_{FeO} \quad (4.50)$$

Qiao *et al.*¹⁷² have outlined a model for estimating the interfacial tension using the excess interfacial tension (γ_{MS}^{xs}) and considering the components of a binary alloy separately with regard to the slag. Values were derived for coefficients by fitting experimental data.

4.7.7 Optical properties

Absorption coefficients (α^)*

The change in absorption coefficient ($\Delta\alpha^*$) of slags containing transition metal oxides (MO) can be estimated from the following: $\Delta\alpha (m^{-1}) = K (\%MO)$

Table 4.10 Details of models developed to calculate the surface tensions of alloys

References	Systems	Details of model and comments
Hajra, Lee, Frohberg ¹⁶²⁻¹⁶⁴	Binaries, ternaries	<p>1. Calculate molar volume of alloy $V = \sum X_i V_i + X_2 V_2 + X_3 V_3$</p> <p>2. Calculate surface area, $s_i = (0.921 V_i^{2/3}) \times 10^4$ for each component, i</p> <p>3. Solve: $1 = \sum \{X_i \exp(\gamma_T - \gamma'_T) s_i / RT\}$ where γ_T and γ'_T are surface tensions of alloy and element, respectively</p>
Small ¹⁶⁵	Fe-O-S	<p>1. $\gamma_T - \gamma = R^* T \Gamma_o \ln \{(1 + K_o a_o + K_s a_s)/(1 + K_s a_s)\} + R^* T \Gamma_s \ln \{(1 + K_o a_o + K_s a_s)/(1 + K_o a_o)\}$ where a is the chemical activity and Γ = surface excess concentration</p> <p>2. Fitted experimental data for surface tension</p>
Tanaka <i>et al.</i> ¹⁶⁶	Binaries, ternaries, molten salts	<p>1. Based on Butler Eqn: $\gamma = \sum \gamma_i l_i + (R^* T / s_i) \ln (X_i^S / X_i^B) + (1/s_i)(G^E - G^B)$ where G^E is the excess free energy which is function of (T, X_i^B), S and B are the surface and bulk.</p> <p>2. $G^E_i = \beta_{\text{alloy}}(G^B)$ where $\beta = (Z^S / Z^B)$ = ratio of coordination in surface and bulk</p> <p>3. $\beta = (Z^S / Z^B) = 0.83$ for alloys $\beta = (Z^S / Z^B) = 0.94$ for ionic mixtures</p> <p>Model successfully calculates effect of non-ideality on surface tension (e.g. negative departures, Fe-Si, positive departures, Cu-Pb). Good agreement with measured values</p>
McNallan, Debroy ¹⁶⁷	Fe-Ni-Cr-S	<p>Based on calculation of γ of Fe-Ni and then effect of Cr and then the effect of S is determined</p> <p>1. $\gamma_{\text{Fe-Ni}} = \gamma_{\text{Fe}} + \{(R^* T / s_{\text{Fe}}) \ln (X_{\text{Fe}}^S / X_{\text{Fe}}^B) + \ln (f_{\text{Fe}}^S / f_{\text{Fe}}^B)\}$ where s = surface area, f = activity coefficients and superscripts S and B refer to the surface and bulk</p> <p>2. $\ln f_{\text{Fe}}^S = (Z^S / Z^B) \ln f_{\text{Fe}}^B$</p> <p>3. $\gamma_{\text{Fe-Ni}} = \gamma_{\text{Fe}} - 0.2 X_{\text{Ni}}$ and effect of Cr on $\gamma_{\text{Fe-Ni}}$ determined and f_S calculated from interaction coefficients.</p> <p>4. $\gamma = \gamma_{\text{Fe}} - A(T - T_o) - R^* \Gamma_s \ln (1 + [k a_s \exp(-\Delta H^{\text{abs}} / R^* T)])$ where ΔH^{abs} = heat of absorption and k is equivalent entropy factor, a_s is activity of S; A = constant, T_o = reference temperature</p>

Su <i>et al.</i> ¹⁶⁸	Commercial alloys, steels Ni-based superalloys	<ol style="list-style-type: none"> 1. Calculate γ 'pure alloy' (γ^0) as in Hajra <i>et al.</i> above 2. Calculate effect of Al (with negative departures from ideality) on γ^0 using correction based on Tanaka's data $\rightarrow \gamma_{corr}^0$ 3. Calculate soluble O and S contents 4. Calculate effect of S and O on γ. $L^* = R^* T \Gamma_o (1 + K_s a_s + K_o a_o) / (1 + K_s a_s)$ $M^* = R^* T \Gamma_s (1 + K_s a_s + K_o a_o) / (1 + K_o a_o)$ and $\Delta\gamma = L^* + M^*$ c: γ (alloy) = $\gamma_{corr}^0 - \Delta\gamma$ Calculated values for steels, Ni-based alloys within $\pm 5\%$ of measured values
Moisou, Burlyev ¹⁶⁹	Steels, Ni-superalloys	Empirical relations based on measurements of binaries – does not include effect of O or S

where K had the following values 910 for FeO, 5 for MnO and 410 for NiO and $\Delta\alpha^* (m^{-1}) = 390 (\%Cr_2O_3) + 370 (\%Cr_2O_3)^2$.¹⁷³

Refractive indices (n)

Susa *et al.*¹⁷⁴ reported that the refractive index (n) of a glass or slag (M_2O-SiO_2) can be estimated from the following relation

$$\begin{aligned} n &= 2(2-3X_{M_2O})n_{BO} + 2X_{M_2O}n_{NBO} = (2n_{NBO}-6n_{BO})X_{M_2O} + 4n_{BO} \\ &= a.n_{BO} + \sum b.n_{NBO} \end{aligned} \quad (4.51)$$

where values of n_{BO} and n_{NBO} were derived from measured data and a and b are the mole numbers of O^0 and O^- , respectively. Values calculated were found to be within 0.4% of measured values.

Priven¹²⁶ reported that refractive indices were dependent upon molar volumes and thus could be calculated using the model for molar volume given in Table 4.4.

4.7.8 Diffusion constants (D)

Most relations for calculating diffusion constants refer to self-diffusion or impurity diffusion at low concentrations. Several theoretical equations have been developed for calculating self-diffusion coefficients and these have been reviewed by Iida and Guthrie.⁷ However, calculations of self- and impurity-diffusivities are usually made relating D to other physical properties.

Relation to molar volume (V)

The following relation has been found to work well for self-diffusivities:⁷

$$D^m (m^2 s^{-1}) = 3.5 \times 10^{-10} (T^m/M)^{0.5} (V^m)^{2/3} \quad (4.52)$$

where M and V are the molecular mass and the molar volume, respectively, of the solvent. The activation energy for diffusion can be calculated from the relation:

$$E_D = b(T^m)^{1.15} \quad (4.53)$$

where b has a value of 2.50 for metals and 2.0 for semi-metals.⁷

Relation to viscosity (η)

The Stokes–Einstein equation gives a relationship with the viscosity:

$$D = kT/b.\pi.\eta.r \quad (4.54)$$

where k = Boltzmann constant and r is the radius of the diffusing species and b has a value of 4 when r (diffusing species) \approx r (solvent) and has a value of 6

when r (diffusing species) $>$ r (solvent). In the modified Stokes–Einstein equation⁷ the diffusion coefficient is given by:

$$(kT/12.6 \eta r) \leq D \leq (kT/10.5 \eta r) \quad (4.55)$$

The Stokes–Einstein relation is not considered to work well in slags and glasses since the diffusing species (cations are small compared with the anions). However, this may not be the case for basic slags where the silicate ions are monomers.

The Eyring relation also relates the D to the viscosity

$$D = kT/\eta\lambda \quad (4.56)$$

where λ = interatomic distance and a value slightly greater than $2r$ has to be adopted to obtain a good agreement with measured values.

Electrical conductivity (κ)

The Nernst–Einstein equation relates D to the electrical conductivity (κ) and concentration (C):

$$\kappa = z^2 \cdot F^2 \cdot DC/R^*T \quad (4.57)$$

where z = valence of diffusing species, R^* = gas constant and F = Faraday constant.

4.8 Acknowledgements

I would like to thank Dr Alistair Fox, Yuchu Su and Dr Zushu Li (Imperial College) and Dr Peter Quested of the National Physical Laboratory for his help and comments.

4.9 References

1. CA Heiple and JR Roper: *Welding J.* 61 (1982) 975s.
2. KC Mills and BJ Keene: *Intl. Mater. Review* 35 (1990) 185.
3. KC Mills, BJ Keene, RF Brooks and A Shirali: *Phil. Trans. Roy. Soc. A* (London) 356 (1998) 911/925.
4. RF Brooks and KC Mills: *Mater. Sci. Eng. A* 178 (1994) 77/81.
5. S Oxley, PN Quested and KC Mills: *Proc. Amer. Vacuum Soc. Conf.*, Santa Fe, NM February (1999) Amer. Vac. Soc. (1999).
6. RW Hamilton, D See, S Butler and PD Lee: *Proc. Inst. British Foundrymen Conf.* (IBF Castcon) held Stratford, June (2000).
7. T Iida and RIL Guthrie: *The physical properties of liquid metals*, Oxford Science (1988).
8. BO Mysen: *Structure and properties of silicate melts*, Elsevier, Amsterdam (1988).
9. BO Mysen: *Earth Science Reviews* 27 (1990) 281/365.

10. ME Fleet: X-ray diffraction and spectroscopic studies on the structure of silicate glasses, in *Short course on silicate melts*, CM Scarfe (ed.), Mineralogical Soc., Ottawa, Canada, October (1986) 1/35.
11. KC Mills: *Trans. ISIJ* 33 (1993) 148/156.
12. Du Sichen, J Bygden and S Seetharaman: *Metall. Trans. B* 25B (1994) 519/525 and 589/595.
13. T Tanaka, M Nakamoto and J Lee: *Proc. Metal Separation Technology* held Copper Mountain, Junre (2004) R E Aune and M Kekkonen (eds) Helsinki Univ. Technol. 135/142.
14. PJ Bray, RV Mulkern and EJ Holupka: *J Non-Cryst. Solids* 75 (1988) 29/36 and 37/44.
15. Jiang Zhongtang and Tang Yongxing: *J Non-Cryst. Solids* 146 (1992) 57/62.
16. Y Waseda and JM Toguri: *The structure and properties of oxide melts*, World Scientific, Singapore (1998).
17. A Navarotsky: *Physics and chemistry of earth materials*, Cambridge Univ. Press, New York (1994).
18. KC Mills and BJ Keene: *Intl Materials Review* 32 (1987) 1/120.
19. S Nakamura, T Hibiya and F Yamamoto, *Proc. Conf. Drop Tower Days*, held Bremen June (1992).
20. G Frohberg, KH Kraatz and H Wever: *Mater. Sci. Forum* 15–18 (1987) 529.
21. S Nakamura, T Hibiya, T Yokota and F Yamamoto: *J Heat Mass Transfer* 33 (1990) 2609/2613.
22. K Nagata and H Fukuyama: *Proc. of Mills Symp. Metals, Slags and Glasses; high temperature properties and phenomena*, held Aug (2002) NPL, Teddington 83/91.
23. KC Mills, BJ Monaghan, RF Brooks and PN Quested: *High Temp. – High Pressures* 34 (2002) 253/263.
24. A Cezairliyan: *Compendium of Thermophysical Property Measurement Methods*, Vol. 2 Recommended Measurement Techniques and Practices, KD Maglic, A Cezairliyan and VE Peletsky (eds), Plenum, New York (1984) 483/517.
25. G Pottlacher, H Jager and T Neger: *High Temp. – High Pressures* 19 (1987) 19/27.
26. SV Lebedev, A Savvatimskii and Yu B Smirnov: *Sov. Phys. Tech. Phys.* 17 (1973) 1400.
27. U Seidel, W Fucke and H Wedle: *Die Bestimmung Thermophysiker Daten Flüssiger Hochschmelzender Metalle mit Schnellen Pulsaufheizexperimenten*. Peter Mannhold, Dusseldorf (1980).
28. D Basak, RA Overfelt and D Wang: *Intl J Thermophys* 24 (2003) 1721/1731.
29. KC Mills, L Courtney, RF Brooks and BJ Monaghan: *ISIJ Intl.* 40 (2000) S120/S129.
30. KC Mills and PD Lee: *Proc. 1st Intl. Symp. Microgravity Research and Applications in Physical Sciences and Biotechnology*, held Sorrento (2000) 555/564.
31. JO'M Bochris, JL White and JD MacKenzie: *Physico-chemical measurements at high temperatures*, London (1959).
32. R Rapp: *Physico-chemical measurements in metals research*, Interscience, New York (1970).
33. *Slag Atlas*, VDEh, Dusseldorf (1995).
34. AF Crawley: *Intl Metals Reviews* 19 (1974) 32.
35. JB Henderson, J Blumm and L Hageman: *Measurement of the properties of an Al-*

- Si casting alloy in solid and liquid regions*, Netzsch-Geratebau GmbH Rept TPS No1-4E (1996).
- 36. K Mukai, L Fang, Z Li and F Xiao: Measurement of the Density of Binary Ni-X (X=Co, W, Ta, Al) Alloys, *Materials Transactions* (2004) 45(5) 1754–1763.
 - 37. RF Brooks, AP Day, KC Mills and PN Quested: *Intl J Thermophys* 18 (1997) 471/480.
 - 38. M. Langen, T Hibiya, M Eguchi and I Egry: *J Crystal Growth* 186 (1998) 550.
 - 39. SJ Roach and H Henein: *Canad. Metall. Quart.* 42 (2003) 175/185.
 - 40. AP Froba and A Leipertz: *Proc (abstracts) of 16th Europ. Conf. on Thermophysical properties*, held London, September (2002) 59/60.
 - 41. Y Kobayashi, Y Nagasaka: *Proc (abstracts) of 16th Europ. Conf. on Thermophysical properties*, held London, September (2002) 103/104.
 - 42. N Kawasaki, K Watanabe and Y Nagasaka: *High Temp. – High Pressures* 30 (1998) 91.
 - 43. RF Brooks, AP Day, RJL Andon, LA Chapman, KC Mills and PN Quested: *High Temp. – High Pressure* 33 (2001) 73/82.
 - 44. T Ejima, Y Sato and T Yamamura: *Proc. 11th Japan Symp. on Thermophys. Properties*, held Kyoto (1990) Japan Thermophysical Soc. 291/294.
 - 45. DH Ferris and PN Quested: *Proc (abstracts) of 16th Europ. Conf. on Thermophysical properties*, held London, September (2002) 255/257.
 - 46. R Roscoe: *Proc. Phys. Soc.* 72 (1958) 576.
 - 47. DA Beckwith and GF Newell: *Theory of oscillation viscometers: the oscillating cup*, Part 2, ZAMP, Vol. VIII (1957) 450.
 - 48. Y Sato: *CAMP-ISIJ* 17 (2004) 154.
 - 49. PA Banerjee and RA Overfelt: *Intl J Thermophys.* 20 (1999) 1791/1800.
 - 50. I Egry, G Lohfer, I Seylam, A Schneider and B Feuerbacher: *Appl. Phys. Lett.* 73 (1998) 462.
 - 51. JF Paradis, Ichikawa and Yoda: *Intl J Thermophys.* 23(2) (2002) 825/842.
 - 52. R Wunderlich and HJ Fecht: *Thermolab Final Report to Europ. Space Agency*, MAP Contract AO-99-022 (2003).
 - 53. H. Fujii K Nogi: Paper presented at High Temp Capillarity Conf., held in San Remo (2004), to be published, *J Interface Sci.*
 - 54. WK Rhim and K Ohsaka: *J Crystal Growth* 208 (2000) 313, see also 257 (2003) 350/358.
 - 55. SJ Roach and H Henein: *Metall. Trans.* In press.
 - 56. JM Vignau, P Azou and P Bastein: *Comp. Rendus Acad. Sci.* 264 (1967) 174/177.
 - 57. Yuchu Su and KC Mills: unpublished work (2004).
 - 58. BJ Keene: *Intl Materials Review* 38 (1993) 157/ 192.
 - 59. Zushu Li, KC Mills, M McLean and K Mukai: *Met. Mater. Trans.*, submitted (2005).
 - 60. JP Garandet, B Vinet and P Gross: *J Coll. Interface Sci.* 165 (1994) 351/354.
 - 61. ME Fraser, WK Lu, AE Hamielec and R Murarka: *Metall. Trans.* 2 (1971) 817.
 - 62. I Egry: *J Mater. Sci* 26 (1991) 2997/3003.
 - 63. BJ Keene, KC Mills and RF Brooks: *Mater. Sci Technol.* 1 (1985) 568.
 - 64. JP Garandet: *Thermolab Final Report to Europ. Space Agency*, MAP Contract AO-99-022, R Wunderlich and HJ Fecht (eds) (2003).
 - 65. G Wille, F Millot and JC Riflet: *Intl J Thermophys.* 23 (2002) 1197/1206 and 1249/1257.

66. I Egry , G Lohofer and G Jacobs: *Proc. 4th Asian Thermophysical Properties Conf*, held Tokyo, September (1995).
67. D Cummings and D Blackburn: *J Fluid Mech.* 224 (1991) 395/416.
68. S. Sauerland, RF Brooks, I Egry and KC Mills: *Proc. TMS Annual conf. on Containerless Processing*, WH Hofmeister and R Schiffman (eds), TMS (1993) 65/69.
69. H Fujii, T Matsumoto and K Nogi: *Acta Mater.* 48 (2000) 2933/39.
70. R Minto and W G Davenport: *Trans. Inst. Min. Metall.* 81C (1972) C36.
71. S Feldbauer and AW Cramb: *Proc. 79th Steelmaking Conf.* (1996) 655.
72. SI Popel, OA Esin and PV Geld: *Dokl. Akad. Nauk SSSR* 74(6) (1950) 1097 see also *ibid.* 83(2) (1952) 253.
73. BJ Keene, *Slag Atlas*, VDEH, Dusseldorf (1995) 407/409.
74. JL Brettonet, LD Lucas and M Olette: *CR Hebd. Seances Acad. Sci. Ser. C* 285 (1977) 45.
75. P V Riboud and L D Lucas: *Can. Met. Quart.* 20 (1981) 199/208.
76. H Gaye, L D Lucas, M Olette and P V Riboud: *Can. Met. Quart.* 23 (1984) 179/191.
77. J Liggieri, F Ravera, M Ferrari, A Passerone and R Miller: *J Coll. Interface Sci.* 186 (1997) 46/52 and 40/46.
78. KD Maglic, A Cezairliyan and VE Peletsy, *Compendium of Thermophysical Property Measurement Methods*, Vol. 1 Survey of measurement methods: Vol. 2 Recommended measurement techniques and practices, Plenum Press, New York (1984).
79. HB Dong and JD Hunt: *Proc. 12th Intl Conf. Thermal Analysis*, held Copenhagen, August (2004).
80. KC Mills, BJ Monaghan, BJ Keene: *Intl Materials Reviews* 41 (1996) 209/242.
81. RA Overfelt et al.: *High Temp. – High Pressure* 34 (2002) 401/409.
82. R Gardon: *Proc. 2nd Intl Conf Thermal Conductivity*, held Ottawa (1962) 167.
83. M Susa, S Kubota, M Hayashi and KC Mills: *Ironmaking and Steelmaking* 28 (2001) 390/395.
84. M Gustavsson, H Nagai and T Okutani: *Proc. 15th Symp. on Thermophysical Properties*, held Boulder, CO June (2003).
85. K Hatori and H Ohta: *Materia Japan* 43 (2004) 129/135.
86. JA Balderas-Lopez: *Revista Mexicana de Fisic* 49 (2000) 353/357.
87. H Ohta, K Nakajima, M Masuda and Y Waseda: *Proc. 4th Intl Conf Molten Slags and Fluxes*, held Sendai (1992) ISIJ, Tokyo (1992) 421/426.
88. BJ Monaghan and PN Quested: *ISIJ Intl* 41 (2001) 1524.
89. H Szegawski and R Taylor: *High Temp. – High Pressures* 30 (1998) 343/350.
90. K Nagata, and KS Goto: *2nd Intl Conf. on Metallurgical slags and fluxes*, held Lake Tahoe, NV (1984) Metall. Soc. AIME, Warrendale, PA 863/873, see also *Trans. JIM* 29 (1988) 133/142.
91. K Takashi and H Fukuyama, *CAMP-ISIJ* 17 (2004) 156.
92. LP Filippov: *Intl J Heat Mass Transf.* 16 (1973) 865/885.
93. VY Zinov'yev, VE Polev, SG Taluts, GP Zinov'yeva and SA Il'inykh: *Phys. Met. Metallog.* 61(6) (1986) 85/92.
94. E Yamasue, M Susa, H Fukuyama and K Nagata: *J Cryst. Growth*, 234 (2002) 121/131.
95. H Ohta, H Shibata, T Emi and Y Waseda: *J Jap. Inst. Metals* 61 (1997) 350/357.

96. SG Teodorescu, RA Overfelt and SI Bakhtiyarov: *Intl J Thermophys.* 22 (2001) 1521/1535.
97. S Krishnan, GP Hansen, RH Hauge and JL Margrave: *High Temp. Sci.* 26 (1990) 143.
98. H Watanabe, M Susa, H Fukuyama and K Nagata: *Intl J Thermophys.* 24 (2003) 223/237.
99. C Cagran, C Brunner, A Seifert and G Pottlacher: *High Temp. – High Pressures* 34 (2002) 669/679.
100. M Susa and K Nagata: *Metall. Trans.* 23B (1992) 331/337.
101. RK Wunderlich and HJ Fecht: *Proc. Symp. on Research and Microgravity Conditions*, held Nordeney, Germany (1998).
102. FJ Grove and PE Jellyman: *J Soc. Glass Technol.* 39 (1955) 3/15T.
103. JR Aronson, IH Bellotti, SW Eckroad, AG Emslie, RK McConnell and PC van Thuna: *J Geophys. Res.* 75 (1970) 3443/3456.
104. A Jambon: *J Geophys. Res.* 87 (1982) 10797/10810.
105. KW Semkow, R Rizzo and LA Haskin and DJ Lindstrom: *Geochim. Cosmochim. Acta* 46 (1982) 1879/1889.
106. HA Walls (Chapter 9C) and TS Lundy (Chapter 9A) in *Physicochemical measurements in metals research*, RA Rapp (ed.), Interscience (1970).
107. AE Le Claire: *Diffusion and mass transport measurements in the characterisation of high temperature materials. Physical and elastic characteristics*, MA McLean (ed.), Inst. of Metals, London (1989) Chapter 5 139/176.
108. JB Edwards, EE Hucke and JJ Martin: *Metall. Rev.* 120 (1968) 13.
109. T Nagata, K Takeo and Y Nagasaka: *Proc. (abstracts) of 16th Europ. Conf. on Thermophysical properties*, held London, September (2002) 104/106.
110. N Ma and JS Walker: *Phys. Fluids* 9 (1997) 1182 and 2789.
111. Y Kawai and Y Shiraishi: *Handbook of Physico-chemical properties at high temperatures*, Special Issue 41, ISIJ, Tokyo (1988).
112. KC Mills: *Recommended values of thermophysical properties for commercial alloys*, Woodhead, Abington (2002).
113. PK Sung, DR Poirier and E McBride: *Mat. Sci and Eng.* A231 (1997) 189/1197.
114. B Vinet, L Magnusson, H Fredriksson and PJ Desre: *J Colloid and Interface Sci.* 255 (2002) 363/374.
115. KC Mills and BJ Keene: *Intl Metals Review* 1 (1981) 21/67.
116. L Battezzati and AL Greer: *Acta Met.* 37 (1981) 1791/1802.
117. A Dinsdale: SGTE data for pure elements, *CALPHAD* 15 (1991) 317/425.
118. JD Margrave: *Mater. Sci. Eng.* A178 (1994) 83/88.
119. YS Touloukian: *Thermophysical properties of high temperature solid materials*, Vol. 1 Elements, Macmillan, New York (1967).
120. YS Touloukian *et al.*: *Thermophysical properties of matter*, Volumes 1–12 , IFI/ Plenum (1970 onwards).
121. P Kubicek and T. Peprica: *Intl Metals Reviews* 28 (1983) 131/157.
122. Landolt Bornstein: *Physikalische Chemische Tabellen*, Springer (1991).
123. GW Kaye and TH Laby: *Tables of physical and chemical constants*, 15th edn, Longmans, London (1995).
124. PF Paradis, T Ishikawa and S Yoda: *J Mater. Sci.* 36 (2001) 5125/5130. See also PF Paradis, T Ishikawa and S Yoda: *Intl J Thermodyn.* 24 (2003) 1121/1136; PF Paradis and WK Rhim: *J Mater. Res.* 14 (1999) 3713/9.

125. J Robinson, AT Dinsdale, LA Chapman, PN Quested, BJ Monaghan, JA Gisby and KC Mills: *Proc. 2nd Intl Conf. of Science and Technology of Steelmaking*, held Swansea, April 2001, IOM, London, 149/160.
126. AI Priven: *Sov. J Glass Phys. Chem.* 14 (1988) 321.
127. KC Mills, AP Day and PN Quested: *Proc. of Nottingham Univ. – Osaka Univ. Joint Symp.*, held Nottingham, October (1995).
128. Y Bottinga and DF Weill: *Amer. J Sci.* 272 (1972) 438. See also *Geochim. Cosmochim. Acta* 46 (1982) 909.
129. A. Kondratiev: *Development of viscosity models for multiphase slag system*. PhD Thesis, Univ. of Queensland, Brisbane (2004).
130. SG Brush: *Chem. Reviews* 62 (1962) 513/548.
131. J Frenkel: *Z. Phys.* 35 (1926) 652/669.
132. J Frenkel: *Nature* 136 (1935) 167/168 and *Trans. Farad. Soc.* 33 (1937) 58/65.
133. HD Weymann: *Kolloid Z Polymer*. 138 (1954) 41/56 and 181 (1962) 131/137.
134. H Eyring: *J Chem. Phys.* 4 (1936) 283/291 and 5 (1937) 726/736.
135. R. Furth: *Sci. Prog.* 37 (1949) 202/218.
136. AK Doolittle: *J Appl. Phys.* 22 (1951) 1471/1475.
137. PV Riboud, Y Ropux, LD Lucas and H Gaye: *Fachber. Huttenprax. Metallweiterverarb.* 19 (1981) 859/869.
138. G Urbain: *Steel Res* 58 (1987) 11/116, see also *Trans. J Brit. Ceram. Soc.* 80 (1981) 139/141.
139. T Iida, H Sakai, Y Kita and K Murakami: *High Temp. Mater. Processes* 19 (2000) 153/164.
140. CL Senior and S Srinivasachar: *Energy and Fuels* 9 (1995) 277/283.
141. KC Mills and S Sridhar: *Ironmaking and Steelmaking* 26 (1999) 262/268.
142. VK Gupta, SP Sinha and B Raj: *Steel India* 21 (1998) 22/29, see also *Steel India* 17 (1994) 74/78.
143. K Koyama: *Nippon Steel Tech. Report* 34 (1987) 41.
144. JW Kim, J Choi, OD Kwon, IR Lee, YK Shin and JS Park: *Proc. 4th Intl Conf on Molten Slags and Fluxes*, held Sendai (1992) ISIJ, Tokyo 468/473.
145. TA Utigard and A Warczok: *Proc. Copper 95 Intl Conf.* (1995) vol. 4, Metall. Soc. of CIM 423/437.
146. RG Reddy, JY Yen and Z Zhang: *Proc. 5th Intl Conf. Molten Slags, Fluxes and Salts*, held Sydney (1997) ISS, Warrendale, PA 203/213, see also *High Temp. Sci.* 20 (1990) 195/202.
147. M Hayashi and S Seetharaman: *CAMP- ISIJ* 16 (2003) 860/863.
148. Ling Zhang and S Jahanshahi: *Metall. Trans. B* 29B (1998) 177/186 and 187/195.
149. T Tanaka, M Nakamoto, J Lee and T Usui: *Sci. Tech. Innovative Ironmaking, Aiming Energy Half Consumption*, held Tokyo, November (2003) 161/164. See also *CAMP-ISIJ* 16 (2003) 864/867.
150. A Kondratiev and E Jak: *Metall. Trans. B* 32B (2001) 1015/1025.
151. KC Mills, L Chapman, AB Fox and S Sridhar: *Scand. J Metall.* 30 (2002) 396/403.
152. T. Lakatos, LG Johansson, B Simmingskold: *Glass Technol.* 13 (1972) 88 and *Glasstekn. Tidstr.* 30 (1976) 7.
153. X Feng and A Barkatt: *Mat. Res. Soc. Symp. Proc.* 112 (1988) 543. See also X Feng, E Saad and IL Pegg: *Nuclear Waste Management III* 457.
154. Y Sasaki and K Ishii: *CAMP-ISIJ* 16 (2003) 867.
155. FY Yan, FJ Wood and KC Mills: *Proc. XVI Intl Glass Conf.*, held Madrid, October

- (1992) vol. 2 177/182.
156. M Hirai: *ISIJ Intl.* 33 (1993) 281/298.
 157. Du Sichen, J Bygden and S. Seetharaman: *Metall. Mater. Trans B* 25B (1990) 519.
 158. EA Moelwyn-Hughes: *Physical Chemistry*, Pergamon, Oxford (1961).
 159. RP Chhabra and DK Sheth: *Z. Metallkunde* 81 (1990) 264/271.
 160. M. Kucharski: *Z. Metallkunde* 77 (1986) 393/396 and 79 (1988) 264/266.
 161. RW Powell and RP Tye: *The Engineer* (1960) 729/732.
 162. JP Hajra, HK Lee and MG Frohberg: *Z. Metallkunde* 82 (1991) 603/608.
 163. HK Lee, JP Hajra and MG Frohberg: *Z. Metallkunde* 83 (1992) 638/643.
 164. JP Hajra, MG Frohberg and HK Lee: *Z. Metallkunde* 82 (1991) 718/720.
 165. WM Small, P Sahoo and K Li: *Scripta Met. et Mater.* 24 (1990) 1155/1158 and 645/649.
 166. T Tanaka and T Iida: *Steel Research* 1 (1994) 21/28.
 167. MS McNallan and T Debroy: *Metall. Trans. B* 22B (1991) 557/559.
 168. Yuchu Su, KC Mills and AT Dinsdale: paper presented at the *High Temp. Capillarity Conf.*, held San Remo, Italy (2004).
 169. LP Moisou and BP Burlyev: *Svar. Proizvodstvo* (1997) (June) 18/20.
 170. J Zhang, S Shu and S Wei: *Proc. of the 6th Intl Conf. Molten Slags, Fluxes and Salts*, held Stockholm, June (2000).
 171. AW Cramb and Jimbo: *Steel Research* 60 (1989) 157/165.
 172. ZY Qiao, LT Kang, ZM Cao and BY Yuan: *CAMP- ISIJ* 16 (2003) 868/871.
 173. M Susa, K Nagata and KC Mills: *Ironmaking and Steelmaking* 20 (1993) 372/378.
 174. M Susa, Y Kamijo, T Kimura and T Yagi: *CAMP- ISIJ* 16 (2003) 872.

4.10 Appendix A: calculation of structural parameters NBO/T and optical basicity

1. (NBO/T)

1. $y_{NB} = \Sigma 2[X_{CaO} + X_{MgO} + X_{FeO} + X_{MnO} + X_{CaO} + X_{Na_2O} + X_{K_2O} + 6(1-f)X_{Fe_2O_3} + -2X_{Al_2O_3} - 2Xf_{Fe_2O_3}]$
2. $X_T = \Sigma X_{SiO_2} + 2X_{Al_2O_3} + 2fX_{Fe_2O_3} + X_{TiO_2} + 2X_{P_2O_5}$
3. $NBO/T = y_{NB}/X_T$ where $f = Fe^{3+}(IV) / (Fe^{3+}(IV) + Fe^{3+}(VI))$

where $Fe^{3+}(IV)$ and $Fe^{3+}(VI)$ represent the fraction of Fe^{3+} in four- and sixfold coordination, respectively.

2. Optical basicity (Λ)

1. $\Lambda = (\Sigma(X_1n_1\Lambda_1 + X_2n_2\Lambda_2 + X_3n_3\Lambda_3 + \dots)) / \Sigma(X_1n_1 + X_2n_2 + X_3n_3 + \dots)$
where n = number of oxygens in oxide e.g. $n = 2$ for SiO_2 or 3 for Al_2O_3 .
2. Λ^{corr} is calculated by deducting the mole fraction of cation required to charge balance the Al^{3+} in the chain, this is usually deducted from the largest cation present, e.g. Ba^{2+} thus $X^{corr}_{BaO} = (X_{BaO} - X_{Al_2O_3})$.

The following values of optical basicity are recommended: $Al_2O_3 = 0.60$: $B_2O_3 = 0.42$: $BaO = 1.15$: $CaO = 1.0$: $FeO = 1.0$: $Fe_2O_3 = 0.75$: $K_2O = 1.4$; $Li_2O =$

1.0: MgO = 0.78: MnO = 1.0: Na₂O = 1.15: P₂O₅ = 0.40: SiO₂ = 0.48: SrO = 1.10: TiO₂ = 0.61: Various Λ values have been cited for CaF₂ 0.43, 0.67 but a value of 1.2 should be used for viscosity calculations.

4.11 Appendix B: notation

a	= Thermal diffusivity ($m^2 s^{-1}$)
C _p	= Heat capacity ($J K^{-1} kg^{-1}$)
D	= Diffusion coefficient ($m^2 s^{-1}$)
E	= Extinction coefficient (m^{-1})
e	= Thermal effusivity ($J s^{0.5} m^{-2} K^{-1}$)
f _s	= Fraction solid
(H _T – H ₂₉₈)	= Enthalpy relative to that at 298K ($J K^{-1} kg^{-1}$)
g	= Gravitational constant ($m s^{-2}$)
k	= Thermal conductivity ($W m^{-1} K^{-1}$)
M	= Molecular mass ($g mol^{-1}$)
N _A	= Avogadro number
R	= Electrical resistivity (Ωm)
R*	= Gas constant ($J K^{-1} mol^{-1}$)
T	= Temperature (K)
X	= Mole fraction
α	= Linear thermal expansion coefficient (K^{-1})
α^*	= Absorption coefficient (m^{-1})
β	= Volume thermal expansion coefficient (K^{-1})
$\Delta^{fus}H$	= Enthalpy of fusion ($J kg^{-1}$)
ϵ	= Emissivity
γ	= Surface tension ($m N m^{-1}$)
η	= Viscosity (Pas)
κ	= Electrical conductivity ($\Omega^{-1} m^{-1}$)
Λ	= Optical basicity
λ	= Wavelength (m)
ρ	= Density ($kg m^{-3}$)
ADL	= Aerodynamic levitation
DSC	= Differential scanning calorimetry
DTA	= Differential thermal analysis
EML	= Electro-magnetic levitation
ESL	= Electro-static levitation
mp	= Melting point (K)
NBO/T	= Number of non-bridging atoms/no. of tetragonal atoms
SLLS	= Surface laser light scattering
THW	= Transient hot wire
USL	= Ultrasonic levitation
WFL	= Wiedemann–Franz–Lorenz rule

- 0g = Micro-gravity measurements
1g = Terrestrial measurements

Subscripts

- c = Phonon conductivity
eff = effective
el = electronic
g = gas
l = liquid
lat = lattice
H = hemispherical
M = metal
N = normal
R = Radiation conductivity
S = slag
s = solid
T = total
R = Radiation conductivity
 λ = spectral

Superscript

- liq = liquidus
m = property value at melting point
sol = solidus
xs = excess

5.1 Introduction

Extraction and refining of metals involve the transfer of mass and heat within each phase and between the phases, one or more of which are in motion. For example, in blast furnace iron making, Fig. 5.1, iron oxide in the form of lumpy ore, sinter or pellet along with coke and limestone, are charged on the top of the furnace continuously. The charge slowly moves down and hot reducing gases produced by burning of coke in front of tuyeres move up through the bed of solids and finally escape through the gas outlet. The heat is transferred from hot gases to solid and at the same time the reducing gases reduce the oxides to metallic iron. At high temperature reduced iron melts and forms liquid metal and gangue in ore, coke ash and lime form the slag. The final product is molten iron containing dissolved carbon and other impurities like silicon, manganese, phosphorous and sulfur and liquid slag, which are tapped from the furnace.

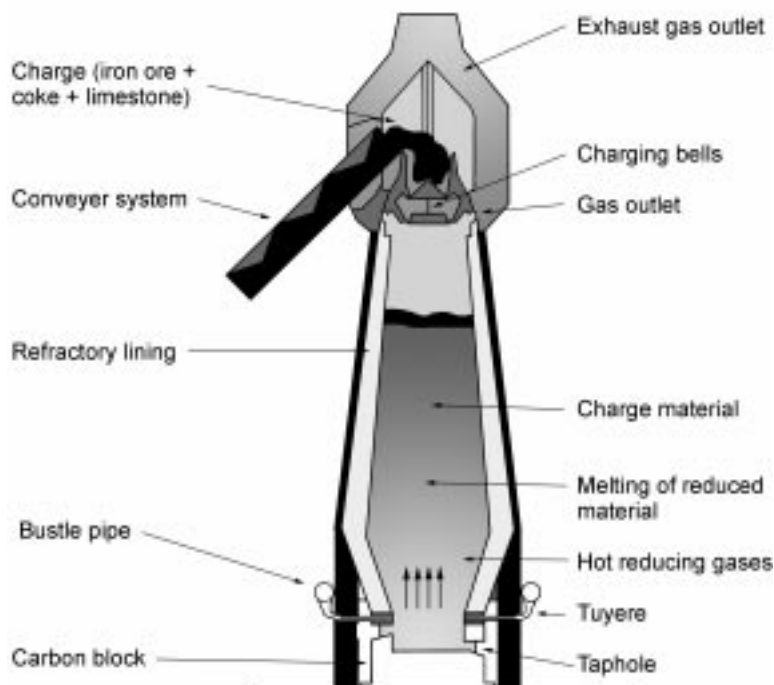
Other metallurgical operations like melting, alloying, casting, joining, heat treatment and metal deformation processes like forging, rolling, etc. also involve heat, mass and momentum transfer. So transport phenomena play a key role in all metallurgical operations.

The present chapter deals with the fundamentals of transport phenomena within a phase and between phases.

5.2 Mass transfer

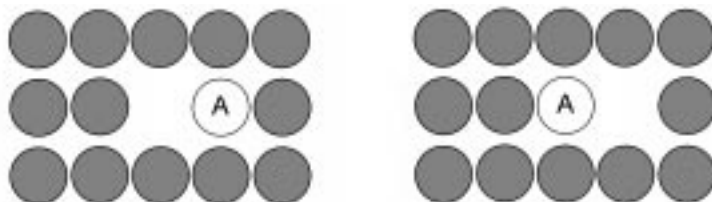
Transfer of a species from one location to another in a mixture of non-uniform composition is known as mass transfer. When a homogeneous solution flows, the species present in the solution moves from one location to another but there is no mass transfer since concentration of species is the same everywhere. So a concentration difference is an essential requirement for mass transfer.

Mass transfer takes place because of molecular motion and bulk flow. Atoms in fluids are in random motion and this causes transfer of a species from one place to another. However this could be noticed only when mixture is not



5.1 Schematic representation of blast furnace.

homogeneous or few radio active atoms are present in the system. The movement of atoms in fluid is easy because the positions of atoms are not rigid. But in solids, atoms move from one lattice site to another by exchanging their position with a neighbouring vacancy, Fig. 5.2. So the movement of atoms in solids is accompanied by movement of the vacancy in the opposite direction. Other mechanisms of movement of atoms are also possible but the vacancy mechanism is most predominant for substitutional solid solutions.



5.2 Diffusion in solid. Atom marked A jumps into vacancy and vacancy moves from left to right.

5.2.1 Mass flux

Figure 5.3(a) shows two non-reacting species A and B which are in contact with each other. The left side has species A and right side has B. Since the concentration of species A and B are not uniform throughout the system, atoms of A and B move in opposite directions. This leads to the decrease of concentration of A in the left side and corresponding increase of the concentration of A in the right side as shown in Fig. 5.3(b). The reverse is the case for concentration profile of B. The process continues till it attains the steady state when concentrations do not change with time. At steady state, the concentration of A becomes the same everywhere, Fig. 5.3(c). Let v_A and v_B be the velocities of A and B respectively. The flux of A, defined as the amount of A crossing the unit area per unit time in a direction normal to the area is

$$N_{Ax} = v_A \cdot C_A \quad (5.1)$$

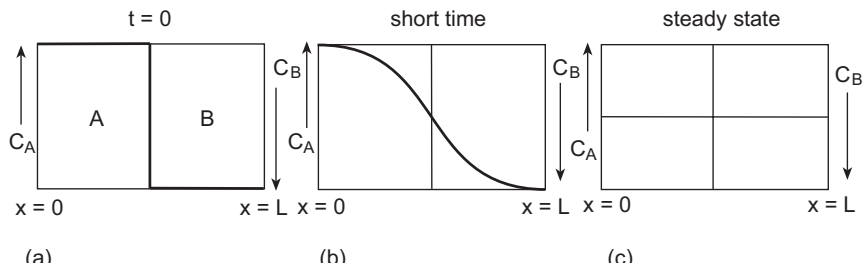
where N_{Ax} is the molar flux of A in x direction and C_A is the molar concentration of A. Equation 5.1 can be written as

$$N_{Ax} = C_A(v_A - v^{av}) + C_A \cdot v^{av} \quad (5.2)$$

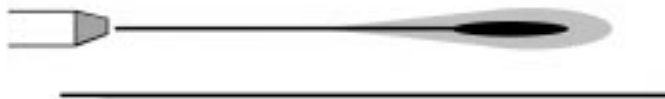
where v^{av} is the average velocity and $(v_A - v^{av})$ is the velocity of A with respect to average velocity. So the first term on the right-hand side measures flux due to molecular motion with respect to average velocity and the second term is the flux due to bulk flow. The flux due to molecular motion with respect to average velocity, J_{Ax} , is given by Fick's law of diffusion as

$$J_{Ax} = C_A(v_A - v^{av}) = -D_{AB} \frac{dC_A}{dx} \quad (5.3)$$

where D_{AB} is the diffusivity of A in A-B. The negative sign in Fick's law shows that the flux is in the direction of decreasing concentration. Fick's law of diffusion gives the flux with respect to average velocity of all the species or with respect to a moving coordinate that moves with velocity v^{av} . Combining equations 5.2 and 5.3,



5.3 Schematic representation of diffusion of two species A and B. (a) Before diffusion. (b) Concentration profiles of A and B after a short time. (c) Steady state concentration profile.



5.4 Diffusion of dye in water flowing through a tube.

$$N_{Ax} = -D_{AB} \frac{dC_A}{dx} + C_A v^{av} \quad (5.4)$$

To understand the physical meaning of the diffusion and bulk flow term in equation 5.4, let us perform a simple experiment. We take a long horizontal glass tube and allow water to flow through it at a very low flow rate and inject some dye along the axis of the tube. If we follow the tip of the dye as it moves through the tube, we will find that a faintly coloured zone just ahead of the deep coloured streak, Fig. 5.4. The velocity of the tip of the streak is v^{av} and the spread of the colour beyond the tip is due to molecular diffusion.

By definition, the average velocity v^{av} is

$$v^{av} = (C_A \cdot v_A + C_B \cdot v_B) / (C_A + C_B) \quad (5.5)$$

Using equation 5.1, equation 5.5 becomes

$$v^{av} = (N_{Ax} + N_{Bx}) / (C_A + C_B) \quad (5.6)$$

Combining equations 5.4 and 5.6

$$N_{Ax} = -D_{AB} \frac{dC_A}{dx} + x_A (N_{Ax} + N_{Bx}) \quad (5.7)$$

where x_A is the mole fraction of A. Definition of average velocity v^{av} , indicates that bulk flow term can be due to molecular motion or external force or both. In solids, and stagnant fluid, there is no bulk flow due to external forces, but the diffusion of atoms and molecules itself lead to bulk flow. In these cases equation 5.7 is the appropriate form of the flux equation. When the bulk flow is primarily due to external forces as in case of Fig. 5.4, the molecular contribution in the bulk flow can be neglected and equation 5.4 is the appropriate form of the equation. The average velocity v^{av} in this case is determined by external forces and is obtained by solving fluid flow problem. Equations 5.1–5.7 have been written in terms of molar fluxes, molar concentration, and mole fraction, but these are valid when the word mole is replaced by mass, i.e. mass flux, mass concentration and mass fraction.

In the three-dimensional case, the flux of A is given by

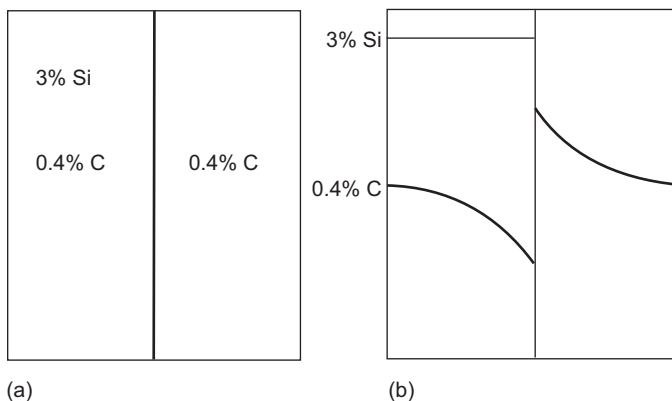
$$\mathbf{N}_A = -D_{AB} \nabla C_A + x_A (\mathbf{N}_A + \mathbf{N}_B) \quad (5.8)$$

Bold letters indicate vectors. The first term on the right-hand side of equation 5.8 is the pure diffusion flux \mathbf{J}_A given by Fick's law and second term is the flux due to bulk flow. The components of the molar fluxes due to molecular motion, \mathbf{J}_A , in different coordinates are given in Table 5.1.

Table 5.1 Components of flux due to binary diffusion

Rectangular	Cylindrical	Spherical
$J_x = -D_{AB} \frac{\partial C_A}{\partial x}$ (A)	$J_{Ar} = -D_{AB} \frac{\partial C_A}{\partial r}$ (D)	$J_{Ar} = -D_{AB} \frac{\partial C_A}{\partial r}$ (G)
$J_y = -D_{AB} \frac{\partial C_A}{\partial y}$ (B)	$J_{A\theta} = -\frac{D_{AB}}{r} \frac{\partial C_A}{\partial \theta}$ (E)	$J_{A\theta} = -\frac{D_{AB}}{r} \frac{\partial C_A}{\partial \theta}$ (H)
$J_z = -D_{AB} \frac{\partial C_A}{\partial z}$ (C)	$J_z = -D_{AB} \frac{\partial C_A}{\partial z}$ (F)	$J_{A\phi} = -\frac{D_{AB}}{r \sin \theta} \frac{\partial C_A}{\partial \phi}$ (I)

According to Fick's law driving force for diffusion is concentration gradient and diffusion takes place only from higher concentration to lower concentration. Darken (1949) found that when two steel bars containing the same carbon but one having silicon are welded together, carbon diffused from the bar containing silicon to the other side. Finally the bar that is free from silicon became richer in carbon than the other one. This is known as uphill diffusion. Figure 5.5 schematically shows the uphill diffusion. According to Fick's law, no diffusion of carbon should take place since carbon concentration in both the bars was initially the same. Darken's experiment clearly demonstrated that the activity gradient is the driving force for diffusion and not the concentration gradient. Silicon increases the activity of carbon and is a driving force for diffusion of carbon from the bar containing silicon to the other bar and the diffusion continues until the activity of the carbon becomes the same in both bars. However, for all usual analysis, Fick's law is used and the activity concept is invoked only to explain the anomaly.



5.5 Schematic diagram of uphill diffusion of carbon. (a) Before diffusion. (b) After diffusion.

Relation between fluxes

Equation 5.7 for N_{Ax} , contains two unknowns N_{Ax} and N_{Bx} , but in fluids a similar equation for N_{Bx} is not an independent equation (see Example 5.2, page 185). Therefore to obtain N_{Ax} , the relationship between the N_{Ax} and N_{Bx} must be known from other physical considerations or laws.

(1) Graham's Law

The ratio of diffusion fluxes in gases are inversely related to the square root of molecular weight or

$$N_{Ax}/N_{Bx} = (M_B/M_A)^{1/2} \quad (5.9)$$

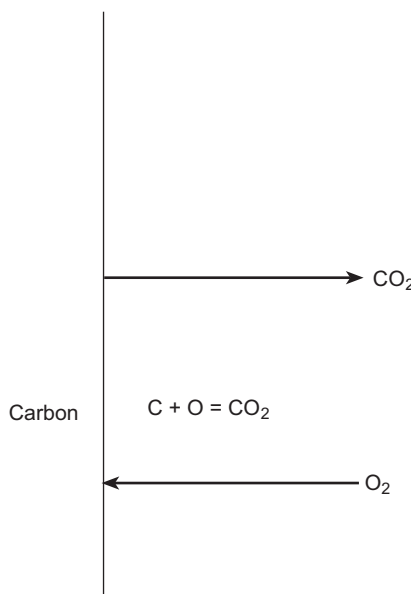
This equation applies to effusion of gases in a vacuum and equal pressure counter diffusion.

(2) Chemical reaction

Let us consider that oxygen is reacting with carbon according to the reaction



Figure 5.6 shows schematically the fluxes on the surface of the carbon block. Oxygen diffuses at the carbon–gas interface for reaction and carbon dioxide



5.6 C-O reaction on the surface of carbon.

formed diffuses away from the reaction interface. Since one molecule of oxygen forms one molecule of CO_2

$$N_{\text{O}_2,x} = -N_{\text{CO}_2,x} \quad (5.11)$$

The above condition indicates that per unit time the number of molecules of oxygen going in one direction is equal to number of molecules of CO_2 going in the opposite direction. This type of diffusion is termed as equimolar counter diffusion.

In the previous case one mole of reactant gas formed one mole of product gas. Let us consider, carbon reacts with oxygen to form CO



If one mole of O_2 comes to the surface of carbon and reacts with it, two moles of CO is produced and go out in the opposite direction. Or the flux of CO is two times that of O_2 and the relationship between the fluxes is

$$N_{\text{O}_2,x} = -\frac{1}{2}N_{\text{CO},x} \quad (5.13)$$

For a reaction of the following type



the fluxes are related by

$$N_{\text{Ax}} = -(n/m) N_{\text{Bx}} \quad (5.15)$$

(3) Flux of inert species

Let us consider that C- O_2 reaction, equations 5.10 or 5.12, takes place in air. Obviously nitrogen present in air will not take part in the reaction so the flux of nitrogen will be zero. In other words, flux of an inert species is always zero.

(4) Dilute solution

If the concentration of the diffusing species A is very small (x_A is very small), the bulk flow term can be neglected since its contribution is very small. In dilute liquid and solid solutions the bulk flow term is neglected.

Example 5.1

Show that for a binary mixture of gases diffusivity of A is same as that of B.

Solution

Let D_{AB} and D_{BA} be the diffusivities of A and B respectively in the mixture. Let us consider that A and B shown in Fig. 5.3 are two gases and the system is isothermal and isobaric. So $(C_A + C_B)$ is constant, or

$$\frac{\partial C_A}{\partial x} + \frac{\partial C_B}{\partial x} = 0 \quad (a)$$

From equation 5.7

$$N_{Ax} = -D_{AB} \frac{\partial C_A}{\partial x} + x_A(N_A + N_B) \quad (b)$$

$$N_{Bx} = -D_{BA} \frac{\partial C_B}{\partial x} + x_B(N_A + N_B) \quad (c)$$

Since $x_A + x_B = 1$, adding equations (b) and (c)

$$D_{AB} \frac{\partial C_A}{\partial x} + D_{BA} \frac{\partial C_B}{\partial x} = 0 \quad (d)$$

From equations (a) and (d) $D_{AB} = D_{BA}$



In the case of diffusion in binary substitutional solid solution, there are three fluxes, that of A, B and vacancies so the above derivation is not applicable. Although concentration of vacancy is very small, the flux is not small. It can be shown that $J_{vx} + J_{Ax} + J_{Bx} = 0$.

Example 5.2

Show that the following two equations are not independent for diffusion in fluids.

$$N_{Ax} = -D_{AB} \frac{dC_A}{dx} + x_A(N_{Ax} + N_{Bx}) \quad (5.7)$$

$$N_{Ax} = -D_{AB} \frac{dC_B}{dx} + x_A(N_{Ax} + N_{Bx}) \quad (5.7a)$$

Solution

Let

$$C_A + C_B = C \quad (a)$$

where C is the total concentration, a constant. Substituting the value of C_A from equation (a) in equation 5.7

$$N_{Ax} = -D_{AB} \frac{d(C - C_B)}{dx} + \frac{C - C_B}{C_A + C_B} (N_{Ax} + N_{Bx}) \quad (b)$$

$$= D_{AB} \frac{dC_B}{dx} - \frac{C_B}{C_A + C_B} (N_{Ax} + N_{Bx}) + N_{Ax} + N_{Bx} \quad (c)$$

Rearranging

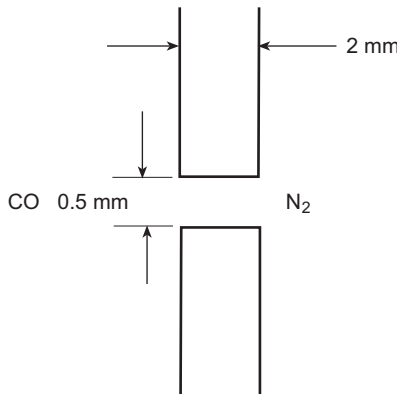
$$N_{Bx} = -D_{AB} \frac{dC_B}{dx} + x_B(N_{Ax} + N_{Bx}) \quad (5.7a)$$

Hence equations 5.7 and 5.7a are not independent equations.



Example 5.3

Carbon monoxide and nitrogen at 2 atm pressure and 300K are separated by a wall of 2 mm thickness, Fig. 5.7. The separating wall has a small hole of 0.5 mm. Calculate the maximum leakage rate of carbon monoxide and nitrogen. The profile of oxygen and nitrogen can be assumed to be linear in the hole. At 300K and 2 atm pressure $D_{CO-N_2} = 1.03 \times 10^{-5} \text{ m}^2/\text{s}$.



5.7 Leakage of CO through a hole.

Solution

The diffusion of N_2 and CO are in opposite directions so it is counter diffusion. Furthermore, the pressure and concentration of gases are the same and the flow of gas inside the hole is only due to molecular motion. So the ratio of fluxes can be calculated by Graham's law, equation 5.9. Since the molecular weights of both CO and N_2 are same, the ratio of molar fluxes is unity. Or $N_{N_2} = -N_{CO}$. So equation 5.7 reduces to

$$N_{N_2} = -D_{CO-N_2} \frac{dC_{N_2}}{dx} \quad (a)$$

The concentration of N_2 in nitrogen side $= P/RT = 2/(0.082300) = 0.081 \text{ kmol.m}^{-3}$. Leakage rate is maximum when concentration of nitrogen on CO side is zero. Since concentration profile is linear, $dC_{N_2}/dx = (C_{N_2}|x - C_{N_2}|0)/x$. Taking the face on the nitrogen side as $x = 0$,

$$\begin{aligned} N_{N_2} &= -1.03 \times 10^{-5} [(0 - 0.081)/(2 \times 10^{-3})] \\ &= 4.17 \times 10^{-4} \text{ kmol.m}^{-2}\text{s}^{-1} \end{aligned}$$

So the leakage rate of nitrogen

$$\begin{aligned} &= N_{N_2} \times \text{area of the hole} = 4.17 \times 10^{-4} \times \pi \times (0.5 \times 10^{-3}/2)^2 \\ &= 8.19 \times 10^{-11} \text{ kmole.s}^{-1} \end{aligned}$$

The leakage rate of carbon monoxide will be the same. ■■■

5.2.2 Diffusivity of gas, liquid and solid

Evaluation of fluxes requires the knowledge of diffusivities. Over the years, considerable efforts have been made to calculate these values based on first principles. But the success has been rather limited. So the primary source of diffusivity is the measured values. However, in the absence of experimentally measured values, empirical and semi-empirical co-relations are used to calculate these.

Diffusivity of gases

According to the kinetic theory of gases, diffusivity of gases are proportional, $T^{1.5}/p$ where T is temperature and p is pressure. This pressure dependence is valid for less than 10 atmospheres but the exponents of temperature for real gases are higher. Chapman–Enskog equation gives a good estimation of binary diffusivity of gases. For details see Reid *et al.* (1977). Fuller, Schettler and Giddings (1966) proposed the following empirical relationship:

$$D_{AB} = \frac{10^{-7} T^{1.75} [1/M_A + 1/M_B]^{1/2}}{p[(V_A)^{1/3} + (V_B)^{1/3}]^2} \quad (5.16)$$

where D_{AB} is in m^2/s , temperature T is in K and p is pressure in atmospheres. V_A and V_B are diffusion volumes of A and B respectively. Diffusion volumes of simple molecules are given in Table 5.2. The above equation predicts diffusivity within 10% in most of the cases. Diffusivity of gas phases is usually in the range of 10^{-5} to $10^{-3} \text{ m}^2/\text{s}$.

Diffusivity through porous solid

Porous solid consists of a number of interconnecting pores (Fig. 5.8). If we take unit area on the surface of the solid, the diffusion takes place only through the area occupied by the pores. Again, gas cannot move in a straight line in the porous solid. It takes a tortuous path. To take into account these two special features of porous solid, diffusivity of gas in porous solid is defined as effective diffusivity

Table 5.2 Diffusion volumes for simple molecules (Fuller *et al.* 1966)

Gas	V_A	Gas	V_A	Gas	V_A
H_2	7.07	Ne	5.59	NH_3	14.9
He	2.88	Ar	16.1	H_2O	12.7
N_2	17.9	CO	18.9	Cl_2	37.7
O_2	16.6	CO_2	26.9	Br_2	67.2
Air	20.1	N_2O	35.9	SO_2	41.1



5.8 Schematic diagram of a porous solid.

$$D_{\text{eff}} = \epsilon D_{AB} / \tau \quad (5.17)$$

where ϵ is porosity of solid and τ is the tortuosity factor. τ measures the ratio of actual path travelled by gas to geometrical diffusion distance.

When gases diffuse through pores it diffuses either by ordinary gas diffusion or Knudsen diffusion or a combination of both. When the pore diameter is much larger than the mean free path, diffusion is ordinary gas diffusion. But if the pore size is smaller than the mean free path, then gas molecules have a higher probability of collision with the pore wall than with each other. Gas flow under this condition is known as Knudsen diffusion. Knudsen diffusion coefficient for diffusion through a cylindrical pore is

$$D_K = 97 r (T/M)^{1/2} \text{ m}^2/\text{s} \quad (5.18)$$

where r is the radius of pore in m, T is the temperature in K and M is the molecular weight. In general, pores are not cylindrical so a correction of tortuosity is required for Knudsen diffusion. Since in porous solid, nature of diffusion depends on the size of pores, effective diffusivity of porous solid is often taken as

$$1/D'_{\text{eff}} = 1/D_{AB} + 1/D_K \quad (5.19)$$

$$D_{\text{eff}} = D'_{\text{eff}} \cdot \epsilon / \tau \quad (5.20)$$

Example 5.4

Find out the pore diameter where molecular and Knudsen diffusivity are comparable for diffusion of H₂-H₂O mixture through a porous solid at 1000K and 1 atm pressure.

Solution

We use equation 5.16, to calculate molecular diffusivity of H₂-H₂O. From Table 5.2, V_{H₂} = 7.07 and V_{H₂O} = 12.7 and molecular weights of H₂ and H₂O are 2 and 18 respectively. Substituting in equation 5.16

$$D_{H_2-H_2O} = \frac{10^{-7}(1000)^{1.75}[1/2 + 1/18]^{1/2}}{[7.07^{1/3} + 12.7^{1/3}]^2} = 7.3 \times 10^{-4} \text{ m}^2/\text{s} \quad (\text{a})$$

Equation 5.18 shows that Knudsen diffusivity of H₂ is greater than that of H₂O. So we should compare the molecular diffusivity of H₂-H₂O mixture with Knudsen diffusivity of H₂O. Knudsen diffusivity of H₂O is

$$D_{H_2O} = 97 r (1000/18)^{1/2} = 723 r \text{ m}^2/\text{s} \quad (\text{b})$$

Both the diffusivities will be same if the pore radius r is

$$r + 7.3 \cdot 10^{-4}/723 = 1.01 \times 10^{-6} \text{ m}$$

So if pore radius is about 1 μm , the contribution of both Knudsen and molecular diffusion will be almost same. If the pore radius is 10 μm , equation 5.19 indicates that the contribution of Knudsen diffusion will be only about 10% of total diffusion. On the other hand, if pore radius is 0.1 μm , the contribution of molecular diffusion will be only 10%. ■■■

Diffusion in liquids

The experimentally measured values of diffusivity are often expressed in the form of the Arrhenius equation

$$D = D_0 \exp(-Q/RT) \quad (5.21)$$

D₀ is the frequency factor, Q is the activation energy for diffusion and R is gas constant. The value of Q for metallic system is mostly less than 16 kJ mol⁻¹. Table 5.3 shows the diffusivity of different solutes in liquid iron at 1873K.

Table 5.3 Diffusivity of solutes in liquid iron at 1873K (Morita 1996)

Solute	C	Si	Mn	S	O	H
Diffusivity $\times 10^9 \text{ m}^2/\text{s}$	4–20	2.5–12	3.5–20	4.5–20	2.5–20	80–200
Solute	N	Ni	Cr	V	Mo	
Diffusivity $\times 10^9 \text{ m}^2/\text{s}$	6–20	4.5–5.6	3–5	4–5	3.8–4.1	

Because of difficulties in measurement at high temperature, uncertainty in measured values is often large. Note that diffusivities of different solutes except hydrogen in liquid iron are of the same order of magnitude irrespective of size of atoms. These values compare quite well with diffusivity of CO_2 in water, $1.9 \times 10^{-9} \text{ m}^2/\text{s}$ at 298K.

Diffusion in solids

In solid solutions we define both intrinsic and inter or mutual diffusivities. The intrinsic diffusivity of an element is the diffusivity of that element in the solution. In a mixture of gases, intrinsic diffusivities of A and B in A-B is denoted by D_{AB} and D_{BA} respectively, but for solids these are denoted by D_A and D_B respectively. In a gas mixture, $D_{AB} = D_{BA}$ (see Example 5.1 on pages 184–5) but in a solid (in general), $D_A \neq D_B$. Inter or mutual diffusivity in solid is the diffusivity of A in B or vice versa and is denoted by D_{AB} . For example, in Cu-Zn alloy, intrinsic diffusivities of Cu and Zn are denoted by D_{Cu} and D_{Zn} respectively and inter or mutual diffusivity by D_{CuZn} . Inter and intrinsic diffusivities are related by

$$D_{AB} = x_B D_A + x_A D_B \quad (5.22)$$

x_A and x_B are mole fractions of A and B in the solution.

Diffusivity in solids follow the Arrhenius equation 5.21 and activation energy of diffusion is quite large. Table 5.4 gives diffusivity of different solutes in iron. It shows that both activation energy for diffusion and diffusivity are strongly related to size of atoms.

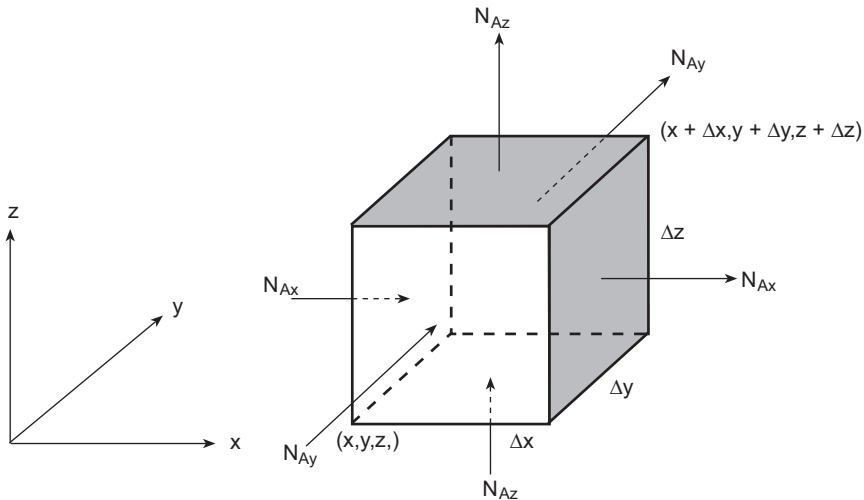
5.2.3 Conservation of mass

Let us consider an elemental volume $\Delta x \Delta y \Delta z$ as shown in Fig. 5.9. Since the mass is conserved, the balance equation is

$$\begin{aligned} &\text{Rate of accumulation of species A in } \Delta x \Delta y \Delta z = \\ &\text{Rate in} - \text{Rate out} + \text{Rate of generation of A} \\ &\text{in } \Delta x \Delta y \Delta z \text{ volume by reaction} \end{aligned}$$

Table 5.4 Diffusivity of solutes in γ iron (Kucera and Stransky 1982)

Diffusing elements	$D_0 \times 10^7 \text{ m}^2 \cdot \text{s}^{-1}$	$Q \text{ kJ mol}^{-1}$	$D \text{ at } 1200\text{K } \text{m}^2 \cdot \text{s}^{-1}$
Hydrogen	8.1	43.2	1.07×10^{-8}
Boron	2.0	87.92	2.98×10^{-11}
Carbon	738	158.98	8.86×10^{-12}
Nitrogen	480	159.1	5.70×10^{-12}
Chromium	4080	286.8	1.34×10^{-16}
Nickel	1090	296.8	1.31×10^{-17}



5.9 Mass balance in a control volume.

In this case there are six faces. Mass flux enters through three faces and goes out through the opposite three faces. N_{Ax} enters at x through the face of area $\Delta y \Delta z$ and goes out through the face at $x + \Delta x$. Similarly, N_{Az} enters at z through the face of area $\Delta x \Delta y$ and goes out at $z + \Delta z$ and N_{Ay} enters at y through the face of area $\Delta x \Delta z$ and goes out at $y + \Delta y$. Hence mass balance equation can be written as

$$\begin{aligned} \frac{\partial(\Delta x \Delta y \Delta z C_A)}{\partial t} = & (\Delta y \Delta z N_{Ax} |_x - \Delta y \Delta z N_{Ax} |_{x+\Delta x}) \\ & + (\Delta x \Delta z N_{Ay} |_y - \Delta x \Delta z N_{Ay} |_{y+\Delta y}) \\ & + (\Delta x \Delta y N_{Az} |_z - \Delta x \Delta y N_{Az} |_{z+\Delta z}) \\ & + \Delta x \Delta y \Delta z R_A \end{aligned} \quad (5.23)$$

where R_A is the rate of generation of A per unit volume by reaction.

Dividing throughout by $\Delta x \Delta y \Delta z$ and taking the limit $\Delta x \rightarrow 0$, $\Delta y \rightarrow 0$, $\Delta z \rightarrow 0$,

$$\frac{\partial C_A}{\partial t} = -\frac{\partial N_{Ax}}{\partial x} - \frac{\partial N_{Ay}}{\partial y} - \frac{\partial N_{Az}}{\partial z} + R_A \quad (5.24)$$

Equation 5.24 is the general mass balance equation of a species in rectangular coordinate. Table 5.5 gives the equation in different coordinate systems. These differential equations along with appropriate boundary conditions are solved to find out the concentration profiles and fluxes in a system. If we are interested in finding out the concentration profile in a cylinder or a system having cylindrical symmetry we use equation B of Table 5.5. Equation C of Table 5.5 is used for

Table 5.5 Equation of continuity of A in different coordinate systems

Rectangular coordinates

$$\frac{\partial C_A}{\partial t} + \frac{\partial N_{Ax}}{\partial x} + \frac{\partial N_{Ay}}{\partial y} + \frac{\partial N_{Az}}{\partial z} = R_A \quad [A]$$

Cylindrical coordinates

$$\frac{\partial C_A}{\partial t} + \frac{1}{r} \frac{\partial}{\partial r} (r N_{Ar}) + \frac{1}{r} \frac{\partial N_{Az}}{\partial \theta} + \frac{\partial N_{Az}}{\partial z} = R_A \quad [B]$$

Spherical coordinates

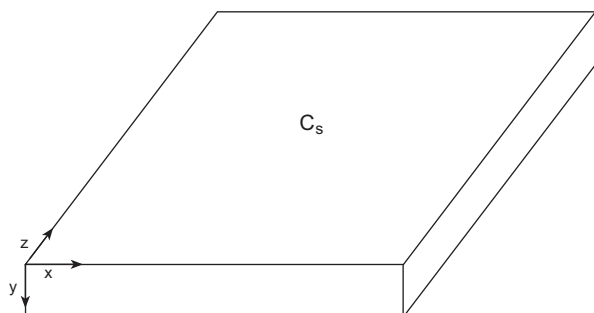
$$\frac{\partial C_A}{\partial t} + \frac{1}{r^2} \frac{\partial}{\partial r} (r^2 N_{Ar}) + \frac{1}{r \sin \theta} \frac{\partial}{\partial \theta} (N_{A\theta} \sin \theta) + \frac{1}{r \sin \theta} \frac{\partial N_{A\phi}}{\partial \phi} = R_A \quad [C]$$

concentration profiles in a sphere. Although any problem can be solved in a rectangular coordinate system, appropriate choice of coordinate system makes the final equation simpler.

Diffusion in solid

Let us consider carburizing of steel as an application of diffusion in solid. A steel plate containing uniform carbon concentration, C_0 , is exposed in a carburizing gas atmosphere. The carburizing atmosphere maintains carbon concentration on the top surface of plate at C_s , Fig. 5.10. We want to find out the carbon concentration profile in the plate.

Carbon diffuses from the top to the interior of the plate in y direction. So concentration gradient of carbon in x and z directions is zero. Furthermore, carbon does not take part in any reaction in the steel plate, so $R_A = 0$. Thereby, the problem involves diffusion of carbon only in y direction and equation 5.24 simplifies to



5.10 Carburizing of steel.

$$\frac{\partial C_C}{\partial t} = - \frac{\partial N_{Cy}}{\partial y} \quad (5.25)$$

where C_C is the concentration of carbon and N_{Cy} is the carbon flux in steel in y direction. Since concentration of carbon in steel is small, we neglect the bulk flow term in the definition of flux given by equation 5.7 and simplify it as

$$N_{Cy} = -D_C \frac{\partial C}{\partial y} \quad (5.26)$$

where D_C is intrinsic diffusivity of carbon in steel.

Substituting equation 5.26 in equation 5.25 and assuming that diffusivity of carbon is constant

$$\frac{\partial C_C}{\partial t} = D_C \frac{\partial^2 C_C}{\partial y^2} \quad (5.27)$$

Equation 5.27 is known as Fick's second law. The initial and boundary conditions are

$$\text{At } t = 0, \quad y > 0, \quad C_C = C_0 \quad (5.28a)$$

$$\text{At } t \geq 0, \quad y = 0, \quad C_C = C_s \quad (5.28b)$$

Normally, the thickness of carburized layer is a fraction of a millimetre only and carbon concentration far away from the top surface remains at C_0 . Thereby, although the plate is of finite thickness, it can be considered as infinity and another boundary condition can be written as

$$\text{At } t > 0, \quad y = \infty, \quad C_C = C_0 \quad (5.28c)$$

To solve equation 5.27 along with equations 5.28a, b and c, we define two new variables

$$\eta = y/2(D_C t)^{1/2} \quad (5.29)$$

$$p = \frac{dC_C}{d\eta} \quad (5.30)$$

We know,

$$\frac{\partial C_C}{\partial t} = \frac{\partial C_C}{\partial \eta} \frac{\partial \eta}{\partial t} = - \frac{y}{4t(D_C t)^{1/2}} \frac{\partial C_C}{\partial \eta} = - \frac{\eta}{2t} \frac{\partial C_C}{\partial \eta^2}$$

$$\frac{\partial C_C}{\partial y} = \frac{1}{2(D_C t)^{1/2}} \frac{\partial C_C}{\partial \eta} \quad \text{and} \quad \frac{\partial^2 C_C}{\partial y^2} = \frac{1}{4D_C t} \frac{\partial^2 C_C}{\partial \eta^2}$$

Using the above relationships and equation 5.30, equation 5.27 can be written as

$$-2\eta p = \frac{dp}{d\eta} \quad (5.31)$$

The variable η given by equation 5.29 has converted the partial differential equation into an ordinary differential equation. This transformation, which reduces the number of independent variables, is known as the similarity transform. The boundary conditions given by equations 5.28 become

$$\text{At } \eta = 0, \quad C_C = C_S \quad (5.32\text{a})$$

$$\text{At } \eta = \infty, \quad C_C = C_0 \quad (5.32\text{b})$$

Integrating equation 5.31,

$$p = A \exp(-\eta^2)$$

where A is a constant. Substituting p from equation 5.30

$$\frac{dC_C}{d\eta} = A \exp(-\eta^2)$$

Integrating in the limit $\eta = 0$ to η and using the boundary condition equation 5.32a,

$$C_C - C_S = A \int_0^\eta \exp(-\eta^2) d\eta \quad (5.33)$$

Using the boundary condition equation 5.32b

$$C_0 - C_S = A \int_0^\infty \exp(-\eta^2) d\eta = A \frac{\sqrt{\pi}}{2}$$

Or,

$$A = 2(C_0 - C_S)/\sqrt{\pi}$$

Hence equation 5.33 becomes

$$(C_C - C_S) = (C_0 - C_S) \operatorname{erf}(\eta) \quad (5.34)$$

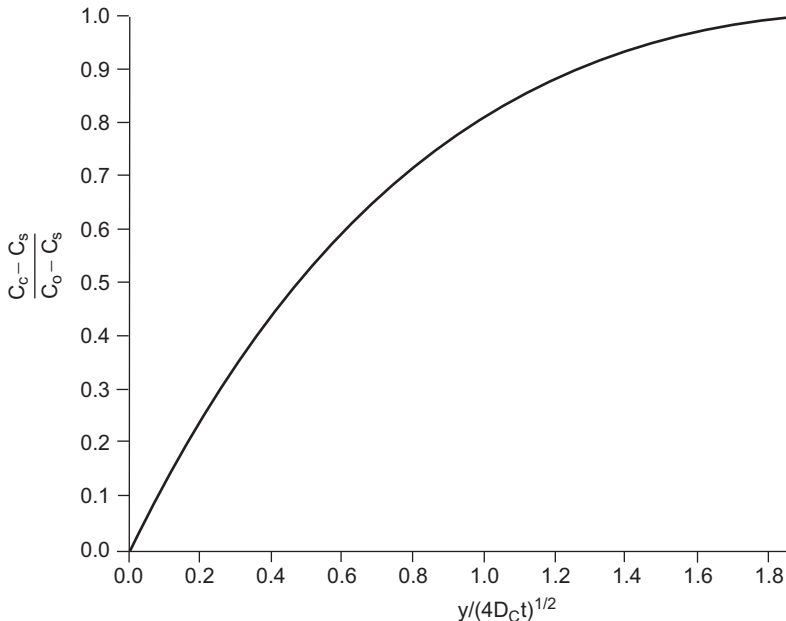
where

$$\operatorname{erf}(\eta) = \frac{2}{\sqrt{\pi}} \int_0^\eta \exp(-\eta^2) d\eta$$

Figure 5.11 shows the dimensionless concentration $(C_C - C_S)/(C_0 - C_S)$ as a function of $y/(4D_{ct})^{1/2}$. This is essentially a plot of $\operatorname{erf}(\eta)$ with η . The figure shows that $\operatorname{erf}(\eta) \approx 1$ when $\eta = 2$. This indicates that if $y/(4D_{ct})^{1/2} > 2$, $C_C = C_0$ or that carbon concentration is the same as the initial concentration. So if maximum time of interest t_{\max} and length in the direction of diffusion, L , are such that $L/(4D_{ct_{\max}})^{1/2} > 2$, the system can be considered as semi-infinite.

Example 5.5

A steel plate with 0.2% carbon is exposed to a carburizing atmosphere at 1223K. Carburizing atmosphere maintains 0.5% carbon on the surface of steel. Calculate



5.11 Variation of $(C_C - C_S)/(C_0 - C_S)$ with $y/(4D_C t)^{1/2}$.

- (a) the concentration of carbon at 1 mm away from the surface after 1 hour, (b) the layer thickness where carbon is greater than 0.3% after 1 hour and (c) what should be the carburizing time if the layer thickness of 0.3% carbon is to be doubled?

Solution

Initial carbon concentration $C_0 = 0.2$, and surface concentration $C_S = 0.5\%$. From Table 5.4, at 1223K, diffusivity of carbon $D_C = 1.2 \times 10^{-11} \text{ m}^2/\text{s}$.

- (a) After 1 hour or 3600s, at $y = 1 \text{ mm}$

$$\eta = y/2(D_C t)^{1/2} = 10^{-3}/\{2(1.2 \times 10^{-11} \times 3600)^{1/2}\} = 2.4$$

$$\text{erf}(2.4) = 1$$

From equation 5.34, $C_C = 0.5 + (0.2 - 0.5) \times 1 = 0.2\%$ or no change in % carbon.

- (b) From equation 5.34, $(0.3 - 0.5) = (0.2 - 0.5)\text{erf}(\eta)$ or $\text{erf}(\eta) = 0.666$. Using Fig. 5.11, $\eta = 0.67$, from the definition of η , $y = 2 \times 0.67 \times (1.2 \times 10^{-11} \times 3600)^{1/2} = 0.28 \text{ mm}$.
- (c) Thickness of the layer having $\%C \geq 0.3\%$ is twice that of (b) or $y = 0.56 \text{ mm}$. Obviously the value of $y/(4t)^{1/2}$ must be same both for (b) and (c). $0.28/(3600)^{1/2} = 0.56/t^{1/2}$ or $t = (0.56/0.28)^2 \times 3600$, or 4 hours. ■■■

Evaporation of liquid

Figure 5.12 shows a volatile liquid A in a cylindrical container of cross-sectional area S. A gas stream of A and B is flowing over container. The gas B is insoluble in liquid A. The system is isothermal and the rate of evaporation is so slow that the liquid level in the container does not change appreciably. We want to find out the rate of evaporation and concentration profile of A in the container at steady state.

The problem involves diffusion in a cylindrical container, so equation B of Table 5.5 is the appropriate equation. But in this case diffusion of A is in z direction only, so the final equation will be the same both in rectangular and cylindrical coordinate systems. If we consider rectangular coordinates, fluxes N_{Ax} and N_{Ay} are zero and for cylindrical coordinate, fluxes N_{Ar} and $N_{A\theta}$ are zero. Table 5.5 shows that equations A and B become identical for this condition. There is no reaction, so rate of generation of A, $R_A = 0$. We are interested in a concentration profile at steady state so $\partial C_A / \partial t = 0$. Hence the conservation equation of species A simplifies to

$$-\frac{dN_{Az}}{dz} = 0 \quad (5.35)$$

Integrating

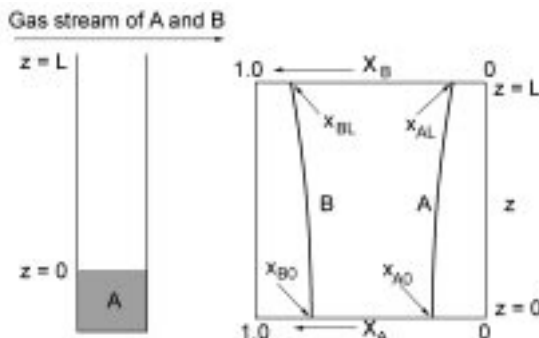
$$N_{Az} = C_1 \quad (5.36)$$

From the definition of flux, equation 5.7

$$N_{Az} = -D_{AB} \frac{dC_A}{dz} + x_A (N_{Az} + N_{Bz}) \quad (5.37)$$

Since the gas B is insoluble in liquid A, the flux of B is zero.

$$N_{Bz} = 0 \quad (5.38)$$



5.12 Evaporation of a liquid A from a container and concentration profiles of A and B.

Using the relation $C_A = C \cdot x_A$ where C is the total concentration of A and B and equation 5.38, equation 5.37 can be written as

$$N_{Az} = -\frac{D_{AB}C}{1-x_A} \frac{dx_A}{dz} \quad (5.39)$$

Substituting the above relationship in equation 5.36

$$-D_{AB}C \cdot \frac{dx_A}{1-x_A} = C_1 dz$$

Integration of the above equation gives

$$D_{AB}C \ln(1-x_A) = C_1 z + C_2 \quad (5.40)$$

Taking the top surface of the liquid as $z = 0$, the boundary conditions are

$$\text{At } z = 0, \quad x_A = x_{A0} \quad (5.41a)$$

$$\text{At } z = L, \quad x_A = x_{AL} \quad (5.41b)$$

The values of x_{A0} and x_{AL} are determined by the vapour pressure of liquid A and the concentration of A in the gas stream that is flowing above the container respectively. From equations 5.40 and 5.41

$$C_2 = D_{AB}C \ln(1-x_{A0}) \quad (5.42)$$

$$C_1 = C \frac{D_{AB}}{L} \ln \frac{1-x_{AL}}{1-x_{A0}} \quad (5.43)$$

Substituting equations 5.42 and 5.43 in equation 5.40 and rearranging

$$\frac{1-x_A}{1-x_{A0}} = \left(\frac{1-x_{AL}}{1-x_{A0}} \right)^{S/L} \quad (5.44)$$

In terms of mole fraction of B, the above equation can be written as

$$x_B/x_{B0} = (x_{BL}/x_{B0})^{Z/L} \quad (5.45)$$

Although the flux of B is zero, the above equation shows that the concentration gradient of B is not zero. Diffusive flux due to concentration gradient is exactly balanced by the flux due to bulk flow. Figure 5.12 shows the concentration profiles of A and B.

$$\text{The rate of evaporation of A} = S N_{Az}|_{z=0} \quad (5.46)$$

Using equations 5.36 and 5.43

$$\text{Rate of evaporation of A} = S C \frac{D_{AB}}{L} \ln \frac{1-x_{AL}}{1-x_{A0}} \quad (5.47)$$

When concentration of A in the gas phase is very small, $\ln(1-x_{AL}) \approx -x_{AL}$ and $\ln(1-x_{A0}) \approx -x_{A0}$ and the above equation simplifies to

$$\text{Rate of evaporation} = SD_{AB}C \frac{x_{A0} - x_{AL}}{L} \quad (5.48)$$

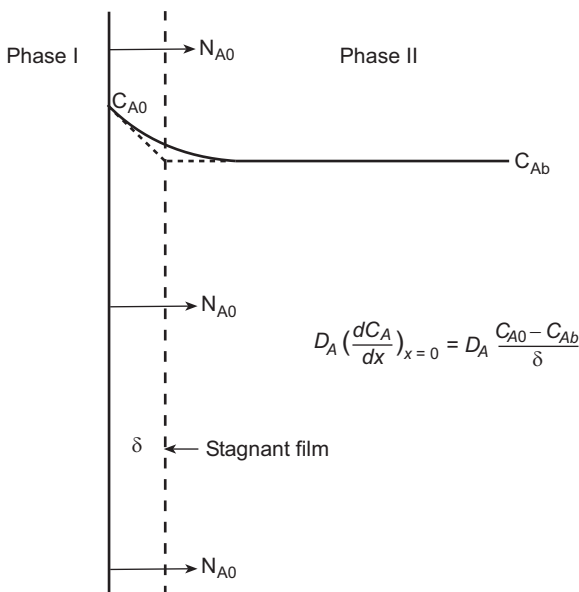
The above equation can also be obtained from equations 5.36 and 5.37 by neglecting the bulk flow term from the later equation.

5.2.4 Interface mass transfer

Quite often we are interested in finding out the rate of transport of a species from one phase to another one. For example, evaporation of a liquid, dissolution of a solid in a liquid, absorption of a gas by liquid, etc. involves transport of a species from one phase to another. These are determined by the flux at the interface between two phases $N_{Ax}|_{x=0}$ or N_{A0} . Figure 5.13 shows the flux at interface. This interphase transport between phases I and II, is calculated using the concept of mass transfer coefficient.

$$\begin{aligned} N_{A0} &= -D_{AB} \left(\frac{dC_A}{dx} \right)_{x=0} + x_{A0}(N_{A0} + N_{B0}) \\ &= k_{MA}(C_{A0} - C_{Ab}) + x_{A0}(N_{A0} + N_{B0}) \end{aligned} \quad (5.49)$$

where N_{A0} is the flux of A from phase I to II, k_{MA} is the mass transfer coefficient of A, C_{A0} and C_{Ab} are concentrations of A in phase II at the interface and bulk respectively and x_{A0} is the mole fraction of A in phase II at the interface. The interface concentration of A in phase II, C_{A0} , is related to the concentration of A



5.13 Transfer of a species from phase I to II.

in phase I. For example: for evaporation of water at 300K, C_{A0} is determined by vapour pressure of water (phase I) at 300K. For removal of nitrogen from liquid steel by argon purging, C_{A0} is determined by the partial pressure of nitrogen in equilibrium with nitrogen dissolved in steel (phase I).

In a number of practical systems x_{A0} is very small and equation 5.49 simplifies to

$$N_{A0} = k_{MA}(C_{Aw} - C_{Ab}) \quad (5.50)$$

A physical picture of mass transfer coefficient can be obtained from film theory. According to this model, at the interface there is a stagnant film of thickness δ . The concentration of A varies linearly in the film as shown by dotted line in Fig. 5.13 and beyond the film; concentration of A is the same as the bulk concentration. So from equation 5.49 we get $k_{MA} = D_{AB}/\delta$. Using this concept quite often we say that at the interface there is a stagnant film.

Mass transfer coefficient is a system property; in the sense it depends on the shape and size of the system from which mass transfer takes place. Besides, it is determined by density, viscosity, diffusivity and velocity of fluid. So

$$k_{MA} = f(\rho, \mu, D_{AB}, v, L) \quad (5.51)$$

where ρ , μ and v are respectively density, viscosity and velocity of fluid and L is the characteristic length of the system. Dimensionless analysis shows that equation 5.51 can be expressed as

$$Sh = f(Re, Sc) \quad (5.52)$$

where Sh , Re and Sc are respectively the Sherwood number, Reynolds number and Schmidt number and are defined as

$$\text{Sherwood number} \quad Sh = k_{MA}L/D_{AB} \quad (5.53)$$

$$\text{Reynolds number} \quad Re = \rho v L / \mu \quad (5.54)$$

$$\text{Schmidt number} \quad Sc = \mu / (\rho D_{AB}) \quad (5.55)$$

The Sherwood number is the ratio of interface or convective mass transfer to diffusive mass transfer rates. The Reynolds number is the ratio inertial force to viscous force and the Schmidt number is the ratio of momentum diffusivity (μ/ρ) to mass diffusivity

Correlations for mass transfer coefficient

The mass transfer from a sphere is mostly calculated by Ranz and Marshall correlation

$$Sh = 2 + 0.6(Re)^{1/2}(Sc)^{1/3} \quad (5.56)$$

The characteristic length for both Sh and Re is the particle diameter. So Re appearing in equation 5.56 is called the particle Reynolds number. When there is

no fluid flow, the above relation predicts $Sh = 2$ which is obtained by theoretical calculation. This correlation is often used for calculation of mass transfer in a packed bed.

Example 5.6

A spherical drop of water of 0.5 mm diameter is falling through dry still air at a velocity of 0.75 ms^{-1} . Assuming that the temperature of water droplet and air is at 300K, calculate the instantaneous evaporation rate. At 300K vapour pressure of water is 0.035 bar. Density and viscosity of air at 300K are 1.177 kg m^{-3} and $18.53 \times 10^{-6} \text{ kg m}^{-1} \text{ s}^{-1}$ respectively. 1 bar = 10^5 Pa and $R = 8.314 \text{ Pa.m}^3.\text{mol}^{-1}\text{K}^{-1}$, Atmospheric pressure = $1.013 \times 10^5 \text{ Pa}$.

Solution

$$\text{Rate of evaporation} = \text{surface area of droplet} \times N_{A0} = \pi(0.5 \times 10^{-3})^2 N_{A0}$$

$$\text{From equation 5.49, } N_{A0} = [k_M(C_{A0} - C_{Ab}) + x_{A0}(N_{A0} + N_{B0})]$$

In the present case A is H_2O and B is air. Since air is not soluble in water, $N_{B0} = 0$,

$$N_{A0} = k_M(C_{A0} - C_{Ab})/(1 - x_{A0})$$

$$\text{Rate of evaporation} = 25\pi \times 10^{-8} [k_M(C_{A0} - C_{Ab})]/(1 - x_{A0})$$

$$C_{A0} = p_{A0}/RT = 0.035 \times 10^5 / (8.314 \times 300) = 1.4 \text{ mole/m}^3$$

$$C_{Ab} = 0$$

$$x_{A0} = p_{A0}/\text{atmospheric pressure} = 0.035 \times 10^5 / 1.013 \times 10^5 = 0.0345$$

$$D_{\text{H}_2\text{O-air}} \text{ at } 300\text{K} = 0.255 \times 10^{-4} \text{ m}^2/\text{s} \text{ from equation 5.16}$$

$$Re = \rho v L / \mu = 1.177 \times 0.75 \times 0.5 \times 10^{-3} / 18.53 \times 10^{-6} = 23.8$$

$$Sc = \mu / (\rho D_{AB}) = 18.53 \times 10^{-6} / (1.177 \times 0.255 \times 10^{-4}) = 0.617$$

$$\text{From equation 5.56, } Sh = 2 + 0.6 \times (23.8)^{1/2} \times (0.617)^{1/3} = 4.49$$

$$K_M = Sh \cdot D_{AB} / L = 4.49 \times 0.255 \times 10^{-4} / 0.5 \times 10^{-3} = 0.229 \text{ m}^2/\text{s}$$

$$\text{So rate of evaporation} = 25\pi \times 10^{-8} \times 0.229 \times 1.4 / (1 - 0.0345) \\ = 26.1 \times 10^{-8} \text{ mole/s}$$



5.3 Heat transfer

When a hot object is kept in atmosphere, heat is transferred from the surface of the object to the surroundings by convection and radiation. As the surface is cooled, heat is transferred from the interior of the object to the surface by conduction. These processes continue until the temperature of the object becomes the same as that of the surroundings. In all the three modes of heat transfer namely, conduction, convection and radiation; the driving force is temperature difference.

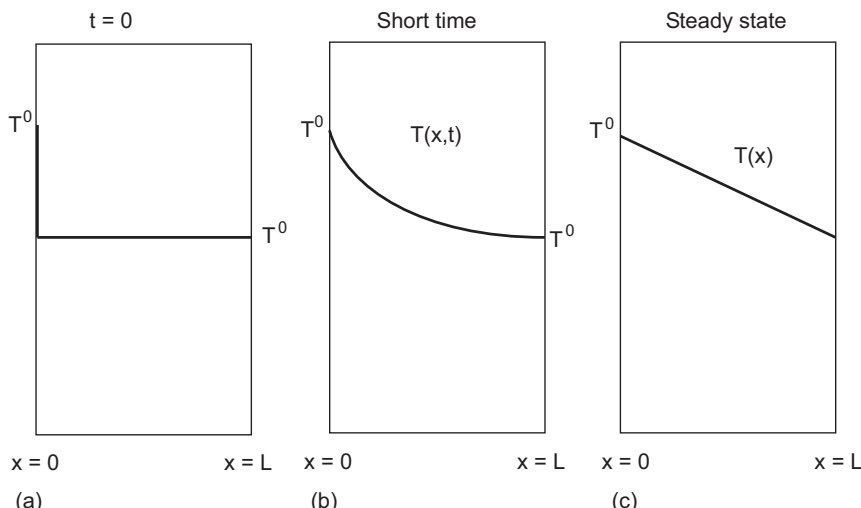
The conduction of heat in solid and liquid takes place due to molecular vibration and that in gas by molecular collision. Convective heat transfer has

two limiting cases: forced and natural. In forced convection the flow is due to external forces whereas in natural convection, it is due to density difference. When a hot object is kept in stagnant air, the heat transfer is by natural convection. The air in contact with the hot object becomes hot and thereby lighter and moves up and cold air from the surroundings occupies the space. This leads to fluid motion that is termed as natural convection. On the other hand, if the hot object is cooled by blowing air over it, the mechanism of heat transfer is forced convection. Both conduction and convection of heat takes place through a material medium, but energy is transported through empty space by radiation.

5.3.1 Conduction

Let us consider a plate that is at a uniform temperature T^0 . At time, $t = 0$, the left face is suddenly raised to a temperature T_0 , Fig. 5.14(a). Due to difference in temperature, heat flows from left to right by conduction and temperature along the length increases with time as shown in Fig. 5.14(b). After sufficiently long time, temperature profile attains the steady state Fig. 5.14(c). Both during steady and unsteady state, heat flows from left to right. This flow of heat is measured in terms of heat flux defined as the amount of heat flowing through unit area per unit time in a direction normal to the area. The heat flux by conduction is given by

$$q_x = -k \frac{dT}{dx} \quad (5.57)$$



5.14 Temperature profile in a slab. (a) The left face of the slab is suddenly raised to T_0 at $t = 0$. (b) Temperature profile after some time. (c) Temperature profile at steady state.

where q_x is the heat flux in x direction W/m^2 , k is the thermal conductivity of material $\text{Wm}^{-1}\text{K}^{-1}$ and dT/dx is the temperature gradient K/m . The negative sign in equation 5.57 indicates that heat flux and temperature gradient are in opposite direction. In Fig. 5.14 temperature decreases with increase of x , dT/dx is negative, and heat flux is positive or it is in direction of increasing x . It should be noted that the flux is a vector and its sign gives the direction of flow. Equation 5.57 is the one-dimensional form of Fourier's law of heat conduction.

In the example above, temperature depends only on its distance from the face or T is a function of x only. But if temperature varies from point to point, i.e., if T is a function of x , y and z , heat will flow in all directions. It is given by

$$\mathbf{q} = -k\nabla T \quad (5.58)$$

The components of heat flux in different coordinate systems are similar to that for molar flux \mathbf{J}_A given in Table 5.1. The above equation is the three-dimensional form of Fourier's law of heat conduction and is valid for a medium whose conductivity is the same in all direction. These types of materials are known as isotropic material. But a number of materials, for example laminated composites, unidirectional fibrous composite material like bamboo etc., are not isotropic, i.e., conductivity is different in different directions. For non-isotropic materials equation 5.58 takes the form

$$\mathbf{q}^m = -\left[\mathbf{i} k_x \frac{\partial T}{\partial x} + \mathbf{j} k_y \frac{\partial T}{\partial y} + \mathbf{k} k_z \frac{\partial T}{\partial z} \right] \quad (5.59)$$

where k_x , k_y and k_z are thermal conductivity of the material and \mathbf{i} , \mathbf{j} , \mathbf{k} are unit vectors in x , y , and z directions respectively.

Example 5.7

Two faces of a stainless steel plate of 0.1 m^2 area and 4 mm thickness are kept at 723K and 323K respectively. The temperature profile in the plate is linear. Calculate the heat flux and total heat transferred in one minute through the plate. Thermal conductivity of stainless steel is $19 \text{ Wm}^{-1}\text{K}^{-1}$.

Solution

The problem involves heat transfer only in one direction and heat flux is given by equation 5.57. Let us assume that the face at temperature 723K as $x = 0$ and that at 323K as $x = \Delta x$. Since the temperature profile is linear, $dT/dx = (T|_{\Delta x} - T|_0)/\Delta x = (323 - 723)/(4 \times 10^{-3}) = -10^5 \text{ K/m}$. So heat flux = $19 \times 10^5 \text{ Wm}^{-2}$. The direction of heat flux is +ve direction of x .

Total heat transferred in one minute

$$\begin{aligned} &= \text{area of the plate} \times \text{heat flux} \times \text{time in seconds} \\ &= 0.1 \times 19 \times 10^5 \times 60 = 1.14 \times 10^7 \text{ J} \end{aligned}$$



5.3.2 Thermal conductivity

According to kinetic theory of gases, thermal conductivity of monatomic gases is independent of pressure and is proportional to square root of temperature. The predicted pressure dependence is valid up to 10 atmospheres but temperature dependent is too weak. The temperature dependence of the thermal conductivity of gas can be expressed as

$$k = k_0(T/T_0)^n \quad (5.60)$$

where k_0 is thermal conductivity at T_0 K. Eucken's equation

$$k = (C_p + 1.25R/M)\mu \quad (5.61)$$

is widely used for estimation of thermal conductivity of gases. C_p , R, M and μ are respectively specific heat, gas constant, molecular weight and viscosity. Table 5.6 gives the thermal conductivity of some common gases. It shows that thermal conductivity of hydrogen is much higher than other gases.

Thermal conductivity of liquid

Thermal conductivity of liquid depends on the nature of the liquid. Liquid metals have a much higher thermal conductivity compared with water or slag. Table 5.7 shows the thermal conductivity of different liquids.

Thermal conductivity of solids

Energy is transferred due to elastic vibrations of the lattice in solids. In the case of metal, besides the above mechanism, free electrons moving through the lattice carry energy. Heat transferred by the latter mechanism is greater than that

Table 5.6 Thermal conductivity of some common gases ($\text{Wm}^{-1} \text{K}^{-1}$)

Gases	H_2	H_2O	CO	CO_2	Air
$k \times 10^3$ at 400K	226	26.1	31.8	24.3	33.8
$k \times 10^3$ at 800K	378	59.2	55.5	55.1	57.3

Table 5.7 Thermal conductivity of liquids ($\text{Wm}^{-1} \text{K}^{-1}$)

Material	Temp. K	k	Material	Temp. K	k
Water	293	0.59	Aluminum	933	91
Glycerol	293	0.29	Copper	1600	174
Slag	1873	4.0	Iron	1809	40.3

Table 5.8 Thermal conductivity of solids at room temperature

Material	Al	Cu	Brass	Fe	Steel	Concrete	Brick
$k \text{ Wm}^{-1}\text{K}^{-1}$	237	398	127	79	52	0.9	0.6

by the former. So thermal conductivity of metal is much higher than that of non-metals. Thermal conductivity of pure metal decreases with temperature. Table 5.8 gives thermal conductivity of some solids.

Thermal conductivity of porous solid is given by

$$k_{\text{eff}} = k(1 - \epsilon) \quad (5.62)$$

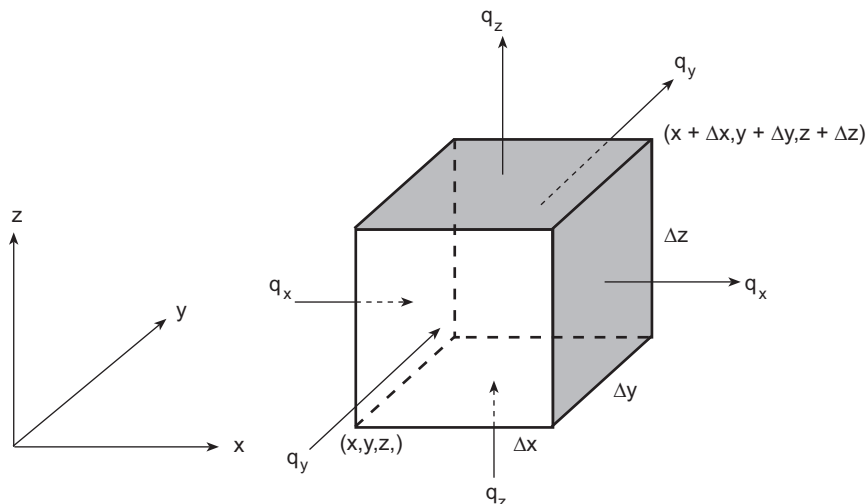
where k_{eff} and k are the thermal conductivity of porous solid and solid respectively and ϵ is the void fraction in solid.

5.3.3 Conservation equation

Let us consider an elemental volume $\Delta x \Delta y \Delta z$ as shown in Fig. 5.15. Since energy is conserved, the balance equation is

$$\begin{aligned} \text{Rate of accumulation of energy in } \Delta x \Delta y \Delta z &= \text{rate in} - \text{rate out} \\ &\quad + \text{rate of generation of energy in } \Delta x \Delta y \Delta z \text{ volume} \end{aligned} \quad (5.63)$$

In Fig. 5.15, heat enters through three faces and goes out through the corresponding opposite three faces. In the case of stationary solid, heat flux is only by conduction. So following the procedure given in Section 5.2.3, we get



5.15 Heat balance in a control volume.

$$\frac{\partial}{\partial t}(\rho C_p T) = -\frac{\partial q_x}{\partial x} - \frac{\partial q_y}{\partial y} - \frac{\partial q_z}{\partial z} + H_G \quad (5.64)$$

where $\rho C_p T$ is the heat content per unit volume and H_G is the rate of heat generation per unit volume. Assuming ρ , C_p and k are constant and using the definition of flux equation 5.58, the above equation can be written as

$$\rho C_p \frac{\partial T}{\partial t} = k \left[\frac{\partial^2 T}{\partial x^2} + \frac{\partial^2 T}{\partial y^2} + \frac{\partial^2 T}{\partial z^2} \right] + H_G \quad (5.65)$$

In the case of fluid, the terms ‘rate in’ and ‘rate out’ in equation 5.63 include heat transfer due to bulk flow as well. Similarly if the solid is in motion, in the direction of motion, the terms ‘rate in’ and ‘rate out’ include heat flux due to bulk motion. Table 5.9 gives the general heat balance equation in different coordinate systems. These equations are valid for solids and incompressible fluids.

Heat generation within a solid can be due to phase transformation, chemical reaction or electrical heating. In the case of fluid besides the above mechanisms, heat generation can be due to viscous dissipation as well. But normally heat generation due to viscous dissipation is very small and is neglected.

Steady state heat conduction

Let us consider heat transfer in the plate shown in Fig. 5.14. The appropriate energy balance equation is equation A in Table 5.9. In this case heat transfer takes place only along the x axis that is normal to the plate face. So, heat flux in y and z directions is zero. The plate is stationary so v_x , v_y and v_z are also zero. At the steady state, $\partial T / \partial t = 0$ and there is no heat generation in the plate, $H_G = 0$. Hence equation (A) of Table 5.9 becomes

Table 5.9 Energy equation for incompressible media in different coordinate systems

Rectangular coordinates

$$\rho C_p \left[\frac{\partial T}{\partial t} + v_x \frac{\partial T}{\partial x} + v_y \frac{\partial T}{\partial y} + v_z \frac{\partial T}{\partial z} \right] = - \left[\frac{\partial q_x}{\partial x} + \frac{\partial q_y}{\partial y} + \frac{\partial q_z}{\partial z} \right] + H_G \quad [A]$$

Cylindrical coordinates

$$\rho C_p \left[\frac{\partial T}{\partial t} + v_r \frac{\partial T}{\partial r} + \frac{v_\theta}{r} \frac{\partial T}{\partial \theta} + v_z \frac{\partial T}{\partial z} \right] = - \left[\frac{1}{r} \frac{\partial}{\partial r} (rq_r) + \frac{1}{r} \frac{\partial q_\theta}{\partial \theta} + \frac{\partial q_z}{\partial z} \right] + H_G \quad [B]$$

Spherical coordinates

$$\begin{aligned} \rho C_p \left[\frac{\partial T}{\partial t} + v_r \frac{\partial T}{\partial r} + \frac{v_\theta}{r} \frac{\partial T}{\partial \theta} + \frac{v_\phi}{r \sin \theta} \frac{\partial T}{\partial \phi} \right] \\ = - \left[\frac{1}{r^2} \frac{\partial}{\partial r} (r^2 q_r) + \frac{1}{r \sin \theta} \frac{\partial}{\partial \theta} (q_\theta \sin \theta) + \frac{1}{r \sin \theta} \frac{\partial q_\phi}{\partial \phi} \right] + H_G \end{aligned} \quad [C]$$

$$\frac{dq}{dx} = 0$$

Integrating,

$$q_x = C_1$$

where C_1 is the integration constant.

Using the definition of heat flux, equation 5.57, the above equation becomes

$$-k \frac{dT}{dx} = C_1 \quad (5.66)$$

Integrating,

$$-kT = C_1x + C_2 \quad (5.67)$$

Integration constants C_1 and C_2 are evaluated from the boundary conditions.

$$\text{At } x = 0, T = T_0 \quad \text{and} \quad x = L, T = T_L$$

Using these conditions in equation 5.67

$$C_1 = k(T_0 - T_L)/L \quad (5.68)$$

$$C_2 = -kT_0 \quad (5.69)$$

and

$$T = T_0 - (T_0 - T_L) \frac{x}{L} \quad (5.70)$$

Quite often we are interested in the case where one face is maintained at temperature T_0 but the other face is exposed to the atmosphere. In this case the boundary conditions are

$$\text{At } x = 0, T = T_0 \quad \text{and} \quad x = L, -k \frac{dT}{dx} = h(T - T_a) \quad (5.71)$$

where h is the heat transfer coefficient and T_a is the ambient temperature. C_2 is same as that given by equation 5.69. Using equations 5.67 and 5.71

$$C_1 = h \left[\frac{-C_1 L + kT_0}{k} - T_a \right]$$

Rearranging

$$C_1 = \frac{T_0 - T_a}{\frac{1}{h} + \frac{L}{k}} \quad (5.72)$$

So

$$T = T_0 - \frac{x}{k} \frac{\frac{T_0 - T_a}{\frac{1}{h} + \frac{L}{k}}}{\frac{1}{h} + \frac{L}{k}} \quad (5.73)$$



5.16 Electrical analogy for heat loss through a plate. $T_{\text{outer face}}$ is the temperature of outer face exposed to atmosphere.

Heat is lost through the face at $x = L$, so the rate of heat lost per unit area is

$$H_{\text{Loss}} = -k \left(\frac{dT}{dx} \right)_{x=L}$$

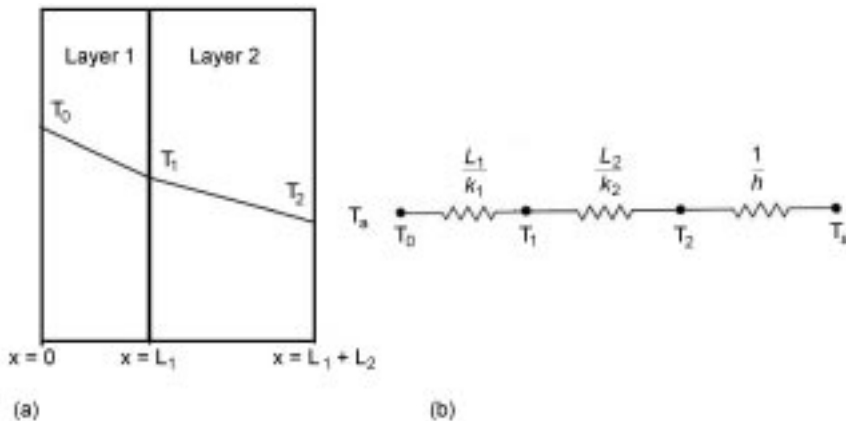
At steady state dT/dx is constant so heat loss per unit area is same as heat flux and is equal to C_1 , see equation 5.67, hence

$$H_{\text{Loss}} = \frac{T_0 - T_a}{\frac{1}{h} + \frac{L}{k}} \quad (5.74)$$

Using an electrical analogue, one can say that heat loss is similar to current, the numerator of above equation is the driving force and the denominator is the resistance for heat loss. Two resistances, one due to plate, L/k , and other one due to the interface, $1/h$, are in series. Figure 5.16 shows the electrical analogue.

Heat loss through composite wall

Let us consider heat flux at the steady state through a composite wall made up of two layers shown in Fig. 5.17(a). The thickness of layers 1 and 2 and their thermal conductivities are L_1 , L_2 and k_1 , k_2 , respectively. Obviously, at the steady state temperature profiles of the layers are given by equation 5.67 and can be written as:



5.17 (a) Temperature distribution in composite wall and (b) electrical analogue of heat flux.

$$\text{For layer 1} \quad T^I = C_1x + C_2 \quad (5.75a)$$

$$\text{For layer 2} \quad T^{II} = C_3x + C_4 \quad (5.75b)$$

The integration constants, C_1 , C_2 , C_3 , C_4 , are determined by the following boundary conditions

$$\text{At } x = 0, \quad T^I = T_0 \quad (5.76a)$$

The outer face is exposed to atmosphere, so

$$\text{At } x = L_1 + L_2, \quad -k_2(dT^{II}/dx) = h(T^{II} - T_a) \quad (5.76b)$$

The walls are in perfect contact, so temperature and heat flux at the interface must be the same. Or

$$\text{At } x = L_1 \quad T^I = T^{II} \quad (5.76c)$$

$$k_1(dT^I/dx) = k_2(dT^{II}/dx) \quad (5.76d)$$

From equations 5.75 and 5.76,

$$C_1 = (k_2/k_1)C_3$$

$$C_2 = T_0$$

$$C_3 = -\frac{T_0 - T_a}{\frac{k_2}{h} + L_2 + \frac{k_2}{k_1}L_1}$$

$$C_4 = L_1C_3(k_2/k_1 - 1) + T_0$$

$$\text{Heat loss} = (-k_2dT^{II}/dx)_{x=L_1+L_2} = -k_2C_3 = -\frac{T_0 - T_a}{\frac{1}{h} + \frac{L_1}{k_1} + \frac{L_2}{k_2}} \quad (5.77)$$

Figure 5.17(b) shows the electrical analogue for heat loss through the composite wall. Using the electrical analogue, we could directly obtain equation 5.77.

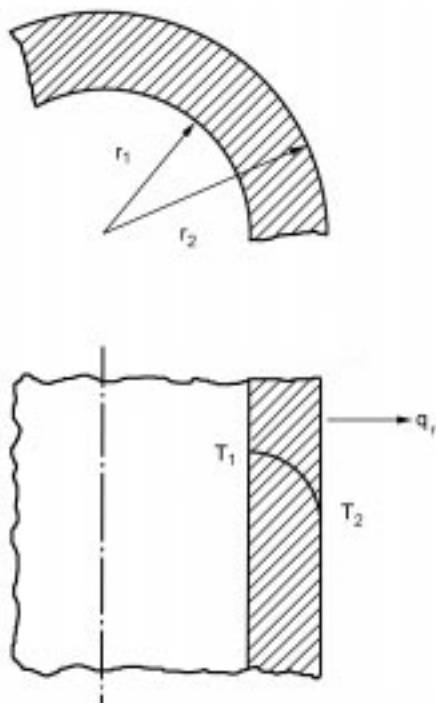
Temperature distribution in a hollow cylinder

Let us consider a hollow cylinder with inner radius r_1 and outer radius r_2 , Fig. 5.18. Inner and outer faces are at T_1 and T_2 respectively. Obviously, the appropriate equation for energy conservation is equation B in Table 5.9. In the hollow cylinder, heat conduction is in the radial direction only; thereby q_z and q_θ are zero. Furthermore, there is no heat generation and all velocity components in equation B are zero, so at steady state the equation simplifies to

$$\frac{d}{dr}(rq_r) = 0 \quad (5.78)$$

Integrating

$$rq_r = C_1$$



5.18 Schematic diagram of a hollow cylinder.

Since

$$q_r = -k \frac{dT}{dr},$$

$$-k \frac{dT}{dr} = C_1/r$$

Integrating

$$-kT = C_1 \ln r + C_2$$

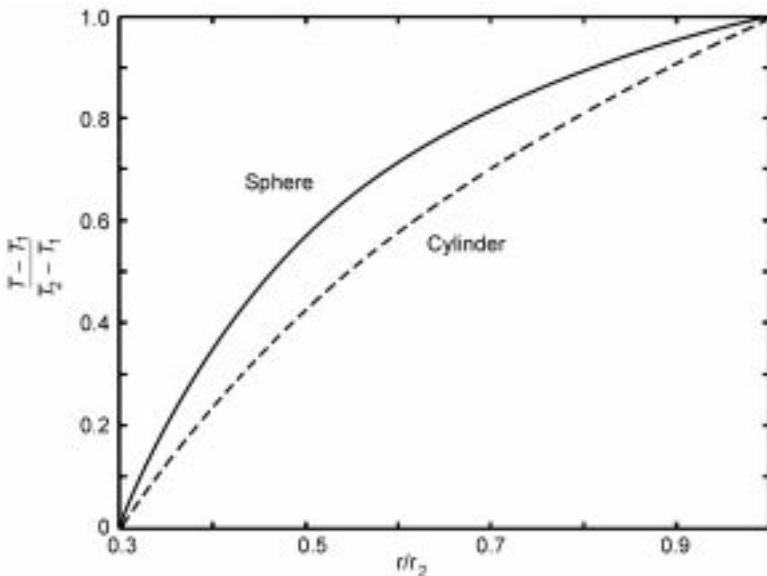
The boundary conditions are

$$\text{At } r = r_1, \quad T = T_1$$

$$\text{At } r = r_2, \quad T = T_2$$

Using the above boundary conditions

$$= T_1 - (T_1 - T_2) \frac{\ln\left(\frac{r}{r_1}\right)}{\ln\left(\frac{r_2}{r_1}\right)}$$



5.19 Temperature distribution in a hollow cylinder and sphere. Ratio of inner to outer radius (r_1/r_2) is 0.3.

The above equation can be written in a dimensionless form as

$$\frac{T - T_1}{T_2 - T_1} = \frac{\ln\left(\frac{r}{r_1}\right)}{\ln\left(\frac{r_2}{r_1}\right)} \quad (5.79)$$

Figure 5.19 shows the dimensionless temperature profile in a hollow cylinder. It shows that temperature profile deviates considerably from linearity.

Steady state temperature distribution in a spherical shell

Let us consider a hollow spherical shell of inner radius r_1 at temperature T_1 and outer radius r_2 at T_2 . Heat conduction takes place only in the radial direction. The appropriate equation is equation C in Table 5.9 which simplifies for the steady state conduction problem without heat generation to

$$\frac{d}{dr}(r^2 q_r) = 0$$

and boundary conditions are

$$\begin{aligned} \text{At } r = r_1, \quad T &= T_1 \\ \text{At } r = r_2, \quad T &= T_2 \end{aligned}$$

The solution of the differential equation along with the above boundary

condition is

$$\frac{T - T_1}{T_2 - T_1} = \frac{\frac{1}{r_1} - \frac{1}{r}}{\frac{1}{r_1} - \frac{1}{r_2}} \quad (5.80)$$

Figure 5.19 shows the dimensionless temperature profile in a hollow sphere. Comparison of temperature profiles in a hollow cylinder and sphere shows that the curvature of the latter is greater.

5.3.4 Heat transfer coefficient

At solid–fluid interface, heat flux from solid to fluid or fluid to solid is defined as

$$q = h(T_s - T_b) \quad (5.81)$$

where T_s is the temperature of solid surface in contact with fluid, T_b is the bulk fluid temperature and h is the heat transfer coefficient, $\text{Wm}^{-2}\text{K}^{-1}$. Equation 5.81 is also used for heat transfer between two fluids. h is often termed as convective heat transfer coefficient to differentiate it from radiative heat transfer coefficient. The value of h depends on characteristic length of body, fluid properties like thermal conductivity, density and specific heat and velocity of fluid. By dimensional analysis it can be shown that

$$\text{Nu} = f(\text{Re}, \text{Pr}) \quad (5.82)$$

where

Nusselt number	$\text{Nu} = hL/k$
Prandtl number	$\text{Pr} = C_p\mu/k = \nu/\alpha$

where L is the characteristic length of the system and $\alpha = k/\rho C_p$ is thermal diffusivity and $\nu = \mu/\rho$ is momentum diffusivity or kinematic viscosity. The Nusselt number measures the ratio of interface or convective heat flux to conductive heat flux and the Prandtl number is the ratio of thermal diffusivity to momentum diffusivity.

The heat transfer from a sphere is often calculated by Ranz and Marshall correlation

$$\text{Nu} = 2 + 0.6(\text{Re}_f)^{1/2}(\text{Pr}_f)^{1/3} \quad (5.83)$$

The characteristic length for both Nu and Re is the particle diameter. The suffix f in Re and Pr indicates that these should be evaluated at the film temperature which is taken as average of surface and bulk temperature. This relationship is also often used for calculation of heat transfer in the packed bed. Comparison of equations 5.56 and 5.83 shows that the relationship between Sh , Re and Sc

number for mass transfer is the same as that between Nu, Re and Pr for heat transfer. This is true not only for a sphere but for other systems as well.

Example 5.8

Show that when a hot sphere is placed in stagnant air, in the absence of natural convection, $\text{Nu} = 2$.

Solution

Let T_0 be the temperature of the sphere or temperature of air in contact with the sphere and T_∞ is the temperature of air far away from it. Stagnant air around the sphere is an infinitely large hollow sphere whose inner radius is the radius of the sphere r_0 and the outer radius $r_2 = \infty$. So equation 5.80 simplifies to

$$T = T_0 - (T_0 - T_\infty) \left(\frac{1}{r_0} - \frac{1}{r} \right) r_0$$

$$T = T_\infty + (T_0 - T_\infty) \frac{r_0}{r}$$

Heat flux at the outer face of the sphere is

$$-k \left(\frac{dT}{dr} \right)_{r=r_0} = k \frac{T_0 - T_\infty}{r_0}$$

Equating the above equation with equation 5.81,

$$h = k/r_0 = 2k/D$$

since in the case of the sphere the characteristic length is the diameter of the sphere, D,

$$\text{Nu} = hD/k = 2$$

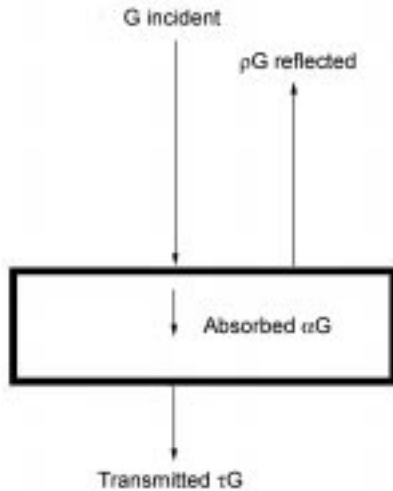


5.3.5 Radiation

A hot body emits radiation in a continuous band of wavelength in the range of 0.1 to 100 microns. This is known as thermal radiation and it includes ultra violet, visible range and infra red of the electromagnetic radiation spectrum. The proportion of different frequencies of radiation emitted by a hot body depends on its temperature and thereby its colour changes with temperature. Like all electromagnetic waves, heat radiation travels through space at the velocity of light.

Emissivity and absorptivity

When radiation falls on an object, a part of it is reflected, a part is transmitted through the object and the rest is absorbed, Fig. 5.20. If G is the flux of radiant



5.20 Schematic illustration of absorption, reflection and transmission of radiation falling on a body.

energy Wm^{-2} , then

$$G = \alpha G + \rho G + \tau G$$

or

$$\alpha + \rho + \tau = 1 \quad (5.84)$$

where α is the fraction of incident radiation absorbed or absorptivity, ρ is the fraction reflected or reflectivity and τ is the fraction transmitted or transmissivity. Most of the solids and liquids are opaque to thermal radiation, so the above equation simplifies to

$$\alpha + \rho = 1 \quad (5.85)$$

For any real body absorptivity α is less than unity and varies with the frequency of radiation. A body for which α is a constant over the entire range of frequency is known as a *grey body*. This is a hypothetical body but we idealize all real bodies as grey bodies for thermal radiation calculations. A limiting case of grey body is $\alpha = 1$ for all frequencies and temperature. This is known as a *black body*. A cavity absorbs all radiation falling on it and hence is a black body.

Let q and q_b be, respectively, total radiant energy emitted per unit area per unit time (Wm^{-2}) by a real surface and a black body when they are at the same temperature. The ratio q/q_b is known as *emissivity* ϵ of the real surface. Or

$$\epsilon = q/q_b \quad (5.86)$$

Let us consider that a grey body of surface area A is enclosed in a cavity and both grey body and cavity are in thermal equilibrium. Obviously, for thermal equilibrium, the energy absorbed by the grey body must be equal to that emitted

by it. Since the cavity is a black body, radiation emitted by it is $q_b \text{ Wm}^{-2}$ and energy absorbed by the grey body is $A\alpha q_b$. Hence

$$Aq = A\alpha q_b \quad (5.87)$$

Comparing equations 5.86 and 5.87

$$\alpha = \epsilon \quad (5.88)$$

So, at a given temperature emissivity and absorptivity are equal for any solid surface. This is *Kirchhoff's law*. Highly polished metal surfaces reflect most of the radiations falling on them so their emissivity is very low. It is in the range of 0.015–0.06. Emissivity of refractory bricks lies between 0.85 and 0.95.

The total energy emitted per unit area per unit time by a black surface is given by the *Stefan–Boltzmann law*.

$$q_b = \sigma T^4 \quad (5.89)$$

The Stefan–Boltzmann constant $\sigma = 5.67 \times 10^{-8} \text{ Wm}^{-2}\text{K}^{-4}$. For non-black bodies, the radiant energy emitted per unit area per unit time is

$$q = \sigma \epsilon T^4 \quad (5.90)$$

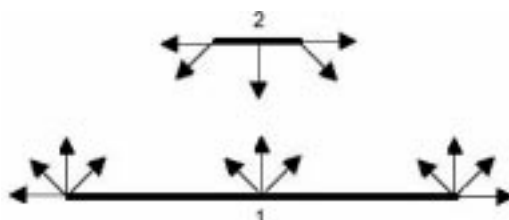
View factor

Let us consider exchange of radiation between two black surfaces 1 and 2 shown in Fig. 5.21. Obviously only a fraction of radiation emitted by surface 1 will be intercepted by surface 2 and vice versa. So radiation energy transferred from 1 to 2 and 2 to 1 can be written as

$$Q_{1 \rightarrow 2} = q_{b1} A_1 F_{12}$$

$$Q_{2 \rightarrow 1} = q_{b2} A_2 F_{21}$$

where F_{12} is the fraction of radiation energy emitted by the unit area of surface 1 which is intercepted or viewed by surface 2 and F_{21} is the fraction of radiation energy emitted by the unit area of surface 2 which is intercepted by surface 1. These are known as the *view factor*. The view factor is a geometric factor and can be calculated analytically. The plots of these values for different geometries



5.21 Radiation exchange between two black bodies.

are available in textbooks on heat transfer. It can easily be proved that the fraction of total energy emitted by surface 1 and intercepted by surface 2 is equal to fraction of total energy emitted by surface 2 and intercepted by surface 1. Or $A_1F_{12} = A_2F_{21}$. This is known as the *reciprocity relation*. Hence net exchange of radiation energy between 1 and 2 is

$$Q_{1 \rightarrow 2} = Q_{1 \rightarrow 2} - Q_{2 \rightarrow 1} = A_1F_{12}(q_{b1} - q_{b2}) = A_2F_{21}(q_{b1} - q_{b2}) \quad (5.91)$$

The definition of the view factor indicates that the view factor for two large parallel plates of equal dimension separated by a small distance is unity since radiation emitted by one plate is fully intercepted by the other. Also, if an object 1 with surface area A_1 is surrounded by object 2 having surface area A_2 , $F_{12} = 1$ since all radiations emitted by surface 1 are intercepted by 2, but $F_{21} < 1$. Using the reciprocity relation, $F_{21} = A_1/A_2$. Since the view factor is the fraction of radiation emitted by a surface and intercepted by another surface, then if a surface 1 is enclosed by surfaces 2, 3, ... n

$$F_{11} + F_{12} + F_{13} + \dots + F_{1n} = 1 \quad (5.92)$$

If the surface 1 is convex, it will not intercept any radiation emitted by itself and $F_{11} = 0$.

Heat exchange between grey bodies

Real bodies are considered as grey bodies where $\alpha < 1$. So when radiation falls on a grey body, a part is reflected back and treatment becomes complex because of multiple reflection of radiation between surfaces. To overcome this problem, we define G as total incident radiation flux on a surface (Wm^{-2}) and J as the total radiation flux leaving the surface (Wm^{-2}). Obviously J has two components, namely radiation emitted by the surface, ϵq_b , and radiation reflected by the surface, ρG . J is known as *radiosity*. So

$$J = \epsilon q_b + \rho G$$

Using equation 5.85 and 5.88,

$$\rho = 1 - \epsilon$$

Hence,

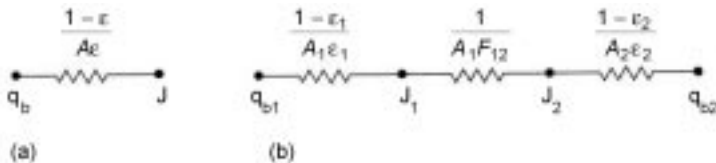
$$J = \epsilon q_b + (1 - \epsilon)G \quad (5.93)$$

Net heat flux leaving the surface is

$$q_{\text{net}} = J - G$$

Substituting the value of G from equation 5.93

$$q_{\text{net}} = \frac{\epsilon}{1 - \epsilon} (q_b - J)$$



5.22 Electrical analogue of radiation heat exchange between grey bodies. (a) Net heat flow from a surface of area A. (b) Heat exchange between two grey bodies.

Therefore net heat flow from a surface of area A is

$$Q_{\text{net}} = \frac{\epsilon}{1-\epsilon} A (q_b - J) \quad (5.94)$$

Using an electrical analogue, net heat flow can be considered as current. The driving force for net heat flow from a surface is $(q_b - J)$ and the resistance is $(1 - \epsilon)/(A\epsilon)$. Figure 5.22(a) shows the electrical analogue for a grey surface.

Now let us consider radiative energy exchange between two grey bodies 1 and 2.

$$Q_{1-2} = Q_{1 \rightarrow 2} Q_{2 \rightarrow 1} = A_1 F_{12} J_1 - A_2 F_{21} J_2$$

Using the reciprocity theorem, the above equation can be written as

$$Q_{1-2} = \frac{J_1 - J_2}{\frac{1}{A_1 F_{12}}} \quad (5.95)$$

Using the electrical analogue, the numerator of the above equation can be identified as the driving force and the denominator as the resistance for heat exchange. To evaluate J_1 and J_2 and thereby Q_{1-2} , we draw the electrical analogue of heat exchange between two grey bodies, shown in Fig. 5.22(b). It shows that the driving force heat flow from surface 1 is $(q_{b1} - J_1)$ and resistance is $(1 - \epsilon_1)/(A_1\epsilon_1)$ (equation 5.94). The driving force for heat exchange between surfaces 1 and 2 is $(J_1 - J_2)$ and resistance is $(1/A_1F_{12})$ (equation 5.95) and finally the driving force for heat flow to surface 2 is $(J_2 - q_{b2})$ and the resistance is $(1 - \epsilon_2)/(A_2\epsilon_2)$. So

$$Q_{1-2} = \frac{q_{b1} - q_{b2}}{\frac{1-\epsilon_1}{A_1\epsilon_1} + \frac{1}{A_1F_{12}} + \frac{1-\epsilon_2}{A_2\epsilon_2}} \quad (5.96)$$

It can be noted that the above equation reduces to equation 5.91 for black bodies.

Let us consider two large parallel plates of equal size separated by a short distance. Here $A_1 = A_2 = A$ and $F_{12} = 1$, hence equation 5.96 simplifies to

$$Q_{1-2} = \frac{A(q_{b1} - q_{b2})}{\frac{1}{\epsilon_1} - 1 + \frac{1}{\epsilon_2}} \quad (5.97)$$

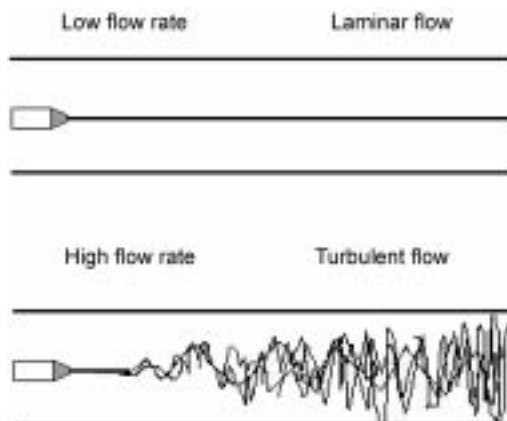
Quite often, we encounter the problem where a small convex grey body is enclosed in an isothermal enclosure. The latter can be treated as a cavity or a black body. Considering the grey body as surface 1 and the enclosure as surface 2, $F_{12} = 1$ and $\epsilon_2 = 1$, so equation 5.96 simplifies to

$$Q_{1-2} = A_1 \epsilon_1 (q_{b1} - q_{b2}) \quad (5.98)$$

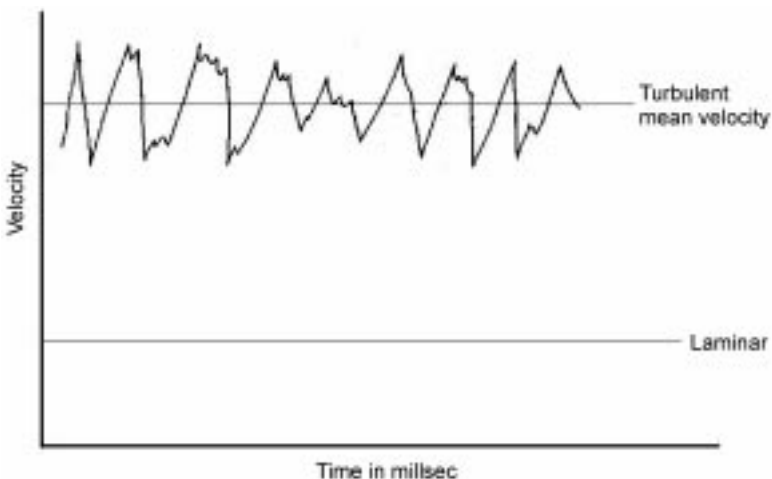
In a real system, gases are mostly present. So heat exchange by radiation between surfaces takes place through them. Gases with symmetric molecules like He, H₂, O₂, N₂, etc. are transparent to thermal radiation so their presence does not affect heat exchange by radiation. But CO, CO₂, H₂O, SO₂, NH₃, HCl, etc. are not transparent to thermal radiation. They absorb and emit thermal radiation in some narrow bands of wavelengths. For example, CO₂ absorbs radiation in wavelength ranges of 2.4–3, 4–4.8 and 12.5–16.5 μm. So if these gases are present in significant amount as in the case of fuel-fired furnaces, their effect on radiation heat exchange cannot be neglected.

5.4 Fluid flow

If we allow water to flow through a long horizontal glass tube and inject a dye into it, we will notice that the dye moves in a straight line at low flow rates of water. But the dye gets dispersed throughout the cross-section of the tube at a short distance from the entry point at high flow rates. Figure 5.23 schematically shows behaviour of dye. This experiment was first performed by Osborne Reynolds in 1883 to show that there are two types of flow behaviour of a fluid. At low flow rates, fluid elements maintain their own path. But at high flow rate, swirling or circular motion is generated within small packets of fluids, known as eddies. These eddies move in random fashion within the fluid and are continuously formed and destroyed by interaction with the surrounding fluid.



5.23 Behaviour of dye streak injected with water in a horizontal tube.



5.24 Schematic diagram of laminar and turbulent velocity at a point at steady state.

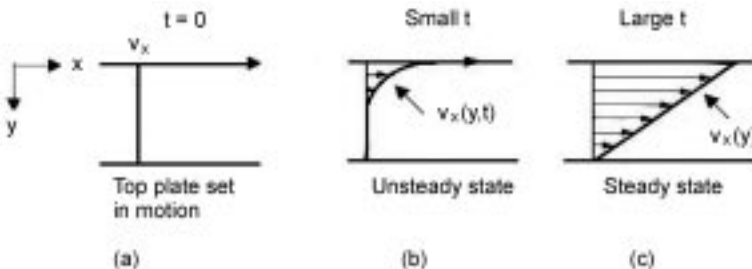
This leads to rapid mixing of dye. The size of eddies can vary from fractions of a millimetre to fairly large values. The first type of flow is known as laminar flow and the second type is known as turbulent flow. Figure 5.24 shows schematically the velocity at a point in laminar and turbulent flow at steady state. Turbulent velocity at a point fluctuates about a mean value because of movements of eddies. This fluctuation is often 20–30% of the mean value.

The transition from laminar to turbulent does not take place suddenly. As velocity is increased a transition region occurs, when the flow becomes unstable and forms local turbulent spots or eddies. With further increases in velocity, local turbulent spots spread and finally the flow becomes fully developed turbulent flow. In the transition region, the dye streak in the pipe flow becomes wavy.

Although most of the flows of metallurgical systems are turbulent, in the present section we will primarily discuss laminar flow.

5.4.1 Newton's law of viscosity

Let us consider a liquid between two parallel plates as shown in Fig. 5.25(a). Initially the liquid is at rest and at time $t = 0$, the top plate is given a constant velocity v_x . The fluid, which is in contact with the top plate, moves with the velocity v_x . The top layer of liquid drags the layer just below it. Similarly this layer in turn drags the layer below it and this continues. Figure 5.25(b) shows the velocity profile after a short time where velocity profile is changing with time. Figure 5.25(c) shows the steady state velocity profile. The velocity of any layer is less than that of the upper one and the velocity of the bottom layer,



5.25 Velocity profile of fluid between two parallel flat plates. (a) At $t = 0$, top plate is set to motion with velocity v_x . (b) Velocity profile after a short time, unsteady state. (c) Velocity profile at steady state.

which is in contact with the stationary plate, is zero. The motion of the top plate has resulted in x momentum (or x component of momentum) which travelled in y direction due to viscous drag. This momentum flux (amount of momentum transferred per unit area per unit time in a direction normal to the area) is given by:

$$\tau_{yx} = -\mu \frac{dv_x}{dy} \quad (5.99)$$

where μ is the viscosity of fluid. The negative sign in the equation shows that the direction of momentum transfer is from high velocity to low velocity. Equation 5.99 is Newton's law of viscosity. The above equation has another meaning. To move the top plate with velocity v_x , a shear force has to be applied. This shear force per unit area or shear stress is τ_{yx} . The subscript yx indicates that the shear force is in x direction and is acting on a plane of constant y . The unit of shear stress is Pa or $\text{kgm}^{-1}\text{s}^{-2}$, the same as that of momentum flux, and the unit of viscosity is $\text{kgm}^{-1}\text{s}^{-1}$ or Pa.s. The fluids that obey this law, i.e. the fluids for which μ is independent of shear rate, (dv_x/dy) , is known as Newtonian fluid. All gases and most of the simple liquids follow Newton's law.

When τ_{yx} is considered as momentum flux, y gives the direction of momentum flux and x the component of momentum. On the other hand when τ_{yx} is considered as shear stress, it is in the x direction and is acting on a fluid surface of constant y . So the direction of momentum flux and shear stress are not the same. Shear stress is always in the direction of velocity or momentum component.

Although equation 5.99 has the same form as that of mass flux given by equation 5.3 or heat flux (equation 5.57), there is a basic difference between this equation and other two. Velocity is a vector but temperature and concentration are scalar. So the heat and mass fluxes are vectors and have three components but the double suffix in τ_{yx} indicates that in three-dimensional problem τ has nine components and it is the stress tensor.

Example 5.9

Two flat plates of area 0.06 m^2 are 0.05 mm apart (Fig. 5.25). The space between the plates is filled by a lubricating oil of viscosity $0.2 \text{ kgm}^{-1}\text{s}^{-1}$. The lower plate is stationary and the upper plate moves with a velocity of 20 mm/s . Calculate the momentum flux from the upper to lower plate at the steady state. What is the force required to keep the upper plate moving?

Solution

At the steady state, the velocity profile is linear as shown in Fig. 5.24. Taking the top plate as $y = 0$,

$$\frac{dv_x}{dy} = (0 - 20 \times 10^{-3}) / (0.05 \times 10^{-3}) = -400 \text{ s}^{-1}$$

Momentum flux

$$\tau_{yx} = -0.2 \times (-400) = 80 \text{ kgm}^{-1}\text{s}^{-2}$$

τ_{yx} is the shear force on the top plate. So the force required to keep the plate moving is

$$\begin{aligned} F &= \tau_{yx} \times \text{area of plate} \\ &= 80 \times 0.06 = 4.8 \text{ N} \end{aligned}$$



5.4.2 Viscosity of gases and liquid

The kinetic theory of gases shows that viscosity of gases is directly proportional to the square root of temperature and independent of pressure. The latter is found to be true when pressure is less than 10 atmospheres but exponents of temperature for real gases are higher. The temperature dependence of viscosity is

$$\mu = \mu_0 (T/T_0)^n \quad (5.100)$$

where μ and μ_0 are viscosity at temperature T and T_0 respectively. The exponent n lies in the range 0.6–1.0.

Table 5.10 gives the viscosity of some common gases

Table 5.10 Viscosity of gases ($\text{kgm}^{-1}\text{s}^{-1}$ or Pa.s)

Gas	H_2	H_2O	CO	CO_2	Air
$\mu \times 10^5$ at 400K	1.09	1.32	2.21	1.94	2.29
$\mu \times 10^5$ at 800K	1.77	2.95	3.54	3.39	3.64

Viscosity of liquids

Viscosities of liquids vary widely depending on the nature of liquid. Viscosities of water and liquid metal are very low but that of slag and some of the organic liquids are very high. Viscosity of liquid decreases with temperature. Table 5.11 shows the viscosity of several liquids.

Table 5.11 Viscosity of liquids ($\text{kgm}^{-1} \text{s}^{-1}$ or Pa.s)

Material	Viscosity
Water at 293K	0.86×10^{-3}
Glycerin at 293K	1.49
Lead at 700K	2.15×10^{-3}
Iron at 2000K	5.6×10^{-3}
Slags	0.1–10

5.4.3 Conservation of momentum

Quite often, we need to find out the velocity distribution in a system. This is obtained by solving the equation of continuity or conservation of mass and conservation of momentum or equation of motion. These equations are

Rate of mass accumulation = rate of mass in – rate of mass out

Rate of momentum accumulation = rate in – rate out
+ sum of forces acting on system

In Sections 5.2.3 and 5.3.3 we have derived the conservation of mass and heat in a differential volume. Following the same procedure, the equation of continuity and conservation of momentum can be derived. The final form of these equations for incompressible Newtonian fluids in different coordinate systems is given in Tables 5.12 and 5.13. The equation of motion given in Table 5.13 is known as *Navier–Stokes* equation. Since all liquids are incompressible and even gases can be considered as incompressible if the velocity is much less than that of sound, these equations have a very wide applicability. The equation of motion contains four unknowns, three components of velocity and pressure. The three equations of motion given in Table 5.13 along with the equation of continuity given in Table 5.12 are the required four equations for the four unknowns.

Flow through a pipe

Let us consider steady state liquid flow through a horizontal pipe as an example of the application of the equation of motion. The flow is laminar and we are

Table 5.12 Equation of continuity for incompressible fluid

Rectangular coordinates

$$\frac{\partial v_x}{\partial x} + \frac{\partial v_y}{\partial y} + \frac{\partial v_z}{\partial z} = 0 \quad [\text{A}]$$

Cylindrical coordinates

$$\frac{1}{r} \frac{\partial}{\partial r} (rv_r) + \frac{1}{r} \frac{\partial v_\theta}{\partial \theta} + \frac{\partial v_z}{\partial z} = 0 \quad [\text{B}]$$

Spherical coordinates

$$\frac{1}{r^2} \frac{\partial}{\partial r} (r^2 v_r) + \frac{1}{r \sin \theta} \frac{\partial}{\partial \theta} (v_\theta \sin \theta) + \frac{1}{r \sin \theta} \frac{\partial v_\phi}{\partial \phi} = 0 \quad [\text{C}]$$

interested in the velocity profile away from the entrance zone where the entrance effect is absent and the flow is fully developed. Since the system is cylindrical, we use a cylindrical coordinate system. Fluid flows in the z direction, so velocity components in the radial and θ direction, v_r and v_θ are zero. Using the above considerations, the equation of continuity in Table 5.12, equation B, simplifies to

$$\frac{\partial v_z}{\partial z} = 0 \quad (5.101)$$

The above equation indicates that v_z is independent of z .

The relevant equation of motion is equation F in Table 5.13. This equation gets simplified for the following reasons:

- (a) Cylindrical symmetry suggests that v_z is independent of θ and the equation of continuity, equation 5.101, shows that v_z is independent of z . So all derivatives of v_z with respect to z and θ are zero.

Table 5.13 Equation for motion for Newtonian fluid with constant ρ and μ

Rectangular coordinates

x component

$$\rho \left[\frac{\partial v_x}{\partial t} + v_x \frac{\partial v_x}{\partial x} + v_y \frac{\partial v_x}{\partial y} + v_z \frac{\partial v_x}{\partial z} \right] = \mu \left[\frac{\partial^2 v_x}{\partial x^2} + \frac{\partial^2 v_x}{\partial y^2} + \frac{\partial^2 v_x}{\partial z^2} \right] - \frac{\partial p}{\partial x} + \rho g_x \quad [\text{A}]$$

y component

$$\rho \left[\frac{\partial v_y}{\partial t} + v_x \frac{\partial v_y}{\partial x} + v_y \frac{\partial v_y}{\partial y} + v_z \frac{\partial v_y}{\partial z} \right] = \mu \left[\frac{\partial^2 v_y}{\partial x^2} + \frac{\partial^2 v_y}{\partial y^2} + \frac{\partial^2 v_y}{\partial z^2} \right] - \frac{\partial p}{\partial y} + \rho g_y \quad [\text{B}]$$

z component

$$\rho \left[\frac{\partial v_z}{\partial t} + v_x \frac{\partial v_z}{\partial x} + v_y \frac{\partial v_z}{\partial y} + v_z \frac{\partial v_z}{\partial z} \right] = \mu \left[\frac{\partial^2 v_z}{\partial x^2} + \frac{\partial^2 v_z}{\partial y^2} + \frac{\partial^2 v_z}{\partial z^2} \right] - \frac{\partial p}{\partial z} + \rho g_z \quad [\text{C}]$$

Table 5.13 Continued

Cylindrical coordinates
r component

$$\begin{aligned} \rho & \left[\frac{\partial v_r}{\partial t} + v_r \frac{\partial v_r}{\partial r} + \frac{v_\theta}{r} \frac{\partial v_r}{\partial \theta} - \frac{v_\theta^2}{r} + v_z \frac{\partial v_r}{\partial z} \right] \\ & = \mu \left[\frac{\partial}{\partial r} \left\{ \frac{1}{r} \frac{\partial}{\partial r} (rv_r) \right\} + \frac{1}{r^2} \frac{\partial^2 v_r}{\partial \theta^2} - \frac{2}{r^2} \frac{\partial v_\theta}{\partial \theta} + \frac{\partial^2 v_r}{\partial z^2} \right] - \frac{\partial p}{\partial r} + \rho g_r \end{aligned} \quad [D]$$

θ component

$$\begin{aligned} \rho & \left[\frac{\partial v_\theta}{\partial t} + v_r \frac{\partial v_\theta}{\partial r} + \frac{v_\theta}{r} \frac{\partial v_\theta}{\partial \theta} + \frac{v_r v_\theta}{r} + v_z \frac{\partial v_\theta}{\partial z} \right] \\ & = \mu \left[\frac{\partial}{\partial r} \left\{ \frac{1}{r} \frac{\partial}{\partial r} (rv_\theta) \right\} + \frac{1}{r^2} \frac{\partial^2 v_\theta}{\partial \theta^2} + \frac{2}{r^2} \frac{\partial v_r}{\partial \theta} + \frac{\partial^2 v_\theta}{\partial z^2} \right] - \frac{1}{r} \frac{\partial p}{\partial \theta} + \rho g_\theta \end{aligned} \quad [E]$$

z component

$$\begin{aligned} \rho & \left[\frac{\partial v_z}{\partial t} + v_r \frac{\partial v_z}{\partial r} + \frac{v_\theta}{r} \frac{\partial v_z}{\partial \theta} + v_z \frac{\partial v_z}{\partial z} \right] \\ & = \mu \left[\frac{1}{r} \frac{\partial}{\partial r} \left\{ r \frac{\partial v_z}{\partial r} \right\} + \frac{1}{r^2} \frac{\partial^2 v_z}{\partial \theta^2} + \frac{\partial^2 v_z}{\partial z^2} \right] - \frac{\partial p}{\partial z} + \rho g_z \end{aligned} \quad [F]$$

Spherical coordinates

r component

$$\begin{aligned} \rho & \left[\frac{\partial v_r}{\partial t} + v_r \frac{\partial v_r}{\partial r} + \frac{v_\theta}{r} \frac{\partial v_r}{\partial \theta} + \frac{v_\phi}{r \sin \theta} \frac{\partial v_r}{\partial \phi} - \frac{(v_\theta^2 + v_\phi^2)}{r} \right] \\ & = \mu \left[\nabla^2 v_r - \frac{2}{r^2} v_r - \frac{2}{r^2} \frac{\partial v_\theta}{\partial \theta} - \frac{2}{r^2} v_\theta \cot \theta - \frac{2}{r^2 \sin \theta} \frac{\partial v_\phi}{\partial \phi} \right] - \frac{\partial p}{\partial r} + \rho g_r \end{aligned} \quad [G]$$

θ component

$$\begin{aligned} \rho & \left[\frac{\partial v_\theta}{\partial t} + v_r \frac{\partial v_\theta}{\partial r} + \frac{v_\theta}{r} \frac{\partial v_\theta}{\partial \theta} + \frac{v_\phi}{r \sin \theta} \frac{\partial v_\theta}{\partial \phi} + \frac{v_r v_\theta}{r} - \frac{v_\phi^2 \cot \theta}{r} \right] \\ & = \mu \left[\nabla^2 v_\theta + \frac{2}{r^2} \frac{\partial v_r}{\partial \theta} - \frac{v_\theta}{r^2 \sin^2 \theta} - \frac{2 \cos \theta}{r^2 \sin^2 \theta} \frac{\partial v_\phi}{\partial \phi} \right] - \frac{1}{r} \frac{\partial p}{\partial \theta} + \rho g_\theta \end{aligned} \quad [H]$$

ϕ component

$$\begin{aligned} \rho & \left[\frac{\partial v_\phi}{\partial t} + v_r \frac{\partial v_\phi}{\partial r} + \frac{v_\theta}{r} \frac{\partial v_\phi}{\partial \theta} + \frac{v_\phi}{r \sin \theta} \frac{\partial v_\phi}{\partial \phi} + \frac{v_r v_\phi}{r} + \frac{v_\theta v_\phi \cot \theta}{r} \right] \\ & = \mu \left[\nabla^2 v_\phi + \frac{2}{r^2 \sin \theta} \frac{\partial v_r}{\partial \phi} - \frac{v_\phi}{r^2 \sin^2 \theta} + \frac{2 \cos \theta}{r^2 \sin^2 \theta} \frac{\partial v_\theta}{\partial \phi} \right] - \frac{1}{r \sin \theta} \frac{\partial p}{\partial \phi} + \rho g_\phi \end{aligned} \quad [I]$$

$$\nabla^2 = \frac{1}{r^2} \frac{\partial}{\partial r} \left(r^2 \frac{\partial}{\partial r} \right) + \frac{1}{r^2 \sin \theta} \frac{\partial}{\partial \theta} \left(\sin \theta \frac{\partial}{\partial \theta} \right) + \frac{1}{r^2 \sin^2 \theta} \frac{\partial^2}{\partial \phi^2}$$

- (b) Since we are considering steady state, the time derivative is zero.
- (c) For a horizontal pipe, the component of acceleration due to gravity in z direction g_z is zero.
- (d) Velocity components in radial and θ direction, v_r and v_θ are zero.

So the z component of the equation of motion in the cylindrical coordinate simplifies to

$$\mu \frac{1}{r} \frac{d}{dr} \left(r \frac{dv_z}{dr} \right) = \frac{dp}{dz} \quad (5.102)$$

Since v_z is a function of r only, the partial derivative is replaced by the total. Integrating,

$$\mu r \frac{dv_z}{dr} = \frac{r^2}{2} \frac{dp}{dz} + C_1$$

Integrating again,

$$\mu v_z = \frac{r^2}{4} \frac{dp}{dz} + C_1 \ln r + C_2$$

The boundary conditions are

At $r = 0$, v_z is finite

At $r = r_0$, $v_z = 0$

Using the above conditions,

$$C_1 = 0 \quad \text{and} \quad C_2 = -\frac{r_0^2}{4} \frac{dp}{dz}$$

Hence

$$v_z = \frac{r^2 - r_0^2}{4\mu} \frac{dp}{dz} \quad (5.103)$$

If the length of pipe is L , and inlet and outlet pressures are P_0 and P_L respectively, $dp/dz = (P_L - P_0)/L$. So the above equation can be written as

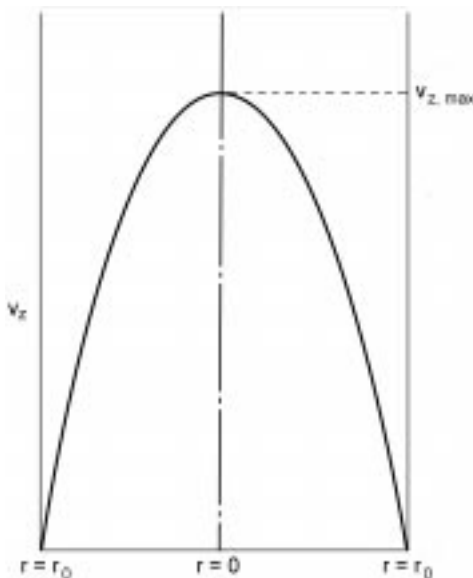
$$v_z = \frac{(r_0^2 - r^2)(P_0 - P_L)}{4\mu L} \quad (5.104)$$

Figure 5.26 shows the parabolic velocity profile. The maximum velocity is at $r = 0$ and has the value

$$v_{z,\max} = \frac{r_0^2(P_0 - P_L)}{4\mu L} \quad (5.105)$$

Volumetric flow rate is given by

$$Q = \int_0^{r_0} 2\pi r v_z dr = \frac{\pi(P_0 - P_L)r_0^4}{8\mu L} \quad (5.106)$$



5.26 Velocity profile of laminar flow in a pipe.

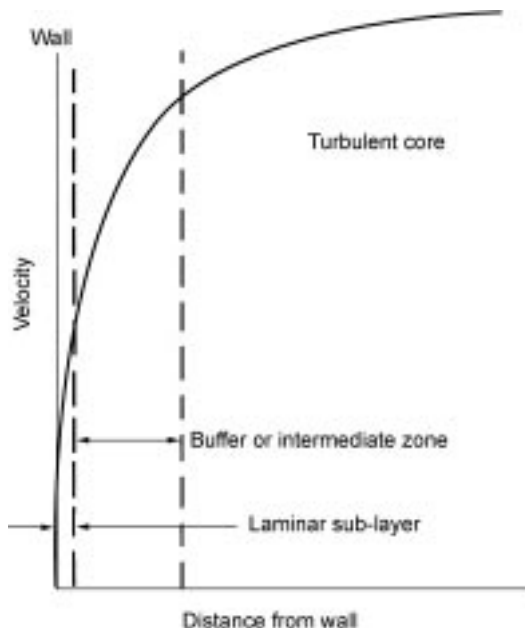
Equation 5.106 is known as the Hagen–Poiseuille law.

The shear force of fluid on the pipe wall is

$$F_z = 2\pi r_0 L \left(-\mu \frac{dv_z}{dr} \right)_{r=r_0} = \pi r_0^2 (P_0 - P_L) \quad (5.107)$$

This shows that viscous force counterbalances the force acting on the fluid. When fluid flows through a vertical pipe, viscous forces counterbalance force due to gravity and pressure.

The above equations are valid for laminar flow, which is obtained for Reynolds number $Re = \rho v_{z,av} D / \mu$, where $D = 2r_0$ and average velocity $v_{z,av} = Q / (\pi r_0^2)$, is less than 2100. Besides, there is no entrance effect. A distance of $L_c = 0.0567 D Re$ is required for the development of the parabolic profile given by equation 5.104. Although the critical Reynolds number for transition from laminar flow is normally taken as 2100, pipe flow can be maintained laminarly even at much higher Reynolds numbers in controlled experiments where all external disturbances are avoided. When the Reynolds number is more than 10,000 the flow is fully turbulent. However, even when the flow is turbulent, it is not turbulent near the wall. Figure 5.27 schematically shows the velocity profile near the wall. Close to the wall, the viscous forces dominate and the flow is laminar. This layer is known as the viscous sub-layer or laminar sub-layer. Some distance away from the wall, the velocity profile is relatively flat. This region is the turbulent core or fully developed turbulent flow. The intermediate region is known as the buffer or intermediate zone. Eddies are generated here. The



5.27 Velocity profile near wall in turbulent flow.

thickness of buffer layer is about six times more than that of viscous sub-layer and total thickness of these two layers is less than a millimetre.

When the flow is fully turbulent velocity distribution follows the relation

$$\frac{v_z}{v_{z,\max}} = \left(1 - \frac{r}{r_0}\right)^{1/7} \quad (5.108)$$

In the case of laminar flow $v_{z,\max}/v_{z,\text{av}} = 2$ and for turbulent flow it is $5/4$.

Example 5.9

Calculate the maximum flow rate of water through a pipe of diameter 20 mm when the parabolic velocity profile given by equation 5.104 is applicable. What is the corresponding pressure drop per metre length of pipe. Assume viscosity and density of water as $0.86 \times 10^{-3} \text{ kgm}^{-1}\text{s}^{-1}$ and 1000 kgm^{-3} respectively.

Solution

Equation 5.104 is valid if Re is less than 2100 or $\rho v_{z,\text{av}} D / \mu = 2100$,

$$\begin{aligned} v_{z,\text{av}} &= (2100 \times 0.86 \times 10^{-3}) / (1000 \times 20 \times 10^{-3}) \\ &= 0.09 \text{ m/s} = 90 \text{ mm/s} \end{aligned}$$

$$\text{Flow rate } Q = \pi r_0^2 v_{z,\text{av}} = 28.3 \times 10^{-6} \text{ m}^3/\text{s}$$

From equation 5.106

$$(P_0 - P_L)/L = (8\mu Q)/(\pi r_0^4)$$

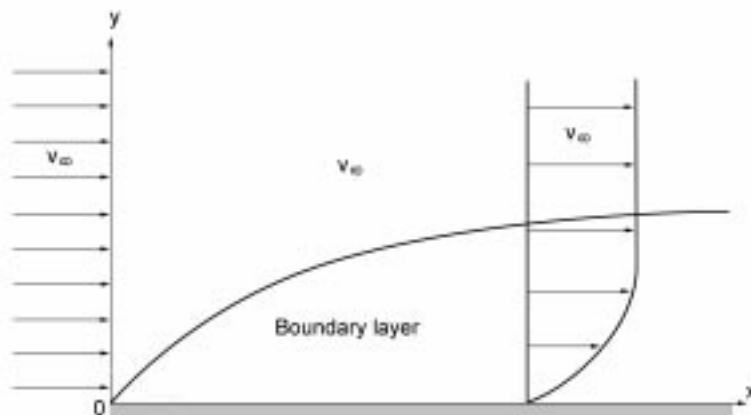
$$= (8 \times 0.86 \times 10^{-3} \times 28.3 \times 10^{-6})/(\pi \times 0.01^4) = 6.2 \text{ Pa}$$

Since kinematic viscosity of water μ/ρ is very low about $10^{-6} \text{ m}^2/\text{s}$, flow is turbulent at a very low flow rate. Liquid metals also have similar low values of kinematic viscosity, so the flow of liquid metal is mostly turbulent. ■■■

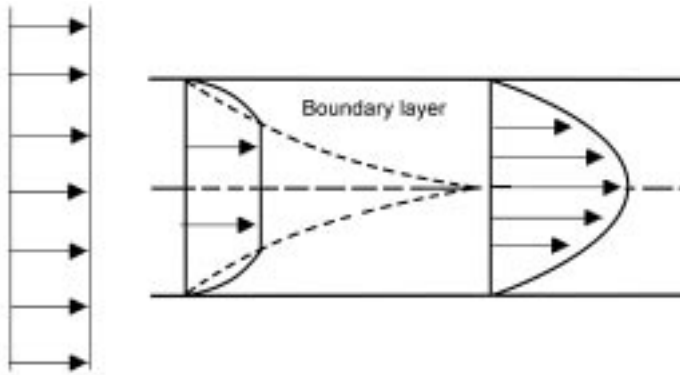
Flow over a flat plate

When a fluid flows over an immersed body, such as a flat plate, the velocity of fluid at the solid–fluid interface is same as that of the immersed body. Viscous forces affect the flow near the solid surface but further away the flow is almost inviscid and velocity is same as that of the free stream. This layer where the velocity of fluid changes from that of the solid to the free stream is known as the boundary layer and this type of flow is known as the boundary layer flow. Figure 5.28 schematically shows the velocity profile over a flat plate. The boundary layer thickness is zero initially and it grows as the fluid moves along the plate. In the case of flow through a duct, the viscous boundary layers grow from the walls and fill the entire duct. So, except at the entrance region, there is no boundary layer separating viscous and inviscid flow, as shown in Fig. 5.29. Flow beyond the entrance region is fully developed flow.

Let us assume that the fluid stream is approaching the stationary flat plate at a uniform velocity v_∞ . The flow is in the x direction. The z direction is normal to the paper. On the left side of the plate the fluid velocity is uniform, $v_x = v_\infty$. But over the entire surface of the plate ($y = 0$), v_x is zero because there is no slip condition and in the entire boundary layer $v_x < v_\infty$. The fluid whose velocity has decreased moves up and this gives rise to the small v_y component in the



5.28 Flow over a flat plate.



5.29 Velocity profile at the entrance region in a duct.

boundary layer. Thereby within the boundary layer there are two components of velocity v_x and v_y and outside the boundary layer there is only v_x . There is no velocity gradient in the z direction, so $\partial v_x / \partial z = \partial v_y / \partial z = 0$. Since it is a steady state problem, the time derivatives are zero. Besides, in the x direction gravity force is zero and we neglect gravity in the y direction. With these simplifications, the equation of continuity, equation A in Table 5.12, and the equations of motion for the x and y components, equations A and B in Table 5.13, in the boundary layer become

$$\rho \frac{\partial v_x}{\partial x} + \frac{\partial v_y}{\partial y} = 0 \quad (5.109a)$$

$$\rho \left[v_x \frac{\partial v_x}{\partial x} + v_y \frac{\partial v_x}{\partial y} \right] = \mu \left[\frac{\partial^2 v_x}{\partial x^2} + \frac{\partial^2 v_x}{\partial y^2} \right] - \frac{\partial p}{\partial x} \quad (5.109b)$$

$$\rho \left[v_x \frac{\partial v_y}{\partial x} + v_y \frac{\partial v_y}{\partial y} \right] = \mu \left[\frac{\partial^2 v_y}{\partial x^2} + \frac{\partial^2 v_y}{\partial y^2} \right] - \frac{\partial p}{\partial y} \quad (5.109c)$$

These equations should be solved for the unknowns v_x , v_y and p subject to no slip boundary condition on the surface of the plate and inlet and exit boundary conditions. These equations are too complex for analytical solution. However, the equations can be simplified from the following considerations:

1. $v_y \ll v_x$, so the y component of the momentum balance equation, 5.109c can be neglected.
2. The terms $\rho v_x \frac{\partial v_x}{\partial x}$ and $\mu \frac{\partial^2 v_x}{\partial x^2}$ in equation 5.109b are the net rate of x component of momentum transfer in the x direction due to bulk flow and viscous flow respectively. The term $\mu \frac{\partial^2 v_x}{\partial x^2}$ can be neglected since viscous diffusion is much smaller than the bulk flow.
3. $\partial p / \partial x$ is negligible.

So the above equations can be simplified to

$$\frac{\partial v_x}{\partial x} + \frac{\partial v_y}{\partial y} = 0 \quad (5.110a)$$

$$\rho \left[v_x \frac{\partial v_x}{\partial x} + v_y \frac{\partial v_x}{\partial y} \right] = \mu \frac{\partial^2 v_x}{\partial y^2} \quad (5.110b)$$

The boundary conditions for all x are

$$\text{At } y = 0, \quad v_x = v_y = 0 \quad (5.111a)$$

$$\text{At } y = \infty, \quad v_x = v_\infty \quad (5.111b)$$

$$\text{At } x = 0 \text{ for all } y, \quad v_x = v_\infty \quad (5.111c)$$

To solve the above equations let us define ‘stream function’ ψ as

$$v_x = \frac{\partial \psi}{\partial y} \quad \text{and} \quad v_y = -\frac{\partial \psi}{\partial x}$$

The substitution of v_x and v_y , defined above, in equation 5.110a shows that the stream function satisfies the equation of continuity so we need to solve only equation 5.110b, which becomes

$$\frac{\partial \psi}{\partial y} \frac{\partial^2 \psi}{\partial x \partial y} - \frac{\partial \psi}{\partial x} \frac{\partial^2 \psi}{\partial y^2} = \nu \frac{\partial^3 \psi}{\partial y^3} \quad (5.112)$$

where $\nu = (\mu/\rho)$ is the kinematic viscosity. To solve the above equation, let us define two dimensionless variables

$$f = \psi / (x\nu v_\infty)^{1/2} \quad (5.113)$$

$$\eta = y(v_\infty/x\nu)^{1/2} \quad (5.114)$$

In terms of these new variables, equation 5.112 becomes an ordinary differential equation.

$$ff'' + 2f''' = 0 \quad (5.115)$$

where

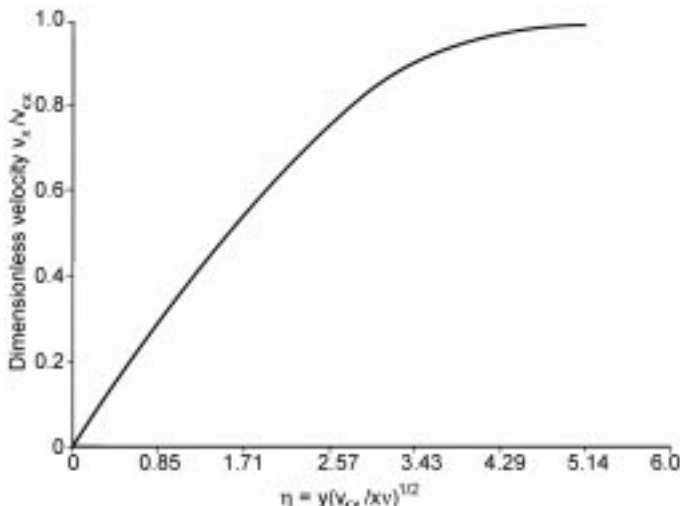
$$f' = \frac{df}{d\eta}$$

The boundary conditions given by equations 5.111(a, b, c) become

$$\text{At } \eta = 0, \quad f = f' = 0$$

$$\text{At } \eta = \infty, \quad f' = 1$$

Equation 5.115 indicates that f and thereby velocity is a function of η only. The equation was first solved by Blasius in 1908 by power series expansion. Figure 5.30 shows the results of numerical solution of the equation. The dimensionless velocity v_x/v_∞ rapidly increases with η and becomes almost unity at $\eta = 5$. The

5.30 Dimensionless velocity vs η .

boundary layer thickness δ is taken as the point where velocity is 99% of the free stream velocity or $v_x/v_\infty = 0.99$. This corresponds to $\eta \approx 5$, so

$$\delta(x) = 5(\nu x/v_\infty)^{1/2} \quad (5.116)$$

The boundary layer thickness grows along the length of flat plate following the square root law and the thickness is inversely proportional to the square root of the free stream velocity. In terms of the Reynolds number, equation 5.116 can be written as

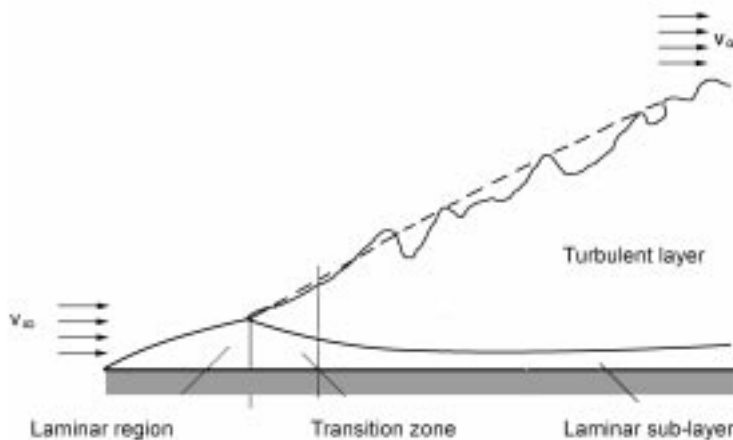
$$\delta(x)/x = 5/\text{Re}_x^{1/2} \quad (5.117)$$

where $\text{Re}_x = \rho v_\infty x / \mu$.

The above equation is valid when the Reynolds number is smaller than 5×10^5 and the flat surface is very smooth. As the fluid moves along the flat surface the Reynolds number increases and the flow becomes unstable which finally leads to a turbulent boundary layer when $\text{Re} > 5 \times 10^6$. Figure 5.31 shows the turbulent boundary layer. The turbulent boundary layer grows much faster along the length of the plate. Because of the fluctuating nature of turbulent flow the edge of boundary layer is not smooth.

Example 5.10

Calculate the boundary layer thickness at the trailing edge of a 0.5 m long plate, for (a) air, (b) water, and (c) mercury at 20 °C when the free stream velocity is 0.2 m/s. ν for air, water and mercury are 1.5×10^{-5} , 0.9×10^{-6} and 1.1×10^{-7} m^2/s , respectively.



5.31 Turbulent boundary layer.

Solution

- (a) For air, $Re_x = v_\infty x / \nu = 0.2 \times 0.5 / 1.5 \times 10^{-5} = 0.67 \times 10^4$
 Since $Re_x < 5 \times 10^5$, equation 5.117 is applicable and
 $\delta = 5 \times 0.5 / (0.67 \times 10^4)^{1/2} \text{ m} = 30.5 \text{ mm}$
- (b) For water, $Re_x = 0.2 \times 0.5 / 0.9 \times 10^{-6} = 1.11 \times 10^5$
 Since this is less than 10^{-6} , $\delta = 5 \times 0.5 / (1.11 \times 10^5)^{1/2} \text{ m} = 7.5 \text{ mm}$
- (c) For mercury, $Re_x = 0.2 \times 0.5 / 1.1 \times 10^{-7} = 0.91 \times 10^6$
 This value lies in the transition range, so the calculated value may not be correct if the plate is not very smooth and the flow is not quiet. However, assuming the equation is valid

$$\delta = 5 \times 0.5 / (0.91 \times 10^6)^{1/2} \text{ m} = 2.6 \text{ mm}$$

The boundary layer thickness is highest for air and lowest for mercury. δ for air is about four times more than that of water and about 11.5 times more than that of mercury. This is because $\nu_{\text{air}}/\nu_{\text{water}}$ is 16.6 and $\nu_{\text{air}}/\nu_{\text{mercury}}$ is 136. ■■■

Example 5.11

A 5 mm thick film of water is flowing over a flat plate of 1 m long. At what distance from the leading edge will the boundary layer thickness be the same as the film thickness. The free stream velocity at the leading edge is 0.5 m/s. ν for water is $0.9 \times 10^{-6} \text{ m}^2/\text{s}$

Solution

We want to know the value of x when $\delta = 5 \text{ mm} = 5 \times 10^{-3} \text{ m}$ and $v_\infty = 0.5 \text{ m/s}$. From equation 5.116

$$\delta(x) = 5(\nu x / v_\infty)^{1/2}$$

So

$$5 \times 10^{-3} = 5(0.9 \times 10^{-6} x/0.5)^{1/2}$$

or

$$x = 0.5/0.9 = 0.55 \text{ m}$$

So 0.55 m is the length of entrance zone. After this the flow is fully developed.



5.4.4 Friction factor and drag coefficient

When a fluid flows through a pipe, shear force acts on the pipe wall. This is called friction force and is defined as

$$F_k = \frac{1}{2} \rho v_{av}^2 f A \quad (5.118)$$

where v_{av} is the average velocity of the fluid, f is the friction factor and A is the surface area on which shear force is acting. For flow through a pipe, $A = \pi D L$. Since F_z defined by equation 5.107 and F_k defined by equation 5.118 are the same,

$$f = \frac{D}{4L} \frac{(P_0 - P_L)}{\frac{1}{2} \rho v_{av}^2} \quad (5.119)$$

By dimensional analysis it can be shown that for fully developed flow, friction factor f depends only on the Reynolds number. For flow in a long tube

$$f = 16/Re \quad Re < 2.1 \times 10^3 \quad (5.120a)$$

$$f = 0.079/(Re)^{1/4} \quad 2.1 \times 10^3 < Re < 10^5 \quad (5.120b)$$

Equation 5.120(a) is obtained from the Hagen–Poiseuille equation.

When the cross-section of pipe is not circular, the effective diameter is calculated using the concept of hydraulic radius. Hydraulic radius is defined as

$$R_h = (\text{cross-sectional area})/(\text{wetted perimeter}) \quad (5.121)$$

For circular tubing hydraulic radius is $D/4$. For non-circular tube equation 5.119 becomes

$$f = \frac{R_h}{L} \frac{(P_0 - P_L)}{\frac{1}{2} \rho v_{av}^2} \quad (5.122)$$

The concept of hydraulic radius is not applicable for laminar flow.

Flow around a sphere

When fluid flows over an immersed object, shear force acting on the fluid is called drag force and is defined as

$$F_k = \frac{1}{2} \rho v_\infty^2 C_D A_p \quad (5.123)$$

where v_∞ is the velocity far away from the immersed object, C_D is the drag coefficient and A_p is the projected area of the solid on the fluid. When fluid flows over a sphere of radius r at a very low flow rate such that the Reynolds number defined as $\rho v_\infty d_p / \mu < 0.1$

$$F_k = 6\pi\mu r v_\infty \quad (5.124)$$

This is known as Stokes law. From equations 5.123 and 5.124 and using $A_p = \pi d_p^2 / 4$ where d_p is the diameter of the sphere, we get

$$C_D = 24/\text{Re} \quad \text{Re} < 0.1 \quad (5.125)$$

For higher flow rates,

$$C_D = 18.5/(\text{Re})^{3/5} \quad 2 < \text{Re} < 5 \times 10^2 \quad (5.126a)$$

$$C_D = 0.44 \quad 5 \times 10^2 < \text{Re} < 2 \times 10^5 \quad (5.126b)$$

When the Reynolds number lies in the range 0.1 to 2 equation 5.125 is often used for estimation of drag force. Equation 5.126b is termed as Newton's Law.

Terminal velocity

Stokes law is often used to calculate the terminal velocity of particles or bubbles in a fluid medium. Let us assume that the density of the particles is greater than that of the fluid medium, so the particle falls down. The downward force acting on the particle is due to gravity and upward forces are buoyant force and drag force. Initially the velocity of the particle will go on increasing because of net downward force. But as velocity increases, the drag force also increases since it is directly proportional to velocity (see equation 5.124), and finally the upward and downward forces are balanced. This velocity, which is attained when the total force acting on the particle is zero, is the terminal velocity. The force balance equation is

$$\frac{4}{3}\pi r^3 (\rho - \rho_f)g = 6\pi\mu r v_t$$

ρ and ρ_f are, respectively, density of particle and fluid and v_t is the terminal velocity. The left-hand side of the above equation is the difference between gravity and buoyant force and the right-hand side is the drag force. So the terminal velocity is

$$v_t = \frac{2}{9} \frac{r^2 (\rho - \rho_f)g}{\mu} \quad (5.127)$$

Example 5.12

Calculate the terminal velocity when a sand particle of $10 \mu\text{m}$ diameter is falling through a water column. Density of sand and water are respectively 2500, 1000 kgm^{-3} respectively and viscosity of water is $9.6 \times 10^{-4} \text{ kgm}^{-1} \text{ s}^{-1}$.

Solution

Using equation 5.127 and $r = 0.5 \times 10^{-5} \text{ m}$

$$\begin{aligned} v_t &= [2 \times (0.5 \times 10^{-5})^2 \times (2500 \times 1000) \times 9.8] / (9 \times 9.6 \times 10^{-4}) \text{ m/s} \\ &= 0.085 \text{ mm/s} \end{aligned}$$

$$\text{Re} = 2500 \times 0.85 \times 10^{-4} \times 10^{-4} / 9.6 \times 10^{-4} = 0.022$$

Since Re is less than 0.1, calculated value of terminal velocity is correct.

*Correlations for packed bed*

The packed bed is made up of solids of different shapes and sizes. The fluid flows through the voids in the bed. In general, the distributions of voids and the particle sizes are not uniform throughout the bed. But for our discussion we assume that distributions of particles, voids and gas are uniform. If the bed is made of spheres of diameter d_p , the contact area between the fluid and solid per unit bed volume is

$$S_p = n 4\pi(d_p/2)^2 \quad (5.128)$$

where S_p is the specific surface area (m^2/m^3) and n is the number of particles per unit volume. Let ϵ be the void fraction in the bed. Then out of unit bed volume $(1 - \epsilon)$ is occupied by the particles and the rest is void. So

$$1 - \epsilon = n 4/3\pi(d_p/2)^3 \quad (5.129)$$

From equations 5.128 and 5.129

$$S_p = 6(1 - \epsilon)/d_p \quad (5.130)$$

If the bed is made up of mixed particle size, d_p is the mean particle size.

In the case of the packed bed, we define superficial velocity as the velocity of gas in the empty tube. Superficial velocity v_0 is related to true average velocity v_b of the gas through the void as

$$v_b = v_0/\epsilon \quad (5.131)$$

If we consider that gas flow through the packed bed is similar to gas flow through a pipe of variable cross-section, the pressure drop and friction factor are related by equation 5.122. Since the cross-section of tube is not constant, hydraulic radius can be defined as the ratio void volume per unit bed volume to

surface area of particles per unit bed volume,

$$R_h = \frac{\epsilon}{S_p} = \frac{d_p \epsilon}{6(1 - \epsilon)} \quad (5.132)$$

Substituting the value of R_h and v_b in equation 5.122

$$f = \frac{(P_0 - P_L)}{\rho v_0^2} \frac{d_p \epsilon^3}{3(1 - \epsilon)L}$$

The bed friction is defined as

$$f_b = \frac{f}{3} = \frac{(P_0 - P_L)}{\rho v_0^2} \frac{d_p \epsilon^3}{(1 - \epsilon)L} \quad (5.133)$$

In the laminar and turbulent flow region, f_b is related to the Reynolds number by

$$f_b = \frac{150}{Re_b} \quad Re_b < 20 \quad (5.134a)$$

$$f_b = 1.75 \quad 10^3 < Re_b < 10^4 \quad (5.134b)$$

where

$$Re_b = \frac{d_b \rho v_0}{\mu(1 - \epsilon)} \text{ is the Reynolds number for the packed bed.}$$

Equations 5.134a and 5.134b are respectively Kozeny–Carman and Burke–Plummer equations. The former is applicable in laminar flow. Ergun combined the above two equations:

$$f_b = \frac{150}{Re_b} + 1.75 \quad 1 < Re < 10^4 \quad (5.135)$$

This equation is known as Ergun's equation.

Combining equation 5.133 and Ergun's equation 5.135 and substituting for Re_b ,

$$\frac{P_0 - P_L}{L} = \left[\frac{150\mu(1 - \epsilon)}{d_b \rho v_0} + 1.75 \right] \frac{\rho v_0^2}{d_p} \frac{1 - \epsilon}{\epsilon^3} \quad (5.136)$$

The above equation shows that the pressure drop in a packed bed is very sensitive to bed porosity and particle size. A decrease in bed porosity or particle size increases pressure drop very significantly.

5.5 Further reading

R.I.L. Guthrie (1989) *Engineering in Process Metallurgy*, Oxford.

F.P. Incropera and D.P. DeWitt (1990) *Fundamentals of Heat and Mass Transfer*, John Wiley, New York.

D.R. Poirier and G.H. Geiger (1994) *Transport Phenomena in Materials Processing*, Publication of TMS.

5.6 References

- Darken, L.S. (1949) *Trans. A.I.M.E.*, vol. 180, 430.
Fuller, E.N., Schettler, P.D. and Giddings, J.C. (1966) *Ind. Eng. Chem.* Vol. 58 no. 5, 18.
Kucera, J. and Stransky, K. (1982) *Mater. Sc. Eng.*, Vol. 52, 1.
Morita, Zen-ichiro (1996) *ISIJ Int.*, Vol. 36, Supplement, S6.
Reid, R.C., Prausnitz, J.M. and Sherwood, T.K. (1977) *Properties of Gases and Liquids*,
3rd edn. McGraw-Hill, New York.

6

Interfacial phenomena, metals processing and properties

K MUKAI, Kyushu Institute of Technology, Japan

6.1 Introduction

We have obtained great technological and academic benefits from describing the nature of metals processing and also by controlling such processes with the aid of thermodynamics and kinetics of bulk phases such as gas, slag and metal. In order to achieve further progress in this area, it is necessary to understand the surface and interface, and to clarify the participation of interfacial phenomena in metallurgical processes. Surface and interfacial tensions of high temperature melts such as slag and steel in iron and steelmaking processes are about 5 to 20 times as large as that of water. In addition, the high temperature melts have remarkably strong surface active agents such as oxygen, sulfur, etc., which are inevitably included in the melts, as shown in Section 6.3.

The subject of interfacial phenomena in relation to iron and steelmaking processes has recently been one of the most attractive fields in metallurgy. There are a number of reasons for this. Further understanding of the kinetics in heterogeneous reactions in metallurgical systems requires more detailed information on interfacial phenomena that occur during the progress of these reactions. These phenomena can reveal more of the microscopic stages of kinetics than did the conventional treatments used in previous studies. Smelting and refining processes developed or improved recently often include various dispersion actions such as the injection of powder agents into liquid steel, degassing of liquid steel with RH, bubble injection through porous plug refractories and slag foaming in bath smelting or during pre-treatment of pig iron in torpedo cars. Control of non-metallic inclusion during the steel refining process is important for the production of much higher quality steels. Detailed information on interfacial phenomena is essential to advance practical operations in these processes.

It is very important to understand the fundamental treatments of the surface and the interface by using interfacial physical chemistry in order to clarify the interfacial phenomena and to apply the results to the improvement and development of metallurgical processing. Interfacial physical chemistry used here

means an academic field which treats interfacial phenomena by using surface chemistry, thermodynamics and kinetics. This is the subject matter for Section 6.2.

In Section 6.3 typical interfacial properties obtained by previous investigators are concisely introduced for the metallurgical systems containing liquid metal and slag.

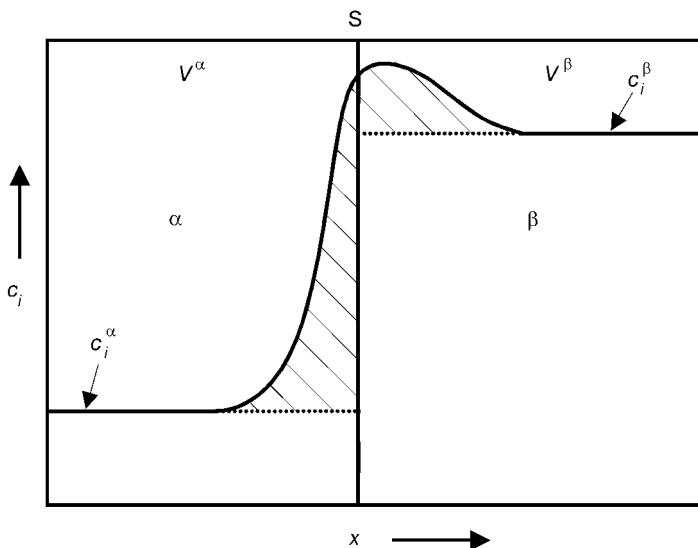
Section 6.4 focuses briefly on several interfacial phenomena which have been recently shown to participate or possibly participate in the processes of metal smelting and refining. Many technological problems have been linked with the interfacial phenomena.

6.2 Fundamentals of the interface

6.2.1 Thermodynamics of interface

Gibbs' dividing surface

Gibbs supposed a dividing surface S (see Fig. 6.1), in order to describe macroscopic surface properties. The dividing surface is always taken parallel to the surface of tension defined later in this section and the thickness of the surface is taken as zero. Figure 6.1 shows concentration distribution of component i , c_i (mol/m^3) in the real surface region and bulk phases of α and β . n_i is the total mole number of the component i , in the volume of $V^\alpha + V^\beta$. If we suppose that c_i^ν (concentration in ν ($= \alpha$ or β phase)) keeps constant from bulk



6.1 Gibbs' dividing surface.

phase ν to the dividing surface S, mole number of the component i in this area is equal to $c_i^\nu V^\nu$. Then, n_i^s given with equation 6.1 means excess mole number of component i at surface and corresponds to the shaded portion of Fig. 6.1:

$$n_i^s = n_i - (c_i^\alpha V^\alpha + c_i^\beta V^\beta) \quad (6.1)$$

Excess quantity per unit surface area, that is, n_i^s/A is called a surface excess quantity of component i , Γ_i (mol/m²), and expressed as equation 6.2:

$$n_i^s = A\Gamma_i \quad (6.2)$$

where A is the surface area.

Similarly the other surface excess quantities are defined in equations 6.3 to 6.6:

$$U^s = U - (u^\alpha V^\alpha + u^\beta V^\beta) \quad (6.3)$$

where U is internal energy and u^ν ($\nu = \alpha, \beta$) is internal energy per unit volume of the phase ν .

$$S^s = S - (s^\alpha V^\alpha + s^\beta V^\beta) \quad (6.4)$$

where S is entropy and s^ν is entropy per unit volume of phase ν .

$$F^s = F - (f^\alpha V^\alpha + f^\beta V^\beta) \quad (6.5)$$

where F is Helmholtz energy and f^ν is Helmholtz energy per unit volume of phase ν .

The surface excess quantities mentioned above can be understood to be the excess quantities which are altogether brought to the dividing surface with infinitesimal thickness. Therefore those excess quantities, for example, n_i^s , vary with the position of the dividing surface within the real surface region as shown in Fig. 6.1. The surface excess quantity is not the absolute value, besides that depends on the position of the dividing surface. In order to solve the above-mentioned inconveniences, Guggenheim introduced two dividing surfaces. However, his treatment is complicated and nowadays is not so popular.

Surface tension

Thermodynamic interpretation

When the surface area A of pure liquid increases by dA , dU^s , the change in internal energy at the surface, is given by equation 6.6:

$$dU^s = dQ^s + \gamma dA \quad (6.6)$$

where dQ^s is the heat absorbed by the surface, γdA means the work which acts on the surface at constant temperature by the change in the surface area dA , and γ is the surface tension which is described later.

For a reversible process,

$$dQ^s = TdS^s \quad (6.7)$$

therefore

$$dU^s = TdS^s + \gamma dA \quad (6.8)$$

Surface excess Helmholtz energy F^s , and its total differential, dF^s , are expressed by equations 6.9 and 6.10, respectively:

$$F^s = U^s - TS^s \quad (6.9)$$

$$dF^s = dU^s - TdS^s - S^s dT \quad (6.10)$$

Equation 6.11 is derived from equations 6.8 and 6.10:

$$dF^s = \gamma dA - S^s dT \quad (6.11)$$

Therefore,

$$f^s \equiv \left(\frac{\partial F^s}{\partial A} \right)_T = \gamma \quad (6.12)$$

Equation 6.12 means that surface tension γ is the surface excess Helmholtz energy per unit surface area. Therefore,

$$\gamma = f^s = u^s - Ts^s \quad (6.13)$$

Equation 6.13 indicates that surface tension contains the entropy term, Ts^s , as well as the internal energy term, u^s ($= U^s/A$), that is known as surface energy.

The relation between f^s and γ for an r -component liquid–gas system is given by equation 6.14:

$$f^s = \gamma + \sum_{i=1}^r \Gamma_i \mu_i \quad (6.14)$$

where $\mu_i = \left(\frac{\partial G}{\partial n_i} \right)_{T, P, n_j (j=1 \dots r, j \neq i)}$ is the chemical potential of the component i .

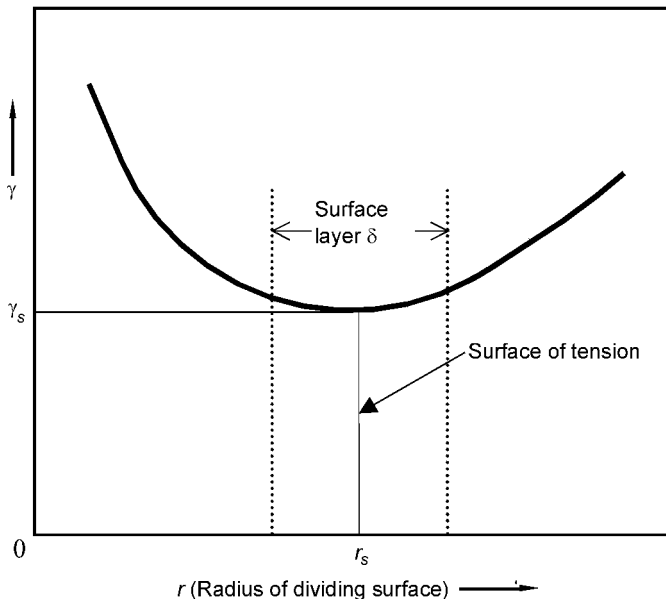
If we choose the dividing surface so as to make

$$\sum_{i=1}^r \Gamma_i \mu_i = 0$$

f^s is equal to γ from equation 6.14, even for an r -component liquid–gas system.

Position of dividing surface

It can be shown on thermodynamic grounds that the surface tension of a plane surface at thermodynamic equilibrium is not dependent upon the position of the



6.2 Relation between surface tension and radius of the dividing surface.

dividing surface. The surface tension of a curved surface, however, varies with the position of the dividing surface as shown in equation 6.15 and Fig. 6.2.

$$\gamma = \gamma_s \left(\frac{r_s^2}{3r^2} + \frac{2r}{3r_s} \right) \quad (6.15)$$

where r is the radius of the dividing surface. As shown in Fig. 6.2, the surface tension has a minimum γ_s at $r = r_s$. The dividing surface at $r = r_s$ is called the surface of tension. The surface of tension is within the surface layer δ (Fig. 6.2). Therefore when r_s is much larger than δ , γ should be regarded as almost constant within the surface layer from equation 6.16:

$$\gamma = \gamma_s (1 + \epsilon^2 + O(\epsilon^3)) \quad (6.16)$$

where $\epsilon = \delta/r_s$.

Radius of curvature

The surface tension γ_s at the surface of tension varies with the change in the radius of curvature r_s for the incompressible liquid as expressed with Tolman's equation 6.17:

$$\frac{\gamma_s}{\gamma_\infty} = 1/(2\lambda_0/r_s + 1) \quad (6.17)$$

where γ_∞ is the surface tension at $r_s \rightarrow \infty$ and λ_0 is the distance between surface of tension and the dividing surface at which $\sum'_{i=1} \Gamma_i \mu_i = 0$. If we take the value $\lambda_0 = 1.6 \times 10^{-10}$ m for water, γ_s/γ_∞ is calculated as follows from equation 6.17: $\gamma_s/\gamma_\infty = 0.997$ at $r_s = 100$ nm, $\gamma_s/\gamma_\infty = 0.97$ at $r_s = 10$ nm. These results indicate that we should take account of the dependency of surface tension on the radius of curvature for materials with the radii less than 100 nm (10^{-5} cm), such as a droplet, nucleus at nucleation, etc. We should also notice that the thermodynamic model cannot be expected to hold for a system containing so few molecules, such as water droplets of radii smaller than 1 nm, for example.

Temperature

For pure liquid, we can obtain equation 6.18 from equation 6.13:

$$\frac{d\gamma}{dT} = \frac{df^s}{dT} = -s^s \quad (6.18)$$

For pure liquid, $d\gamma/dT$ has generally negative values, which indicate $s^s > 0$. $s^s > 0$ means that entropy at the surface is larger than for the bulk liquid. Several empirical relations between surface tension and temperature are proposed, for example, as expressed by equations 6.19 and 6.20:

$$\gamma = (k/v^{1/2/3})(T_c - T) \quad (6.19)$$

where v^1 is molar volume, T_c is critical temperature, k is constant and is about 2.1×10^{-7} J/deg for most liquids. Equations 6.19 was proposed by Eötvös in 1886. Equation 6.19 does not hold accurately in the vicinity of T_c . Katayama and Guggenheim proposed equation 6.20 in order to improve equation 6.19:

$$\gamma = \gamma_o(1 - T/T_c)^{11/9} \quad (6.20)$$

where γ is constant and depends on the kind of liquid.

Surface stress

In the case of a solid, we have to distinguish between surface tension and surface stress. Surface tension is defined in terms of work, γdA (see equation 6.6) retaining the same surface condition, such as keeping the number of atoms at the unit surface area constant. Another way to expand the surface by dA is to stretch the distance between atoms at the surface. In this case the number of atoms at the surface is kept constant and the work is expressed by gdA . g is called surface stress, and is related to surface tension γ by equation 6.21 (Shuttleworth's equation):

$$g = \gamma + (\partial\gamma/\partial\omega)_N \quad (6.21)$$

where ω is the elastic surface strain and N is the total number of atoms at the surface. Since a liquid surface deforms in a completely plastic manner, g is equal to γ for the liquid surface.

6.2.2 Mechanical aspects of surface tension

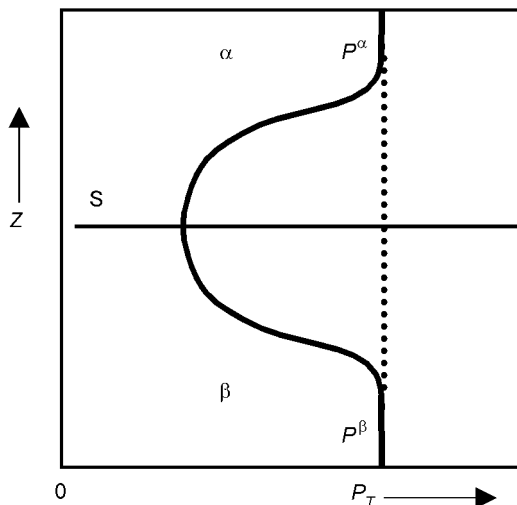
Mechanical definition

As pointed out by Young, a system composed of two fluids such as liquid and gas which contact each other, behaves, from a mechanical standpoint, as if it consisted of two homogeneous fluids separated by a uniformly stretched membrane of infinitesimal thickness. Surface tension has been defined from a macroscopic standpoint as the tractional force, γ , acting across any unit length of line on this fictitious membrane. Surface tension has the dimensions of force per unit length and is usually expressed in $\text{N}\cdot\text{m}^{-1}$.

The real surface in the above mentioned system has a finite thickness, that is, the surface layer (or region) as shown in Fig. 6.3. For this system, the surface tension is defined from a mechanical standpoint by equation 6.22 (the Bakker equation):

$$\gamma = \int_{-\infty}^{\infty} (p_N - p_T(z)) dz \quad (6.22)$$

where p_N is normal pressure to the surface and equal to p , the hydrostatic pressure in the system, $p_T(z)$ is tangential pressure. $p_T(z)$ exerts normally across a plane parallel to the z axis and varies with z as shown in Fig. 6.3,



6.3 Variation of tangential pressure $P_T(z)$ with z .

while p is required, from the condition of hydrostatic equilibrium, to be the same value even in the surface layer. If we can describe $p_T(z)$ from the molecular distribution functions of the fluid by using ‘molecular dynamics’, for example, the surface tension can be rigorously expressed with the aid of equation 6.22.

Surface tension, γ , as a force of traction, can be available even for the system which is not in a thermodynamic equilibrium state.

Laplace’s equation

When a spherical surface of radius with curvature r maintains mechanical equilibrium between two fluids α and β phases at different pressures p^α and p^β and the interface is assumed to be of zero thickness, the condition for mechanical equilibrium provides a simple relation between p^α and p^β :

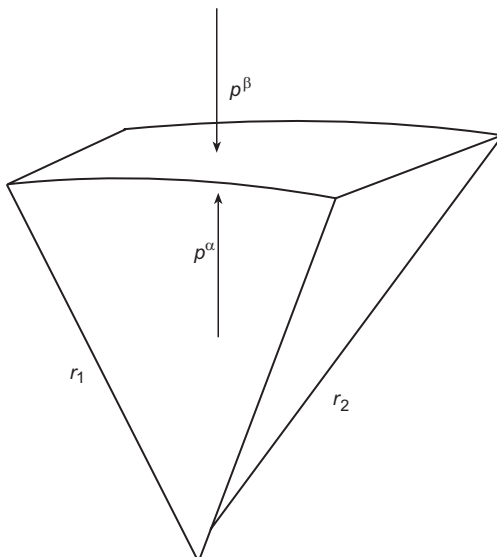
$$p^\alpha - p^\beta = 2\gamma/r \quad (6.23)$$

Equation 6.23 is known as the Kelvin relation.

If, instead of a spherical surface, we consider any surface, the condition of mechanical equilibrium at each point in the surface is given by Laplace’s equation (6.24):

$$p^\alpha - p^\beta = \gamma \left(\frac{1}{r_1} + \frac{1}{r_2} \right) \quad (6.24)$$

where r_1 and r_2 are the two principal radii of curvature of the surface as shown in Fig. 6.4.



6.4 Pressure difference between phase α and β in mechanical equilibrium.

Laplace's equation (6.24) provides a fundamental base for measuring surface tension in static state such as the capillary rise method, the sessile drop method, the pendant drop method, the maximum bubble pressure method, etc.

Marangoni effect

Surface tension as a trational force is available for describing the behaviour of the system which is not in a thermodynamical equilibrium state. The surface (or interfacial) tension difference, or gradient, on the surface (or interface) of liquid, for example, in the direction x , can change the motion of liquid due to the surface shear stress τ_s , written as

$$\tau_s = \frac{d\gamma}{dx} = \frac{\partial\gamma}{\partial T} \cdot \frac{dT}{dx} + \frac{\partial\gamma}{\partial c} \cdot \frac{dc}{dx} + \frac{\partial\gamma}{\partial\varphi} \cdot \frac{d\varphi}{dx} \quad (6.25)$$

Equation 6.25 indicates that the surface (or interfacial) tension gradient is caused by the gradients of temperature T , concentration c of the surface active component in the liquid and electric potential φ at the interface between two liquids.

In hydrodynamics, the surface (or interfacial) tension difference or gradient participating in the above dynamics is called the Marangoni effect.¹ The motion of liquid induced by the Marangoni effect is called Marangoni flow or Marangoni convection. The non-dimensional number defined by equations 6.26 and 6.27 is called the Marangoni number, M_a , which characterizes the Marangoni convection:

$$M_a = (\partial\gamma/\partial T) \cdot \Delta T \cdot L/a\eta \quad (6.26)$$

$$M_a = (\partial\gamma/\partial c) \cdot \Delta c \cdot L/D\eta \quad (6.27)$$

where ΔT is temperature difference, L is the characteristic length of the system, a is thermal diffusivity, η is viscosity, Δc is the concentration difference of the surface active component and D is the diffusion coefficient of the surface active component.

Since liquid metals and slags generally have high surface or interfacial tension and also have strong surface active components such as oxygen and sulfur in liquid iron (see Section 6.3.1), both factors are favorable to the occurrence of Marangoni convection in systems where these are present.

Even in the field of gravity on the Earth, occurrences of the Marangoni effect in metallurgical systems have been observed in the following: (a) Marangoni convection of molten silicon² and salts³ due to temperature gradient, (b) spreading and shrinking of slag droplets on the metal due to changes in applied potential,⁴ and (c) Marangoni flow of slag film⁵ and metal surface^{6,7} due to concentration gradient, which is described in further detail in Sections 6.4.1 and 6.4.2.

Since the Marangoni convection is most intensive at and around liquid–gas and liquid–liquid interfaces, it effectively promotes mass transfer in the region

of the concentration boundary layer, resulting in the acceleration of the heterogeneous reaction rate when the reaction rate is limited by the mass transfer process (see Section 6.4.2). The Marangoni effect also participates in the surface dilatational viscosity which is closely related to many interfacial phenomena in metallurgical processes (see Section 6.2.3).

The interfacial tension gradient, which is induced along the interface between a liquid and foreign particle by the concentration gradient or temperature gradient, would propel the foreign particle in the direction of decreasing interfacial tension.⁸ This phenomenon is also taken as a kind of Marangoni effect (in a broad sense). The movement of fine particles driven by the interfacial tension gradient should have a close relationship to certain phenomena in iron and steelmaking processes, such as the occurrence of bubble and inclusion-related defects and nozzle clogging (see Section 6.4.5).

6.2.3 Physical chemistry of interfacial phenomena

Here interfacial phenomena will be treated from a physicochemical standpoint.

Adsorption

The composition of the surface layer is usually different from that of the two bulk phases. This phenomena is called ‘adsorption’. The real concentrations in the surface layer are not uniform but vary continuously through its thickness. A macroscopic definition of adsorption can be arrived at by employing Gibbs’ dividing surface described in Section 6.2.1.

Gibbs’ adsorption equation

Gibbs’ adsorption equation in general form is given by equation 6.28:

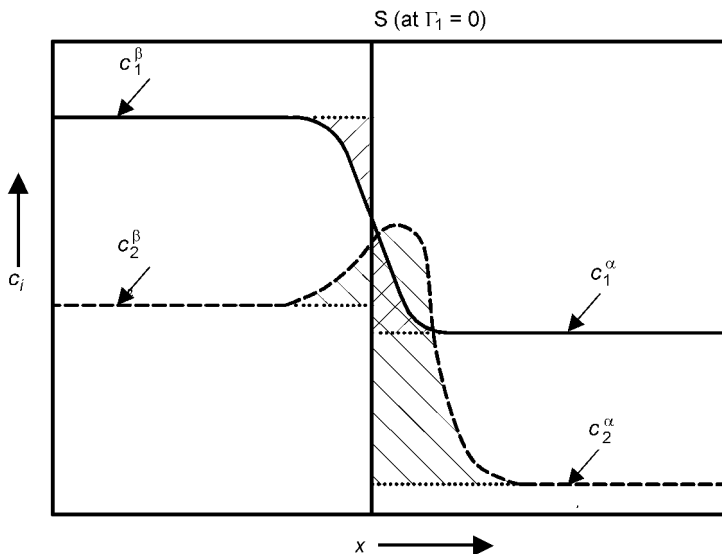
$$d\gamma + s^s dT + \sum_{i=1}^r \Gamma_i d\mu_i = 0 \quad (6.28)$$

Equation 6.28, which is due to Gibbs, is derived by employing thermodynamics and the concept of the dividing surface.

At constant temperature, equation 6.28 reduces to

$$d\gamma = - \sum_{i=1}^r \Gamma_i d\mu_i \quad (6.29)$$

Since Γ_i depends on the position of the dividing surface, it is possible and convenient to make a special choice for the position of this surface in such a manner as to make Γ_1 zero. We shall denote Γ_i defined in this way as $\Gamma_{i(1)}$. Then we have equation 6.30 instead of equation 6.29:



6.5 Adsorption of component 2 at the dividing surface which makes Γ_1 zero.

$$d\gamma = - \sum_{i=2}^r \Gamma_{i(1)} d\mu_i \quad (6.30)$$

Equation 6.30 is known as Gibbs' adsorption equation.

For the system composed of components 1 and 2, equation 6.30 reduces to

$$d\gamma = -\Gamma_{2(1)} d\mu_2 \quad (6.31)$$

$\Gamma_{2(1)}$ means the adsorption of component 2 at the surface which makes the adsorption of component 1 zero, as shown in Fig. 6.5.

The value $\Gamma_{2(1)}$ can be calculated from the experimentally obtained slope of γ vs $\ln a_2$ (or c_2) based on the equations 6.32 and 6.33:

$$\Gamma_{2(1)} = -\frac{1}{RT} \left(\frac{\partial \gamma}{\partial \ln a_2} \right)_T \quad (6.32)$$

$$\Gamma_{2(1)} = -\frac{1}{RT} \left(\frac{\partial \gamma}{\partial \ln c_2} \right)_T \quad (\text{for ideal solution}) \quad (6.33)$$

where a_2 is the activity of the component 2.

It should be noticed that $\Gamma_{2(1)}$ is not absolute concentration but the relative quantity, the excess surface quantity (see Fig. 6.5).

Adsorption of surface active elements such as oxygen and sulfur at the liquid iron surface (see Section 6.3.1) reduces the reaction rate between nitrogen gas and liquid iron (see Section 6.4.2). Adsorptions at slag surface and slag–metal interface also closely relates to surface dilatational viscosity (the area viscosity), ζ_s , given by equation 6.34:⁹

$$\Delta\gamma = \zeta_s \frac{1}{A} \frac{\partial A}{\partial t} \quad (6.34)$$

where $\Delta\gamma$ is the corresponding change in the surface tension to that in the surface area A and t is time.

Equation 6.34 is analogous to Marangoni viscosity, ζ_M , given by the following equation:

$$\Delta\gamma = \zeta_M \frac{1}{A} \frac{\partial A}{\partial t} \quad (6.35)$$

Therefore, ζ_s and ζ_M include the rate of attainment of equilibrium between the bulk phase and adsorbed surface (which contains, Gibbs elasticity^{10,11}) as well as its own properties of adsorbed surface layer. In other words, the ζ_s and ζ_M may be called ‘Gibbs–Marangoni’ viscosity.

Surface dilatational viscosity is closely related to the following interfacial phenomena:¹² foaming, coalescence of bubbles, droplets and solid particles in liquid and also dispersion of bubbles, droplets as well as solid particles into liquid. The involvement of mold powder or slag by the molten steel should be also influenced by ζ_M . All of the above mentioned phenomena include the elemental processes of (a) surface (interface) expansion or shrink, (b) drainage and (c) break of the melt film.

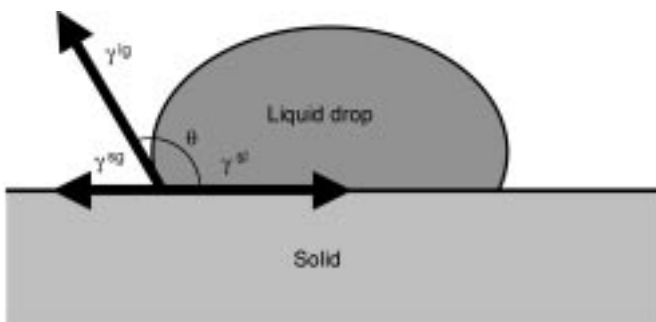
Wetting

Wetting of solid (s) by liquid (l) without any kinds of reaction is characterized by contact angle θ as shown in Fig. 6.6, or with the quantity of Helmholtz energy changes for wettings shown in Fig. 6.7 and equations 6.36, 6.37 and 6.38:

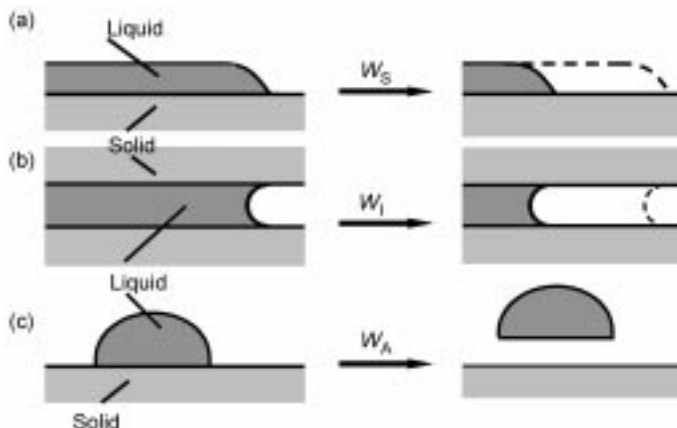
$$W_S = \gamma^{sg} - \gamma^{lg} - \gamma^{sl} \quad (6.36)$$

$$W_I = \gamma^{sg} - \gamma^{sl} \quad (6.37)$$

$$W_A = \gamma^{lg} + \gamma^{sg} - \gamma^{sl} \quad (6.38)$$



6.6 Contact angle θ and interfacial tension γ_{ij} for the system of gas–liquid–solid.



6.7 Three types of wetting for gas–liquid–solid system.

where g means gas phase and γ^{ij} is the interfacial tension between phases i and j. Modes of wetting, (a), (b) and (c) in Fig. 6.7, correspond to different forms of wetting, namely spreading wetting, immersional wetting and adhesional wetting, respectively. Two terms which are widely used in this context are the spreading coefficient, W_S (defined in equation 6.36) and the work of adhesion, W_A (defined in equation 6.38). Equations 6.40, 6.41 and 6.42 are derived from equations 6.36, 6.37 and 6.38 when Young's equation (equation 6.39) can be applied to the systems in Fig. 6.6.

$$\gamma^{sg} = \gamma^{sl} + \gamma^{lg} \cos \theta \quad (6.39)$$

$$W_S = \gamma^{lg}(\cos \theta - 1) \quad (6.40)$$

$$W_I = \gamma^{lg} \cos \theta \quad (6.41)$$

$$W_A = \gamma^{lg}(1 + \cos \theta) \quad (6.42)$$

Equations 6.40, 6.41 and 6.42 are valuable for practical use because γ^{lg} and θ can be determined experimentally.

For $\theta = 0^\circ$, hence $W_S = 0$, spreading wetting occurs spontaneously. For $\theta \leq 90^\circ$, hence $W_I \geq 0$, immersional wetting occurs and for $\theta \leq 180^\circ$, hence $W_A \geq 0$, adhesional wetting occurs spontaneously.

Young's equation indicates that contact angle θ depends on the interfacial tension γ^{sg} , γ^{sl} and γ^{lg} which are closely related to the interfacial Helmholtz energy f^s as shown by equation 6.12. Since the Helmholtz energy is a function of chemical composition of the system and temperature, the contact angle also depends on the chemical composition of the system and temperature. The chemical composition of the drop varies with the dissolution of the substrate materials into the drop, resulting in the change in the contact angle. When a new phase or compound are generated at the drop–substrate interface by the reaction

between the drop and substrate, the contact angle corresponds to the system of the drop and generated phase or compound in equilibrium.

For the case where the surface of the substrate is not smooth, the Wenzel equation (6.43)¹³ is used instead of Young's equation (6.39):

$$R'(\gamma^{sg} - \gamma^{ls}) = \gamma^{lg} \cos \theta' \quad (6.43)$$

where R' is roughness factor and given with A/A_o . A and A_o are actual surface area and geometrical surface area of the substrate, respectively, and θ' is the apparent contact angle for the rough surface. When the wettability between the drop and substrate is poor, the rough interface between the drop and the substrate tends to form a composite interface which consists of the liquid–solid interface (wetting area) and the interface including small gas phase between the liquid and solid (non-wetting area). The Wenzel equation (6.43) is not available for the above case and we have to find another expression¹⁴ on θ' .

We often observe the advancing contact angle θ_a and the receding contact angle θ_r , that is, a hysteresis of wetting. The following causes for the hysteresis have been proposed: (1) friction between drop and solid surface, (2) adsorbed layer (film) at solid surface, (3) surface roughness. We may add one more cause, that is, surface stress of the solid surface (see Section 6.2.1) as a mechanism for the hysteresis, and these four causes may participate together in the hysteresis.

For the wetting in non-equilibrium state, we should add the kinetic factor for describing the contact angle θ . In the case of very rapid spreading of the drop on the solid surface, the spreading velocity may be limited by the hydrodynamic flow of the drop at the advancing front of the drop, and hence the contact angle may be dominated by the flow characteristics.

When adsorption, dissolution and chemical reaction between the drop and substrate material do not reach the equilibrium state and the reaction rate is determined by the mass transfer process, the contact angle may be influenced by the mass transfer rate and time.

Influence of radius of curvature

We will consider one component system composed of two phases which are separated by the interface with radius of curvature r in a thermodynamic equilibrium state. We also suppose that no chemical reactions occur other than the transfer of matter from one phase to the other.

For mechanical equilibrium, the pressure of α phase (Fig. 6.4), p^α is larger than that of β phase as indicated by equation 6.24. Since Gibbs energy G and hence chemical potential μ_i increases with increasing pressure, G and μ_i of α phase are larger than those of β phase. The above difference in Gibbs energy and chemical potential between α and β phases influences the physicochemical properties of α phase such as vapor pressure, melting temperature, solubility, etc.

On vapor pressure

Vapor pressure of pure liquid droplet with radius r increases with decreasing r . The quantitative description of the phenomena is known as the Kelvin equation (6.44):

$$\ln p_r/p_o = \frac{2\gamma^{\text{lg}}}{r} \frac{\nu^1}{RT} \quad (6.44)$$

where p_r and p_o are the vapor pressure at radius r and ∞ , respectively, γ^{lg} is the surface tension of the droplet and ν^1 is the molar volume of the droplet. ν^1 is supposed to be constant at any radius.

In the case of a bubble with radius r in liquid, equation 6.45 can be derived:

$$\ln \frac{p_r}{p_{i,o}} = -\frac{2\gamma^{\text{lg}}}{r} \frac{\nu^1}{RT} \quad (6.45)$$

Equation 6.45 indicates that the vapor pressure in the bubble decreases with decreasing r , which is the reverse mode to that of droplet.

For the droplet of mixture, the following analogous equation 6.46 is given:

$$\ln \frac{P_i}{p_{i,o}} = \frac{2\gamma^{\text{lg}}}{r} \frac{\nu_i^1}{RT} \quad (6.46)$$

where p_i and $p_{i,o}$ are the partial pressures of component i at the radius r and ∞ , respectively, ν_i^1 is the partial molar volume of component i .

On heat of evaporation

The heat of evaporation of pure liquid droplets decreases with decreasing r as expressed by equation 6.47:

$$\Delta_e h_r - \Delta_e h_o = -\frac{2\gamma^{\text{lg}} \nu^1}{r} \quad (6.47)$$

where $\Delta_e h_r$ and $\Delta_e h_o$ are the molar heat of evaporation at radius r and ∞ , respectively.

On boiling point

Equation 6.48 expresses the relation between boiling point of pure substance and radius of curvature of liquid droplets under constant pressure of the gas phase:

$$\ln T_r/T_o = -\frac{2\gamma^{\text{lg}}}{r} \cdot \frac{\nu^1}{\Delta_e h} \quad (6.48)$$

where T_r is the boiling temperature of the droplet at radius r , T_o is the boiling temperature of bulk liquid ($r \rightarrow \infty$) at given constant pressure. Equation 6.48 indicates $T_r < T_o$. This is the phenomenon of supercooling of a saturated vapor.

On melting point

Equation 6.48 may be extensively applied to the system of small solid particle with the radius r and bulk liquid. The melting point T of the small solid particle will be given by equation 6.49:

$$\ln T_r/T_o = -\frac{2\gamma^{sl}}{r} \cdot \frac{\nu^s}{\Delta_f h} \quad (6.49)$$

where T_r is the normal melting point at the some external pressure, ν^s is the molar volume of solid and $\Delta_f h$ is the molar heat of fusion.

On solubility

The solubility of pure solid particle (component 1) depends on radius r of the particle as expressed by equation 6.50:

$$\frac{2\gamma^{sl}}{r} = \frac{RT}{\nu_1^{s,o}} \ln \left\{ (\gamma_1 x_1) / (\gamma_{1,o} x_{1,o}) \right\} \quad (6.50)$$

where $\nu_1^{s,o}$ is the molar volume of pure solid 1, x_1 and $x_{1,o}$ are the mole fractions of component 1 in the solution which, at the same T and P of the solution, is in equilibrium with the solid particle with radius r and a large particle ($r \rightarrow \infty$), respectively. γ_1 is the activity coefficient of the component 1.

For the ideal solution, equation 6.50 reduces to equation 6.51:

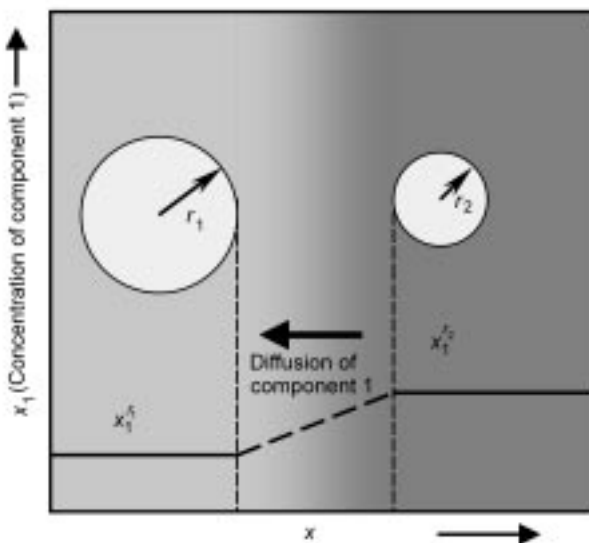
$$\frac{2\gamma^{sl}}{r} = \frac{RT}{\nu_1^{s,o}} \ln (x_1 / x_{1,o}) \quad (6.51)$$

Equation 6.51 is known as the Freundlich–Ostwald equation. Equation 6.51 predicts that the solution in equilibrium with a solid particle of component 1 increases in the concentration, x_1 , as the solid decreases in its radius. In other words, small solids are more soluble than large ones. In a solution in contact with solids of different radii of curvature, the larger solid will grow at the expense of the smaller one as shown in Fig. 6.8. The above mentioned phenomena is known as Ostwald ripening.

In relation to phase rule

For very small particles, intensive properties such as vapor pressure, boiling point, melting point, solubility, etc. depend on its radius of curvature as described above. The results indicate that the phase rule for the system where the contribution of surface quantity should be taken account of must be different from the one for the system composed of bulk phases, neglecting the contribution of the interface.

We suppose the following system: number of independent components, r , number of bulk phases, ν , number of types of surface, ξ , number of independent



6.8 Ostwald ripening.

chemical reactions, q . For simplicity, we also suppose that each type of surface has only one surface phase. For this system, the number of degrees of freedom is given by equation 6.52 instead of equation 6.53 for the system composed of bulk phase, neglecting the interface:

$$f = r + 1 - q \quad (6.52)$$

$$f = r + 2 - \nu - q \quad (6.53)$$

The equations from (6.44) to (6.51) are subject to the phase rule (6.52).

Thermodynamics of nucleation

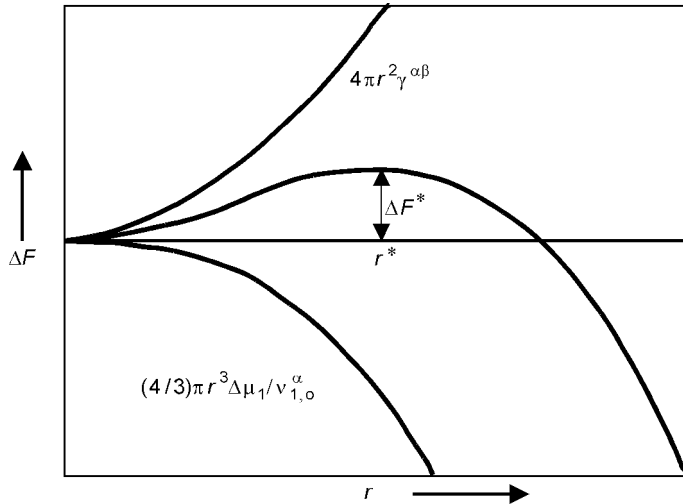
Homogeneous nucleation

We shall consider the change in Helmholtz energy when a nucleus of α phase generates in β phase (g or l). We suppose that the system after nucleation has the same total number of molecules in the same total volume and temperature to those of the system before the nucleation.

The change in Helmholtz energy, $(\Delta F)_{T,V}$, is given by equation 6.54:

$$(\Delta F)_{T,V} = F - F_o \quad (6.54)$$

where F is the total Helmholtz energy of the system after nucleation and F_o is that before the nucleation. For simplicity, we assume that the bulk β phase is sufficiently large that the removal of the small amount of material needed to form the nuclei does not alter appreciably either the pressure or composition of

6.9 Free energy of formation of an embryo (α) as a function of embryo size r .

the bulk phase. Under the above assumptions, we have, finally, the following equation (6.55):

$$(\Delta F)_{T,V} = \sum_{i=1}^r n_i^\alpha \Delta \mu_i + \gamma^{\alpha\beta} A \quad (6.55)$$

where

$$\Delta \mu_i = \mu_i^\alpha(T, P^\beta, x_2^\alpha, \dots, x_r^\alpha) - \mu_i^\beta(T, P^\beta, x_2^\beta, \dots, x_r^\beta)$$

However, we have to notice that the above assumption does not hold in general. For the case of Al_2O_3 nucleation in liquid iron, for example, we have to take account of the composition change of the liquid iron (bulk phase) which alters the Helmholtz energy of the bulk phase.¹⁵

We shall apply equation 6.55 to the case where a droplet of component 1 (α phase) nucleates in the β phase. $(\Delta F)_{T,V}$ is given by equation 6.56 and Fig. 6.9:

$$(\Delta F)_{T,V} = \frac{4}{3} \frac{\pi r^3}{v_1^{\alpha,\circ}} \Delta \mu_1^\circ + 4\pi r^2 \gamma^{\alpha\beta} \quad (6.56)$$

For equilibrium state, that is, at the critical nuclei (we denote *), $(dF)_{T,V} = 0$. When the nucleus grows, we will have the following differential:

$$\left(\frac{\partial F}{\partial r} \right)_{T,V} = \frac{4\pi r^{*2}}{v_1^{\alpha,\circ}} \Delta \mu_1^\circ + 8\pi r^* \gamma^{\alpha\beta} = 0 \quad (6.57)$$

Therefore,

$$r^* = -\frac{2\nu_1^{\alpha,o}\gamma^{\alpha\beta}}{\Delta\mu_1^o} \quad (6.58)$$

$$(\Delta F^*)_{T,V} = \frac{4}{3}\pi r^{*2}\gamma^{\alpha\beta} \quad (6.59)$$

For the nucleation of the droplet of pure component 1 from gas phase at the above equilibrium state,

$$\Delta\mu_1^o = RT \ln p_{1,o}^o/p_{1,r}^o \quad (6.60)$$

where $p_{1,o}^o$ and $p_{1,r}^o$ are the equilibrium vapor pressures of the pure liquid at $r \rightarrow \infty$ and r , respectively. $p_{1,r}^o$ is then regarded as the vapor pressure at supersaturated state for the nucleation. Substituting equation 6.60 into equation 6.58, we obtain Kelvin's equation (6.44).

Heterogeneous nucleation

We will consider the heterogeneous nucleation of δ phase at the interface between α phase (gas or liquid) and solid(s) as shown in Fig. 6.10. The nucleus forms a lens on the plane interface between α phase and solid. We suppose the same assumptions to homogeneous nucleation that pressure and composition both of α and solid phases do not change before and after the nucleation. At the equilibrium, that is, critical nucleus,

$$(\Delta F^*)_{T,V} = \frac{2}{3}\gamma^{\alpha\delta}\pi r^{*\alpha\delta^2}(1 - \cos\theta - \frac{1}{2}\cos\theta\sin^2\theta) \quad (6.61)$$

where $r^{*\alpha\delta}$ is the radius of the lens and θ is the contact angle (Fig. 6.10).

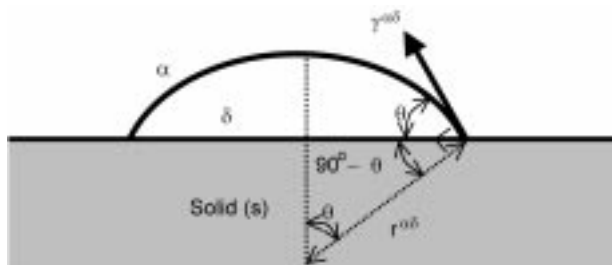
For $\theta < 180^\circ$,

$$1 + \cos\theta + \frac{1}{2}\cos\theta\sin^2\theta > 0$$

then we can derive the following relation

$$(\Delta F^*)_{T,V,het} < (\Delta F^*)_{T,V,hom} = \frac{4}{3}\pi r^{*\alpha\alpha^2}\gamma^{\alpha\delta} \quad (6.62)$$

The relation (6.62) explains that heterogeneous nucleation is thermodynamically more advantageous than homogeneous nucleation for $\theta < 180^\circ$.



6.10 Lenticular nucleus (δ) on a plane interface between α phase and solid.

Kinetics of nucleation

We shall define the number, I , of critical nuclei of α phase (component 1) which are formed in β phase, in unit time in unit volume of bulk phase in a state of supersaturation at a temperature T . The nucleation proceeds in a quasi-stationary state in which critical nuclei are formed at the expense of embryos, followed by their removal from the embryo population by their growth into the nucleated phase, finally the bulk phase.

Equations 6.63 and 6.64^{16,17} are usually used for condensed systems as the quantitative expression of I .

$$I = A \exp(-\Delta F^*/kT) \quad (6.63)$$

$$A = n^* (\gamma^{\alpha\beta}/kT)^{1/2} (2\nu_1^{\alpha,o'}/9\pi)^{1/3} n(kT/h) \quad (6.64)$$

where n^* is the number of molecules on the surface of critical nuclei given by equation 6.65, $\nu_1^{\alpha,o'}$ is the volume of one molecule of the nucleated phase α given by equation 6.66 and n is the number of molecules of component 1 per mole of parent phase β .

$$n^* = 4\pi r^{*2} / \{M_1 / (\rho_1^{\alpha,o} N_o)\}^{2/3} \quad (6.65)$$

$$\nu^{\alpha,o'} = (M_1 / \rho_1^{\alpha,o}) / N_o \quad (6.66)$$

where M_1 and $\rho_1^{\alpha,o}$ is the molecular weight and density of α phase of component 1, respectively. N_o is the Avogadro's constant.

*Dispersion and coalescence*¹⁸

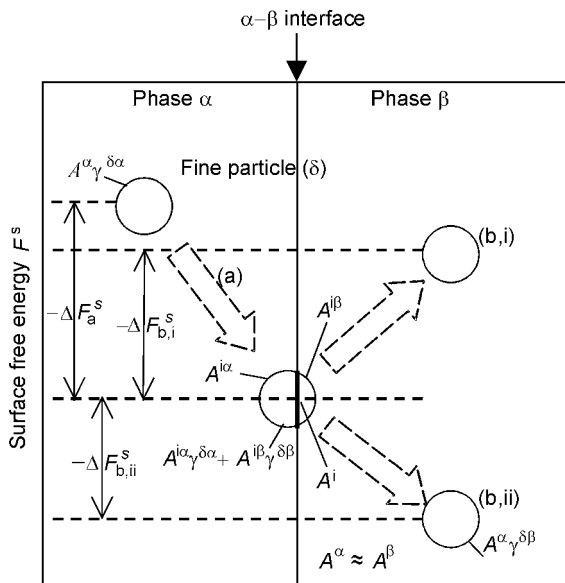
Since the dispersion system composed of fine particles (dispersion phase δ) and dispersion medium (phase α) is thermodynamically unstable, the dispersed particles tend to coalesce with each other or to be absorbed into the same phase (to the particle) which contacts with the dispersion medium.

When the phase β contacting with the dispersion medium is different from the phase of the particle (δ), from the thermodynamic point of view, (a) $\Delta F_a^s < 0$ and $\Delta F_{b,i}^s > 0$ should be satisfied for the particle in the dispersion medium to adhere to the $\alpha-\beta$ interface or (b) the relations of $\Delta F_a^s < 0$ and $\Delta F_{b,ii}^s < 0$ are needed for the particle to go through the interface and transfer into phase β . ΔF_a^s and ΔF_b^s are given by equations 6.67 and 6.68, respectively. The above behaviors of the particle are also explained by Fig. 6.11.

$$\Delta F_a^s = A^{i\alpha} \gamma^{\delta\alpha} + A^{i\beta} \gamma^{\delta\beta} - A^i \gamma^{\alpha\beta} - A^\alpha \gamma^{\delta\alpha} \quad (6.67)$$

$$\Delta F_b^s = A^\beta \gamma^{\delta\beta} - (A^{i\alpha} \gamma^{\delta\alpha} + A^{i\beta} \gamma^{\delta\beta} - A^i \gamma^{\alpha\beta}) \quad (6.68)$$

where $\gamma^{\delta\alpha}$ and $\gamma^{\delta\beta}$ is the interfacial tension between the particle (phase δ) and phase α and that between the particle and phase β , respectively. $\gamma^{\alpha\beta}$ is the interfacial



6.11 Thermodynamic illustration for the system of fine particle in phase α and β or at the α - β interface.

tension between the phases α and β . A^α and A^β is the interface area between the particle and phases α and β , respectively and A^i is the interface area between phases α and β . When the particle straddles the interface between two phases, the original interface will disappear and be replaced by two separate interfaces.

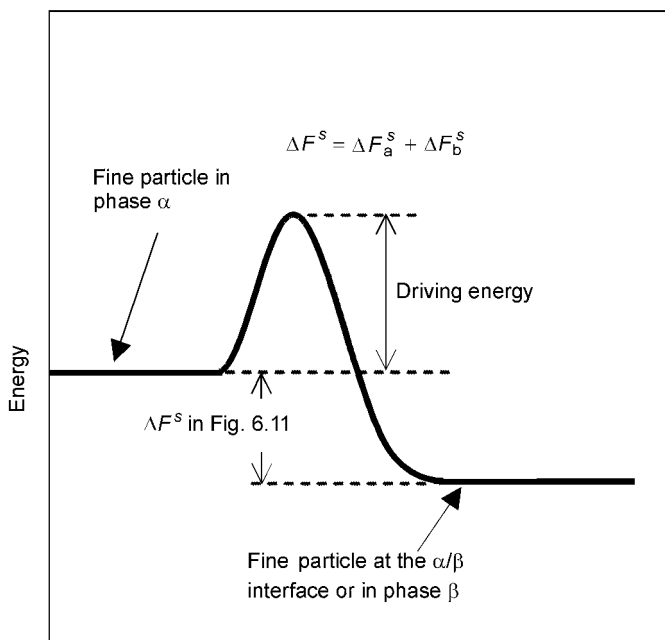
In practical operations, we often encounter kinetic problems, that is, (a) how to drive the particle toward the interface and or into phase β via the α - β interface, or (b) how to keep the dispersed system stable as long as possible.

Figure 6.12 shows schematically thermodynamic and kinetic processes of the dispersed particle separation. The driving energy in Fig. 6.12 is caused by the viscous drag force when the particle moves toward the phase β , electric double layer, Saffman force, van der Waals force, etc. The energy for overcoming the driving energy can be supplied by gravity (for example, density difference between the particle and phase α), mechanical agitation, applied potential, the force caused by interfacial tension gradient between the particle and the phase α (see the section on the Marangoni effect, page 245), etc.

6.3 Interfacial properties of a metallurgical melts system

6.3.1 Surface tension

The group of liquid metal generally has the highest surface tension among all kind of liquids.¹⁹ The surface tension of liquid slag is lower than that of liquid



6.12 Schematic illustration of kinetic and thermodynamic processes of dispersed particle separation.

metal although it is larger than those of water and organic materials. Since the surface tension has the internal energy term as expressed by equation 6.13, it reflects bond energy and then depends on the bond types in liquids, that is, metallic bond (liquid metal), covalent bond (liquid slag), ionic bond (liquid slag), and van der Waals bond (molecular liquid).

Pure liquid usually has a negative temperature coefficient of surface tension, which indicates that the surface excess entropy s^s (see equation 6.18) is positive. $s^s > 0$ means that the degree of order of atom or molecule configuration at the surface is lower than that in bulk phase (see equation 6.4). We can evaluate the value of the entropy term in equation 6.13 for liquid iron as about -700 mN/m from its temperature coefficient, $d\gamma/dT = -0.40 \text{ mN/(m}\cdot\text{K)}$, which is the average value of those summarized by Keene²⁰ from recently obtained experimental data. The absolute value of the entropy term is equivalent to 40% of the surface tension value 1800 mN/m . The result may indicate that we should take account of the contribution of entropy term for the prediction of surface tension of liquid metal.

Liquid metal usually has strong surface active elements. Table 6.1²⁰ shows surface activities of several solutes in liquid iron. Especially oxygen, sulfur and nitrogen, which are inevitably included in liquid steel during the iron and steelmaking process as shown in Table 6.1,²⁰ are remarkably surface active to

Table 6.1 Surface activities of solute¹⁹

Solute (<i>i</i>) in Fe	Mean value of approximate surface activities (mNm ⁻¹ [mass% <i>i</i>] ⁻¹) relative to iron	Approximate range (in mass%) over which surface activity was derived
C	-19	0–2.2
Mn	-51	0–4.9
N	-5580	0–0.025
O	-26190	0–0.0086
Si	-26	0–2.5
S	-10990	0–0.029

liquid iron in comparison with surface activeness for the system of water-surfactant ($\text{C}_8\text{H}_{17}\text{SO}_3\text{Na}:i$) solution, $-88 \text{ mNm}^{-1}[\text{mass\%}i]^{-1}$, ($0\sim 0.1 \text{ mass\% } i$).²¹

The temperature coefficient of surface tension of liquid iron alloy increases with increasing oxygen and sulfur concentration and becomes a positive value after reaching zero at around 70 ppm (on a mass basis) for oxygen in liquid iron²² and 60 ppm (on a mass basis) for sulfur in 304 and 306 stainless steels.²³ The above behavior in the temperature coefficient of surface tension may cause a drastic change in the metal pool shape for TIG welding due to the change in the direction of Marangoni convection in the metal pool.^{22–24}

The temperature coefficient of surface tension of liquid silicate slag also has a positive value in the range of high SiO_2 concentration.

6.3.2 Interfacial tension between slag and metal

Interfacial tension between slag and liquid iron alloy measured experimentally has generally as large a value as surface tension of liquid metal, and also has a strong surface active element such as oxygen and sulfur.²⁵

We have to notice that many interfacial tension values reported previously are measured in non-equilibrium state. When the slag–metal system, for example, $\text{SiO}_2\text{-CaO-FeO}$ slag–iron alloy, is in equilibrium state, the number of freedom for the system is 2. Therefore, if temperature and pressure are fixed, the number of freedom is equal to zero, which means that all of the composition of slag and metal phases are fixed and we cannot change the composition of the metal phase independently of slag composition.

When we apply the Gibbs' adsorption equation (6.30) to the system containing the slag–metal interface, in principle, we should pay attention to confirming whether the system is in equilibrium state or not. In addition, for non-equilibrium state, during sulfur transfer from liquid iron drop to slag phase via the interface, for example, the iron drop in the slag phase is observed to be deformed into a depressed flat shape.²⁶ If we apply the Laplace equation to the

non-equilibrium system in order to obtain the interfacial tension between the drop and slag phase, we will obtain an unusual low interfacial tension value²⁷ from the analysis of the depressed drop shape. Here we also pay attention to confirming whether the depressed drop is in equilibrium of statics or not. If the deformation of the drop is dominantly caused by the Marangoni convection at the interface induced by the transfer of the surface active element sulfur, we cannot apply, in principle, the Laplace equation to the system and the unusual low interfacial tension value, obtained with the aid of the Laplace equation, is regarded as just an apparent one.

6.3.3 Wetting of ceramics by liquid metal and slag at high temperature

In general, the liquids which react well with ceramics show good wettability between the liquid and the solid, that is, θ is smaller than 90° . On the other hand, when the ceramic is substantially inert against the liquid, θ tends to be larger than 90° , which means poor wettability.

Almost all the liquid iron alloy–solid oxide systems show poor wettability, except for a few, for example, the Al(l)-SiO₂(s) system.²⁸ Oxygen in the liquid iron reduces the contact angle θ between the iron and alumina. However, when oxygen concentration is smaller than about 100 ppm (on a mass basis), the wetting behavior tends to become complicated.²⁹ SiC, Si₃N₄ graphite and diamond are not wetted by those metals which have a very low solubility in those materials.²⁸ On the other hand, SiC is wetted well by liquid iron, cobalt and nickel which have a pretty high solubility for carbon on SiC.²⁸

Liquid slag usually dissolves solid oxides well and also wets them well. On the other hand, in general, graphite is not wetted well by liquid slag which hardly dissolves carbon.

6.4 Interfacial phenomena in relation to metallurgical processing

In this section, we will consider several interfacial phenomena which do, or may, participate in the metal smelting and refining processes, studied mainly by our research group. Many papers have already been published on this topic by various investigators besides ourselves.

6.4.1 Local corrosion of refractories at slag–gas and slag–metal interfaces^{5,30}

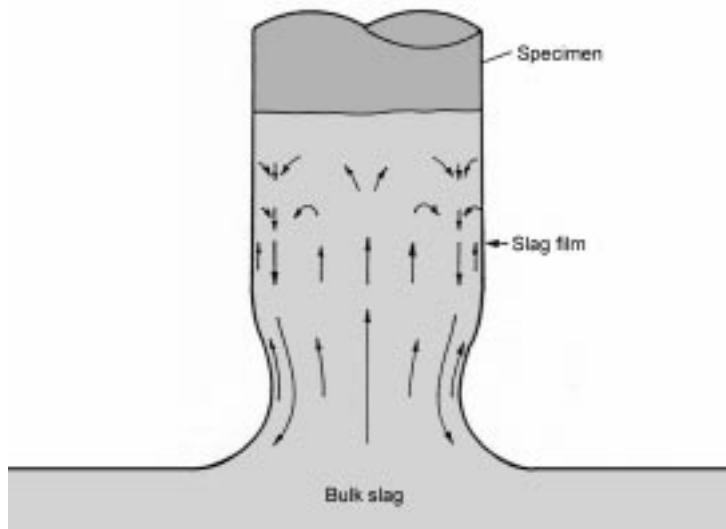
It has been well known that refractories composed of oxides, oxides–graphite and oxides–graphite–carbide are corroded locally at slag–gas (slag surface) or slag–metal interface in the fields of glass technology and iron and steelmaking.

The local corrosion of refractories is a serious problem for these industries because it limits the life of the refractories. Several kinds of ideas had been proposed on the mechanism of this local corrosion, such as interfacial turbulence, vaporization, oxygen potential, electrochemical reaction.

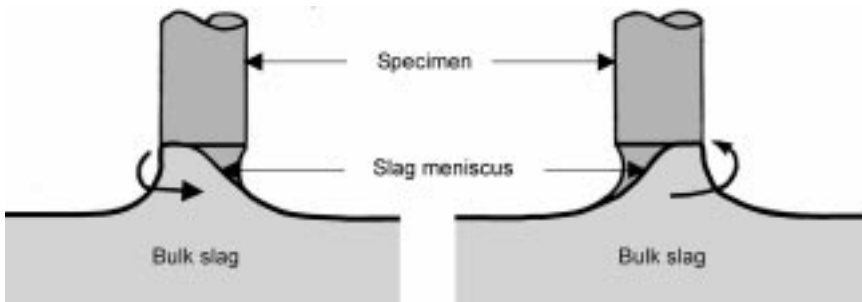
Recent investigations have led to the following conclusions by combining optical or X-ray radiographic techniques, aiming by direct observation of the phenomena which occur in the local corrosion zone, with the conventional immersion test.

(1) Local corrosion of oxide refractories and trough materials composed of oxide and SiC at the slag–gas and slag–metal interfaces is essentially caused by the active motion of the slag film formed by the wettability between the refractory and the slag. The slag film motion accelerates the dissolution rate of the refractory by breaking down the diffusion layer of the dissolved component from the refractory. The active film motion is dominantly induced by the Marangoni effect and/or change in the form of slag film (slag meniscus) due to the variation of interfacial tension and its density.

The flow pattern of the slag film (or slag meniscus) is different between the following two systems: (i) For the system where the dissolved component from refractory into the slag increases interfacial tension, the typical flow patterns are as those shown in Fig. 6.13 which was observed for the systems of $\text{SiO}_2(\text{s})-(\text{PbO}-\text{SiO}_2)\text{slag}$. The following systems are regarded as having a similar flow pattern to that of $\text{SiO}_2(\text{s})-(\text{PbO}-\text{SiO}_2)$ slag system: $\text{SiO}_2(\text{s})-(\text{PbO}-\text{SiO}_2)\text{slag-Pb(l)}$, magnesia–chrome refractory – $(\text{CaO}-\text{Al}_2\text{O}_3-\text{SiO}_2-\text{FeO})\text{slag}$, and blast furnace trough material – $(\text{CaO}-\text{Al}_2\text{O}_3-\text{SiO}_2)\text{slag-(Fe-C) alloy}$. (ii) For the



6.13 A typical flow pattern of slag film for the rod silica specimen dipped in $\text{PbO}-\text{SiO}_2$ slag.

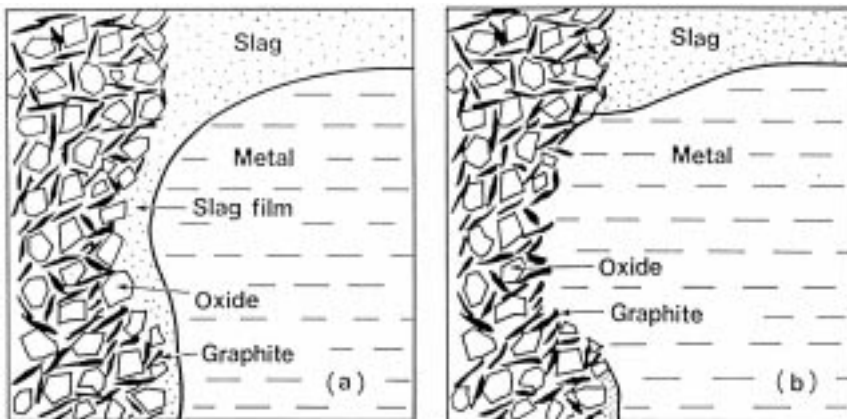


6.14 A rotational slag meniscus motion for the rod silica specimen dipped in $\text{FeO}-\text{SiO}_2$ slag.

system where the dissolved component from refractory into the slag decreases interfacial tension, the typical motions of the slag meniscus are shown in Fig. 6.14 which was observed for the system of $\text{SiO}_2(s)$ – $(\text{FeO}-\text{SiO}_2)$ slag system. The local corrosion zone of this system forms a steeper groove and narrower vertical zone than those of the case (i) above. The horizontal cross-section of the prism specimen of this system remains square during the entire corrosion process, while in the system described in (i), the cross-section of the prism specimen changes its shape from square to round. The flow pattern of the following practical refractory systems belongs to system (ii): blast furnace trough material– $(\text{CaO}-\text{Al}_2\text{O}_3-\text{SiO}_2)$ slag and magnesia-chrome refractory – $(\text{CaO}-\text{Al}_2\text{O}_3-\text{SiO}_2-\text{FeO})$ slag – Fe(l) .

SiO_2 scarcely decreases the surface tension of $\text{Na}_2\text{O}-\text{SiO}_2$ slag. When the SiO_2 specimen is partially immersed in this slag, a slag film is also formed above the slag level. However, neither film motion nor local corrosion is detected experimentally in this system.

(2) Local corrosion of refractories composed of oxide and graphite at the slag–metal interface is caused by the cyclic dissolution of oxide and graphite into the slag and metal phase, respectively. As shown in Fig. 6.15, when the wall of the Al_2O_3 -C or MgO -C refractory is initially covered with a slag film (Fig. 6.15a), the film not only wets the oxides, but dissolves them in preference to graphite. This changes the interface to a graphite-rich layer. Since the metal phase wets graphite better than the slag, the metal phase creeps up the surface of the specimen, as indicated in Fig. 6.15b, and dissolves graphite in preference to the oxides. Once the graphite-rich layer disappears due to dissolution into metal, the slag can again penetrate the boundary between the metal and the specimen, and the process is repeated. This cycle produces a local corrosion zone at the metal–slag interface. The up-and-down motion of the slag–metal interface shown in Fig. 6.15 was clearly observed using X-ray radiographic techniques. The Marangoni flow of the slag film is also considered to play an important role in the local corrosion of oxide–graphite refractory at the metal–slag interface during the stage shown in Fig. 6.15a and also the evolution of gas bubbles influence the dissolution process.



6.15 Schematic representation of the manner in which local corrosion of oxide-graphite refractory proceeds.

The local corrosion of oxide-graphite refractory also occurs at the interface of slag-oxidative gas. The manner in which the local corrosion occurs in this system is essentially the same as that for the oxide refractory-slag-liquid steel system when the oxidative gas phase, which removes the graphite in the refractory by oxidizing it, is replaced with a liquid steel phase and the present system is turned upside down.

6.4.2 The rate of heterogeneous reaction between gas and metal or slag and metal

The local corrosion of refractory described in Section 6.4.1 is a typical case of the heterogeneous reaction of the systems, refractory (solid)-slag-gas and refractory-slag-metal where the Maragoni effect accelerates the reaction rate. The rate of heterogeneous reaction of gas-metal and slag-metal is also seriously influenced by the addition of surface active agents such as oxygen, sulfur, etc. In particular, the reaction rate between nitrogen gas and liquid iron has been studied by many investigators. As a result, there is general agreement that surface active elements such as oxygen, sulfur, etc., inhibit the absorption rate of nitrogen into molten iron and also the desorption rate of nitrogen from liquid iron. Surface active elements at the surface of the liquid iron can be explained to affect reaction rates through a surface blocking mechanism.^{31,32}

Almost all the previous investigations were conducted under actively stirred conditions of metal phase, such as induction heating of metal, levitation of metal drop, free falling of metal drop, etc. When the metal is heated by an electric resistance furnace, that is, non-inductive heating, it is reasonably explained that the rates both of nitrogen absorption and desorption are dominantly influenced by the Marangoni convection.^{33,34} Nitrogen is a pretty strong surface active agent

although it is not as strong as oxygen or sulfur. Local differences in nitrogen concentration on the surface of liquid iron, which is generated by the blowing of nitrogen onto the surface or blowing argon gas onto the surface of liquid iron containing nitrogen, induces Marangoni convection (interfacial turbulence), resulting in the acceleration of the gas–metal reaction rate. Oxygen in the metal reduces the extent of surface activeness of nitrogen,³⁵ which suppresses the Marangoni convection caused by the local difference in nitrogen concentration on the surface and, as a result, decreases the rate of nitrogen–metal reaction.

We may deduce that oxygen acts on the rate of nitrogen–gas reaction in the following two ways: (1) surface blocking by the adsorbed oxygen on the liquid iron surface, and (2) reduction of the Marangoni convection induced by local differences in nitrogen concentration on this surface due to weakening of the surface activeness of nitrogen by the oxygen.

6.4.3 Bubble injection and slag foaming

Bubble injection

Bubble volume V_B (cm³) detached from the orifice plate immersed in liquid can be described by equation 6.69,³⁶ which was obtained experimentally, when orifice diameter d_o (cm) in equation 6.69 is replaced by d_{1m} , the maximum diameter of the periphery of a bubble adhering to the plate during its growth stage:

$$V_B = 0.0814 (V_G d_o^{0.5})^{0.867} \quad (6.69)$$

where V_G is gas flow rate (cm³/s). d_{1m} increases with increasing θ , resulting in an increase in the bubble volume V_B as predicted by equation 6.69. θ is the contact angle between liquid and orifice.

When bubbles are formed, for example, on the porous plug refractory, an increase in d_{1m} due to poor wettability between liquid steel and the oxide porous plug leads to the coalescence of adjacent bubbles on the surface of the plug. This coalescence may result in the formation of large bubbles in liquid steel. X-ray *in situ* observation revealed that the bubble formed on the oxide porous plug immersed in liquid Fe-C alloy is much larger than that on the same plug immersed in water.³⁷ Argon gas injected through porous refractory of the inner wall of the immersion nozzle may form a gas curtain (or film) between the boundary of liquid steel and the inner wall due to the poor wettability between liquid steel and the porous oxide refractory.³⁷ The gas curtain may effectively prevent the clogging of immersion nozzle in continuous casting of liquid steel.

Slag foaming

The main cause of slag foaming in iron and steelmaking processes is considered to be the high speed evolution of fine CO bubbles from the interface between

slag and metal due to metal–slag reaction.^{38,39} The fine CO bubble can be formed due to the good wettability between slag and liquid Fe-C alloy. Interfacial turbulence caused by the Marangoni convection may also participates in facilitating the fine CO bubble generation.

Foam stability can be expressed using the foam index $\Sigma(s)$ given by equation 6.70,⁴⁰ which was obtained semi-empirically:

$$\Sigma = 115\eta_s^{1.2}/\gamma_s^{0.2}\rho_sd_B^{0.9} \quad (6.70)$$

where η_s , γ_s and ρ_s are viscosity (N·s/m²), surface tension (N/m) and density (kg/m³) of slag, respectively.

Equation 6.71⁴¹ predicts that the foam height h_f is facilitated by the high speed evolution of the CO bubble, that is, large u_s , the superficial gas velocity and generation of CO bubbles with small diameter d_B :

$$h_f = u_s \cdot \Sigma \quad (6.71)$$

6.4.4 Penetration of slag or metal into refractory

Penetration of slag into refractory usually accelerates the rate of dissolution or abrasion of refractory into liquid slag and also the penetration layer of the refractory induces structural spalling, resulting in the shortening of the refractory life. Liquid slag penetrates very rapidly into MgO refractory because of the good wettability between the slag and MgO. Penetrated height h is linked with time, t by equation 6.72, which was obtained for the initial stage of the slag penetration by *in situ* observation with the aid of high temperature X-ray radiographic techniques:⁴²

$$h = kt^{1/2} \quad (6.72)$$

where k is constant and should depend on pore radius, surface tension and viscosity of slag, contact angle between slag and refractory, pore structure of refractory (for example, labyrinth factor), etc.

Refractories composed of oxide and graphite, such as magnesia–carbon and alumina–carbon are very effective for suppressing the slag penetration because the carbon acts as an inhibiting material for slag penetration due to the poor wettability between carbon and slag.

Usually liquid metal does not penetrate spontaneously into oxide refractory because of the poor wettability between the metal and oxide.

In general, porous purging plugs made of oxide are used to blow an inert gas into the molten steel. The life of a porous purging plug is determined by how deep the molten steel penetrates into the plug. The observed quantitative results obtained with the aid of high temperature X-ray radiography⁴³ indicates that the liquid steel penetration into porous refractory under external hydrostatic pressure is influenced by the structure and size distribution of pores in the

refractory, and also the chemical reaction between the steel and refractory, which mainly reduces the size of pore and contact angle between the liquid steel and refractory.

6.4.5 Interaction of foreign particles with solid–liquid interface

In the steelmaking process, the interaction between foreign particles in liquid steel and a solid–liquid interface should participate in the occurrence of bubble and inclusion-related defects in steel products and nozzle clogging in continuous casting of steel.

Many studies have been done theoretically and experimentally on the engulfment and pushing of foreign particles by the solidifying interface.^{44,45} The following factors were thought to have great influences on the engulfment or pushing of foreign particles: the size of foreign particles, solidifying velocity and the difference between the thermal conductivity of foreign particles and liquid. Various analytical models have been proposed for describing a critical solidifying velocity V_c in relation to the above mentioned factors by taking account of the forces of buoyant, viscous drag, Saffman and van der Waals forces acting on the particle in the vicinity of the advancing interface. The particle will be pushed ahead of the interface or engulfed by the interface depending on whether its velocity normal to the local interface is smaller or greater than some critical velocity, V_c . However, those models could not describe precisely the observed results.⁴⁵

During the solidification of molten steel, a boundary layer, in which the concentration and temperature gradients exist, is formed in front of the solidifying interface. Once inclusions and bubbles enter the boundary layer, concentration gradients of O, S, Ti, etc., can produce an interfacial tension gradient around the particle, and in turn, could result in a driving force acting on the particle. This driving force could make the particle move towards the solidifying interface and promote the engulfment of the foreign particles.²¹ The model taking account of the force caused by the surface tension gradient provides a reasonable explanation of the fact that bubble defects in practical continuous casting operations increase with the increase of surface active element concentrations in molten steel.⁴⁶

The clogging of the immersion nozzle in the continuous casting process results mainly from alumina build-up on the inner wall of immersion nozzle. Recently various models for explaining the mechanism of nozzle clogging were proposed. However, none of them could fully succeed in clarifying the mechanism. The force caused by the interfacial tension gradient between inclusion and liquid steel acting on the inclusion may hold a key to solve this technological problem of nozzle clogging. That may be the reason why very little inclusion is built up on the inner wall when the inner wall of the alumina-graphite nozzle is covered with high Al₂O₃ material, for the high Al₂O₃ material

intercepts the SiO and CO gas (generated in the nozzle) transfer via the inner wall–liquid steel interface into the steel, resulting in the reduction of the concentration gradient of Si and C in the vicinity of the interface.⁴⁶

6.5 Further reading

The thermodynamic part of Section 6.2 has been compiled with reference to publications 1 and 2 and quoting partially from references 3 and 4.

1. R. Defay and I. Prigogine (translated by D.H. Everett), *Surface Tension and Adsorption* (1966) New York, John Wiley and Sons, Inc.
2. S. Ono and S. Kondo, ‘Molecular Theory of Surface Tension in Liquids’, in S. Flügge, *Handbuch der Physik, Band X* (1960) Berlin, Springer-Verlag, 134–280.
3. J.G. Kirkwood and I. Oppenheim, *Chemical Thermodynamics* (1962) New York, McGraw-Hill.
4. C. Herring, ‘The Use of Classical, Macroscopic Concepts in Surface-Energy Problems’, in R. Gomer and C.S. Smith, *Structure and Properties of Solid Surfaces* (1953) Chapter 1, Chicago, Univ. Chicago Press, 5–72.

6.6 References

1. C. Marangoni, ‘Über die Ausbreitung der Tropfen einer Flüssigkeit auf der Oberfläche einer anderen’, *Ann. Phys. Chem.* (1871) **143**, 337–354.
2. T. Hibiya, S. Nakamura, K. Mukai, Z.G. Niu, N. Imaishi, S. Nishizawa, S. Yoda and M. Koyama, ‘Interfacial phenomena of molten silicon: Marangoni flow and surface tension’, *Phil. Trans. R. Soc. Lond. A* (1998) **356**, 899–909.
3. T. Nakamura, K. Yokoyama, F. Noguchi and K. Mukai, ‘Direct Observations of Marangoni Convection in Molten Salts’, *Materials Science Forum* (1991) **73–75**, 153–158.
4. K. Mukai, J.M. Toguri, I. Kodama and J. Yoshitomi, ‘Effect of Applied Potential on Interfacial Tension between Liquid Lead and PbO-SiO₂ Slags’, *Canadian Metallurgical Quarterly* (1986) **25**(3), 225–231.
5. K. Mukai, ‘Marangoni flows and corrosion of refractory walls’, *Phil. Trans. R. Soc. Lond. A* (1998) **356**, 1015–1026.
6. J.K. Brimacombe and F. Weinberg, ‘Observations of Surface Movements of Liquid Copper and Tin’, *Metallurgical Transactions* (1972) **3** (Aug.), 2298–2299.
7. S. Kimura, Y. Nabeshima, K. Nakajima and S. Mizoguchi, ‘Behavior of Nonmetallic Inclusions in Front of the Solid–Liquid Interface in Low-Carbon Steels’, *Metallurgical and Materials Transactions B* (2000) **31B** (Oct.), 1013–1021.
8. K. Mukai and W. Lin, ‘Motion of Small Particles in Solution with an Interfacial Tension Gradient and Engulfment of Particles by Solidifying Interface’, *Tetsu-to-Hagané* (1994) **80**(7), 527–532.
9. F.V. Vader, T.F. Erkens and V. Tempel, ‘Measurement of Dilatational Surface Properties’ *Trans. Faraday Soc.* (1964) **60**, 1170–1177.
10. J.A. Kitchener, ‘Confirmation of the Gibbs Theory of Elasticity of Soap Film’, *Nature* (1962) **194**, 676–677.
11. J.A. Kitchener, ‘Elasticity of Soap Films: an Amendment’, *Nature* (1962) **195**, 1094–1095.

12. S. Seetharaman, K. Mukai and D. Sichen, 'Viscosities of slags – an overview, *VII Int. Conf. Molten Slags Fluxes and Salts*', Cape Town, The South African Institute of Mining and Metallurgy (2004), 31–41.
13. R.N. Wenzel, 'Resistance of Solid Surfaces to Wetting by Water' *Ind. Eng. Chem.* (1936) **28**, 988–994.
14. A.B.D. Cassie and S. Baxter, 'Wettability of Porous Surfaces' *Trans. Faraday Soc.* (1944) **40**, 546–551.
15. K. Wasai and K. Mukai, 'Thermodynamics of Nucleation and Supersaturation for the Aluminum-Deoxidation Reaction in Liquid Iron', *Metallurgical and Materials Transactions B* (1999) **30B**(Dec.), 1065–1074.
16. D. Turnbull and J.C. Fisher, 'Rate of Nucleation in Condensed Systems', *J. Chem. Phys.* (1949) **17**(1), 71–73.
17. J.H. Hollomon and D. Turnbull, 'Nucleation', Chapter 7 in B. Chalmers, *Progress in Metal Physics*, London, Pergamon Press (1953) **4**, 342–343.
18. K. Mukai, T. Matsushita and S. Seetharaman, 'Motion of Fine Particles in Liquid Caused by Interfacial Tension Gradient in Relation to Metals Separation Technologies', *Metal Separation Technologies III*, Copper Mountain, Colorado, Helsinki Univ. of Technology (2004), 269–273.
19. R.E. Boni and G. Derge, 'Surface Tensions of Silicates', *Trans. Met. Soc. AIME* (1956) **206**, 53–59.
20. B.J. Keene, 'Review of data for the surface tension of iron and its binary alloys', *International Materials Reviews* (1988) **33**(1), 1–37.
21. Z. Wang, K. Mukai and I.J. Lee, 'Behavior of Fine Bubbles in Front of the Solidifying Interface', *ISIJ International* (1999) **39**(6), 553–562.
22. K. Mukai and N. Shinozaki, 'Melting and Flow Behavior of Fe-O Melts Heated by Plasma Arc', *Materials Transactions, JIM* (1992) **33**(1), 45–50.
23. K.C. Mills and B.J. Keene, 'Factors affecting variable weld penetration', *International Materials Reviews* (1990) **35**(4), 185–216.
24. K. Ishizaki, N. Araki and H. Murai, 'Interfacial Tension Theory on the Phenomena of Arc Welding (Chapter 9)', *J. Jpn Weld. Soc.* (1965) **34**(2), 146–153.
25. B.J. Keene, 'Interfacial Tension between Ferrous Melts and Molten Slags', *NPL Report DMM(D)115* (Nov.) (1991) 1–206.
26. P. Kozakevitch, G. Urbain and M. Sage, 'Sur la tension interfaciale fonte/laitier et le mécanisme de désulfuration', *Revue de Metallurgie* (1955) **LII**(2), 161–172.
27. A.A. Deryabin, S.I. Popel and L.N. Saburov, 'Non-equilibrium Interfacial Tension and Adhesion in the System of Liquid Metal-Oxide', *Izv. A. N. SSSR Metally* (1968) **5**, 51–59.
28. K. Nogi (2001), 'Wettability between Liquid Metals and Ceramics', Chapter 3, in T. Toshio *et al.*, *Wettability Technology Handbook* (2001) Techno System Co. Ltd, 127–145.
29. N. Shinozaki, N. Echida, K. Mukai, Y. Takahashi and Y. Tanaka, 'Wettability of Al₂O₃-MgO, ZrO₂-CaO, Al₂O₃-CaO Substrates with Molten Iron', *Tetsu-to-Hagané* (1994) **80**(10), 743–752.
30. K. Mukai and Z. Tao, 'Local corrosion of refractories in iron and steelmaking processes', *Recent Res. Devel. in Metallurg. and Materials Sci.* (1998) **2**, 17–24.
31. M. Byrne and G.R. Belton, 'Studies of the Interfacial Kinetics of the Reaction of Nitrogen with Liquid Iron by the ¹⁵N-¹⁴N Isotope Exchange Reaction', *Metall. Trans. B* (1983) **14B**, 441–449.

32. J. Lee and K. Morita, 'Interfacial Kinetics of Nitrogen with Molten Iron Containing Sulfur', *ISIJ International* (2003) **43**(1), 14–19.
33. Z. Jun and K. Mukai, 'The Influence of Oxygen on the Rate of Nitrogen Absorption into Molten Iron and Marangoni Convection', *ISIJ International* (1998) **38**(3), 220–228.
34. Z. Jun and K. Mukai, 'The Rate of Nitrogen Desorption from Liquid Iron by Blowing Argon Gas under the Condition of Non-inductive Stirring', *ISIJ International* (1999) **39**(3), 219–228.
35. Z. Jun and K. Mukai, 'The Surface Tension of Liquid Iron Containing Nitrogen and Oxygen', *ISIJ International* (1998) **38**(10), 1039–1044.
36. L. Davidson and E.H. Amick Jr., 'Formation of Gas Bubbles at Horizontal Orifices', *A. I. Ch. E. J.* (1956) **2**(3), 337–342.
37. Z. Wang, K. Mukai and D. Izu, 'Influence of Wettability on the Behavior of Argon Bubbles and Fluid Flow inside the Nozzle and Mold', *ISIJ International* (1999) **39**(2), 154–163.
38. Y. Ogawa and N. Tokumitsu, 'Observation of Slag Foaming by X-ray Fluoroscopy', Sixth Int. *Iron and Steel Congress*, Nagoya, ISIJ (1990), 147–152.
39. K. Mukai, 'Some Views on the Slag Foaming in Iron and Steelmaking Processes', *Tetsu-to-Hagané* (1991) **77**(6), 856–858.
40. Y. Zhang and R.J. Fruehan, 'Effect of the Bubble Size and Chemical Reactions on Slag Foaming', *Metallurgical and Materials Transactions B* (1995) **26B** (Aug.), 803–812.
41. K. Ito and R.J. Fruehan, 'Study on the Foaming of CaO-SiO₂-FeO Slags', *Metallurgical Transactions B* (1989) **20B** (Aug.), 509–514.
42. K. Mukai, Z. Tao, K. Goto, Z. Li and T. Takashima, 'In-situ observation of slag penetration into MgO refractory', *Scandinavian Journal of Metallurgy* (2002) **31**, 68–78.
43. T. Matsushita, T. Ouchi, K. Mukai, I. Sasaka and J. Yoshitomi, 'Direct Observation of Molten Steel Penetration into Porous Refractory', *J. Technical Association of Refractories, Japan* (2003) **23**(1), 15–19.
44. K. Mukai, 'Engulfment and Pushing of Foreign Particles Such as Inclusions and Bubbles at Solidifying Interface', *Tetsu-to-Hagané* (1996) **82**(1), 8–14.
45. R.W. Smith, X. Zhu, M.C. Tunnicliffe, C.L. Russell and W.M.T. Gallerneault, 'The Capture of Suspended Particles as a Crystallising Phase Advances into Its Melt', 1st Int. Sympo. *Microgravity Research & Applications in Physical Sciences & Biotechnology*, Sorrento, ESA SP-454 (2001), 613–620.
46. K. Mukai and M. Zeze, 'Motion of Fine Particles under Interfacial Tension Gradient in Relation to Continuous Casting Process', *Steel Research* (2003) **74**(3), 131–138.

The kinetics of metallurgical reactions

S S R I D H A R , Carnegie Mellon University, USA and
H Y S O H N , University of Utah

7.1 Introduction

Metallurgical processes such as extraction, refining, casting or annealing, almost always involve multiple phases and the kinetics are often coupled with the rate of movement of boundaries (surfaces and interfaces) between phases. Therefore, the emphasis of this chapter is on the fundamentals of heterogeneous reactions.

7.2 Fundamentals of heterogeneous kinetics

The recovery of metal values from their ores requires heterogeneous reactions between phases. Pyrometallurgical reactions such as the reduction of metal oxides and sulfides, the various types of roasting of metal sulfides, and hydrometallurgical operations such as leaching and solvent extraction are some examples.

Heterogeneous reactions take place at a phase boundary between the reacting phases, unlike homogeneous reactions that take place over the entire volume of a given phase. Therefore, heterogeneous reactions always accompany the transfer of mass between the reaction interface and the bulk phase, in addition to the rate of the chemical reaction. Additionally, many chemical reactions are accompanied by the absorption or liberation of heat, and hence the transport of heat must also be considered. For this reason, most heterogeneous reactions involve a rather complex set of steps. Most reactions in metallurgical processes are between solids and fluids in which the solid participates as a reactant that undergoes chemical changes. Although reactions between immiscible liquid phases and between a gas and a liquid are also heterogeneous in nature, the discussion in this section will largely involve the analysis of fluid–solid reactions. Most gas–liquid and liquid–liquid reactions are rate-controlled by mass transfer, and thus their analysis reduces to a problem of mass transfer combined with chemical equilibrium at the interface.

The individual component steps of the overall heterogeneous reaction process are described in this section.

7.2.1 Reactions involving adsorption and desorption

Most heterogeneous reactions occurring in metallurgical systems are described with rate expressions that are of first order with respect to the fluid reactant and product. Although often justified, they are not always correct, and even when the use of the first-order dependence is reasonable, it applies only in the range of concentrations in which the data have been collected. Extrapolation beyond this range of concentrations is risky. The reason for this is that heterogeneous reactions involve the adsorption and desorption of the reactants and products present in the fluid phase. These processes make the general rate expression nonlinear (Szekely *et al.*, 1976).

Furthermore, the rates of the intrinsic chemical reactions cannot be estimated to any reasonable degree of reliability and are highly specific to the chemical as well as the physical nature of the substances involved. Thus, these rates can only be obtained by experiments. This is in contrast to transport properties, which can be estimated to reasonable accuracy without the need of experiments. This applies in large measure to turbulent flows and mass transfer through the pores of a porous solid.

Let us consider the following fluid–solid reaction to represent heterogeneous reactions:



Rather comprehensive review and derivation of the rare expressions for reactors involving adsorption, desorption, and surface reaction have been presented by Szekeley *et al.* (1976). The resulting rate expressions have somewhat different forms depending on which among the above steps controls the overall rate. However, they all are special cases of the following expression, in terms of the molar rate of consumption of the fluid reactant per unit area of the reaction interface:

$$(-\dot{m}_A) = \frac{k(C_A^m - C_C^n/K_C)}{1 + K_1 C_A^i + K_2 C_C^j} \quad (7.2)$$

or

$$= \frac{k_p(p_A^m - p_C^n/K_p)}{1 + K'_1 p_A^i + K'_2 p_C^j}$$

The terms in the denominators arise from the adsorption and desorption of the fluid species. For liquid–solid reactions, the molar concentration is used in the rate equation. For gas–solid reactions, either the molar concentration or the partial pressure has been used in the literature. Partial pressure is preferred for gas–solid reactions because it more accurately represents the activity of a gaseous species and K_p in the rate equation is the thermodynamic equilibrium constant. In this chapter, however, the molar concentration is used to simultaneously treat both the gas–solid and liquid–solid reaction systems. For a gas–solid reaction at equilibrium, $\dot{m}_A = 0$ and

$$K_C = \frac{C_C^n}{C_A^m} = \frac{(p_C/RT)^n}{(p_A/RT)^m} = \frac{p_C^n}{p_A^m} (RT)^{m-n} = K_p (RT)^{m-n} \quad (7.3)$$

For a liquid–solid reaction, K_C is related to the thermodynamic equilibrium constant through the activity coefficients. Many reactions can be described by a simple kinetic expression with $m = n = 1$ and $K_1 = K_2 = 0$ in equation 7.2, which represents a first-order reversible reaction. This further simplifies to the often used first-order rate expression when K_C or K_p is large, i.e. the reaction is irreversible.

7.2.2 Heat and mass transfer

Diffusion in a binary mixture

The transport of species in the fluid phase occurs as a result of concentration differences. The movement of a species in a binary mixture of species A and C in the presence of a concentration gradient and in the absence of turbulence is described by Fick's first law of diffusion:

$$N_i = -CD_{AC}\nabla x_i + x_i(N_A + N_C) \quad (7.4)$$

Here the molar flux is defined with respect to fixed coordinates and is expressed as

$$N_i = x_i C u_i \quad (7.5)$$

It is noted that, for equimolar counter diffusion,

$$N_A = -N_C \quad (7.6)$$

In equation 7.4, the second term on the right-hand side refers to the flux of species A resulting from the bulk motion of the fluid, and the first term is due to the diffusion superimposed on the bulk flow.

The binary molecular diffusivity D_{AC} is a function of temperature and pressure. For gases at low density the molecular diffusivity is relatively independent of mole fraction, whereas for liquids the dependence on concentration can be significant. Extensive literature is available on the estimation of diffusivities. The diffusivities of gases can, in general, be estimated more accurately (Bird *et al.*, 2002; Reid *et al.*, 1973; Satterfield, 1970) than those in a liquid phase (Bird *et al.*, 2002; Reid *et al.*, 1973).

Multicomponent diffusion

Although theories of binary diffusion are sufficient to describe most metallurgical systems, there are situations where multicomponent diffusion must be considered. The rigorous equation to describe the mass flux may be found elsewhere (Bird *et al.*, 2002). However, a simplified equation for the molar flux results if the species are assumed to behave ideally (Bird *et al.*, 2002):

$$\nabla x_i = \sum_{j=1}^n \frac{1}{CD_{ij}} (x_i N_j - x_j N_i) \quad (7.7)$$

where D_{ij} is the binary diffusivity. The calculation of the concentration gradient in multicomponent diffusion through the solution of the rigorous Stefan–Maxwell equations is rather complex.

In some instances, it is convenient to define an effective binary diffusivity D_{im} so that the flux of i in a multicomponent system can be expressed by a relation analogous to equation 7.4 (Bird *et al.*, 2002):

$$N_i = -CD_{im}\nabla x_i + x_i \sum N_j \quad (7.8)$$

Certain approximations can be made to evaluate D_{im} for special cases, and one that has proved useful when the variation of D_{im} is considerable is to assume a linear dependence on concentration (Reid *et al.*, 1973). Satterfield (1970) provides the following equation:

$$D_{im} = (1 - x_i) \left(\sum_{j \neq i} \frac{x_j}{D_{ij}} \right)^{-1} \quad (7.9)$$

Conduction

The conduction of heat is governed by Fourier's law:

$$q = k\nabla T \quad (7.10)$$

Here, q is the heat flux vector and k is thermal conductivity. Methods for estimating thermal conductivities of gases, liquids, and solids are available in the literature (Bird *et al.*, 2002; Reid *et al.*, 1973).

Transfer in porous media

Many solid reactants have some porosity, allowing the fluid phase to diffuse in while reacting with it. Additionally, in recent times much attention has been directed towards feed preparation so that solids have sufficient porosity and yet have sufficient strength to withstand the physical forces in the reactor. Extensive investigations have been made on heat and mass transfer in porous solids (Szekely *et al.*, 1976; Satterfield, 1970).

The conduction of heat in a porous solid is also described by Fourier's law of conduction, as stated in equation 7.10, but the thermal conductivity of a porous solid is not well understood. The usual approach is to define an effective thermal conductivity that relates the heat flux to the temperature gradient. Experimentally measured values of effective thermal conductivity are most reliable. Some methods of estimating this parameter, however, are available. Two extreme types of behavior are considered, with real systems occupying an intermediate position. The first type is a solid made up of a continuous solid

phase containing closed and isolated pores filled with a fluid that has a thermal conductivity much lower than that of the solid. Most porous pellets are described by this case. The effective thermal conductivity for such a solid is expressed as (Francl and Kingery, 1954)

$$k_e = k(1 - \epsilon) \quad (7.11)$$

In the second case, the fluid is considered to be a continuum, and the solid is made up of small particles that are in point contact with the neighboring particles (Kunii and Smith, 1960). This picture best describes loose compacts of fine powders. The effective thermal conductivity depends largely on that of the fluid.

The transport of matter in a porous solid matrix is an important step in heterogeneous reactions since fluid molecules must diffuse through the pores to gain access to the solid surface. Factors that complicate the description of pore diffusion are:

- (a) The volume occupied by the solid is not available for mass transfer.
- (b) The diffusion path is quite tortuous.
- (c) Molecular diffusion or Knudson diffusion or both play an important role, depending on the pore size.
- (d) Bulk flows, sometimes with large pressure gradients, may develop within the solid (Evans and Song, 1973; Evans, 1972). This may occur when there is a net generation of product gases with the chemical reaction. When the pores are small, a large pressure gradient may develop.

The effective diffusivity of the fluid in the pores of the solid is in general much smaller than the molecular diffusivity and includes the various factors discussed above. Comprehensive discussions on the earlier work can be found in (Szekely *et al.*, 1976; Satterfield, 1970; Smith, 1970; Mason and Marrero, 1970).

A widely used treatment of pore diffusion is attributed to Mason and co-workers (1970; 1967). For a binary mixture in an isothermal system,

$$N_A = -D_{Aeff} \nabla C_A + x_A \delta_A N - x_A \gamma_A (C_T B_0 / \mu) \nabla P \quad (7.12)$$

and

$$N - \beta_A N_A = - \left(\frac{D_{BK}}{RT} \right) \left(1 + \frac{pB_0}{D_K} \right) \nabla P \quad (7.13)$$

where

$$N = N_A + N_C, \quad \text{i.e., total flux} \quad (7.14)$$

$$1/D_{Aeff} = 1/D_{AK} + 1/D_{ACeff} \quad (7.15)$$

$$\delta_A = D_{Aeff}/D_{ACeff} \quad (7.16)$$

$$\gamma_A = D_{Aeff}/D_{AK} \quad (7.17)$$

$$\beta_A = 1 - D_{CK}/D_{AK} \quad (7.18)$$

and

$$1/D_K = x_A/D_{AK} + x_C/D_{CK} \quad (7.19)$$

Here, B_0 is a parameter characteristic of the solid, and μ is the viscosity of the fluid. In equation 7.12, the first term on the right-hand side refers to the diffusive flux resulting from the concentration gradient, the second term is the bulk flow term, and the third is the viscous flow term. Under certain circumstances the bulk flow and viscous flow terms may be neglected. When equimolar counter-diffusion is encountered or when the mole fraction of the transferred species is small, the bulk flow term may be neglected.

The effective diffusivities are estimated as follows:

$$D_{ACeff} = D_{AC}(\epsilon/\tau) \quad (7.20)$$

where ϵ is the porosity and τ is the tortuosity factor characteristic of the solid; and

$$D_{AK} = \left(\frac{4}{3}\right) \left(\frac{8RT}{\pi MA}\right)^{1/2} K_0 \quad (7.21)$$

where K_0 is a constant characteristic of the solid that has a unit of length.

The dusty gas model of Mason *et al.* (1967), which assumes the solid to be made up of spherical particles of radius r_g , gives

$$K_0^{-1} = \left(\frac{128}{9}\right) \left(\frac{n_d \tau}{\epsilon}\right) r_g^2 \left(1 + \frac{\pi}{8}\right) \quad (7.22)$$

Additional developments and reviews on diffusion in porous media are given in the literature (Abbasi *et al.*, 1983; Ohmi *et al.*, 1982; Gavalas and Kim, 1981; McCune *et al.*, 1979; Chen and Rinker, 1979; Alzaydi *et al.*, 1978; Pismen, 1974; Youngqvist, 1970; Wakao and Smith, 1962).

Convective heat and mass transfer

In a heterogeneous reaction system, the transfer of heat and mass between the interface and the bulk fluid is an important step in the overall process. The rate of mass transfer between the bulk fluid and the surface of a solid is expressed as

$$N_A = k_m(C_{As} - C_{Ab}) \quad (7.23)$$

where C_{As} and C_{Ab} are respectively the concentration of the species A at the surface of the solid and that in the bulk fluid, and k_m is the external mass-transfer coefficient. The above equation assumes that the flux is proportional to the concentration difference. Bird *et al.* (2002) have suggested that a more rigorous equation that includes a net flow normal to the interface is

$$N_A = k_m(C_{As} - C_{Ab}) + x_A(N_A + N_C) \quad (7.24)$$

where the second term is the net flow normal to the interface. In most fluid–solid systems, $x_A \ll 1$ or equimolar counterdiffusion takes place so that $N_A = -N_B$. In either case, equation 7.24 reduces to equation 7.23. Considering that x_A may vary significantly between the interface and the bulk fluid, Han and Sohn [2004] developed the following expression for the average mole fraction to be used in place of x_A in equation 7.24:

$$1 + (\nu - 1)\tilde{x}_A = \frac{[1 + (\nu - 1)x_{As}] - [1 + (\nu - 1)x_{Ab}]}{\ln \frac{1 + (\nu - 1)x_{As}}{1 + (\nu - 1)x_{Ab}}} \quad (7.25)$$

where

$$\nu = -\frac{N_C}{N_A} \quad (7.26)$$

Frequently, the mass-transfer coefficient is expressed as the Chilton–Coburn j factor, defined as

$$j_D = \frac{Sh}{ReSc^{1/3}} \quad (7.27)$$

Various correlations of this form are available in the literature (Evans, 1979; Malling and Thodos, 1967; Wilson and Geankoplis, 1966; Rowe *et al.*, 1965).

A correlation for mass transfer involving single spheres that has found wide application is that by Ranz and Marshall (1952):

$$Sh = 2.0 + 0.6 Re^{1/2} Sc^{1/3} \quad (7.28)$$

It must be pointed out that at a low Reynolds number the effect of natural convection can become significant, and correlations including this effect must be used (Steinberger and Treybal, 1960).

The description of external heat transfer is similar to that of external mass transfer. The heat flux to the solid surface is expressed as

$$q = h(T_s - T_b) \quad (7.29)$$

where h is the heat-transfer coefficient and T_s and T_b are the temperatures of the solid surface and the bulk fluid, respectively. The form of the empirical correlations for heat transfer can be obtained in a manner similar to that of the mass-transfer correlation. By analogy with mass transfer, the Ranz–Marshall equation for heat transfer may be written as

$$Nu = 2.0 + 0.6 Re^{1/2} Pr^{1/3} \quad (7.30)$$

and additionally it may be assumed that the Chilton–Coburn j factors are identical for mass and heat transfer, i.e.,

$$j_D = j_H \quad (7.31)$$

where

$$j_H = \frac{Nu}{RePr^{1/3}} \quad (7.32)$$

At high temperatures, the solid may receive heat from its surrounding by radiation in addition to convection described above. The rate of radiative transfer is described by the Stefan–Boltzman equation. As an example, the expression for simple radiative heat transfer between two surfaces of equal emissivity may be written for the surface with a unit view factor as follows:

$$q_r = \sigma\epsilon(T_e^4 - T_s^4) \quad (7.33a)$$

where q_r is the radiative flux, ϵ is the emissivity and σ is the Stefan–Boltzman constant. The description of radiative transfer in general is quite complex and is strongly dependent on the system geometry. While the above equation is a fairly good approximation, it is generally suggested that the relative importance of radiation and convection be determined prior to including a description of radiative transfer. For this purpose, it is convenient to define a radiative heat-transfer coefficient, h_r ,

$$h_r = \sigma\epsilon(T_e^2 + T_s^2)(T_e + T_s) \quad (7.33b)$$

and

$$q_r = h_r(T_e - T_s) \quad (7.33c)$$

Then, h_r may be combined with h to give the total heat-transfer coefficient.

When two surfaces that are not oriented parallel to one another exchange radiative heat, the radiation incident on each surface is only part of the total emissive power and depends on the surface geometries and orientations. This is accounted for by a so-called view factors (F_{ij}) which can be computed but are tabulated in textbooks for simple cases (Poirier and Geiger, 1994). If two surfaces (1 and 2) have arbitrary shapes and orientations, the net radiative exchange will be:

$$q_{1 \rightarrow 2} = F_{12}\sigma\epsilon_1 T_1^4 - F_{21}\sigma\epsilon_2 T_2^4 \quad (7.33d)$$

The view factors have two important properties; (i) the reciprocity relation:

$$\mathbf{A}_i \cdot \mathbf{F}_{ij} = \mathbf{A}_j \cdot \mathbf{F}_{ji}$$

and (ii) that the sum of all view factors for a given surface equals unity, i.e.

$$\sum_{j=1}^n \mathbf{F}_{ij} = \mathbf{1}$$

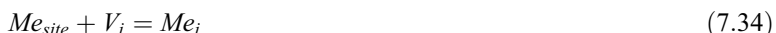
Radiative heat transfer in an enclosure consisting of surfaces of different temperatures and radiative properties requires more complex treatment (Modest, 1993). The procedure becomes even more difficult when involving suspended particulate and temperature variations within the volume of the enclosure (Hahn and Sohn, 1990b; Perez-Tello *et al.*, 2001b).

7.3 Solid-state reactions

7.3.1 Reaction in a single phase

Point defect formation and elimination

In metals, point defects are not charged and thus the condition of electro-neutrality does not arise as it does for ionic crystals. Thus in metals single defects form rather than pairs of oppositely charged defects. In general, single defects such as vacancies or interstitials form at sites such as dislocation, grain boundaries (low and high angle) and surfaces according to the following equilibria:



and



Here, the subscript ‘site’ refers to a defect generation site.

Homogenization of compositional gradients

These reactions are diffusional processes where inequalities in concentrations and thus chemical potential gradients are equilibrated through transport of mass. In the cases where the non-equilibrium is caused by a single interstitially dissolved element at dilute amounts, the process can be readily described by an appropriate mathematical solution to Fick’s first and second laws for diffusion:

$$\bar{J} = -D \cdot \nabla C \quad (7.36)$$

$$\frac{\partial C}{\partial t} = D \nabla^2 C \quad (7.37)$$

Here J is the flux of atoms per unit area, D is the diffusion coefficient and C is the concentration of the diffusing species. For isotropic solids, the diffusion coefficient can be taken as a constant whereas, for non-isotropic solids, D will be described by a 3×3 matrix.

The appropriate solution to Fick’s laws can be found by solving the equations above, using the geometry of the system and boundary conditions. For more complex solutions, monographs on the mathematics of diffusion (Crank, 1956) or thermal conduction (Fourier’s laws are mathematically identical to Fick’s laws for these cases) can be used to find solutions (Carslaw and Jaeger, 1959).

An example of simple one-dimensional diffusion processes and their appropriate mathematical descriptions is discussed below.

In order to make an electronic component, boron has to be implanted into silicon. To do this, a thin silicon film containing boron is deposited on one surface of a 2 mm thick silicon wafer. The thickness of the film is $\delta \mu\text{m}$ and boron concentration is $C_0 \text{ atoms/m}^3$. Diffusion coefficient of B in Si is $D \text{ m}^2/\text{s}$. If the silicon wafer can be assumed to be semi-infinite compared to the deposited

film, the concentration of B in the Si wafer will be described by the following solution to Fick's second law:

$$C = \frac{\delta C_0}{\sqrt{\pi D t}} \exp\left(-\frac{x^2}{4 D t}\right) \quad (7.38)$$

In non-dilute binary substitution systems such as diffusion couples several complications arise with respect to the mathematical treatment of the problems. First, if fluxes of the two elements are substantially different there will be a net movement of vacancies, which can cause the so-called Kirkendall shifts (Smigelskas and Kirkendall, 1947). This is a process by which mass is transported due to stress gradients caused by the vacancies without involving diffusional processes. Second, large concentration gradients invalidate the equality of concentration gradients to chemical potential gradients, i.e. activity coefficients need to be considered. Third, the intrinsic diffusion coefficients themselves are likely to vary. In the case of a binary semi-infinite diffusion couple problem like the one shown in Fig. 7.1, the two intrinsic diffusion coefficients that vary with position can be replaced with a so-called chemical diffusion coefficient (Darken and Gurry, 1953):

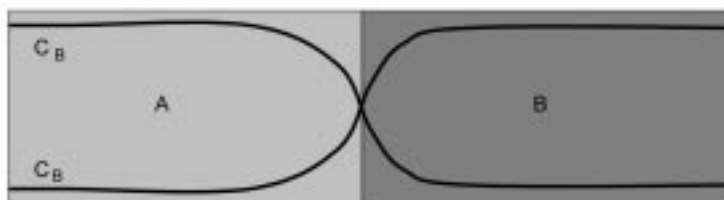
$$\tilde{D} = (N_2 D_1^* + N_1 D_2^*) \left(1 + \frac{d \ln \gamma_1}{d \ln N_1}\right) \quad (7.39)$$

Here, N_1 and N_2 are the mole fractions, γ_1 is the activity coefficient of component 1 and D_1^* and D_2^* are the tracer diffusion coefficients of 1 and 2.

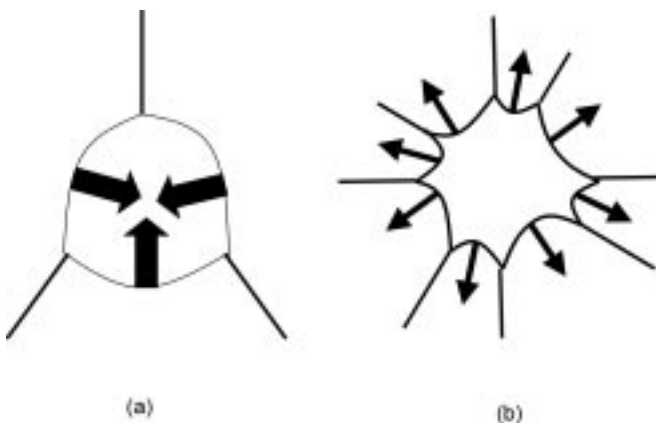
The tracer diffusion coefficients differ from the intrinsic ones in that they are not affected by activity coefficients but they may nevertheless vary with composition. The chemical diffusion coefficient can now be used in Fick's second law but since it is a function of composition and space, analytical solutions cannot be readily obtained.

Evolution of grains

In polycrystalline metal alloys, a random grain structure is inherently unstable since grains will more often than not have a net curvature and thus all the grain boundary tension forces are not balanced. Therefore, when annealed grain boundaries will tend to migrate towards their centers of curvature. The force on



7.1 Binary diffusion couple.



7.2 Two-dimensional grain model.

a boundary of curvature r , will be of the magnitude γ/r . The effect of curvature can be exemplified by the two-dimensional model shown in Fig. 7.2.

At the junction between three grains of equal boundary energy, a force balance necessitates that a 120° angle is formed. Therefore, a grain is only stable when it has six boundaries. If the number of boundaries around a grain is fewer than six, the boundaries will all curve in a convex manner towards the grain (see Fig. 7.2a) and the grain will tend to shrink. The opposite will occur when the number of boundaries is greater than six (see Fig. 7.2b). As a result, during annealing there will be an increase in the mean grain size and a decrease in the number of grains. This process is known as grain growth. Atomistically, atoms detach themselves from the high pressure concave side of the boundary (the shrinking grain) and attach themselves on the low-pressure convex side (the growing grain).

The pressure difference across a boundary can be related to a potential – or free energy difference:

$$\Delta G = \frac{2\gamma V_m}{r} \quad (7.40)$$

where V_m is the molar volume, and ΔG is the free energy difference, per atom, between two grains adjacent to a curved boundary. It should be mentioned that while ΔG is the driving force behind all grain boundary motion, it is governed by dislocation strain-energies rather than grain curvatures in the case of recrystallization. The effect of ΔG on the grain migration kinetics can be described in the same way for recrystallization and grain growth. The flux of atoms from grain 1 to grain 2 can be expressed as an activated process (Porter and Easterling, 1992):

$$J_{1 \rightarrow 2} = A_2 n_1 \nu_1 \exp\left(-\frac{\Delta G^*}{RT}\right) \left(1 - \exp\left(-\frac{\Delta G}{RT}\right)\right) \quad (7.41)$$

Here, J is the net flux, A_2 is the probability that a migrating atom from grain 1 will attach to grain 2, n_1 is the number of atoms in a favorable position to jump in grain 1, ν_1 is the atom vibration frequency and ΔG^* is the activation energy needed for an atom to escape from grain 1.

If the boundary is to move at a velocity, the flux J should be equal to $v/(V_m/N_a)$, where N_a is the Avogadro's number and we get, assuming a sufficiently high temperature such that $RT \gg \Delta G$:

$$\nu = \frac{A_2 n_1 \nu_1 V_m^2}{N_a R T} \exp\left(-\frac{\Delta G^*}{R T}\right) \cdot \frac{\Delta G}{V_m} \quad (7.42)$$

which means that the velocity should be, at a constant temperature, proportional to the driving force,

$$v \propto \frac{\Delta G}{V_m} \quad (7.43)$$

The proportionality constant is defined as M = mobility of the grain boundary.

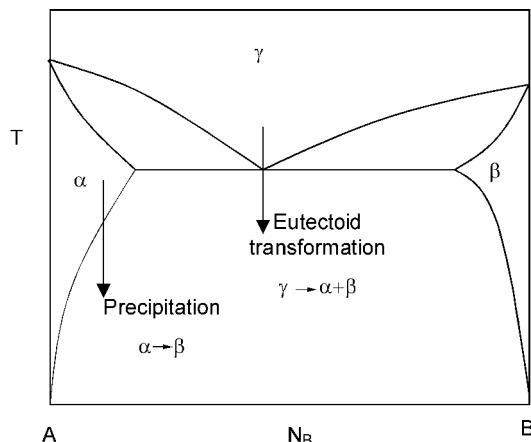
7.3.2 Multiphase reactions

Phase transformations can be grouped into those that require long-range diffusion and those that do not. The majority belong to the former category.

Diffusional transformations

Two examples of phase transformations are indicated in the phase diagrams in Fig. 7.3.

In the first case, the precipitation transformation is:



7.3 Examples of phase transformation.

where α of a certain composition transforms to α of a different composition and β of yet a different composition.

The second case is a eutectoid transformation where,



where γ of a certain composition transforms to α and β of different compositions.

In both the cases, solute redistribution is needed for the transformations and this is achieved through diffusion. These types of transformations proceed through, first, nucleation and then growth, and when applicable this could be followed by coarsening (Ostwald ripening). This text is only intended to provide a brief introduction to the subject of phase transformations and thus the discussion that follows on nucleation and growth will focus on the first type, i.e. precipitation of a second phase from a matrix. The eutectoid case is naturally more complicated since two new phases are formed simultaneously.

Nucleation

When a small amount of new phase β forms from a matrix of α the free energy will change according to:

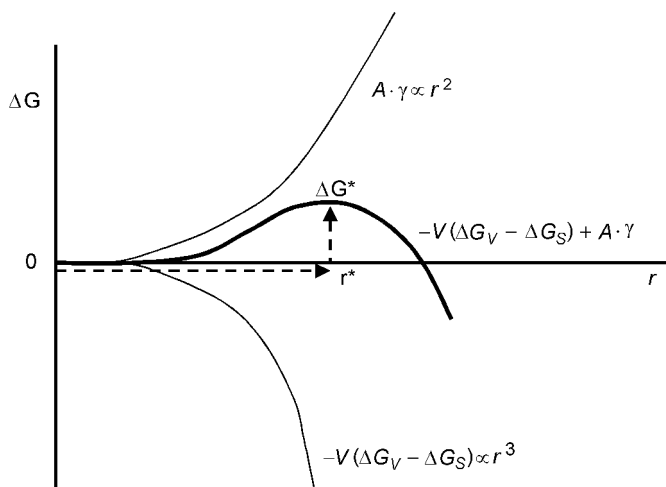
$$\Delta G = V(\Delta G_S + \Delta G_V) + A\gamma_{\alpha/\beta} \quad (7.46)$$

In this equation, V is the volume of the β -phase embryo and A is its interfacial area with the matrix. The terms ΔG_V is the free energy change ($= \Delta H - T\Delta S$) for the reaction, $\alpha \rightarrow \beta$. Assuming that we are at a temperature and composition where β is thermodynamically favorable, this term will be negative and thus contribute to a lowering of the energy. The term ΔG_S is the strain energy due to lattice misfit between α and β and contributes with a positive term. γ is the interfacial energy between α and β and this also contributes with a positive term. It should be mentioned that the equation above is written by assuming that the interfacial energy is isotropic. If this was not the case, the term should be replaced by a summation of contributions from all areas. If the β -embryo assumes a spherical shape, with radius r , the equation above can be written as:

$$\Delta G = -\frac{4}{3}\pi \cdot r^3(\Delta G_S - \Delta G_V) + 4\pi r^2 \cdot \gamma_{\alpha/\beta} \quad (7.47)$$

This equation is plotted as a function of radius in Fig. 7.4.

It can be seen that the free energy goes through a maximum (ΔG^*), at a critical $r = r^*$, and then decreases with size. Thus, β -embryos that are larger than this critical size will spontaneously grow. Depending on the nature of the interface between the phases, ΔG_S and $\gamma_{\alpha/\beta}$ will contribute in different ways. If the interface is coherent, then the interfacial energy will be low whereas the strain energy will be high. On the other hand the opposite will be the case for incoherent interfaces. In general, the interfacial energy plays a greater role and thus



7.4 Energy change during nucleation.

homogeneous nucleation is favored primarily as precipitates that are coherent with the matrix. While this is not possible due to the difference in most systems between matrix and precipitate crystal structures, a coherent meta-stable precipitate often nucleates first. The formation of GP zones is an example of this.

By differentiating the equation and finding the maximum, ΔG^* and r^* can be evaluated as:

$$r^* = \frac{2\gamma_{\alpha/\beta}}{(\Delta G_V - \Delta G_S)} \quad (7.48)$$

$$\Delta G^* = \frac{16\pi\gamma_{\alpha/\beta}^3}{3(\Delta G_V - \Delta G_S)^2} \quad (7.49)$$

The number of β -like clusters per unit volume of size r^* , in a system of totally C_0 atoms per unit volume, is:

$$C^* = C_0 \exp\left(\frac{-\Delta G^*}{kT}\right) \quad (7.50)$$

A fraction, f , of these critical clusters is assumed to grow per unit time, by receiving an additional atom from the matrix.

$$f = \omega \exp\left(-\frac{\Delta G_m}{kT}\right) \quad (7.51)$$

where, ΔG_m is the free energy of migration and ω is a factor that depends on the area of the critically sized cluster and atom vibration frequency. The nucleation rate per unit volume is then:

$$\frac{1}{V} \frac{dN}{dt} = \omega C_0 \exp\left(\frac{-\Delta G^*}{kT}\right) \exp\left(-\frac{\Delta G_m}{kT}\right) \quad (7.52)$$

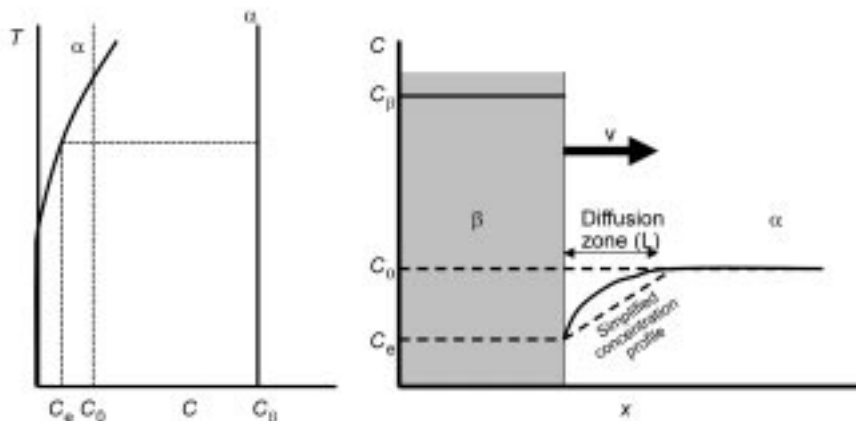
When nucleation of a precipitate occurs at a location where the precipitate replaces a high energy area, the nucleation can be facilitated. This is due to the fact that a high energy interface will be covered by the precipitate and this will in part compensate for the interfacial free energy term in equation 7.47. This will result in a lowering of the critical free energy for nucleation. The degree of lowering is dependent on the specific heterogeneous site, e.g. grain boundary, dislocation, vacancy cluster, non-metallic inclusion, etc. as well as precipitate shape. This is called heterogeneous nucleation and is the primary mode of nucleation for non-coherent precipitates.

Growth

A precipitate's final size and shape is dependent on the rates of growth of the various interfaces it forms with the matrix. The growth rate is often a diffusion problem and most attention has been on transformations that occur upon cooling, i.e. growth of an undercooled stable phase in a thermodynamically unstable matrix phase. The following treatment developed by Zener (1949) is for a planar interface (incoherent interfaces are most likely planar) that grows in one dimension. A planar precipitate grows according to Fig. 7.5.

The region adjacent to the precipitate (which is rich in solute) has been depleted of the solute. The interface is assumed to be in equilibrium and the concentration vs distance in the depleted region is approximated to be linear. It is, furthermore, assumed that the precipitate is sufficiently far from other precipitates that soft impingement (overlap of diffusion fields) does not occur. If the interface advances at a rate, v ($= dx/dt$), a mass balance at the interface gives,

$$\nu \cdot (C_\beta - C_e) = J_{solute} = -D \frac{(C_0 - C_e)}{L(t)} \quad (7.53)$$



7.5 Schematic precipitate growth.

At any time, the diffusion length $L(t)$ can be evaluated from a solute balance between precipitate and depleted zone:

$$(C_\beta - C_0)x = \frac{1}{2}L(t)(C_0 - C_e) \quad (7.54)$$

Combining the two equations above results in:

$$\nu = \frac{dx}{dt} = \frac{D(C_0 - C_e)^2}{2x(C_\beta - C_e)(C_\beta - C_0)} \quad (7.55)$$

Integration results in:

$$x = \frac{(C_0 - C_e)}{(C_\beta - C_e)^{0.5}(C_\beta - C_0)^{0.5}} \sqrt{Dt} \quad (7.56)$$

If the molar volume remains relatively constant, the concentrations in the equations above can be replaced by mole-fractions (N).

In the case of a one-dimensional growth of a non-planar front such as a needle, the effect of curvature on the equilibrium interface concentration (the Gibbs–Thompson effect) needs to be considered. The resulting growth rate can be shown to be (Jones and Trivedi, 1971):

$$\nu = D \frac{(X_0 - X_e)}{k(X_\beta - X_r)} \frac{1}{r} \left(1 - \frac{r^*}{r} \right) \quad (7.57)$$

Here, X_r is interface concentration in the matrix, which is different from the planar equilibrium value due to the curvature. r^* is the critical nuclei radius and r is the radius of the advancing tip. The diffusion length is proportional to the growing tip radius r . k in the above equation is the proportionality constant and from the diffusion solution is close to 1 (Porter and Easterling, 1992).

The thickening of a plate where edges are faceted often occurs through a ledge mechanism. This means that atoms can only attach themselves at the edges. The growth rate can be shown to be (Laird and Aaronson, 1969):

$$\nu = \frac{D(X_0 - X_e)}{k(X_\beta - X_e)\lambda} \quad (7.58)$$

Here, λ is the spacing between ledges.

While the models discussed so far assume that diffusion is the rate-limiting step, it should be mentioned that there is also the possibility of interface reaction controlling the transformation rate. This is the case in single component (pure) metals where the transformation is governed by an activation energy barrier analogous to a first order chemical reaction.

Combining nucleation and growth kinetics

In general, the fraction transformed during a reaction $\alpha \rightarrow \beta$ will depend on the temperature history since both nucleation and growth are strong functions of temperature. The volume at time t of a β grain that nucleated at time τ will be

(for three-dimensional spherical growth):

$$V = \frac{4}{3}\pi\nu^3(t - \tau)^3 \quad (7.59)$$

At low transformation fractions, the volume contributed from all β grains per unit total volume is N (nucleation rate):

$$f = \sum V = \frac{4}{3}\pi N\nu^3 \int_0^t (t - \tau)^3 d\tau = \frac{\pi}{3}N\nu^3 t^4 \quad (7.60)$$

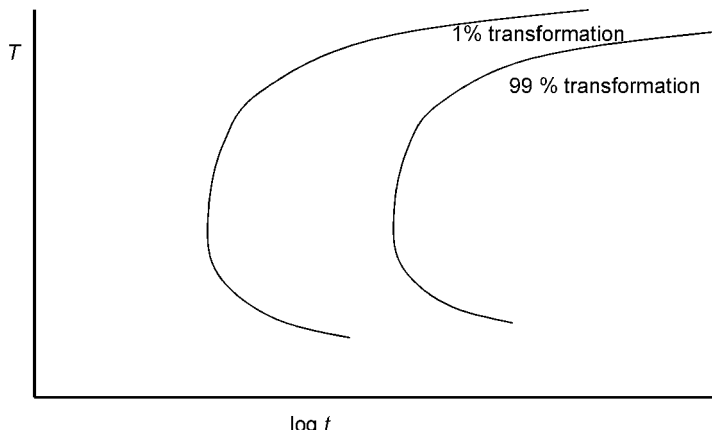
The nucleation rate (N) has been assumed to be constant. If one considers impingement, which will slow down the rate,

$$f = 1 - \exp\left(-\frac{\pi}{3}N\nu^3 t^4\right) \quad (7.61)$$

This is known as the Johnson–Mehl–Avrami equation (Porter and Easterling, 1992) and will result in the classic C-shaped curve when the fraction transformed (f) is plotted in a diagram with temperature (T) as the y-axis and time (t) as the x-axis. A schematic of such a diagram, called a TTT-diagram (for time–temperature–transformation) is shown in Fig. 7.6. The C-shape is caused by a slow nucleation rate at high T and a slow growth (caused by slow diffusion) at low T .

Phase transformation upon heating

So far the discussion has focused upon phase transformations that occur upon cooling. The combined nucleation and growth behaviors, resulted in the TTT type behavior, i.e. the transformation is limited by nucleation at low undercooling (high temperature) and by growth at low temperatures. Also, the growth rates themselves have terms for both supersaturation (which increases with undercooling) and diffusion (which decreases with undercooling). The resulting rate of transformation vs temperature would then exhibit a maxima. In



7.6 Time–temperature–transformation (TTT) diagram.

the case of heating above a transformation temperature, both the driving force and diffusion rate increase with temperature. Therefore the effect of increasing temperature is continuously to accelerate the transformation rate.

Coarsening

In order to lower the total interfacial energy, a multiphase alloy will strive to shift the size distribution of precipitates towards as small number of large precipitates as possible. The rate of this process is strongly dependent on temperature and, thus, is a concern in high temperature applications and processes.

Depending on the process history, a certain size distribution of the second phase precipitates will be present in the matrix as a result of nucleation and growth. The chemical potential of solutes in the matrix adjacent to a precipitate will vary depending on the precipitate–matrix interface curvature due to the Gibbs–Thomson effect. Therefore there will be a chemical potential difference between two spherical precipitates of different sizes. This difference will be:

$$\Delta G_\gamma = \Delta \mu = RT \ln \left(\frac{N_1}{N_2} \right) = 2\gamma V_m \left(\frac{1}{r_1} - \frac{1}{r_2} \right) \quad (7.62)$$

As can be seen, the solute concentration will be higher in the matrix near the smaller particle. As a result, the solute diffuses from the regions adjacent to smaller particles to the regions near larger ones and the larger particles grow at the cost of the smaller ones that shrink and eventually disappear altogether. As a result, the average particle radius r_a among the particle population increases with time whereas the total number of particles decreases with time. If diffusion is the slowest step the rate of coarsening has been found to be (Wagner, 1961):

$$r_a^3 - r_o^3 = kt \quad (7.63)$$

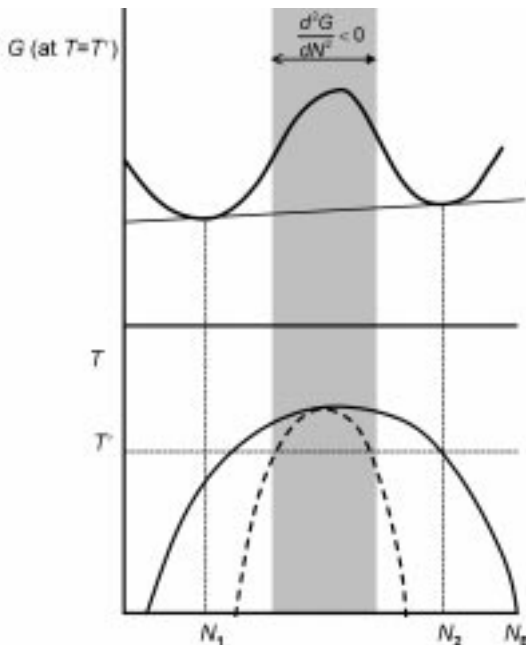
where r_o is the mean starting radius. k is a kinetic constant that equals $D * \gamma * N_e$, where N_e is the mole fraction of solutes at equilibrium with very large precipitates.

Spinodal decomposition

In the discussion of nucleation and growth of a second phase, it was assumed that a sharp boundary existed between the matrix and precipitating phase. In the case of spinodal decomposition, the transformation proceeds while maintaining a coherent and non-distinguishable boundary.

In the case of spinodal decomposition, the free energy *vs* composition has a behavior as that is shown in Fig. 7.7, which is characteristic of a miscibility gap.

Note that, inside the so-called spinodal region, the second derivative of Gibbs energy is negative. This means that any infinitesimal fluctuation in composition would lead to an energy decrease for the alloy and would be expected to grow spontaneously. Let us consider a one-dimensional binary decomposition case in



7.7 Free energy vs composition for spinodal decomposition.

the spinodal region. Sinusoidal fluctuations may or may not result in decomposition into two phases as shown in Fig. 7.7. Based on Fick's second law solution, it can be shown (Cahn, 1968) that fluctuations will be stable under certain condition. A small free energy change can be written as a sum of the chemical (ΔG_c), strain (ΔG_s) and gradient (ΔG_γ) parts.

The chemical energy is:

$$\Delta G_c = \frac{1}{2} \frac{d^2 G}{dN^2} (\Delta N)^2 \quad (7.64)$$

The strain energy:

$$\Delta G_s = \eta^2 \frac{E}{(1-v)} V_m (\Delta N)^3 \quad (7.65)$$

Here E is Young's modulus, v is Poisson's ratio and $\eta = \frac{1}{a} \frac{da}{dN}$, where a is the lattice parameter.

The gradient energy arises due to non-similar nearest neighbors and is thus related to unlike atom pairs:

$$\Delta G_\gamma = K \frac{(\Delta N)^2}{\lambda} \quad (7.66)$$

Here K is the so-called gradient energy, which depends on the differences in bond energies between like and unlike pairs. λ is the wavelength of the sinusoidal fluctuation. The total energy change can then be written:

$$\Delta G = \left(\frac{d^2G}{dN^2} + \frac{2K}{\lambda^2} + 2\eta^2 \frac{E}{(1-v)} V_m \right) \frac{(\Delta N)^2}{2} \quad (7.67)$$

Fluctuations will according to this equation be stable when the term within the brackets is negative. By using a flux equation with a chemical potential gradient and solving Fick's second law, the kinetics of the decomposition are obtained (Cahn, 1968) as (after neglecting the non-linear terms):

$$\Delta N = N(t) - N(t=0) = \cos \frac{2\pi}{\lambda} x \cdot \exp \left(-A \left(\frac{2\pi}{\lambda} \right)^2 + B \left(\frac{2\pi}{\lambda} \right)^4 \right) t \quad (7.68)$$

Here

$$A = M \left(\left(\frac{\partial^2 G}{\partial N^2} \right) + \eta^2 \frac{2E}{1-v} \right)$$

and

$$B = 2KM/V_m$$

M is the mobility

$$M = \frac{ND}{RT}$$

Ordering

In some binary systems such as Cu-Zn or Cu-Au there is a strong negative deviation of the activities. This corresponds to a negative enthalpy of mixing. In general this is indicative of the fact that the components tend to strongly attract one another. This leads, at low temperatures, where the dis-ordering effect of entropy and thermal motion is weak, to the formation of the so-called super structures. In these structures the atoms organize themselves to maximize the dissimilar bonds and minimize the similar ones. In general, the ordering tendency increases with decreasing temperature below a critical temperature T_c . The internal energy and enthalpy are continuous across this temperature and thus this is a second order transformation. The common mechanism (Porter and Easterling, 1992) is through nucleation and growth. An ordered region is referred to as a domain. Both interfacial energy and strain energy are expected to be low, and therefore nucleation is relatively easy and occurs homogeneously.

Martensitic transformations

Martensitic transformations are brought about by a movement of the interface between parent and product phases. As the interface advances, atoms in the parent lattice re-align into the more energetically favorable martensite structure. The displacement of atoms is relatively small (less than one inter-atomic spacing) in magnitude and no compositional changes occur. Instead, the atomic re-alignment results in a shape deformations and a change in symmetry from the

original lattice. The martensitic transformation that FCC lattice undergoes to form a BCT is described by a process called the Bain distortion (Reed-Hill and Abbaschian, 1992). Since no diffusion is involved, these transformations are called diffusionless. The growth rates of martensite are extremely fast and approach the speed of sound and therefore nucleation is what primarily controls the grain size. Nucleation is thought to occur heterogeneously (Reed-Hill and Abbaschian, 1992). The interfacial energy is relatively low but the shear associated with the Bain transformation contributes to an elastic strain energy that hinders homogeneous nucleation. The free energy of an ellipsoidal martensite embryo platelet with radius a and thickness $2c$ is:

$$\Delta G = 2\pi a^2 \gamma + \frac{2(2-v)}{8(1-v)} 2(s/2)^2 \mu ac^2 - \frac{4}{3} \pi a^2 c \cdot \Delta G_v \quad (7.69)$$

The second term is the elastic strain energy term where s is the strain, v is Poisson's ratio and μ is the shear modulus. The most likely heterogeneous nucleation sites are thought to be dislocations whose strain energy field assists nucleation. The nucleation energy barrier can be reduced by the dislocation interaction energy (Porter and Easterling, 1992):

$$\Delta G_d = 2\mu s \pi \cdot ac \cdot \bar{b} \quad (7.70)$$

Here b is the burgers vector of the dislocation.

7.4 Gas–solid reactions

Gas–solid reactions, being heterogeneous reactions, occur at phase boundaries, and thus always accompany the transfer of mass and heat between the reaction interface and the bulk phase. The overall gas–solid reaction involves a combination of the following individual steps:

1. Transfer of the gaseous reactants and the gaseous products between the bulk gas and the external surface of the solid particle.
2. Diffusion of the gaseous reactants and the gaseous products within the pores of the solid, if the solid contains open porosity.
3. Chemical reaction between the gaseous reactant and the solid at the gas–solid interface.
4. Transfer of the reaction heat within the solid.
5. Transfer of heat between the external surface of the solid and the surroundings by convection and radiation.
6. Changes in the structure of the solid due to chemical reaction and heat.

The rate-controlling step can change depending on reaction conditions, and thus the rate information obtained under a given set of conditions may not be applicable under another set of conditions. Furthermore, there may not be a single rate-controlling step because several steps may have comparable effects on determining the overall rate. The relative importance of these steps could also

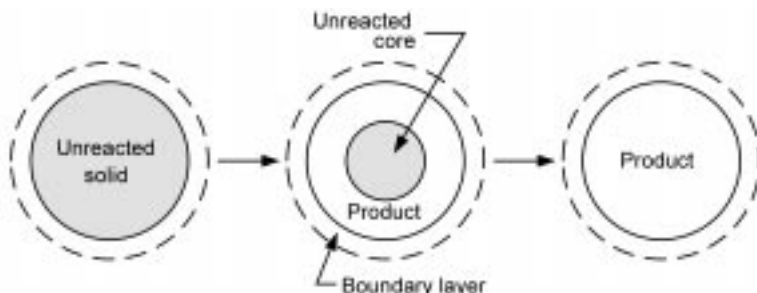
change in the course of the reaction. Therefore, understanding how the individual reaction steps interact with each other is important in determining not only the rate-controlling step under given reaction conditions but also whether more than a single step must be considered in expressing the rate over the entire duration of the reaction. The treatments of the above individual component steps were discussed in Section 7.2 Fundamentals of heterogeneous kinetics on page 270.

Because the transfer of mass and, to a lesser extent, heat constitutes an important aspect of a gas–solid reaction, the quantitative analysis of the overall rate must necessarily take into account the geometry and structure of the solid before, during, and after the reaction. Although there are other types of gas–solid reactions, the most important group of reactions in metallurgical and materials processing operations consists of those in which a solid reacts with a gas to produce a coherent layer of porous products. Therefore, this section will mainly be concerned with this type of reaction, which is given by equation 7.1. For the analysis of other types of gas–solid reactions, the reader is referred to other references (Szekely *et al.*, 1976).

7.4.1 Reaction of an initially non-porous solid producing a porous product layer

In this type of gas–solid reaction, the reaction progresses in a topochemical manner from the outer surface of the solid towards its interior, as depicted in Fig. 7.8. The reaction forms a coherent porous product (or ash) layer around the unreacted portion of the solid, with the chemical reaction taking place at the sharp interface between the two zones. This shrinking-core picture has been applied to a wide range of reactions. Szekely *et al.* (1976) generalized the results of many previous investigators on reactions that are isothermal and of first order with respect to the gaseous reactant. They formulated the following equation incorporating chemical kinetics, diffusion through porous product layer, and external mass transfer, as well as the three basic geometries of the solid:

$$g_{F_p}(X) + \sigma_s^2 [p_{F_p}(X) + 4X/Sh^*] = t^* \quad (7.71)$$



7.8 Reaction of an initially non-porous solid that forms a coherent layer of porous product (the shrinking-core reaction system).

where F_p is the shape factor (= 1, 2, or 3 for a slab, a long cylinder, or a sphere), and

$$t^* \equiv \left(\frac{bk}{\alpha_B \rho_B} \right) \left(\frac{A_p}{F_p V_p} \right) \left(C_{Ab} - \frac{C_{Cb}}{K} \right) t \quad (7.72)$$

$$\sigma_s^2 \equiv \left(\frac{k}{2D_{eA}} \right) \left(\frac{V_p}{A_p} \right) \left(1 + \frac{1}{K} \right) \quad (7.73)$$

$$Sh^* \equiv \frac{(D_A \cdot \delta) d_p}{D_{eA}} = \left(\frac{D_A}{D_{eA}} \right) \left(\frac{k_{mAd} d_p}{D_A} \right) = \left(\frac{D_A}{D_{eA}} \right) Sh \quad (7.74)$$

$$g_{F_p}(X) \equiv 1 - (1 - X)^{1/F_p} \quad (7.75)$$

and

$$p_{F_p}(X) \equiv X^2 \quad \text{for } F_p = 1 \quad (7.76a)$$

$$\equiv X + (1 - X) \ln(1 - X) \quad \text{for } F_p = 2 \quad (7.76b)$$

$$\equiv 1 - 3(1 - X)^{2/3} + 2(1 - X) \quad \text{for } F_p = 3 \quad (7.76c)$$

It has been shown (Szekely *et al.*, 1976) that chemical reaction controls the overall rate when $\sigma_s^2 < 0.1$ or 0.01 depending on the range of tolerable error (<10% or <1%, respectively). On the other hand, pore diffusion and external mass transfer control the overall rate ($g_{F_p}(X)$ becomes negligible) when $\sigma_s^2 > 10$ or 100.

Individual forms of equation 7.71 were used for various metallurgical reactions (Lu and Bitsianes, 1968; Seth and Ross, 1966; St. Clair, 1965; Themelis and Gauvin, 1963; Kawasaki *et al.*, 1963; McKewan, 1960). Sohn and Sohn (1980) subsequently showed that the right-hand sides of equations 7.76a to 7.76c can be derived as a single combined term given by

$$p_{F_p}(X) \equiv 1 - \frac{F_p(1 - X)^{2/F_p} - 2(1 - X)}{F_p - 2}; \quad \begin{array}{l} \text{conversion function for} \\ \text{pore-diffusion control} \end{array} \quad (7.77)$$

$p_2(X)$ for a long cylinder can be obtained by applying L'Hospital's rule to the right-hand side of equation 7.77, resulting in the familiar expression given by equation 7.76b.

The effect of changing particle size due to the difference in the volumes of the reactant and the product solids can be incorporated by redefining $p_{F_p}(X)$ as follows, if one neglects the change in the mass-transfer coefficient with the small change in particle size in the last term of equation 7.71 (Szekely *et al.*, 1976):

$$p_{F_p}(X) \equiv zX^2 \quad \text{for } F_p = 1 \quad (7.78a)$$

$$\equiv \frac{[Z - (Z - 1)(1 - X)] \ln [Z - (Z - 1)(1 - X)]}{Z - 1} \quad (7.78b)$$

$$+ (1 - X) \ln(1 - X) \quad \text{for } F_p = 2 \quad (7.78b)$$

$$\equiv 3 \left\{ \frac{Z - [Z - (Z - 1)(1 - X)]^{2/3}}{Z - 1} - (1 - X)^{2/3} \right\}$$

for $F_p = 3$ (7.78c)

where Z is the volume of the product solid formed from unit volume of the reactant solid. It can be shown (Sohn, 1980) that the right-hand sides of equations 7.78a to 7.78c (and those of equations 7.76a to 7.76c as special cases) can be derived as a single term given by

$$p_{F_p}(X) \equiv \frac{F_p}{F_p - 2} \left\{ \frac{Z - [Z - (Z - 1)(1 - X)]^{2/F_p}}{Z - 1} - (1 - X)^{2/F_p} \right\} \quad (7.79)$$

The expressions of $p_{F_p}(X)$ for $Z = 1$ and/or $F_p = 2$ can again be obtained by applying L'Hospital's rule.

When there is a substantial change in the gas volume upon reaction, Sohn and Sohn (1980) obtained the following approximate solution to replace equation 7.71:

$$t^* = g_{F_p}(X) + \sigma_s^2 \left(\frac{\theta}{\ln(1 + \theta)} p_{F_p}(X) + \frac{4(1 + \theta)X}{Sh^*} \right) \quad (7.80)$$

where

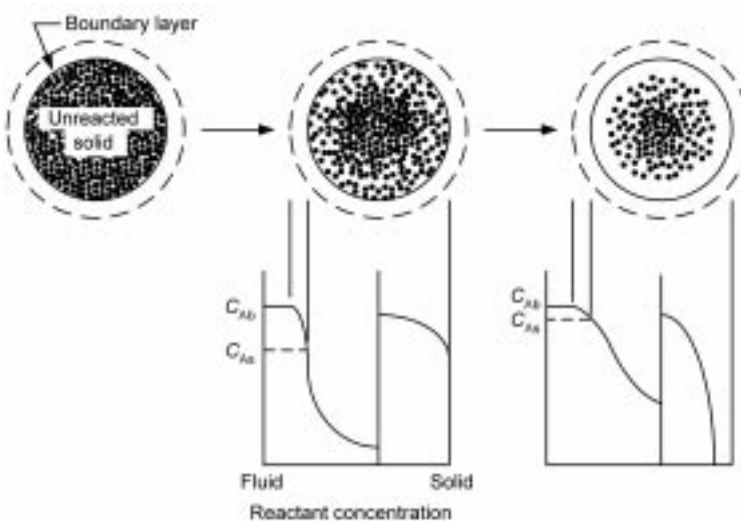
$$\theta = (\nu - 1)(C_{Ab}/C_T) \quad (7.81)$$

Sohn and Szekely (1972a) analyzed the system in which the reaction order with respect to the gaseous reactant is different from unity. In many gas-solid reactions, substantial enthalpy changes accompany the reactions. Such non-isothermal systems are more difficult to analyze than the isothermal systems discussed above, and may exhibit multiple steady states and thermal instability. These aspects have been reviewed elsewhere (Szekely *et al.*, 1976).

The shrinking-core model is attractive for its conceptual and mathematical simplicity. It should be noted, however, that its validity is limited to the reaction of a non-porous solid occurring at a well-defined sharp reaction interface. In general, the improper application of the shrinking-core model to the reaction of a porous solid results in an erroneous analysis of experimental data. Thus, one may obtain incorrect dependence of the rate on reaction conditions and physical parameters such as temperature, gaseous reactant concentration, and particle size. The proper analysis of the reaction of porous solids is discussed below.

7.4.2 Reaction of a porous solid

Many solid reactants have some initial porosity, allowing diffusion and chemical reactions to occur simultaneously in a diffuse zone. The progress of reaction in a porous solid is illustrated in Fig. 7.9. Reaction takes place throughout the particle or pellet volume, and the concentration of the gaseous reactant decreases



7.9 Reaction of an initially porous solid.

as it diffuses into the interior of the particle while reacting on its path. The reaction given by equation 7.1 taking place in a porous solid can be described mathematically by formulating the conservation equations for the gaseous and the solid reactants, and for energy if substantial heat effect is involved.

The conservation of gaseous species per unit volume of the pellet (including the pore space) is given by

$$\nabla \cdot \underline{N}_i = R_i; \quad i = A \text{ or } C \quad (7.82)$$

This equation incorporates the pseudo-steady-state approximation, which states that the accumulation term can be neglected for gas–solid reactions (Bischoff, 1963; 1965; Luss, 1968).

For many heterogeneous reactions, the molar rate of consumption of the gaseous reactant per unit area of the reaction interfaces is given by the Langmuir–Hinshelwood rate equation, discussed earlier and expressed by equation 7.2.

The molar rate of consumption of the solid reactant per unit volume of the solid is expressed by

$$\rho_B \frac{\partial w}{\partial t} = b(-\dot{m}_A)S_v = b(-\dot{m}_A)S_v^o \cdot f(w) \quad (7.83)$$

where w is the local fractional conversion of the solid reactant, S_v^o is the initial surface area per unit volume of the solid, and $f(w)$ represents the relative variation of the specific surface area S_v with solid conversion.

The fluxes of gaseous species, N_i , must, in general, be related to concentrations through the Stefan–Maxwell equations (Eddings and Sohn, 1993; Szekely *et al.*, 1977; Szekely and El-Tawil, 1976). However, for a binary

mixture or by using an effective binary diffusivity, one may use the simpler relationship given below:

$$N_i = -C_T D_{ei} \nabla x_i + x_i \sum_{j=1}^n N_j \quad (7.84)$$

The rate of production of gaseous species i per unit volume, R_i , is related to the rate of reaction of the solid reactant through stoichiometry, as follows:

$$R_A = \frac{\alpha_B \rho_B}{b} \frac{\partial w}{\partial t} = -\alpha_B (\dot{m}_A) S_v^o f(w) \quad (7.85a)$$

$$R_C = \frac{c \alpha_B \rho_B}{b} \frac{\partial w}{\partial t} = c \alpha_B (\dot{m}_A) S_v^o f(w) \quad (7.85b)$$

When the solid temperature changes during the reaction, the conservation of energy is described by

$$\rho c_p \frac{\partial T}{\partial t} = -\underline{\nabla} \cdot \underline{q} + (-\Delta H) \cdot (-R_A) \quad (7.86)$$

The simultaneous solution of equations 7.82, 7.83 and 7.86 with appropriate boundary conditions yields the profiles of the gaseous species concentrations as functions of position inside the solid. Using these concentration profiles, the local conversion of solid, w , can be obtained as a function of time by solving equation 7.83 together with equation 7.2. The overall conversion X is then calculated by integrating the local conversion over the entire solid volume.

Closed-form solutions to the governing equations have been obtained for certain special cases. When the reaction involves a substantial heat effect, these equations must in general be solved using a numerical technique. Even in such a case, the conversion-vs-time relationship for a diffusion-controlled irreversible reaction ($K \rightarrow \infty$) is given by equation 7.71 or 7.80 without the $g_{F_p}(X)$ term. Various models for a reaction between a porous solid and a gas have been formulated, the differences among which are largely equivalent to the use of different dependences of rate on solid conversion, $f(w)$.

The grain model

This model assumes that the porous solid is made up of small non-porous grains of a uniform size that each react according to the chemical-reaction-controlled shrinking-core scheme discussed above (Szekely *et al.*, 1976; Sohn and Szekely, 1972b; Szekely and Evans, 1970). This picture, although rather unrealistic and restrictive, provided an early basis for the incorporation of solid structure in analyzing gas–solid reactions. Furthermore, the analysis of this system also provided us with the foundation for more realistic and less restrictive descriptions of gas–solid reactions in the subsequent work, as will be discussed later.

The generalized grain model developed by Sohn and Szekely (1972b), which encompasses many other specific models to represent similar configurations

(Szekely and Sohn, 1973; Tien and Turkdogan, 1972; Szekely and Evans, 1970; Ishida and Wen, 1968; Ausman and Watson, 1962), was formulated for an isothermal, first-order reaction with equimolar counterdiffusion (or diffusion at low concentrations). It was also assumed that the diffusion of the reactant gas through the product layer around the individual grain offers little resistance to the overall rate. This assumption is usually valid for small grains but can readily be relaxed (Sohn and Szekely, 1974; Calvelo and Smith, 1972). Sohn and Szekely (1972b) considered porous solids in which the pellet and the grain may each have the shape of a slab, a long cylinder, or a sphere – nine possible combinations. In their development, they used the following equation for the reaction of the grains in lieu of equation 7.83:

$$-\rho_B \frac{\partial r_c}{\partial t} = bk \left(C_A - \frac{C_C}{K} \right) \quad (7.87)$$

where r_c is the position of the reaction interface within the grain, and ρ_B is the molar density of the solid reactant. It is noted that equation 7.87 is a special form of equation 7.83 for grains reacting according to the chemical-reaction-controlled shrinking-core scheme by considering that

$$w = 1 - (r_c/r_g)^{F_g} \quad (7.88)$$

The term R_A is now given as

$$R_A = -\alpha_B k \left(\frac{A_g}{V_g} \right) \left(\frac{A_g r_c}{F_g V_g} \right)^{F_g-1} \left(C_A - \frac{C_C}{K} \right) \quad (7.89)$$

It is noted that

$$F_g V_g / A_g = r_g, \quad (7.90)$$

the initial radius or half thickness of the grain.

The case of flat grains ($F_g = 1$) corresponds to models of Ausman and Watson (1962) and Ishida and Wen (1968). (It is noted that in this case, R_A in equation 7.89 is independent of r_c . It must, however, be set equal to zero when r_c reaches zero since there no reaction and hence no consumption of A – an often forgotten requirement.) When $F_g \neq 1$, equations 7.82 and 7.83 must be solved numerically, even for an isothermal, first-order reaction. For systems in which the effective diffusivity remains unchanged upon reaction, Sohn and Szekely (1972b) obtained the following approximate solution for the conversion-vs-time relationship:

$$t_g^* \cong g_{F_g}(X) + \hat{\sigma}^2 [p_{F_p}(X) + 4X/Sh^*] \quad (7.91)$$

where

$$t_g^* \equiv \left(\frac{bk}{\rho_B} \right) \left(\frac{A_g}{F_g V_g} \right) \left(C_{Ab} - \frac{C_{Cb}}{K} \right) t \quad (7.92)$$

$$\hat{\sigma}^2 \equiv \frac{\alpha_B F_p k}{2D_e} \left(\frac{A_g}{F_g V_g} \right) \left(\frac{V_p}{A_p} \right)^2 \left(1 + \frac{1}{K} \right) \quad (7.93)$$

and $g_i(X)$ and $p_i(X)$ have been defined in equations 7.75 and 7.76. The results of these analyses were applied to the reduction of nickel oxide pellets with hydrogen by systematically designed experiments (Szekely *et al.*, 1973).

Equation 7.91 has a number of noteworthy characteristics. The equation is valid for the nine combinations of F_g and F_p over the entire range of $\hat{\sigma}$ approaching zero (chemical reaction control) and infinity (pore diffusion control); it is also exact at the conversion values of zero and unity. In other words, the time for complete conversion is exactly predicted by equation 7.91 even for an intermediate value of $\hat{\sigma}$ for which the equation is valid only approximately for $0 < X < 1$. This property was originally determined by the comparison of equation 7.91 with the exact numerical solution of equation 7.82 together with equations 7.87 and 7.89 (Sohn and Szekely, 1972b). Subsequently, a rigorous mathematical proof of this interesting property has been developed (Sohn *et al.*, 1985).

The above analyses of the grain model have been made for the case of a constant effective diffusivity. In many gas–solid reactions, the product solid layer has a substantially different effective diffusivity than the reactant. One of the simplified methods of incorporating this structural change is to assign different effective diffusivities to the completely and partially reacted zones. Szekely and Sohn (1973) reported the results of computation for this two-diffusivity system made up of grains of various geometries.

The law of additive reaction times

Based on the conversion-vs-time relationships for porous and nonporous solids discussed above, Sohn (1978) developed the ‘Law of Additive Reaction Times’. This law is applicable for an isothermal reaction in which the effective diffusivity of the solid remains constant during the reaction. The law states that

$$\text{Time required to attain a certain conversion} \cong \text{Time required to attain the same conversion under the conditions of rapid inter-grain pore diffusion} + \text{Time required to attain the same conversion under the rate control by inter-grain pore diffusion and external mass transfer} \quad (7.94a)$$

or

$$t = t(X)|_{\hat{\sigma} \rightarrow 0} + t(X)|_{\hat{\sigma} \rightarrow \infty} \quad (7.94b)$$

$$= a \cdot g(X) + a \cdot \hat{\sigma}^2 [p_{F_p}(X) + 4X/Sh^*] \quad (7.94c)$$

where a is a constant term containing the chemical-reaction-rate constant. In general, the term $t|_{\hat{\sigma} \rightarrow 0}$ is related to $f(w)$ in equation 7.83 by

$$\begin{aligned} t(X)|_{\hat{\sigma} \rightarrow 0} &= \frac{\rho_B}{b(-\dot{m}_A)_b S_v^o} \int_0^x \frac{dw}{f(w)} \\ &= \frac{\rho_B}{bkS_v^o(C_{Ab} - C_{Cb}/K)} \int_0^x \frac{dw}{f(w)} = a \cdot g(X) \end{aligned} \quad (7.95)$$

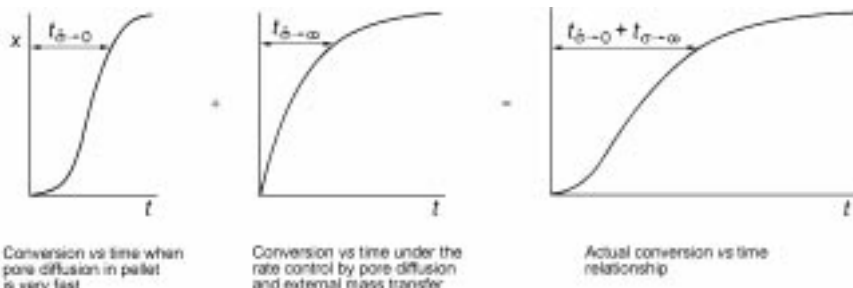
in which $(-\dot{m}_A)_b$ is $-\dot{m}_A$ at bulk conditions. From equation 7.71 or 7.91, the term $t|_{\hat{\sigma} \rightarrow \infty}$ is given by

$$\begin{aligned} t(X)|_{\hat{\sigma} \rightarrow \infty} &= \left(\frac{V_p}{A_p} \right)^2 \frac{\alpha_B \rho_B F_p}{2bD_e(C_{Ab} - C_{Cb})} \left(1 + \frac{1}{K} \right) [p_{F_p}(X) + 4X/Sh^*] \\ &= a \cdot \hat{\sigma}^2 [p_{F_p}(X) + 4X/Sh^*] \end{aligned} \quad (7.96)$$

The conversion function $g(X)$ should be chosen in such a way that its magnitude varies between 0 and 1 as X varies from 0 to 1 (not always possible, e.g. the nucleation-and-growth kinetics expression given by equation 7.101 below) – typically the entire function containing X in the last term in equation 7.95, leaving all the constant coefficient in a . It is noted that any constant arising from the integration in equation 7.95 goes into a . Then, $\hat{\sigma}^2$ is defined by dividing by a the constant term that multiplies the conversion function $p(X)$ in equation 7.96. A different choice of $g(X)$ does not affect the validity of equation 7.94a to 7.94c: the appropriate selection of $g(X)$ and thus the constant a will, however, result in the definition of $\hat{\sigma}^2$ in such a way that the numerical criteria for chemical-reaction control and pore-diffusion control will remain, respectively, $\hat{\sigma}^2 < 0.1$ and $\hat{\sigma}^2 > 10$.

Figure 7.10 illustrates how the law of additive reaction times can be applied in general if we have information on the chemical reaction rate in the absence of the resistance due to intra-pellet diffusion and that on the rate controlled by intra-pellet diffusion. Equations 7.71, 7.80 and 7.91 are examples of the mathematical expressions of this law. This law is exact for the reaction of a non-porous solid following the shrinking-core scheme. It is approximately valid for the reaction of a porous solid with constant effective diffusivity. In the latter case, the exact solution must in general be obtained by numerical solution of the governing second-order differential equations.

The law of additive reaction times, which results in a closed-form solution, is



7.10 Graphical representation of the law of additive reaction times.

even more useful in the analysis of multi-particle systems involving various particle sizes and changes in gas concentration and solid temperature, because the solution is explicit in time. Thus, in a differential form it yields the instantaneous conversion rate dX/dt as a function of solid conversion (X) and other conditions at any time. This allows the application of the approximate solution to systems in which conditions vary with time (and position in the reactor) as long as the temperature within a particular pellet is spatially uniform at any given time (Sohn, 1978). It has further been shown (Sohn, 1978) that this law is valid regardless of the dependence of rate on solid conversion. The general applicability and usefulness of this law have been verified using a wide variety of gas–solid reaction systems. Some of these cases will be discussed below.

Structural changes such as sintering, swelling, and softening are complex and not well understood. If information is available, the effects of such changes on effective diffusivity and chemical reactivity could be incorporated into the governing equations. When there is a substantial heat effect, the analysis becomes much more complex with the possible existence of multiple steady states and instability (Szekely *et al.*, 1976). Many metallurgical systems involve solids with high thermal conductivities. In such cases, temperature within the solid may be sufficiently uniform and resistance to heat transfer may be limited to the external heat transfer between the external surface and the bulk gas stream. For such systems, the reaction rate in the form of dX/dt can still be obtained from equation 7.91 by writing it in a dimensional form and expressing the temperature-dependent parameters as functions of temperature. The validity of this approach has been verified (Sohn, 1978), as illustrated in the following Example A.

Example A: Porous solids in which the reaction of the solid follows the nucleation-and-growth kinetics

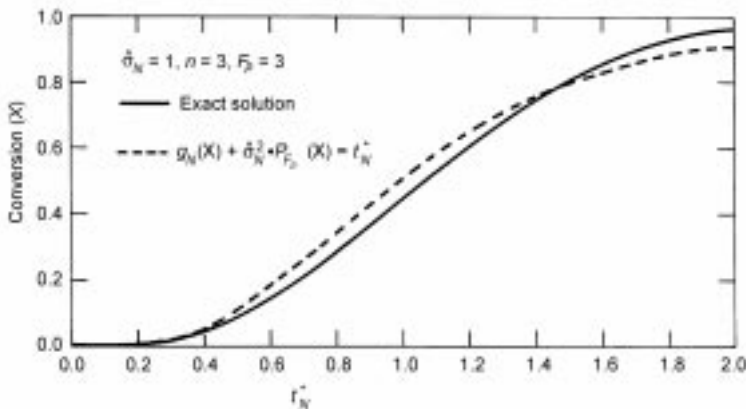
Gas–solid reactions usually involve the adsorption of gaseous reactants at preferred sites on the solid surface and the formation of nuclei of the solid product. For small particles the period of the formation and growth of nuclei occupies essentially the entire conversion range. The conversion-vs-time relationship in this case is given by the nucleation-and-growth kinetics. A frequently used form of such a rate expression, which is attributed to Erofeev (Young, 1966), is

$$[-\ln(1 - w)]^{1/n} = mt \quad (7.97)$$

Sohn (1978) obtained the following equation by applying equation 7.94b to this system:

$$t_N^* = g_N(X) + \hat{\sigma}_N^2 [P_{F_p}(X) + 4X/Sh^*] \quad (7.98)$$

where



7.11 Comparison of equation 7.98 with the exact solution ($Sh^* = 4$).

$$t_N^* \equiv \frac{bkS_v^o}{\rho_B} \left(C_{Ab} - \frac{C_{Cb}}{K} \right) t \quad (7.99)$$

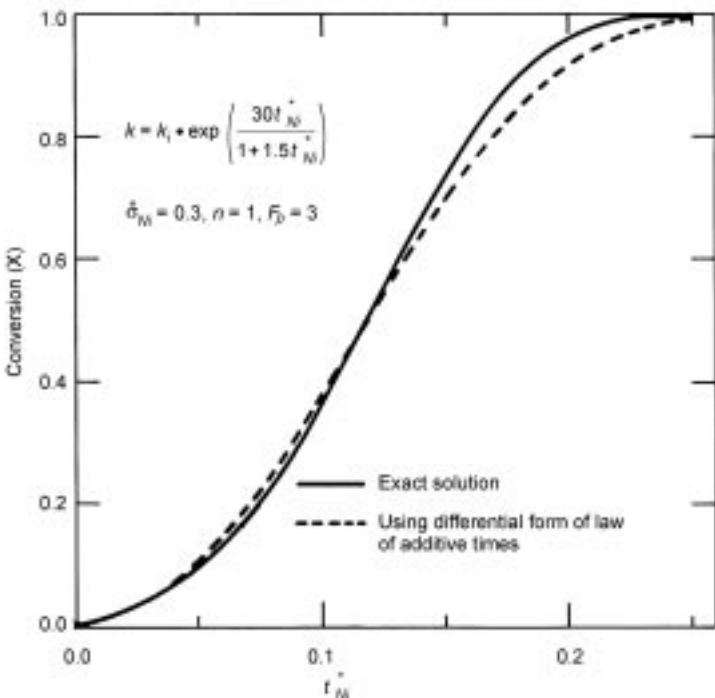
$$\sigma_N^2 \equiv \frac{\alpha_B F_p k S_v^o}{2D_e} \left(\frac{V_p}{A_p} \right)^2 \left(1 + \frac{1}{K} \right) \quad (7.100)$$

$$g_N(X) \equiv [-\ln(1-X)]^{1/n} \quad (7.101)$$

A comparison between equation 7.98 and the exact numerical solution of the governing differential equation (7.82), with the corresponding equation 7.83 obtained from the differential form of equation 7.97, is shown in Fig. 7.11. This comparison is made for the case of $\sigma_N^2 = 1$, i.e., when chemical kinetics and pore diffusion are equally significant, which represents the severest test of the approximate solution. Other appropriate rate expressions for $f(w)$ in equation 7.83 could be used giving rise to the corresponding forms of $g_N(X)$ according to equation 7.95. Sohn and Kim (1984a) applied equation 7.98 to reanalyze the data on the hydrogen reduction of nickel oxide pellets (Szekely *et al.*, 1973) and determined that this equation gave a better overall representation of this reaction system than the original grain model approach.

As discussed above, a major advantage of the approximate solution such as equation 7.98 is that it is time-explicit. This allows the approximate solution to be applied, in a differential form in terms of dX/dt , to the situation in which bulk conditions change with time (as long as the temperature within the solid remains spatially uniform). Figure 7.12 shows an example of this in which the uniform solid temperature varies linearly with time, causing the system to shift from chemical control to mixed control to pore diffusion control as the conversion increases from zero to unity. It is seen that the application of the law of additive reaction times (in the differential form) yields a very satisfactory result.

A special case of the rate expression given by equation 7.97 is the case of $n = 1$, which is equivalent to the ‘first-order’ rate dependence on the fraction of



7.12 Comparison of the differential form of the law of additive reaction times with the exact numerical solution for the case of changing temperature.

the solid reactant remaining unreacted. Among the many gas–solid reactions treated with this rate expression, the most familiar one is the reaction of carbon dispersed in a matrix of an inert solid, such as the removal of carbonaceous residue from the organic binder used in ceramic forms and the regeneration of coked catalysts. It has been shown for such systems (Sohn and Wall, 1989) that equation 7.98 is not only valid but also superior to other closed-form approximate solutions of the governing differential equations.

Example B: Application to liquid–solid reactions

An example of such an application is the ferric chloride leaching of galena (PbS). There were conflicting conclusions drawn for the controlling reaction mechanism depending on the conditions under which the reaction was carried out. By applying the law of additive reaction times, Sohn and Baek (1989) showed that the different behaviors could be included within a unified rate expression encompassing them as special cases of the overall behavior, and equation 7.94 gave an excellent representation of the experimental data in the region of mixed control.

Example C: The grain-pellet system with intra-grain diffusion effect

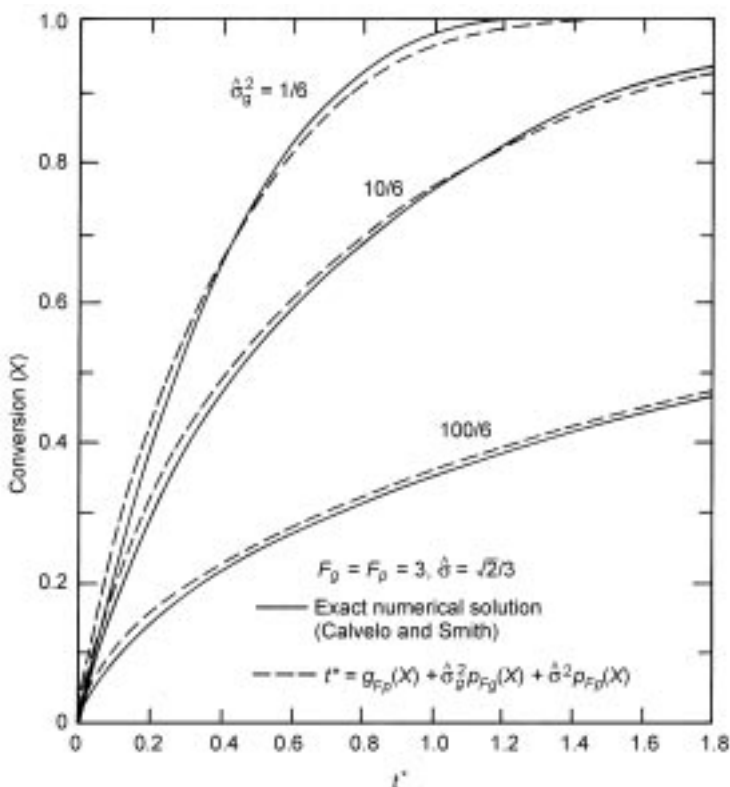
When diffusion through the product layer around each grain presents a substantial resistance, the $t|_{\delta \rightarrow 0}$ term is obtained from equation 7.71 without the last term. Thus, the application of equation 7.94b yields (Sohn and Szekely, 1974; Calvelo and Smith, 1972):

$$t_g^* \cong [g_{F_g}(X) + \hat{\sigma}_g^2 p_{F_g}(X)] + \hat{\sigma}^2 [p_{F_p}(X) + 4X/Sh^*] \quad (7.102)$$

where

$$\hat{\sigma}_g^2 \equiv \left(\frac{k}{2D_g} \right) \left(\frac{V_g}{A_g} \right) \left(1 + \frac{1}{K} \right) \quad (7.103)$$

For the reaction of a spherical pellet made up of spherical grains, equation 7.102 was found closely to represent the exact numerical solution obtained by Calvelo and Smith (1972), as illustrated in Fig. 7.13.



7.13 Comparison of equation 7.102 with the exact numerical solution in Calvelo and Smith (1972).

Example D: The reaction of a porous solid with a gas accompanied by a volume change in the gas phase

In this case, the application of the law of additive reaction times, expressed by equation 7.95b, yields

$$t(X) \cong a \cdot g(X) + a \cdot \hat{\sigma}^2 \left[\frac{\theta}{\ln(1+\theta)} p_{F_p}(X) + \frac{4(1+\theta)}{Sh^*} X \right] \quad (7.104)$$

This equation is the porous solid counterpart of equation 7.80 for an initially non-porous solid. It has been shown (Sohn and Bascur, 1982) that equation 7.104 gives a very satisfactory representation of the exact numerical solution of the governing differential equation that includes the bulk flow effects due to the volume change in the gas phase upon reaction.

Other examples of the application of the law of additive reaction times can be found in the literature (Eddings and Sohn, 1993; Sohn and Xia, 1986, 1987; Sohn and Chaubal, 1986; Sohn and Braun, 1980).

The effect of chemical equilibrium on gas–solid reaction kinetics and the falsification of activation energy

The correct and meaningful analysis of reaction kinetics requires a careful incorporation of equilibrium considerations. Surprisingly, this is all too frequently neglected, especially in the analysis of reactions involving interactions between a solid and a fluid. Sohn (2004) has critically examined this problem quantitatively and developed mathematical criteria for the importance of K when its value is small.

With reference to equations 7.72, 7.73, 7.92, 7.93, 7.99 and 7.100, it is seen that equilibrium consideration is not necessary for an irreversible reaction ($K \rightarrow \infty$) with the K term disappearing from the equations. However, the term that depends on the rate constant k , $g(X)$, becomes insignificant as $K \rightarrow 0$. Then, k 's in the remaining terms t^* and σ^2 cancel each other, i.e., chemical kinetics do not affect the overall rate, with the overall rate becoming proportional to K and diffusivity (when $C_{Cb} = 0$). This result leads to several significant conclusions (Sohn, 2004):

- (1) *The overall rate of a reaction with small K tends to be controlled by mass transfer, i.e. k_f does not appear in the overall rate expression.* Physically, this means that, as $K \rightarrow 0$, the presence of even a small concentration of the fluid product near the reaction interface brings the condition there close to equilibrium. Thus, the ability of the system to remove the fluid reactant (mass transfer) becomes the critical step.
- (2) *The overall rate of a reaction with small K tends to be slow.* As $K \rightarrow 0$, the concentration of the fluid product at the interface becomes small even at equilibrium (rapid chemical kinetics) and the concentration difference of the fluid reactant between the bulk and the interface, which is related to that of the fluid product by the reaction stoichiometry, becomes small. Thus, the

mass transfer rates of the reactant and product in the fluid phase become correspondingly slow. The smaller the value of K , the slower the overall reaction. (Thermodynamics has a direct effect on the reaction rate! This, even if the bulk fluid contains no product species.)

- (3) *The apparent activation energy of the overall rate is falsified.* Because the overall rate in this case is proportional to K , when $C_{Cb} = 0$, the temperature dependence of the overall rate is determined by the temperature dependence of K . Since

$$\Delta G^0 = \Delta H^0 - T\Delta S^0 \quad (7.105)$$

Based on the thermodynamic relationship that

$$K = \exp\left(-\frac{\Delta G^0}{RT}\right) \quad (7.106a)$$

K can be expressed as

$$K = \exp\left(-\frac{\Delta H^0}{RT}\right) \cdot \exp\left(\frac{\Delta S^0}{R}\right) \quad (7.106b)$$

Considering that ΔS^0 , ΔH^0 , and $D_A(RT)^{1-c}$ are weak functions of temperature, equations 7.71, 7.91 and 7.98 reduce to

$$p_{F_p}(X) + 4X/Sh^* = (\text{const}) \exp\left(-\frac{\Delta H^0}{RT}\right) \cdot (C_{Ab}) \quad (7.107)$$

Thus, the apparent Arrhenius activation energy of the overall rate will be equal to ΔH^0 , the standard enthalpy of the reaction, if the rate is analyzed under the assumption of chemical reaction control. Furthermore, in most cases a large positive ΔG^0 value means a large positive ΔH^0 value. Thus, the apparent activation energy will be large.

It is usually stated that the temperature dependence of a mass-transfer controlled reaction is weak, i.e., the apparent activation energy is small. It is also usually assumed that large apparent activation energy (larger than a few kilocalories per mol) indicates a rate control by chemical kinetics. These statements are not necessarily correct for systems with small K values, with the apparent activation energy approaching the standard enthalpy of reaction (ΔH^0), which is typically large for a fluid–solid reaction with a small K value (a large positive value of ΔG^0).

Sohn (2004) derived a similar result for a fluid–solid reaction that produces only fluid products or with a solid product that is continuously removed from the surface of the reactant solid.

Complex gas–solid reactions

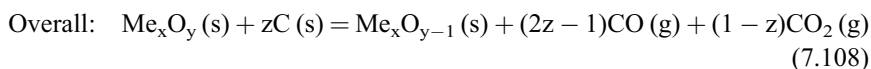
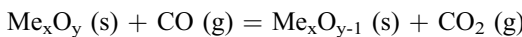
The ideas and principles discussed in the previous sections have been applied to the quantitative analysis of complex gas–solid reaction systems. Examples are

listed below. The reader is referred to the references given in each case for further details.

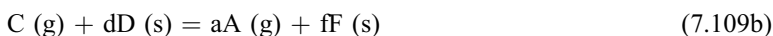
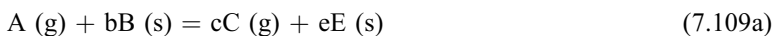
Solid–solid reactions proceeding through gaseous intermediates with a net production of gases

A number of such reactions are of considerable importance in metallurgical processes. These reactions may be considered as coupled gas–solid reactions, and can thus be analyzed in light of the mathematical analyses developed in the previous parts of this chapter.

The most important example is the carbothermal reduction of metals oxides. These reactions proceed through the intermediates of CO and CO₂, according to the following mechanism:

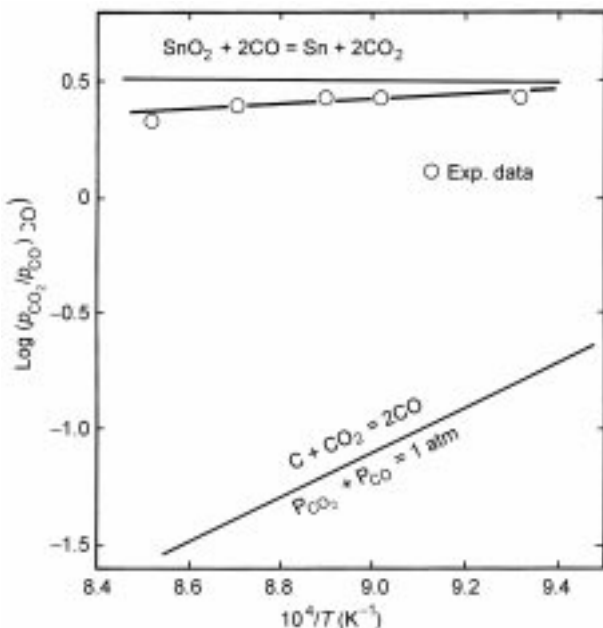


The reduction of iron oxides (Otsuka and Kunii, 1969; Rao, 1971), the reaction between ilmenite and carbon (El-Guindy and Davenport, 1970), the reduction of tin oxide (Padilla and Sohn, 1979), and the reaction between chromium oxide and chromium carbide (Maru *et al.*, 1973) are some examples. In all these reactions, there is a net generation of gaseous species CO and CO₂ resulting in a bulk flow of the gas mixture from the reaction zone. These reactions can be expressed by the following general equations:



In order for this reaction to be self-sustaining without requiring an external supply of gaseous reactants and with a net generation of gaseous species, the condition $ac > 1$ must be satisfied.

In the early investigations, the kinetics of solid–solid reactions was analyzed for specific conditions in which one of the gas–solid reactions controls the overall rate. The studies on the carbothermic reduction of hematite (Rao, 1971), the reaction between ilmenite and solid carbon (El-Guindy and Davenport, 1970), the carbothermic reduction of stannic oxide (Padilla and Sohn, 1979), and the reaction between chromium oxide and chromium carbide (Maru *et al.*, 1973) make use of the assumption of such a single controlling reaction. Padilla and Sohn (1979) showed experimentally that for their experimental conditions this assumption is valid by directly measuring for the first time the partial pressures of the intermediate gases. This experimental evidence is given in Fig. 7.14, which indicates that the SnO₂–CO reaction is very fast (near equilibrium), and



7.14 Observed values of p_{CO_2}/p_{CO} ratios compared with the computed equilibrium values for the component reactions in the carbothermic reduction of stannic oxide.

thus the overall rate of reaction is controlled by the C–CO₂ reaction taking place at the observed p_{CO_2} and p_{CO} .

Sohn and Szekely (1973) developed a theoretical basis for analyzing the general case in which both reactions affect the overall rate and for establishing a criterion for the controlling step. Let us consider a uniform mixture of solids B and D. They may be in the form of small particles or pellets that undergo reactions of the types discussed in Sections 7.3.1 and 7.3.2. We shall here consider isothermal systems and the case of uniform gas concentrations between the particles or pellets of solids B and D. This latter condition is applicable when the overall reaction, and thus the overall gas production, is reasonably fast. This condition is also valid if the mixture is placed in a container with only a small opening that allows the gas product to exit but does not allow the back diffusion of any gas from the surroundings. From the mass balances of the gaseous species, the rates of net generation of the gaseous species are given as follows:

$$\frac{dn_A}{dt} = -v_1 + av_2 \quad (7.110a)$$

$$\frac{dn_C}{dt} = cv_1 + v_2 \quad (7.110b)$$

where v_1 and v_2 are the net forward rates of reactions 7.109a and 7.109b, respectively, per unit volume of the solid mixture. These terms can be expressed,

using equations 7.85 and 7.85b, as follows:

$$v_1 = \left(\frac{\alpha_B \rho_B}{b} \right) \frac{dX_B}{dx} \quad (7.11a)$$

$$v_2 = \left(\frac{\alpha_D \rho_D}{d} \right) \frac{dX_D}{dt} \quad (7.11b)$$

The reaction rate terms, dX_i/dt , depend on the reaction mechanism of each solid. It can be given by any of the solutions given earlier for the reaction of a single solid such as the differential form of equations 7.71, 7.83, 7.91 or 7.94b. It must be noted that the bulk concentration terms in these equations are now the interstitial concentrations, which vary with time as the reaction progresses.

If the total pressure of the system is maintained constant, the following relationships hold:

$$\frac{dn_A}{dt} = \frac{C_A}{V_p} \frac{dV}{dt} \quad (7.112a)$$

$$\frac{dn_C}{dt} = \frac{C_C}{V_p} \frac{dV}{dt} \quad (7.112b)$$

where dV/dt is the rate of volume generation of the gas mixture, and V_p is the volume of the mixture. We have made a pseudo-steady-state assumption that the gas-phase concentrations at any time are at the steady-state values corresponding to the amounts and sizes of the solids at that time, namely, $CdV/dt \gg VdC/dt$.

We also have the condition that

$$C_A + C_C = C_T \quad (7.113)$$

Equations 7.110 to 7.113 may be solved for C_A and C_C . Using these values, the rates of reaction of the solids may then be obtained from the appropriate expressions used for dX_B/dt and dX_D/dt . Integration of these rates over dt will yield incremental values of X_B and X_D . Using the new values of X_B and X_D , equations 7.110 to 7.113 are solved again to obtain C_A and C_C at the next time step. The procedure is repeated to give conversions as functions of time. In certain simple cases, analytical solutions are possible (Sohn and Szekely, 1973).

Solid-solid reactions proceeding through gaseous intermediates with no net production gas

This situation arises when $ac = 1$ in reactions represented by equations 7.109a and 7.109b. An example is the oxidation of metal sulfides with lime in the presence of water vapor to produce the corresponding oxides (Sohn, 1983; Sohn and Kim, 1984b, 1987, 1988; Soepriyanto *et al.*, 1989). This reaction can in general be expressed by the following:



Using this scheme, selected metal sulfides such as molybdenum disulfide and zinc sulfide can be transformed into the corresponding oxides without producing a sulfur-containing gas. The role of lime in this process is twofold: (1) it improves the thermodynamics of the reaction between sulfide and steam, which has a very low equilibrium constant due to the positive Gibbs free energy change, by eliminating hydrogen sulfide, and (2) the reaction between hydrogen sulfide and lime fixes sulfur as calcium sulfide which can be further treated to recover sulfur.

Reactions 7.114a, b, c involve no net consumption or generation of the gaseous intermediates, and the gaseous species do not appear in the overall stoichiometry. The gaseous species simply act as carriers of oxygen and sulfur atoms. In this respect, the mechanism for this type of reaction might be termed ‘catalysis by gases’ (Sohn, 1991).

The kinetics of this reaction can be described by equation 7.110. The difference between this case and the reactions with net generation of gases is that, since no gases are formed or consumed,

$$v_1 = av_2 \quad (7.115)$$

Equations 7.111 and 7.113 are also valid in this case. The solution of these equations gives the conversion as a function of time. Using this approach, the detailed kinetics of reactions of various sulfide minerals with lime has been described (Sohn and Kim, 1987, 1988; Soepriyanto *et al.*, 1989; Sohn, 1991).

Successive gas–solid reactions in which the reactant gas reacts with the first solid, producing an intermediate gas which in turn reacts with the second solid

Two notable examples, in which successive gas–solid reactions play a major role, utilize lime as a scavenger of sulfur-containing gases. The first is the hydrogen reduction of metal sulfides in the presence of lime (Kay, 1968; Habashi and Yostos, 1977; Sohn and Rajamani, 1977; Shah and Ruzzi, 1978; Rajamani and Sohn, 1983; Sohn and Won, 1985; Won and Sohn, 1985), which can be represented by the following general scheme:



In this reaction scheme, lime serves two purposes: (1) it fixes sulfur in the solid, thereby reducing the emission of hydrogen sulfide into the atmosphere, and (2)

the presence of lime improves the otherwise unfavorable thermodynamics of reaction 7.116a by removing hydrogen sulfide from the gas phase. Reaction 7.116b is highly favorable thermodynamically. The second example is the roasting of sulfide minerals in the presence of lime (Haver and Wong, 1972; Bartlett and Haung, 1973; Haung and Bartlett, 1976).

Sohn and co-workers (Sohn and Rajamani, 1977; Rajamani and Sohn, 1983; Sohn and Won, 1985) developed a model for successive gas–solid reactions in a porous pellet. The model takes into consideration the effects of the relative amounts of the solids, grain sizes, the pellet size and porosity, and the diffusion of gaseous species, as well as the effect of improved thermodynamics in systems represented by the first example. The model describes not only the rates of reaction of the solid reactants but also the fraction of the intermediate gas (the sulfur-containing gases in the above examples) that is captured by the second solid (lime in the above examples).

Staged reaction of a solid with a gas in which the solid forms a series of thermodynamically stable intermediate phases

A notable example of such a system is the gaseous reduction of hematite (Fe_2O_3) to iron through the successive formation of magnetite (Fe_3O_4) and wustite (FeO) (Sohn and Chaubal, 1984; Sohn, 1981).

Simultaneous reactions between solid reactants and gases

This type of system can be described by writing the expressions for the consumption of the gaseous reactants by the different solids as well as the conversion of different solids by reaction with different gases in equations 7.82 and 7.83 together with equations 7.2 and 7.3 and solving the resulting equation by a numerical method. The reader is referred to the literature for further detail (Sohn and Braun, 1980, 1984; Lin and Sohn, 1987; Paul *et al.*, 1992).

Multiparticle systems

In the above sections, the discussion mainly involved the analysis of reactions taking place in a single particle or pellet of solids. The eventual objective for studying single particle systems is, of course, to apply the results to the analysis and design of multiparticle systems of industrial importance. Examples of multiparticle gas–solid contacting equipment include packed beds, moving beds, fluidized beds, and rotary kilns. The extension of single particle studies to multiparticle systems will depend on the nature of the particulate assemblages, the mode of gas–solid contacting, and the spatial variation of the gas properties within the system. Therefore, general analyses of these processes will not be presented here, and the reader is referred to the literature for developments in this area (Zhou and Sohn, 1996; Paul *et al.*, 1992; Sohn, 1991; Rhee and Sohn,

1990; Sohn and Lin, 1990; Gao *et al.*, 1983; Herbst, 1979; Szekely *et al.*, 1976; Evans and Song, 1974).

7.5 Liquid–liquid reactions

There are instances during treatment of molten metals where reactions between immiscible molten phases need to be considered. Most often this involves the partition of a solute or impurity element between the two phases. As a general picture, imagine the interface between two phases as shown in Fig. 7.15 and the partition of an element i .

From a kinetic point of view, the rate controlling step is one or several of the following:

- (i) Reactant species has to move between the bulk of phase 1 to the interface.
- (ii) Reaction has to take place at the interface between phases 1 and 2.
- (iii) Reactant has to move between the interface and the bulk of phase 2.

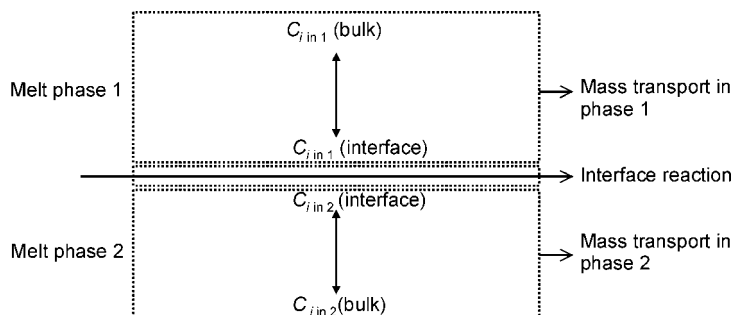
At high temperatures, in the absence of surface active elements that might sterically hinder the reaction, the chemical reaction is often rapid enough to establish local equilibrium and avoid concentration build up at the interface. The flux of the solute can then be written,

$$J_i = k_1(C_1^i - C_1^b) = k_2(C_2^b - C_2^i) \quad (7.117)$$

Here the k s are mass transfer coefficients. It should be noted that if the species i could be in different chemical forms depending on the phase, i.e. Ca and Ca^+ . The partition coefficient is defined as: $m = C_1^i/C_2^i$. The interfacial concentrations can then be eliminated from the equation 7.117 to yield:

$$J_i \left(\frac{1}{k_1} + \frac{m}{k_2} \right) = mC_2^b - mC_1^b \quad (7.118)$$

For the case where the interface is not in equilibrium, a similar expression can be derived, assuming that forward and back reactions are simple:



7.15 Schematic of a liquid–liquid interface.

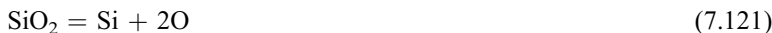
$$J_i \left(\frac{1}{k_1} + \frac{1}{k_{rxn}} + \frac{m}{k_2} \right) = mC_2^b - mC_1^b \quad (7.119)$$

Here an additional resistance term containing the chemical reaction rate constant has been added.

Reactions between molten metals and slags are an example of liquid–liquid reactions. During metal extraction and liquid state processing slags are often used to achieve a multitude of purposes such as thermal insulation, contamination prevention, lubrication, and heat transfer control. Generally, industrial slags and fluxes contain SiO_2 , Me_xO (metal oxides) and, depending on the slag, additional compounds like Al_2O_3 , CaF_2 and P_2O_5 . The ratio $\text{SiO}_2/\text{Me}_x\text{O}$ is an indication of the degree of polymerization. In this section some of the fundamental aspects of chemical reactions between slags and metals are discussed with the case of FeO/Fe as an example. The activation energy for the interfacial reaction is 120 kcal per mole (Richardson, 1974) for a reaction between molten iron and slag:



Due to the relatively low activation energy this reaction is expected to be mass transport controlled. Slags have in general higher viscosities and due to their ionic/polymeric nature the transport of $\text{Fe}^{2+}-\text{O}^{2-}$ in the slag phase is likely the rate determining step. In general, the activation energy for the chemical reaction step is expected to be related to the enthalpy change. When transferring species from a slag to a metal, more bonds have to be broken than formed, since the solutes share ionic bonds in the slag phase. Thus, the activation energies would be expected to be high for those elements that share many bonds in the slag structure such as Si. The activation energy for the reaction,



is 270 kcal per mole.

One of the noteworthy aspects of melt–melt reactions is the ability to achieve large interfacial areas to enhance reaction rates. Kozakevitch (Kozakevitch *et al.*, 1955 and Kozakevitch, 1969) followed the desulfurization of liquid steel by molten slag by using X-rays to observe the change in the shape of a sessile drop of the steel in liquid slag (held in a crucible). It was noted that there was a marked change in the shape of the drop from non-wetting to wetting and then back to non-wetting conditions. These changes are equivalent to the following changes in the metal–slag interfacial tension (γ_{ms}):

- (i) a high initial γ_{ms} ;
- (ii) a reduction to a very low γ_{ms} value while there is rapid desulfurization;
- (iii) an increase in γ_{ms} to its initial value when desulfurization is complete.

Studies on the deposphorization of steel have yielded similar behavior (Jakobsson *et al.*, 1998).

These dramatic changes in γ_m associated with rapid mass transfer are usually referred to as dynamic interfacial tension. When γ_{ms} is very low, any disturbance or turbulence can cause droplets of one phase to move into the other phase. This is usually referred to as emulsification and the formation of a metal emulsion in the slag phase (or vice versa) leads to fast kinetics for the refining reactions because of the huge surface area/mass ratio. Thus from a refining process viewpoint a low interfacial tension is advantageous and modern metal production processes make use of this.

7.6 Solid–liquid reactions

7.6.1 Solidification

The transformation of an element of liquid into solid will follow a heat balance:

$$\rho c_p \frac{\partial T}{\partial t} = L \frac{\partial f_s}{\partial t} - Q \frac{S}{V} \quad (7.122)$$

where ρ , c_p and L are the density, specific heat capacity and latent heat of the metal respectively. S and V are the surface area and volume of the element and f_s is the fraction solid. Q is the net heat flux from the volume element. This equation can be closed by specifying an f_s-t-T relationship if Q and f_s can be identified. Q is dependent upon the thermal field caused by the structure around the element, the mold characteristics and fluid flow in the melt. The fraction solid, f_s , depends on the solidification kinetics, which is governed by the rates of nucleation and growth which are also influenced by fluid flow. The strong interdependence of melt fluid flow, heat transfer and crystal growth complicates the theoretical treatment of solidification. Recently, studies have presented numerical modeling techniques that can simulate solidification structures ranging from dendrite morphology (as reviewed in Boettinger *et al.*, 2000) to microporosity (as reviewed in Lee *et al.*, 2001) and particle pushing (Stefanescu *et al.*, 1998). The dendrite morphology models range from phase field simulations which accurately track the development of a dendritic grain in simplified thermal conditions to cellular automata models which track only the dendrite tip locations in complex geometries for the prediction of grain structures (Gandin *et al.*, 1993). Microporosity models range from analytic solutions to complex simulations of the interactions of pores and the developing microstructure (Lee *et al.*, 2001). Particle pushing models have also spanned a range from analytic solutions (Stefanescu *et al.*, 1998) to the use of phase field (Ode *et al.*, 2000). One common feature of many of these models is their highlighting of the importance of the kinetics of solidification processes upon the final structure. Information on high temperature kinetics is, however, difficult to obtain, especially on nucleation rates.

7.6.2 Metal–melt refractory reactions

Refractory vessels that contain molten metals and slags are subjected to degradation due to chemical or mechanical attack by the molten phases. Chemical attacks occur through the reduction of oxide compounds in the refractory by more reactive elements in the melt.

For example, at high Al levels, there can be a significant reaction with the MgO in the refractories according to:



This reaction rate can be controlled by the mass transport of Al to the reaction site or by the gas phase mass transport of Mg vapor away from the reaction site since its partial pressure is equal to or less than 1 atmosphere. It is also possible that the Mg (v) can react to produce undesired spinel inclusions in the metal melt.

Erosion at the slag–gas or slag–metal interfaces is usually referred to as ‘slag line attack’. It is caused through the establishment of Marangoni flows at the interfaces. Mukai (1998) investigated this form of erosion for oxide refractories and MgO/C refractories. For oxide materials (e.g. SiO₂) and systems where the dissolution of SiO₂ leads to an increase in surface tension, the region of the slag film in longer contact with the refractory will have higher SiO₂ contents. These regions will have higher surface tension and Marangoni flow will occur towards these regions. Since these regions occur at the top of the slag film there will be a flow of slag up the refractory until the Marangoni forces are balanced by buoyancy forces. However, if SiO₂ dissolution causes a decrease in surface tension of the slag the erosion pattern is different with rotational and cyclical ‘up and down’ motions of the slag.

The erosion of MgO/C and Al₂O₃/C refractories occurs by a two-stage process. When MgO particles protrude from the surface the refractory will be wetted by the slag and the slag will dissolve the MgO leaving C particles protruding from the surface. Under these conditions the metal phase will wet the refractory better than the slag. The metal thereupon dissolves the carbon leaving MgO protruding from the surface and the whole process is then repeated.

Tsotridis and Hondros (1998) developed a mathematical model to predict erosion wear in vessels. This accounted for interfacial wear due to both thermo- and diffuso-capillary flows and erosion in the lower part of the vessel due to buoyancy flows.

7.6.3 Electrochemical reactions

Electrochemical reactions are a type of chemical reaction where electric energy is consumed or created. An electrochemical reaction could be e.g.:



This is a reduction reaction. The quantitative link between electrical energy and chemical reactions was established by Faraday (see, for example, Uhlig and Revie, 1985) who found that, for a reaction such as the one above, the loss of product A (in moles = m) is related to a current at A according to: $m \cdot n \cdot F = it$. The chemical free energy of the reaction is ΔG_A and a corresponding reversible potential can be computed, using the Nernst equation, $\Delta G_A = -nFE_A$ (where F is Faraday's constant).

The reaction above cannot occur by itself since the electrons consumed need to be supplied by a different reaction, called an oxidation reaction.



The two reactions have to occur at a location called electrodes, where electrons, ions and reactants (A and B are usually solids or gases) have to be present. The electrode where oxidation occurs is called the anode and the one where reduction occurs is called the cathode. The electrons given off at the anode are supplied to the cathode through an electronic conducting phase. To close the circuit, an ionic current is passed between the electrodes through an ionic pathway, called the electrolyte. The entire electrochemical system, consisting of electrodes, electrolyte and electron lead, is called an electrochemical cell. The overall cell reaction is the sum of anode and cathode reactions and the cell free energy and reversible cell potential can be calculated accordingly. There are two basic types of electrochemical cells. In galvanic cells (see Fig. 7.16a), the cell free energy is negative and thus the reversible cell potential is positive. In these types of cells, to which most corrosion cells, fuel cells and batteries belong, electrical energy is released. The second type is electrolysis cells (Fig. 7.16b), which have a negative cell potential and thus are not spontaneous. Electrolytic metal extraction processes are examples of this latter type.

For an in-depth understanding of electrochemical kinetics there are several excellent textbooks available (e.g. Bard and Faulkner, 2001). In this chapter, the topic is introduced in two cases, corrosion in an aqueous solution and electrolytic Al extraction.

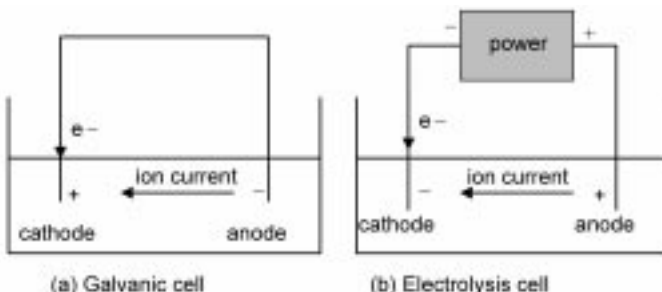
Corrosion of Zn in a de-aerated environment

Consider Zn metal reacting to form ions in the presence of water according to:



The standard half cell potential of this anodic oxidation reaction is: $E_{Zn}^0 = 0.763$ V (Uhlig and Revie, 1985) vs the standard hydrogen potential at room temperature. The Zn ions dissolve in the water that serves as an electrolyte. The electrons are supplied through the Zn metal itself and delivered to a cathodic reduction reaction:





7.16 (a) Galvanic cell and (b) electrolysis cell.

The standard half cell potential vs the standard hydrogen electrode is 0 V for this reaction. This reaction will have to occur at the Zn surface too and therefore the exact location of the anode and cathode cannot be specified. This cell can be viewed as the case in Fig. 7.16a, with the Zn dissolution reaction occurring at the anode and the hydrogen reduction reaction at the cathode. Applying Kirchoff's law to the cell, one obtains:

$$E_{\text{H}} - |\eta_{\text{H}}| + E_{\text{Zn}} - |\eta_{\text{Zn}}| - i \cdot \sum R_{ohm} = 0 \quad (7.128)$$

In this equation, E_H and E_{Zn} are the reversible cell potentials:

$$E_H = E_H^0 - \frac{RT}{2F} \ln \left(\frac{P_{H_2}}{a_{H^*}} \right) \quad (7.129)$$

and

$$E_{\text{Zn}} = E_{\text{Zn}}^0 - \frac{RT}{2F} \ln \left(\frac{a_{\text{Zn}^{2+}}}{1} \right) \quad (7.130)$$

The terms η_H and η_{Zn} are called over-potentials and account for the kinetic resistances at the electrodes. In general they include the effects of (i) charge transfer reaction resistance, (ii) mass transport resistance and (iii) intermediate chemical reaction and adsorption effects. As a result, they are non-linear functions of current, which can be derived similarly to what was done for reaction rate theory but adding the effect of electrical potential on stabilizing or de-stabilizing the presence of electrons:

$$|\eta_H| = \frac{RT}{\alpha_H F} 2.3 * \log \left(\frac{i}{i_{0,H}} + \frac{C_{H^*}(0,t)}{C_{H^*}^*} \right) \quad (7.131)$$

Here, α is the transference number (between 0 and 1), usually close to 0.5. $i_{0,H}$ is the exchange current of the charge transfer reaction and is a measure of the electrocatalytic nature of the electrode. Roughly it corresponds to the chemical reaction rate constant. The second term in the parenthesis is the ratio between reactant concentration at the electrode and in the bulk that depends on the mass transport of reactants to the reaction site. It should be mentioned that the mass transport is carried out through migration, diffusion and fluid flow. The combined flux equation being:

$$\bar{J}_{H^*} = -D_{H^*} \nabla C_{H^*} - \frac{Z_{H^*} F}{RT} D_{H^*} C_{H^*} \nabla E + C_{H^*} \bar{v} \quad (7.132)$$

A corresponding equation to equation 7.131 exists for the anode, but in this case there are presumably no mass transfer effects, since there are no gradients for the reactant Zn:

$$|\eta_{Zn}| = \frac{RT}{\alpha_{Zn} F} 2.3 * \log \left(\frac{i}{i_{Zn}} \right) \quad (7.133)$$

The Ohmic resistances consist of the resistance to electrons in leads and contacts and the resistance to ions in the electrolyte:

$$\sum R_{ohm} = R_{lead} + R_{contact} + R_{electrolyte} \quad (7.134)$$

The electrolyte resistance can be evaluated from the mobility of all ions present and the geometry and size of the electrolyte. By solving equations 7.128 to 7.134, a short circuit current will be found and this current corresponds to the corrosion current. From the corrosion current, the loss of Zn due to dissolution can be readily computed, using Faraday's law.

Electrolytic Al production

Hall, an American, and Herault, a Frenchman, simultaneously engineered a process to produce metallic aluminum from a molten salt based on cryolite and alumina ($\text{Na}_3\text{AlF}_6\text{-Al}_2\text{O}_3$). This mixture forms a low melting eutectic (approx. 1000 °C) salt mixture as opposed to pure alumina, which melts above 2000 °C.

At the cathode, Al is produced according to:



At the anode:



and the overall cell reaction is:



In this case the net cell potential ($E_{cathode} - E_{anode}$) is negative = -1.2 V and thus, external power is needed to drive the reaction. Examining Fig. 7.16b and using Kirkhoff's law one obtains for this electrolysis cell:

$$E_{imposed} = -E_{cell} + |\eta_{anode}| + |\eta_{cathode}| + i \cdot \sum R_{ohmic} \quad (7.138)$$

At the cathode, the mass transfer of ions is suggested to cause the overpotential of approximately 0.46 V (Hayes, 1993). At the anode the step:



is sluggish and causes an overpotential of 0.41 V.

Ohmic losses, including electrolyte resistance contribute to 1.9 V. The imposed cell potential thus amounts to about 4.4 V. When computing the energy needed to produce a tonne of Al, this corresponds to about 250 GJ per tonne of Al. This can be compared to the production of steel through the blast furnace route, which costs only roughly 30 GJ/tonne.

7.7 Gas–liquid reactions

There are several important cases where molten metals react with a gas phase such as:

1. Metal droplets in reacting gases (e.g. during atomization).
2. Gas bubbles in melts (e.g. during purging during steelmaking).
3. Reaction between continuous gas and a metal phase (vacuum de-gassing or reoxidation).

In general, the mass transfer depends on the flow in the two fluid phases and the reaction kinetics depends on the nature of the interface.

7.7.1 Melt reoxidation

Reoxidation of a molten steel surface as a result of unwanted reaction between reactive elements in melt with air is a cause of exogenous inclusions that can get entrained into the melt and lead to lowering product quality (Farrell *et al.*, 1970). Melt reoxidation with air can take place at a number of locations in the steelmaking process where the melt is temporarily exposed to the atmosphere. It is likely to happen primarily (Lindenberg and Vorwerk, 1981) at melt surfaces that happen to be uncovered in the ladle furnace, tundish or continuous casting mold, or at refractory joints and nozzles between these three vessels. In the latter case, reoxidation occurring at or near nozzles due to air aspiration can lead to deposits on the walls that results in clogs that prevent a uniform steel melt flow which degrades process control (Rastogi and Cramb, 2001). Sasai (Sasai, 2001; Sasai and Mizukami, 2001) studied how reoxidation caused by air leads to Al_2O_3 build-up in the tundish nozzle, and found that during stable casting modest reoxidation resulted solely from oxidation by air on the tundish bath surface, whereas during teeming the reoxidation increased fivefold and was caused primarily by oxidation at the tundish inlet.

The reoxidation process involves: (i) transport of oxygen to the melt, (ii) mass transport in the melt (iii) precipitation of the oxide phase and growth of the oxide precipitate into a macro-inclusion.

Gas phase mass transfer to a melt has been extensively studied and documented in the literature (e.g. Fruehan, 1998). Sasai and Mizukami (2000) developed models based on experimental results (Sasai and Mizukami, 1996, 1998) to predict the melt reoxidation rates in the tundish based on gas phase mass transfer through the tundish inlet and top covering tundish powder.

Precipitation of the oxide phase follows a chemical reaction between metallic elements in the melt (unreacted deoxidation reactants such as Al, Si or Ca and/or Fe) and oxygen dissolved in the melt, and the thermodynamic basis of this reaction is essentially similar to the much studied (Turkdogan, 1996) deoxidation equilibrium that takes place in the ladle. It should, however, be mentioned that, unlike deoxidation that occurs under isothermal conditions (at about 1600 °C) where thermodynamic data are abundant, reoxidation occurs more often under significantly lower and often changing temperatures where published interaction coefficient data are more scarce.

7.7.2 Melt evaporation

The evaporation of a solute, such as Mn, under near vacuum conditions, from a melt can be controlled by one or a combination of the following factors:

1. Mass transfer from the melt to the surface:

$$J = k_m(C_b - C_i) \quad (7.140)$$

where, k_m is the mass transfer coefficient and C_b and C_i are the solute concentrations in bulk and interface respectively.

2. Evaporation kinetics (Richardson, 1974, p. 486):

$$J = \frac{44 \cdot 33A\alpha}{\sqrt{MT}} (p^0 \gamma C_i - p^i) \quad (7.141)$$

where, M is the molecular mass, α is the vaporization constant, γ is the activity coefficient, p^0 is the vapor pressure over the pure solute and p^i is the impurity vapor pressure near the interface.

3. Gas phase mass transfer:

$$J = \frac{k_g}{RT} (p^i - p^b) \quad (7.142)$$

where k_g is the gas phase mass transport coefficient, and p^b is the pressure of the solute in the bulk gas.

7.7.3 Gas bubbles rising in metals

During gas purging, bubbles rise through a molten metal bath and react during their ascent with solutes in the melt. The rate is determined by either mass transport in the gas or melt or chemical reaction.

In the case of inert gas purging, where rising Ar bubbles absorb impurities, it is possible that mass transfer inside the bubble can be the rate controlling step. According to Bradshaw and Richardson (1970) the mass transfer coefficients in the gas phase, for the case of N and H in steel, were estimated to be half of the mass transfer coefficients in the melt phase. In the cases of H or N where the gas partial pressure in equilibrium with the melt is very low, this could result in a

slow mass transport kinetics whereas for gases which have a higher equilibrium pressure (CO), the concentration difference term will result in gas phase mass transfer being less important.

Mass transfer in the melt phase

Gas bubbles encountered during purging in metallurgical processes are usually larger than 1 cm in diameter. For such bubbles, if mass transport is assumed to occur only across the cap of a rising cap-shaped bubble, the mass transfer coefficient has been developed for the case of laminar flow over the cap (Baird and Davidson, 1962):

$$k = 0.975 \cdot d^{-1/4} D^{1/2} g^{1/4} \quad (7.143)$$

Here, d is the equivalent spherical diameter, D is the diffusion coefficient in the melt and g is gravity.

The resulting transfer rate of gas into the bubble is:

$$J = k(C_b - C_i) \quad (7.144)$$

Here, C_b and C_i are the concentrations of the solute in the bulk melt and in the melt at the bubble surface, respectively.

7.7.4 Foaming

Foams are widely used in the iron- and steelmaking processes since they provide rapid refining of metal droplets held in the foam due to the enormous (surface area/mass) ratio. Foaming slags are also used in electric arc furnaces (EAF) to stabilize the arc and improve energy efficiency.

There is a general agreement (e.g., Cooper and Kitchener, 1959) that the principal factors promoting foaming are:

- a low surface tension of slag (γ_s) (P_2O_5 , Na_2O , oxide additions cause a decrease in γ_s);
- high bulk and surface viscosities which retard draining of the slag film (P_2O_5 and SiO_2 are both surface active and will congregate preferentially at the surface and will tend to increase the surface viscosity);
- the presence of solids in the slag (since this will increase viscosity and tend to lock the bubbles and prevent their escape);
- low temperature since this will increase slag viscosity and encourage the formation of solids (a high solidification temperature of the slag would also be beneficial);
- high surface elasticity.

Although there is a general agreement on the factors affecting foam stability there is still some disagreement about the relative importance of the various factors.

7.7.5 Sulfide smelting and converting reactions

These reactions take place at sufficiently high temperatures, where the chemical reactions are very rapid. Thus, the overall rate of the process is determined by mass transfer between the gas and the molten phase. Further, in most operations, the process is designed and operated under the conditions in which mass transfer is also very rapid. Therefore, the overall rate is often determined by the supply rate of the oxygen-containing process gas, which is dependent on other factors such as heat generations and removal, erosion of refractory and gas injectors, melt splashing and sloshing, etc.

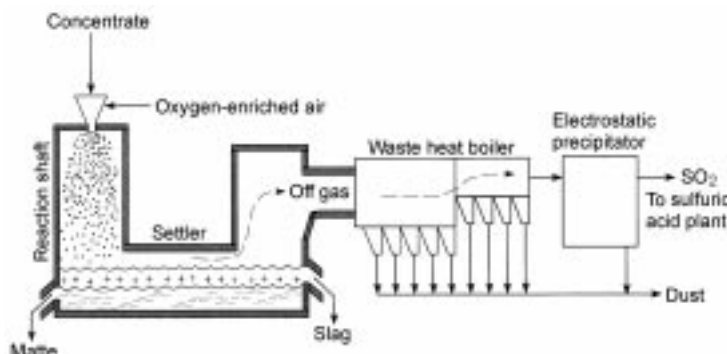
The major reactions in sulfide smelting and converting steps are the oxidation of sulfur and iron, as discussed in Section 7.2. Another critical factor is the removal and distribution of minor elements. The rates of their removal also depend on the injection rate of the process gas, but an important additional factor in this respect is the equilibrium relationships that describe the distribution ratios of the minor elements among the gas, slag, and matte or metal phases. The minor element removal stops with the gas injection at the end of the iron and sulfur removal. In the case of the fire-refining process in which the removal of the impurities is the main objective, the process continues until the impurity concentrations become sufficiently low. In both cases, the rate of impurity removal is largely dependent on the gas supply rates and the thermodynamics of impurity distribution. Much work has been done in this respect, and the reader is referred to the literature for details (Nagamori and Sohn, 2000; Kim and Sohn, 1998a, 1998b, 1997, 1996; Chaubal and Nagamori, 1988; Nagamori and Chaubal, 1982; Nagamori and Mackey, 1978).

7.8 Comprehensive process modeling

In traditional metallurgical process modeling, it was possible to incorporate only the simplified aspects of fluid flow, mixing, and mass/heat transfer into the analysis of process rates and reactor design. As a result, accurate and realistic incorporation and simulations of many aspects of complex processes have not been possible. With the advent of high-speed, high-capacity computing devices and technologies, complex processes have become amenable to analysis and modeling. This has also resulted in the merging of various disciplines in formulating detailed descriptions of complex processes. Developments that exemplify this in the field of metallurgical process modeling are discussed in this section.

7.8.1 Flash smelting process

The flash smelting process is important in the production of non-ferrous metals from sulfide minerals. A schematic diagram of this process is given in Fig. 7.17. In this process, fine, dried mineral particles and fluxes are injected into the



7.17 Schematic diagram of a flash smelting process.

furnace with industrial oxygen or oxygen-enriched air. The sulfide particles are ignited and burn in the turbulent gas jet. The design and operation of a flash-smelting furnace has largely remained an art, despite the fact that the process has been in commercial use for a long time and is currently the dominant sulfide-smelting process. This is mainly due to the difficulty of quantifying the complex interactions of the individual sub-processes, i.e. the turbulent fluid flow, convective heat and mass transfer, chemical reactions, and radiative heat transfer.

A reliable mathematical model starts with good understanding of identifiable component processes followed by assembling them into the overall description of the process. The model equations are written based on the continuity of mass and the conservation of momentum and energy for the gas and the particle phases (Hahn and Sohn, 1990a; Perez-Tello *et al.*, 2001b). The time-averaged equations for the conservation of fluid properties can be expressed in the following general form:

$$\nabla \cdot (\rho \vec{v} \phi) - \nabla \cdot (\Gamma_\phi \nabla \phi) = S^\phi \quad (7.145)$$

where ϕ is the dependent variable, Γ_ϕ is the coefficient for the diffusive transfer, and S^ϕ is the source term. Table 7.1 shows all the gas phase governing equations. The particle phase is often described using the Lagrangian framework, the governing equation being listed in Table 7.2. Further details of the model equations can be found elsewhere (Hahn and Sohn, 1990a; Perez-Tello *et al.*, 2001b).

The next sub-process to include is the gas–particle reactions, i.e. the oxidation of sulfur and iron in the mineral particles. To describe the ignition transient as well as the main combustion period following the ignition, information on the intrinsic kinetics of the mineral particle oxidation is needed. This information is preferably obtained by carrying out separate experiments (Chaubal and Sohn, 1986). Appropriate measures must be taken to ensure the determination of the intrinsic kinetics.

The ability of the computer model to describe the dispersion of the particles in the turbulent gas jet of a flash-smelting furnace shaft was verified by the use of a non-reacting model system (Yasuda and Sohn, 1995). Sohn and co-workers

Table 7.1 Gas phase equations

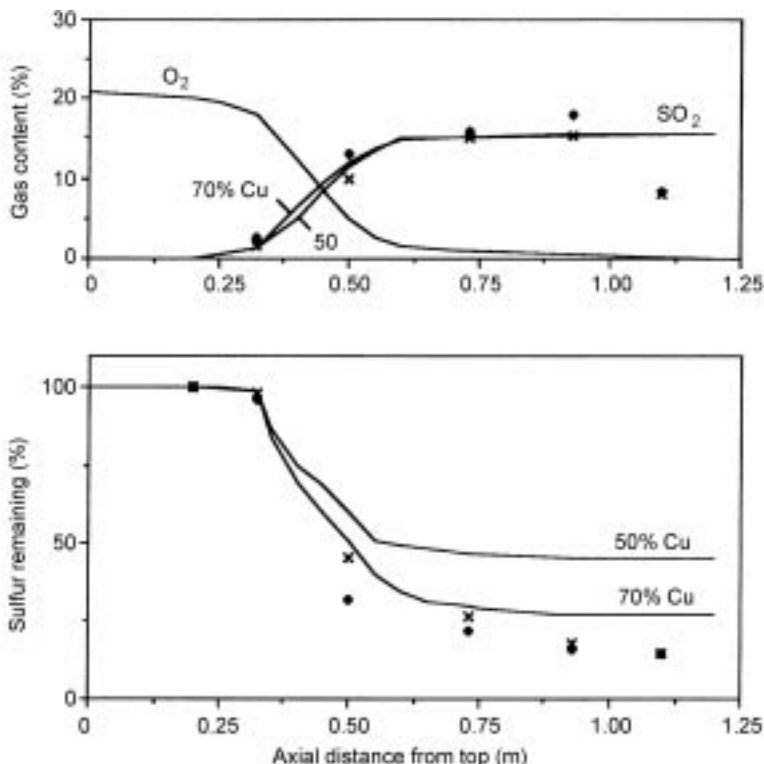
Equation	ϕ	Γ_ϕ	S^ϕ	
Continuity	1	0	S_p^m	(A-1)
x-Momentum	\bar{u}_g	μ_e	$-\frac{\partial p}{\partial x} + \frac{\partial}{\partial x} \left(\mu_e \frac{\partial \bar{u}_g}{\partial x} \right) + \frac{\partial}{\partial y} \left(\mu_e \frac{\partial \bar{v}_g}{\partial x} \right) + \frac{\partial}{\partial z} \left(\mu_e \frac{\partial \bar{w}_g}{\partial x} \right) - \frac{2}{3} \frac{\partial}{\partial x} (\bar{\rho}_g k) + \bar{\rho}_g g_x + S_p^u$	(A-2)
y-Momentum	\bar{v}_g	μ_e	$-\frac{\partial p}{\partial y} + \frac{\partial}{\partial x} \left(\mu_e \frac{\partial \bar{u}_g}{\partial y} \right) + \frac{\partial}{\partial y} \left(\mu_e \frac{\partial \bar{v}_g}{\partial y} \right) + \frac{\partial}{\partial z} \left(\mu_e \frac{\partial \bar{w}_g}{\partial y} \right) - \frac{2}{3} \frac{\partial}{\partial y} (\bar{\rho}_g k) + \bar{\rho}_g g_y + S_p^v$	(A-3)
z-Momentum	\bar{w}_g	μ_e	$-\frac{\partial p}{\partial z} + \frac{\partial}{\partial x} \left(\mu_e \frac{\partial \bar{u}_g}{\partial z} \right) + \frac{\partial}{\partial y} \left(\mu_e \frac{\partial \bar{v}_g}{\partial z} \right) + \frac{\partial}{\partial z} \left(\mu_e \frac{\partial \bar{w}_g}{\partial z} \right) - \frac{2}{3} \frac{\partial}{\partial z} (\bar{\rho}_g k) + \bar{\rho}_g g_z + S_p^w$	(A-4)
Turbulent kinetic energy	k	μ_e/σ_k	$G - \bar{\rho}_g \epsilon$	(A-5)
Dissipation rate	ϵ	μ_e/σ_ϵ	$(\epsilon/k)(C_1 G - C_2 \bar{\rho}_g \epsilon)$	(A-6)
Sulfur mass fraction	f	μ_e/σ_f	S_p^f	(A-7)
Reacted oxygen ratio	η	μ_e/σ_η	S_p^η	(A-8)
Enthalpy	\bar{h}_g	μ_e/σ_h	$Q_{rp}^h + Q_{rg}^h + \bar{u}_g \frac{\partial p}{\partial x} + \bar{v}_g \frac{\partial p}{\partial y} + \bar{w}_g \frac{\partial p}{\partial z} + S_p^h$	(A-9)
where:				
$G = \mu_t \left\{ 2 \left[\left(\frac{\partial \bar{u}_g}{\partial x} \right)^2 + \left(\frac{\partial \bar{v}_g}{\partial y} \right)^2 + \left(\frac{\partial \bar{w}_g}{\partial z} \right)^2 \right] + \left(\frac{\partial \bar{u}_g}{\partial y} + \frac{\partial \bar{v}_g}{\partial x} \right)^2 + \left(\frac{\partial \bar{u}_g}{\partial z} + \frac{\partial \bar{w}_g}{\partial x} \right)^2 + \left(\frac{\partial \bar{v}_g}{\partial z} + \frac{\partial \bar{w}_g}{\partial y} \right)^2 \right\}$		(A-10)		
$\mu_e = \mu_t + \mu_i$				(A-11)
$\mu_t = C_\mu \bar{\rho}_g k^2 / \epsilon$				(A-12)
$S_p^m = S_p^f - S_p^\eta$				(A-13)

Table 7.2 Particle phase equations

Motion	$m_p \frac{d\langle \mathbf{V} \rangle}{dt} = m_p \frac{3}{4} C_D \frac{\rho_g}{\rho_p} \frac{1}{d_p} \langle \mathbf{U} \rangle - \langle \mathbf{V} \rangle (\langle \mathbf{U} \rangle - \langle \mathbf{V} \rangle) + (m_p - m_g) \mathbf{g}$	(B-1)
Particle dispersion (cloud model)	$\sigma_{ii}^2(t) = 2 \int_0^t \langle v_i'^2(t_1) \rangle \int_0^t R_{ii}^p(\tau) d\tau dt_1$	(B-2)
Species mass balance	$\frac{dn_i}{dt} = \sum_{j=1}^{j=q} R_{ij}^r - R_i^v$	(B-3)
Energy	$\frac{d}{dt}(m_p h_p) = H_r + Q_{rp} - Q_p - H_v$	(B-4)

(Perez-Tello *et al.*, 2001a; Sohn and Seo, 1990; Sohn *et al.*, 1988) carried out experiments in a laboratory flash furnace under various operating conditions and compared the results with the experimental data (Hahn and Sohn, 1990a; Perez-Tello *et al.*, 2001b). They also verified their model results against the independent measurements obtained in a pilot plant by Outokumpu personnel (Hahn and Sohn, 1990a), providing further evidence of the reliability of the mathematical model. The mathematical model provides a realistic representation of the process because it is built based on either first principles or well-established correlations for individual sub-processes developed independently. One can thus use the mathematical model with much greater confidence to describe, analyze, and design the sulfide-smelting processes. An example is the application of this mathematical model to the description of minor-element behavior (Seo and Sohn, 1991), which is an important problem in any smelting process.

Figure 7.18 shows a typical comparison between the model predictions and laboratory measurements in terms of the SO₂ concentration in the gas and sulfur content in the particles at various axial positions along the centerline of the furnace shaft (Hahn and Sohn, 1990a). The discrepancy toward the bottom of the furnace is due to the air leaking into the furnace through an opening through which the sample probe is inserted. It is particularly noteworthy that the model adequately predicts the particle ignition point, after which the reaction is very fast. A similar comparison between the model predictions and measurements obtained by Outokumpu Co. in their pilot plant is shown in Fig. 7.19. The top figure shows the SO₂ and O₂ concentrations along the central axis from the burner, as well as the amount of oxygen used in the oxidation of metal contents. The second graph is for the case in which the feed gas was preheated. Considering the complexity of the process and the fact that the pilot-plant measurements were made completely independently from our computation, the agreement is noteworthy. The bottom graph compares the temperature profiles for these two cases.

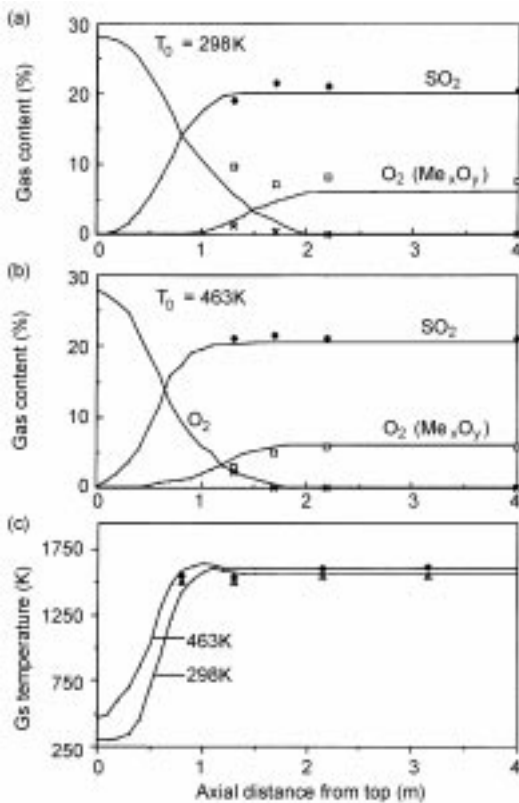


7.18 Comparison of the computed and measured results along the centerline of a laboratory flash furnace shaft. (Conditions for the tests are given in Hahn and Sohn (1990a).)

7.8.2 Fluidized-bed reactors for gas–solid reactions

In a fluidized-bed reactor, the solid particles are dragged upward as clouds or wakes by the gas bubbles and descend by gravity in the emulsion phase, as shown in a schematic representation in Fig. 7.20. Fresh particles may be fed continuously to the bed and discharged either through an overflow pipe or by entrainment of gases. Particle size and density may change, and particles of the same size have different residence time in the bed. All of these must be accounted for in order to predict and control the behavior of the solids in a fluidized-bed process.

Zhou and Sohn (1996) investigated the fluidized-bed chlorination of rutile by $CO-Cl_2$ mixtures, using the bubble assemblage model to describe the bed behavior with several new features. An experimentally determined, particle-size-dependent reaction-rate expression of the chlorination kinetics was incorporated to calculate the concentration profile of reactant gases in the bed. This rate expression is more realistic than those previously used (Youn and Park, 1989; Fuwa *et al.*, 1978). The particle-size distribution in the bed was



7.19 Comparison of the computed and measured results along the centerline of an Outokumpu pilot flash furnace shaft. ($\text{O}_2 (\text{Me}_x\text{O}_y)$ denotes the percent of input O_2 consumed to produce metal oxides. Conditions for the tests are given in Hahn and Sohn (1990a).)

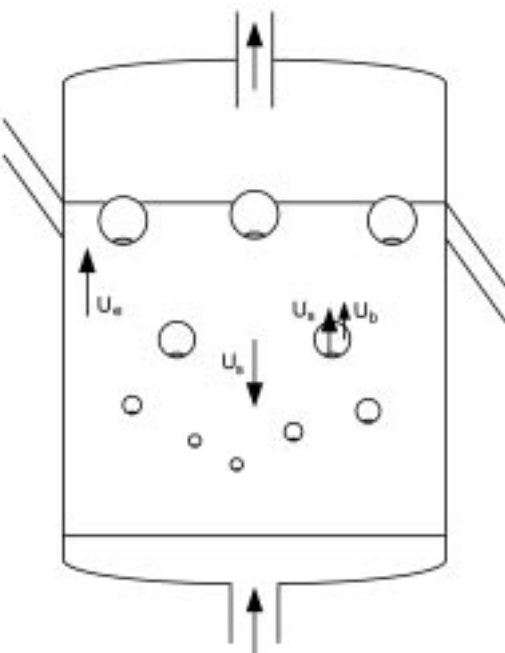
calculated by a population balance. The model assumes that the solid particles are well mixed throughout the bed, but the gas concentrations vary with the bed height. This makes the model applicable to industrial application where the concentrations of reactant gases may change substantially along the bed height.

The gases flow through the bubble and emulsion phases, while exchanging mass between the phases. The gas-phase mass balances in these two phases can be expressed as follows:

$$-f_{g,b}U_b \frac{dC_{Ab}}{dz} = \delta K_{be}(C_{Ab} - C_{Ae}) + f_{g,b}(-r_{g,b}) \quad (7.146)$$

$$-f_{g,e}U_e \frac{dC_{Ae}}{dz} = \delta K_{be}(C_{Ae} - C_{Ab}) + f_{g,e}(-r_{g,e}) \quad (7.147)$$

where $f_{g,j}$ is the fraction of the bed volume occupied by gas in phase j ; K_{be} is the interchange coefficient for gas between the bubble and the emulsion phases based on the bubble volume; and $r_{i,j}$ is the consumption rate of reactant gas i per



7.20 A schematic representation of the bubbling fluidized bed.

unit volume of the fluidized bed at a particular height in phase j ; and δ , the fraction of the bed volume occupied by the bubbles, is given by [Kunii and Levenspiel, 1991],

$$\delta = \begin{cases} \frac{U_0 - U_{mf}}{U_b + U_{mf}} & \text{when } U_b \cong \frac{U_{mf}}{\epsilon_{mf}} \\ \frac{U_0 - U_{mf}}{U_b} & \text{when } U_b \cong 5 \frac{U_{mf}}{\epsilon_{mf}} \end{cases} \quad (7.148)$$

The rate expression for the chlorination of rutile was experimentally determined as follows (Sohn *et al.*, 1998):

$$\frac{dr}{dt} = -k_v(RT)^{1.29} C_{co}^{0.55} C_{Cl_2}^{0.74} \quad (7.149)$$

The mathematical model developed in this work considers the separate variations of the gas concentrations in the bubble and emulsion phases with bed height. With the assumption of steady state and perfect mixing of solid particles in the bed, an overall mass balance of the solid gives (Kunii and Levenspiel, 1968; Levenspiel *et al.*, 1968)

$$F_0 - F_1 - F_2 = \sum_{\text{all } r} \left(\begin{array}{c} \text{rate of solid consumption in} \\ \text{size interval } r \text{ to } r + dr \\ \text{in the whole bed} \end{array} \right) \quad (7.150)$$

and

$$\left(\begin{array}{l} \text{Rate of mass} \\ \text{consumption in the} \\ \text{size interval } r \text{ to} \\ r + dr \text{ per unit} \\ \text{volume of the bed} \end{array} \right) = \left(\begin{array}{l} \text{Rate of mass} \\ \text{consumption in the} \\ \text{size interval } r \text{ to} \\ r + dr \text{ in bubble} \\ \text{phase per unit} \\ \text{volume of the bed} \end{array} \right) + \left(\begin{array}{l} \text{Rate of mass} \\ \text{consumption in the} \\ \text{size interval } r \text{ to} \\ r + dr \text{ in emulsion} \\ \text{phase per unit} \\ \text{volume of the bed} \end{array} \right) \quad (7.151)$$

In the bubble phase,

$$\left(\begin{array}{l} \text{Rate of mass} \\ \text{consumption in the} \\ \text{size interval } r \text{ to} \\ r + dr \text{ in bubble} \\ \text{phase per unit} \\ \text{volume of the bed} \end{array} \right) = \rho \left(\begin{array}{l} \text{Number of particles in} \\ \text{the interval } r \text{ to } r + dr \\ \text{in bubble phase per} \\ \text{unit volume of the bed} \end{array} \right) \left(\begin{array}{l} \text{Rate of volume} \\ \text{decrease for one} \\ \text{particle in} \\ \text{bubble phase} \end{array} \right) \\ = \rho \left(\frac{y_b w P_1(r) dr}{\rho \left(\frac{4}{3} \pi r^3 \right)} \frac{dV}{dt} \right) \quad (7.152)$$

A similar equation is written for the emulsion phase. In the preceding equations, F_o is the feed rate of solids with a particle-size density function of $P_o(r)$; F_1 is the withdrawal rate of solids with a particle-size density function of $P_1(r)$; F_2 is the elutriation rate of solids with a particle-size density function of $P_2(r)$; ρ is the mass density of solid; y_b is the fraction of the entire solid present in the bubble phase; w is the solid weight per unit volume of the bed; r is the particle radius; and V is the volume of a particle.

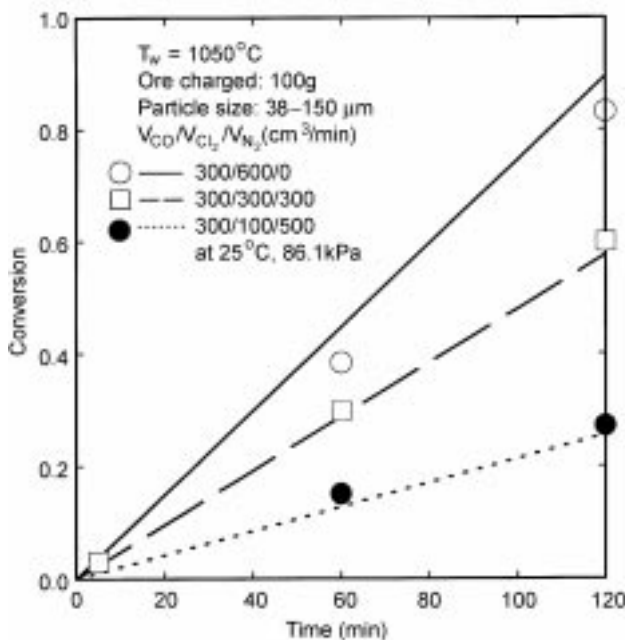
The mass balance of solid in the particle-size interval r to $r + dr$ in terms of rate gives,

$$\left(\begin{array}{l} \text{Solids} \\ \text{entering in} \\ \text{the feed} \end{array} \right) - \left(\begin{array}{l} \text{Solids} \\ \text{leaving in} \\ \text{overflow} \end{array} \right) - \left(\begin{array}{l} \text{Solids} \\ \text{leaving in} \\ \text{carryover} \end{array} \right) \\ + \left[\left(\begin{array}{l} \text{Solids} \\ \text{shrinking} \\ \text{into the} \\ \text{interval from} \\ \text{a larger size} \end{array} \right) - \left(\begin{array}{l} \text{Solids} \\ \text{shrinking} \\ \text{out of the} \\ \text{interval to a} \\ \text{smaller size} \end{array} \right) \right] - \left(\begin{array}{l} \text{Solids} \\ \text{consumption} \\ \text{due to the} \\ \text{shrinkage within} \\ \text{the interval} \end{array} \right) = 0 \quad (7.153)$$

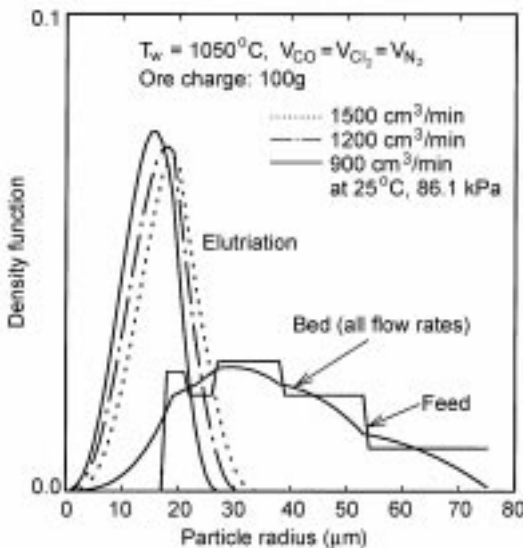
The formulation of the quantitative expressions of the various terms in the above conceptual balance equations is described elsewhere (Zhou and Sohn, 1996). The resulting model equations were applied to the cases of single-sized and multi-sized feeds.

To verify the mathematical model, batch experiments were carried out using a deep bed across which significant changes in gas concentrations occurred. Since the gas-phase dynamics are much faster than changes in the solid particles, the steady-state model was applied to each time increment, yielding the solid-particle-size distribution and the amount of solids remaining in the bed after each time increments. The mathematical model was tested by comparing the computed results with the results of experiments under carefully selected conditions in which both the chlorination kinetics and mass-transfer effects play a significant role. In this way, generally valid verification of the model was obtained.

Examples of the model predictions compared with the experimental results are shown in Fig. 7.21 for a feed with a wide size distribution. It is seen that the mathematical model yields results that are in good agreement in terms of overall conversion *vs* time. The calculated results of the particle size distributions in the bed and in the elutriation are given in Fig. 7.22.



7.21 Experimental data *vs* model prediction for the fluidized-bed chlorination of rutile particles with a wide size distribution. (The feed particle size distribution can be found in Fig. 7.22.)



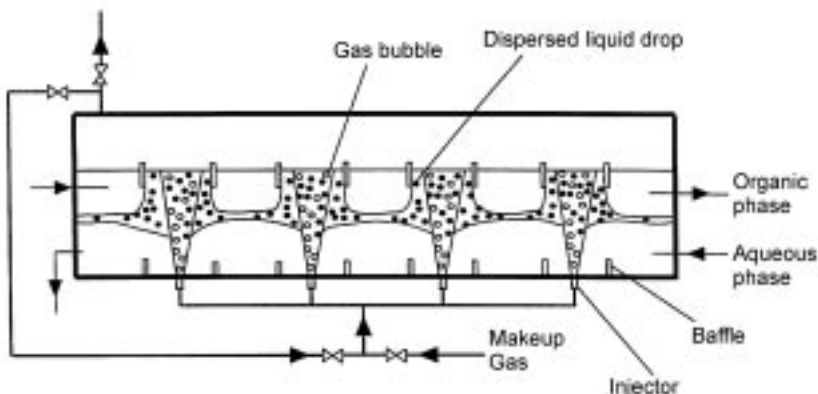
7.22 Computed particle-size density function in the bed and elutriation for the fluidized-bed chlorination of rutile particles with a wide size distribution.

7.8.3 Bottom-gas-injected solvent extraction process

Solvent extraction is used to separate, purify, and concentrate metal values in aqueous solutions (Blumberg, 1988; Lo *et al.*, 1983; Ricci, 1980). Two characteristics of the solvent extraction process make it an attractive method for purifying and concentrating solutes dissolved in a solvent: first, solutes can be selectively removed and second, they can be concentrated from a dilute solution. Most solvent extraction processes for metal extraction use mixer-settler contactors (Lo *et al.*, 1983). In the nuclear industry, the most often used contactors are the pulse columns and the mixer-settlers, but more recently the centrifugal extractors have become popular for certain applications.

Ideally, the contactor must be simple with few, if any, moving parts. The simplest of these is the spray column in which the heavy and the light phases flow counter-currently in a vertical vessel. Although these types of contactors have the advantages of simple structure with no moving parts, they suffer from relatively low throughput rates (due to their dependence on the small density difference between the two liquid phases) and, most importantly, from severe backmixing which greatly reduces the extraction efficiency and thus necessitates large heights.

The mixer-settler equipment, on the other hand, can be operated under conditions wherein near equilibrium between the two phases is assured. However, it has the disadvantages of considerable complexity of construction and operation due to the requirement of impellers for stirring, interstage pumping, and piping. Furthermore, cleaning and maintenance are quite difficult, especially when



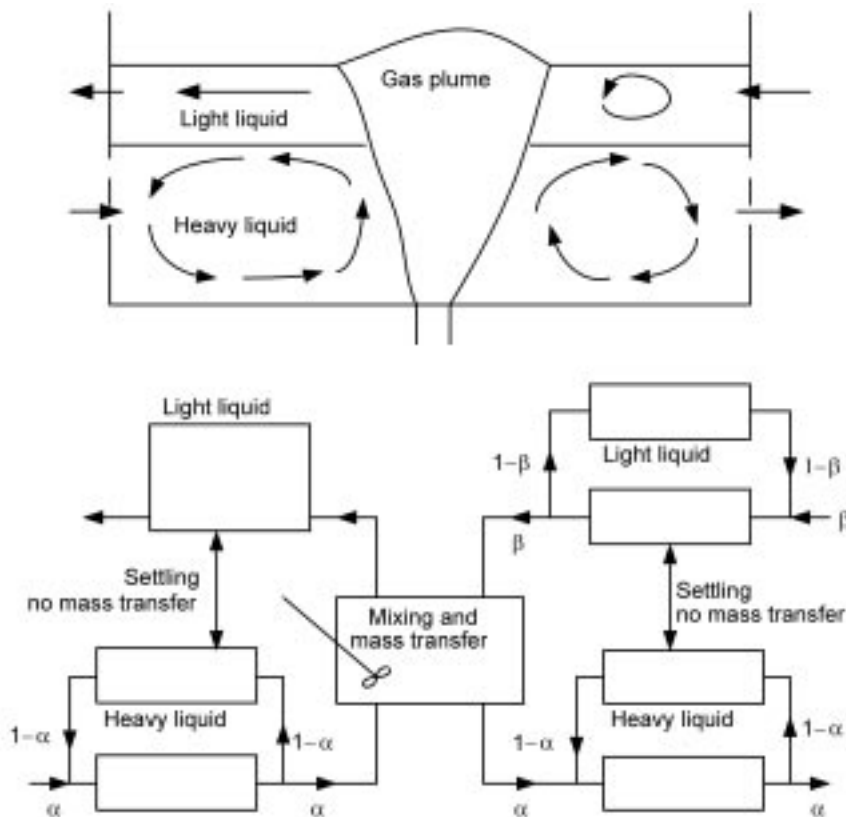
7.23 Schematic diagram of the novel SOHNEX solvent extraction process.

corrosive and/or particle-laden liquids are processed (Laddha and Degaleesan, 1978).

Other types of contactors that are in use all have internal structures that add varying degrees of complexity and limit the throughput rate per unit volume of the equipment.

A new solvent extraction process that overcomes the disadvantages of the existing processes described above is the SOHNEX process (Sohn and Doungdeethaveeratana, 1998). The process is carried out in a horizontal countercurrent contactor, in which the liquid-liquid emulsion is generated by a series of bottom-blown gas jets, as shown in Fig. 7.23. The gas jet creates a plume zone consisting of an emulsion of the two liquids that contains a large interfacial area for rapid mass transfer. The two liquids then disengage and flow in the opposite directions before entering another plume zone. Since the agitation of the two phases and the formation of the emulsion are caused by gas jets, this contactor has no mechanical moving parts and few internal accessories. Thus, the process combines the simplicity of a cylindrical vessel having no moving parts with the contacting efficiency of a mixer-settler as shown below. The equipment is inexpensive to build and operate, and is easy to clean. The agitation by a gas jet provides a milder and more uniform shear than by a mechanical agitator, and thus generates more uniform droplets (Zaidi and Sohn, 1995) (with fewer very small ones) that coalesce more easily in the phase disengagement zone between the plumes.

The overall fluid flow and mixing phenomena in such a channel reactor were investigated, and its residence-time distribution (RTD) was analyzed based on an ideal-reactor-network model (Iyer and Sohn, 1994). In this model, the plume region above an injector was modeled as a continuous stirred tank reactor (CSTR). Since the gas is injected with high energy and the bath is rather shallow, the fluids in the plume region are very well mixed as in a CSTR. Observation of the fluid flow around each plume indicated that a recirculating



7.24 Flow configuration and ideal-reactor-network model of the bottom-gas-injected solvent extraction process.

flow is set up on either side of the plume (Iyer and Sohn, 1994). Thus, these regions were modeled as recycle plug-flow reactors. A schematic diagram of the combination of ideal reactors used to model the region around each plume, including the plume itself, is shown in Fig. 7.24. The model has a single unknown parameter, α (Fig. 7.24), the throughput fraction through the combined recycle reactor section. This parameter was determined from the experimental RTD results and correlated against operating variables. All other model variables are determined as functions of α and the known operating conditions.

The model equations are based on the RTD response of the individual ideal reactors. The RTD response $E(t)$ of a plug-flow reactor (PFR) to a pulse input can be written as

$$E(t) = \delta(t - \tau_P) \quad (7.154)$$

where δ is the Dirac delta function and τ_P is the mean residence time of the PFR.

The CSTR response to a similar pulse input is

$$E(t) = \tau_C^{-1} \exp\left(-\frac{t}{\tau_C}\right) \quad (7.155)$$

where τ_C is the mean residence time of the CSTR, and the RTD response for the recycle reactor in the heavy phase is

$$E(t) = \alpha(1 - \alpha)^n \{ \delta[t - \tau_P - n(\tau_P + \tau_R)] \} \quad (7.156)$$

where τ_R is the mean residence time of the top recycle reactor, and

$$n = \text{integer} \left[\frac{t - \tau_P}{\tau_P + \tau_R} \right]$$

Considering a CSTR with a normalized input function $Y(t)$ such that

$$\int_{t=0}^{\infty} Y(t) dt = 1 \quad (7.157)$$

the RTD response to the input function introduced between time 0 and $d\theta$ is given by

$$\delta E = \tau_C^{-1} [Y(0) d\theta] \exp\left(-\frac{t}{\tau_C}\right) \quad (7.158)$$

The RTD response to the input function introduced between any time θ and $\theta + d\theta$ is represented by

$$\delta E = \tau_C^{-1} [Y(\theta) d\theta] \exp\left[-\frac{t - \theta}{\tau_C}\right] \quad (7.159)$$

Therefore, the RTD at any time t is given by

$$E(t) = \int_{\theta=0}^t \tau_C^{-1} Y(\theta) e^{(t-\theta)/\tau_C} d\theta \quad (7.160)$$

The model equations for the various combinations of ideal reactors can be obtained by combining the responses of the individual reactors. The RTD of the first recycle reactor unit and CSTR combination can be expressed as follows:

$$E_1(t) = \sum_{i=1}^n \left\{ \alpha(1 - \alpha)^{n-1} \left[\int_{\theta=0}^{t-\tau} e^{-\tau_{P1}} \tau_{C1}^{-1} Y(\theta) e^{(t-\tau-\theta)/\tau_{C1}} d\theta \right] \right\} \quad (7.161)$$

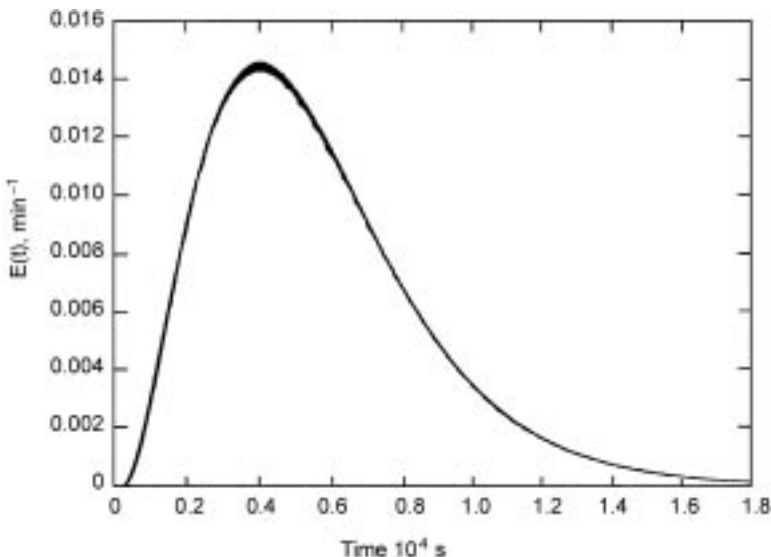
where $\tau = (2i + 1)\tau_{P1}$ and

$$n = \text{integer} \left[\frac{t - \tau_{P1}}{2\tau_{P1}} \right]$$

assuming $\tau_p = \tau_R$ (Iyer and Sohn, 1994), while that for the recycle section following the CSTR can be written as

$$E_2(t) = \sum_{i=1}^n \alpha(1 - \alpha)^{n-1} [E_1(t - \tau)] \quad (7.162)$$

where $\tau = \tau_{P1} + (2i + 1)\tau_{P2}$ and



7.25 Computed and experimental residence time distribution in the heavy phase of the bottom-gas-injected countercurrent liquid–liquid process. ($\alpha = 0.025$. Detailed test conditions are given in Iyer and Sohn (1994).)

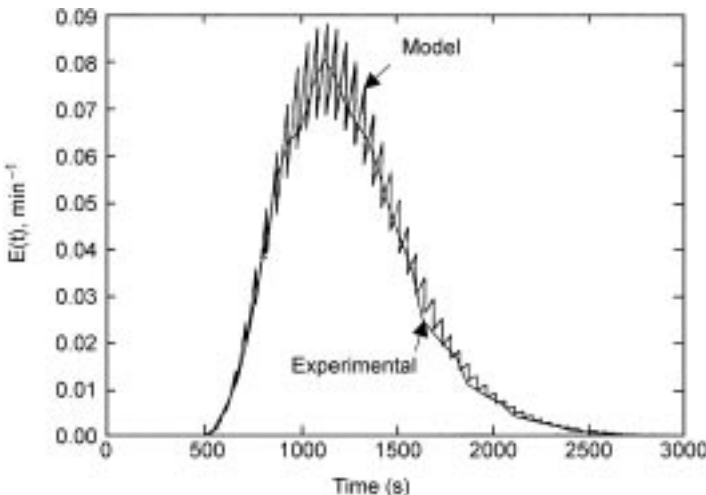
$$n = \text{integer} \left[\frac{t - \tau_{P1} - \tau_{P2}}{2\tau_{P1}} \right]$$

These equations can be extended similarly to further identical sections down the length of the reactor by using the response of the previous section as the input function to the next section.

The value of α was determined as the value that gives the best match between the experimental and calculated values for the peak time and the average residence time (the lowest combined difference). A comparison of experimental results with model predictions of heavy-liquid RTD behavior for three different cases is shown in Figs 7.25, 7.26 and 7.27. It can be seen that there is an overall excellent fit between the predicted and the experimental RTD curves. The fluctuation in the $E(t)$ value is due to the response characteristics of the idealized recycle reactor unit. The recycle reactor output consists of pulses at intervals of $(\tau_P + \tau_R)$ (assumed equal in this work (Iyer and Sohn, 1994)) entering the CSTR. When the CSTR's nominal residence time is small (large α), the magnitude of the fluctuation becomes large. Even for the largest value of α , the time for the peak and the average residence time are represented satisfactorily. Figure 7.28 presents the correlation for α against the experimental conditions represented by ϵ formulated by a dimensional analysis:

$$\epsilon = \left(\frac{\rho_1 Q_{L1}}{\rho_g Q_g} \right) \left(\frac{h_1}{L} \right) \left[1 + \frac{h_2}{h_1} \frac{\rho_2}{\rho_1} \right] \left(\frac{\pi d_{inj}^2}{4A_1} \right)^2 \quad (7.163)$$

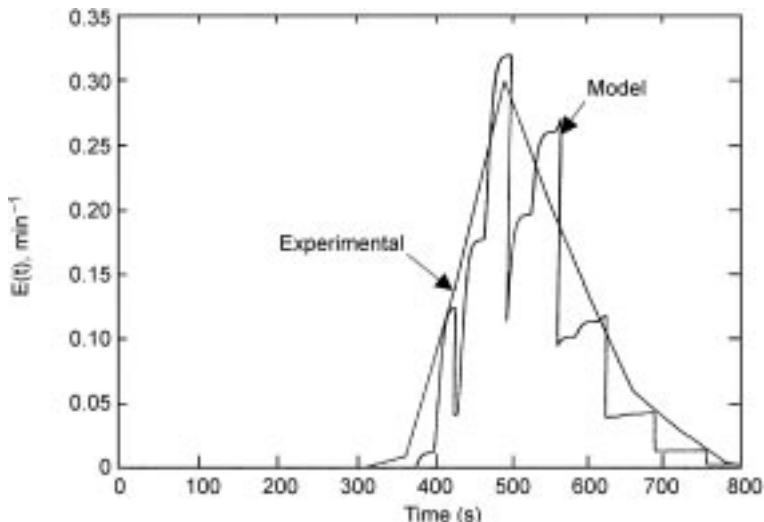
where ρ is the density, Q is the volumetric flow rate, h is the liquid depth, L is



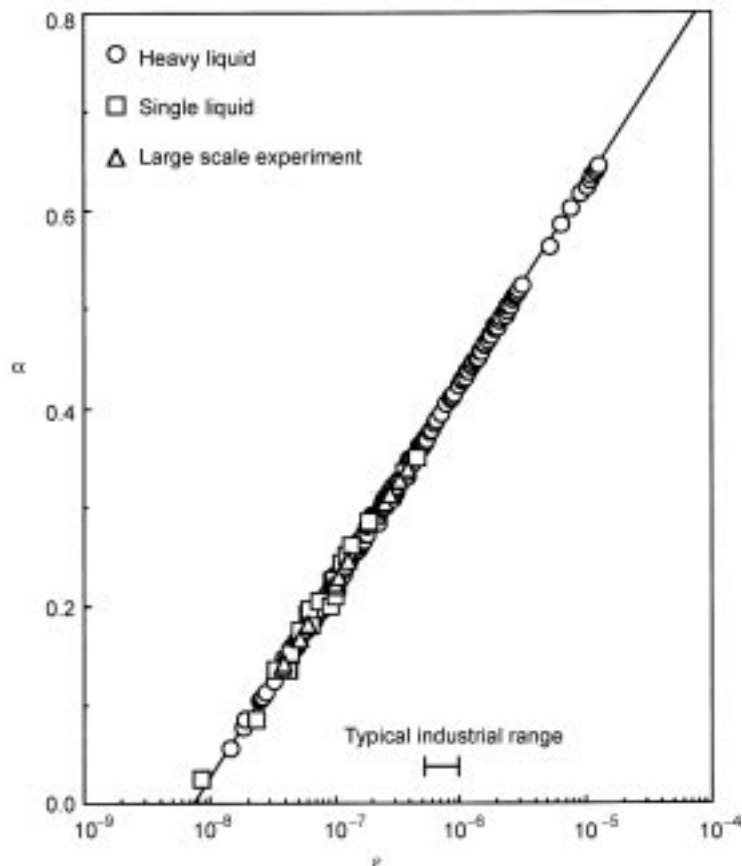
7.26 Computed and experimental residence time distribution in the heavy phase of the bottom-gas-injected countercurrent liquid–liquid process. ($\alpha = 0.225$. Detailed test conditions are given in Iyer and Sohn (1994).)

the distance between the adjacent gas injectors, A is the cross-sectional area perpendicular to the overall liquid flow, and the subscripts 1 and 2 represent, respectively, the heavy and the light liquid phases. The correlation is represented by

$$\alpha = 0.2 \log_{10} \epsilon + 1.623, \quad \text{for } 8 \times 10^{-9} < \epsilon < 2 \times 10^{-5} \quad (7.164)$$



7.27 Computed and experimental residence time distribution in the heavy phase of the bottom-gas-injected countercurrent liquid–liquid process. ($\alpha = 0.644$. Detailed test conditions are given in Iyer and Sohn (1994).)



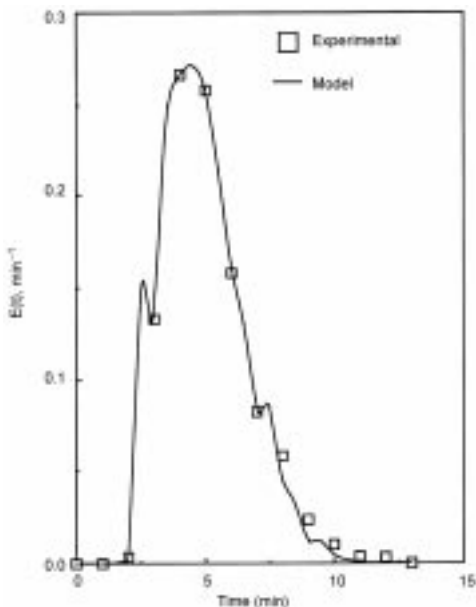
7.28 Variation of α with ϵ in the heavy phase of the bottom-gas-injected countercurrent liquid-liquid process.

For the light phase, the model equations are similar to those for the heavy-liquid calculations. The response of the first recycle reactor and CSTR combination is identical to equation 7.161. For the PFR unit downstream of the CSTR, the RTD response is given by

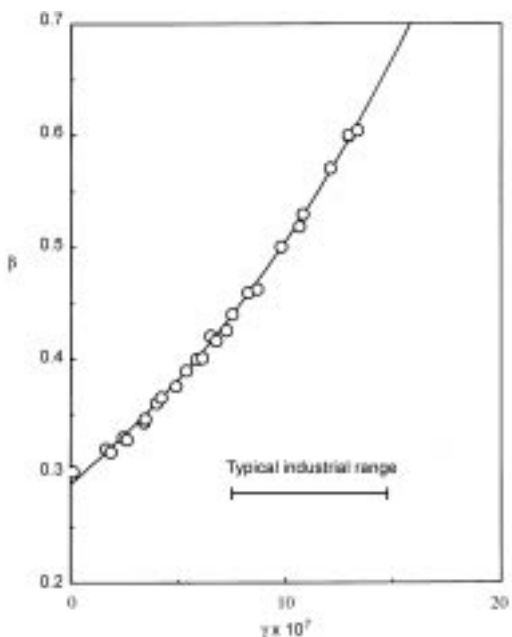
$$\begin{aligned} E_2(t) &= 0 && \text{for } 0 < t < \tau_{P1} \\ &= E_1(t - \tau_{P2}) && \text{for } t > \tau_{P2} \end{aligned} \quad (7.165)$$

These equations can also be extended, as in the heavy-liquid case, to additional identical sections throughout the length of the reactor by using the response of the previous section as the input function to the next section. A comparison of model predictions with experimental results for the light-phase is shown in Fig. 7.29.

The correlation for the parameter β for the recycling zone of the light phase is given in Fig. 7.30. The operating conditions are represented, based on a dimensional analysis, by a single dimensionless group γ defined by



7.29 Computed and experimental residence time distribution in the light phase of the bottom-gas-injected countercurrent liquid–liquid process. ($\beta = 0.601$. Detailed test conditions are given in Iyer and Sohn (1994).)



7.30 Variation of β with γ in the light phase of the bottom-gas-injected countercurrent liquid–liquid process.

$$\gamma = \frac{\rho_2 Q_{L2}}{\rho_g Q_g} \frac{h_1}{L} \left[1 + \frac{h_2}{h_1} \frac{\rho_2}{\rho_1} \right] \left(\frac{\pi d_{inj}^2}{4A_2} \right)^2 \quad (7.166)$$

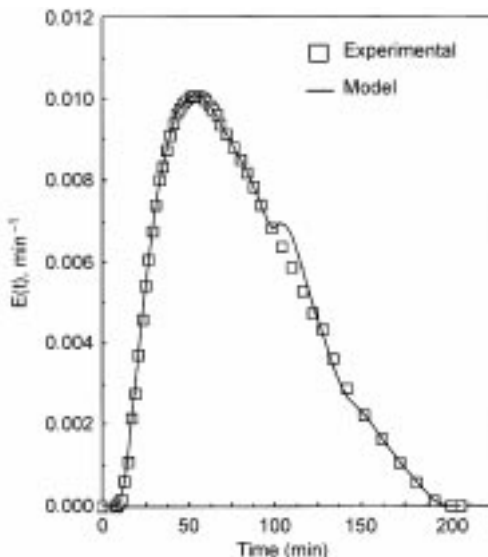
and the correlation equation is

$$\beta = 0.288 \times 10 * *(2.46 \times 10^5 \gamma), \quad \text{for } \gamma < 1.4 \times 10^{-6} \quad (7.167)$$

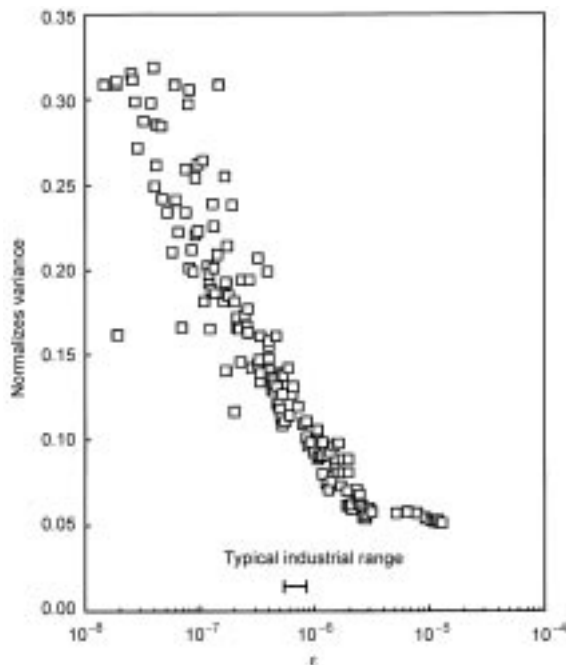
The correlation for α was applied to operations in a much larger vessel (1 m diameter and 7.2 m length) to test its suitability for scale-up. A comparison between the experimental result and the model prediction is shown in Fig. 7.31, which shows an excellent agreement.

The residence-time distribution represents the degree of backmixing of fluid elements as they flow through a vessel. The degree of backmixing can be represented by the normalized variance $\sigma_\theta^2 = \sigma^2/\bar{t}^2$ of the residence-time distribution (Levenspiel, 1999). Iyer and Sohn (1994) developed correlations for σ_θ^2 for the heavy and light phases of the bottom-gas-injected counter-flow system against the dimensionless groups ϵ and γ , respectively, as shown in Figs 7.32 and 7.33. The range of σ_θ^2 between 0.05 and 0.3 for the heavy phase corresponds to the degree of backmixing for 3 to 20 CSTRs in series. The σ_θ^2 values ranging from 0.1 to 0.15 for the light phase are equivalent to the degree of backmixing in 5 to 11 CSTRs in series. This is quite comparable to the mixer-settler systems commonly used in metallurgical solvent extraction, in which a mixer cell is equivalent to a CSTR.

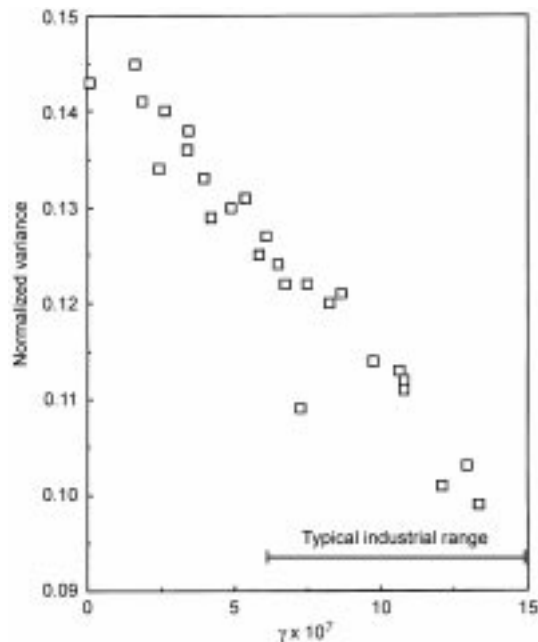
This work has shown how a judiciously constructed network of ideal reactors can be used to represent the residence time distribution of a system in which



7.31 Computed and experimental residence time distribution in the heavy phase of a large-scale model of the bottom-gas-injected countercurrent liquid–liquid process. ($\alpha = 0.181$. Detailed test conditions are given in Iyer and Sohn (1994).)



7.32 Variation of normalized variance σ_{θ}^2 with ϵ in the heavy phase of the bottom-gas-injected countercurrent liquid-liquid process.



7.33 Variation of normalized variance σ_{θ}^2 with γ in the light phase of the bottom-gas-injected countercurrent liquid-liquid process.

rather complex flows of liquids take place. The ideal-reactor-network model discussed here further enables one to analyze and predict the rate of mass exchange between the two liquid phases by mass transfer and chemical reaction when combined with the emulsion characteristics discussed earlier and the mass transfer characteristics in such liquid–liquid emulsions (Iyer and Sohn, 1993).

7.9 References

- Abbasi MH, Evans JW and Abramson IS (1983) ‘Diffusion of gases in porous solids: Monte Carlo simulations in the Knudsen and ordinary diffusion regimes’, *AICHE J*, 29, 617–24.
- Alzaydi A, Moor A and Rai A (1978) ‘Combined pressure and diffusional transition region flow of gases in porous media’, *AICHE J*, 24, 35–42.
- Ausman JM and Watson CC (1962) ‘Mass transfer in a catalyst pellet during regeneration’, *Chem Eng Sci*, 17, 323–29.
- Baird MHI and Davidson JF (1962) ‘Annular jets – I Fluid dynamics’, *Chem. Engng. Sci.*, 17, 467–72.
- Bard E and Faulkner L (2001) *Electrochemical Methods: Fundamentals and Applications*, NY, John Wiley and Sons.
- Bartlett RW and Haung HH (1973) ‘The lime-concentrate-pellet roast process for treating copper sulfide concentrates’, *J Metals*, 25(12), 28–34.
- Bird RB, Stewart WE and Lightfoot EN (2002) *Transport Phenomena*, 2nd edn, New York, Wiley.
- Bischoff KB (1963) ‘Accuracy of the pseudo steady state approximation for moving boundary diffusion problems’, *Chem Eng Sci*, 18, 711–13.
- Bischoff KB (1965) ‘Further comments on the pseudo steady state approximation for moving boundary diffusion problems’, *Chem Eng Sci*, 20, 783–84.
- Blumberg R (1988) *Liquid–Liquid Extraction*, New York, Academic Press.
- Boettinger WJ, Coriell SR *et al.* (2000) ‘Solidification microstructures: recent developments, future directions’, *Acta Mat*, 48, 43–70.
- Bradshaw AV and Richardson FD (1970) *Chemical engineering in the iron and steel Industry*, A symposium, London, Institution of Chemical Engineering.
- Cahn J (1968) ‘Spinodal decomposition’, *Trans. AIME*, 242(2), 168–80.
- Calvelo A and Smith JM (1972) ‘Intrapellet transport in gas–solid, non-catalytic reactions’, *Proc Chemeca '70, no 3*, London, Butterworth, 1–46.
- Carslaw HS and Jaeger JC (1959) *Conduction of heat in solids*, 2nd edn, Glasgow, Oxford University Press.
- Chaubal PC and Nagamori N (1988) ‘Thermodynamics for arsenic and antimony in copper matte converting – computer simulation,’ *Metall Trans B*, 19B, 547–56.
- Chaubal PC and Sohn HY (1986) ‘Intrinsic kinetics of the oxidation of chalcopyrite particles under isothermal and non-isothermal conditions’, *Metall Trans B*, 17B, 51–60.
- Chen OT and Rinker RG (1979) ‘Modification of the dusty-gas equation to predict mass transfer in general porous media,’ *Chem Eng Sci*, 34, 51–61.
- Cooper CF and Kitchener JA (1959) ‘Current concepts in the theory of foaming’, *JISI*, 193, 48–55.
- Crank J (1956) *Mathematics of diffusion*, Glasgow, Oxford University Press.
- Darken LS and Gurry RW (1953) *Physical chemistry of metals*, Intl. Student Edition, NY, McGraw-Hill Book Company, Inc.

- Eddings EG and Sohn HY (1993) 'Simplified treatment of the rates of gas-solid reactions involving multicomponent diffusion', *Ind Eng Chem Res*, 32, 42–48.
- El-Guindy MI and Davenport WG (1970) 'Kinetics and mechanism of ilmenite reduction with graphite', *Metall Trans*, 1, 1729–34.
- Evans JW (1972) 'Gas-solid reactions: the viscous flow term', *Can J Chem Eng*, 50, 811–14.
- Evans JW (1979) 'Mass transfer with chemical reaction', *Minerals Sci Eng*, 11, 207–23.
- Evans JW and Song S (1973) 'Gas-solid reactions: the viscous flow term (non-equimolar fluxes)', *Can J Chem Eng*, 51, 616–17.
- Evans JW and Song S (1974) 'Application of a porous pellet model to fixed, moving, and fluidized bed gas-solid reactors', *Ind Eng Chem Process Des Dev*, 13, 146–52.
- Farrell JW, Bilek PJ and Hilti DC (1970) 'Inclusions originating from reoxidation of liquid steels', *Electric Furnace Proceedings* 28, Pittsburgh, TMS-AIME, 64–86.
- Franc J and Kingery WD (1954) 'Thermal conductivity: IX, Experimental investigation of effect of porosity on thermal conductivity', *J Am Ceram Soc*, 37, 99–107.
- Fruehan RJ (1998) *The Making, Shaping and Treating of Steel*, Pittsburgh USA, The AISE Steel Foundation, 24.
- Fuwa A, Kimura E and Fukushima S (1978) 'Kinetics of iron chlorination of roasted ilmenite Ore, Fe₂TiO₅ in a fluidized bed', *Metall Trans B*, 9B, 643–52.
- Gandin CA, Rappaz M and Tintillier R (1993) '3-Dimensional probabilistic simulation of solidification grain structures application to superalloy precision castings', *Met. Trans. A*, 24A, 467–79.
- Gao HW, Sohn HY and Wadsworth ME (1983) 'A mathematical model for the solution mining of primary copper ore: Part I. Leaching by oxygen-saturated solution containing no gas bubbles', *Metall Trans B*, 14B, 541–51; 'Part II. Leaching by solution containing oxygen bubbles', 553–58.
- Gavalas GR and Kim S (1981) 'Periodic capillary models of diffusion in porous solids', *Chem Eng Sci*, 36, 1111–22.
- Habashi F and Yostos BI (1977) 'Copper from Chalcopyrite by direct reduction', *J Metals*, 29(7), 11–16.
- Hahn YB and Sohn HY (1990a) 'Mathematical modeling of sulfide flash smelting Process: Part I. Model development and verification with laboratory and pilot-plant measurements for Chalcopyrite concentrate smelting', *Metall Trans B*, 21B, 945–58.
- Hahn YB and Sohn HY (1990b) 'Mathematical modeling of sulfide flash smelting process: Part II. Quantitative analysis of radiative heat transfer', *Metall Trans B*, 21B, 959–66.
- Han G and Sohn HY (2004) 'Interphase mass transfer with bulk flow normal to the phase boundary', *Korean J Chem Eng*, 21, 34–40.
- Haung HH and Bartlett RW (1976) 'Oxidation kinetics of a lime-copper concentrate pellet', *Metall Trans B*, 7B, 369–74.
- Haver FP and Wong MM (1972) 'Making copper without pollution', *Mining Eng*, 24(6), 52–53.
- Hayes P (1993) *Process Principles in Minerals and Metals Production*, Brisbane, Hayes Publishing Co.
- Herbst JA (1979) 'General approach to describing rate processes in multiparticle systems,' in *Rate Processes of Extractive Metallurgy*, Sohn HY and Wadsworth ME (eds), New York, Plenum, 53–112.
- Ishida M and Wen CY (1968) 'Comparison of kinetic and diffusional models for solid–gas reactions', *AIChE J*, 14, 311–17.
- Iyer KM and Sohn HY (1993) 'Mass transfer analysis for pyrometallurgical channel reactors with high-strength bottom gas injection', in *Extractive Metallurgy of*

- Copper, Nickel and Cobalt, Vol 1 Fundamental Aspects, Reddy RG and Weizenbach RN (eds), Warrendale, Pennsylvania, TMS, 223–43.
- Iyer KM and Sohn HY (1994) ‘Physical and mathematical modeling of pyrometallurgical channel reactors with bottom gas injection: Residence time distribution analysis and ideal-reactor-network model’, *Metall Mater Trans B*, 25B, 207–19.
- Jakobsson A, Nasu M, Mangwiwo J, Mills KC and Seetharaman S (1998) ‘Interfacial tension effects on slag–metal reactions’, *Phil. Trans. Roy. Soc.*, 356, 996–1001.
- Jones GJ and Trivedi R (1971) ‘Lateral growth in solid-solid phase transformations’, *Journal of Applied Physics*, 42 (11), 4299–4304.
- Kawasaki E, Sanscrainte I and Walsh TI (1963) ‘Kinetics of reduction of iron oxide with carbon monoxide and hydrogen’, *AICHE J*, 8, 48–52.
- Kay H (1968) ‘Hydrogen reduction of molybdenite using sulfur acceptors. Part I: calcium oxide’, in *High Temperature Refractory Metals*, Krivsky WA (ed.), New York, Gordon and Breach, 33–44.
- Kim HG and Sohn HY (1996) ‘Thermodynamic modeling of minor-element behavior in in-bath copper smelting and converting with calcium ferrite slag’, *Trans Inst Mining Metall Sec C*, 105, C151–63.
- Kim HG and Sohn HY (1997) ‘Minor-element behavior and iron partition during the cleaning of copper converter slag under reducing conditions’, *Can Metall. Quart*, 36, 31–37.
- Kim HG and Sohn HY (1998a) ‘Effects of CaO, Al₂O₃ and MgO additions on the copper solubility, Ferric/Ferrous ratio and minor-element behavior of iron-silicate slags’, *Metall Mater Trans B*, 29B, 583–90.
- Kim HG and Sohn HY (1998b) ‘Minor-element behavior in copper smelting and converting with the use of tonnage oxygen’, *Trans Inst Mining Metall Sec C*, 107, C43–C59.
- Kozakevitch P (1969) ‘Foams and emulsions in steelmaking’, *J. Metals*, 21(7), 57–68.
- Kozakevitch P, Urbain G and Sage M (1955) ‘Stresses on the interface iron slag and the mechanism of desulphurization’, *Rev. Metallurg.*, 52, 161–71.
- Kunii D and Levenspiel O (1968) ‘Bubbling bed model for kinetic process in fluidized beds. Gas–solid mass and heat transfer and catalytic reactions’, *Ind Eng Chem, Process Des Develop*, 7, 481–92.
- Kunii D and Levenspiel O (1991) *Fluidization Engineering*, New York, Wiley.
- Kunii D and Smith JM (1960) ‘Heat transfer characteristics of porous rocks’, *AICHE J*, 6, 71–78.
- Laddha GS and Degaleesan TE (1978) *Transport Phenomena in Liquid Extraction*, New York, McGraw-Hill, 209–431.
- Laird C and Aaronson HI (1969) ‘The growth of g-plates in an Al-15% Ag alloy’, *Acta Metallurgica*, 17(4), 505–19.
- Lee PD, Chirazi A and See D (2001) ‘Modeling microporosity in Aluminum-Silicon alloys: a review’, *J. Light Metals*, 1, 15–30.
- Levenspiel O (1999) *Chemical Reaction Engineering*, 3rd edn, New York, Wiley.
- Levenspiel O, Kunii D and Fitzgerald T (1968) ‘The processing of solids of changing size in bubbling fluidized beds’, *Powder Technol*, 2, 87–96.
- Lin HK and Sohn HY (1987) ‘Mixed-control kinetics of oxygen leaching of chalcopyrite and pyrite from porous primary ore fragments’, *Metall Trans B*, 18B, 497–504.
- Lindenberg HU and Vorwerk H (1981) *Proceedings of the 2nd International Conference on Clean Steel held at Balatonfüred*, London, The Metals Society, 241–50.
- Lo TC, Baird MHI and Hanson C (eds) (1983) *Handbook of Solvent Extraction*, New York, Wiley.

- Lu W-K and Bitsianes G (1968) 'Chemical kinetics of gaseous reduction of hematite', *Can Metall Quart*, 7, 3–13.
- Luss D (1968) 'On the pseudo steady state approximation for gas solid reactions', *Can J Chem Eng*, 46, 154–56.
- Malling GF and Thodos G (1967) 'Analogy between mass and heat transfer in beds of spheres: contributions due to end effects', *Int J Heat Mass Transfer*, 10, 489–92.
- Maru Y, Kuramasu Y, Awakura Y and Kondo Y (1973) 'Kinetic studies of the reaction between Cr₂3C₆ particles and Cr₂O₃ particles', *Metall Trans*, 4, 2591–98.
- Mason EA and Marrero TR (1970) 'The diffusion of atoms and molecules', *Advan Atom Mol Phys*, 6, 155–232.
- Mason EA, Malinauskas AP and Evans RB (1967) 'Flow and diffusion of gases in porous media', *J Chem Phys*, 46, 3199–216.
- McCune CC, Fogler HS and Kline WE (1979) 'An experimental technique for obtaining permeability-porosity relationships in acidized porous media', *Ind Eng Chem Fundam*, 18, 188–91.
- McKewan WM (1960) 'Kinetics of iron oxide reduction', *Trans Metall Soc AIME*, 218, 2–12.
- Modest MF (1993) *Radiative Heat Transfer*, New York, McGraw-Hill.
- Mukai K (1998) 'Marangoni flows and corrosion of refractory walls', *Phil. Trans. Roy. Soc., (London)*, 336A(1739), 1015–26.
- Nagamori M and Chaubal PC (1982) 'Thermodynamics of copper matte converting: Part III. steady-state volatilization of Au, Ag, Pb, Zn, Ni, Se, Te, Sb and As from slag, matte and metallic copper', *Metall Trans B*, 13B, 319–29.
- Nagamori M and Mackey PJ (1978) 'Thermodynamics of copper matte converting: Part I. Fundamentals of the Noranda process', *Metall Trans B*, 9B, 255–65.
- Nagamori M and Sohn HY (2000) 'Dissolution of lead and bismuth in white metal (CuS0.5) at matte smelting temperatures', *Metall Mater Trans B*, 31B, 543–46.
- Ode M, Lee JS, Kim SG, Kim WT and Suzuki T (2000) 'Numerical simulation of the critical velocity for particle pushing/engulfment transition in Fe-C alloys using a phase-field model', *ISIJ Int.*, 40, 153–60.
- Ohmi M, Usui T and Nakajima K (1982) 'Theory on effective diffusivities of Bi-disperse porous solids at constant pressure and influence of an inert gas', *Trans ISIJ*, 22, 30–38.
- Otsuka K and Kunii D (1969) 'Reduction of powdery ferric oxide mixed with graphite particles', *J Chem Eng Japan*, 2, 46–50.
- Padilla R and Sohn HY (1979) 'Reduction of stannic oxide with carbon', *Metall Trans B*, 10B, 109–15.
- Paul BC, Sohn HY and McCarter MC (1992) 'Model for ferric sulfate leaching of copper ores containing a variety of sulfide minerals: Part I. modeling uniform size ore fragments', *Metall Trans B*, 23B, 537–48.
- Perez-Tello M, Sohn HY, St. Marie K and Jokilaakso A (2001a) 'Experimental investigation and 3-D computational fluid dynamics modeling of the flash converting furnace shaft: Part I. Experimental observation of copper converting reactions in terms of converting rate, converting quality, changes in particle size, morphology, and mineralogy', *Metall Mater Trans B*, 32B, 847–68.
- Perez-Tello M, Sohn HY and Smith PJ (2001b) 'Experimental investigation and 3-D computational fluid dynamics modeling of the flash converting furnace shaft: Part II. Formulation of 3-D computational fluid dynamics model incorporating the particle cloud description', *Metall Mater Trans B*, 32B, 869–86.
- Pismen LM (1974) 'Diffusion in porous media of a random structure', *Chem Eng Sci*, 29, 1227–36.

- Poirier DR and Geiger GH (1994) *Transport phenomena in materials processing*, Warrendale (PA), TMS, 381–86.
- Porter DA and Easterling KE (1992) *Phase transformations in metals and alloys*, 2nd edn, London (UK), Chapman & Hall.
- Rajamani K and Sohn HY (1983) ‘Kinetics and sulfur fixation in the reduction or oxidation of metal sulfides mixed with lime’, *Metall Trans B*, 14B, 175–80.
- Ranz WE and Marshall WR Jr (1952) ‘Evaporation from drops Part I’, *Chem Eng Prog*, 48, 141–46.
- Rao YK (1971) ‘The kinetics of reduction of hematite by carbon’, *Metall Trans*, 2, 1439–47.
- Rastogi R and Cramb AW (2001) ‘Inclusion formation and agglomeration in aluminum killed steels’, *Proceedings of the 60th Steelmaking Conference Proceedings*, held at Baltimore (MD) 25–28 March 2001, Warrendale (PA), ISS, 1047–87.
- Reed-Hill R and Abbaschian R (1992) *Physical metallurgy principles*, 3rd edn, Boston (USA), PWS-KENT Publishing Company.
- Reid RC, Prausnitz JM and Sherwood TK (1973) *The Properties of Gases and Liquids*, 2nd edn, New York, McGraw-Hill.
- Rhee K-I and Sohn HY (1990) ‘The selective chlorination of iron from ilmenite ore by CO–Cl₂ mixtures: Part II. mathematical modeling of fluidized-bed process’, *Metall Trans B*, 21B, 331–40.
- Ricci L (ed.) (1980) *Separation Techniques: I. Liquid–Liquid Systems*, New York, McGraw-Hill.
- Richardson FD (1974) *Physical Chemistry of Melts in Metallurgy*, Volume 2, London, Academic Press.
- Rowe PN, Claxton KT and Lewis JB (1965) ‘Heat and mass transfer from single sphere in an extensive flowing fluid’, *Trans Inst Chem Eng*, 43, T14–31.
- Sasai K (2001) *Oxygen in Steelmaking: Towards Cleaner Steels*, Chapter 3.1, London, The Institute of Materials.
- Sasai K and Mizukami Y (1996) ‘Effect of stirring on oxidation rate of molten steel’, *ISIJ International*, 36(4), 388–94.
- Sasai K and Mizukami Y (1998) ‘Effects of tundish cover powder and teeming stream on oxidation rate of molten steel in tundish’, *ISIJ International*, 38(4), 332–38.
- Sasai K and Mizukami Y (2000) ‘Reoxidation behavior of molten steel in tundish’, *ISIJ International*, 40(1), 40–47.
- Sasai K and Mizukami Y (2001) ‘Mechanism of alumina adhesion to continuous caster nozzle with reoxidation of molten steel’, *ISIJ International*, 41(11), 1331–1339.
- Satterfield CN (1970) *Mass Transfer in Heterogeneous Catalysis*, Cambridge, Massachusetts, MIT Press.
- Seo KW and Sohn HY (1991) ‘Mathematical modeling of sulfide flash smelting process: Part III. Volatilization of minor elements’, *Metall Trans B*, 22B, 791–99.
- Seth BBL and Ross HU (1966) ‘Application of a generalized rate equation to the gaseous reduction of iron oxide’, *Can Metall Quart*, 5, 315–28.
- Shah ID and Ruzzi PL (1978) ‘Pentlandite: Preparation, hydrogen reduction in the presence of lime to yield an iron-nickel alloy’, *Metall Trans B*, 9B, 247–53.
- Smigelskas AD and Kirkendall EO (1947) ‘Zinc diffusion in a-brass’, *Trans. Met. Soc. AIME*, 171, 130–42.
- Smith JM (1970) *Chemical Engineering Kinetics*, 2nd edn, New York, McGraw-Hill.
- Soepriyanto S, Olson FA and Sohn HY (1989) ‘The selective oxidation of mixed metal sulfides with lime in the presence of steam without emitting sulfur-containing pollutants’, *Metall Trans B*, 20B, 237–42.
- Sohn HY (1978) ‘The law of additive reaction times in fluid-solid reactions’, *Metall*

- Sohn HY, 1980) 'The effect of oxygen pressure on the leaching of copper from chalcopyrite ore containing pyrite under simulated solution-mining conditions', *Minerals Metall Processing*, 7, 163–68.
- Sohn HY and Rajamani K (1977) 'Successive gas–solid reactions in a porous pellet: Application to the reaction of metal sulfides in the presence of lime', *Chem Eng Sci*, 32, 1093–101.
- Sohn HY and Seo KW (1990) 'Flash combustion of sulfide mineral particles in a turbulent gas jet', in *Multiphase Transport and Particulate Phenomena*, Vol. 3, Veziroglu T N (ed.), *Proceedings of the 5th Miami International Symposium on Multi-Phase Transport and Particulate Phenomena*, December 12–14, 1988, Miami Beach, Florida, New York, Hemisphere Publishing Corp, 501–42.
- Sohn HY and Sohn H-J (1980) 'The effect of bulk flow due to volume change in the gas phase on gas–solid reactions: Initially nonporous solids', *Ind Eng Chem Process Des Dev*, 19, 237–42.
- Sohn HY and Szekely J (1972a) 'The effect of reaction order in non-catalytic gas–solid reactions', *Can J Chem Eng*, 50, 674–76.

- Sohn HY and Szekely J (1972b) 'A structural model for gas–solid reactions with a moving boundary – III. A generalized dimensionless representation of the irreversible reaction between a porous solid and a reactant gas', *Chem Eng Sci*, 27, 763–78.
- Sohn HY and Szekely J (1973) 'Reactions between solids through gaseous intermediates – I. Reactions controlled by chemical kinetics', *Chem Eng Sci*, 28, 1789–801.
- Sohn HY and Szekely J (1974) 'The effect of intragrain diffusion on the reaction between a porous solid and a gas', *Chem Eng Sci*, 29, 630–34.
- Sohn HY and Wall DR (1989) 'Application of the law of additive reaction times to the regeneration of coked catalyst pellets', *Chem Eng Sci*, 44, 442–44.
- Sohn HY and Won S (1985) 'Successive gas–solid reaction model for the hydrogen reduction of cuprous sulfide in the presence of lime', *Metall Trans B*, 16B, 645–61.
- Sohn HY and Xia YN (1986) 'Effect of nonuniform distribution of solid reactant on fluid–solid reactions. 1. Initially nonporous solids', *Ind Eng Chem Process Des Dev*, 25, 386–94.
- Sohn HY and Xia YN (1987) 'Effect of nonuniform distribution of solid reactant on fluid–solid reactions. 2. Porous solids', *Ind Eng Chem Research*, 26, 246–54.
- Sohn HY, Johnson SH and Hindmarsh AC (1985) 'Application of the method of lines to the analysis of single fluid–solid reactions in porous solids', *Chem Eng Sci*, 40, 2185–90.
- Sohn HY, Seo KW, Chaubal PC and Hahn YB (1988) 'Laboratory studies on the flash smelting of copper concentrate', in *Flash Reaction Processes, Proceedings of the 1988 Center for Pyrometallurgy Conference, Salt Lake City, Utah, June 15–17, 1988*, Robertson DGC, Sohn HY and Themelis NJ (eds), published by the Center for Pyrometallurgy, University of Missouri–Rolla, Rolla, Missouri, 145–66.
- Sohn HY, Zhou L and Cho K (1998) 'Intrinsic kinetics and mechanism of rutile chlorination by CO + Cl₂ mixtures', *Ind Eng Chem Research*, 37, 3800–05.
- St. Clair HW (1965) 'Rate of reduction of an oxide sphere in a stream of reducing gas', *Trans Metall Soc AIME*, 233, 1145–52.
- Stefanescu DM, Juretzko FR, Catalina A, Dhindaw BK, Sen S and Curreri PA (1998) 'Particle engulfment and pushing by solidifying interfaces. II. Microgravity experiments and theoretical analysis', *Metall Mater Trans. A*, 29A, 1697–1706.
- Steinherger RL and Treybal RE (1960) 'Mass Transfer from a solid soluble sphere to a flowing liquid stream', *AIChE J*, 6, 227–32.
- Szekely J and El-Tawil Y (1976) 'The reduction of hematite pellets with carbon monoxide–hydrogen mixtures', *Metall Trans B*, 7B, 490–92.
- Szekely J and Evans JW (1970) 'A structural model for gas–solid reactions with a moving boundary', *Chem Eng Sci*, 25, 1091–107.
- Szekely J and Sohn HY (1973) 'The effect of structure on the reaction between a porous solid and a gas', *Trans Inst Mining Met*, 82, C92–100.
- Szekely J, Lin CI and Sohn HY (1973) 'A structural model for gas–solid reactions with a moving boundary – V. An experimental study of the reduction of porous nickel–oxide pellets with hydrogen', *Chem Eng Sci*, 28, 1975–89.
- Szekely J, Evans JW and Sohn HY (1976) *Gas–Solid Reactions*, New York, Academic Press.
- Szekely J, Choudary M and El-Tawil Y (1977) 'On the reaction of solids with mixed gases', *Met. Trans. B*, 8B, 639–43.
- Themelis NJ and Gauvin WH (1963) 'A generalized rate equation for the reduction of iron oxides', *Trans Metal. Soc AIME*, 227, 290–300.
- Tien RH and Turkdogan ET (1972) 'Gaseous reduction of iron oxides: Part IV.

- mathematical analysis of partial internal reduction-diffusion control', *Metall Trans*, 3, 2039–48.
- Tsotridis G and Hondros ED (1998) 'Modeling of the erosion of refractories by Marangoni flow', *Phil. Trans. Roy. Soc., (London)*, 336A (1739), 1013–14.
- Turkdogan ET (1996) *Fundamental of Steelmaking*, London, The Institute of Materials.
- Uhlig HH and Revie RW (1985) *Corrosion and Corrosion Control*, 3rd edn, Chapter 2, NY (USA), John Wiley & Sons.
- Wagner C (1961) 'The theory of precipitate change by redissolution', *Z. Elektrochem*, 65, 581.
- Wakao N and Smith JM (1962) 'Diffusion in catalyst pellets', *Chem Eng Sci*, 17, 825–34.
- Wilson EJ and Geankoplis CJ (1966) 'Liquid mass transfer at very low Reynolds numbers in packed beds', *Ind Eng Chem Fundam*, 5, 9–14.
- Won S and Sohn HY (1985) 'Hydrogen reduction of Cu₂S in the presence of lime', *Trans Inst Mining Metall*, 94, C140–45.
- Yasuda Y and Sohn HY (1995) 'Experimental and theoretical study of particle dispersion phenomena in a turbulent gas jet of the flash-smelting process by the image analysis technique', *Metall Mater Trans B*, 26B, 637–46.
- Youn I-J and Park KY (1989) 'Modeling of fluidized bed chlorination of rutile', *Metall Trans B*, 20B, 959–66.
- Young DA (1966) *Vol 1 Decomposition of Solids, of The International Encyclopedia of Physical Chemistry and Chemical Physics, Topic 21 Solid and Surface Kinetics*, Tompkins FC (ed.), London, Pergamon Press.
- Youngqvist GR (1970) 'Diffusion and flow of gases in porous solids', *Ind Eng Chem*, 62 (8), 52–63.
- Zaidi A and Sohn HY (1995) 'Measurement and correlation of drop-size distribution in liquid–liquid emulsions formed by high-velocity bottom-gas injection', *ISIJ International*, 35, 234–41.
- Zener C (1949) 'Theory of growth of spherical precipitates from solid solution', *J. Appl. Phys.*, 20, 950–53.
- Zhou L and Sohn HY (1996) 'Mathematical modeling of fluidized bed chlorination of rutile', *AICHE J*, 42, 3102–12.

7.10 Appendix: notation

- a constant in equation 7.94c or radius of ellipsoidal martensite nuclei, lattice parameter or chemical activity
- A gaseous reactant or in the case of equation 7.41 a probability of attachment
- A_g, A_p external surface area of an individual grain and the pellet, respectively
- b number of moles of solid B reacted per mole of gaseous reactant A
- \bar{b} burgers vector
- B solid reactant
- c, d stoichiometry coefficients or thickness of ellipsoidal martensite nuclei
- C gaseous product or total molar concentration
- C_i molar concentration of gaseous species i
- d_p thickness of a slab or diameter of a cylinder or a sphere
- D solid product or diffusivity

D_{ei}	effective diffusion coefficient of gaseous species in the porous solid
D_g	effective diffusion coefficient of gaseous species in the product layer around a grain
D_K	Knudsen diffusion coefficient
E	Young's modulus or electrochemical potential
F_g, F_p	shape factors for the grain and pellet, respectively (= 1, 2, or 3 for flat plates, long cylinders, or spheres, respectively)
F	Faraday's constant = 96587°C/equivalents
F_{ij}	View factor for radiaton heat transfer between surfaces i and j
f	fraction
$g(X)$	conversion function defined by equations 7.75, 7.95 or 7.101
g	gravity
G	Gibbs free energy or activation energy
h	convective heat transfer coefficient
$(-\Delta H)$	heat of reaction
i	current
i_0	exchange current
J	flux (unit of species per area and time)
k	reaction-rate constant, thermal conductivity or Boltzmann's constant
k_m	external-mass-transfer coefficient
K	equilibrium constant or gradient energy
L	diffusion length
m	apparent rate constant, equation 7.97 or partition coefficient
M	mobility
$(-\dot{m}_A)$	molar rate of consumption of the gaseous reactant A per unit area of solid
n_d	number of grains of solid reactant per unit volume of porous solid, $3(1 - \epsilon)/4\pi r_g^2$
n_i	number of moles of species i per unit volume of the solid mixture including the pore space, in the case of equation 7.41 the number of atoms in a favorable position, or number of charge equivalents in Faraday's law
\underline{N}_i	molar flux vector for species i
N_a	Avogadro's number
N_i	mole fraction of species I
Nu	Nusselt number, hd_p/k
p_i	partial pressure of species i
$p(X)$	conversion function defined by equations 7.76 or 7.79
P	total pressure
Pr	Prandtl number, $C_p\mu/k$
\underline{q}	heat flux vector
r_c	position of reaction interface in a non-porous particle
r_g	original radius of the grain
s	strain

R_i	rate of production of species i per unit volume of the pellet
R	ideal gas constant
Re	Reynolds number, $d\mu\rho/\mu$
r	radius
S_v, S_v^o	surface area per unit volume of the solid (not pellet) at any time and its initial value, respectively
s	indicates strain energy or solid
Sc	Schmidt number, $\mu/(\rho D_{AB})$
Sh	Sherwood number, $k_m d_p/D_{AB}$
Sh^*	modified Sherwood number defined by equation 7.74
t	time
t^*, t_g^*, t_N^*	dimensionless times defined by equations 7.72, 7.92 and 7.99, respectively
T	temperature
\underline{u}	bulk velocity vector
u_i	velocity of species i
v_1, v_2	net forward rates of reactions 7.109a and 7.109b, respectively, per unit volume of the solid mixture including the pore space
v	velocity
V_g, V_p	volume of a grain or the pellet, respectively
w	local fraction conversion of solid reactant
x	distance
x_i	mole fraction of fluid species i
X	overall fractional conversion of solid reactant
Z	volume of product solid formed from unit volume of reactant solid or charge of an ion

Greek symbols

α_B, α_D	fractions of pellet volume initially occupied by solid reactants B and D , respectively
α_i	transference number for the electrochemical half-cell reaction i
α, β	denotation of phases
δ	boundary layer thickness or thickness of deposited thin film
ϵ	porosity or emissivity
θ	volume change parameter defined by equation 7.81
v	number of gaseous products formed from one mole of gaseous reactant, atomic vibration frequency or Poisson's ratio
η	indicates a parameter in equation 7.65 or overpotential
ρ_B, ρ_D	true molar densities of solids B and D , respectively
$\hat{\sigma}_g, \hat{\sigma}_N, \sigma_s$	gas-solid reaction moduli defined by equations 7.93, 7.103, 7.100 and 7.73, respectively
γ	interfacial tension or a phase
ω	factor in equation 7.51 that depends on the area of the critically sized cluster and atom vibration frequency

- λ spacing between ledges or wavelength of the sinusoidal concentration fluctuation
- τ indicates time of nucleation
- μ shear modulus or chemical potential

Subscripts

- A, C gaseous species A and C , respectively
- b bulk stream value
- B, D solid species B and D , respectively
- e effective or environment
- eff effective
- g grain
- i species i , based on initial conditions or interface
- $1, 2, 3 \dots$ species in a system
- o starting value
- \rightarrow indicates a process going from one state to another
- m indicates molar quantity or melt
- s solid
- b bulk
- i interface

Superscripts

- * when associated with D indicates radioactive tracer diffusion constant, when associated with G indicates an activation energy and when associated with r or C indicates a critical radius or concentration respectively
- 0 reference state
- p pellet
- s surface or solid
- T total

Thermoanalytical methods in metals processing

O N M O H A N T Y , The Tata Iron and Steel Company, India

8.1 Introduction

8.1.1 Specific heat

The quantity of heat required to raise the temperature of a unit mass by one degree is called the specific heat C and the molar heat capacity represents the heat capacity of one mole of a substance. The numerical values are given in units of calories/mol/ $^{\circ}\text{C}$ or in calories/gm/ $^{\circ}\text{C}$. The specific heat can be measured under constant pressure (C_p) or constant volume (C_v). In metallic materials it is C_p which is of greater relevance as it can be directly measured experimentally and C_v can be estimated from C_p using the relation

$$C_p - C_v = \frac{\alpha^2 V T}{\beta} \quad (8.1)$$

where

$$\alpha \rightarrow \text{Coefficient of volume expansion} = \frac{1}{V} \left(\frac{dV}{dT} \right)_P$$

$$\beta \rightarrow \text{Compressibility coefficient} = -\frac{1}{V} \left(\frac{dV}{dP} \right)_T$$

$V \rightarrow$ Molar volume

The molar heat capacity of a binary alloy is estimated from the heat capacities of the constituent elements, as per the Neumann–Kopp rule.

Thus,

$$C_p = X_1 C_{p1} + X_2 C_{p2} \dots \quad (8.2)$$

where X_1, X_2 are the atom fraction of the constituents.

When the variation of enthalpy ($Q = E + PV$) with temperature (T) is known, C_p ($= dQ/dT$) is determined at a given temperature by graphically or numerically determining the slope of the $Q - T$ plot. By the same argument given the specific heat variation with temperature, the enthalpy could be determined by integration (either graphical or numerical).

8.1.2 Specific heat of crystals and phase transition

As a material is heated, a variety of disorders can occur; each involves absorption of thermal energy and therefore, a contribution to the specific heat of the material. When the temperature of a body is raised, the amplitude of vibration of the atoms would increase, the frequency remaining constant. The amount of vibrational energy absorbed when the temperature is raised by one degree is known as vibrational heat capacity and when expressed for unit mass of the material, it is known as vibrational specific heat. The variation of vibrational specific heat with temperature has been investigated first by Einstein and then modified by Debye in order to comply with the observed data at different temperatures.¹ The Debye expression thus becomes:

$$C_v = 3R \left[\frac{12T^3}{\theta^3} \int_0^{\theta/T} \frac{x^3 dx}{e^x - 1} - \frac{3\theta/T}{e^{\theta/T} - 1} \right] \quad (8.3)$$

where

$$\theta = \text{Debye characteristic temperature} = \frac{h\nu_m}{\kappa}, \quad x = \frac{h\nu}{kT}$$

$\kappa \rightarrow$ Boltzmann's const.; $\nu_m \rightarrow$ maximum frequency of vibration

The above expression is similar to Einstein's expression but yields better results at lower temperatures compared to the Einstein expression; the latter assuming a constant frequency (ν_m) of vibration for all atoms. The Debye characteristic temperatures are given in Table 8.1.

Beyond the Debye–Einstein characteristic temperature (i.e. $T/\theta = 1.0$) the C_v per gm atom for all metals tend to assume a limiting value of ~ 6 cal/gm atom and at 0°K it goes to zero. The value of $\theta = h\nu/\kappa$ (the form being same in both the Einstein and Debye approaches) depends on ν and plays a crucial role in relating to the elastic properties of the materials. The frequency of vibration (ν) is given by

$$\nu = \left(\frac{1}{2\pi} \right) \sqrt{\frac{ya}{m}} \quad (8.4)$$

where, $y \rightarrow$ elastic const. of the material, $a \rightarrow$ atomic spacing, $m \rightarrow$ atomic mass.

Since $y \approx 10^{11}$ dynes/cm², $a \approx 10^{-8}$ cm, $m \approx 10^{-23}$ gm, ν comes out to be of the order of 10^{12} – 10^{13} per second; substituting this in the relation $\theta = h\nu/\kappa$ gives

Table 8.1 Debye characteristic temperatures (θ) of selected metals

Material (diamond) →	Na	Al	Cu	Ag	Fe	Pb	Be	C
Debye temp. (θ) →	150	385	315	215	420	88	1000	2000

the characteristic temperatures in the order of 50–500°K; which is in agreement with the observed value. Further, it may be seen that v increases with increasing strength of binding (increasing ‘y’) and with decreasing mass. Consequently, strongly bound crystals of light atoms, e.g. diamond, have high characteristic temperatures, and weakly bound crystal of heavy atoms, e.g. lead, have low characteristic temperatures. It has already been shown that the quantity experimentally measured is C_p and the C_v is derived from this using equation 8.1.

The free energy change at any given temperature is given by the general expression

$$F = E_o - \int_0^T \left(\int_0^T \frac{C_p}{T} dT \right) dT \quad (8.5)$$

where $E_o \rightarrow$ internal energy, $C_p \rightarrow$ specific heat. The second term in equation 8.5 essentially represents entropy(s), that is $(\partial F / \partial T)$, at constant pressure.

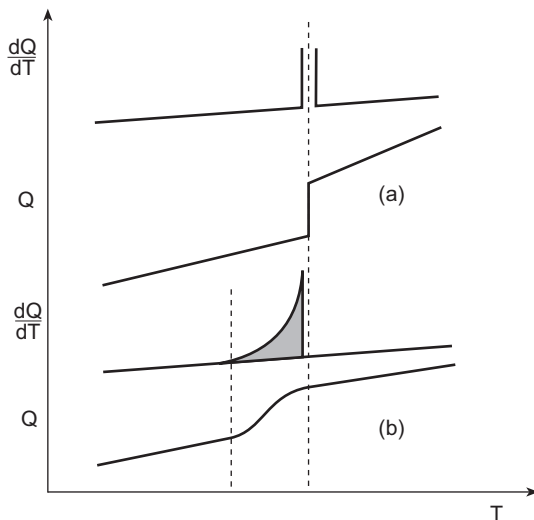
The expression shows that as the temperature increases, the free energy drops and it decreases as the specific heat increases. Thus, if there are two phases, A and B, and A has lower E_o and lower specific heat, then A would be more stable at lower temperature but, at sufficiently higher temperature, the phase B will be stabler. A large specific heat is associated with a low characteristic temperature and hence with a low vibrational frequency. The vibrational frequency decreases as the strength of the binding of the lattice decrease. The more weakly bound phase B in the above situation (that has higher E_o) has a larger vibrational specific heat; hence higher entropy. This phase would therefore be more stable at higher temperatures. Barrett discovered that Li, stable at room temperature in the bcc form has an fcc structure at liquid air temperature.² The polymorphism in iron is somewhat complex; here bcc structure (α -iron) is replaced by the fcc structure (γ -iron) above 910°C; but the bcc phase re appears (as δ -iron) at temperatures above 1400°C. Here, the magnetic change (ferro to para on heating) and the electronic specific heat (that becomes prominent in transition metals such as iron) are responsible for the observed phase changes.¹

A discontinuous change in the heat content takes place during melting (at constant temperature) and also during several allotropic/structural transformations. Here, the entropy change (dQ/dT) would be infinite. Transformation at Curie temperature also shows a similar change. The order-disorder transformation in β – brass exemplifies another type of transformation that takes place over a temperature; here C_p at transformation is large, but finite.

The $Q - T$ and $(dQ/dT) - T$ variations are shown in Fig. 8.1(a) and (b) for first and second types of transformations, respectively.

8.1.3 Estimation of thermal effects

As has been shown, the heat content can increase abruptly at melting and this increment is equal to the latent heat. Usually, the specific heat of liquid is higher



8.1 Variation $Q-T$ and $(dQ/dT)-T$ for (a) isothermal and (b) non-isothermal transformations.

than that of solid and therefore, a supercooled liquid would manifest higher C_p . The latent heat also depends on the temperature of transformation and as supercooling increases the latent heat decreases. The extent of heat effects would decide the accuracy required and therefore the experimental technique to be used. The solid state phase transformations for instance, are associated with low heat effects demanding more sensitive equipment for monitoring the transformations. From the foregoing it will be seen that if there is a structural change taking place during heating or cooling, it will be accompanied by discontinuities or abnormal curvature in a time-temperature curve. Under suitable conditions these curves can be analyzed to identify the temperature or the temperature range associated with a transformation.

Direct and inverse thermal methods

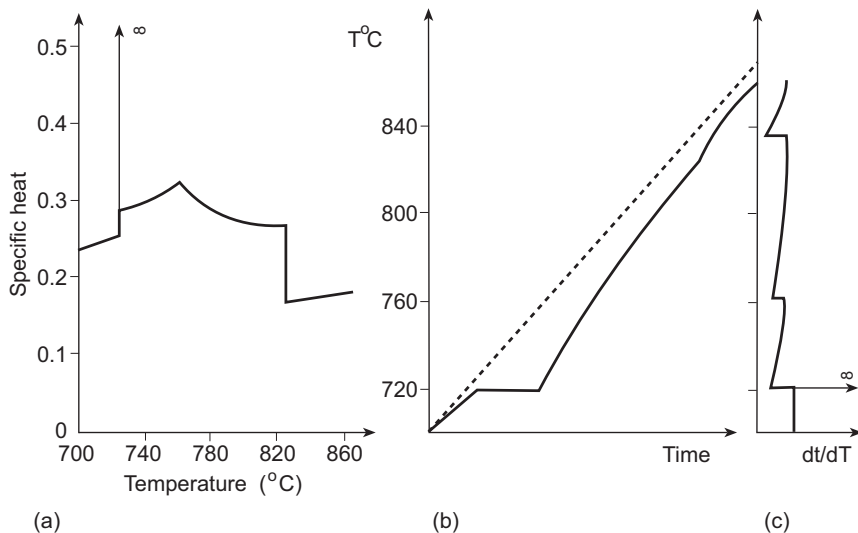
The simplest technique is to place a specimen in a furnace which is designed to have a negligible temperature gradient in a zone that is larger than the dimension of the specimen. The specimen could be self-supported if the investigation is all in the solid state or else, need a crucible when solid-liquid transformation is under study. The furnace is to be heated or cooled linearly and the temperature of the specimen is recorded at suitable time intervals. For measuring temperature a calibrated thermocouple or a pyrometer is used; the thermocouple needs to be sheathed, if liquid alloys are used. The rate of heating or cooling should be so adjusted as to avoid a pronounced temperature gradient across the specimen. A recommended rate is 1–2 °C/min for a specimen of about 20 mm diameter, this is

expected to produce a gradient not exceeding $0.1\text{ }^{\circ}\text{C}$ between the outer to the centre while studying S-L transformations.

The method of inverse rate cooling would sometimes show more sensitive points of transition. Here, the time taken to heat or cool through a small uniform temperature interval is noted and plotted against the corresponding temperature. However, the inverse rate method does not give any additional information and the accuracy may go down especially when isothermal transformation with supercooling are studied, in comparison to the normal cooling curves.

The characteristics would be complicated in case of non-isothermal transformations particularly when there are overlapping reactions; for example, in the steels, during heating or cooling. For analyzing these curves, the fundamental knowledge on specific heat would be useful. In Fig. 8.2 the specific heat curve for carbon-steel (a) specific heat; (b) a somewhat ideal direct heating curve; and (c) an inverse heating curve are shown.³

In the real life situation, the heating and cooling curves appear different in form. While one makes an allowance for rounding-off the discontinuities, reference is usually made to cooling curves. The magnitude of the upper discontinuity is more pronounced in an experimental cooling curve due to undercooling. Owing to gradual changes in specific heat on heating, it is difficult to detect the upper change point during heating. Since the actual specific heat change is small on heating, it is replaced in practice by the irregularity shown as a dotted line in Fig. 8.2(c). From the above discussion it would be evident that care needs to be taken to distinguish between fluctuations due to internal structural changes in the specimen.



8.2 Specific heat and heating curves for a 0.2% carbon-steel (a) specific heat (b) direct (c) inverse rate.

Differential thermal analysis (DTA)

Small changes in thermal effects are emphasized through this technique. Here, the difference in temperature (ΔT) between a standard and a specimen is plotted against the temperature of the specimen. The standard has to be a material that undergoes no transformation in the temperature range of investigation. The specimen and standard could be placed side by side, or the standard may be in the form of a thick-walled hollow cylinder, surrounding the specimen, care taken to ensure that the specimen and the standard do not touch each other. The latter method is considered very sensitive.

One may record the differential heating or cooling curves, these are of importance in solid state transformations.

8.1.4 Introduction to specific thermoanalytical methods

Thermal analysis as defined by the international confederation for thermal analysis (ICTA) and accepted by the IUPAC and ASTM refers to a group of techniques in which a physical property of a substance, or its reaction products is measured as a function of temperature while the substance is subjected to a controlled temperature programme. Therefore one could cover a number of techniques here. A comprehensive table has been provided by Gallagher,⁴ simplified in Table 8.2.

As would be evident, a wide spectrum of methods can come under thermoanalytical methods as long as the measurement is conducted under a controlled temperature environment. Keeping in view the small space available and the level of treatment being rather basic, four general techniques are dealt with in this chapter, namely: (i) thermogravimetry (TG); (ii) differential thermal analysis (DTA) and differential scanning calorimetry (DSC); and (iii) evolved gas analysis (EGA). It is also known that two or more techniques are to be

Table 8.2 Principal thermoanalytical methods

Property	Technique	Acronym
Mass	Thermogravimetry	TG
Apparent mass (change by induced magnetic field)	Thermomagnetometry	TM
Volatiles	Evolved gas detection Evolved gas analysis	EGD EGA
Radioactive decay	Emanation thermal analysis	ETA
Temperature	Differential thermal analysis	DTA
Heat or heat flux	Differential scanning calorimetry	DSC
Dimension	Thermodilatometry	DA

employed when a critical conclusion is to be drawn from the results. Thus, a combination of TG and DTA in several metallic systems is quite valuable. Similarly in many polymeric systems mass change (TG) and evolved gas (EGA) would be useful. The other important feature of today's equipment is deriving benefits from the power of computer and electronics. As a result, the cost of the equipment in general is on the decline, while both the accuracy and precision have gone up.

8.2 Thermogravimetry (TG)

The basic components constituting the TG apparatus include a defined (in weight) sample and controlled furnace; facilities to pick up and record the temperature (as well as the facility to create a temperature programme that is capable of sensing the mass both during heating and during cooling). The data on temperature and mass changes are fed to a data acquisition system. The present day electromagnetic balances possess high sensitivity, temperature stability and reasonable freedom from vibration. Details of electrobalances (in particular, the Cahn electrobalance) are given in many literature.⁵ A typical sensitivity of $0.1\text{ }\mu\text{g}$ is possible. Although most commercial TG apparatus uses such electrobalances, other special purpose sensors for mass change are also made use of. For example, the resonant frequency of a piezo electric crystal (e.g. quartz) varies with the mass deposited on the crystal surface. It is observed that as small as $1\text{ pg}\text{cm}^{-2}$ can be detected.⁶ Such ultra sensitivity enables the vapourization and deposition rates to be measured. However, there are limitations on the temperature range and careful handling is required to avoid interference from external factors.

Accuracy of thermal methods, depends to a large extent, on the uniformity and precision of the heating system. The exact nature of the experimental arrangement and the type of material used for various components of the system depends mostly on the manufacturers. For example, most instruments have a furnace external to the sample compartment. In some instruments, however, the furnace is built inside the sample chamber and hence in the same gaseous environment as the sample. This arrangement is primarily used for very small samples. Such miniature furnaces allow shorter test-to-test times. However, while dealing with heterogeneous samples (such as coal, mineral, etc.) one has to use a larger sample for getting bulk characteristics; requirements for larger samples also arise where the change in mass is extremely small (e.g. thin films).

Up to a temperature of $1000\text{--}1200^\circ\text{C}$ the heating elements used are either Nichrome or Kanthal alloys. Tubes and accessories are usually made of fused quartz, that would hold the samples and maintain atmosphere. An aluminium sample container is often used up to around 600°C because of good thermal conductivity and comparatively lower cost for tests. In the elevated temperature range of $1500\text{--}1700^\circ\text{C}$, the heating elements are silicon carbide, molybdenum

disilicide, platinum or platinum alloys. Similarly, for holding the samples one uses platinum or alumina, and for containing atmospheric gases mullite or alumina are used. There are also instruments that facilitate experimentation above 1700°C (for testing refractory materials). Here, the heating elements such as molybdenum, tungsten or graphite need to be protected against oxygen. The design of furnaces for heating can be quite complex and fascinating. One finds, for example, the use of radiant heating capable of heating rates of 500°C/min, up to 1200°C. Similarly, various focal arrangements are available for infrared heating. A point to note is that the rate of cooling in all these instruments cannot attain such rates.⁴

8.2.1 TG and DTG curves

One can use a thermogravimetric (TG) curve in which a wt % is plotted against temperature. The use of the per cent weight is more useful than absolute value since the former can provide a tool for comparing the behaviour of several materials. On the same plot, one can also superimpose the derivative of the TG curve; these would be known as DTG curves. While the DTG curves enhance resolution, it is customary to smooth the data prior to the differentiation; otherwise the noise also gets amplified in the process. It may be mentioned that the DTG plots are used for kinetic analysis as they represent in many situations, the actual rate of the reaction. In many cases, the inorganic/organic compounds participating in the reaction can be identified by the characteristic temperature as well as by the actual determination of the stoichiometry (this determination is more convenient from the TG plot rather than the DTG plot).

8.2.2 Sources of error

The errors are generated both in the measurement of mass as well as measurement of temperature. Some of the errors in the measurement of temperature come from the heating rate, thermal conductivity, sensor arrangement and electronic drift, etc. The uncertainties in the measurement of mass starts from the buoyancy effect; atmosphere turbulence; condensation and reaction, electrostatic and magnetic forces as well as the electronic drift. The treatment of the sources of error and their minimization has been dealt with by Gallagher.⁴ It would be important to note that the parameters affecting the error also interact among themselves thereby affecting the overall reaction in a complex manner. For example, if the thermal decomposition of a material (such as CaC₂O₄.H₂O) involves the evolution of CO and the atmosphere of experimentation is air or oxygen (in place of Argon) then the exothermic oxidation of CO to CO₂ would take place on the surface or in the interstices of the powder. The heat generated can instantaneously (temporality) heat up the material and raise its temperature; the nearby thermocouple may not be able to register this change. Further, the

thermobalance, if it registers this change, would show a folding back of the curves when the abscissa is temperature. In such situation, a plot of wt% against time would be better.

8.2.3 Isothermal TG and other miscellaneous methods

These methods have been used extensively to study the variable stoichiometry of materials and to determine phase equilibrium kinetics uses are made by measuring the rate of change of mass. However, care needs to be taken to avoid errors. It may be further mentioned that isothermal TG has been commonly used in the study of corrosion and oxidation of metals.⁷ One needs to have high precision particularly while studying the early processes in corrosion and also the reaction of thin films (that represent only a very small fraction of the total change).

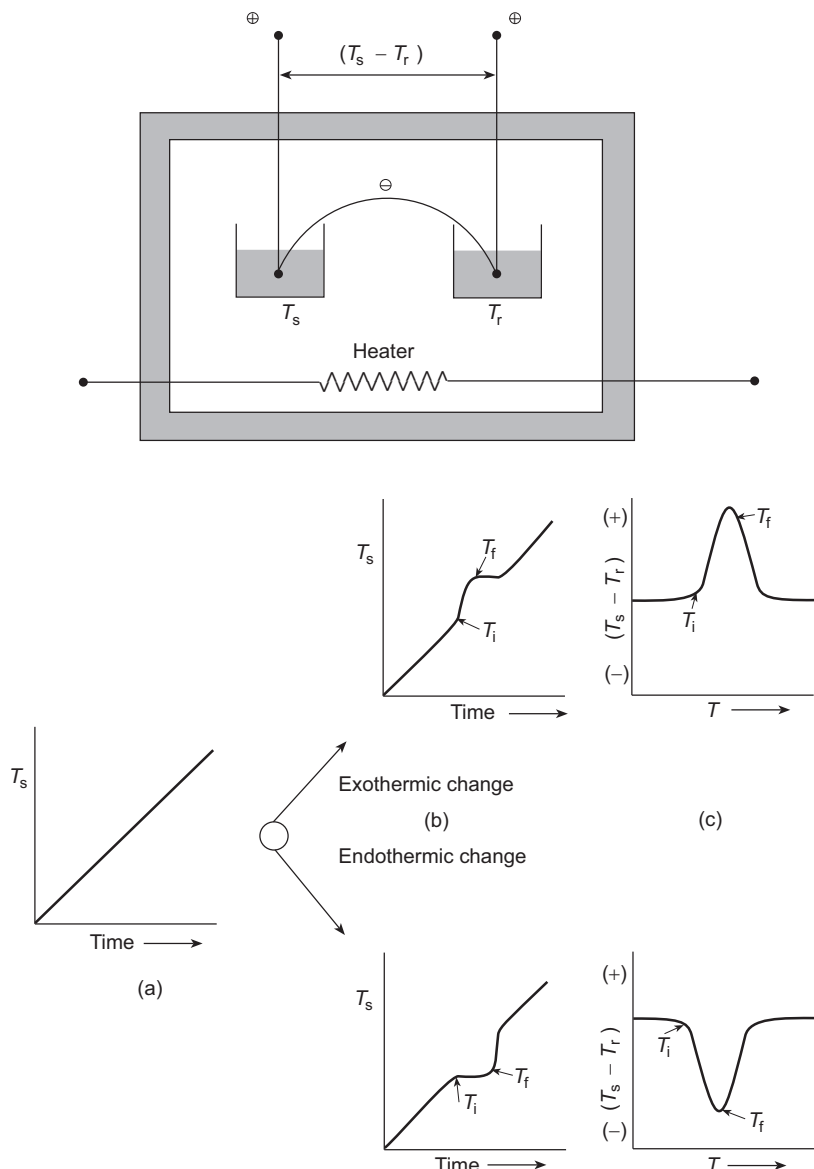
Experiments are sometimes conducted where a magnetic field gradient is superimposed, then the method of TG is said to be thermomagnetometry (TM). If the sample is paramagnetic an apparent weight gain or loss (depending on the direction of the field gradient) takes place that can provide additional information. An interesting example of the proximate analysis of coal and lignite is found in literature⁸ using TG and TM in a controlled atmosphere. This work by Alymer and Rowe⁸ demonstrates that the technique can give reasonably accurate results comparable to the more involved and time consuming ASTM methods.⁸ In particular, the hematite present in the ash of the coal can be determined by TM once the initial measurement is done by the TG for determining the moisture and volatiles and, thereafter, the fixed carbon (the last one under oxidizing atmosphere while the first two are determined under inert atmosphere).

8.3 Differential thermal analysis (DTA) and differential scanning calorimetry (DSC)

8.3.1 Differential thermal analysis (DTA)

It was Le Chatelier, in 1887, who demonstrated that the rate of change of temperature of a body at equal increments of time could provide some additional information, hence the name, differential thermal analysis.⁹ However, it was soon realized by Roberts-Austen that a better method than simple differentiation of the heating/cooling curve, would be to compare the temperatures of the sample with a reference material.¹⁰ This method is today known as differential thermal analysis (DTA).

One places an inert reference material (possessing similar C_p) alongside a specimen of study and tracks the difference in temperature between the two. Here, the reference material and the sample would be subjected to the same



8.3 General principle and arrangement of DTA (i = initial, f = final).

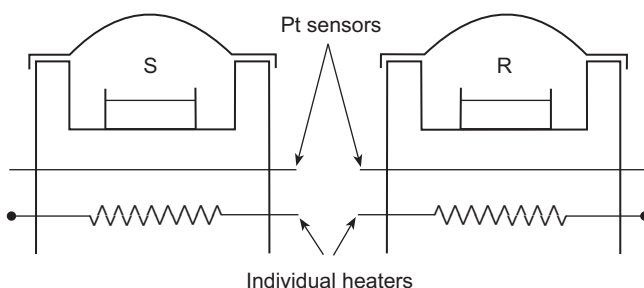
fluctuation in the temperature and therefore would respond similarly, the effects would thus get cancelled out. The baseline would consequently remain nearly unaffected. The basic DTA apparatus and a typical plot are shown in Fig. 8.3(a, b, c). During heating if the sample undergoes an endothermic reaction the reference sample would show a higher temperature thus ΔT

($= T_s - T_r$) would be negative. By the same logic, if there is an exothermic reaction occurring in the specimen while heating, the ΔT ($= T_s - T_r$) would be positive. A change in the specific heat (C_p) or the thermal conductivity of the sample would result in a change in the slope in the $\Delta T - T$ plot and a step in the baseline of the curve.

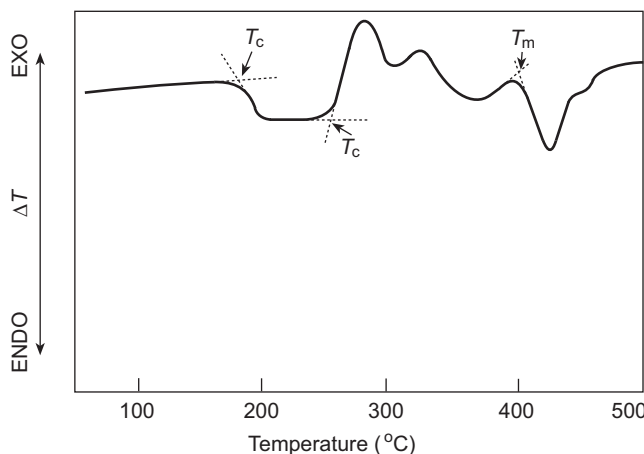
The DTA-curve is primarily used for detecting and characterizing thermal processes (such as endothermic/exothermic) qualitatively. One would also comment on the reversibility of the reaction, as well as on the order of the reaction. The DTA method is extensively used for determining phase diagrams. Under ideal conditions, the area under a DTA peak should be proportional to the enthalpy of the reaction causing the peak. However, factors such as changes in the thermal transport properties and the sensitivity of detectors influence the results.

8.3.2 Differential scanning calorimetry (DSC)

Some of the problems mentioned in relation to DTA can be addressed in the differential scanning calorimetry (DSC) apparatus. The original DSC was developed by Perkin Elmer Co. in 1964 and was designated as ‘power compensation’ type.^{11,12} Figure 8.4 shows a simple schematic of this apparatus. Here, ‘S’ and ‘R’ would refer, as earlier to the specimen and reference respectively. The Pt-resistance thermometers are coupled into a bridge circuit. The difference in temperature ΔT ($= T_s - T_r$) is kept as zero by sensing any imbalance and actuating a heater in the sample or the reference portion of the cell. Thus, the power needed to keep the bridge circuit in balance is proportional to the change in the heat capacity or enthalpy taking place. The integral of the power over the time of the event gives the energy difference between the sample and the reference. If power is supplied to the sample, it is taken as positive by convention; this refers to an endothermic reaction situation (since this would lead to the temperature of the sample falling behind that of the reference). Thus, in the endothermic situation, ΔH is taken to be positive and in this sense it is the opposite of the situation in the



8.4 Schematic of a power compensation DSC.



8.5 DTA curve for a glass at $20\text{ }^{\circ}\text{C min}^{-1}$ in N_2 .¹³

DTA. Consequently, an endothermic process is positive in DSC while it is negative in the DTA.

Apart from the above, there is a second type of DSC that is based on the ‘heat flux’ mode. Such a DSC is similar in operation to a DTA apparatus. However, here the temperature dependence of thermal transport and sensor sensitivity are built into the hardware and software systems. Some of the present day equipment has a switch to operate either in the DTA or DSC-heat flux mode. It is important to note that many reactions are not reversible (e.g. metastable to stable; polymerization; tempering of quenched steel, etc.). Therefore, a comparison of the heating curve with the cooling curve (or a reheat process) would provide information on the specific phenomenon. Thus, if a glass is heated in the DTA (Fig. 8.5) one observes the following:¹³

1. A base line shift associated with ΔC_p at the glass transition (T_g).
2. Two overlapping exothermic processes (metastable to stable and amorphous to crystalline starting at T_c).
3. Melting of the two ordered phases resulting in two overlapping endothermic peaks (starting at T_m).

The point to note is that, on reheating (after slow cooling) of the same glass one would observe only the two endothermic melting points as the other transitions are already over.

The DSC data can also be used to determine the heat capacity, C_p of a substance by comparison with a known standard (usually sapphire, Al_2O_3).⁵ One important issue in DTA or DSC is the determination of the baseline. The extrapolated onset of the reaction (as in Fig. 8.5) is very common; however other techniques are also used.⁴ The computerized equipment has the capability of adjusting the baseline with the help of a stored baseline.

8.3.3 Calorimetric analysis

A broad description would be provided for the measurement of enthalpy and specific heat.

Enthalpy can be evaluated by the method of mixtures involving the measurement of a small rise in temperature of a vessel and its contents when a hot sample is dropped into it. The use of drop calorimeters and the errors to be taken care of are dealt with in classical books on heat.¹² In many cases, it is desirable to heat the specimen in a suitable container either to avoid contamination by reactive materials or because the specimen is either a liquid or a powder. In this case, the enthalpy of the container needs to be determined separately. If the hot sample is dropped directly into the calorimeter fluid (usually water, though aniline and paraffin oil has also been used), there is a possibility of localized evaporation or splashing. Some workers attempt to minimize the effect by dropping the sample into a metal vessel surrounded by liquid; this method, however, suffers from inertia in heat exchange and therefore introduces errors. To a large extent this deficiency has been rectified by ice calorimetry.³ In this set-up, the heat of the specimen cause the melting of ice; the quantity can be determined from the volume of the ice water mixture. It has been shown to have high accuracy if properly calibrated.^{15,16} In general, the method of mixture can yield very accurate results if the specimen undergoes no transformation within the range of temperatures studied. If the quenching does not interfere with the transformation, and if the material displays an equilibrium structure at room temperature, then the method is satisfactory even if a transformation takes place. Whenever quenching results in a non-equilibrium structure, it is necessary to measure enthalpy through the measurement of specific heat.

The direct measurement of specific heat involves the estimation of change in temperature of a specimen subjected to a small increment in heat. The method is useful in studying phase transformation; especially those associated with irreversible changes in specific heat, i.e recrystallization of cold worked material; tempering reaction in steel, etc. In some experiments specific heat is measured by pulse heating either by laser or by passing a heavy current.¹⁷ Liquid metal solution calorimetry has been extensively used for measuring the heat of solution, mixing,¹⁸ formation,¹⁹ cold working²⁰ and annealing²¹ and many other solid state processes. The liquid tin solution calorimeter was introduced in 1952.²² As is known the heat (energy) effects associated with solid state is difficult to determine; these processes are primarily slow, specially when diffusion is involved. Metal solution calorimetry is preferred because it possesses a well-defined energy at a given concentration, temperature and pressure. Further, the dissolution of a solid in the liquid metal is more rapid than most solid state processes. The enthalpy difference between the mechanical mixture and an alloy of the same composition can be determined as the difference in their heat effects

on dissolution under otherwise identical conditions. Some details about the liquid metal solution can be found out from literature.²³

8.4 Evolved gas analysis (EGA) and detection (EGD)

As has already been pointed out, the EGD refers to the qualitative determination of volatile species that are evolved. The EGA technique on the other hand, involves the quantitative determination of the volatile species. Details of the technique can be found in literature.⁴

Both EGA and EGD can be employed in determining the consumption of reactive gases such as H₂, O₂, CO₂, H₂O and so on. Although these can be employed as standalone equipment, they are more often used in conjunction with TG, DTA or DSC, etc. in which the output carrier gas stream from any of these is taken for analysis.

The specific method for sampling can vary depending upon the nature of the sensor and the sensitivity desired. For higher sensitivity, one could accumulate the products over a period of time and analyze them periodically using the analytical equipment. If the analytical equipment is dedicated online equipment, the rate of sampling is dictated by the nature of the equipment and the rate of change of the gas phase.

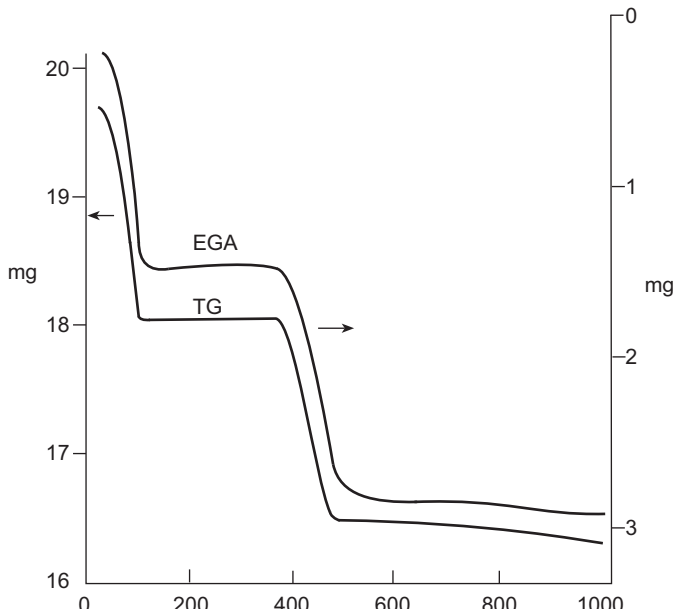
Analytical gas chromatography instruments are discontinuous in operation whereas Fourier Transformed Infra Red (FTIR) equipment can be used both in the continuous as well as discontinuous mode. The mode is decided by (i) rate of change in composition of the gas stream, (ii) the storage capacity in the data acquisition system, and (iii) the time needed to scan the spectrum of wavelengths or mass numbers etc.

One issue in EGA/EGD is the compatibility between the carrier gas and the product gases, both from the consideration of direct reaction and interference in analysis. Similarly, the materials of construction should not change the composition through absorption, catalysis, etc. It is also important to note that many gases condense in the cooler portions of the exhaust train before arriving at the sensor; thus one would need heated transfer lines here. Increasing the flow rate of the gas is used to enhance direct correlation by shortening the delay; however beyond a limit the carrier gas rate would increase the noise level or the sensitivity of the initial equipment (TG, DTA, DSC, etc.) and dilute the concentration of the evolved gas to very low levels affecting its detection. There are situations where the thermoanalytical equipment operates at a different pressure (e.g. mass spectrometry requiring a vacuum of 10⁻⁵ torr or less). A special interfacing would then be required; it may be advisable at times to perform the measurements separately rather than online.

The detectors and analyzers can vary, mostly depending upon the physical nature of the gases involved. If the system is static (i.e. not a flowing atmosphere) then either pressure or volume can be used as detectors for EGD. A

controlled rate TG instrument can be used in this case.²⁴ Gas density could be used in a flowing system. A carrier gas such as He is used for improved signal. Thermal conductivity would be a good indicator in this case.

Methods used for EGD are quite selective depending upon the nature of the problem. Broad band optical absorption or emission has been used successfully with filters that can improve selectivity; aerosols can be detected in this manner. Flame ionization detectors, as in gas chromatography have been used to detect organic matters quite accurately. A selective approach to EGD involves passing evolved gas through solids or liquids that will absorb a specific type (acidic or basic) of gases. The method can be a quantitative EGA in such situations. Gas analyzers used in process stream analysis or environment monitoring have also been used for EGA. Dew point detectors can be used to detect water losses from a sample or that formed by reactions such as reduction of oxides by hydrogen. In Fig. 8.6 a comparison of TG and EGA curves is shown for the thermal decomposition of hydrated barium hydroxide.²⁵ The agreement would seem very good. One can combine flow rate and dew point to provide quantitative information. The evolution of oxygen or its consumption from a gas mixture can be monitored using standard oxygen analyzers. When oxidation-reduction phenomena are investigated, the use of an oxygen analyzer on the exit system is recommended.⁴



8.6 Comparison of the TG and EGA curves for water loss from hydrated barium hydroxide.²⁶

Studying the evolution of radioactive gases is done by emanation thermal analysis (ETA) which is a unique method of analysis using the evolution of radioactive gases. During heating of the radioactive sample, radioactive gas is released, the rate of which is dependent upon the reaction, transformation, porosity, change in surface area, etc. Commercial equipment is available for ETA and one comes across information such as the dependence of emanation from tungsten on its crystallographic orientation.²⁶

As far as methods of analysis in EGA are concerned the Fourier Transformed Infra Red (FTIR) method is widely used because it is simpler and less expensive. This has been used in studies involving organic materials and polymers. Mass spectroscopy (MS) is more accurate but expensive. Gas chromatography is used less widely due to the longer time of analysis. Several interesting examples of EGA plots and their application in finding clues to the behaviour of material have been given by Gallagher.⁴ Examples of corrosion studies on copper (using the corrosion products and doing MS scan) are available.²⁷ Reduction of oxides to form metals has been studied by EGA and DTG; these have been based on weight loss and the dew point of the gas stream.²⁸ One interesting example is the study of thin films semiconductor technology. Since the films are very thin, other techniques are difficult, and the occluded Ar (used during the sputtering of thin films) is of concern. Here, MS-EGA and Rutherford backscattering have been successfully used to determine the amount of Ar by Hong *et al.*²⁹ Similarly, the polymers (particularly, PVC) have been widely subjected to TG and FTIR-EGA in order to study their thermal degradation and also to find out the nature of volatile products that can form when fire occurs; these can be crucial from the environmental standpoint.⁴

8.5 References

1. Cottrell, A.H.: *Theoretical Structural Metallurgy*, Edward Arnold Ltd, London (1944).
2. Barrett, C.S.: *Phys. Rev.*, 72 (1947) 245.
3. Cherepin, V.T. and Mallik, A.K.: *Experimental Techniques in Physical Metallurgy*, Asia Publishing House, Bombay, Calcutta, London, New York (1967) 187.
4. Gallagher, P.K.: *Thermo Analytical Methods in Materials Science and Technology*, Cahn, R.W. *et al.* (eds) Vol. 2A, Characterisation of Metals, Part-I, VCH Verlag (1992).
5. Brown, M.E.: *Introduction to Thermal Analysis*, Chapman & Hall (1988).
6. Plant, A.F.: *Industrial Research*, July (1971) 36.
7. Evans, U.R.: *The Corrosion and Oxidation of Metals*, St Martinus Press, New York (1960).
8. Aylmer, D.M. and Rowe, M.W.: *Thermochimica Acta*, 78 (1984) 81.
9. Le Chatelier, H. (a) *Compt. Rend. Hebd. Seanc. Acad. Sci., Paris* (1987) 104, 1143 and 1517. (b) *Bull. Soc. Fr. Miner.*, 10 (1887) 204.
10. Roberts-Austen, W.C.: (a) *Proc. Inst. Mech. Eng.*, 1 (1899) 35. (b) *Metallographist*, 2 (1899) 186.

11. O'Neill, M.J.: *Anal. Chem.*, 36 (1964) 1238.
12. Watson, E.S. et al.: *Anal. Chem.*, 36 (1964) 1233.
13. Vogel, E.M. and Gallagher, P.K.: *Mater Lett.*, 4 (1985) 5.
14. Kubashevski, O. and Evans, E.L.: *Metallurgical Thermochemistry*, 2nd edn, Pergamon Press, London (1957).
15. Butcher, K.L. and Nickson, G.H.: *Trans. Faraday Soc.*, 54 (1958) 1195.
16. Vallee, R.E.: *Review Sci. Instr.*, 33 (1962) 856.
17. Nathan A.M.: *J. Appl. Physics*, 22 (1951) 234.
18. Kleppa, O.J.: *J. Phy. Chem.*, 59 (1955) 175.
19. Orr, R.L. et al.: *Rev. Sci. Instr.*, 28 (1957) 767.
20. Bever, M.B. and Ticknor, L.B.: *Acta Met.*, 1 (1953) 116.
21. Greenfiled, P. and Bever, M.B.: *Acta Met.*, 4 (1956) 433.
22. Ticknor, L.B. and Bever, M.B.: *Trans. AIME*, 194 (1952) 194, 941.
23. Howlett, B.W. et al.: *Rev. Sci. Instr.*, 33 (1962) 619.
24. Rouquerol, J.: *Thermochim. Acta*, 144 (1989) 209.
25. Gallagher, P.K. and Gyorgy, E.M.: *Thermal Analysis*, Vol. 1 Birkhauser Verlag Basel (1980) 113.
26. Balek, V.: *Thermochim. Acta*, 110 (1987) 222.
27. Nassau, K. et al.: *Corrosion Science*, 27 (1987) 669.
28. Gallagher, P.K. et al.: *J. Thermal Analysis*, 23 (1982) 185.
29. Hong, M. et al.: *J. Appl. Physics*, 59 (1986) 551.

Part II

Improving process and product quality

Improving process design in steelmaking

D SICHEN, Royal Institute of Technology, Sweden

9.1 Introduction

The design of a process requires teamwork, since it must take many major factors into consideration, such as the aims of the process – the product(s), the choice and availability of the raw materials, the environmental constraints, the energy consumption and the cost of the production.

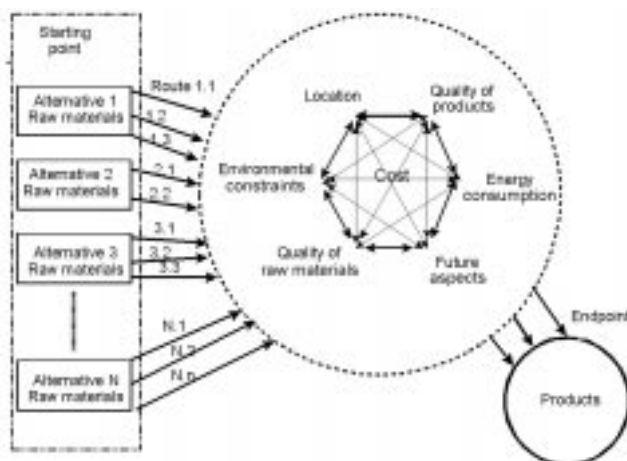
Any analysis of the process route should begin with the identification of the aim or aims of the process, namely the products in the present discussion. This should be followed by the examination of the potential raw materials. Only after knowing the endpoint (the products) and the possible starting point(s), can one start looking for the process route. There will be a number of processing alternatives as shown schematically in Fig. 9.1.

Environmental regulations would rule out several possible routes. The availability of the raw materials would further reject a couple of options. The remaining production routes, however, are usually still multiple, and choosing the production route is, in fact, always an optimization process. It depends on the choice of the raw materials, energy consumption, the quality required of the final products, the extent of pollution and the cost. In the optimization process, the potential processing route has very often to be modified. Therefore, the final choice of the process route and, consequently, the design of the process have usually to go through a number of planning cycles. The present chapter does not intend to discuss the optimization process. Instead, it focuses on the fundamentals of the technical design or development of the individual route. Hence, we shall confine ourselves only to the chemical engineering aspects in this chapter, while leaving the economical and environmental concerns to the readers' further study.

9.2 Overview of process design

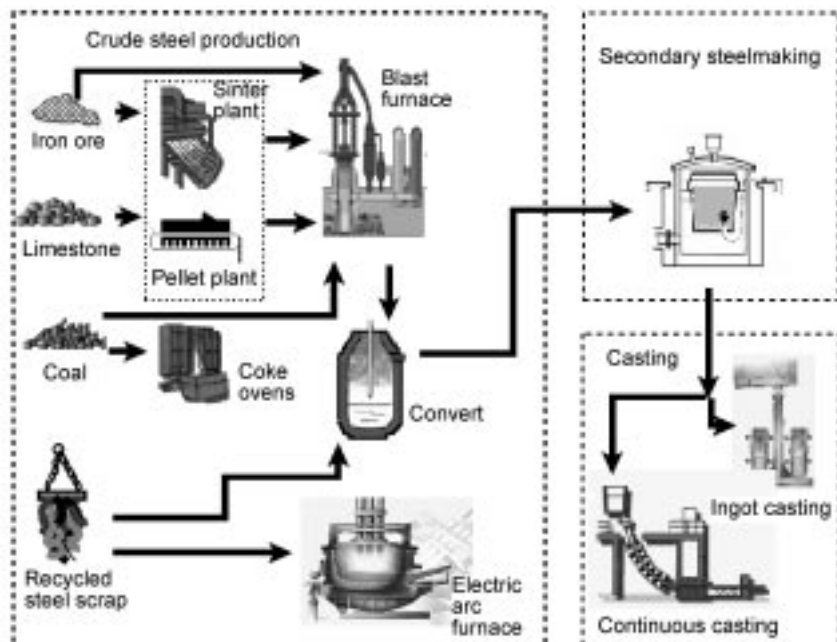
9.2.1 Whole process

A production line, *viz.* the whole process is usually composed of a number of sub-processes. The design of a production line requires a comprehensive



9.1 Alternative processing routes.

investigation and optimization to make the final choice of the process route. While this choice would put specific demands on the design of the sub-processes, the design of the individual sub-processes might, in turn, lead to reconsideration and modification of the preliminary design of the production line. We shall discuss the steelmaking process as an example.



9.2 Production line(s) for steelmaking.

Figure 9.2 presents schematically the production line(s) for steelmaking. The whole process can be divided into three major steps before metal forming.

Step 1 Crude steel production

There are two major process routes for making crude steel today. The choice of the production route presents a very good example of how the raw materials influence the process design. The use of iron ore as the main starting material is usually associated with the route of the basic oxygen converter. On the other hand, the electric arc furnace would be the alternative when the steel plan operates mainly on recycled steel scraps. The former requires a charge of molten iron, which is produced in blast furnaces.

The raw materials for producing molten iron are iron ore, coking coal and fluxes – mainly limestone. Preparation of the charge materials plays an essential role to ensure the gas flow through the burden column. Iron ores are charged in the form of lump ores, sinters and pellets. The use of pellets and sinters is a typical example of rationally utilizing natural resources. The preparation and enrichment processes in the iron ore mines result in very fine-grained ores. An optimized process design will naturally include the sub-process to agglomerate the accumulated fine-grained ores by means of pelletizing or sintering.

Pelletizing involves the forming of ore fines (pellet feed) and concentrates with grain sizes of well under 1 mm into pellets of around 10 to 15 mm in diameter by addition of a binding agent. The pellets are first formed in rotating drums or on rotary discs and thereafter dried and indurated at temperatures above 1273K.

Sintering is made by charging a mixture of ore fines together with coke breeze, fluxes, in-plant returns and return fines onto a circulating grate, or sinter strand, and igniting the coke breeze contents in the surface. A flame front passes through the layer of the mixture over the strand length and agglomerates the mixture into coarse lumps of ore.

With the increasing demand from environmental regulation, there has been a trend of replacing sinters by pellets, since the sintering process leads to more serious pollution. The trend of replacing sintered ore by pellets illustrates how the environmental issue affects the design of a whole process. Similarly, to reduce the release of CO₂, SO₂ and other polluting gases in coke production, much effort has been made to increase the amount of coal injection into the blast furnace. Unfortunately, many existing blast furnaces have not been designed to facilitate this operation. This example indicates that a process design might need modification with the development of environmental regulations, availability of natural resources and so on. The facilities for future modification should always be an important aspect in designing a process.

The hot metal from the blast furnace contains impurities such as carbon, silicon, sulphur and phosphorus. These are removed in a converter. While a

number of types of converters are available nowadays, converters having combined blowing are more commonly adopted. In such operations, pure oxygen at high pressure is blown into the vessel through a water-cooled lance above the molten metal; at the same time inert stirring gases and/or oxygen are additionally injected through the converter bottom. The bottom blowing was beneficially introduced in view of its high efficiency in enhancing the mass transfer process in the molten steel. It is a typical example of the improvement of a process design by considering the mass transfer aspect. Converter process is still a necessary step before secondary steelmaking, though studies are being carried out to look into the possibility of combining the converter process with the secondary steelmaking process.

Increasing importance is being attached to scrap recycling for reasons of optimum raw materials utilization and environmental protection. Electric arc furnaces functioning as the melting unit have been more widely employed recently, since this enables the transformation of electrical energy into melting heat with high efficiency and high energy density. Another important advantage of an arc furnace is that it can produce any steel grade, regardless of the charge (scrap, DRI, hot metal, as well as any combinations). The need for recycling and the environmental advantage of using electrical energy are among the main reasons for the increasing role of EAFs in steelmaking.

Step 2 Secondary steelmaking

In the case of both the basic oxygen process route and the electric arc furnace route, the molten steels, after being tapped (poured) from the furnace, undergo a further stage of processing before casting. This step is usually called secondary steelmaking. A number of routes are available. In general, the process should facilitate operations such as stirring with argon and induction, adding alloys, vacuum de-gassing and arc heating. The ladle furnace is one of the attractive alternatives. The objective in all cases is to fine-tune the chemical composition of the steel, to improve the homogenization of temperature, to remove impurities and to reduce the number of inclusions.

The design of this step depends greatly on the design of step 1. For example, to determine the flow rate of argon gas and the stirring time, one must take into account the nitrogen and hydrogen levels in the crude molten steel coming from either the converter or the electric arc furnace. Similarly, the deoxidation practice must be designed on the basis of the initial oxygen level in the crude molten metal.

As the standard of steel cleanliness is continuously increasing with time and technological improvements, the control of impurity level and non-metallic inclusion population has become a serious concern of the steel producers. Consequently, secondary steelmaking has become increasingly important in all modern steel industries. It has become one of the crucial aspects in designing the

steelmaking process. In order to make the secondary steelmaking process more efficient, even some modifications are made in the production line. For example, many steel plants have introduced a sub-process of desulphurization using calcium carbide in a torpedo furnace before sending the hot metal to the converter. This practice lightens the load of the desulphurization in secondary steelmaking. Introducing the torpedo furnace into the process line is an example whereby an individual sub-process (secondary steelmaking in the present case), in turn, leads to the modification of the initial design of the production line.

Step 3 Casting

After the secondary steelmaking, the steel is cast. Nowadays, the continuous casting process is widely used throughout the world, although the ingot route is retained for certain applications, e.g. high alloying tool steels. The use of ingot casting is sometimes necessary to avoid chemical segregation in the case of high alloy steels. It is also needed when the amount of production is not so high as to meet the requirements of continuous casting. The choice of the casting process is a good example of how the process design is governed by the final product.

The routes for producing iron and steel, as well as product developments have reached a very advanced state. Still, the steel industry continues to face challenges with regard to innovations in plant and process engineering, product development, and product application. The present section has only discussed briefly the steelmaking process. New thinking and new designs of the steelmaking processes will always be needed with the advance of technology. Although different metallurgical processes require different designs, the discussions in general would be similar. Since the purpose of this chapter is not to introduce the different metallurgical processes, but only the principal factors influencing process design, it will leave the particular processes to readers' further study.

9.2.2 Sub-process

As discussed in the previous section, a production line generally consists of a number of sub-processes. Each sub-process fulfils a number of specific tasks. While the present section will introduce the principal factors that need careful consideration in the design of a sub-process, the consideration of these factors will be further elaborated in later discussions.

We could first take ladle treatment as an example to illustrate the key factors for process design. In the modern steel industry, a ladle no longer functions only as a container for transportation, but also as a very important reactor for refining. An advanced ladle would facilitate the removal of impurities, such as oxygen, sulphur, hydrogen and nitrogen. It would also enable the final adjustment of the alloying elements to meet the target of the steel compositions. The design of the

ladle treatment must take the following points into consideration to fulfil the above-mentioned tasks.

(i) Thermodynamic constraints

A process will always proceed towards but not beyond the thermodynamic equilibrium. For example, in the case of most of the steel grades, one would like to reduce the hydrogen content to a minimum level in the ladle. On the other hand, the minimum hydrogen concentration (or precisely, the hydrogen activity) is directly related to the partial pressure of hydrogen in the system. The dehydrogenation reaction is described as:



$$\Delta G_1^o = -2(36480 + 30.46 \cdot T) \text{ J} \quad (9.2)$$

$$K_1 = \exp\left(\frac{2(36480 + 30.46 \cdot T)}{R \cdot T}\right) \quad (9.3)$$

K_1 is the equilibrium constant of reaction 9.1. Assuming the hydrogen activity equals its concentration in a dilute solution, K_1 can be expressed as:

$$K_1 = \frac{P_{H_2}}{[\text{mass}\%H]^2} = \frac{P_{\text{total}} \cdot X_{H_2}}{[\text{mass}\%H]^2} \quad (9.4)$$

In the above equation, P_{H_2} is the partial pressure of hydrogen, P_{total} is the total pressure and X_{H_2} is the mole fraction of hydrogen gas. Hence, a low hydrogen concentration in the liquid would need vacuum treatment to meet the thermodynamic constrain.

(ii) Mass balance

In the design of a process, mass balance is a crucial issue. As mentioned earlier, deoxidation is one of the most important tasks in ladle treatment. Usually, aluminium or/and ferrous silicon alloy are employed for this purpose. In the case of aluminium deoxidation, the dissolved oxygen content in the liquid steel would depend on the aluminium activity in the steel, which in turn is related to the alumina activity in the slag.

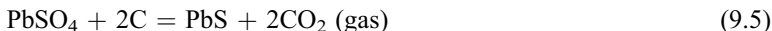
The addition of aluminium will change the final equilibrium. The final aluminium activity in the metal and the alumina activity in the slag will be reached by the transfer of the aluminium element from the metal to the slag. In this transferring process, mass balance must be maintained, *viz.* the total amount of Al loss in the metal phase must equal to the total amount of Al coming to the slag. Hence, the amount of Al addition must be calculated on the base of the mass balance. Since in many cases the reactions cannot reach thermodynamic equilibrium, the calculated amounts of the addition should be considered as minimum.

(iii) Reaction rates

Like most of the metallurgical processes, ladle process is also heterogeneous in nature. A heterogeneous reaction always involves a number of reaction steps. For slag–metal reactions in a ladle treatment, the reaction rates would depend on the mass transfers in both liquid metal and liquid slag, the kinetic condition of the interface, the kinetics of the chemistry and the heat transfer. A comprehensive analysis of all these steps would be a precondition for a reliable estimation of the reaction rate, which is one of the key factors of process design.

While the above discussion shows the importance of thermodynamic constraints, mass balances and reaction rates in the design of ladle process, these factors, in general, should always be taken into account in the design of most of the processes. We could take the smelting of lead in a rotary furnace as another example.

There are two major smelting practices in secondary lead production, namely the silicate system and soda–iron system. The soda–iron system is generally adopted using short rotary furnace. In the furnace, lead sulphate is firstly converted to lead sulphide by the reaction,



The sulphide is then reduced by iron through the reaction,



The battery paste contains also certain amounts of PbO and PbO₂. The lead oxides are reduced by carbon forming CO and CO₂ gases. To form slag, soda ash (Na₂CO₃) is added. The slag can generally be expressed by the formula FeSNa₂S(O).

Both reactions 9.5 and 9.6 are heterogeneous and endothermic in nature. The preconditions for the reactions to take place and proceed are: (i) a reducing atmosphere is maintained in the reactor, so that thermodynamic constraints are met; (ii) correct quantities of the raw materials are adopted, so that correct mass balance is obtained; (iii) a high enough furnace temperature is maintained, so that the reactions can proceed at a reasonable rate; (iv) the furnace charge is well mixed, so that the solid reactants have good contact with each other; (v) heat must be supplied to the reaction sites, so that the temperature is not decreased by the endothermic reactions. Failure in meeting any of these preconditions results in the failure of the process.

9.3 Thermodynamics and mass balance

9.3.1 Thermodynamic description

Most of the metallurgical processes are heterogeneous in nature, involving a number of phases, such as liquid slag, liquid metal, solid refractory and gas. Of

them, slag and metal, which are always solutions, play essential roles in many of extraction and refining processes. A design of a sub-process, e.g. ladle treatment, would demand a reliable thermodynamic descriptions of all the phases. Since slags and liquid metals are solutions, their thermodynamic descriptions would need mathematical models. Unfortunately, none of the existing thermodynamic models is reliable for all slag systems. Even in the case of liquid metals, solution models are usually only reliable in certain composition ranges. Hence, the choice of models is always a compromising process. This process requires an in-depth understanding of the models and experience. The present chapter does not intend to make the choice for the readers. Instead, it will introduce briefly some of the solution models, so that the readers are prepared for the later discussion.

Slag models

A number of slag models are available in the literature with varying degrees of success. They may be classified into two main groups, namely structural based models^{1–5} and empirical or semi-empirical models.^{6–14} The latter type is the most commonly used one. Since empirical and semi-empirical models are based on experimental information, the quality of the experimental data has a strong effect on the results of the model calculations.

Kapoor and Frohberg⁶ developed a model, in which the structure of silica melts are represented by symmetric and asymmetric cells composed of one oxygen ion surrounded by two equal or two different cations. This model was later extended to multicomponent systems by Gaye and Welfringer,⁷ known as the IRSID model. The IRSID model has been applied to a number of multicomponent systems and good agreement between the results of model calculation and experimental data has been reported.⁷

The two-sublattice model developed by Hillert *et al.*⁸ for ionic solutions assumes that one sublattice is occupied by cations and the other one by anions and neutral species. Even in this model, complex anionic species are used.⁸ It should be mentioned that difficulties have been encountered in choosing the suitable species in both the two-sublattice and the IRSID models.⁹ The fractions of different species optimized in this way are somewhat arbitrary, as very little experimental evidence is obtained to support the same.

Pelton and Blander¹⁰ developed a model based on the well known quasi-chemical approach to describe the silicate systems. Difficulties arise when a system contains a liquid phase exhibiting strong structural ordering at a certain composition. By choosing the composition of orthosilicate as the maximum ordered, they were able to describe a number of ternary silicate systems using solely the information from the binary systems.

Temkin¹¹ developed a model for the ideal mixing of molten salts. For mixing of two liquid salts AX and BY, where A and B are cations and X and Y are anions, the ideal entropy of mixing may be expressed as:

$$\Delta S_M = -R[y_A \ln(y_A) + y_B \ln(y_B) + y_X \ln(y_X) + y_Y \ln(y_Y)] \quad (9.7)$$

where y_A , y_B , y_X , y_Y are the ionic fractions of the ions A, B, X and Y. The assumption that the mixing between the salts is ideal gives the expression for the Gibbs energy of mixing:

$$\Delta G_M = -T \cdot \Delta S_M \quad (9.8)$$

The use of the regular solution model to describe the thermodynamics of silicate melts was originally suggested by Lumsden.¹² A silicate melt is considered as a matrix of oxygen ions, O^{2-} with different cations including Si^{4+} distributed in it. Ban-Ya and Shim¹⁴ have successfully applied the regular solution approach to a number of binary, ternary and quaternary silicate systems.

Combining the approaches of Temkin,¹¹ Lumsden¹² and Hillert,⁸ a model for ionic melts has been developed at KTH.^{15,16} According to this model, an oxide melt is considered to consist of a matrix of oxygen ions with various cations distributed in it. In a system containing m different oxides, $C1_{c1}O_{a1}$, $C2_{c2}O_{a2}$, ..., $Ci_{ci}O_{ai}$, ..., $Cm_{cm}O_{am}$, the cations and anions can be grouped into two separate subgroupings:

$$(C1^{\nu 1}, C2^{\nu 2}, \dots Ci^{\nu i} \dots Cm^{\nu m})_p (O^{2-})_q \quad (9.9)$$

where p and q are stoichiometric numbers, $Ci^{\nu i}$ stands for cations, the superscript represents the electrical charge. The thermodynamics of the melt is expressed by the next-nearest-neighbour interactions, *viz.*, the interactions between different cations in the presence of O^{2-} . Consideration of the next-nearest-neighbour interactions necessitates the use of the cation fractions defined as:

$$y_{Ci} = \frac{N_{Ci}}{\sum_{j=1 \text{ to } m} N_{Cj}} \quad (9.10)$$

In equation 9.10, N_{Ci} is the number of moles of cation $Ci^{\nu i}$ and the summation covers all the cations. If $X_{Ci_{ci}O_{ai}}$ and $G_{Ci_{ci}O_{ai}}^o$ represent the mole fraction and the standard Gibbs energy of oxide $Ci_{ci}O_{ai}$, the integral Gibbs energy of a solution can be expressed as:

$$G^m = \sum X_{Ci_{ci}O_{ai}} \cdot G_{Ci_{ci}O_{ai}}^o + RTp \sum y_{Ci} \ln y_{Ci} + G^E \quad (9.11)$$

G^E , the excess Gibbs energy of the solution in equation 9.11 is described as:

$$G^E = f(T, y_{Si^{4+}}) + \sum_{i=1 \text{ to } m-1} \left(\sum_{j=i+1 \text{ to } m} y_{Ci} y_{Cj} \Omega^{Ci, Cj(O)} \right) \quad (9.12)$$

$\Omega^{Ci, Cj(O)}$ in the above equation represents the interaction between cations Ci and Cj when O^{2-} ions are present. This interaction is a function of temperature and composition. The presence of the function, $f(T, y_{Si^{4+}})$ in equation 9.12 is due to

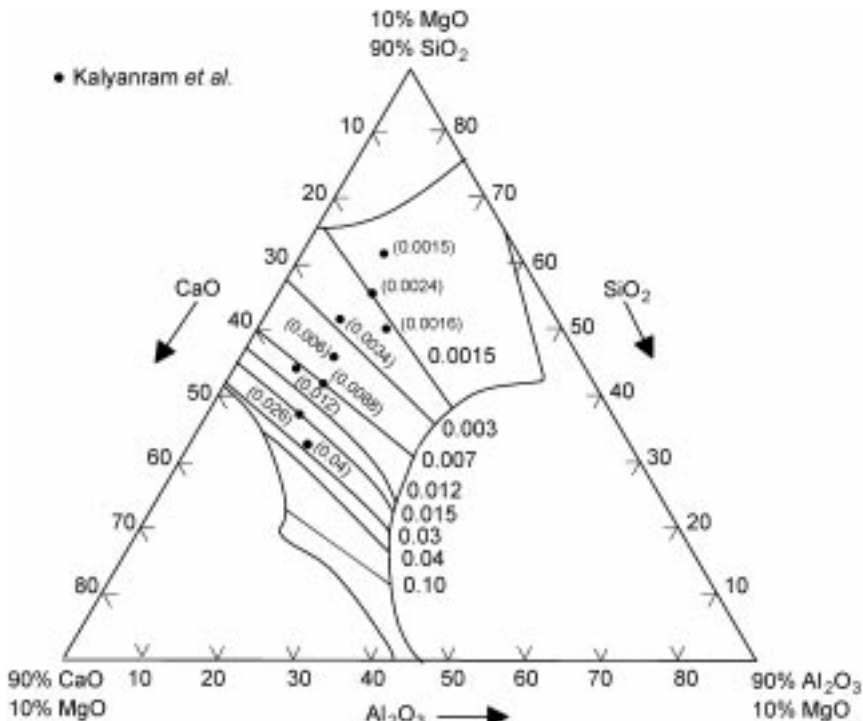
the fact that the excess Gibbs energy is not zero as the composition approaching pure SiO_2 when the hypothetical standard state for silica is adopted.^{15,16}

According to Temkin's theory,¹¹ the activity coefficient of $C_{i_{ci}O_{ai}}$ is related to the activity coefficient of the corresponding cation, $C_{i_{ci}}$, which, in turn, is expressed by the partial excess Gibbs energy of the same species:

$$\gamma_{C_{i_{ci}}O_{ai}} = \gamma_{C_{i_{ci}}}^{ci} \cdot \gamma_O^{ai} = \gamma_{C_{i_{ci}}}^{ci} = \exp \left[\frac{G_{C_{i_{ci}}^{i+}}^E}{RT} \right] \quad (9.13)$$

As an example,¹⁵ Fig. 9.3 presents the calculated CaO activities using this model at constant MgO content (mass pct $\text{MgO} = 10$) and at 1773K in the $\text{Al}_2\text{O}_3\text{-CaO-MgO-SiO}_2$ system. The experimental data by Kalyanram *et al.*¹⁷ are also included for comparison. Considering the extremely low activity values, the agreement between the values predicted by the model and the experimental results can be considered reasonable.

The slag compositions in different industrial processes differ greatly. In Table 9.1, some typical slag compositions, relevant to the steel industry, used in the blast furnace (BF), electric arc furnace (EAF) and ladle furnace (LF) are presented. As an example of the model calculations, the effect of the

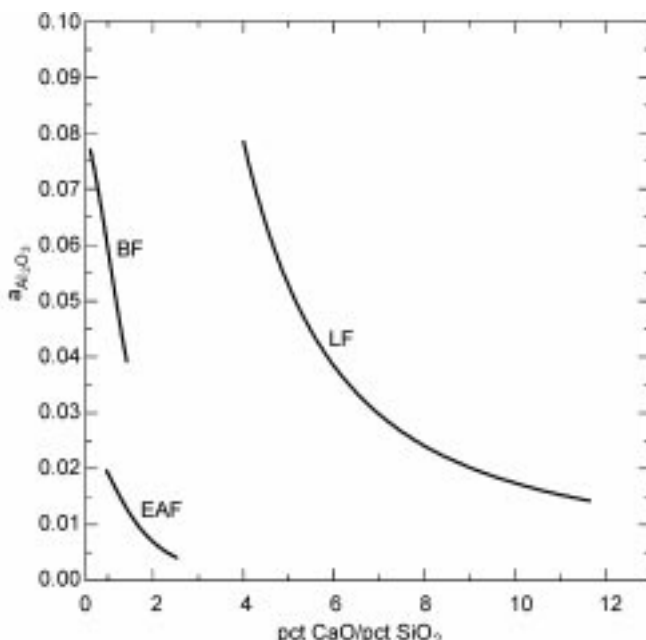


9.3 Calculated CaO activities at constant MgO content (mass pct $\text{MgO} = 10$) and at 1773K in the $\text{Al}_2\text{O}_3\text{-CaO-MgO-SiO}_2$ system.

Table 9.1 Some typical slag compositions of the electric arc furnace (EAF), blast furnace (BF), and ladle furnace (LF) processes

Oxide	Compositions in mass pct		
	EAF	BF	LF
Al ₂ O ₃	10	13	33
CaO	40	32	54
FeO	15	2	0.5
MgO	9	17	7
MnO	5	2	0.5
SiO ₂	21	34	5

replacement of SiO₂ by CaO on the activities of alumina in the case of BF, EAF and LF slags is illustrated in Fig. 9.4. In the calculation for each type of slag, the contents of the other components given in Table 9.1 were kept constant. It is seen in Fig. 9.4 that the activity of alumina is lower in the EAF slag than in the BF slag at the same mass pct CaO/mass pct SiO₂ ratio. It is also seen that an increase of the mass pct CaO/mass pct SiO₂ ratio leads to a considerable decrease of the alumina activity, irrespective of the type of the slag. However, the decrease in alumina activity with the increasing mass pct CaO/mass pct SiO₂



9.4 The effect of the replacement of SiO₂ by CaO on the activities of alumina in the case of BF, EAF and LF slags.

ratio is more profound in the case of BF and EAF slags. The substantial variations of the oxide activities with slag composition again emphasizes the importance of the thermodynamic consideration in the process design.

Solution models for liquid metal

A number of solution models are currently available. Wagner's model¹⁸ is the most commonly used one. For dilute solutions, the model describes the activity coefficient γ_i for a solute i by Taylor series,

$$\ln \gamma_i = \ln \gamma_i^o + \sum_{j=2}^N X_j \frac{\partial \ln \gamma_j}{\partial X_j} = \ln \gamma_i^o + \sum_{j=2}^N X_j \epsilon_i^{(j)} \quad (9.14)$$

In this model, the derivatives higher than first order are not considered. The reference state γ_i^o is an infinitely dilute solution with respect to the solute i . The use of only first order derivatives restricts the use of Wagner's equation to very low concentrations of the solute concerned.

In practical application, it is usually preferable to use concentration of mass per cent and the Henrian standard state. In this case, Wagner's equation is given by:

$$\ln f_i = \sum_{j=2}^N [\%_j] \frac{\partial \ln f_j}{\partial [\%_j]} = \sum_{j=2}^N [\%_j] e_i^{(j)} \quad (9.15)$$

The relationship between $\epsilon_i^{(j)}$ and $e_i^{(j)}$ is

$$\epsilon_i^{(j)} = \frac{230 e_i^{(j)} M_j}{M_{solv}} + \left(1 - \frac{M_j}{M_{solv}} \right) \quad (9.16)$$

where M_j and M_{solv} are the atomic weight for component j and for the solvent.

To extend the model calculation to higher concentrations, second-order interaction parameters have been adopted by Lupis and Elliot.¹⁹ However, only a limited number of interaction parameters higher than first order is available.

A number of models have been developed on the basis of Wagner's model. For example, Pelton and Bale^{20,21} have proposed the Unified Interaction Parameter Model (UIPM) taking into consideration the influence of the solvent. Harja *et al.*²² have modified Wagner's method for ternary systems by using boundary conditions that apply to concentrated solutions. The same method has later been adopted by Ma, Ohser and Janke,²³ but has been extended to a multicomponent system. While these models have been found to have improved performance in the case of concentrated solutions, the lack of the model parameters has in many cases limited the use of these models.

Other types of solution models are also available in the literature. Since the present chapter is to introduce the use of the solution model in process design, it is not going to list all the thermodynamic models. Interested readers may find them in the literature.^{18–27}

9.3.2 Mass balance constraints

Although in many processes, the system would not reach thermodynamic equilibrium, a thorough thermodynamic evaluation is still necessary to examine the limit of the reaction. In a heterogeneous process, equilibrium is usually reached by the fluxes of the involved elements from one phase to another by interface reactions. Hence, mass balance must be taken into account along with the thermodynamic constraints to estimate the amounts of the raw materials required and the final compositions of the phases participating the reaction(s).

We shall take desulphurization in the ladle treatment as an example to illustrate this aspect. For the sake of clarity, we shall assume, at this point, that the slag composition is constant. A detailed discussion taking all the parallel reactions into consideration will be presented in the next section.

The desulphurization can be expressed by the equation:

$$[S]_{\text{metal}} + (O^{2-})_{\text{slag}} = [O]_{\text{metal}} + (S^{2-})_{\text{slag}} \quad (9.17)$$

The ability of a slag to take up sulphur from a metallic phase is often expressed as sulphide capacity, C_S , which is defined as:²⁸

$$C_S = (\text{mass \% } S) \sqrt{\frac{P_{O_2}}{P_{S_2}}} \quad (9.18)$$

where P_{O_2} and P_{S_2} are the partial pressures of oxygen and sulphur gases prevailing in the adjacent of the slag phase. In the case of slag–metal reaction, P_{O_2} and P_{S_2} are related to the activities of oxygen and sulphur in the liquid metal through the following reactions:



The sulphur partition ratio, L_S is related to the sulphide capacity by the following relationship:

$$L_S = \frac{(\text{mass \% } S)_{\text{slag}}}{[\text{mass \% } S]_{\text{metal}}} = C_S \frac{f_S K_{19}}{a_O K_{20}} \quad (9.21)$$

where a_O and f_S are the activity of oxygen and activity coefficient of sulphur in the liquid metal, respectively. K_{19} and K_{20} in equation 9.21 stand for the equilibrium constants of reactions 9.19 and 9.20. The equilibrium constants K_{19} and K_{20} are well established for liquid iron and can be found in the literature.²⁹ If the values of a_O and f_S are known, the partition of sulphur between the slag and metal can be evaluated on the basis of the sulphide capacity of the slag using equation 9.21. For simplicity, we could assume the slag composition as well as a_O and f_S are constant. It should be pointed out that the composition of the slag, a_O and f_S in the metal would vary. These variations will be considered in the

next section. Our task at this point is to estimate preliminarily the amount of slag required to bring down the initial sulphur content in the liquid metal, $[mass\%S]_{metal,0}$ to the desired value, $[mass\%S]_{metal,\infty}$ when the slag composition is known.

Usually, the slag having an initial sulphur concentration $(mass\%S)_{slag,0}$ is not in thermodynamic equilibrium with the metal with respect to sulphur. The chemical potential difference will drive the flux of sulphur from metal to slag to satisfy equation 9.21,

$$L_S = \frac{(mass\%S)_{slag,0} + \Delta(mass\%S)_{slag}}{[mass\%S]_{metal,0} - \Delta[mass\%S]_{metal}} = C_S \frac{f_S K_{19}}{a_O K_{21}} \quad (9.21')$$

To maintain the mass balance, $\Delta(mass\%S)_{slag}$ is related to $\Delta[mass\%S]_{metal}$ by the following equation:

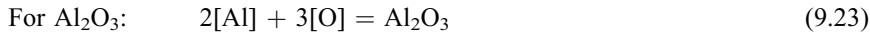
$$\Delta[mass\%S]_{metal} \frac{W_{metal}}{100} = \Delta(mass\%S)_{slag} \frac{W_{slag}}{100} \quad (9.22)$$

where W_{metal} and W_{slag} are the weight of the liquid metal and the slag, respectively. Using equations 9.21' and 9.22, one can estimate the value of W_{slag} on the basis of the sulphide capacity, C_S (assuming a_O and f_S are known).

In some cases, the industry would want to find a suitable slag composition with a desired amount of slag. In such case, one can evaluate the sulphide capacity using equations 9.21' and 9.22. The range of the slag composition can be determined using the sulphide capacity models³⁰⁻³² on the basis of the evaluated C_S . In fact, it is very often a compromising procedure to determine the amount and the composition of the slag in most of the practices.

9.3.3 Thermodynamics and mass balance in ladle treatment

In order to further demonstrate the principle of the consideration of thermodynamic constraints and mass balance in detail, we shall discuss this aspect in the case of ladle treatment. In the previous section, the slag composition was assumed constant. In a real industrial practice, slag composition changes with time mostly because of the deoxidation and the corrosion of the refractory lining. In addition to the variation of the slag composition, the concentrations of the dissolved elements in the liquid metal also vary with time. To account for the composition changes of both liquid metal and slag, all the parallel chemical reactions should be considered simultaneously. Let us take the deoxidation by aluminium addition as an example to illustrate how mass balance should be considered. Ladle slag usually contains Al_2O_3 , CaO , FeO , MgO , MnO and SiO_2 . Since the solubilities of Mg and Ca in the liquid iron are very low,³³ their fluxes from one phase to another would not affect the mass balance with respect to oxygen appreciably. Hence, the following reactions should be considered in the design of a process.



The addition of Al would not only change the concentration of aluminium in the liquid metal and disturb the equilibrium of reaction 9.23, but also disturb the equilibriums of the reactions 9.24 to 9.26. To reach a new equilibrium between the slag and metal, the fluxes of Al, Fe, Mn, Si and O are generated. These fluxes would result in the concentration changes, $\Delta X_{\text{Al}_2\text{O}_3}$, ΔX_{FeO} , ΔX_{MnO} and ΔX_{SiO_2} in the slag as well as concentration changes, $\Delta[\text{mass\%Al}]$, $\Delta[\text{mass\%Fe}]$, $\Delta[\text{mass\%Mn}]$, $\Delta[\text{mass\%Si}]$, and $\Delta[\text{mass\%O}]$ in the liquid metal. To maintain the mass balance and the thermodynamic equilibrium, the following relationships must be kept.

$$K_{\text{Al}_2\text{O}_3} = \frac{\gamma_{\text{Al}_2\text{O}_3} ({}^0X_{\text{Al}_2\text{O}_3} + \Delta X_{\text{Al}_2\text{O}_3})}{f_{\text{Al}}^2 ({}^0[\text{mass\%Al}] - \Delta[\text{mass\%Al}])^2 \cdot f_O^3 ({}^0[\text{mass\%O}] - \Delta[\text{mass\%O}]^3)} \quad (9.27)$$

$$K_{\text{FeO}} = \frac{\gamma_{\text{FeO}} ({}^0X_{\text{FeO}} + \Delta X_{\text{FeO}})}{f_{\text{Fe}} ({}^0[\text{mass\%Fe}] - \Delta[\text{mass\%Fe}]) \cdot f_O ({}^0[\text{mass\%O}] - \Delta[\text{mass\%O}])} \quad (9.28)$$

$$K_{\text{MnO}} = \frac{\gamma_{\text{MnO}} ({}^0X_{\text{MnO}} + \Delta X_{\text{MnO}})}{f_{\text{Mn}} ({}^0[\text{mass\%Mn}] - \Delta[\text{mass\%Mn}]) \cdot f_O ({}^0[\text{mass\%O}] - \Delta[\text{mass\%O}])} \quad (9.29)$$

$$K_{\text{SiO}_2} = \frac{\gamma_{\text{SiO}_2} ({}^0X_{\text{SiO}_2} + \Delta X_{\text{SiO}_2})}{f_{\text{Si}} ({}^0[\text{mass\%Si}] - \Delta[\text{mass\%Si}]) \cdot f_O^2 ({}^0[\text{mass\%O}] - \Delta[\text{mass\%O}]^2)} \quad (9.30)$$

In these equations, the superscript ‘0’ on the left side of each concentration denotes the concentration before aluminium addition, γ and f stand for the activity coefficient of the oxide in the slag and the activity coefficient of the element in the liquid metal, respectively.

The concentration change of an element in the metal is related to the mole fraction change of its oxide in the slag,

$$\Delta X_{\text{Al}_2\text{O}_3} = \frac{\rho_{\text{metal}} \cdot V_{\text{metal}}}{\rho_{\text{slag}} \cdot V_{\text{slag}}} \cdot \frac{{}^0M_{\text{slag}}}{100} \cdot \frac{1}{2 \cdot M_{\text{Al}}} \cdot \Delta[\text{mass\%Al}] \quad (9.31)$$

$$\Delta X_{\text{FeO}} = \frac{\rho_{\text{metal}} \cdot V_{\text{metal}}}{\rho_{\text{slag}} \cdot V_{\text{slag}}} \cdot \frac{{}^0M_{\text{slag}}}{100} \cdot \frac{1}{M_{\text{Fe}}} \cdot \Delta[\text{mass\%Fe}] \quad (9.32)$$

$$\Delta X_{\text{MnO}} = \frac{\rho_{\text{metal}} \cdot V_{\text{metal}}}{\rho_{\text{slag}} \cdot V_{\text{slag}}} \cdot \frac{{}^o M_{\text{slag}}}{100} \cdot \frac{1}{M_{\text{Mn}}} \cdot \Delta[\text{mass\%Mn}] \quad (9.33)$$

$$\Delta X_{\text{SiO}_2} = \frac{\rho_{\text{metal}} \cdot V_{\text{metal}}}{\rho_{\text{slag}} \cdot V_{\text{slag}}} \cdot \frac{{}^o M_{\text{slag}}}{100} \cdot \frac{1}{M_{\text{Si}}} \cdot \Delta[\text{mass\%Si}] \quad (9.34)$$

In the above equations, ρ_{metal} and V_{metal} are the density and volume of the metal; ρ_{slag} and V_{slag} are the density and volume of the slag, ${}^o M_{\text{slag}}$ is the mole weight of the slag. It is noted that the concentration change of oxygen is due to the reactions 9.23 to 9.26. Hence,

$$\begin{aligned} \Delta[\text{mass\%O}] &= \frac{3}{2} \cdot \frac{M_O}{M_{\text{Al}}} \cdot \Delta[\text{mass\%Al}] + 2 \cdot \frac{M_O}{M_{\text{Si}}} \cdot \Delta[\text{mass\%Si}] \\ &\quad + \frac{M_O}{M_{\text{Mn}}} \cdot \Delta[\text{mass\%Mn}] + \frac{M_O}{M_{\text{Fe}}} \cdot \Delta[\text{mass\%Fe}] \end{aligned} \quad (9.35)$$

where, M_i stands for the molar weight of the element i .

In order to calculate the slag composition and steel composition at equilibrium, equations 9.27 to 9.35 should be solved simultaneously. While the activity coefficients of the oxides can be evaluated using the thermodynamic model for ionic melts developed at KTH,^{15,16} Wagner's model¹⁸ could be employed to calculate the activity coefficients of the dissolved elements in the liquid metal. It should be pointed out that the use of the KTH model and Wagner's model is only an example. The readers could also use other thermodynamic models for the slag and metal. However, the principle of the calculation would be the same.

One could also take the desulphurization into consideration by including equations 9.21' and 9.22. Consequently, one more term corresponding to sulphur should be included in equation 9.35:

$$\begin{aligned} \Delta[\text{mass\%O}] &= \frac{3}{2} \cdot \frac{M_O}{M_{\text{Al}}} \cdot \Delta[\text{mass\%Al}] + 2 \cdot \frac{M_O}{M_{\text{Si}}} \cdot \Delta[\text{mass\%Si}] \\ &\quad + \frac{M_O}{M_{\text{Mn}}} \cdot \Delta[\text{mass\%Mn}] + \frac{M_O}{M_{\text{Fe}}} \cdot \Delta[\text{mass\%Fe}] - \frac{M_O}{M_S} \cdot \Delta[\text{mass\%S}] \end{aligned} \quad (9.36)$$

This practice is very important for the design and even the optimization of the ladle treatment. For instance, in many steel plants, EAF slag is tapped into the ladle along with the molten steel. In the EAF slag, the FeO content is usually very high. One would always face the choice regarding when aluminium should be added for deoxidation. A calculation as discussed in this section would reveal that Al should definitely be added after the deslagging procedure. Big amount of Al added to the ladle in the presence of the EAF slag would contribute mostly to reduce the FeO in the slag and therefore help very little to reduce the oxygen activity in the liquid metal.

9.4 Kinetics – mass transfer and heat transfer

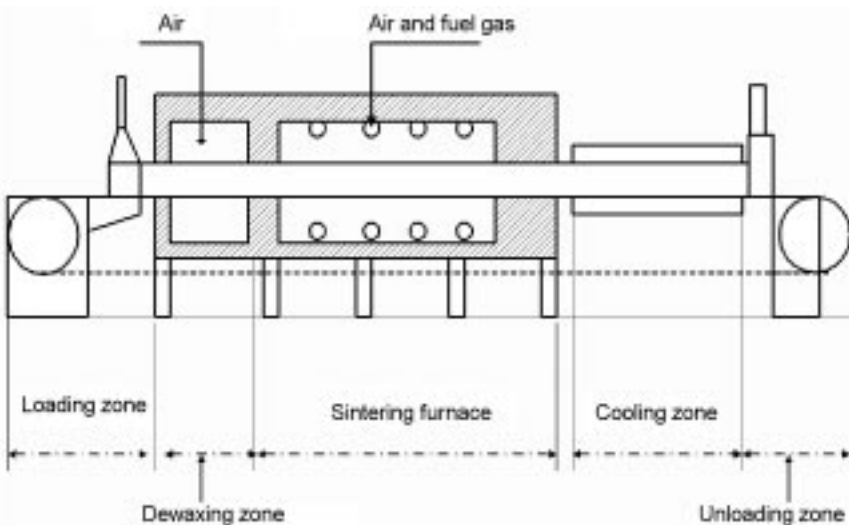
Very often, a process is far from thermodynamic equilibrium. While a thermodynamic analysis would reveal the driving force of the process, a reliable estimation of the process time would require an in-depth understanding of the reaction mechanism and good knowledge of the reaction rate.

The kinetic aspects of heterogeneous reaction have been discussed in Chapter 7. In an industrial process, the situation would be much more complicated. To elaborate the discussion, the sintering process in a belt furnace is taken as an example. Belt furnaces are widely used in metallurgical industries, particularly for sintering process.^{34,35} Figure 9.5 presents the schematic diagram of a typical gas fired belt furnace unit. It consists of a continuous sintering furnace with a preheating zone, a few metres of sintering zone and a cooling zone. The unit is also equipped with a conveyance system driven by a driving unit. In the case of sintering, the temperature profile in the furnace plays a crucial role. For instance, too high temperature during initial part of sintering cycle could lead to premature release of the binder and increased porosity. During the cooling part of the cycle, the temperature needs to be well controlled to avoid undesired reactions, e.g. reoxidation. To design the process, the following considerations must be made.

1. Mass transfer

The mass transfer can further be divided into three steps:

- Mass transfer in each individual particle of the sintered material.
- Mass transfer of the gas through the bed of the sintered material.
- Mass transfer in the gas phase.



9.5 Schematic diagram of a typical gas-fired belt furnace unit.

2. Heat transfer

As in the case of mass transfer, the heat transfer may also be divided into three steps:

- (a) Heat transfer in each individual particle of the sintered material.
- (b) Heat transfer through the bed of the sintered material.
- (c) Heat transfer in the gas phase.

3. Chemical reactions within the individual particle.

4. Chemical reactions between the gas and solid particles.

5. Possibly, chemical reactions in the gas phase.

While mass transfer and heat transfer depend very much on the fluid flow of the gas, they also depend on the temperature profile. On the other hand, the temperature distribution, in turn, is influenced by the mass transfer and heat transfer. The situation is further complicated by the presence of the chemical reactions, as any chemical reaction would affect both the mass balance and heat balance. Hence, a reasonable process design should take all the factors into consideration. Fortunately, with the advance of the modern computer technology, this kind of comprehensive consideration is becoming more and more practically possible.

In some cases, the rate of a process is controlled by only one or a number of steps. The dehydrogenation process in ladle treatment is one of such examples. The process consists of a number of steps, namely:

1. Transport of dissolved hydrogen in the liquid metal to the surface of the gas bubble.
2. Interface reaction including the formation of H₂ gas and its desorption.
3. Transport of H₂ gas from the gas–metal interface.

When a ladle is purged by argon gas, the mass transfer in the gas bubbles is a fast process.³⁶ Usually, vacuum treatment in combination with argon-purging is carried out after deoxidation of the steel. The oxygen level is very low at this stage. Since the occupation of the oxygen atoms on the bubble surface is not appreciable, the interface reaction including the formation of H₂ gas and its desorption is also fast. The enthalpy change associated with the interfacial reaction would not substantially affect the temperature at the steel–bubble interface. Hence, the dehydrogenation process is mostly controlled by the hydrogen transfer in the liquid metal. Nowadays, the velocity distribution in an argon stirred ladle can be calculated by computerised fluid dynamic (CFD) with acceptable accuracy. Utilising the CFD results, one can estimate the circulation of the flow and therefore the hydrogen concentration in the vicinity of the argon gas plume. In the gas–metal mixing region, local equilibriums are established at different vertical positions. The moles of H₂ gas carried away by the bubbles per second at location *i* can be estimated by

$$\left(\frac{dn_{H_2}}{dt}\right)_{i,local} = -\frac{1}{2} \left(\frac{dn_H}{dt}\right)_{i,local} = -\frac{1}{2} \frac{d[mass\%H]_{i,local}}{dt} \frac{m_{Fe(i,local)}}{100 \cdot M_H} \quad (9.37)$$

$m_{Fe(i,local)}$ in equation 9.37 is the mass of iron, which could be associated to a control volume. Since hydrogen is carried away by argon,

$$\left(\frac{dn_{H_2}}{dt}\right)_{i,local} = \frac{\dot{n}_{Ar(i,local)}}{60 \cdot 22.4} X_{H_2} \quad (9.38)$$

where $\dot{n}_{Ar(i,local)}$ is the volume flow rate of argon at location i . The local equilibrium leads to,

$$K_1 = \frac{P_{H_2}}{[mass\%H]_{i,local}^2} = \frac{P_{total(i,local)} \cdot X_{H_2(i,local)}}{[mass\%H]_{i,local}^2} \quad (9.39)$$

inserting 9.39 in 9.38,

$$\left(\frac{dn_{H_2}}{dt}\right)_{i,local} = \frac{\dot{n}_{Ar(i,local)}}{60 \cdot 22.4} \cdot \frac{K_1}{P_{total(i,local)}} \cdot [mass\%H]_{i,local}^2 \quad (9.40)$$

The combination of 9.37 and 9.40 gives

$$\begin{aligned} \left(\frac{dn_{H_2}}{dt}\right)_{i,local} &= \frac{\dot{n}_{Ar(i,local)}}{60 \cdot 22.4} \cdot \frac{K_1}{P_{total(i,local)}} \cdot [mass\%H]_{i,local}^2 \\ &= -\frac{1}{2} \frac{d[mass\%H]_{i,local}}{dt} \frac{m_{Fe(i,local)}}{100 \cdot M_H} \end{aligned} \quad (9.41)$$

The use of this equation along with the results of the mass transfer in the bulk of liquid metal would be able to predict the dehydrogenation process with an acceptable accuracy. The predicted dehydrogenation time would be very valuable in the process design with respect to hydrogen refining.

9.5 Optimization of interfacial reactions

Metallurgical processes are very often heterogeneous in nature. Most of the reactions take place at the interfaces. While it is a common knowledge that optimization of the interfacial reactions plays a crucial role in the design of a process, the lack of in-depth understanding of the interface is very often an obstacle for the optimization. Recently, more and more attention has been drawn to the studies of interfaces.

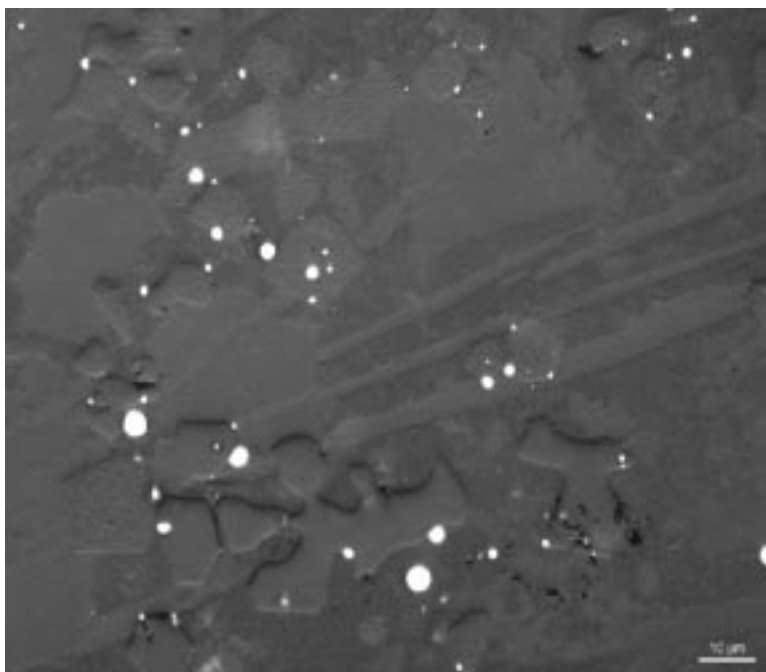
In fact, the optimization of interfacial reaction would essentially rely on the precision of the description of the interface. Since different processes involve different types of interfaces, it is impossible to discuss all of them. The present section will take some examples to illustrate the consideration of the interfaces.

9.5.1 Slag–metal mixing

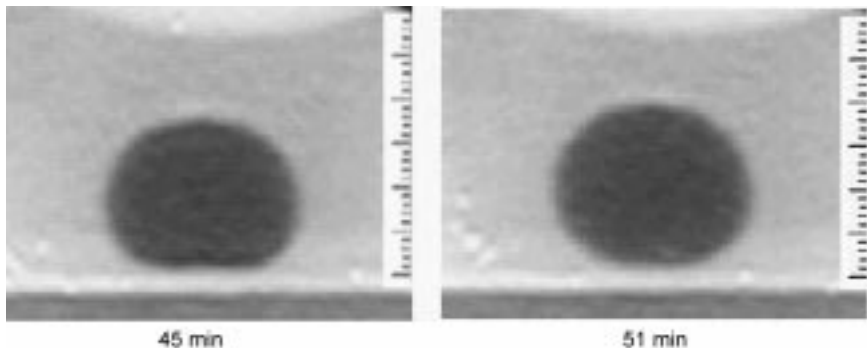
In steelmaking, slag–metal mixing is a very common phenomenon and it occurs due to the shear at the slag–metal interface caused by excessive liquid steel flow.³⁷ This mixing leads to emulsification of steel in slag, which increases the total interfacial area and consequently the rate of slag–metal reactions.

The factors that affect the emulsification are slag layer thickness (or slag volume), velocity of the liquid flow and the fluid properties like viscosity, density and interfacial tension.³⁷

It is found by a cold model study³⁸ that slag–metal mixing takes place only when a critical velocity (along the interface) is achieved. Below this velocity, flow is streamlined and no mixing is possible. The value of the critical velocity would depend on the properties of both liquids, namely density, viscosity and interfacial tension. It is interesting to point out that when a mixing flow is stabilized, the fraction of water in the oil–water mixing zone is very small, only a few percents. In a stabilized mixing layer, oil becomes small spherical droplets. Surrounding each oil droplet, a thin water film is formed. These oil droplets tightly packed together, so that water occupies only the voids of the drops. The amount of water in the films surrounding the oil droplets and in the voids is very small. This is in accordance with the observation found in a ladle. In a recent study,³⁹ the slag–metal mixing zone in a ladle was sampled and



9.6 Microphotograph of the mixing zone taken from an argon stirred ladle.



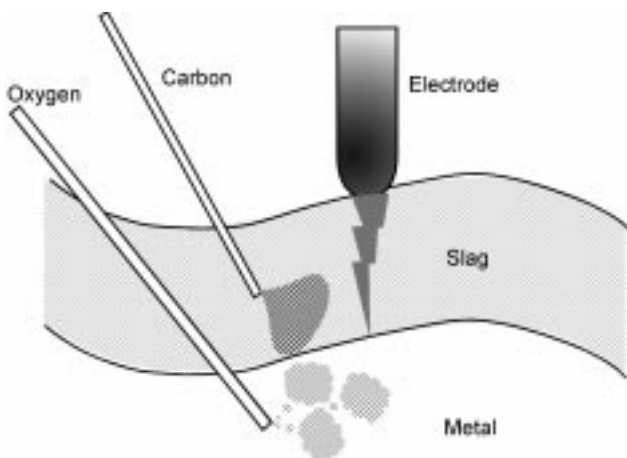
9.7 X-ray images of the iron drops surrounded by a slag in the sulphurization process.

analyzed. Figure 9.6 presents the microphotograph of the mixing zone. It is clearly seen in this figure that metal presents in the form of very fine particles. The maximum size of the metal particles is about $140\text{ }\mu\text{m}$. Chemical analysis showed that the amount of iron present in the mixing zone is about 1 per cent. The small size of the metal particles and the low content of iron in the mixing zone suggest that the metal–slag system could be very similar with the water–oil system. In the mixing zone, slag takes the form of small spherical droplets, while metal forms a film around each slag sphere. It is reasonable to expect that the size of the slag droplets and the metal film thickness would be a function of the physical properties of the two liquids as well as the flow. A mathematical description of the slag mixing is highly desired for designing the processes involving slag–metal reactions.

It should be mentioned that physical properties of both liquid metal and slag vary along the process. Consequently, the behaviour of slag–metal mixing would vary as well. In Fig. 9.7, the X-ray images of the iron drops surrounded by a slag in sulphurization process are compared.⁴⁰ The change of the contact angle due to the change of sulphur content in the metal drop is well brought out in the figure. Hence, knowledge of the variation of the physical properties in general and interfacial tension in particular would be essential in a precision design of a process.

9.5.2 Foaming

The foaming slag practice in the electric arc furnace (EAF) is nowadays a standard technique in the production of low-alloyed steels. The foam covers the electrodes and arcs and thereby enhances the heat exchange to the liquid steel and at the same time protects the refractory wear from the heat radiation. Furthermore, the surrounding slag stabilizes the electric arc. The results of creating a foaming slag in the EAF would be an increased energy efficiency and productivity, and reduced refractory wear and electrode consumption.



9.8 Slag foaming generated by carbon and oxygen injection.

In the EAF, slag foaming is generated by carbon and oxygen injection as schematically shown in Fig. 9.8. In this practice, oxygen is injected by lance into the liquid steel and thereby oxidising Fe to FeO_x . FeO_x floats up and comes into the slag phase. However, FeO_x is reduced in the next step by carbon injection into the slag. FeO_x may also react with dissolved carbon in the metal phase. In both cases, CO gas is formed. When the rate of CO generation is high enough and the physical properties of the slag favour the residence of the small gas bubbles in the slag, foam is generated.

The most important physical properties of slag with respect to foaming are the viscosity, surface tension and density. These physical properties are directly dependent on the slag composition and temperature. The optimum amount of FeO_x in the slag normally lies in the range of 15–25 per cent.⁴¹ The relatively large FeO_x content and the fact that the reduction rate of FeO_x with carbon is relatively high make the slag foaming practice in low-alloyed steel production an easily controlled process.

On the other hand, difficulties have been encountered to control the slag forming in stainless steel production. It is difficult to obtain sufficient foaming and at the same time avoid chromium oxidation. This difficulty could be due to (i) the low reduction rate of chromium oxide, (ii) the precipitation of chromium oxide particles, which will not only affect the fluidity of the slag but also the interfacial situation, and (iii) the variations of the physical properties of the slag.

Generating slag foam implies a creation of a huge surface area between slag and CO gas. A stabilized foam would also require a sufficient long residence time of the gas bubbles in the slag. Unless the interfacial phenomena between slag and gas are well understood, optimum operation parameters can not be obtained. This is true in both process design and process optimization.

9.5.3 Denitrogenation

Denitrogenation is a common practice in both AOD converter and ladle refining to produce steels of appropriate nitrogen contents. For this purpose, the liquid steel is usually purged by argon gas. Knowledge of the denitrogenation rate is extremely important in determining the process time and argon flow.

The denitrogenation process involves a number of steps, namely:

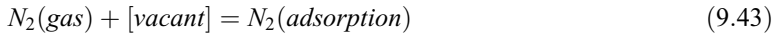
1. Transport of dissolved nitrogen in the liquid metal to the surface of the gas bubble.
2. Interface reaction including the formation of N₂ gas and its desorption.
3. Transport of N₂ gas from the gas–metal interface.

It is well known that the surface active elements in the iron, e.g. oxygen and sulphur significantly decrease the rate of interface reaction. This effect is found to be almost identical in adsorption and desorption processes. Hence, it is necessary to take the nitrogen desorption into consideration in designing or optimization of the process.

Nitrogen is only slightly surface active on liquid iron.⁴² The surface sites are either vacant or occupied by oxygen or sulphur. The number of unoccupied sites on the surface is

$$\phi_{vacant} = 1 - \phi_O - \phi_S \quad (9.42)$$

In the case of adsorption, the interface reaction can be expressed as:



The rate of adsorption would be proportional to the nitrogen pressure and the number of sites available for nitrogen molecules,

$$\frac{dn_{N_2}}{dt} \propto \phi_{vacant} \cdot P_{N_2} = (1 - \phi_O - \phi_S)P_{N_2} \quad (9.44)$$

The adsorption phenomena and adsorption isotherms have been discussed in detail in Chapter 4. The readers can get help in that chapter regarding the descriptions of ϕ_O and ϕ_S . In the case of high coverage with oxygen, the number of unoccupied sites on the surface is inversely proportional to the concentration of oxygen in the melt. Consequently, the rate of adsorption (or desorption) of nitrogen would be inversely proportional to the oxygen concentration in the liquid iron,

$$\frac{dn_{N_2}}{dt} \propto \frac{P_{N_2}}{[mass\%O]} \quad (9.45)$$

9.5.4 Effect of interfacial energy on the separation of inclusions by bubble floatation

The standard of steel cleanliness has continuously been changing with time and technological improvements. Controlling the non-metallic inclusion population

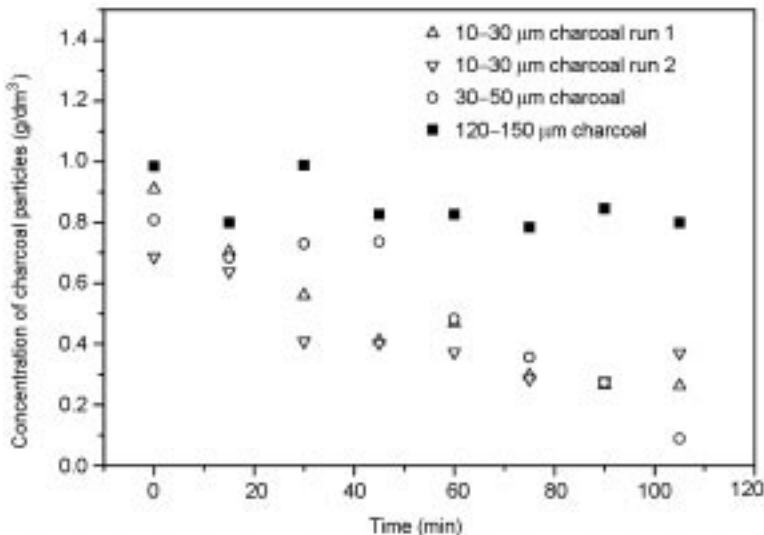
has become a serious concern of the steel producers. Inclusions could be separated from the steel melt by a number of mechanisms, viz. separation to the slag by buoyancy force, attachment to the refractory wall and floatation by attaching on the gas bubbles. In all these mechanisms, interfacial phenomena play a crucial role. To demonstrate this aspect, we will take the inclusion separation by bubble floatation as an example.

Inclusion removal by injecting gas through the liquid steel has since long been a matter of interest of many researchers. Since the introduction of floatation coefficient,⁴³ this concept has been used by many researchers to determine whether a type of solid particles or liquid drops can be captured by the rising gas bubbles and separated from the liquid in a liquid–particle (or drop)–gas system. The floatation coefficient is defined as

$$F = \gamma_{lg} - \gamma_{pg} + \gamma_{pl} \quad (9.46)$$

where γ_{lg} , γ_{pg} and γ_{pl} stand for the surface tension of the liquid, surface tension of the dispersed phase and the interfacial tension between the dispersed phase and liquid, respectively. A necessary condition for the attachment of the dispersion phase to the gas bubbles would be a positive F .

While a positive floatation coefficient is a necessary condition for the separation of a dispersed phase from the bulk phase by gas bubbles, it is not a sufficient condition. The insufficiency of this condition has been demonstrated by the results of the charcoal–water–gas system.⁴⁴ The concentrations of charcoal in the deionized water are plotted as functions of time for four experiments in Fig. 9.9. An initial concentration of mass content of 0.1 per cent



9.9 Concentrations of charcoal in the deionized water as functions of time for four different experiments.

charcoal was employed for all cases. While the charcoal concentrations decrease with time in the case of the small particles in the ranges 10–30 and 30–50 µm, the concentration of the charcoal particles in the size range 120–150 µm is almost constant. A flow rate of 0.41 Nl/min would pass 36.9 litres of gas in 1.5 hours through the water bath, which was only 0.8 litres.⁴⁴ It is reasonable to believe that the charcoal particles had a very high probability of meeting the gas bubbles during such a time period. The floatation coefficient of the charcoal–water–gas system is 105 mN/m.⁴⁴ If a positive floatation coefficient would ensure the attachment of the particles on the bubbles, most of the particles would have been removed from the bath. The controversy between the experimental observation and the floatation coefficient evidently demonstrates that the floatation coefficient is only a necessary but not a sufficient condition for separation of particles or drops from the bulk liquid by gas bubbles.

In order to predict the removal of inclusions having particle sizes at µm level from steel, new models taking into account interfacial energies, drag force, buoyancy force and gravity force are needed.

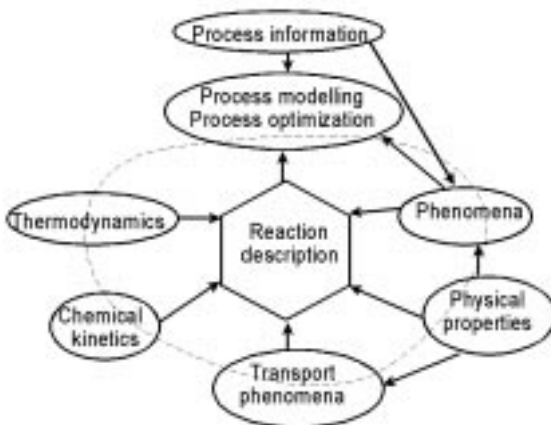
9.6 Micro-modelling

Mathematical modelling of process is no longer only an academic exercise nowadays. With the advance of computer technology, modelling has become more and more a powerful tool for process design and optimization.

Modelling of materials processes requires a fundamental understanding of the process based on thermodynamics, transport phenomena and kinetics of the steps involved. This aspect has been discussed in detail in the previous sections. While a traditional thermochemical model often lacks the input from kinetics and transport phenomena, computerized fluid dynamic (CFD) models often lack a thermodynamic and kinetic basis. Furthermore, CFD models need accurate input of thermophysical data, such as the viscosities of the various molten phases and the interfacial tensions, to generate reliable mapping of flow patterns in reactors.

Futuristic process models, referred to as ‘macro-models’ should be structured using the reaction models that are parts of the gross process. Such reaction models referred to as ‘micro-models’ may be advantageously used as building blocks. The micro-models, in fact, are reaction descriptions based on experimental thermochemical and kinetic information. The latter needs to be complemented by thermophysical data, essentially to describe the heat transfer and mass transfer phenomena involved. The philosophy underlying this is illustrated in Fig. 9.10.

To further elaborate this aspect, the sulphur refining in ladle treatment is taken as an example.⁴⁵ Conventionally, the two-film theory has been used for many decades to describe the slag–metal reactions. When using this theory, a mass-transfer coefficient is employed to describe the rate of the overall reaction

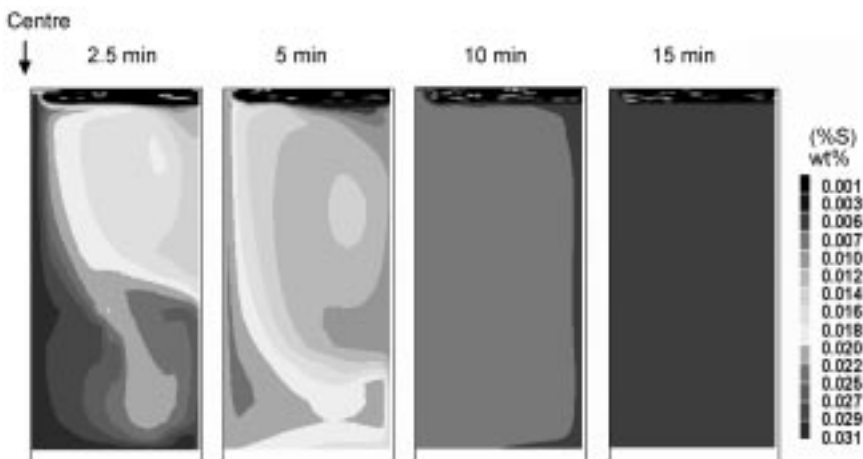


9.10 Philosophy underlying the micro-modelling approach.

between slag and metal. It utilizes an artificial interfacial area on the basis of the assumption of a flat interface between slag and metal. However, it is well known that in most steelmaking processes when gas stirring is applied, liquid metal becomes entrapped in the slag phase, forming a slag–metal mixing zone.^{38,45} The exchange rate between slag and metal in this mixing zone is enormous. In view of the unrealistic nature of the two-film theory when applied to ladle treatment, a new attempt is made using micro-modelling approach⁴⁵ to describe the desulphurization process in ladle refining.

In the model construction, a number of micro-model blocks (see Fig. 9.10) are taken into account.

1. *Thermodynamic block.* The Al_2O_3 activity in the slag is calculated using the IRSID model.^{7,45} The sulphide capacity of the slag is evaluated using the model developed at KTH.^{15,16} The activities of various elements in the liquid metal are calculated using the dilute-solution model.¹⁸
2. *Physical property block.* While most of the physical properties are taken from the handbooks, the viscosity of the slag is evaluated using KTH model.⁴⁶
3. *Transport block.* The fluid flow, mass transfer and heat transfer are described by corresponding conservation equations and calculated by using the commercial CFD code, Phoenics. In the model, the $k-\epsilon$ model is adopted to simulate the turbulence.⁴⁷
4. *Phenomenon block.* Ladle treatment involves both gas–metal reaction and slag–metal reaction. The models for the flows of gas–metal as well as slag–metal are incorporated in the CFD model. Interested readers can find the details in the published papers.⁴⁵
5. *Kinetic block.* In view of the high process temperature, the chemical reaction at the slag–metal interface, (in the mixing zone in the present



9.11 Change of sulphur concentration in steel during refining, when 80 l/min argon gas is injected into 100 tons of steel.

case) is considered to be very fast, so that thermodynamic equilibrium is established locally and dynamically in the slag–metal mixing zone. By considering the volume of mixing between slag and metal and the thermodynamic equilibrium in the two-phase zone, the calculations of interfacial area and the mass-transfer coefficients for different elements are avoided.

Figure 9.11 shows the change of sulphur concentration in steel during refining, when 80 l/min argon gas is injected into 100 tons of steel. Argon is injected through a centrally located porous plug in the bottom of the ladle. Since the ladle is axially symmetric, only half of the ladle is shown in the two-dimensional plane in Fig. 9.11. When argon is injected, it lifts the steel up towards the upper part of the ladle due to buoyancy forces. At the steel–slag interface, the flow is directed towards the ladle wall. In the steel–slag region, instability is created, which causes the steel and slag to mix and enhances the sulphur refining reaction. This reaction continues as long as the volume element of steel is transported along the steel–slag interface. Therefore, the steel close to the ladle wall in the upper part of the ladle contains less sulphur than the steel bulk at the beginning of the sulphur refining operation. From the figure, it is also possible to see that the fluid flow along the ladle wall causes steel of a lower sulphur content to be transported down into the bulk of the steel, where it is mixed with steel containing a higher sulphur content. After about 10 minutes, sulphur is rather homogeneously distributed in the ladle. The predicted sulphur content in the steel for this case is 0.007 wt% to 0.008 wt% after 15 minutes of gas-stirring. Actual plant data for a 15-minute gas-stirring period with the same gas flow gives a sulphur content of 0.005 wt% to 0.010 wt%. However, it is very difficult

in a plant situation to know if the gas flow is constant during injection. Very often gas leaks out through cracks in the refractory, etc. It should also be pointed out that the phenomenon model employed in this approach for the slag–metal mixing⁴⁵ should only be considered very preliminary. It requires further improvement on the basis of rigorous theoretical consideration and experimental verification. However, the comparison shows that by building the process model of a gas-stirred ladle using the micro-models as building blocks, it is possible to predict desulphurization with acceptable accuracy.

9.7 Conclusions

In this chapter, the principal factors in process design have been briefly discussed. The focus has been given to the theoretical consideration. However, this consideration is far from sufficient. Very often, a lot of phenomena in the process are poorly understood. It is also very common that the thermodynamic data are missing or subjected to larger uncertainties. Even the physical properties and kinetic data are not available in many occasions. The unavailability (or/and the uncertainty) of the basic data would hinder us from finding out the optimum solutions. When, inevitably, we hit the wall of our understanding, experimental investigations must be carried out. These investigations should include (i) laboratory experiments, (ii) physical model experiments, (iii) pilot plant experiments, and finally (iv) industrial experiments. Interested readers should read the corresponding chapters in the book and other literature to prepare their knowledge for a promising process design.

9.8 References

1. Toop GW and Samis CS, ‘Activities of ions in silicate melts’, *Trans. TMS-AIME*, 1962, **224**, 878–887.
2. Masson CR, ‘Thermodynamics and constitution of silicate slags’, *J. Iron Steel Inst.*, 1972, **210**, 89–96.
3. Masson CR, Smith IB and Wihiteway SG, ‘Activities and ionic distributions in liquid silicates: application of polymer theory’, *Can. J. Chem.*, 1970, **48**, 1456–1464.
4. Lin PL and Pelton AD, ‘A Structural Model for Binary Silicate Systems’, *Metall Trans B*, 1979, **10**, 667–675.
5. Jeffes JHE, ‘The relationship of structure and thermodynamic properties of polyanionic compounds’, *Canadian Met. Quart.*, 1981, **20**, 37–50.
6. Kapoor ML and Frohberg MG, *Int. Metallurgical Chemistry – Applications in Ferrous Metallurgy*, Sheffield, July 1971, Iron Steel Inst., 17–23.
7. Gaye H, Riboud BA and Welfringer J, ‘Slag Modelling: a Tool for Evaluating Metallurgical Treatments’, *Process Technology Proceedings*. Vol. 6; Washington, DC, USA, 6–9 April, 1986, 631–639.
8. Hillert M, Jansson B, Sundman B and Ågren J, ‘A Two-Sublattice Model for Molten Solutions With Different Tendency for Ionization’, *Metall. Trans. A*, 1985, **16A**, 261–266.

9. Selleby M, 'An assessment of the Ca-Fe-O-Si system', *Metall. Trans. B*, 1997, **28B**, 577–596.
10. Pelton AD and Blander M, 'Thermodynamic Analysis of Ordered Liquid Solutions by a Modified Quasichemical Approach – Application to Silicate Slags', *Metall. Trans B*, 1986, **17B**, 805–815.
11. Temkin M, 'Mixtures of fused salts and ionic solutions', *Acta Phys. Chim. URSS*, 1945, **20**, 411–420.
12. Lumsden J, *Physical Chemistry of Process Metallurgy, Part 1*, New York, Interscience, 1961, 165–205.
13. Sommerville ID, Ivanchev I, Bell HB, *Int. Metallurgical Chemistry – Applications in Ferrous Metallurgy*, Sheffield, July 1971, Iron Steel Inst., 23–25.
14. Ban-Ya S and Shim J-D, 'Application of the Regular Solution Model for the Equilibrium of Distribution of Oxygen Between Liquid Iron and Steelmaking Slags', *Canadian Metall. Quarterly*, 1982, **21**, 319–332.
15. Björkvall J, Sichen Du and Seetharaman S, 'Thermodynamic model calculations in multicomponent liquid silicate systems', *Ironmaking and Steelmaking*, 2001, **28**, 250–257.
16. Björkvall J, Doctoral Thesis, Department of Materials Science and Engineering, Royal Institute of Technology, Stockholm, ISSN 1403-493X, ISBN 91-7170-523-6, 24 March, 2000.
17. Kalyanram MR, Macfarlane TG and Bell HB, 'The activities of calcium oxide in slags in the systems CaO-MgO-SiO₂, CaO-Al₂O₃-SiO₂ and CaO-MgO-Al₂O₃-SiO₂ at 1500°C', *J. Iron Steel Inst.*, 1960, **195**, 58–64.
18. Wagner C, *Thermodynamics of Alloys*, Reading MA, Addison-Wesley, 1952.
19. Lupis CHP and Elliott JF, 'Generalized interaction coefficients', *Acta Metallurgica sinica*, 1966, **14**, 529–538.
20. Pelton AD and Bale CW, 'A modified interaction parameter formalism for non-dilute solution', *Metallurgical and Materials Transcription*, 1986, **17A**, 1211–1215.
21. Pelton AD, 'The polynomial representation of thermodynamic properties in dilute solution', *Metallurgical and Materials Transcription B*, 1997, **28B**, 869–876.
22. Harja JP, Reddy SR and Frohberg MG, 'Deviation and consistency of partial function of the ternary system involving interaction coefficients', *Metallurgical and Materials Transcription B*, 1995, **26B**, 495–502.
23. Ma ZT, Ohser J and Janke D, 'Thermodynamic treatment of multicomponent system using interaction parameters', *Acta metallurgica sinica*, 1997, **10**(2), 375–385.
24. Darken LS, 'Thermodynamics of binary metallic solutions', *TMS-AIME*, 1967, **239**, 80–89.
25. Reddy RG and Reddy SR, 'Thermodynamic properties of quaternary systems', *Minerals, Metals and Materials Society/AIME*, 1999, 243–253.
26. Tao DP, 'Prediction of thermodynamic properties of multicomponent liquid alloy by binary infinite dilute activity coefficients', *Metallurgical and Materials Transcription B*, 2001, **32B**, 1205–1211.
27. Guochang J and Kuagdi X, 'A discussion on thermodynamics of pyrometallurgy for ferroalloys', *China Science and Technology Press, 8th International Ferroalloys Congress Proceedings*, 1998, 290–293.
28. Richardson FD, *Physical Chemistry of Melts in Metallurgy*, vol.2, Academic Press, London, 1974, 291–296.
29. Engh TA, *Principles of Metal Refining*, Oxford University Press, Oxford, 1992, 51.

30. Nilsson R, Sichen Du and Seetharaman S, 'Estimation of sulphide capacities of multi-component silicate melts' *Scand. J. Metal.*, 1996, **25**, 128–134.
31. Young RW, Hassall GJ, Duffy JA and Xu Z, 'Use of Optical Basicity Concept for Determining Phosphorus and Sulphur Slag–Metal Partitions', *Ironmaking and Steelmaking*, 1992, **19**, 201–219.
32. Reddy RG and Blander M, 'Modeling of Sulfide Capacities of Silicate Melts', *Metall. Trans. B*, 1987, **18B**, 591–596.
33. Han Q, *Rare earth, alkaline earth and other elements in metallurgy*, 1998, Japan Technical Information Service, Tokyo, Japan, 42–55.
34. Martinez GP, 'Gas-Fired Belt Furnace Cuts Sintering Costs', *Meta Powder Report*, 1992, **47**, 31–33.
35. Saxena N, Dwyer J, Haring N, Kirschner M and Nayar H, 'Predicting part temperatures during sintering under production conditions using a simple PC-based model' Advances in Powder Metallurgy and Particulate Materials, 1996, vol. 3, Washington DC, USA, June 16–21, 1996, 12.43–12.55.
36. Brandberg J, Johansson E, Magnelöv M, Rutqvist E and Sjöström U, *Steel Grips*, *in press*, 2005.
37. Cramb AW, Chung Y, Harman J, Sharan A and Jimbo I, 'The slag/metal interface and associated phenomena. A history of pneumatic steelmaking', *Iron and Steelmaker (USA)*, 1997, **24**(3), 77–83.
38. Dayal P and Sichen Du, Unpublished work, Department of Materials Science and Engineering, Royal Institute of Technology, SE-100 44 Stockholm, 2004.
39. Beskow K, Dayal P, Björkvall J and Sichen Du, *Ironmaking and Steelmaking*, *in press*, 2005.
40. Jakobsson A, Viswanathan NN, Sichen Du and Seetharaman S, 'Interfacial phenomena in some slag–metal reactions', *Metall & Materials Trans. B*, 2000, **31B**, 973–980.
41. Görnerup M and Jacobsson H, 'Foaming Slag-Practice in Electric Stainless Steelmaking', Iron and Steel Society/AIME, 55th Electric Furnace Conference Proceedings, Chicago, USA, 1998 57–69.
42. Pehlke RD and Elliott JF, 'Solubility of nitrogen in liquid iron alloys II. Kinteica', *Trans. Metallurgical Society of AIME*, 1963, **227**, 844–855
43. Elliott JF, 'The role of interfaces in pyrometallurgical processes', *Extractive Metallurgy 85 Symposium*, London, September 1985, c171–c178.
44. Kumar J, Tripathi N and Sichen Du, 'Importance of interfacial phenomena in the removal of inclusions by gas bubbles from steel – An experimental study using cold model', *Steel Grips*, 2003, **1**, 133–139.
45. Jonsson L, Sichen Du and Jönsson P, 'A new approach to model sulphur refining in a gas-stirred ladle – a coupled CFD and thermodynamic model', *ISIJ International*, 1998, **38**, 260–267.
46. Ji F-Z, Sichen Du and Seetharaman S, 'Viscosities of multi-component silicate melts at high temperatures', *International J. of Thermophysics*, 1999, **20**, 309–322.
47. Launder BE and Spalding DB, 'The numerical computations of turbulent flows', *Comp. Meth. In Appl. Mech. & Eng.*, 1974, **3**, 269.

10.1 Introduction

The formation of solid from a liquid is an interesting phenomenon as the following issues are experimentally observed:

- The initiation of solidification requires either undercooling or supersaturation.
- Most common examples of the initiation of solidification are heterogeneous where the first solid forms on a pre-existing solid surface.
- If the pre-existing heterogeneous sites are removed from the liquid, the initiation of solidification appears in the body of the liquid and the number of observed growing crystals is a function of either undercooling or supersaturation.
- At high cooling rates in multicomponent or structurally complex liquids, glass formation occurs when the liquid is supercooled to its glass transition temperature before the onset of crystal formation. In this manner amorphous solids can be formed.
- During solidification at high cooling rates it is possible to produce metastable crystalline phases where the first phase to precipitate is not the thermodynamically most stable phase. Transition through metastable states to the stable state can often occur during the solidification process.
- After the initiation of solidification, it is common to observe the formation of cells and dendrites during the growth phase of solidification.
- Three types of solidification structure are commonly seen in castings: equiaxed, columnar and eutectic.
- Solidification structures are commonly observed to coarsen during the solidification process.
- Partitioning of elements (segregation) between the solid and the liquid is common.
- The dissipation of latent heat through the growing shell or into an undercooled liquid often controls the solidification rate in metals and leads to recalescence of the liquid and solid in undercooled growth.

- Growth rate can be controlled by atom attachment at the interface, mass transfer in the liquid, heat transfer or a mixture of these processes.
- Generally there is a volume change during solidification that leads to either porosity or swelling in castings depending upon the sign of the change.
- The process of solidification commonly causes fluid flow due to Marangoni and natural convection related to thermal and composition gradients induced during the process.

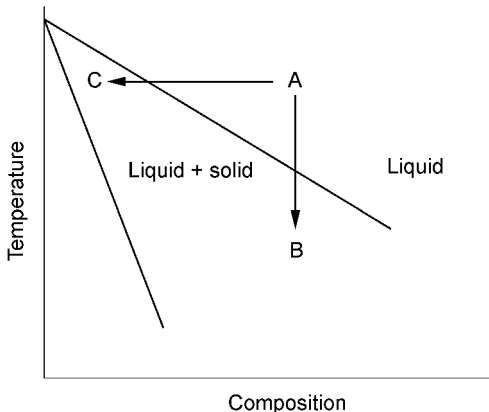
From the above observations it is clear that in order to understand solidification and casting there is a very complex interplay between many factors. There are a number of excellent texts on solidification that have been written over the last twenty years^{1–10} and this subject continues to develop. In this chapter it is the intention to give an introduction to our current understanding of the phenomena that are related to the initiation of solidification and to the factors that control growth rates. These issues will then be discussed with respect to issues in the casting of steels.

10.2 Solidification fundamentals

10.2.1 The conditions necessary for solidification

Solidification is the formation of a solid from a liquid or a gas. Solidification generally occurs during cooling but can also occur at constant temperature by chemical change of the system. For example, if a pure liquid metal, which is initially at a temperature above its melting point, is cooled continuously, at some temperature below its equilibrium melting point, solid will form. The temperature at which solidification actually occurs (T_i) when subtracted from the equilibrium melting temperature (T_m), is the undercooling (ΔT) necessary for the initiation of solidification. This phenomenon was first recognized by Fahrenheit in 1724.¹⁰ Similarly, if a liquid binary solution is held at constant temperature and its chemistry is changed by adding or removing one of the constituents, at some point, when the equilibrium solubility for the constituent is exceeded, solid will be precipitated. In this case, we will refer to solidification as being from a supersaturated liquid or gas. From these two examples, it can be seen that the initiation of solidification normally occurs by undercooling below an equilibrium temperature or by supersaturation above an equilibrium composition.

We can view this process schematically for solutions in Fig. 10.1 where a partial phase diagram for a binary solution is drawn. If the starting position is A, then solidification can be initiated by (1) reducing temperature below the position of the equilibrium liquidus (from A to B) or (2) increasing the composition at constant temperature past the equilibrium liquidus (from A to C). While path 1 is well recognized, path 2 is not as obvious; however, if one considers a binary alloy where the solute readily evaporates at processing



10.1 Schematic of a solidification process in a binary solution.

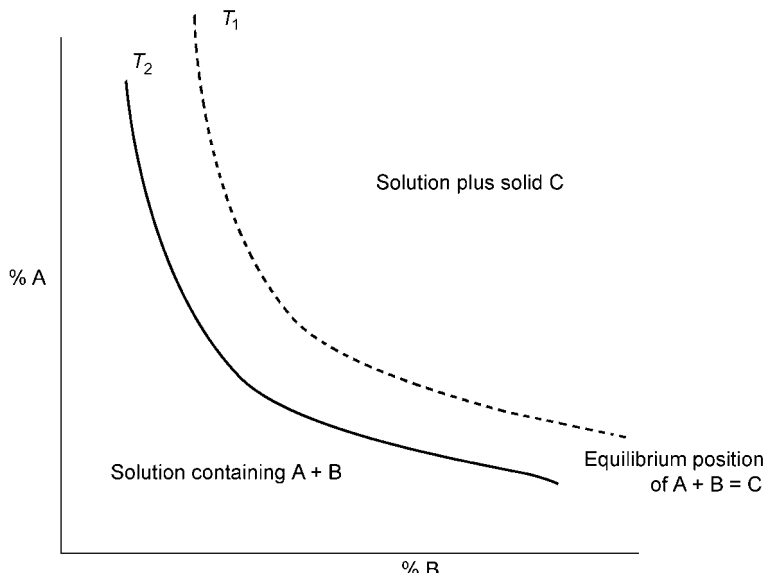
temperatures, the alloy, if held at constant temperature, will naturally follow path 2. In this diagram the liquidus and solidus curves are, by definition, calculated using bulk thermodynamic properties or measured during melting experiments.

Solidification can also occur by chemical reaction. For example, in liquid metals there is significant solubility of oxygen and sulfur that increases with temperature. As most casting processes initiate at temperatures significantly above the liquidus, oxides and sulfides will precipitate during cooling. These precipitation reactions are also driven by chemical and/or thermal changes.

Figure 10.2 is a schematic of an equilibrium diagram indicating the conditions for precipitation of C from a solution containing A and B. The solid and dashed lines are the equilibrium position for A and B in solution and in equilibrium with pure solid C at temperatures T_1 and T_2 (where $T_1 > T_2$). In this diagram decreasing temperature stabilizes solid C. If one begins with a solution of A and B at temperature T_1 and then one adds B at some concentration above that indicated by the dashed line, solid C will precipitate and grow until the concentration of A and B in solution is that given by the diagram, taking into account the stoichiometry of the reaction. The supersaturation necessary to initiate precipitation of solid C is related to the position of the equilibrium line and can be manipulated by decreasing temperature. Thus increasing composition and decreasing temperature can both lead to a critical supersaturation and the formation of solid C.

10.2.2 Issues of thermodynamics

In order to understand solidification, we must first understand phase diagrams of the type schematically shown in Figs 10.1 and 10.2. These diagrams are



10.2 Equilibrium diagram for the precipitation of C from a solution containing A and B.

constructed using bulk thermodynamic parameters and denote regions of stability where bulk parameters are important; however, during solidification, the first solid to form occurs by atom clustering either within the bulk (homogeneously) or on surfaces (heterogeneously). In addition, during solidification, there is formation of a solid that has both volume and a surface. Thus, if we look at the energy change during the solidification process, we can immediately see that for homogeneous nucleation of solid within a liquid mass, then the total change in free energy (ΔG) must be related to the volume free energy change plus the energy necessary to create the surface:¹¹

$$\Delta G = \Delta G_v \cdot V_s + \gamma_{s/l} \cdot A_s \quad (10.1)$$

where ΔG_v is the free energy change per unit volume created and $\gamma_{s/l}$ is the interfacial energy per unit area between the solid and the liquid. As the volume free energy can be calculated in two different ways, depending upon whether temperature or chemical change is driving precipitation, we can write ΔG_v as follows:

$$\begin{aligned} \Delta G_v &= \Delta H_{v,l \rightarrow s} - T \Delta S_{v,l \rightarrow s} \approx \frac{\Delta H_{v,l \rightarrow s}}{T_M} \Delta T \\ &\approx -\frac{\Delta H_{v,s \rightarrow l}}{T_M} \Delta T \approx \Delta S_{v,l \rightarrow s} \Delta T \end{aligned} \quad (10.2)$$

$$\Delta G_v = \Delta G^o + RT \ln Q = RT \ln \frac{Q}{K_E} = -RT \ln S \quad (10.3)$$

where ΔH_v and ΔS_v are enthalpy and entropy change per unit volume respectively of the phase transformation; T_M is the equilibrium temperature for the phase transformation; $\Delta T = T_M - T$ and is the undercooling; ΔG^o is the standard Gibbs free energy for the reaction; K_E is the equilibrium constant for the reaction; Q is the reaction product calculated using the initial activities of the components and S is the supersaturation ratio (K_e/Q). Thus one can relate ΔG_v to the undercooling (ΔT), if we assume that for a small range of undercoolings that the thermal contribution due to the phase transformation ($\Delta S = \Delta H/T_M$) accounts for more than 99% of total change of entropy, or to the natural logarithm of the supersaturation ratio (S). Equation 10.2 is Volmer's equation from 1939 and equation 10.3 is that of Guggenheim from 1957.

If we assume that the solid precipitates as a sphere, then equation 10.1 must go through a maximum at small radii, as the volume term must become smaller than the area term, as $r^3 < r^2$, when $r < 1$. A schematic of this situation is given in Fig. 10.3 where the maximum free energy is ΔG^* and the radius corresponding to the maximum is r^* .

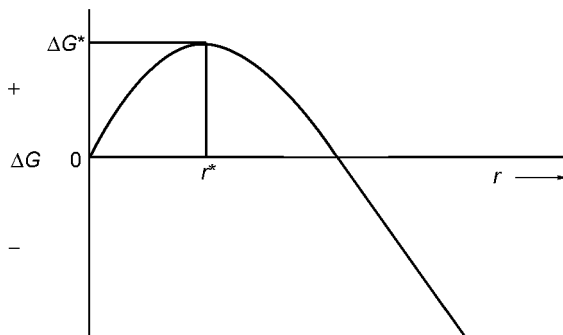
From equation 10.1, assuming solidification is driven by undercooling, the critical radius, r^* , and the critical free energy, ΔG^* can be written as follows:

$$r^* = \frac{2\gamma_{s/l}}{\Delta G_{v,s \rightarrow l}} = \frac{2\gamma_{s/l}}{\Delta H_{s \rightarrow l}} \frac{T_M}{\Delta T} \quad (10.4)$$

$$\Delta G^* = \frac{16}{3}\pi \frac{\gamma^3}{\Delta G_{v,s \rightarrow l}^2} = \frac{16}{3}\pi \frac{\gamma^3 T_M^2}{\Delta H_{v,s \rightarrow l}^2 \Delta T^2} \quad (10.5)$$

Thus both the critical radius and the critical free energy decrease with increasing undercooling.

For a reaction driven process, r^* and ΔG^* can be written as follows:



10.3 Schematic of the total free energy as a function of radius for a sphere.

$$r^* = \frac{2\gamma_{s/l}}{\Delta G_{v,s \rightarrow l}} = \frac{2\gamma_{s/l}}{RT \ln S} \quad (10.6)$$

$$\Delta G^* = \frac{16}{3}\pi \frac{\gamma^3}{\Delta G_{v,s \rightarrow l}^2} = \frac{16}{3}\pi \frac{\gamma^3}{(RT \ln S)^2} \quad (10.7)$$

where r^* and ΔG^* decrease with decreasing temperature and increasing supersaturation.

The nucleation of a phase was viewed by Gibbs¹¹ and Volmer and Weber¹² as a heterophase fluctuation in an undercooled or supersaturated phase where numbers of atoms must cluster together to form the potential starting points for the phase transformation. In Fig. 10.3, at small radii ΔG is positive and reaches a maximum as a function of r . Thus if we use Gibbs view of fluctuations, this maximum represents an unstable condition as, if a fluctuation occurred in the system that leads to the formation of a sphere of radius r^* , then any change to the size of the droplet due to evaporation or condensation, would lead to the droplet either diminishing or growing, as both processes would lead to a decrease in the free energy of the cluster. Thus r^* is the smallest radius that has the potential to increase in size. Equations 10.4 to 10.7 are related to one's assumption of the geometry associated with the solidification process and would change if one assumed a different geometric shape and a number of such relationships can be developed, if one changes geometry.

The most obvious change in geometry is to assume that the solidification process occurs on a pre-existing surface (heterogeneous nucleation). If one assumes a spherical cap which forms an equilibrium shape on a pre-existing surface, then Young's relation can be used to relate the various surface energies via an equilibrium contact angle (θ) where:

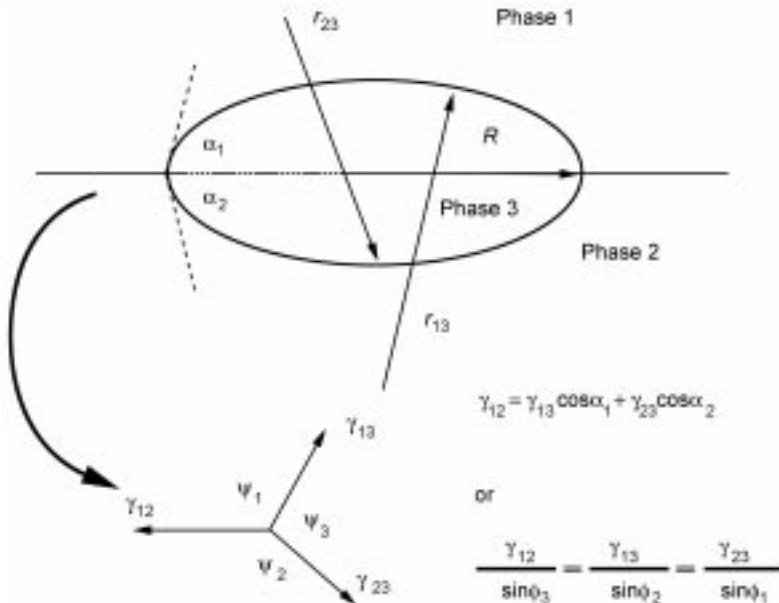
$$\gamma_{c-l} = \gamma_{c-s} + \gamma_{s-l} \cos \theta \quad (10.8)$$

and γ_{c-g} is the surface energy between the pre-existing solid and the liquid, γ_{c-s} is the interfacial energy between the pre-existing solid and the newly solidified material and γ_{s-l} is the interfacial energy between the newly formed solid and the liquid. This leads to the following relationship for ΔG^* :

$$\Delta G_{het}^* = \frac{1}{4}[2 + \cos \theta][1 - \cos \theta]^2 \Delta G_{hom}^* = S(\theta) \Delta G_{hom}^* \quad (10.9)$$

The function $S(\theta)$ varies from 0 to 1 as θ varies from 0 to 180. Thus wetting conditions lead to very small values of ΔG^* . Of course, as r^* is related to the shape of the curve (where $d\Delta G/dr = 0$), not its maximum value, heterogeneous nucleation does not change the critical radius; however, it strongly affects the volume of the critical nucleus and thus the number of atoms that must cluster together in order to form a critical nucleus:

$$\frac{V_{het}^*}{V_{hom}^*} = S(\theta) = \frac{\Delta G_{het}^*}{\Delta G_{hom}^*} \quad (10.10)$$



10.4 Nucleation at a liquid–liquid interface.

In the above discussion, it was assumed that the pre-existing solid was flat; however, if one assumes that surfaces are rough, the concave areas are more effective in decreasing the necessary volume for nucleation than either flat or convex areas, thus heterogeneous nucleation is favored in valleys rather than hills.

Another interesting issue is to consider solid nucleation at a liquid–liquid interface¹¹ as shown schematically in Fig. 10.4. In this figure the various interfacial energies are related as shown.

In this case:

$$\begin{aligned} \frac{\Delta G_{het}}{\Delta G_{hom}} &= f(\alpha) \\ &= \left[2 - 3\cos \alpha_1 + \cos^3 \alpha_1 + \left(\frac{1 - \cos^2 \alpha_1}{1 - \cos^2 \alpha_2} \right)^{3/2} (2 - 3\cos \alpha_2 + \cos^3 \alpha_2) \right] \quad (10.11) \end{aligned}$$

10.2.3 Effects of size

Another way of looking at this thermodynamic problem is to understand the effect of surface energy on the equilibrium position of the reaction. The first attempts to understand this issue was in the formation of liquid droplets from the vapor where surface energies and contact angles are apparently easy to measure. It is well known that the effect of surface energy on a droplet is to increase the

pressure inside the droplet. This change in pressure is described by the Young–Laplace equation which can be written for a sphere as:

$$\Delta P = P_{in} - P_{out} = \gamma\kappa = \gamma\left(\frac{1}{r_1} + \frac{1}{r_2}\right) = \frac{2\gamma}{r} \quad (10.12)$$

$$d\Delta P = \gamma d\kappa \quad (10.13)$$

where κ is curvature and assuming that γ is a constant.

In general:

$$dG = VdP - SdT \quad (10.14)$$

thus, assuming that the total pressure is not affected by the formation of a droplet, it is easy to show that the change in the equilibrium temperature due to radius for a sphere is:

$$\Delta T_r = \frac{\gamma VT_M}{\Delta H_{l-g}} \kappa = \Gamma\kappa = \frac{2\Gamma}{r} \quad (10.15)$$

$$\Delta S \Delta T = \frac{2\gamma V}{r} \quad (10.16)$$

and Γ is the Gibbs–Thompson coefficient and equals $\gamma V / \Delta S_{l-g}$. Equation 10.16 is often called the Thompson–Gibbs relation. Thus, the equilibrium condensation temperature for a droplet decreases with decreasing radius. In fact, this is a general finding. When one nucleates small droplets or particles, the equilibrium phase diagram will change and the equilibrium position for the reaction will always occur at a lower temperature than that given in a phase diagram that was determined from bulk samples. Of course, this means that undercooling is necessary for the formation of droplets and particles from a vapor or a liquid. A similar equation can be developed for the effect of radius on equilibrium partial pressure. This equation is generally referred to as the Kelvin equation:

$$RT \ln \frac{P}{P^0} = V \left[\frac{2\gamma}{r} + [p - p^0] \right] \approx \frac{2\gamma V}{r} \quad (10.17)$$

and relates the equilibrium partial pressure of a droplet (P') to its size. Equation 10.17 indicates that as radius decreases, the equilibrium partial pressure must increase. In equation 10.17, P^0 is the equilibrium partial pressure for a flat interface. The similarities between equations 10.16 and 10.17 indicate different manners by which the chemical potential can be derived. If the liquid is wetting to the solid, Kelvin also showed that in capillaries:

$$RT \ln \frac{P''}{P^0} = -\frac{2\gamma V}{r} \quad (10.18)$$

the equilibrium partial pressure for condensation will be less in a capillary than on a flat surface, again indicating why concavities can be better sites for the onset of nucleation.

Equation 10.16, Kelvin's equation, also indicates an unstable equilibrium position, if one considers the result of small fluctuations in radius for a droplet in equilibrium with its surroundings. First, assume that one has a population of mono-sized droplets in equilibrium with the vapor phase. If the droplet spontaneously becomes larger by condensation, the new equilibrium partial pressure for the new larger droplet size will be lower than the pressure that previously was in equilibrium with the smaller droplet. The new larger droplet is now in a situation where the actual pressure of the vapor from which the droplet condensed is now above its new equilibrium partial pressure. This condition will cause the droplet to further grow to reduce its local pressure to the equilibrium pressure corresponding to its size. This process will continue and the droplet will grow. Similarly, if a droplet decreases due to evaporation, the new equilibrium partial pressure necessary for the droplet will now be higher than the actual pressure and the droplet will continue to evaporate. Obviously, there must be mass balance as the total mass of droplets will not change, thus some droplets will grow and others will decrease. Of course, these changes in local equilibrium will lead to gradients in chemical potential between droplets and the driving force for mass transfer between the droplets. In materials science, this phenomenon is known as Ostwald ripening, and the coarsening of structures is also very common in solidification as the system reduces its total surface area and moves to its lowest energy state by reduction of surface area.

Thompson derived the effect of temperature on precipitation of droplets as a function of radius, where the effect of radius was to reduce the equilibrium temperature for the transformation in the following manner:

$$\ln \frac{T}{T_o} = -\frac{2\gamma V^n}{\Delta H_{vap} r} \quad (10.19)$$

showing the necessity for undercooling. In the derivation of Thompson's equation, it is assumed that $\Delta S = \Delta H/T$; if, however, $\Delta S = \Delta H/T_M$, is assumed, equation 10.15 results which is a clearer derivation and is preferred.

Gibbs' approach to nucleation and the Kelvin equation are yielding results that are similar in that an unstable position occurs during nucleation. These two views can be easily reconciled by considering the precipitation of droplets using the natural variables of volume, pressure, area and number of moles. Thus rewriting our thermodynamic equations for nucleation in terms of the Helmholtz free energy (F) where:

$$dF = -PdV - SdT + \gamma dA + \mu_i dn_i \quad (10.20)$$

it can be shown that at low values of supersaturation, that:

$$\Delta F = \gamma 4\pi r^2 - \frac{4\pi r^3}{3V^n} RT \ln \frac{P'}{P^0} \quad (10.21)$$

If the maximum of this function is found ($dF/dr = 0$), Kelvin's equation results. Of course, the maximum must occur at r^* and thus Kelvin's equation is satisfied for droplets of a critical radius. Using Kelvin's equation, it is possible to calculate the size of a critical radius for droplet formation. For example, at 0°C and at a supersaturation of 4.2, water droplets are observed in water vapor. This leads to a calculation of r^* of 0.8 nanometers which is a cluster of approximately 70 water molecules. For solidification of a solid phase one must change the various constants to those of the solid. For example, equation 10.16 would be written with the solid–liquid interfacial tension and the entropy change for solidification.

This discussion of droplets leads to some interesting issues in solidification:

1. The formation of very small particles necessitates that surface energy must be included in our description of equilibrium. Thus, current equilibrium phase diagrams cannot predict the onset of solidification as they are based upon bulk observations or calculations using bulk properties. Thus equilibrium phase diagrams as a function of particle size are necessary and a diagram of this type was recently calculated by Tanaka *et al.*¹³ for the system copper–lead. Similar affects of particle size have been measured by Sambles¹⁴ who noted that the melting temperature of pure gold decreased markedly (by more than 100K) when the particle size decreased below 20 nanometers.
2. Solidification structures will naturally coarsen due to the influence of curvature on local equilibrium.

The discussion of the thermodynamics of solidification so far has lead us to understand that the equilibrium phase diagram does not necessarily help us in our understanding of the initiation of solidification and that, when solidification occurs by fluctuations of small groups of atoms or molecules, the phase diagram must be altered due to the affect of radius on the equilibrium position.

10.2.4 Nucleation rate and the formation of non-equilibrium solids

In addition to the effect of radius, one must also include the effect of cooling rate when discussing solidification, as it is possible to undercool liquids to the point that the liquid begins to exhibit solid-like behavior. For example, the undercooled liquid can fail in a brittle mode at low temperatures or deform plastically at higher temperatures. Thus, not only can the phase diagram be changed by particle size, it should also take into account the effect of cooling rate on the potential for metastable phase formation and glass formation. Clearly this is beyond the realm of thermodynamics alone.

Following the view that small fluctuations are responsible for the initiation of solidification,^{11,12} it was postulated that the homogeneous nucleation rate (J)

should be proportional to the number of critical size nuclei (n_c^*), that is a nuclei with a radius r^* , where:

$$J \propto n_c^* \quad (10.22)$$

and that the number of these nuclei would follow the Frenkel size distribution equation (10.23), where one assumes that the entropy change of the solid–liquid system must be included by calculating the free energy of mixing of embryos (potential nuclei) with the liquid atoms (n_l) by assuming an ideal mixing model:

$$n_c^* = n_l \exp\left(\frac{-\Delta G_c^*}{k_b T}\right) \quad (10.23)$$

If the clusters evolve by a bimolecular reaction with forward and reverse rates of monomer addition where critical size nuclei grow by addition of atoms at the interface, an expression for the steady state nucleation rate can be derived assuming an activated process:

$$J = N_s \nu n_c^* \quad (10.24)$$

$$J = N_s \frac{kT}{h} \exp\left(\frac{-\Delta G_d}{k_b T}\right) n_l \exp\left(\frac{-\Delta G_c^*}{k_b T}\right) \quad (10.25)$$

where N_s is the number of atoms adjacent to the interface and in a position where a potentially successful jump is possible and ν is the jump frequency of an atom from the liquid to the solid, ΔG_d is the activation energy at the solid–liquid interface for a successful jump of an atom in the liquid to the surface of the nuclei and h is Planck's constant. ΔG_d is the kinetic barrier to nucleation and ΔG_c^* is the thermodynamic barrier to nucleation. This can also be written (from equations 10.5 and 10.7) as:

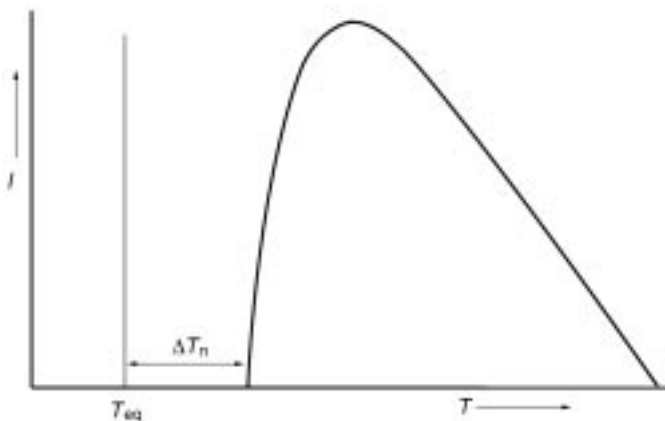
$$J = N_s \frac{kT}{h} \exp\left(\frac{-\Delta G_d}{k_b T}\right) n_l \exp\left(-\frac{16}{3kT} \pi \frac{\gamma^3 T_M^2}{\Delta H_{v,s \rightarrow l}^2 \Delta T^2}\right) \quad (10.26)$$

$$J = N_s \frac{kT}{h} \exp\left(\frac{-\Delta G_d}{k_b T}\right) n_l \exp\left(-\frac{16}{3kT} \pi \frac{\gamma^3}{(RT \ln S)^2}\right) \quad (10.27)$$

Equation 10.26 is plotted schematically in Fig. 10.5 where the nucleation rate goes through a maximum as temperature decreases. ΔT_n in Fig. 10.5 is the undercooling necessary for an observable nucleation rate of 1 nuclei per cm^3 per second. In metals it is very difficult to actually measure the maximum in Fig. 10.5 due to difficulties in accessing extreme undercoolings; however, such results are often seen in liquid oxides and in polymers.

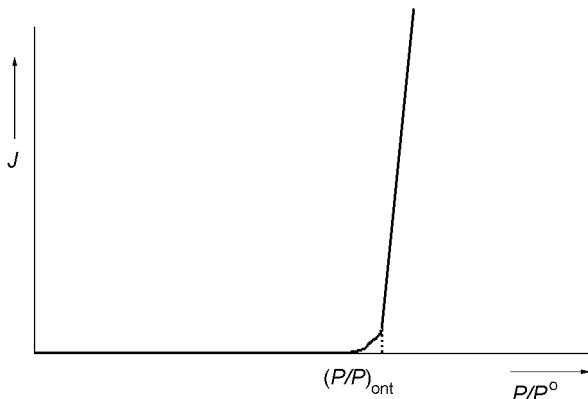
Equation 10.27 is plotted schematically in Fig. 10.6, where in this case, the nucleation rate continues to increase with increasing supersaturation.

The time to nucleate is proportional to the reciprocal of the nucleation rate. Thus time–temperature–transformation (TTT) curves can be derived from the

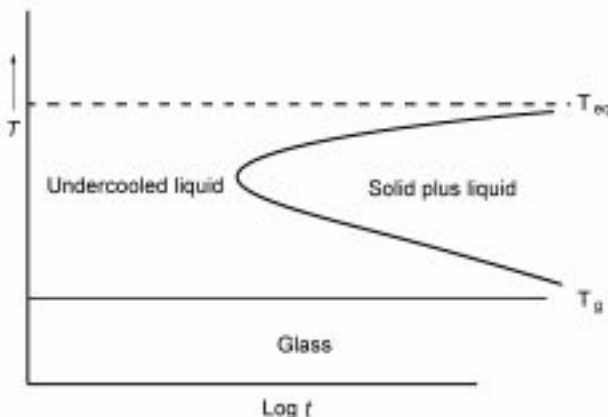
10.5 Nucleation rate (J) as a function of temperature.

nucleation rate and such a curve is shown schematically in Fig. 10.7. In this figure the dashed line indicates the position of the first observable solid in an experiment.

Other curves could also be drawn to denote the fraction of solidification and to indicate the progression of solidification with time. In Fig. 10.7 the equilibrium position of the phase transformation is noted, as is the glass transition temperature. Thus this figure schematically shows the position of the possible phases and indicates the stability regimes (with temperature and time) of the liquid, the glass and the area where the solid crystallizes from the liquid. Theoretically all liquids should be able to be formed at high cooling rates; however, the realm of achievable cooling rate is well defined and only those liquids that can be cooled quickly enough to avoid solid precipitation can be made as glasses.



10.6 The effect of supersaturation on the nucleation rate.



10.7 Schematic TTT curve.

Alternatively,^{1,8} if the jump frequency is calculated from:

$$\nu = \frac{D_l}{a^2} \quad \text{and} \quad N_s = \frac{4\pi(r^*)^2}{a^2} \quad (10.28)$$

then, for typical metals, where J is measured per cm^3 per second:

$$J = \left(\frac{D_l}{a^2} \right) \left(\frac{4\pi(r^*)^2}{a^2} \right) n_l \exp \left(\frac{\Delta G^*}{kT} \right) \approx 10^{34} \exp \left(\frac{\Delta G^*}{kT} \right) \quad (10.29)$$

The above discussion of nucleation rate concerns homogeneous nucleation, if one takes into account the fact that a heterogeneous nucleation site exists, then equation 10.29 can be rewritten as:

$$\begin{aligned} J_{het} &= \frac{D}{a^2} \frac{2\pi r_{cr}^2 (1 - \cos \theta)}{a^2} n_a \exp \left(\left[-\frac{\Delta G_{hom}^*}{k_b T} \right] f(\theta) \right) \\ &\approx 10^{24} \exp \left(\left[-\frac{\Delta G_{hom}^*}{k_b T} \right] f(\theta) \right) \end{aligned} \quad (10.30)$$

where n_a is the number of atoms in contact with the surface of potential nucleating sites (approximately taken as 10^{24} in this calculation⁵). Of course, this means that $J \propto N_a$ where N_a is the area of the nucleant and related to the number and size of the nucleating particles.

From equation 10.30, heterogeneous nucleation is promoted by:

- A stable solid material that exists in the liquid above the solidification temperature. This solid can be physically added and mixed or precipitated from solution during cooling.
- A low contact angle between the precipitated solid and the heterogeneous nucleating surface.

- A large surface area of the potential nucleant.

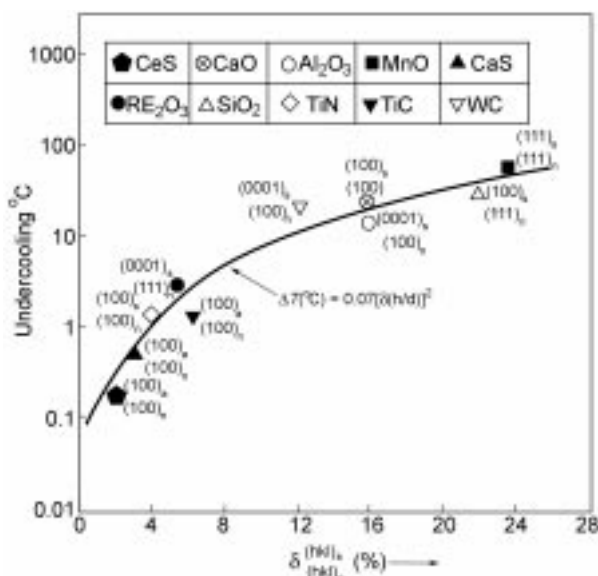
The contact angle between solids in a liquid is not a readily measurable contact angle in non-transparent liquids. In addition liquid–solid interfacial energies are not easily determined, thus the use of Young's relation (equation 10.8) to determine nucleating species is not particularly useful. Thus other criteria are necessary to allow the identification of potential nucleating species.

Knowledge of surface structure is useful in the determination of potential nucleants. If one assumes that epitaxy is important then nucleation should occur on planes that have a low misfit or disregistry with the plane to be precipitated. Bramfit calculated the disregistry (δ) as follows:

$$\delta = \sum_{i=1}^3 \delta_{(hkl)_s}^{(hkl)_n} = \left[\frac{|(d[uvw]_n^i \cos \gamma) - d[uvw]_s^i|}{d[uvw]_n^i} \right] \times 100\% \quad (10.31)$$

where $(hkl)_s$ and $(hkl)_n$ are low-index planes in the solid and nucleant, $[uvw]_s$ and $[uvw]_n$ are low-index directions in the $(hkl)_s$ and $(hkl)_n$ planes respectively, $d[uvw]$ is the spacing along $[uvw]$, γ is the angle between $[uvw]_s$ and $[uvw]_n$ and i is one of the three directions of the crystal with minimum index. Bramfit¹⁵ used this parameter to explain the difference in efficiency of heterogeneous nucleants of δ ferrite by measuring the degree of undercooling during solidification as shown in Fig. 10.8.

Of course, measurement of the undercooling for initiation of solidification is the most accurate assessment of the effectiveness of a nucleant.



10.8 Effect of lattice disregistry on undercooling.¹⁶

10.3 The growth of solids

In the discussion of growth rates there are a number of issues. The first is, what is controlling the growth rate? There are three potential general answers: interface kinetics, mass transfer or heat transfer; however, mixed results are also possible. In addition there are two major types of interface: flat and diffuse. If the interface is diffuse as in most metals, growth will be continuous, while if the interface is flat as in oxides, for example, the interface will grow laterally and the interface will be faceted. The entropy of fusion is often used to determine which type of interface will predominate and if $\alpha = \Delta S/R < 2$; the interface will be diffuse.

10.3.1 Interface dominated growth rates

Once nucleated, particles must grow and although the nucleation process is outside of our abilities to observe in liquids, one can certainly observe the growth stage after nucleation. In the above discussion of nucleation, it was assumed that growth was in an undercooled liquid and atom attachment to an interface controlled the growth rate and the jump frequency at the interface was very important. If one follows this viewpoint and assumes that growth is an activated process, then the Wilson–Frenkel relation results:

$$R = \frac{D}{a} \left[1 - \exp\left(\frac{\Delta G_{\text{crystallization}}}{k_b T}\right) \right] = \frac{D}{a} \left[1 - \exp\left(\frac{\Delta H_{\text{crystallization}} \Delta T}{k_b T T_m}\right) \right] \quad (10.32)$$

and, if diffusivity is related to viscosity via the Stokes–Einstein relation, it follows that:

$$R = \frac{k_b T}{3\pi a^2 \eta} \left[1 - \exp\left(\frac{\Delta H_{\text{crystallization}} \Delta T}{k_b T T_m}\right) \right] \quad (10.33)$$

This relation can be used to predict the growth rate as a function of temperature for crystobollite precipitation from fused silica, as shown in Fig. 10.9.

If one assumes that not all sites on a surface are appropriate and that a successful jump occurs only in specific positions, then a correction factor f can be attached to equation 10.33 and for a growing monolayer, if $f = \Delta T/2\pi T_M$:

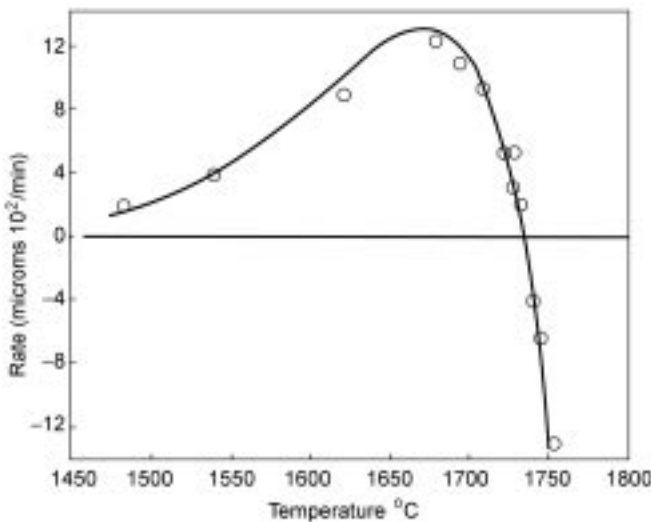
$$R = \frac{\Delta T k_b T}{6\pi^2 T_M a^2 \eta} \left[1 - \exp\left(\frac{\Delta H_{\text{crystallization}} \Delta T}{k_b T T_m}\right) \right] \quad (10.34)$$

If equations 10.33 and 10.34 are approximated by the following approximation, if $1 - \exp(-x) = x$, then equation 10.33 indicates that:

$$R \propto \Delta T \quad (10.35)$$

and equation 10.35 indicates that:

$$R \propto \Delta T^2 \quad (10.36)$$



10.9 The growth or melting rate of crystoballite as a function of temperature.⁶

If one assumes that growth is by a screw dislocation emerging at a surface, a similar relation to equation 10.36 is found. In metals the undercoolings associated with surface growth mechanisms are very small and only at high growth rates do interface kinetics become an issue.

As already noted the growth phase of solidification is easily observed and if one assumes that there is a steady state nucleation rate, that the growth rate is constant and the liquid is consumed by the growth of the particles, the following general Kolmogorov, Johnson, Mehl, Avrami (KJMA) equation can be developed:⁵

$$X_t = 1 - \exp \left[-c_g \int_0^t J_t \left[\int_0^t G_t dt \right]^d dt \right] \quad (10.37)$$

where X_t is the fraction transformed, c_g is a shape factor, J_t is the nucleation rate, G_t is the growth rate and d represents the dimensionality of growth.

For example, if we had growth of a sphere at constant growth rate and a constant nucleation rate (J_v), then as c_g is $4\pi/3$, $d = 3$, and G_t is a constant, the Johnson–Mehl equation results:

$$1 - X_t = \exp \left(-\frac{\pi J_v R^3}{3} t^4 \right) \quad (10.38)$$

From this equation, if J_v and R are known as a function of temperature and we assume small values of X_t , it follows that:

$$X_t \cong \frac{\pi J_v [R]^3}{3} t^4 \quad (10.39)$$

If the limit of observation for X_t is assumed to be 10^{-6} the time when the first observation of solidification at a given temperature T could be calculated from a knowledge of J_v and R . For example, using equations 10.29 and 10.32, for homogeneous nucleation followed by growth by the monolayer model, the TTT curve could be calculated.

Although the above growth models seem reasonable in pure liquid oxides where undercooling is easy and heat transfer is not an issue; however, in metals with a high latent heat of solidification or during highly exothermic reactions, heat transfer tends to control the growth rate after the initial formation of solid. In multicomponent solutions mass transfer in the liquid can become rate controlling rather than atom attachment.

10.3.2 Heat transfer dominated growth rates

In heat transfer dominated solidification, the rate of solidification is determined solely by the ability to transfer heat away from the interface. In undercooled liquids heat can be transferred either to the liquid or into the growing shell. The amount of solidification is thus related to the heat flux removed from the interface. If the amount of heat released during solidification is measured per unit mass and the thermal gradient in the solid (dT/dx) is G_s and the thermal gradient in the liquid is G_l , then the interface heat balance for a planar interface is as follows:

$$k_s G_s - k_l G_l = \Delta H \rho R \quad (10.40)$$

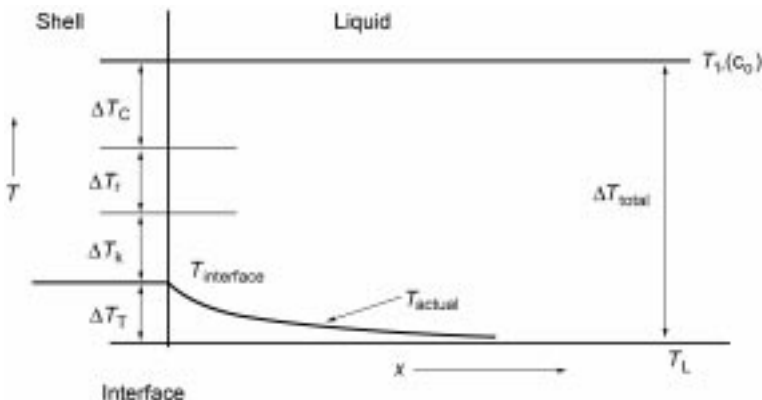
where ρ is the density and k_s and k_l are the thermal conductivities of the solid and liquid respectively. Thus the maximum growth rate occurs when G_l is negative (undercooled) and G_s is positive (normal solidification). The relation also shows that an interface can be stabilized ($R = 0$) by ensuring that $k_s G_s = k_l G_l$. If convection heat transfer controls thermal transport in the liquid then equation 10.40 would be rewritten as follows:

$$k_s G_s - h_l(T_b - T_t) = \Delta H \rho R \quad (10.41)$$

To avoid the necessity of solving for h_l it is not uncommon in calculations to substitute a fictitious effective conductivity in equation 10.40 to account for a higher rate of heat transport than would be calculated from conduction heat transfer.

The first issue in any heat transfer problem in solidification is to define the interface temperature, as it is that temperature that will define the temperature that the heat must flow from. The starting point is, of course, the equilibrium phase diagram and to calculate the interface temperature one must first take into account the effect of chemistry (ΔT_c), and, if the interface has curvature, then this undercooling must also be included (ΔT_r), such that:

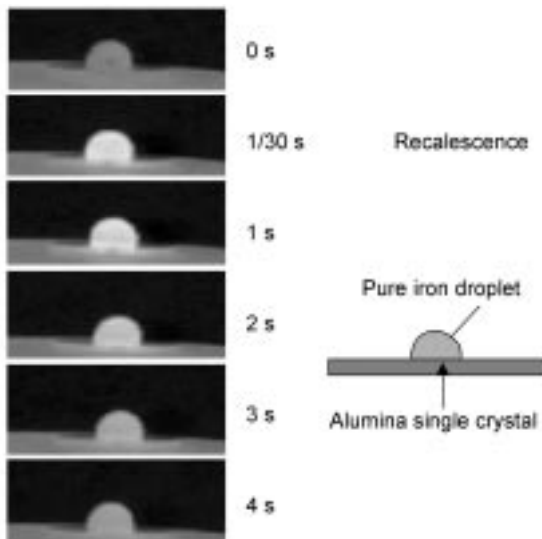
$$T_{int} = T_{Mpt} - \Delta T_c - \Delta T_r \quad (10.43)$$



10.10 Schematic of thermal profile in liquid and solid for undercooled growth of an alloy.

It is also assumed that when solidification is initiated, the interface temperature immediately attains T_{int} as calculated in equation 10.37. Of course, there must also be a kinetic undercooling (ΔT_k) to allow heat transfer and there can also be a pressure undercooling (ΔT_p); however, both of these corrections are usually small and are normally ignored.⁹ A schematic of a thermal profile for undercooled solidification is given in Fig. 10.10 where the various undercoolings are marked.

An example of undercooled growth can be seen in Fig. 10.11 where liquid iron is undercooled until solidification occurs on an alumina substrate. In this



10.11 Example of undercooled solidification.¹⁵ Photograph by H. Shibata.

case the undercooling for initiation of solidification is 211°C and the droplet fully recalesces in the time of 1 frame of the video camera.

Transient moving boundary problems of this type are Stefan problems and, if one looks at the situation where a semi-infinite solution of the transient heat transfer equation is appropriate and can be used to determine thermal gradients:

$$\frac{\partial T}{\partial t} = \alpha \frac{\partial^2 T}{\partial x^2} \quad (10.44)$$

it follows that the growth rate for a plane front growing into an undercooled liquid is:

$$R = \lambda \sqrt{\frac{\alpha}{t}} \quad (10.45)$$

where

$$\sqrt{\pi} \lambda \exp(\lambda^2) \operatorname{erfc} \lambda = \frac{C_p \Delta T_t}{\Delta H} = St \quad (10.46)$$

where erfc is the error function complement, ΔT_t is the thermal undercooling of the liquid and St is the Stefan number. It should be noted that when the Stefan number equals or is greater than 1, this function has no solution. If the Stefan number equals 1, $C_p \Delta T = \Delta H$ and this means that the heat given out during solidification can recalesce the liquid to its equilibrium point. At Stefan numbers greater than 1, the solidification process cannot recalesce the liquid to its equilibrium point and this is termed hypercooling. Under this condition the interface temperature would not be easily determined and this solution is not appropriate.

Upon nucleation of a solid the first solid formed is a sphere and the interface conditions must include the fact that the interfacial area is increasing. Equation 10.40, the interface heat balance must be rewritten for spherical growth as follows:

$$k_s G_s - k_l G_l = \Delta H \rho R - \frac{1}{A} \frac{\gamma d(A)}{dt} = (\Delta H \rho - \kappa \gamma) R \quad (10.47)$$

Where the growth rate is increased due to the formation of surface, i.e. less energy needs to be conducted as it is consumed in surface creation. Mullins showed that spheres in undercooled liquids become unstable very quickly and rather than grow as spheres begin to grow as cells or dendrites.

If we assume that the sphere is growing in an undercooled liquid of temperature T_∞ , then the growth rate of the sphere will be:

$$R = \left(\frac{dr}{dt} \right)_{r=r_p} = - \frac{k_l}{\Delta H \rho} \left(\frac{dT}{dr} \right)_{r=r_p} = \frac{k_l}{\Delta H \rho} (T_i - T_\infty) \left(\frac{1}{r_p} + \frac{1}{\sqrt{\pi \alpha t}} \right) \quad (10.48)$$

where T_i is the interface temperature. At longer times equation 10.48 will tend to the steady state solution where:

$$R = \frac{k_l}{\Delta H \rho} \frac{(T_i - T_\infty)}{r_p} \quad (10.49)$$

The progression of radius with time will then be:

$$r_p = \sqrt{r_{p,o} + \frac{K_l(T_i - T_\infty)}{\Delta H \rho} t} \quad (10.50)$$

where $r_{p,o}$ is the starting radius. To determine the length of time it takes to reach a steady state solution, the characteristic time (τ) can be determined where

$$\tau \approx \frac{r_p^2}{\alpha_l} \quad (10.51)$$

in metals where α_l is approx $10^{-5} \text{ m}^2/\text{sec}$, for a τ of less than 0.1 sec, r_p must be less than 0.1 mm. Thus for very small spheres the steady state solution would be appropriate; otherwise the full transient solution is necessary.

As we have already noted, T_i is a function of r for very small radii and:

$$T_i = T_{mpt} - \frac{2\Gamma}{r} \quad (10.52)$$

Therefore equation 10.49 can be rewritten as:

$$R = \frac{k_l}{\Delta H \rho} \frac{\left(\Delta T - \frac{2\Gamma}{r_p} \right)}{r_p} \quad (10.53)$$

where $\Delta T = T_{Mpt} - T_\infty$. Thus the growth rate will become zero when $\Delta T = 2\Gamma/r_p$ as T_i will tend to T_∞ and the driving force for heat transfer will be eliminated.

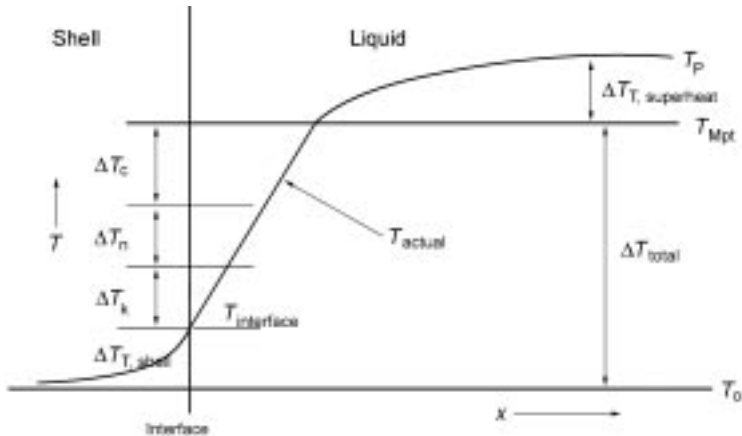
As previously noted, Mullins has shown that spherical growth is unstable, perturbations form and grow where these perturbations develop with a tip radius that is constant. A general problem in solidification is to determine the relationship between the radius and growth rate. If one considers this problem as a cylinder growing with a hemispherical cap into an undercooled liquid, one develops a relationship very similar to equation 10.49 for steady state growth:

$$\frac{rR}{2\alpha} = \frac{C_p(T_i - T_\infty)}{\Delta H} \quad (10.54)$$

which, if taking into account the effect of radius on the interface temperature, is written as:

$$Pe_T = \Omega \left(1 - \frac{\Delta T_r}{\Delta T} \right) \quad (10.55)$$

where Pe_T is the thermal peclet number and Ω is the inverse of the Stefan number. Thus in equation 10.54 or 10.55, if the radius is known the growth rate can be calculated and vice versa. A more complete solution for this diffusion



10.12 Schematic of the temperature profile for normal solidification.

problem was first given by Ivantsov for a geometry that is closer to that of a real dendrite where, if we correct for capillarity:

$$I(P) = \Omega \left(1 - \frac{\Delta T_r}{\Delta T} \right) \quad (10.56)$$

where

$$I(P) = Pe_T \exp(Pe_T) E_1(Pe_T)$$

and

$$E_1(Pe_T) = -0.577 - \ln(Pe_T) + \frac{4Pe_T}{Pe_T + 4}$$

The above discussion concerns undercooled growth; however, solidification is often initiated by cooling against a mold. A schematic of the thermal profile for normal solidification is given in Fig. 10.12.

Normal solidification is the most common mode of growth and, if one assumes perfect contact at the mold–shell interface and thermal gradients in both the shell and the mold, Schwartz's semi-infinite solution of the Stefan problem results, where:

$$R = \lambda \sqrt{\frac{\alpha_{shell}}{t}} \quad (10.57)$$

and λ is calculated as follows:

$$\frac{T_m - T_o]C_p^s}{\Delta H \sqrt{\pi}} = \lambda \exp \lambda^2 \left[\sqrt{\frac{(k\rho C_p)_{shell}}{(k\rho C_p)_{mold}}} + \operatorname{erf} \lambda \right] \quad (10.58)$$

And the mold shell interface temperature is calculated from the following relation:

$$T_s = T_o + [T_m - T_o] \left[\frac{\sqrt{\frac{(k\rho C_p)_{shell}}{(k\rho C_p)_{mold}}}}{\sqrt{\frac{(k\rho C_p)_{shell}}{(k\rho C_p)_{mold}}} + erf \lambda} \right] \quad (10.59)$$

Of course, reality is always more complicated than these simplifications and, if one considers the situation of undercooling a liquid against a mold, there would be heat transfer in both directions at the interface. In this case, equation 10.60 gives the expression for the growth rate where λ can be determined as follows:⁷

$$\frac{St_s}{\lambda \sqrt{\pi} \exp(\lambda^2) erf(\lambda)} + \frac{St_{initial}}{v\lambda \sqrt{\pi} \exp(v\lambda^2) erf(v\lambda)} = 1 \quad (10.60)$$

and

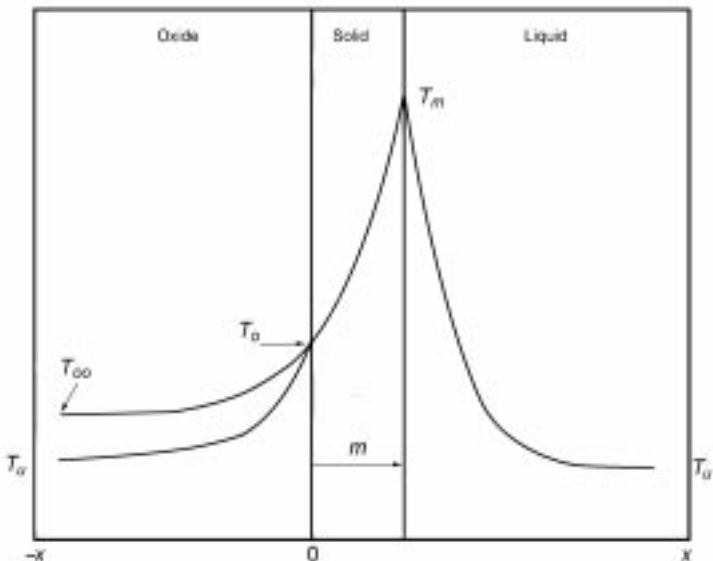
$$St_s = \frac{c_{p(s)}(T_m - T_s)}{\Delta H} \quad \text{and} \quad St_{initial} = \frac{c_{p(l)}(T_m - T_{initial})}{\Delta H}$$

$$v = \sqrt{\frac{\alpha_s}{\alpha_l}}$$

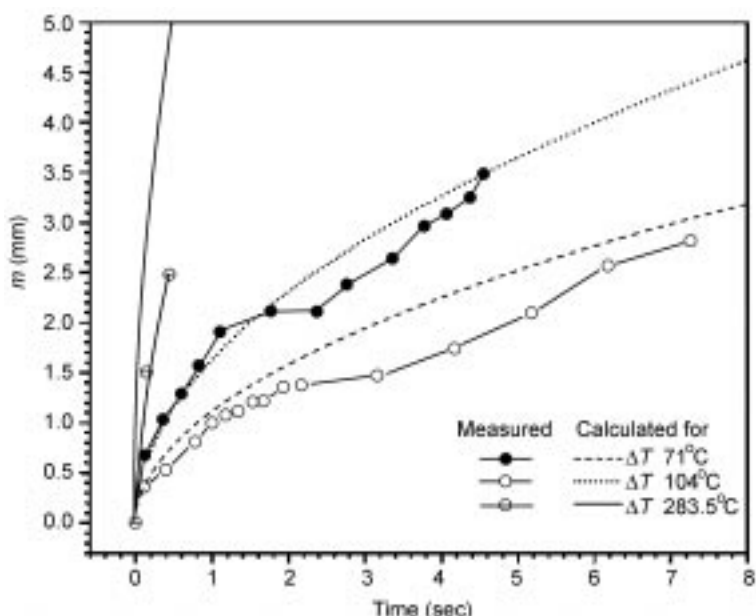
The situation in Fig. 10.11 is typical of an undercooled solidification problem where the system cools to a temperature before solidification is initiated and then when solidification occurs the growing front immediately attains the equilibrium interface temperature and, heat is conducted into the liquid and into the shell. In this case there is heat transfer through the shell and the alumina pedestal that the iron droplet rests upon, thus this solution must be a combination of a Schwartz solution and the undercooled solution as shown in Fig. 10.13.

Experimentally measured results versus this simplified model are shown in Fig. 10.14 where fair agreement between experimentally measured results is observed at higher undercoolings but not at lower undercoolings due to complete recalculation of the droplet before completion of solidification.

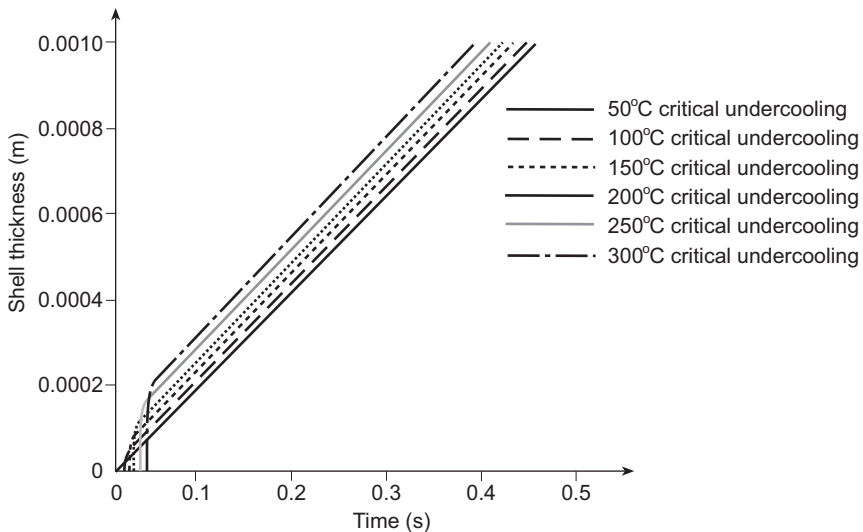
Another more practical condition for undercooled growth would be against a cooled metal mold where, if we assume that solidification occurs by nucleation, then initially the liquid against the mold would be undercooled until the temperature reaches the level necessary for activation of a heterogeneous nuclei. Once the front is nucleated there will be a transfer of heat into the liquid and through the steel. Once the undercooled liquid has been reheated, all thermal gradients will be through the shell and there will be a transition from undercooled growth to normal solidification. There is no analytical method to represent this situation therefore a numerical solution is necessary. Results from such a calculation are given in Fig. 10.15 where as the critical undercooling for nucleation is increased there is a longer time before solidification is initiated.



10.13 Schematic of the temperature profile for undercooled growth.¹⁵



10.14 Growth of a liquid iron shell as a function of undercooling.¹⁵



10.15 Shell profile calculations as a function of the critical undercooling for nucleation against a mold wall.

This initiation time is followed by a rapid rise in growth rate due to the combined modes of heat transfer. As the undercooled liquid is recrystallized, the solution becomes that for normal solidification. It can be seen that as the ability to undercool increases, the time to solidification is decreasing. This occurs because the efficiency of heat transfer is greatest when the liquid contacts the mold. Once the shell is formed the total heat flux decreases. Clearly this effect is most obvious when casting small sections.

The assumption of perfect contact at the shell–mold interface is not normally accurate and in reality there is a complex situation that is found where the shell is in intermittent contact with the mold leading to a complex conduction–convection and radiation problem. This complex situation is overcome by assuming that Newton's law can be invoked and that a heat transfer coefficient for the mold can be determined.

In actual molds it is common that all of the resistances to heat transfer are important and it is common to write the heat flux equation as a sum of resistances using Newton's law and assuming an analog to electrical resistance, the heat balance can be written as:

$$Q = hA(T_p - T_o) = \frac{(T_p - T_o)}{\mathfrak{R}} = \rho_s \Delta H R \quad (10.61)$$

where T_p is the temperature of the liquid and T_o is the temperature of the medium removing heat from the mold. Resistance for heat transfer coefficients will be $1/hA$ and for conduction will be L/kA where L is the distance over which heat is conducted.

Thus, for a water-cooled mold where there is a mold thickness and a growing shell with intermittent contact, the total resistance to heat transfer \Re would be calculated as follows:

$$\Re = \frac{1}{h_{water} A} + \frac{L_{mold}}{k_{mold} A} + \frac{1}{h_{interface} A} + \frac{L_{shell}}{k_{shell} A} + \frac{1}{h_{liquid} A} \quad (10.62)$$

In the above equations the heat transfer coefficients for the fluid against the mold and the liquid against the shell must be determined from a knowledge of fluid flow in the system and $h_{interface}$ is a complicated heat transfer coefficient that includes conduction, convection and radiation terms. The conduction terms come from point contacts with the mold, the convection and radiation terms are due to heat transfer across the valleys between the point contacts. In radiation heat transfer the heat flux is described by Stefan's law, where:

$$Q \propto (T_1^4 - T_2^4) \quad (10.63)$$

The radiation contribution to heat transfer can be significant for high temperature metals. It is often assumed that the interface h is a simple sum of heat transfer coefficients that account for the three modes of heat transfer:

$$h_{interface} = h_{conduction} + h_{convection} + h_{radiation} \quad (10.64)$$

It is therefore no surprise that $h_{interface}$ is very difficult to calculate as it is a function of time, local mold geometry and the detailed thermal conditions within the mold and analytical solutions of the real casting problems are not possible.

If the interface resistance dominated heat transfer, then

$$m = \frac{h_{int}[T_M - T_o]t}{\rho \Delta H} \quad (10.65)$$

$$R = \frac{h_{int}[T_M - T_o]}{\rho \Delta H} \quad (10.66)$$

In the case where resistance to heat transfer is in the shell and at the interface, Adams developed the following solution to this problem:

$$m = -\frac{k_s}{h} \pm \sqrt{\frac{k_s^2}{h^2} + \frac{2k_s[T_M - T_o]}{a \rho \Delta H} t} \quad (10.67)$$

where

$$a = \frac{1}{2} \pm \sqrt{\frac{1}{4} + \frac{C_{p(s)}[T_M - T_s]}{3 \Delta H}}$$

Now if $h \gg k_s$

$$m = -\frac{k_s}{h} \pm \sqrt{\frac{2k_s[T_M - T_o]}{a \rho \Delta H} t} \quad (10.68)$$

and

$$R = \sqrt{\frac{k_s[T_M - T_o]}{a \rho \Delta H t}} \quad (10.69)$$

In alloys where there is a significant freezing range where solidification begins at the interface temperature (T_i) and ends at the effective solidus temperature (T_s) there is zone where the fraction of solid varies from 0 at T_i to 1 at T_s . In this area of the changing fraction of solid, cells and dendrites develop in normal and undercooled solidification. It is normal to view this area as a separate zone of solidification and assume that in the mushy zone the total enthalpy consists of an enthalpy of the liquid H_l and an enthalpy of the solid H_s and to partition the release of latent heat to correspond to the temporal evolution of the fraction of solid (f), where:

$$\frac{\partial H}{\partial T} = \Delta H \frac{\partial f_s}{\partial t} + f_l \frac{\partial H_l}{\partial t} + f_s \frac{\partial H_s}{\partial t} \quad (10.70)$$

and equation 10.43 can be rewritten as follows:

$$\left[1 - \frac{\Delta H}{c_p} \left(\frac{\partial f_s}{\partial t} \right) \right] \frac{\partial T}{\partial t} = \alpha \frac{\partial^2 T}{\partial x^2} \quad (10.71)$$

For equilibrium solidification the use of this approach is straightforward; however, in all other conditions, it is strongly influenced by segregation and numerical solution is necessary.

If equation 10.43 is written to include an energy source term such that:

$$\frac{\partial T}{\partial t} = \alpha \frac{\partial^2 T}{\partial x^2} + \frac{\dot{Q}}{\rho C_p} \quad (10.72)$$

and, assuming $\dot{Q} = \rho \Delta H \frac{\partial f_s}{\partial t}$ that, then:⁹

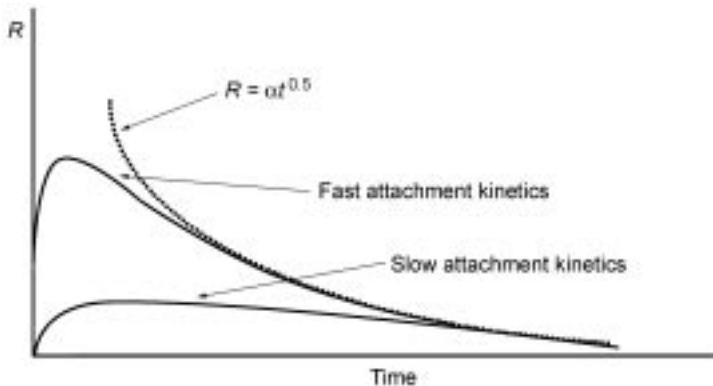
$$\frac{\partial T}{\partial t} = \alpha \frac{\partial^2 T}{\partial x^2} + \frac{\Delta H}{C_p} \frac{\partial f_s}{\partial t} \quad (10.73)$$

which is equivalent to equation 10.70, as

$$\frac{\partial f_s}{\partial t} = \frac{\partial f_s}{\partial T} \frac{\partial T}{\partial t}$$

The partitioning of the latent heat across the actual liquidus to solidus gap leads to a change in the gradient of cooling in the mushy zone. If internal temperature gradients in the shell are small, then the cooling rate of a casting can be calculated as follows:

$$\frac{\partial T}{\partial t} = -\frac{hA(T_p - T_o)}{\rho C_p \nu} \left[1 - \frac{\Delta H}{C_p} \frac{\partial f_s}{\partial T} \right] \quad (10.74)$$



10.16 Schematic of growth rate as a function of time.

Even in heat transfer dominated processes, at the initiation of solidification, the potential heat flux and therefore growth rate is very high. The ability to grow a front by heat transfer cannot be faster than the ability to add atoms to the front; therefore, the growth rate at very small times must be limited by this issue. This is schematically shown in Fig. 10.16.

10.3.3 Mass transfer dominated growth

In conditions where dissipation of heat is not controlling the solidification rate or during isothermal solidification, it is possible to find conditions where transport of mass in the liquid controls the growth rate.

The mass balance at a planar interface in one dimension can be written as:

$$D_s \left(\frac{dC_s}{dx} \right)_{x=x_i} - D_l \left(\frac{dC_l}{dx} \right)_{x=x_i} = R(C_l^i - C_s^i) = RC_l^i(1 - k_{eq}) \quad (10.75)$$

where C_l^i and C_s^i are the interface composition of the interface and the interface composition of the solid respectively and k_{eq} is the equilibrium partition coefficient determined from a phase diagram and it is assumed that at all growth rates interfacial equilibrium is maintained. Equation 10.75 is similar in form to equation 10.40, the heat balance at the interface. However, there is one significant difference, in the heat flux equation all heat energy must travel from liquid to solid to complete solidification and after solidification a casting can be cooled to one isothermal temperature; however, in the transport of mass, it is normal that the time to cool a casting to an isothermal temperature is much shorter than the time to ensure chemical homogenization of a casting. This means that gradients in composition that arise due to the solidification process will remain in the casting, unless some thermal treatment is carried out after casting. Another difference is that composition can be stored in the liquid where heat cannot; thus during solidification the composition of the liquid can increase or decrease, depending upon the phase

diagram, the rate of mixing in the liquid and the diffusive flux into the solid. This leads to the condition that both the liquid and solid compositions can be transient and gross changes in composition are possible during solidification.

For example, under equilibrium conditions where mass transfer is rapid in both liquid and solid the final composition of the solid will be the composition of the liquid; however, in conditions where diffusion in the solid is very slow and can be ignored, the compositional profile will be described by the Gulliver Scheil equation:

$$C_s = kC_0(1 - f_s)^{k-1} \quad (10.76)$$

where the composition of the solid will vary continuously from solidification start to finish. In castings this variation is seen perpendicular to the growth direction of a cell or dendrite and leads to phenomena of segregation. As it is possible for solute to increase in the liquid between cells or dendrites, the last solidification temperature of a casting is determined by this segregation and the effective solidus temperature is a function of the phase diagram and the local thermal and mass fields. For this reason there are many models that have been developed to allow this determination and numerical solutions are necessary to determine the segregation amount accurately.

The interface temperature is also strongly affected by composition (equation 10.43) and, in alloy solidification where heat transfer is important, any change in interface composition will result in a change in interface temperature.

The phenomenon of interface instability was explained in detail by Mullins and Sekerka, where, following the approach of Kurtz, the marginal stability criterion can be written as follows:

$$-\Gamma\omega^2 - [\bar{k}_l G_l \xi_l + \bar{k}_s G_s \xi_s] + m G_c \xi_c = 0 \quad (10.77)$$

where ω is $2\pi/\lambda$, λ is the wavelength of a small perturbation, \bar{k} is an average thermal conductivity for the liquid and the solid, ξ is a term to correct the thermal and compositional terms due to local interface conditions, m is the slope of the liquidus and G_c is the compositional gradient in the liquid. In this equation terms that are negative favor a planar interface, while positive terms favor instability of the interface. In this case a gradient of composition in the liquid always favors instability as does a negative thermal gradient in the liquid. Thus alloys and under-cooled liquids exhibit instabilities that result in formation of cells and dendrites.

Mullins and Sekerka wrote a form of the equation 10.77 for low Peclet number liquids as follows:

$$\left[\frac{R}{D} \Delta T_o - \left(\frac{2k_l G_l}{k_l + k_s} + \frac{\Delta H R}{k_l + k_s} \right) - \frac{k \Gamma R^2}{D^2} \right] = 0 \quad (10.78)$$

and if λ is equated to the tip radius of a perturbation and, as assumed by Langer and Muller-Krumbharr, that the marginal stability criterion allows the calculation of the tip radius, it can be found that the tip radius in all cases is

very small (larger than a critical radius), thus in diffusional growth situation we are most often looking at dendrite growth and models of growth are very similar to the heat transfer solutions where the transient solution of the mass transfer equation will have the following form for a growing sphere from its own vapor:

$$R = \frac{dR_p}{dt} = \frac{DM_{wtA}}{\rho} (C_\infty - C_s) \left(\frac{1}{R_p} + \frac{1}{\sqrt{\pi Dt}} \right) \quad (10.79)$$

which at longer times gives the steady state solution:

$$R = \frac{dR_p}{dt} = \frac{DM_{wtA}}{\rho r_p} (C_\infty - C_s) \quad (10.80)$$

In the case of solidification of an alloy, if we assume that equation 10.75 describes the steady flux balance at the interface and assuming that we can ignore the term for diffusion in the solid:

$$-D_l \left(\frac{dC_l^i}{dr} \right)_{x=x_i} = R(C_l^i - C_s^i) = RC_l^i(1 - k_{eq}) \quad (10.81)$$

and

$$R = \frac{D}{r} \frac{[C_l^i - C_\infty]}{[1 - k_{eq}]C_l^i} \quad (10.82)$$

In a manner similar to that for solidification due to heat transfer we can write the relation for the growth a cell as a hemispherical cap as follows:

$$Pe_c = \Omega_c \left(1 - \frac{r_c}{r} \right) \quad (10.83)$$

where Pe_c is the compositional Peclet number ($rR/2D$) and Ω_c is the dimensionless supersaturation:

$$\frac{[C_l^i - C_\infty]}{[1 - k_{eq}]C_l^i}$$

In a similar manner Ivantsov's solution can be used to describe the diffusion at the tip of a paraboloid of revolution, where:

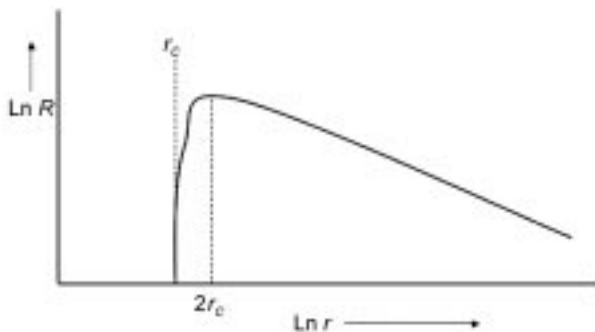
$$I(Pe_c) = \Omega_c \left(1 - \frac{r_c}{r} \right) \quad (10.84)$$

and

$$I(P) = Pe_c \exp(Pe_c) E_1(Pe_c)$$

$$E_1(Pe_c) = -0.577 - \ln(Pe_c) + \frac{4Pe_c}{Pe_c + 4}$$

Steady solutions are appropriate in many mass transfer situations as the characteristic time to achieve equilibrium at the interface (τ) is $\sim r_p^2/D$ and, for small radii, the characteristic time is small enough to be ignored.



10.17 Schematic of growth rate versus radius for diffusion controlled growth of a paraboloid.

Equation 10.84 is schematically shown in Fig. 10.17 where the growth rate exhibits a maximum.

10.4 The casting of steels

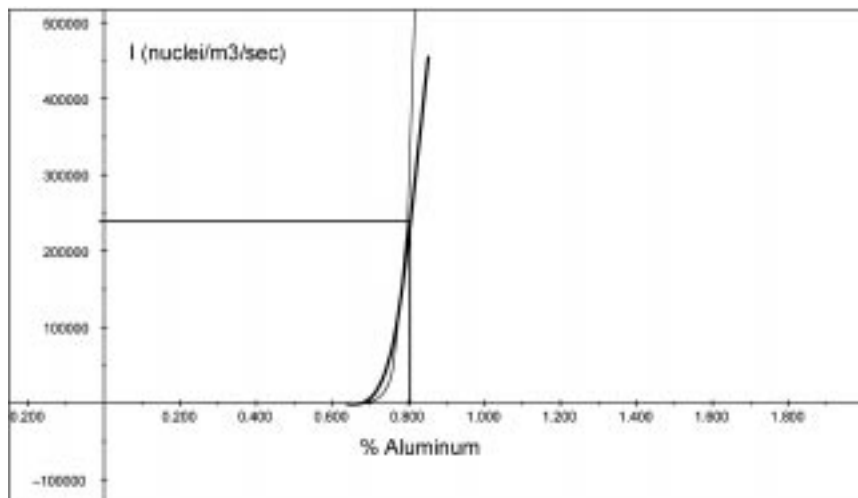
There are two main industrial methods for steel casting: ingot casting and continuous casting.¹⁵ Ingot casting is currently only used in foundries and in special products casting while continuous casting accounts for the majority of the steel cast in the world. There are two major types of continuous casting machines in which either the mold oscillates and there is a liquid oxide layer between the mold and the steel shell, or the mold rotates and there is direct contact between the mold and the shell of the casting.

In the casting of steels there are a number of initial solidification related issues:

- Solidification can be initiated heterogeneously, by the oxides and nitrides that are precipitated in the liquid steel during processing.
- In oscillation mold casters, the liquid oxide layer between the oscillating mold and the shell is a potential glass former and thus tends to become a mixture of crystallized solid and glass as it is cooled.
- The surface of cast steels in oscillating mold casters contains ‘oscillation marks’ that are related to the mold oscillation cycle itself.
- In the rotating mold or in ingot casting there can be an interaction between the steel grade and the mold surface that can affect the solidification structure at the surface of the casting.

10.4.1 The precipitation of oxides

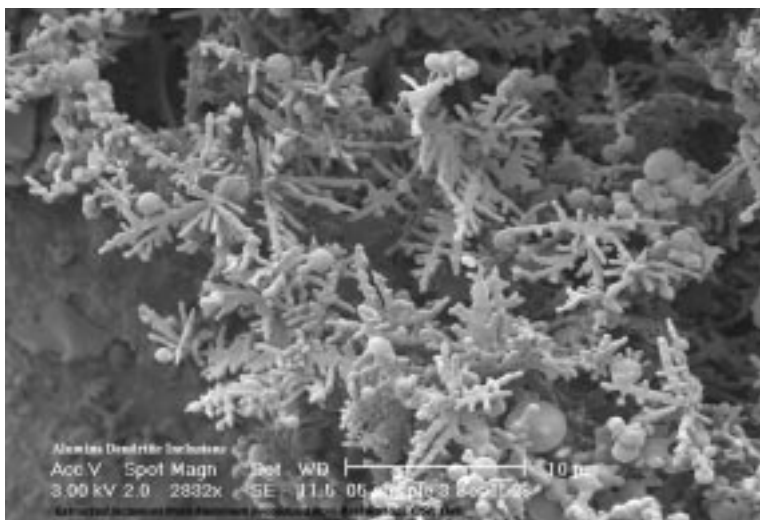
Liquid steels at high temperatures always contain soluble oxygen and it is normal practice to control the level of soluble oxygen by adding deoxidizers.



10.18 Nucleation rate for alumina formation in liquid iron.

Aluminum is the most common deoxidizer addition to liquid steels and solid alumina forms by reaction with the aluminum and oxygen that are dissolved in liquid steel. An example of the homogeneous nucleation rate at constant dissolved oxygen content (0.008%) and as a function of aluminum content is given in Fig. 10.18, where equation 10.27 was used to calculate the nucleation rate. Use of equation 10.6 gives a critical radius of 9 angstroms for homogeneous nucleation of alumina. This calculation is dependent on the initially assumed conditions, for example, a starting oxygen content of 0.008% was used; however, this data indicates significant supersaturation is necessary before there is a significant nucleation rate for alumina precipitation. Once nucleated, growth occurs rapidly to eliminate the supersaturation of aluminum and oxygen in the liquid. For conditions in liquid iron where there is significant liquid stirring due to natural convection or gas injection spheres of alumina can grow to micron sizes in minutes; however, as seen in Fig. 10.19, at high growth rates, alumina dendrites are commonly seen. The situation is more complex than it first appears, as at liquid steel temperatures alumina particles can easily agglomerate, sinter and also coarsen. In Fig. 10.20, an equiaxed dendrite of alumina can be easily seen. Both primary and secondary arms are clearly seen radiating from a central position; however, close inspection indicates that secondary arms are spheroidizing, causing necks in the secondary arms and eventually disconnecting from the primary arm. This is the effect of minimization of surface energy that causes the dendritic array to coarsen and degrade to spheres and rods rather than the extended dendritic array.¹⁸⁻²⁰

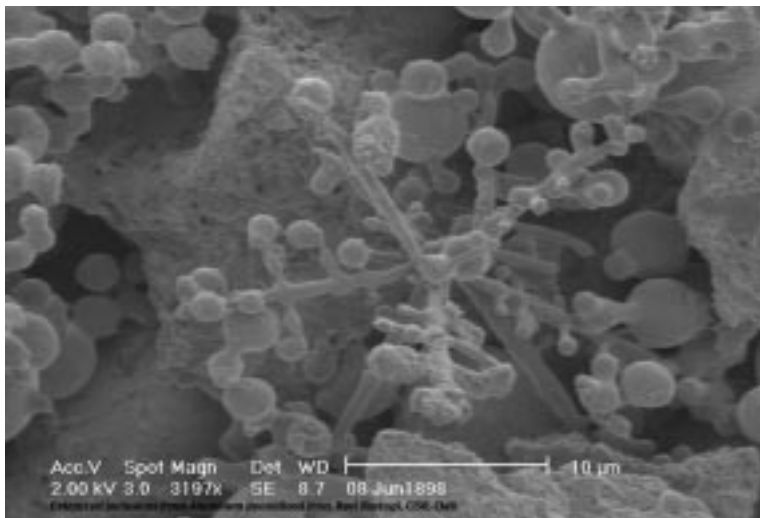
Thus in the observation of alumina inclusions one must understand the thermal history of the inclusion to fully appreciate the structure that is observed.



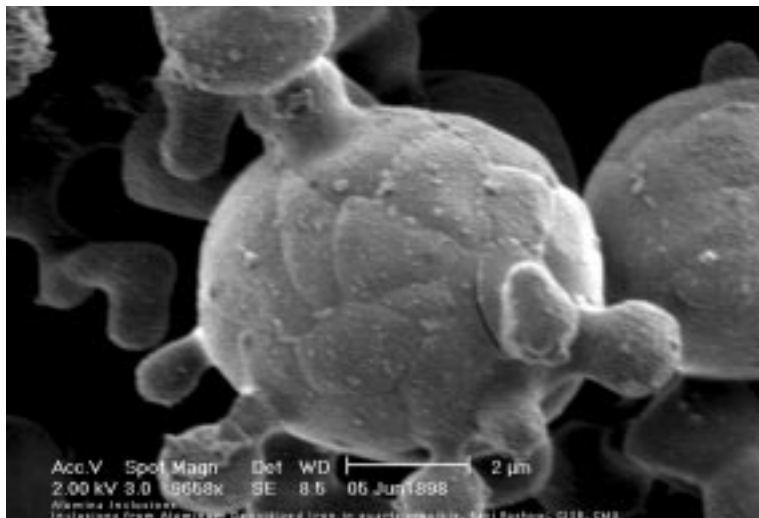
10.19 Morphology of alumina in a deoxidation experiment.¹⁸ Photograph by R. Rastogi.

For example fully spheroidized alumina inclusions can be found at low growth rates as shown in Fig. 10.20.

There are many other deoxidation techniques and it is possible to form a variety of inclusions chemistries in liquid steel. In titanium treated steels, titanium nitride precipitates during cooling and alumina is a heterogeneous nucleation site for titanium nitride. Thus it is common in titanium treated steels



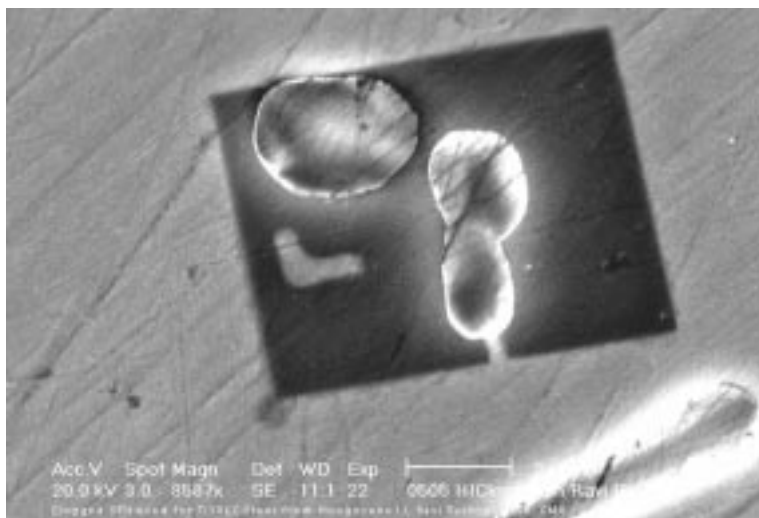
10.20 An equiaxed alumina dendrite exhibiting coarsening.¹⁸ Photograph by R. Rastogi.



10.21 Spheroidized alumina particle.¹⁹ Photograph by R. Rastogi.

to find alumina particles that are completely surrounded by titanium nitride. An example is shown in Fig. 10.21 for a titanium stabilized ultra low carbon steel where the cubic titanium nitride surrounds the alumina.

The precipitation of one inclusion on a pre-existing inclusion in liquid steels is not unusual and manganese sulfide commonly precipitates on alumina during solidification, for example. The inclusions precipitated in liquid steel are also heterogeneous nucleating agents for solidification. This has been well



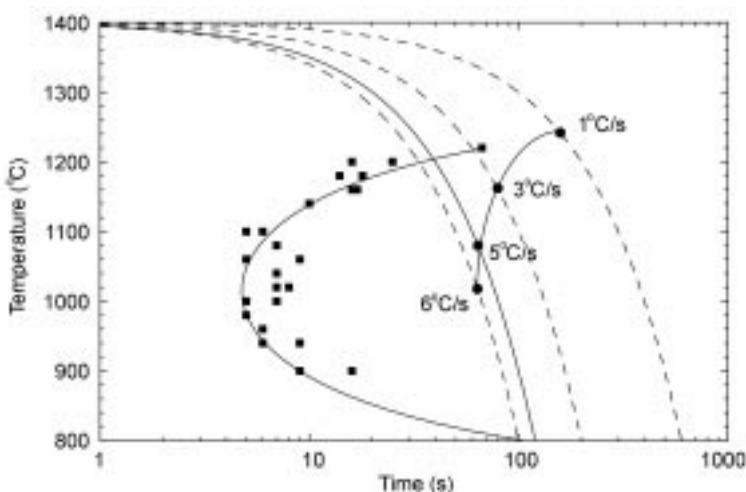
10.22 Titanium nitride particles in solid steel.¹⁹ Photograph by R. Rastogi.

recognized in the welding literature and is only recently becoming interesting to the bulk casting world where fully equiaxed continuous castings are now possible in stainless steel grades where titanium is the primary deoxidant and titanium nitride can be precipitated before solidification (Fig. 10.22). This area termed ‘oxide metallurgy’ by Nippon Steel and is now an area of research focus in addition to nucleation of solidification structures, transformation structures also nucleate from the various inclusions that precipitate during casting and heat treatment.

10.4.2 The solidification of mold slags

Mold slags are multicomponent oxides that are based on the calcium silicate system where there are additions of soda, boria, alumina, magnesia and Lithia, in addition to small amounts of calcium fluoride. These oxides, although bright at steelmaking temperatures, are optically transparent as long as FeO and MnO and titania levels are strictly controlled. This leads to the development of the single and double hot thermocouple techniques that allowed the solidification behavior of slags to be fully understood. For example, from the work of Kashiwaya *et al.*^{21,22} and Orrling *et al.*,^{23–27} both the TTT and CCT curve of a mold slag was determined and is shown in Fig. 10.23.²⁷

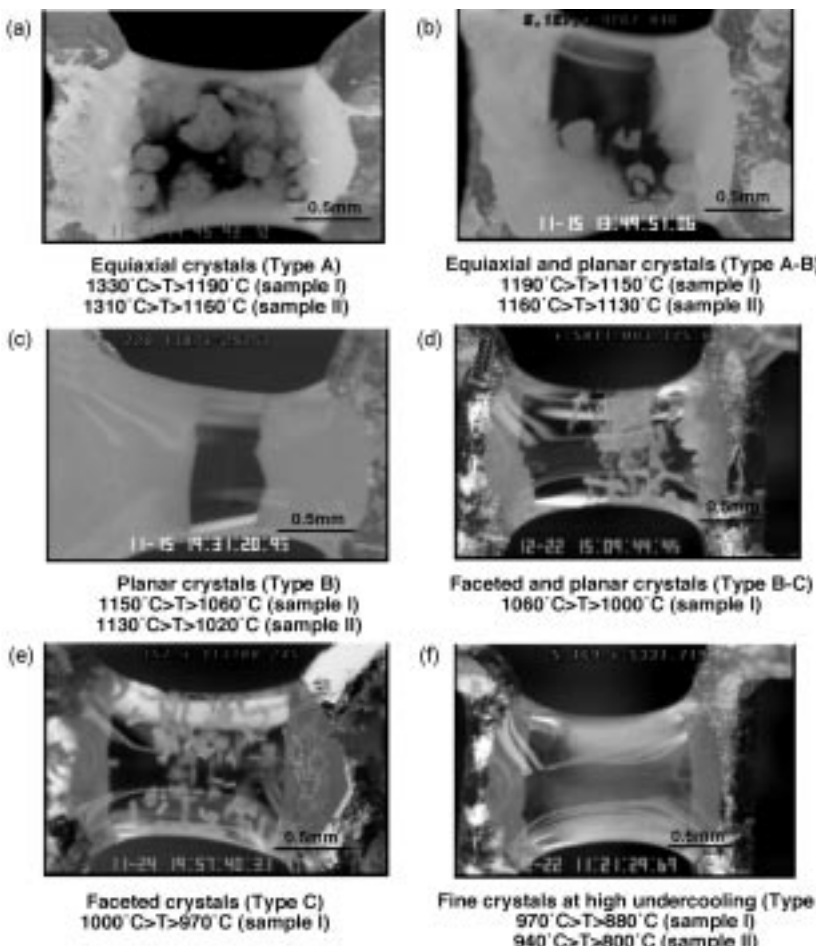
From Fig. 10.23 we can see the typical C shape of the TTT curve and the fact that from continuous cooling experiments the time to solidification start is extended. Both curves are for the first observation of solid. As the liquidus of this slag is approximately 1260°C it is relatively easy to undercool these slags by more than 300°C in TTT mode. The criterion for glass formation in these



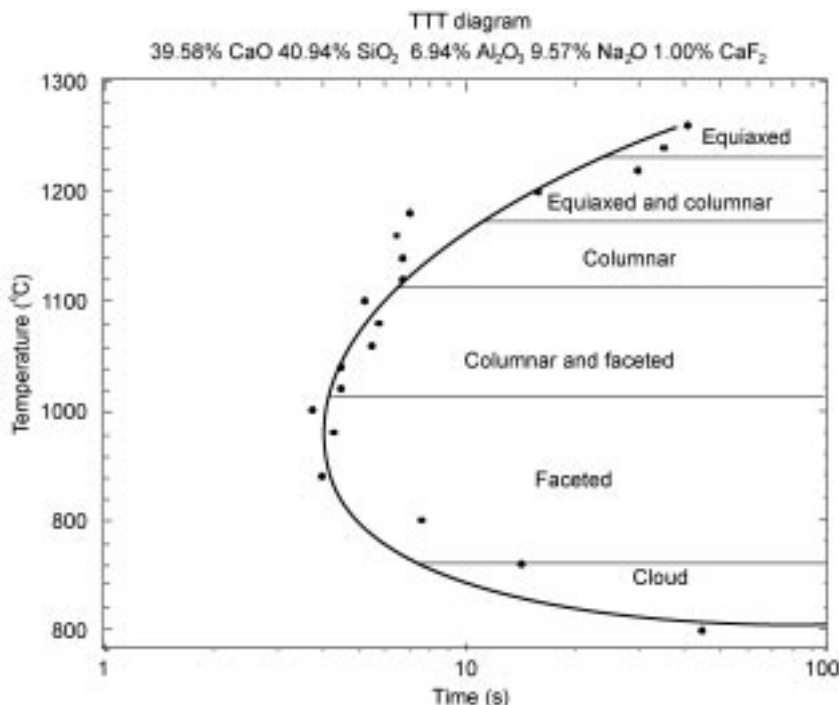
10.23 The TTT and CCT curve of an industrial mold slag.²⁷

experiments is that the cooling rate should be greater than 6°C per second and at thermal gradients above this crystallization can be completely avoided. In these thermocouple techniques solidification at higher temperatures always occurs on the thermocouples as the platinum/rhodium of the thermocouple wire is a heterogeneous nucleation point for solidification of the oxide; however, as the temperature decreases the effect of the thermocouple as a nucleating agent diminishes until eventually there is no effect and solid is seen to precipitate and grow within the bulk of the liquid.

Orrling noted that the morphology of the solidification process is determined by the details of the solidification path (Fig. 10.24) and in the measurement of TTT diagrams using the DHTT made the map shown in Fig. 10.25.



10.24 Examples of the different solidification structures during construction of a TTT curve.²⁷ Photograph by C. Orrling.

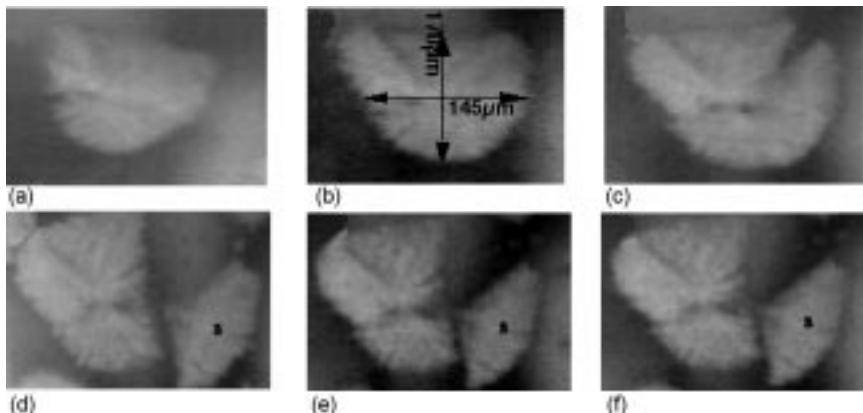


10.25 Map of solidification structures observed during the construction of a TTT diagram.²⁷

Orrling noted that at high temperature, slightly below the liquidus that solidification initiated against the thermocouple itself; however, at temperatures above 1200°C the system was physically stirred due to slight variations in temperature. The fluid flow resulted in the nucleated particles eventually being removed from the thermocouple surface where they would continue to grow in the undercooled liquid as equiaxed crystals. In addition, Orrling noted that the equiaxed crystals as they grew were not stable and frequently broke apart due to the local fluid flow conditions (see Fig. 10.26). These dendrite fragments would then subsequently grow. The structure was then completely equiaxed.

As the temperature was decreased, the amount of observable stirring in the system decreased due to the increasing viscosity of the liquid and eventually the crystals did not detach from the thermocouples and complete columnar growth was observed where both fronts would grow from each thermocouple and meet in the middle (Fig. 10.24c). Of course, at intermediate temperatures, where stirring was still observable, a columnar zone with an equiaxed zone between both fronts was noted. This was due to dendritic fragmentation as noted above.

As the temperature was further decreased, an area of very small faceted crystals appeared between the two growing columnar zones (Fig. 10.24d) and, as



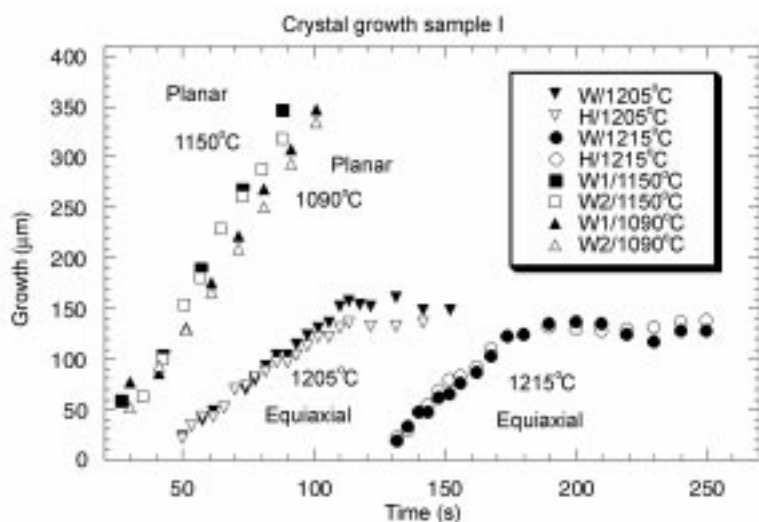
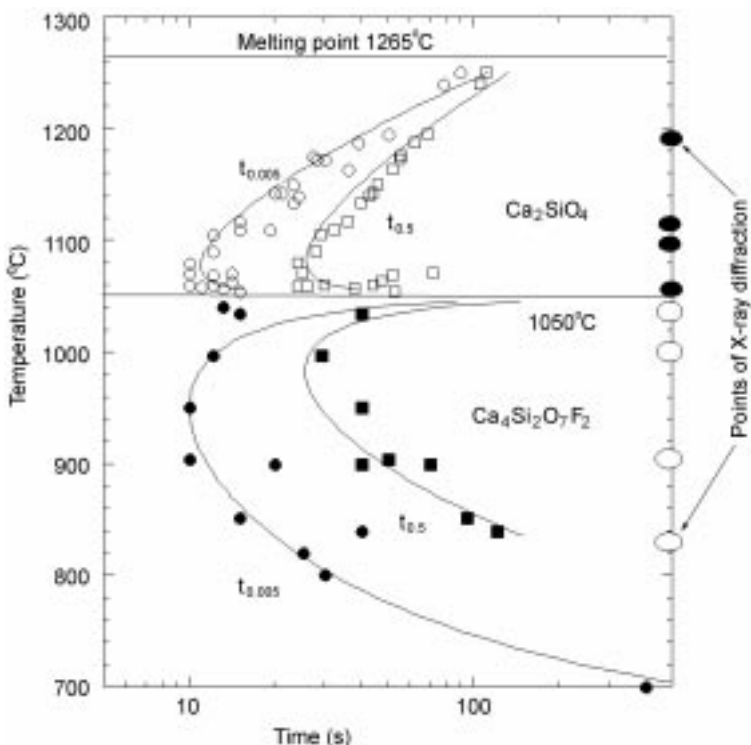
10.26 Dendrite fragmentation at 1220 °C due to fluid flow.²⁵ Photograph by C. Orrling.

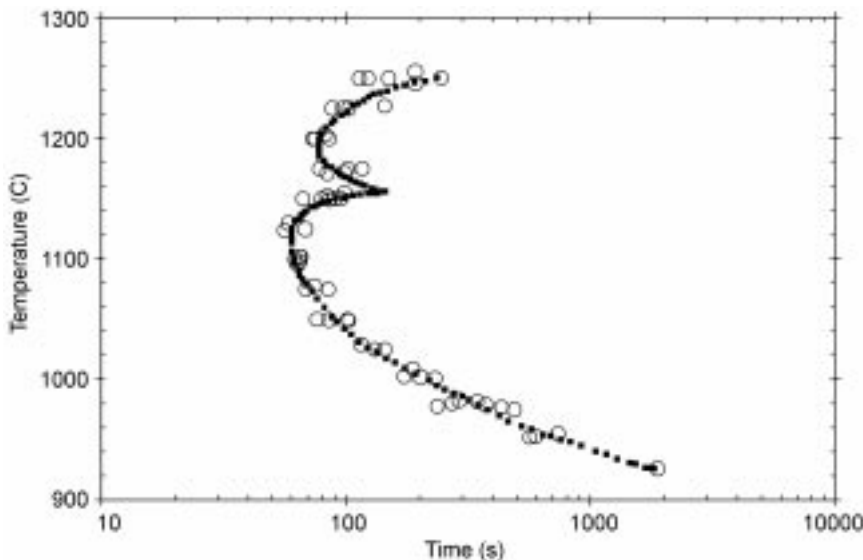
the temperature was further decreased, the extent of the faceted crystals increased until at temperatures below 1000°C only faceted crystals were observed (Fig. 10.24e) and no precipitation on the thermocouples could be discerned.

As the temperature was further decreased the crystals became very fine and the density of crystals increased until it appeared ‘cloud-like’ (Fig. 10.24f). This occurred at 400°C undercooling. This type of map was typical of all oxides studied and indicated the strong effect of fluid flow on structure and also of growth kinetics on structure as growth was always controlled by diffusion and thus decreased with decreasing temperature. In addition, the mode of nucleation changed from nucleation against the thermocouple to nucleation with the body of the liquid. X-ray analysis suggested the composition of the crystal formed in this slag was larnite ($\beta\text{-Ca}_2\text{SO}_4$).

Growth rates in these studies were always linear, as shown in Fig. 10.27, and suggested that the steady state approximation is appropriate and the diffusivity is controlling growth rates where growth rates as a function of tip radius fits Ivantsov’s solution (equation 10.84).

The precipitation of multiple phases is also observed in the solidification of mold slags. For example, from the first ever example of a TTT of a mold slag by Kashiwaya *et al.*²² two different crystal chemistries were determined by X-ray diffraction. The presence of a defined crystal chemistry was determined solely by the temperature of the isothermal hold during construction of a TTT curve (Fig. 10.28) where dicalcium silicate (Ca_2SiO_4) was found at temperatures above 1040°C and cuspidine ($\text{Ca}_4\text{Si}_2\text{O}_7\text{F}_2$) at temperatures below 1040°C. In this situation dicalcium silicate will transform to cuspidine, if held at temperatures below 1040°C and diffusion rates are reasonable. The mold slag measured in this study contained 7.6% Na_2O and 6.5% Al_2O_3 . As both elements do not appear in

10.27 Linear growth kinetics for both columnar and equiaxed dendrites.²⁵10.28 TTT diagram for an industrial mold slag.²⁰



10.29 TTT diagram of a 46% lime–46% silica–6% alumina–2% soda slag.²⁹

the crystal that is precipitated then significant segregation occurs during solidification of the mold slag. Double nosed TTT curves are quite common and in a simpler system shown in Fig. 10.29, dicalcium silicate (Ca_2SiO_4) was the high temperature phase while tricalcium silicate (Ca_3SiO_5) was the lower temperature phase. In addition to TTT and CCT curves the fraction solidified as a function of time can also be determined as seen in Fig. 10.30 where the results fit the form of equation 10.38, the Johnson–Mehl equation where constant growth and nucleation rate are assumed.

The above results suggest that to understand the solidification behavior of a mold slag, it is necessary to have an accurate history of the thermal conditions that the slag has endured as the structure of the slag will evolve with time.

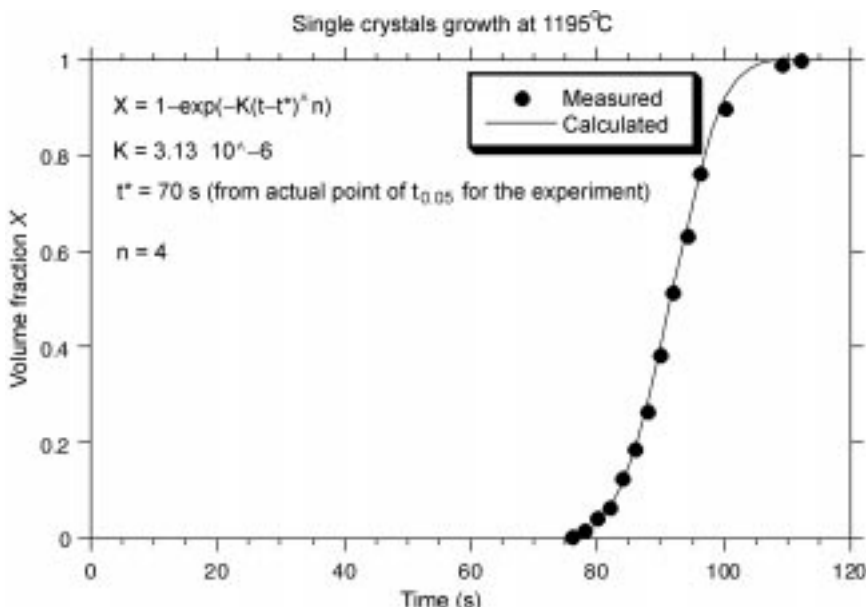
In a continuous casting mold the resistances to heat transfer can be written in a manner equivalent to equation 10.62, where,

$$\Re = \frac{1}{h_{\text{water}} A} + \frac{L_{\text{mold}}}{k_{\text{mold}} A} + \frac{d}{k_{\text{mold slag}} A} + \frac{L_{\text{shell}}}{k_{\text{shell}} A} + \frac{1}{h_{\text{liquid}} A} \quad (10.85)$$

or

$$\Re = \frac{1}{h_{\text{water}} A} + \frac{L_{\text{mold}}}{k_{\text{mold}} A} + \frac{1}{k_{\text{mold slag}} A} + \frac{L_{\text{shell}}}{k_{\text{shell}} A} + \frac{1}{h_{\text{liquid}} A} \quad (10.86)$$

where d is the mold slag thickness and $k_{\text{mold slag}}$ is an effective conductivity for the mold. $h_{\text{mold slag}}$ could also be determined as in equation 10.63 and the conduction, radiation and convection terms calculated separately. Note that as the slag thickness decreases, this resistance decreases and the heat transfer rate



10.30 Example of the evolution of the fraction of solid during the solidification of a slag.²⁷

will increase. However, as we have seen from the above discussion of the solidification behavior of slags, we can expect that the liquid slag will first chill against the mold giving a glass region. At the same time, next to the beginning shell, the slag will be liquid and there will be a large gradient between these positions as mold slag films are quite small (less than 1 mm). Between these two endpoints solidification will initiate and the fraction of solid and the morphology will be strictly dependent upon the exact nature of the cooling conditions in the flux layer. As one travels down the mold it will continue to cool on the shell side and the crystalline structure will continue to evolve. Liquid slags wet copper very well as they deeply undercool and, initially, perfectly wet the mold; however, as the crystals precipitate, they undergo anomalous expansion and cause stresses that can lead to detachment from the mold wall. The small interface voids can occur which can lead to local hot spots and further crystallization. It is of no surprise that the average heat flux in continuous casters is variable with time.

In continuous caster molds this resistance to heat transfer of the mold slag determines the potential casting rate and thermal profile in the shell as it exits the mold and chemistry change in the flux is used to modify heat transfer rates. Until this point we have not introduced atmospheric effects into the discussion; however, calcia-based slags are very hydroscopic and have a significant solubility for water vapor. Orrling *et al.* and Prapakorn *et al.* have shown the extreme sensitivity of solidification behavior to moisture content in the

atmosphere where growth rates are higher and the solidification starts at shorter times and higher temperatures in humid atmospheres.^{25,29}

It is not unusual in continuous cast structures to observe a fine structure on the surface followed by a columnar zone. Often this fine surface structure is referred to as a chill zone; however, it is very difficult to determine the exact nature of this zone by metallography. This fine structure is an indication of undercooling in the mold and as the liquid steel near the top of a mold is in contact with a liquid slag. Thus nucleation at this interface is quite difficult and should require a significant undercooling. Thus nucleation can be heterogeneous on the inclusions that are natural to the system and are transported into this area by bulk fluid flow or by nucleation on solid particles at the mold slag–steel interface. The nature of the initial solidification zone will be determined by the nature of the local fluid flow, the density of potential heterogeneous nuclei in the bulk of the steel and the density of potential nuclei on the slag–steel interface.

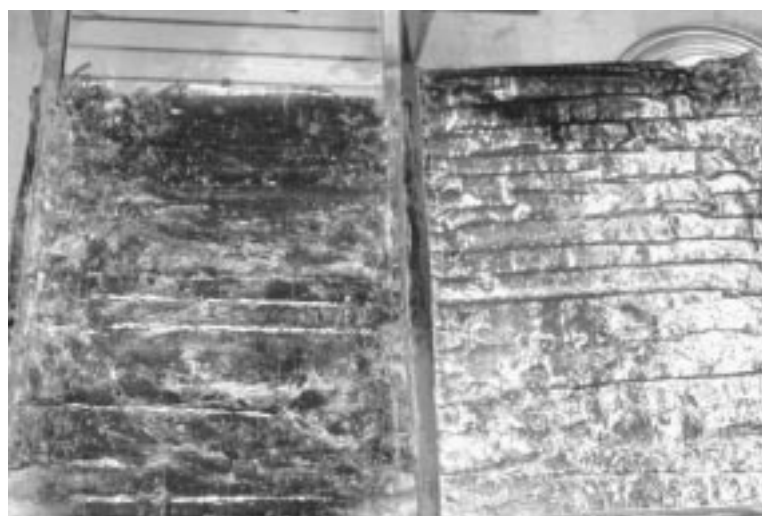
10.4.3 The surface of steel cast continuously in an oscillating mold

During the continuous casting of steel it is common to see surface marks on the surface of cast material. Generally there is at least one mark per oscillation cycle of the mold. This is shown in Fig. 10.27 where the steel surface is shown on the right-hand side of the picture (b) and the slag surface sticking to the mold is shown on the left-hand side of the picture (a). Thus, in operation, both sides would be in contact and the slag surface would be an exact fit to the steel surface.³⁰

The surface topography of continuous cast steels is dependent upon the thermal conditions in the mold and the steel grade that is cast (Fig. 10.31). In general ultra low carbon steels, which tend to have very low solute content, exhibit deep marks that also form hook structures in the surface of the cast slab where it appears that the liquid meniscus solidified and then was subsequently overflowed. In peritectic steels there are also deep marks but the steel surface itself is also wrinkled where in medium carbon grades the oscillation marks are very small and are more like undulations (Fig. 10.32).

In the formation of oscillation marks in ultra low carbon steels, where hook formation is common, recent work has shown that in this case the mark is formed by an increased rate of heat transfer during the negative strip period of mold oscillation due to the liquid meniscus moving closer to the mold wall. Negative strip time is defined as the period during which the mold is moving downwards faster than the strand, while the remaining duration of the oscillation cycle is called the positive strip period. For sinusoidal oscillation, negative strip time is quantified by the following equation:

$$t_n = \frac{1}{\pi f} \arccos \left(\frac{v_c}{\pi s f} \right) \quad (10.87)$$

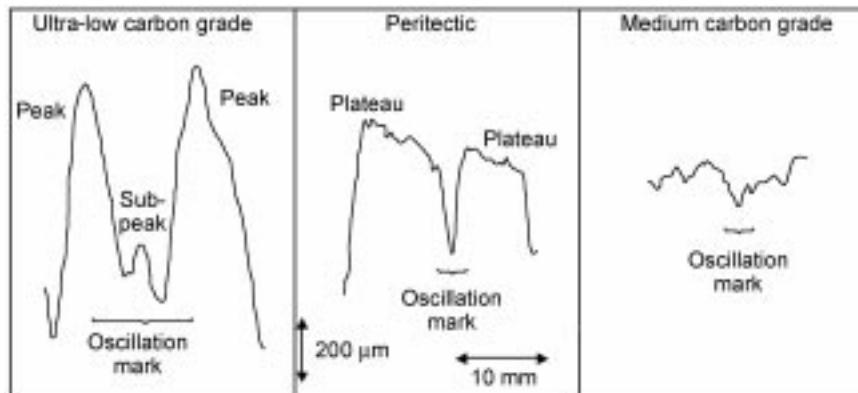


10.31 The surface of continuous cast steel: (a) is the mold slag sticking to the mold and (b) is the surface of the steel.²⁷ Photographs by A. Badri.

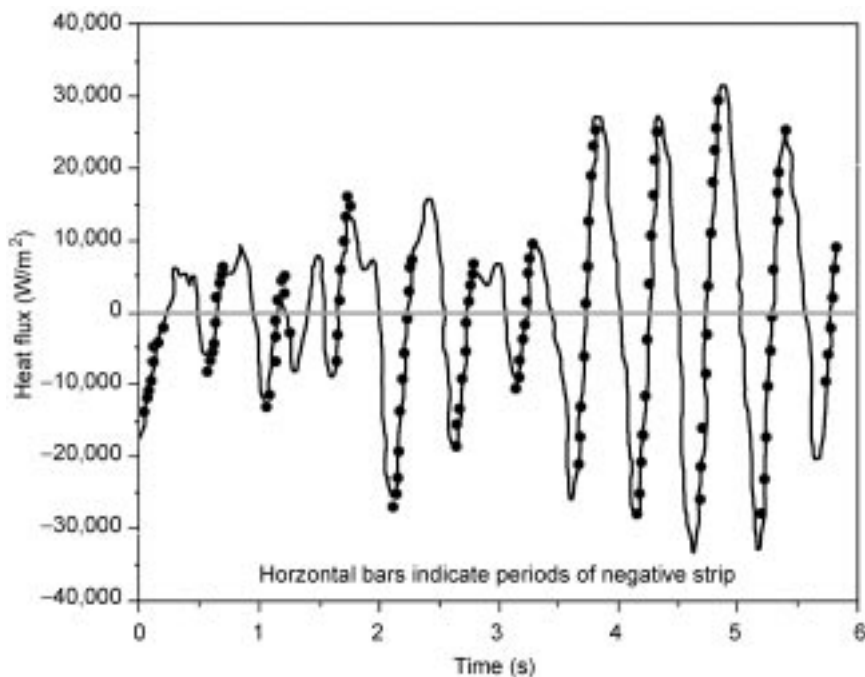
where t_n is the negative strip period, f is the frequency of oscillation (Hz), v_c is the casting speed, and s is the stroke.

Thermal measurements and heat flux calculations by Badri *et al.* have documented this increased heat transfer rate during the negative strip time of mold oscillation (Fig. 10.33) and have shown that local changes in meniscus position during the negative strip time that give rise to increased heat transfer rates are one mechanism of mark formation.^{30–32} Details of this mechanism are shown schematically for an overflow type of mark in Fig. 10.34.

In Badri's work,³⁰ there are two necessary conditions for the formation of a solidified meniscus. First, the mold conditions at the meniscus must be such that



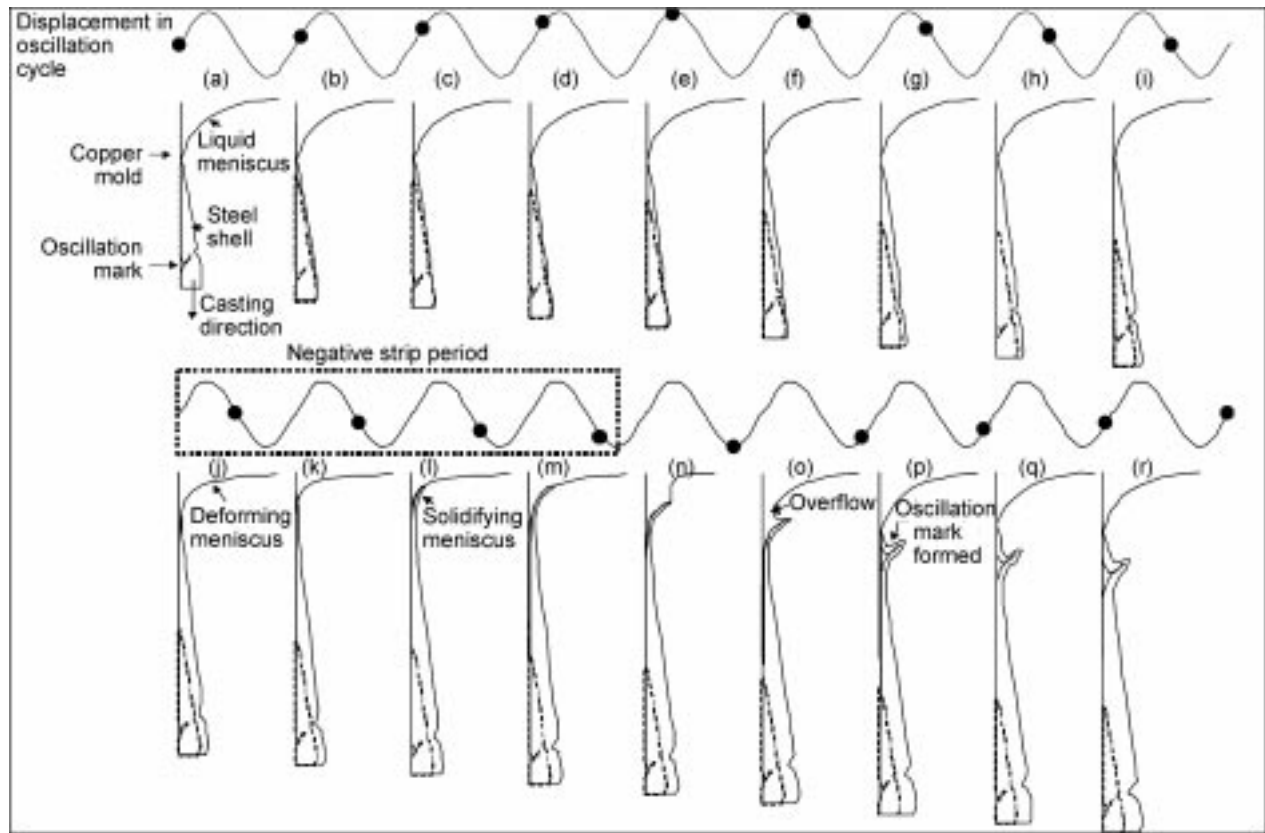
10.32 Profile of oscillation marks as a function of steel grade.³⁰



10.33 Variation of heat flux about an average value during the continuous casting of an ultra-low carbon steel (horizontal bars are the negative strip time).³⁰

the potential for heat transfer is sufficient to cause solidification of the curved meniscus. Second, the liquid meniscus must deform such that the liquid comes into close proximity with the copper mold. The simultaneous occurrence of these two necessary conditions provides the sufficient condition for the solidification of the meniscus. The final necessary condition determines the type of mark that forms. The frozen meniscus can be overflowed to form a subsurface hook-type oscillation mark, or, if the frozen meniscus lacks strength, the rising liquid can force the shell back to the mold, forming a depression-type mark. Therefore, the first two necessary conditions must occur simultaneously, followed by the third condition, to create a series of events necessary and sufficient for the formation of oscillation marks (Fig. 10.34). It should be noted that meniscus movement can be caused by fluid flow as well as mold oscillation and the extra marks that are often seen in continuous cast surfaces are often due to loss of level control and wave motion in the mold of the continuous caster.

During the negative strip period, where there is little relative motion between the mold and the shell, undercooled growth of dendrites combined with normal solidification might be expected and dendrites will grow along the meniscus as noted first by Saucedo.³³



10.34 Schematic of the formation of an overflow oscillation mark.³⁰

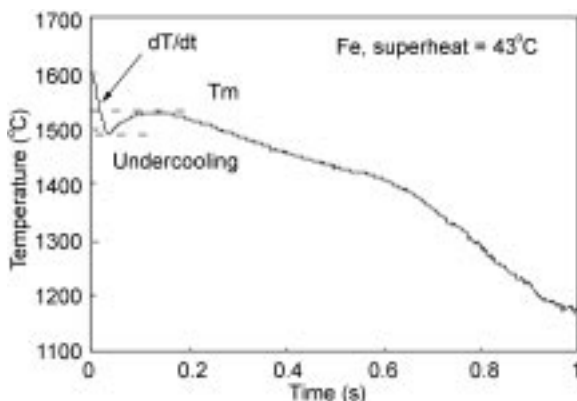
10.4.4 Undercooling and initial solidification

It is clear that in order to have an equiaxed zone one must have an undercooled liquid in contact with the solid where one can transfer heat and allow growth in all directions. Undercooled growth thus occurs when the liquid temperature is below the interface temperature. This can occur by cooling the liquid below its equilibrium transformation temperature or by compositional segregation during the solidification process. Liquid iron and its alloys can be easily undercooled during normal steel deoxidation practices; however, recent work has indicated that inclusion engineering in steels can result in large equiaxed zones due to nucleation on pre-existing solid inclusions at low undercoolings.

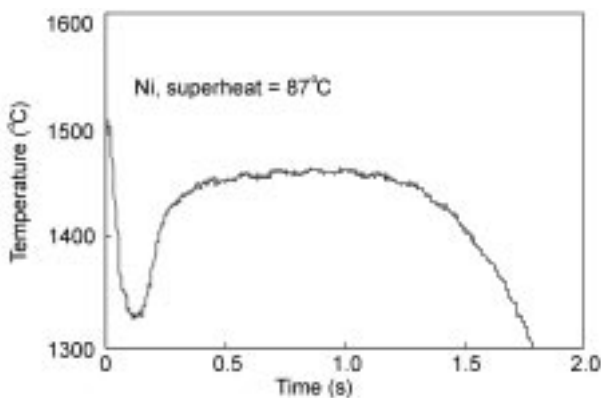
The undercooling of liquid steel against a mold surface has been studied in detail by Mizukami *et al.*^{34–37} Using a small hole in a mold to observe the surface temperature of the cast surface, Mizukami *et al.* were able to observe significant undercoolings and very high initial heat transfer rates using the ejected droplet method.³⁴ Subsequent developments of the technique have lead to fully instrumented molds able to measure both shell surface temperature and the thermal profile in the mold.^{38–42}

Mizukami *et al.*'s technique³⁴ has allowed the measurement of undercoolings at very short times and the measurement of very high initial heat transfer rates where there is adequate contact between the mold and the liquid. For example, from the studies of Todoroki *et al.*⁴² both nickel and iron were observed to significantly undercool before recalescing to their equilibrium temperature (Figs 10.35 and 10.36). Relationships between the cooling rate and the undercooling were also measured (Fig. 10.37) where in alloys higher cooling rates and higher undercoolings were measured.

In general, in droplet experiments as superheat of the droplet increases the measured heat flux increases and the surface of the casting becomes smoother.



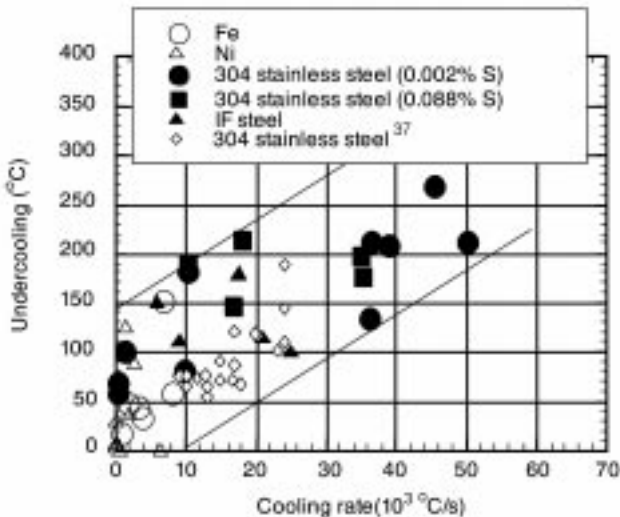
10.35 Measurement of the undercooling of liquid iron using Mizukami's technique.³⁷



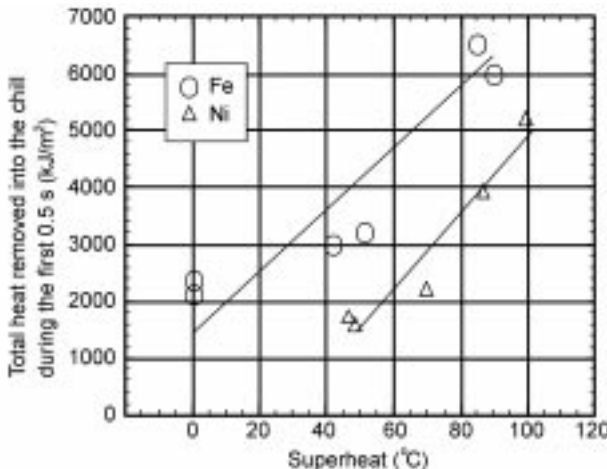
10.36 Measurement of the undercooling of liquid nickel using Mizukami's technique.³⁷

This is due to better wetting of the liquid to the mold. For example, in Fig. 10.38 the total heat removed in a droplet experiment in 0.5 seconds is plotted as a function of superheat and the cast surface roughness is plotted as a function of superheat in Fig. 10.39.

The effect of superheat on the cast surface roughness and heat transfer rate are linked as higher heat transfer rates suggest better contact between the mold and the shell. This should also result in the overall cooling rate of a casting being higher (at least in the first millimeter cast where contact resistance is still a



10.37 Relationship between cooling rate and achieved undercooling on a water cooled copper mold.³⁷

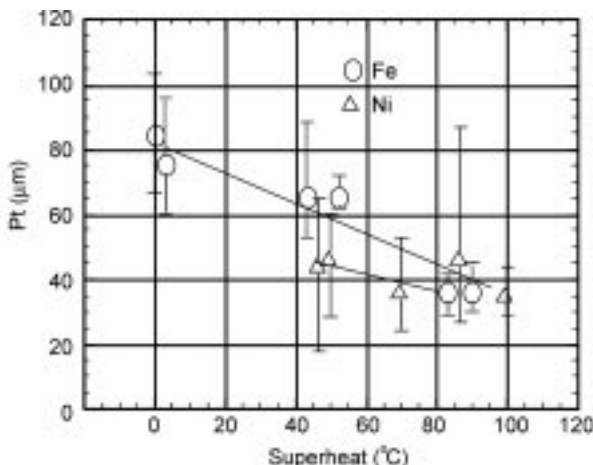


10.38 Relationship between superheat and heat removed.³⁷

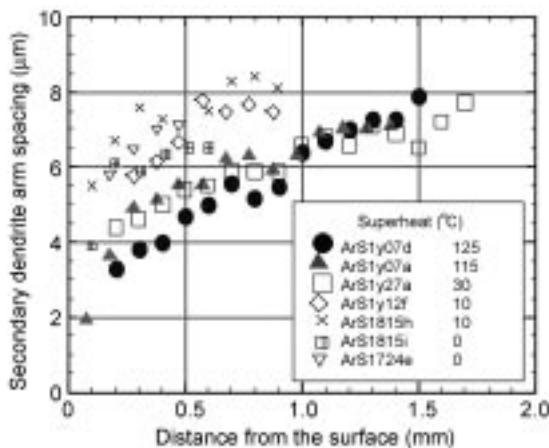
greater resistance to heat transfer than conduction in the shell. This is shown clearly in Fig. 10.40 where the secondary dendrite arm spacing is shown to decrease as superheat increases.

Local cooling rate can be calculated from the values of the measured secondary dendrite arm spacing using an empirical relationship between secondary dendrite arm spacing and the local cooling rate developed by Mizukami *et al.*:³⁷

$$\lambda_2 = 100T^{-0.35} \quad (10.88)$$



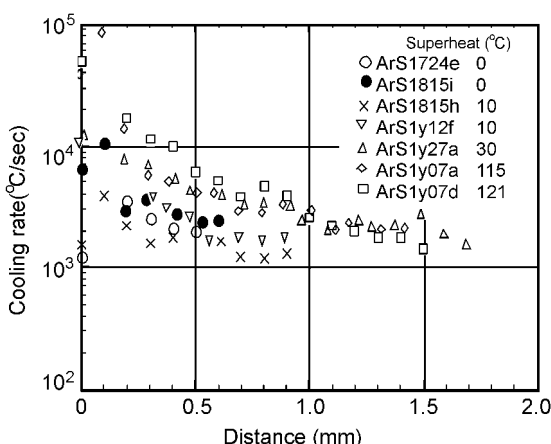
10.39 Effect of superheat on roughness of the cast surface.³⁷



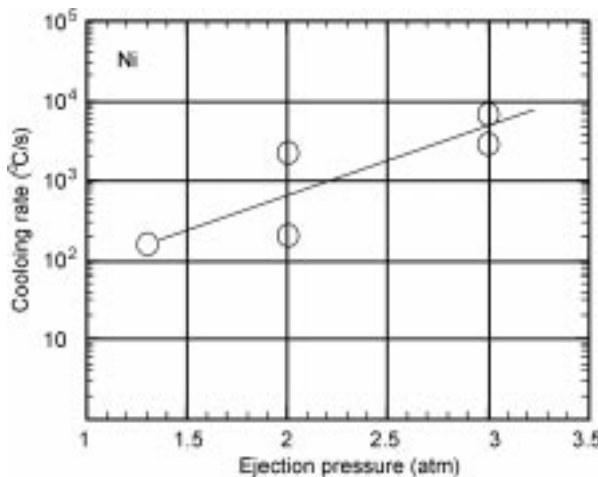
10.40 Effect of superheat on secondary dendrite arm spacing.

where λ_2 is secondary arm spacing (μm) and T is local cooling rate ($^{\circ}\text{C}/\text{s}$). Using equation 10.88 the secondary dendrite arm spacings were converted to cooling rates and these results are shown in Fig. 10.41. Extrapolations of the local cooling rates are in agreement with the cooling rates obtained by the surface temperatures of the solidified steel.

In these results the effect of superheat is perhaps counter-intuitive as one would expect increased superheat to increase gradients in the liquid and increase the amount of heat transferred through the interface from the liquid, thus reducing the growth rate via equation 10.40. However, as nucleation does not occur until the temperature is significantly reduced, the effect of superheat in droplet experiments is to extend the time before solidification initiates and to



10.41 Cooling rate in the casting as a function of superheat.



10.42 Effect of ejection pressure on surface cooling rate.

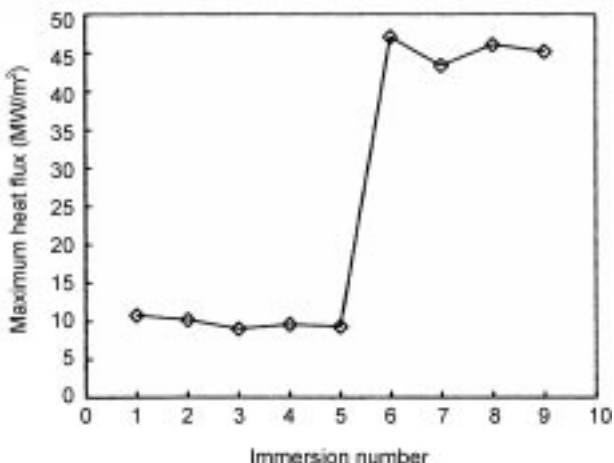
allow better contact of the liquid to the mold before the shell is formed. As there is considerable stirring in ejected droplets the superheat is dissipated very quickly before the onset of solidification and significant undercooling is possible due to the high heat transfer rates that are possible due to improved contact between the mold and the shell. Thus any factor that reduces the equilibrium temperature for solidification start (e.g. composition) will have a similar effect as it will allow better contact of the liquid alloy to the mold surface before initiation of solidification.

Another method of improving contact is to fill a mold more quickly. This can be accomplished by increasing ejection pressure (Fig. 10.42) and if the liquid covers the mold more quickly, the cooling rate increases due to better contact.

10.4.5 Interactions between the mold and the steel shell

During casting in an oscillating mold caster there is always a solid/liquid oxide between the steel shell and the mold; however, in twin roll, horizontal and ingot casting, the shell comes into direct contact with the mold. This leads to the opportunity for material to be transported during solidification from the steel to the mold surface and to affect the heat transfer rate. This was shown by first by Strezov *et al.*^{43,44} in dip experiments (Fig. 10.43) and by Evans^{45,46} in droplet experiments where in Mn-Si killed steels MnO-SiO₂ coats the mold surface and leads to an increase in the heat transfer rate.

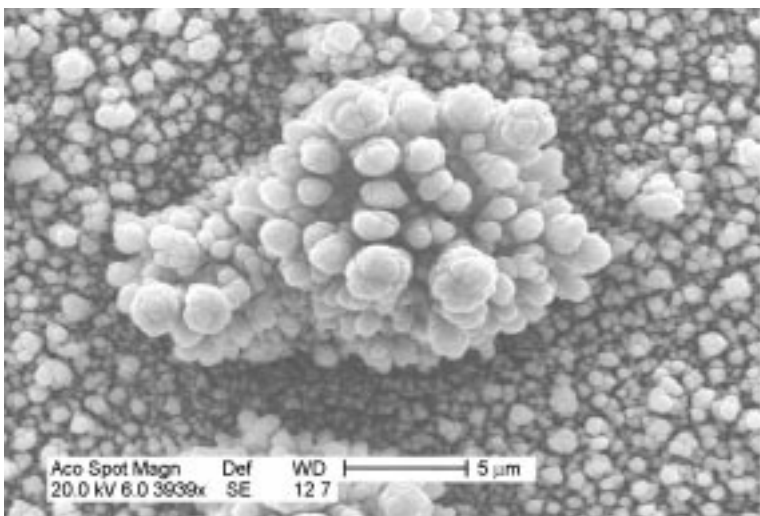
Misra *et al.*^{38,39} later showed this to be a quite general phenomenon in steels when liquid oxides are the stable natural oxide and showed that, due to contact angle changes during cooling, the natural liquid inclusions can be physically ejected onto the surface of the mold. Evaporation is also a mechanism by which



10.43 Maximum heat flux as a function of repeated immersion.⁴³

material can be transported onto mold surfaces and in aluminum killed steels where the natural inclusions are solid, MnS films are found to build up on mold surfaces.^{38,39} In high manganese content steels, Mn evaporation rates are high and MnO is deposited onto mold surfaces (Fig. 10.44).^{47,48}

When a liquid contacts a mold there is not perfect contact between the liquid and the mold and, on the microscale, the liquid sits on top of the peaks of the roughness of the mold. Thus there is intermittent contact between the mold and



10.44 MnO deposits on the mold surface during the casting of a high manganese steel. Photograph by P. Nolli and M.E. Valdez.

the liquid and there will be a significant contact interfacial heat transfer coefficient. Initially, there will be gas in the voids between the mold and the liquid and convection and radiation heat transfer will control the rate of heat loss in these areas. A detailed description of this contact between the mold and the liquid would be determined by the wettability between the liquid steel and the mold, the ease of undercooling and the initial superheat (to allow contact before solidification), the time for nucleation, the liquid coverage velocity and the pressure under which the liquid is pressed against the mold. If casting in a vacuum, one could force complete wetting by supplying enough force to overcome the surface tension forces. The presence of surface films changes the wettability between the liquid and the surface and tends to fill in the valleys of the roughness. In addition, if the deposited film can melt during the solidification process, one goes towards perfect wetting of the deposited film to the shell and the elimination of areas of voids. Thus one can eliminate the contact resistance and replace that resistance with a conduction resistance for heat transfer through the deposited film. Thus, as long as the film is thin, and the new conduction resistance is less than that for intermittent contact, the total heat flux will increase.

Thus in twin roll casting, or in any casting where there can be interaction between the steel and the mold, heat flux can vary locally and with time due to the deposition of material on the mold surface. This can lead to significant increases in heat flux, which if controlled can lead to increased productivity, but, if uncontrolled, can lead to local variation in heat transfer rates and the onset of cracking.⁴⁸

10.5 Conclusion

The contact between a liquid and a mold controls the details of initial heat transfer rates in steel castings and is a key issue in the understanding of the initial solidification structures that can be formed. In conventional casting the solidification structure of a mold flux is a key component in the understanding of heat transfer and recent studies have shown that mold slags are easy glass formers and thus solidification structures are quite variable and determined by local thermal gradients; however, TTT and CCT diagrams can be very useful in understanding this behavior. Surface oscillation marks are caused by variation in meniscus position during mold oscillation that affects local heat transfer rates. This can lead to hook type marks in grades with small liquidus to actual solidus gaps. In twin roll or ingot casting solidification structures are controlled by the relative velocity between the mold and the steel, the chemical nature of the surface of the mold, superheat and steel chemistry. Undercooling and extremely high heat transfer rates can be measured at short times when liquid steel comes into contact with a water-cooled mold and leads to very fine microstructures at the casting surface.

10.6 Acknowledgements

All professors are only as good as their students and co-workers. Thus most figures and photographs from a research group are taken from the work of a graduate student or a visiting researcher. In this chapter I'd like to thank C. Orrling, A. Badri, M.E. Valdez, R. Rastogi, N. Phinichka, P. Misra, H. Todoroki, I. Jimbo, T. Suzuki, Y. Kashiwaya and H. Shibata for their contributions both intellectually and artistically.

10.7 References

1. M. Flemings: *Solidification Processing*, 1974, Butterworths, London.
2. W. Kurtz and D.J. Fisher: *Fundamentals of Solidification*, 1984, Trans Tech Publication, Switzerland.
3. W.A. Tiller: *The Science of Crystallization: Macroscopic Phenomena and Defect Generation*, 1991, Cambridge University Press, London.
4. W.A. Tiller: *The Science of Crystallization: Microscopic Interfacial Phenomenon*, 1991, Cambridge University Press, London.
5. V. Alexiades and A.D. Solomon, *Mathematical Modeling of Melting and Freezing Processes*, 1993, Hemisphere Publishing Corporation.
6. Dimo Katsiev: *Nucleation*, 2000, Butterworth Heineman.
7. B. Mutaftschiev: *The Atomic Nature of Crystal Growth*, 2001, Springer Verlag, Berlin.
8. S. Davis: *The Theory of Solidification*, 2001, Cambridge University Press, London.
9. D.M. Stefanescu: *Science and Engineering of Casting Solidification*, 2002, Kluwer Academic/Plenum Publishers.
10. M. Rappaz, C. Beckermann and R. Trivedi (eds), *Solidification Processes and Microstructures*, TMS, 2004.
11. J.W. Gibbs, *The Scientific Papers, Vol. 1: Thermodynamics*, 1961, Dover Publications, New York
12. M. Volmer and A. Weber: *Z. Phys. Chem.*, 119, 1926, 277.
13. T. Tanaka, M. Nakamoto and J. Lee: *Metal Separation Technologies III*, R.E. Aune and M. Kekkonen (eds), Helsinki University Publishing, 2004, 135–142.
14. J.R. Sambles: *Proc. Roy. Soc. London A*, vol. 423 A, 339–351.
15. B.L. Bramfitt: Effect of Carbide and Nitride Addition on the Heterogeneous Nucleation, Behaviour of Liquid Iron, *Met. Trans*, vol. 1, no. 7, July 1970.
16. O. Grong, *Metallurgical Modeling of Welding*, 2nd edn, The Institute of Materials, 1997.
17. M.E. Valdez, H. Shibata, S. Sridhar and A.W. Cramb: ‘The Solidification Rate of Undercooled Pure Liquid Iron’, TMS/AIST Conference, New Orleans, September 2004.
18. A.W. Cramb and M. Byrne (eds), *Making Shaping and Treating of Steel – Vol. 3, Casting*, AISE, 2003.
19. R. Rastogi, doctoral thesis, Carnegie Mellon University, 2000.
20. R. Rastogi and A.W. Cramb: Inclusion Formation and Agglomeration in Aluminum Killed Steels, 84th Steelmaking Conference Proceedings, 2001, 789–829.
21. Y. Kashiwaya, C.E. Cicutti and A.W. Cramb: Crystallization Phenomena of Mold

- Slag for Continuous Casting, *ISIJ International*, vol. 38, no. 4, 1998, 357–365.
- 22. Y. Kashiwaya, C.E. Cicutti and A.W. Cramb: ‘Crystallization Behaviour of Slags’, *Steelmaking Conference*, 1998, vol. 81, 185–191.
 - 23. C. Orrling, A. Tilliander, Y. Kashiwaya and A.W. Cramb: ‘Melting and Solidification of Slags’, *Steelmaking Proceedings*, 1999, vol. 82, 417–425.
 - 24. C. Orrling, S. Sridhar and A.W. Cramb: *In situ Observation of the Role of Alumina on the Solidification Behavior of Slags*, *ISIJ*, 2000, 877–885.
 - 25. C. Orrling and A.W. Cramb: ‘The Effect of Water Vapor on Mold Slag Crystallization’, *Met Trans B*, 2000, vol. 31B, 403–406.
 - 26. C. Orrling, Y. Fang, N. Phinichka, S. Sridhar and A.W. Cramb: ‘Observation and Measurement of Solidification Phenomena at High Temperatures’, *JOM-e*, July 1999 (<http://www.tms.org/pubs/journals/JOM/9907/Orrling-9907.html>).
 - 27. C. Orrling, doctoral thesis, Carnegie Mellon University, 2000.
 - 28. C.T. Mutale, T. Claudon and A.W. Cramb: ‘Observation of the Crystallization Behavior of a Slag containing 46 wt.% CaO, 46 wt.% SiO₂, 6 wt.% Al₂O₃, and 2 wt.% Na₂O using the Double Hot Thermocouple Technique’, unpublished research.
 - 29. K. Prapakorn, C. Orrling and A.W. Cramb: ‘The Solidification Behavior of Calcium Aluminate in Dry and Wet Atmospheres’, *European Casting Conference*, vol. 2, 2002, 733–742.
 - 30. A. Badri, doctoral research, Carnegie Mellon University, 2003.
 - 31. A. Badri, T.T. Natarajan, C.C. Snyder, K.D. Powers, F.J. Mannion, and A.W. Cramb: ‘A Mold Simulator for the Continuous Casting of Steel, Part 1, Steel Shell Solidification Profiles’, *Met Trans B*, 2004, vol. 36B, no. 3, 355–372.
 - 32. A. Badri, T.T. Natarajan, C.C. Snyder, K.D. Powers, F.J. Mannion, M. Byrne and A.W. Cramb: ‘A Mold Simulator for the Continuous Casting of Steel, Part 2, The Formation of Oscillation Marks During the Continuous Casting of Low Carbon Steels’, *Met Trans B*, 2004, vol. 36B, no. 3, 373–416.
 - 33. I.G. Saucedo: *Continuous Casting, Volume 9: Initial Solidification and Strand Surface Quality of Peritectic Steels*, 1997, ISS–AIME, Warrendale, PA, 131–141.
 - 34. H. Mizukami, T. Suzuki and T. Umeda: *Tetsu-to-Hagane*, 77, 10, 1991, 1672.
 - 35. H. Mizukami, T. Suzuki and T. Umeda: *Tetsu-to-Hagane*, 78, 4, 1992, 580.
 - 36. H. Mizukami, T. Suzuki and T. Umeda: *Tetsu-to-Hagane*, 78, 8, 1992, 1369.
 - 37. H. Mizukami, T. Suzuki, T. Umeda and W. Kurtz: *Material Science and Eng A*, 173, 1993, 36.
 - 38. N. Phinichka, P. Misra, Y. Fang and Alan W. Cramb: ‘Initial Solidification Phenomena in the Casting of Steels’, *Innovation and Excellence in Continuous Casting*, 2nd edn, Stahl Eisen, 2003, 65–78.
 - 39. P. Misra, N. Phinichka and A.W. Cramb: ‘The Effect of the Presence of Liquid Films on a Copper Mold Surface on the Rate of Heat Transfer during the Solidification of Steel Droplets’, *ISS Transactions 2003*, Iron and Steelmaker, vol. 30, no. 10, 2003, 46–55.
 - 40. H. Todoroki, R. Lertarom, I. Jimbo, T. Suzuki and A.W. Cramb: ‘Solidification of Steel Droplets against a Water Cooled Copper Mold’, *Proceedings of the McLean Symposium*, ISS, 1998, 155–175.
 - 41. H. Todoroki, R. Lertarom, I. Jimbo, T. Suzuki and A.W. Cramb: ‘Initial Solidification of Iron, Nickel and Steel Droplets’, TMS Meeting, San Diego, 1998.
 - 42. H. Todoroki, Y. Suzuki and A.W. Cramb: ‘Initial Solidification of Iron, Nickel and Steel Droplets’, *ISS Transactions*, 1999, I&SM, vol. 26, no. 4, 57–71.

43. L. Strezov and J. Herbertson, 'Experimental studies of interfacial heat transfer and initial solidification pertinent to strip casting', *ISIJ International*, 38(9), 1998, 959–966.
44. L. Strezov, J. Herbertson and G.R. Belton: 'Mechanism of initial melt/substrate heat transfer pertinent to strip casting', *Metallurgical and Materials Transaction B*, 31B, October 2000, 1023–1030.
45. T. Evans, PhD Thesis, University of Newcastle, 2000.
46. T. Evans and L. Strezov: *Metallurgical and Materials Transaction B*, 31B, October 2000, 956–966.
47. D. Choo, P. Nolli, P. Misra, M.J. Ha and A.W. Cramb: 'The Effect of Surface Oxide Films on Heat Transfer Behavior in the Strip Casting Process', *AISE Conference*, Pittsburgh, 2003.
48. P Nolli, D.K. Choo and A.W. Cramb: 'The Effect of Surface Oxide Films on Heat Transfer Behavior in the Strip Casting Process', *TMS/AIST Conference*, September 2004.

G E N G B E R G , SSAB Tunnplåt AB and MIK Research AB (MIKRAB) and
L K A R L S S O N , Dalarna University, Sweden

11.1 Introduction

Metal working processes encompass a wide range of strain, strain rates and temperatures. Strains range from less than 0.01 (for example in skin-pass rolling of interstitial free steel) up to around 1 (cold rolling of strip, extrusion, etc.). Typical strain rates and temperatures are given in Table 11.1 (which is partly an extract from Frost and Ashby (1982)).

For plastic forming processes the most important characteristics of the material are:

- the ability to distribute strains;
- the deformation resistance; and
- the resulting properties of the formed part.

Table 11.1 Characteristics of metal working processes and typical values for some common testing methods

Process	Strain rate (s^{-1})	Temperature
Cold working (rolling, forging, levelling, ...)	1–2000	RT, slight adiabatic heating
Wire drawing (sheet, tube drawing)	1–20 000	RT–0.3 T_m , adiabatic heating
Explosive forming	10–1000	RT
Machining	100–100 000	RT–0.4 T_m , adiabatic heating
Warmworking (rolling, forging, ...)	1–1000	0.35–0.5 T_m
Hotworking (rolling, forging, ...)	1–1000	0.55–0.85 T_m
Extrusion	0.1–100	0.7–0.95 T_m
<hr/>		
Testing method		
Tensile	up to 1000	RT
Tensile and compression	up to 100	up to T_m
Hopkinson bar	up to ~ 4000	RT

RT: room temperature, T_m : melting temperature in degrees Kelvin.

The ability to distribute strains is mainly governed by the work hardening and strain-rate sensitivity. It is also affected by the strain path.

The purpose of this paper is to outline the, in our view, most essential material properties for metal working processes and the microstructural reasons for them. We recognise that the presence and development of crystallographic texture is quite an important part but our purpose is not to give an extensive description of this, only to point out some consequences. For further reading we recommend a book by Kocks, Tomé and Wenk (1998). Another aspect that is only briefly covered is the influence of stress states and changes in strain paths during processing or between consecutive process steps.

11.2 Work hardening

As commonly accepted the flow stress, σ , is usually proportional to the square root of the dislocation density, ρ . For a polycrystalline material the proportionality constant can be seen as the product of the Taylor factor, m , the strength of the barriers (such as attractive junctions between dislocations), α , the shear modulus, G , and Burgers' vector, b . The rates of dislocation generation and recovery/annihilation thus determines the work hardening rate.

$$\sigma = \sigma_0 + m \cdot \alpha \cdot G \cdot b \cdot \sqrt{\rho} \quad (11.1)$$

$$\frac{d\rho}{dt} = \left(\frac{d\rho}{dt} \right)_{\text{generation}} + \left(\frac{d\rho}{dt} \right)_{\text{recovery}} \quad (11.2)$$

σ_0 are all other contributions to the flow stress except deformation hardening. Dislocation generation is affected mainly by other dislocations, their ability to cross-slip and grain and phase boundaries. Recovery is usually considered to be due to cross-slip and climb and of course recrystallisation contributes to annihilation of dislocations.

11.2.1 Single phase materials

The shear strain obtained by slip of one dislocation is given by the relative displacement of the dislocation in the slip plane times Burgers' vector over the height. For $\Delta\rho$ dislocations per unit area slipping an average distance of L during the time increment Δt the relation to the normal strain increment, $\Delta\epsilon$, can be written as

$$\left(\frac{d\rho}{dt} \right)_{\text{generation}} = \frac{m}{b \cdot L} \cdot \frac{d\epsilon}{dt} \quad (11.3)$$

The mean free distance of slip is for Frank networks limited by the distance between individual dislocations, $\sim 1/\sqrt{\rho}$, while for heterogeneous dislocation structures by the cell or subgrain sizes. This implies that strain hardening varies

between linear and parabolic. The tendency to form substructures is closely related to the ability of dislocations to leave their original slip plan, either by cross-slip or a combination of cross-slip and climb. Both are thermally activated processes, cross-slip by bringing two partials together allowing them to slip on a secondary slip system and climb by diffusion. Body centred cubic (bcc) metals normally have very large stacking fault energies and a large number of possible slip systems while a large variety of stacking fault energies is found for face centred cubic (fcc) metals.

During deformation grains change their shapes and rotate. In order to account for the different changes in individual grains it has been proposed that additional, ‘geometrically necessary’, dislocations are created at the boundaries to accommodate the differences (Ashby 1971). The corresponding geometrical dislocation slip distance is proportional to the grain size, d . For small grain sizes this is manifested as an increased hardening rate (Chandrasekaran 2003).

Bergström has proposed a model where the recovery term is due to remobilisation of dislocations (Bergström 1983). In his formulation

$$\left(\frac{d\rho}{dt}\right)_{\text{recovery}} = -\Omega \cdot \rho \cdot \frac{d\epsilon}{dt} \quad (11.4)$$

where Ω is measure of remobilisation. Another approach is to assume that dislocations are increasing their link length by diffusion controlled climb (Friedel 1964). We can write this as

$$\left(\frac{d\rho}{dt}\right)_{\text{recovery}} = -M \cdot \rho^2, \quad M = \frac{D_s G b^3}{kT \cdot \ln(l/b)} \quad (11.5)$$

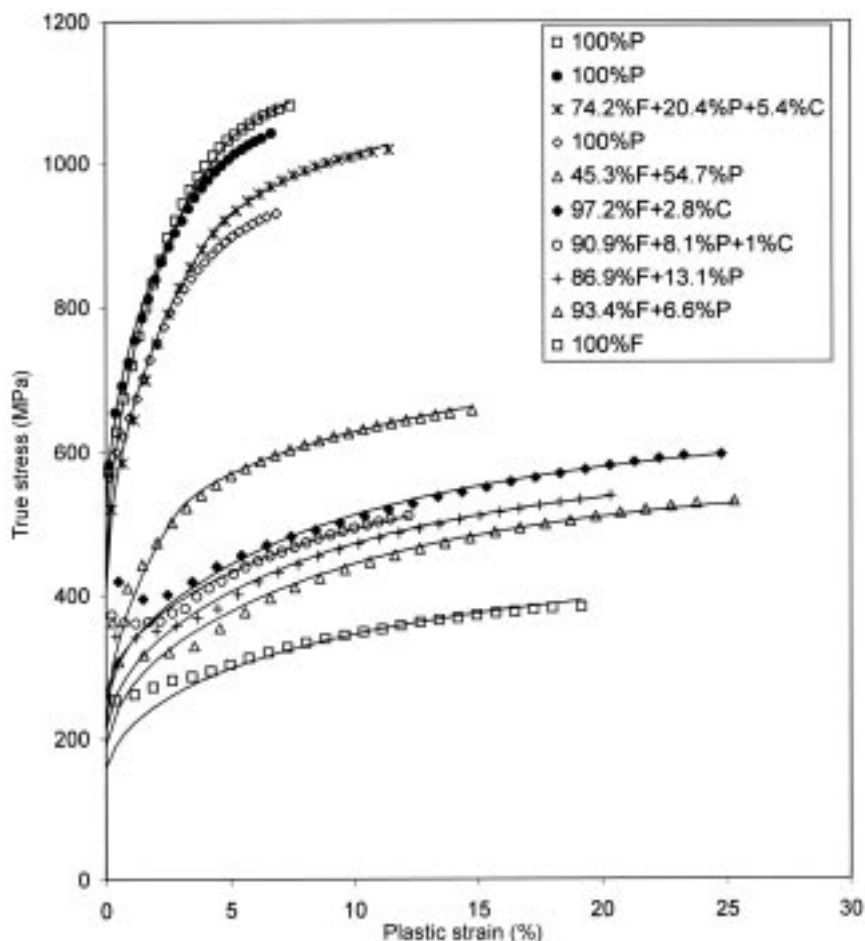
where M is the mobility for the process, D_s is the self-diffusion coefficient, k is Boltzmann’s constant and l is the average dislocation link length.

Elements in solid solution will affect the generation process mainly by changing the stacking fault energy and the recovery process by reducing the mobility.

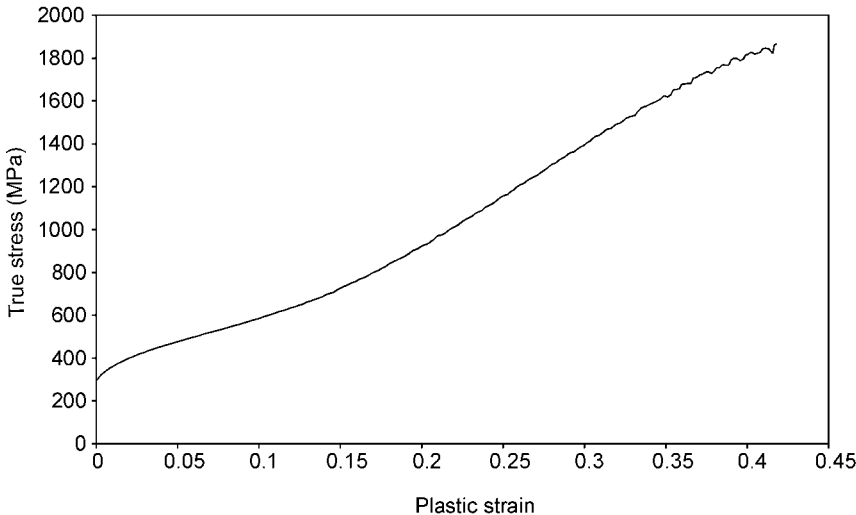
11.2.2 Multi-phase materials

When we are considering secondary phases in a continuous matrix their effect will depend on their size relative to the average dislocation link length. When the second phase is smaller then it will constitute a barrier to a single dislocation and can be treated as conventional precipitation hardening. In this case the effect on work hardening is insignificant (extra dislocation length is created, for example, as Orowan loops around the particles). If, on the other hand, the second phase is larger than the dislocation mean link length then we have to consider the phases as regions of different plastic properties. The less deforming phases (or constituents) will cause the generation of geometrically necessary dislocations in the softer parts in the same way as was discussed above for

grains in a polycrystalline material (Ashby 1971). For spherical, hard particles in a soft matrix the effect is given by a geometrical slip distance, g_0 , proportional to f/r (fraction over particle radius). The geometrical slip distance will vary with the shape of the constituents. The flow stress can then be described by a law of mixtures. This approach has been successful in the description of the flow stress for dual phase steel as well as for ferritic perlitic steels, see Fig. 11.1 (Engberg and Carlsson 2002; Kömi *et al.* 2004). For steels with TRIP (transformation induced plasticity) properties the increase in hardening is substantial. In Fig. 11.2 one example is given showing the effect of martensite formation in a 304-type stainless steel.



11.1 Lines: model, points: observations. F = ferrite with different amounts of pearlite, P and cementite, C.



11.2 Tensile test of 304-type stainless steel.

The flow stress can now be expressed by

$$\sigma = \sum f_i \cdot \sigma_i \quad \text{for constant strain} \quad (11.6)$$

$$\epsilon = \sum f_i \cdot \epsilon_i \quad \text{for constant stress} \quad (11.7)$$

$$\sigma_i = \sigma_{0i} + m\alpha Gb\sqrt{\rho_i} \quad (11.8)$$

$$\frac{d\rho_i}{dt} = \frac{m}{b} \cdot \left(\frac{1}{L} + \frac{1}{d} + g_i \right) \cdot \frac{d\epsilon_i}{dt} + \left(\frac{d\rho_i}{dt} \right)_{recovery} \quad (11.9)$$

where g_i is the geometrical slip distance caused by the difference in plastic deformation of phase i and all other constituents, j .

$$g_i = \sum_j g_{0j} \cdot \left(1 - \frac{d\epsilon_j}{d\epsilon_i} \right) \quad (11.10)$$

11.3 Rate effects

The strain rate sensitivity is important in the distribution of plastic strain. The effect on the magnitude of the flow stress is also of importance, for example, in crash members in automobiles, in deciding the roll forces needed during skin-pass rolling, etc. The rate dependence is due to thermally activated deformation (Peierls–Nabarro barriers, solute atoms, etc.) at low to ambient temperatures, below $0.5 T_m$, and to diffusion controlled processes (climb, recrystallisation) at higher temperatures.

11.3.1 Low to ambient temperatures

Thermal barriers for dislocation slip can, as indicated, be overcome by thermal activation. This can only be true for sufficiently small barriers such as given in Table 11.2. The work needed to overcome the barrier can be written as

$$H = H_0 - \int_0^A \tau^* dA \quad (11.11)$$

where H_0 is the work needed without the assistance of applied stress, τ^* the stress in excess of athermal barriers (thermal stress) and A the activation area (length of dislocation times distance travelled during the activation event). The strain rate obtained at a given thermal stress is then given by the product of the mobile dislocation density, ρ_m , the attack frequency, ω , and the probability of overcoming the barrier (as given by an Arrhenius expression). The shape of the barrier and the mobile dislocation density will then give the thermal stress. For ferritic steels a good approximation of the Peierls–Nabarro barrier is obtained by putting the activation area inversely proportional to the thermal stress and to assume a constant mobile dislocation density. This will lead to a simple relation

$$\frac{d\epsilon}{dt} = c_1 \cdot \left(\frac{\sigma^*}{c_2} \right)^{T/c_3} \quad (11.12)$$

where c_i are constants. For fcc metals the Peierls–Nabarro barriers are normally small and the effect is quite small (can often be neglected). For bcc and hexagonal (hcp) metals the effect can be quite large.

Atoms in solid solution can play a significant role. In ferrite a strong elastic interaction is found for interstitial atoms (C, N) while substitutional atoms give a considerably smaller contribution. In fcc metals they can contribute substantially. In dilute solutions the atoms can be regarded as point obstacles with the barrier given by the elastic interaction. If the barriers are strong, then the dislocations are best described as partially flexible and the Friedel process (see, for example, Brown and Ham 1971) can be assumed to prevail. For C in ferrite this will lead to an expression of the form

Table 11.2 Approximate activation areas for some thermally activated barriers

Mechanism	Normalised activation area, A/b^2
Peierls-Nabarro	10–100
Cutting of forest dislocations	100–10 000
Non conservative motion of jogs	100–10 000
Cross-slip	10–100
Solute atoms	10–100

$$\sigma^* = \left[1 + c_2 \cdot T \cdot \ln \left(\frac{d\epsilon}{dt} \right) \right]^3 \cdot c_1 \cdot G \cdot \sqrt{x} \quad (11.13)$$

where x is the atomic fraction of carbon. c_i are material parameters (Engberg and Carlsson 2002).

Static strain ageing in ferritic steels gives rise to the Lüders' strain during tensile testing. The localisation of strain to the band(s) gives local strain rates much in excess of the nominal ones. The sharper the plastic front, caused, for example, by a finer grain size where the individual grain boundaries constitute barriers for front movement, the higher the strain rate and consequently the higher is the yield stress and the yield elongation. With an increased nominal strain rate the yield stress increase is larger than what is obtained during homogeneous deformation (see, for example, Yoshitake *et al.* 1996). This is of importance, for example, during skin-pass rolling, where commonly a fixed total elongation is prescribed, at accelerations or decelerations giving rise to substantial changes in needed roll force.

11.3.2 Warm to hot working temperatures

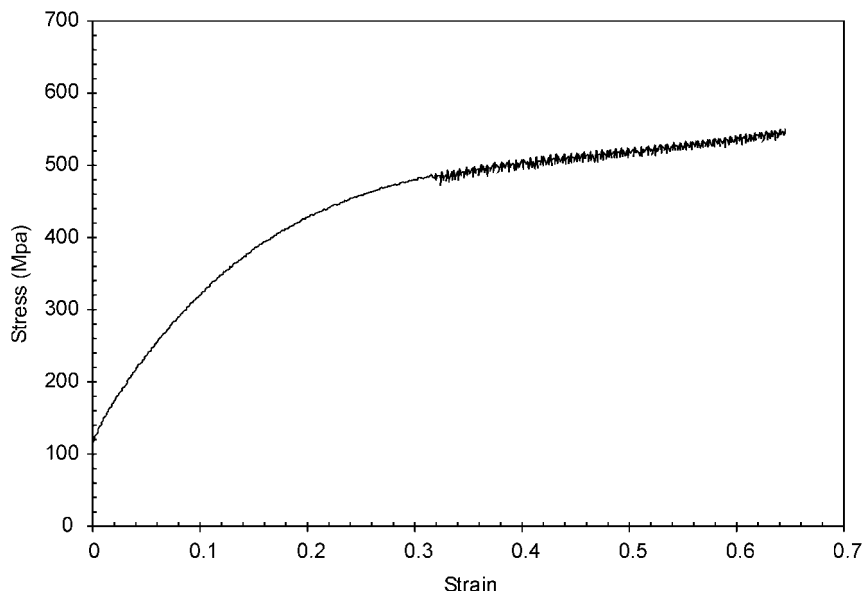
Above around $0.3 T_m$ recovery by cross-slip mechanisms are thought to occur and above $0.5 T_m$ climb becomes significant. This has a very significant effect on the temperature and strain-rate dependency of the flow stress. Also, recrystallisation will become of importance. The dislocation generation mechanisms will remain as given above. It has, however, been suggested that the generation of point defects, vacancies, due to cutting of forest dislocations or other dislocation interactions can be of importance as this will increase the diffusivity. One classic example of this effect is found in dynamic strain ageing of substitutional alloys. In Fig. 11.3 one example of the phenomenon is shown for a 316-austenitic stainless steel deformed at 400°C . The effect increases with strain as more vacancies are created and the diffusivity increases.

The generation of vacancies is also counteracted by diffusion to various sinks, such as dislocations, grain boundaries, etc. A simple description is given by

$$\frac{dx_v}{dt} = c_1 b \frac{d\epsilon}{dt} \sqrt{\rho} - c_2 D_m x_v (x_v - x_{v0}) \sqrt{\rho} \quad (11.14)$$

where x_v is the vacancy concentration, x_{v0} the same at thermal equilibrium, D_m the migration part of the diffusion coefficient and c_i are material parameters (Siwecki and Engberg 1997). The first term on the right-hand side gives the generation and the second term the annihilation of vacancies.

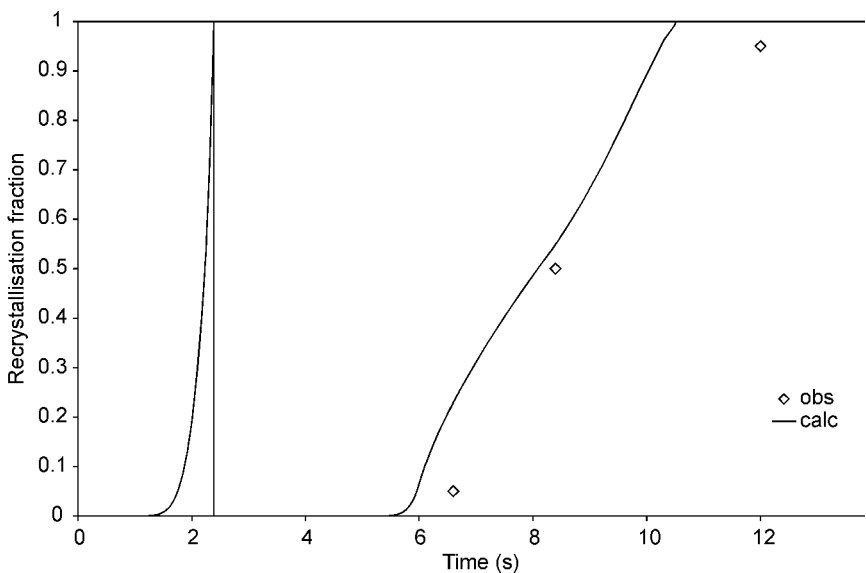
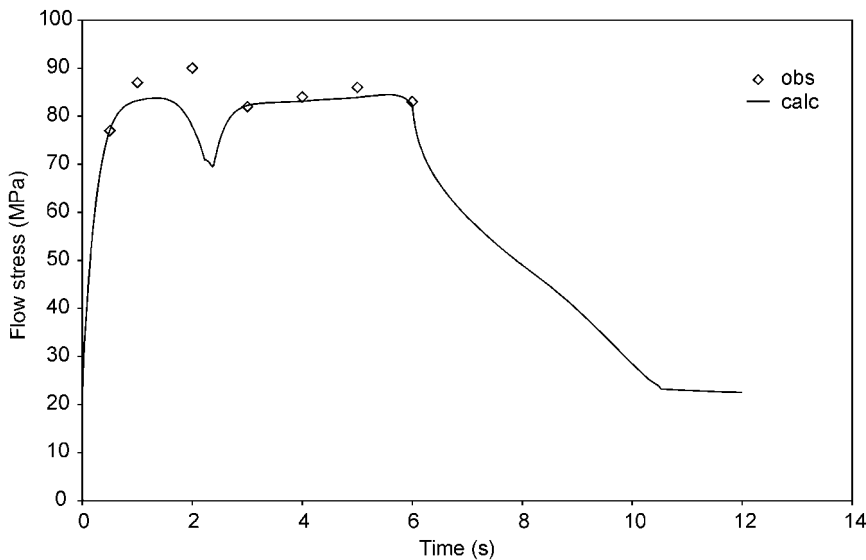
Recrystallisation is traditionally described by a JMAK (Johnson-Mehl, Avrami, Kolmogorov) type expression combined with regression formulas for



11.3 Dynamic strain ageing in a 316-type stainless steel.

the influence of strain, strain rate, alloy composition, etc. New grains appear on grain and phase boundaries and on shear bands (see, for example, Sellars 1997). It has been suggested that subgrains take an active part in the nucleation process of new recrystallised grains. Humphreys (1997) proposed that a part of the subgrains could undergo abnormal growth and that for some critical size of the abnormal subgrains they were sufficiently large to be able to grow as new grains. This idea was tested on a stainless steel (Wang *et al.* 2003) with seemingly good results. The possibility of subgrains acting as nuclei for recrystallisation should, of course, also be valid during deformation but here the subgrain size is decided by the deformation conditions and the material properties.

Preliminary results from applying a slightly modified version of the model have been tried on a CMn-steel, see Fig. 11.4. Here we allow one deformed grain size and one recrystallised. The flow stress is given by a law of mixtures and is also affected by the need for geometrically necessary dislocations when the softer, recrystallised part constitutes a continuous network. As is seen the major features of both flow stress, including dynamic recrystallisation, and recrystallised fraction are described. In fact, the figure display dynamic and metadynamic recrystallisation (starts during deformation and is completed after deformation). After deformation we also see the characteristics of a stress relaxation experiment, as performed by deforming to a given strain and then stop the testing machine and keep the total strain constant. First, the softening is rapid while recrystallisation still takes place and then we just see the effects of recovery.



11.4 Comparison of model calculations with experimental data for recrystallisation and flow stress in a CMn-steel (Karjalainen and Pertula 1996).

11.4 Interaction with phase transformations

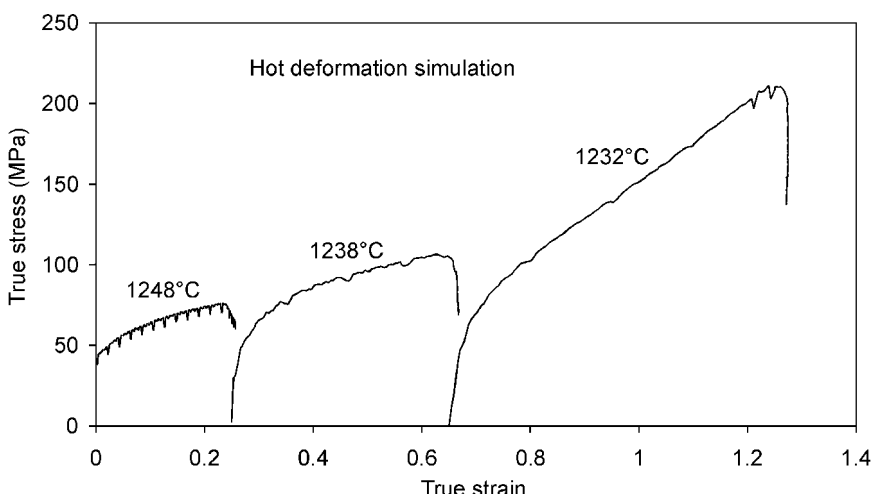
During hot deformation, phase transformations can also occur. Microalloying with Ti, Nb and V has been successfully used to produce high strength hot-rolled steel for several decades. Precipitation of $(\text{Ti},\text{Nb})(\text{C},\text{N})$ takes place on dislocations during hot rolling and gives significant effects by retarding and even completely stopping recrystallisation. In Fig. 11.5 one example is given where the flow stress is clearly affected by precipitation in the third consecutive deformation step.

The effect of precipitation is fourfold:

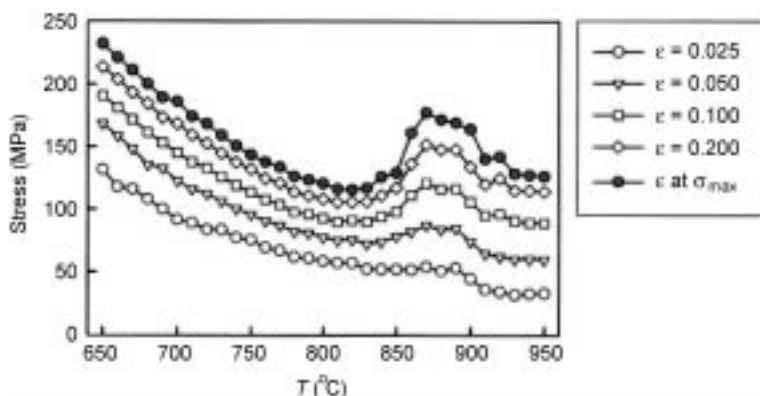
- it gives precipitation hardening;
- it retards and eventually blocks recovery;
- it retards and eventually blocks recrystallisation;
- it retards and eventually blocks grain/phase boundary movement.

The ability to block recrystallisation has been utilised in controlled rolling of HSLA steel. The purpose is to obtain heavily deformed austenite grains, ‘pancakeing’, with strain accumulated in several of the last passes. The subsequent phase transformation then yields a fine ferrite grain size and correspondingly good properties.

So far we have mainly discussed precipitation but, of course, phase transformations can also occur on a more massive scale. For ferritic steels it is the transformation from austenite to ferrite or ferrite plus carbide. For very low carbon steels the temperature interval for the transformation is small and thus large changes in volume fractions can occur. As ferrite is considerably softer than austenite at a given temperature, the flow stress drops significantly with



11.5 Hot compression tests, performed at SIMR, of a Ti-Nb HSLA steel.



11.6 Flow stress from hot compression tests of a 0.05% C steel (Bodin 2002).

increasing volume fraction of ferrite. The flow stress behaviour has been studied extensively. A simple law of mixtures seems to catch the main changes, although as discussed above it is expected that when austenite is the minority phase in a continuous matrix of ferrite, an increase in work hardening should be obtained. In Fig. 11.6 one example is given for a 0.05% C steel, where, also, the increased work hardening is obvious.

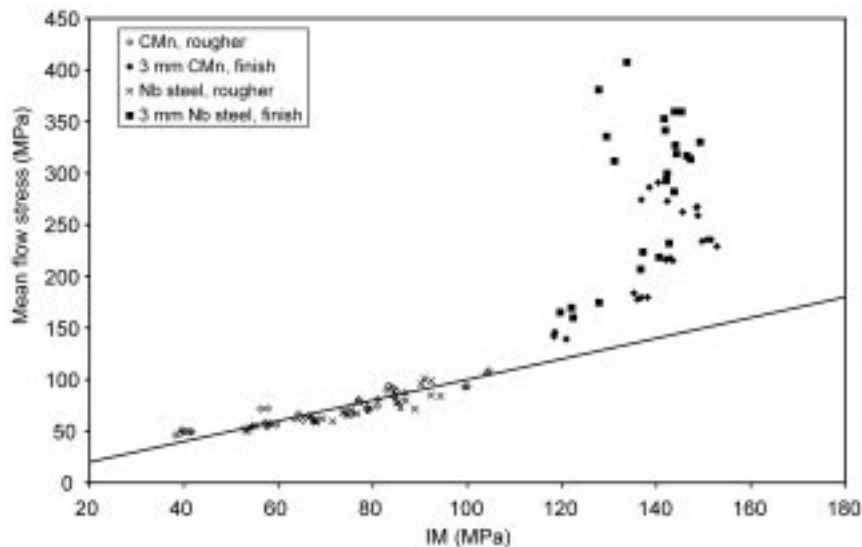
11.5 Examples of material behaviour during processing

The intention here is to give some examples of material behaviour during processing. All examples are taken from SSAB Tunnplåt AB.

11.5.1 Hot rolling

Mill data from the hot strip mill has been used to calculate the mean flow stress in each pass, assuming the material to be elastic – ideally plastic. The roll force model used was a classical slab method with constant friction assumed in the roll gap. For the roughing mill (reversible 4-high) both roll force and roll torque were available so the friction coefficient could be evaluated in addition to the flow stress for each pass. The values were close to 0.3 so it was decided to use this for all calculations, also for the finishing, six-stand (4-high), tandem mill. As torque is not measured in the finishing mill only flow stress values could be obtained for this part.

Hot compression test results for CMn-steels have been collected and evaluated at the Swedish Institute for Metals Research (SIMR) (Sandberg and Siwecki 1985). The data for the CMn-steels were obtained in the temperature range 800–1200°C and the strain-rate interval 0.001–1100 s⁻¹. The carbon and manganese contents varied between 0.01–0.19% and 0.2–1.5% respectively. From the regression formulas of this analysis mean flow stress values corresponding to



11.7 Calculated mean flow stresses from mill data.

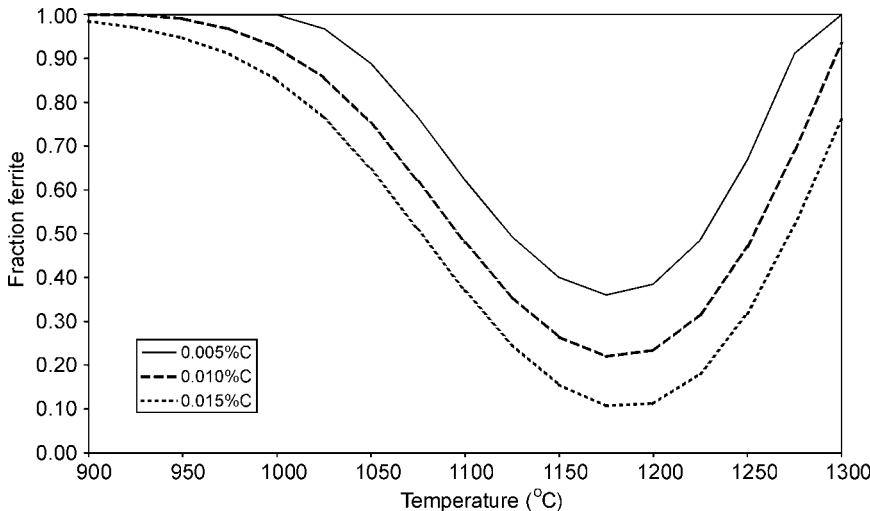
strains, strain-rates and temperatures for the same rolling passes as above have been calculated. The hot compression data were all of single stroke type, meaning that the starting structure was fully recrystallised in all cases.

In Fig. 11.7 results for one CMn-steel and one Nb-microalloyed steel are displayed. During roughing the two types of data coincide, meaning that complete recrystallisation is obtained between the successive passes. In the finishing mill the two datasets start to diverge. This can only be interpreted as the result of strain accumulation between successive passes, interpass times are not sufficiently long to allow complete recrystallisation. The effect is stronger for the microalloyed steel due to the presumed effect of strain induced precipitation of niobium carbonitrides.

During rolling of high silicon steel (used for their magnetic properties) the material behaviour has sometimes caused problems with unexpected increases in width during roughing. The reason for this was found in variations in the temperature of the slab as it entered the mill and was due to the position of the slab in the reheating furnace. If the first end of the slab was close to a skid mark then the temperature was 20 to 40 degrees lower than usual. An examination of the phase diagram shows that this will lead to an increased amount of ferrite and consequently to a softer material, see Fig. 11.8.

11.5.2 Cold rolling

As a part of an ECSC project (Vanel *et al.* 2004) a set of experiments were conducted in the five-stand tandem mill at SSAB Tunnplåt. The mill was run at a



11.8 Volume fraction of ferrite for a 1.85% Si steel. Calculated by ThermoCalc.

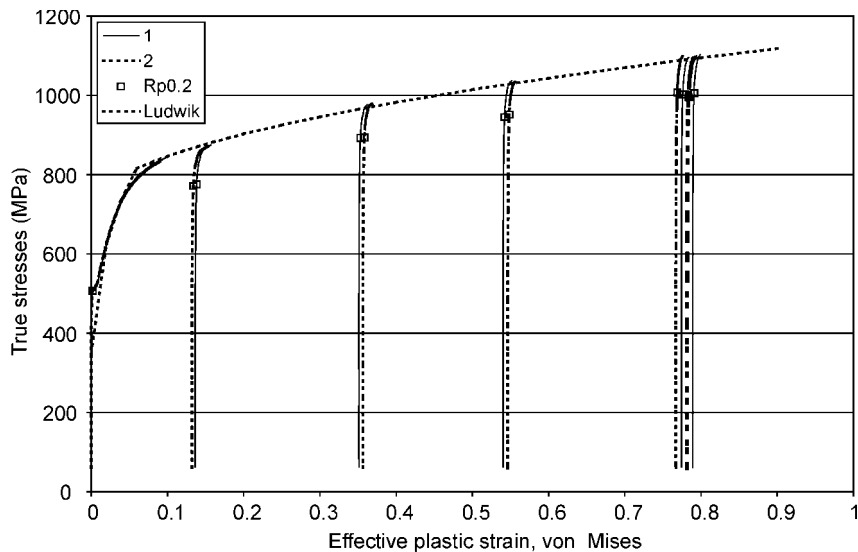
low speed of 30 m/minute and emergency stopped. This enabled us to extract material before and between the stands and after the last stand. This material was then carefully characterised by tensile testing in three different directions in the plane of the sheet (along the rolling direction, RD, transverse to the rolling direction, TD, and 45 degrees in between). Tests were also performed by compression testing in the normal direction (performed on stacks of sheet by SIMR). Finally, the material was also characterised by texture measurements and calculations of Taylor factors (and also by SIMR).

In Fig. 11.9 results from tensile testing of a 0.45% C steel in the rolling direction are displayed. The change in deformation from rolling to uniaxial tension gives a change in the yield surface, causing yield at a lower stress than would be expected if the material showed isotropic hardening in accordance to previous findings (see, for example, Kocks *et al.* 1998; Granlund 1997). The isotropic yield surface is then approached as deformation continues and we have assumed that the transient effects are overcome when R_m is reached in the tensile tests.

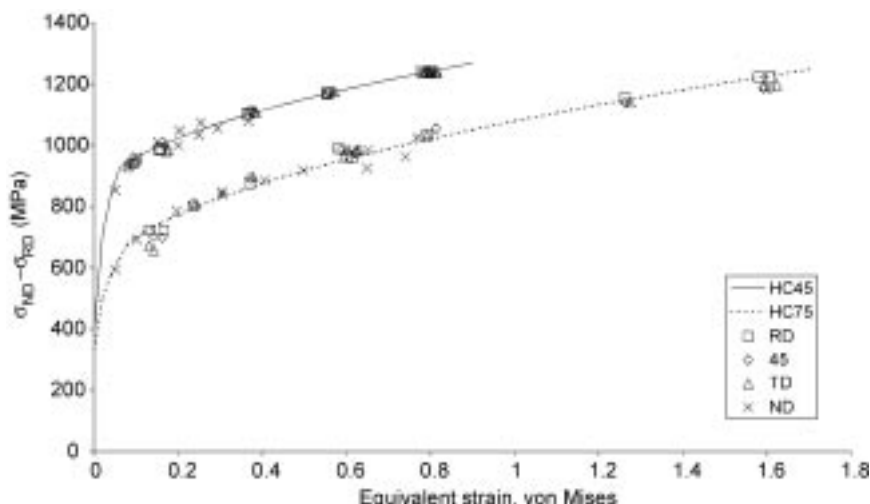
The next step was to bring all data together in a total description. The first obvious trial was to use the Taylor factors depicted from the texture measurements. This, however, was not successful. In a second trial we simply used the Hill yield criterion,

$$p_1 \cdot (\sigma_{11} - \sigma_{22})^2 + p_2 \cdot (\sigma_{22} - \sigma_{33})^2 + p_3 \cdot (\sigma_{33} - \sigma_{11})^2 + 2 \cdot p_4 \cdot \sigma_{12}^2 + 2 \cdot p_5 \cdot \sigma_{23}^2 + 2 \cdot p_6 \cdot \sigma_{31}^2 = k(\epsilon) \quad (11.15)$$

with much better success. The result is shown in Fig. 11.10 where data from all types of tests are displayed in the form of the plane strain flow stress. It also



11.9 Uniaxial stress-strain curves for a 0.45% C steel (HC45). Test direction parallel to rolling direction (RD). Tests before and after each stand in the tandem mill. Double tests. Fitted Ludwik model.



11.10 Flow stress in plane strain compression for a 0.45% C steel (HC45) and a 0.75% C steel (HC75). Symbols: experimental points from tensile and compression tests in different directions and before and after each stand in the tandem mill.

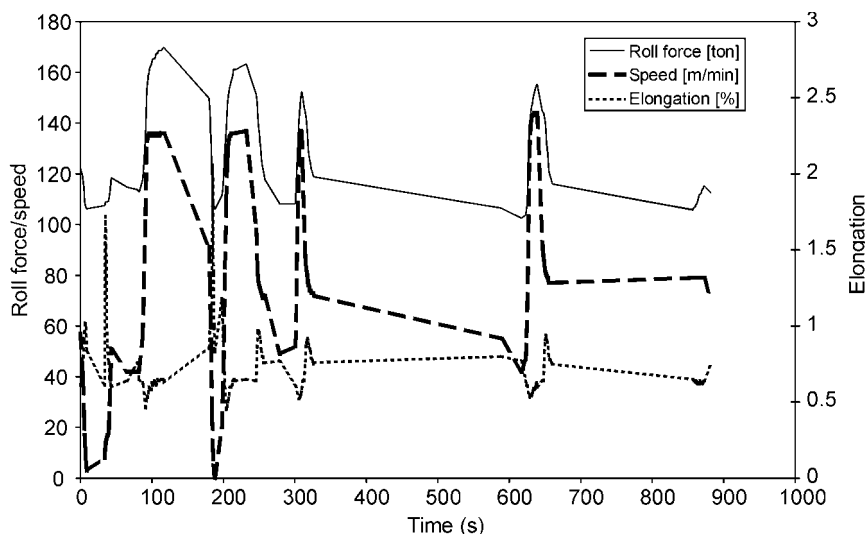
turned out that the data could be well described by applying two sets of the classic Ludwik equation. At low strains we expect this behaviour as we have a two constituent microstructure, ferrite plus pearlite, and the creation of geometrically necessary dislocations should prevail. At higher strains the statistically stored dislocations will dominate, giving the lower hardening rate. An interesting feature is that the work hardening is almost identical for both steels at high strains. The logical explanation is that in both cases deformation by statistical dislocations in ferrite dominates.

11.5.3 Skin-pass rolling

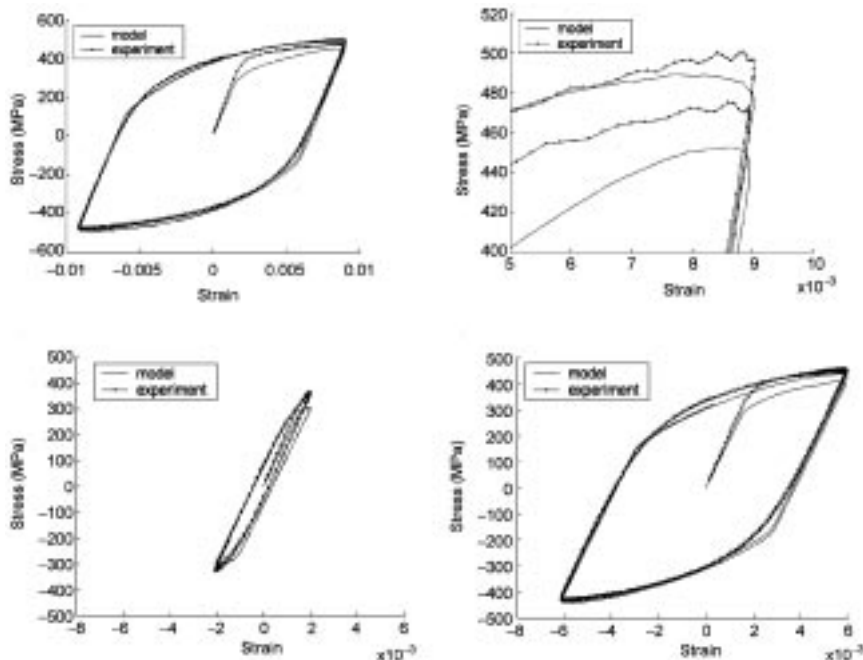
Speed changes are frequent in skin-pass mills, both in standalone mills and mills incorporated in continuous lines. A speed change will, in addition to the effect on the oil film in the roll bearings, also lead to a significant change in the flow stress of a ferritic steel. One typical example is given in Fig. 11.11. Here it is very clear that speed changes causes concurrent changes in the roll force. A comprehensive description of this can be found in Wiklund and Sandberg (2002).

11.5.4 Levelling

Roll levelling of sheet subjects the outer fibres of the material to a series of tensile and compressive strains in the levelling direction of the sheet (often the rolling direction). The first cycles are used to get sufficient plastic deformation



11.11 Logged data from a skin-pass mill in a continuous annealing line.



11.12 Experimental hysteresis loops and model results for DP 600 at different strain amplitudes.

into the material in order to decrease variations in the incoming material. The subsequent cycles, with successively decreasing strains, are then used to redistribute the internal stresses to a low level across the thickness of the material. For a high strength steel like DP 600 (dual phase with R_m minimum 600 MPa) the strains typically start around 1%. Tests have been performed at SIMR with fully reversed tensile/compressive testing under strain control. Some results are shown in Fig. 11.12. As is seen the Bauschinger effect is significant. The usual way to model this is to impose a back stress due to the deformation history. Domkin (2003) has applied one such model combined with a dislocation based model for work hardening and strain rate and the results are also shown in the figure.

11.6 Development trends

The material behaviour during and after metal working processes are incorporated into process control systems in more detail. Prediction of product properties can be used to change the set-up of the process, as has been utilised by VAI-Q (Andorfer *et al.* 2000) to change coiling temperatures during hot strip rolling. This is achieved by using the actual temperature after roughing and calculating the expected properties using the initial set-up. Deviations from

target properties are then used to adjust the coiling temperature. The core of their system is a set of physical-metallurgical models that depict the microstructural evolution during hot rolling and the relation of microstructure to mechanical properties using information of the time-temperature-deformation sequence (Andorfer *et al.* 1999).

In summary, the geometry, time and initial temperature together with the material composition are fed into the model (knowledge-based, physical) and results in predictions of rolling load and power, shape, microstructure and mechanical properties. For future uses it has been suggested (Sellars 2000) that the sequence is reversed, meaning that desired properties (mechanical, geometrical, etc.) are used as input and results in a specification of the material, time, initial temperature, geometry, load and power of the process.

In FE modelling of metal working processes the description of the material behaviour plays an increasingly important role and more complex material models are used in simulations (for example, crash simulations, see Engberg and Carlsson (2002)).

11.7 References

- Andorfer J, Auzinger D and Hubmer G (1999) 'Two years experience with VAI-Q – an online system for controlling the mechanical properties of hot rolled strip', AISE.
- Andorfer J, Hribernig G, Luger A and Samoilov A (2000) 'Operational experience with the metallurgical control of the mechanical properties of hot rolled strip', in *THERMEC 2000*, Las Vegas, USA.
- Ashby MF (1971) 'The deformation of plastically non-homogeneous alloys', in Kelly A and Nicholson RB, *Strengthening Methods in Crystals*, London, Applied Science Publ., 137–190.
- Bergström Y (1983) 'The plastic deformation of metals – a dislocation model and its applicability', *Reviews on Powder Metallurgy and Physical Ceramics*, 2, 79–265.
- Godin A (2002) Intercritical deformation of low-alloy steels, Dissertation, Delft University, ISBN 90-805661-2-8.
- Brown LM and Ham RK (1971) 'The deformation of plastically non-homogeneous alloys', in Kelly A and Nicholson RB, *Strengthening Methods in Crystals*, London, Applied Science Publ., 10–135.
- Chandrasekaran D (2003) Grain Size and Solid Solution Strengthening in Metals, Dissertation, KTH, Stockholm, ISBN 91-7283-604-0.
- Domkin K (2003) 'Physically Based Models of Metal Plasticity', Licentiate thesis, Luleå University of Technology, 2003: 30.
- Engberg G and Carlsson B (2002) 'The strain-rate sensitivity and deformation hardening of ferritic steels', in *Int. Conf. New Developments in Sheet Metal Forming Technology*, Fellbach.
- Friedel J (1964) *Dislocations*, Oxford, Pergamon Press.
- Frost HJ and Ashby MF (1982) *Deformation-mechanism Maps*, Oxford, Pergamon Press.
- Granlund J (1997) 'Structural Steel Plasticity', Dissertation, Luleå University of Technology, 1997: 24.
- Humphreys FJ (1997) 'A unified theory of recovery, recrystallization and grain growth,

- based on the stability and growth of cellular microstructures – I. The basic model’, *Acta Mater.*, 45, 4231–4240.
- Karjalainen LP and Perttula J (1996) ‘Characteristics of static and metadynamic recrystallization and strain accumulation in hot-deformed austenite as revealed by the stress relaxation method’, *ISIJ International*, 36(6), 729–736.
- Kocks UF, Tomé CN and Wenk H-R (1998) *Texture and Anisotropy – Preferred orientations in polycrystals and their effect on materials properties*, Cambridge University Press.
- Kömi J, Ruha P, Engberg G, Borggren U, Karlberg M, Abajo Martinez N, Lopéz J and Karjalainen P (2004) ‘The prediction of the mechanical properties of hot-rolled strip products by means of hybrid methods’, Luxembourg, EUR 20939 EN.
- Sandberg A and Siwecki T (1985) ‘Evaluation of microstructure development and rolling loads in connection with hot strip rolling of CMn-steels and Nb-microalloyed steels’, Stockholm, Swedish Institute for Metals Research, IM-2060.
- Sellars M (1997) ‘Microstructure Modelling in Hot Deformation’, in Hutchinson B, Andersson M, Engberg G, Karlsson B and Siwecki T, *Thermo-Mechanical Processing in Theory, Modelling and Practice, [TMP]²*, Stockholm, The Swedish Society for Materials Technology, 35–51.
- Sellars CM (2000) ‘State of the art of microstructural modelling’, in *VAI-Q Symposium*, Linz.
- Siwecki T and Engberg G (1997) ‘Recrystallization Controlled Rolling of Steels’, in Hutchinson B, Andersson M, Engberg G, Karlsson B and Siwecki T, *Thermo-Mechanical Processing in Theory, Modelling and Practice, [TMP]²*, Stockholm, The Swedish Society for Materials Technology, 121–144.
- Vanel L, Bourdon G, Depreitere, Uijtdebroeks H, Ablewhite J, DeLaRue T, Rudkins N, Engberg G and Pettersson K (2004) ‘Heavy reductions on first stands of a tandem cold mill’, Luxembourg, EUR 20929 EN.
- Wang X, Siwecki T and Engberg G (2003) ‘A Physical Model for Prediction of Microstructure Evolution during Thermomechanical Processing’, in ‘Thermec 2003’, Madrid, part 5, 3801–3806.
- Wiklund O and Sandberg F (2002) ‘Modelling and Control of Temper Rolling and Skin Pass Rolling’, in Lenard JG, *Metal Forming Science and Practice*, Oxford, Elsevier Science, 313–343.
- Yoshitake A, Sato K and Okita T (1996) ‘Impact absorbed energy of hat square column in high strength steels’, SAE SP-1172, 960020, 7.

Understanding and improving powder metallurgical processes

F LEMOISSON and L FROYEN,
Katholieke Universiteit Leuven, Belgium

12.1 Introduction

Powder metallurgy (PM) represents a market of about eight billion dollars/year and a production exceeding one million tons/year. Powder metallurgy allows the production of near-net-shape components, implying material saving, combined with better properties, which can make PM processes competitive compared to the conventional casting, forging or machining route.

PM compounds are used in many fields such as energy, automotive, aerospace, medical industries, and for many applications such as electrodes for glass production (e.g. Mo), wires of lamps (e.g. W), soft magnetic cores (e.g. Fe-Ni, Fe-Si), tools (e.g. WC-Co), dies (e.g. high speed steel), bearings, gears, brakes, injection moulds (e.g. stainless steel), gas turbine blades (e.g. superalloys), medical implants (e.g. Ti-alloys), and aircraft wing weight (e.g. W, ODS). A wide range of materials can be processed by powder metallurgy such as light alloys (Al, Mg, Ti), stainless steels, high speed steels, Ni- and Co-based superalloys, ODS materials, refractory metals, etc. For refractory metals (e.g. W, Mo, Ta) powder metallurgy is the only economical way of production because of their very high melting temperatures. Moreover, materials produced by powder metallurgy have a much finer microstructure (down to nano-scale) and a micro-scale instead of a macro-scale segregation provided by conventional metallurgy which highly increases the properties of the PM component.

12.2 Production processes for powders

There are numerous processes, which allow the production of powders with a wide range of characteristics (composition, size, size distribution, shape, microstructure and purity). In fact, these characteristics have to be adapted to subsequent production steps of the component and its application field. For example, the required particle shape depends on the process used to obtain the final product. Spherical atomised powders are needed when the powders are used for thermal spraying, loose powder sintering or hot consolidation

(extrusion, isostatic pressing) rather than for cold pressing. In the last case irregular powders are more suited in order to guarantee a sufficiently high green strength for handling. Another example concerns mechanically alloyed (MA) powders: these powders are smaller (particles of a few μm with a grain size of a few nm) than those (10 to $100\mu\text{m}$) for conventional powder metallurgy processes and, therefore, special consolidation methods such as hot compaction followed by hot extrusion, or direct hot extrusion have to be used.

Powder contamination is also an important criterion for many applications. The amount and the type (inclusions, superficial oxidation, etc.) of contamination depends on the powder production process. It can originate from initial impurities of the powder, containers, fluids (e.g. solvent) or additives (e.g. binders), atmosphere, etc.

Powder production processes can be classified in mechanical, atomisation, physical, chemical and plasma routes.

12.2.1 Mechanical routes

Mechanical routes are mainly used for the production of hard metal and ceramic powders. They deal with the production of powder by means of four different forces (impaction, attrition, shear, and compression) involved separately or in combination.¹ Impaction produces powder by fracturing the material submitted to a high and rapid load (striking of one object by another). Attrition is the production of particles created by the rubbing action between two bodies. Shear consists in fracturing particles along their shear planes (e.g. cleavage). Compression involves fracture of the particle under compressive forces (crushing or squeezing of particulate material).

Under the influence of those forces the powders can undergo fracture, deformation (work hardening), cold-welding in varying degrees or polymorphic transformation. This results in particles size reduction (grinding or comminution), solid state alloying (mechanical alloying), polymorphic transformation (mechanical milling), shape change (flaking in the case of ductile material), mixing or blending of two or more materials and contamination.

Grinding, mechanical alloying and mechanical milling will be discussed in more detail followed by an overview of the different milling technologies and a particular process called the ‘Coldstream’ process.

Grinding

Particle size reduction by mechanical means is called grinding.² The objective is to produce a powder with a specific particle size distribution adapted to the subsequent process steps.

During grinding, particles fracture when the applied stresses exceed the particle strength globally (massive fracture) or locally (fine wear debris is

considered to be formed by attrition). The rate of particle size reduction increases with frequency of stress application and magnitude of the stress. However, particle size reduction rate typically decreases during the grinding process, for example, due to the increase in fracture resistance of the smaller particles.¹

Impact energy depends on the specific mill design. It increases with mill speed, density and size of milling media (ball, rod, etc.). High impact energy is required to produce fine powders. However, very high mill speeds could lead to high wear of the balls inducing high contamination, excessive heating and lower powder yields.

The size of the milling media (typically 20:1 for ball:powder diameter) also influences size, morphology and microstructure of the powder. To produce fine powders, it is recommended to mill in several steps while reducing successively the milling media size, as one milling step usually induces a particle size reduction of about factor 10.

An increase in ball to powder ratio increases the impact frequency and the total energy consumption per second while the average impact energy per collision decreases. Typical values of this ratio range from 5 to 30. For the amorphisation of a powder this ratio may approach 100.

Additives (surface-active agents or process control agent (PCA) and lubricant) are used to nullify autohesion (Van der Waals forces) and so inhibit agglomeration, to reduce welding (atomic bonding) and/or to lower the surface tension of the material (proportional to the energy required to create new surfaces). Their aims are to shorten milling times and/or to produce finer powders.^{1,5} The most widely used PCAs are alcohols, stearic acid and ethyl acetate.¹ Small amounts of these additives remain in the powder and are responsible for contamination in C, H and/or O, which can reach 0.5 to 3 wt%.⁴

Mechanical milling

Mechanical milling leads to polymorphic transformation of the powder. It comprises high-energy ball milling of uniform (often stoichiometric) composition powders, such as pure metals, intermetallics, or prealloyed powders (stainless steel), where material transfer is not required for homogenisation, contrary to mechanical alloying. For example, mechanical milling of ordered intermetallics can induce disordering or amorphisation.⁸

Mechanical alloying

Mechanical alloying (MA) is a dry, high-energy ball milling technique. MA can be used for many different material systems such as metals, intermetallics, ceramics and composites (cermets, and metal matrix composites).

During MA of powder particles from ductile–ductile or ductile–brittle material systems, the impact with the milling balls repeatedly plastically deforms

the powder particles (flattening), creates new surfaces (fracture) and enables the particles to weld together (rewelding). A process control agent (PCA) (0.5 to 4 wt%) is usually added to allow fracture of the particle and to reduce but not to eliminate cold welding, as it is one basic mechanism of mechanical alloying.⁸ After a short time of MA, the particles have a characteristic layered structure build-up from different starting powders (material transfer). With increasing MA time, the particles become work hardened and fracture by a fatigue failure mechanism and/or by the fragmentation of fragile flakes. As MA proceeds, the internal structure of the particles (grain size, lamellar spacing, etc.) is steadily refined to nanometer dimensions even if the particle size becomes constant. For brittle–brittle material systems, smaller and smaller parts of the harder constituent are incorporated into the less hard one as MA proceeds.

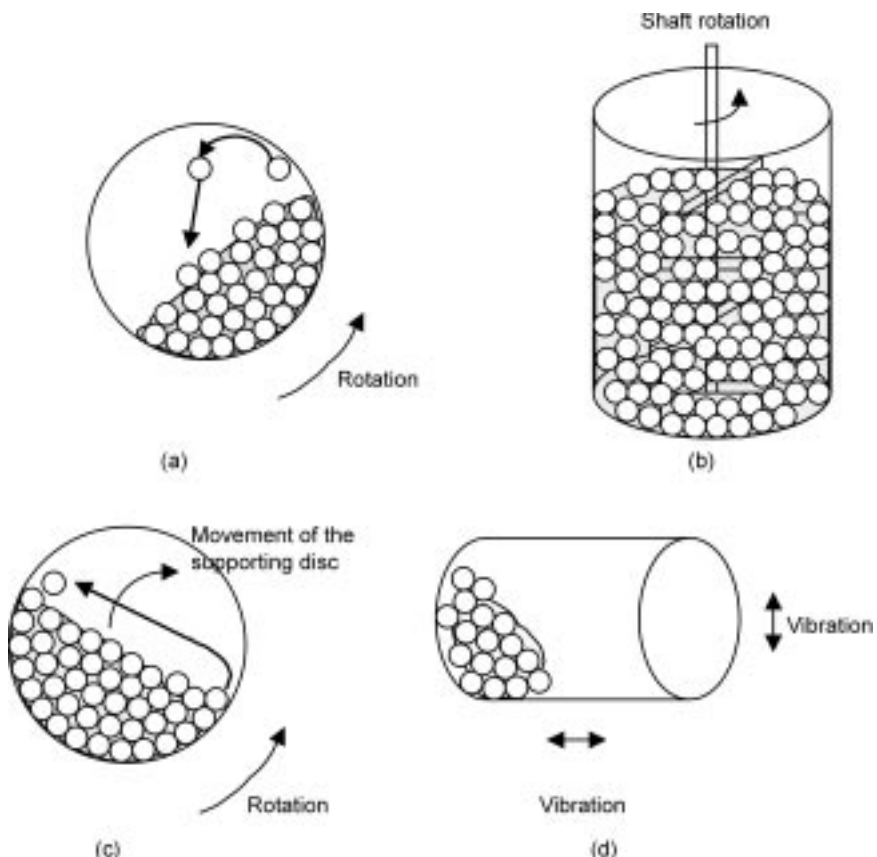
In the 1960s, MA was mainly used to produce ODS (oxide-dispersion strengthened) materials. These have a high strength at room and elevated temperatures, as well as excellent oxidation and hot corrosion resistance. The elevated temperature strength of these materials is due to the uniform dispersion (with a spacing of around 100 nm) of very fine (5 to 50 nm) oxide particles (Y_2O_3 , ThO_2 and La_2O_3) in a nickel- or iron-base superalloys.⁶ These dispersoids inhibit dislocation motion in the metal matrix. It also retards or inhibits the recovery and recrystallisation processes and so increases the creep resistance of the alloy.

Moreover, MA allows the production of metastable phases, such as supersaturated solid solutions (extension of solid solubility limits), non-equilibrium crystalline or quasi-crystalline intermediate phases, amorphous (glassy) alloys, alloying of difficult to alloy elements (e.g. elements which are immiscible under equilibrium conditions).^{5,7} For example solid solutions in the systems Cu-Fe, AlSb-InSb, Cu-Co have been obtained. MA also favours chemical reactions at lower temperature (chemical displacement).

The main applications concerns the ODS materials, which are used in the glass, energy production, and aerospace industries. But as the producing costs are high, the MA materials are niche materials.

Milling technologies

Different kind of mills are suitable for grinding, mechanical alloying and mechanical milling such as horizontal mills (tumbler ball mill), stirred mill (attritor, e.g. Szegvari attrition mill¹), planetary ball mill, vibrating mill (tube vibrating mill, Sweco vibrating mill and shaker vibrating mill (e.g. Spex is a lab-scale mill³)). Their working principles and operating conditions are summarised in Fig. 12.1 and Table 12.1. The classification on a scale of increasing mill energy is: horizontal ball mill, attritor, planetary ball mill and vibrating ball mill. For example, a process that takes only a few minutes in the SPEX mill can take hours in an attritor and a few days in a commercial tumbler ball mill.



12.1 Principle of the different mills: (a) horizontal mills,³ (b) Szegvari attrition mill,¹ (c) planetary ball mill,³ (d) shaker vibrating mill (e.g. SPEX is a lab-scale mill).³

The choice of a milling technique is determined by many parameters. For example, attrition mills are more efficient than tumbler ball mills for mixing and blending WC-Co cutting tool powders because of short milling time, production of fine particle size (submicron sized) and enhanced smearing of Co onto carbide particles. However, as the product output is relatively low with attrition mills, tumbler ball mills are usually used for production runs of over 100 kg/day. Moreover, powder contamination, which is an important criterion for many applications, can be due to the initial purity of the powder, the milling equipment (design), the milling operating conditions (mill speed, balls size and material, atmosphere) and/or the use of process control agent. It increases with milling time, milling intensity and with the reduction of the difference of strength/hardness between the powder and the milling balls.

Table 12.1 Typical operating conditions of the different mills

	Vibrating mill	Planetary ball mill	Vertical attritor	Horizontal attritor	Horizontal ball mill
Cycle time (h)	0.01–0.5	1–10	0.1–10	0.1–10	> 10
Powder amount	> 1 kg (industry) 1 g (laboratory)	10–100 g	100 kg (industry) 100 g (laboratory)	100 kg (industry) 100 g (laboratory)	> 1 ton
Mill speed (rpm)	1000 (industry) 3300 (laboratory)	80–400	60 (industry) 300 (laboratory)	1800	10–50
Ball diameter (mm)	1–10	6–30	6–10	6–10	6–25
Ball filling level		50–70%	70%	30%	50%
Powder filling level		1:10 powder to ball weight ratio	1:10 powder to ball weight ratio	1:10 powder to ball weight ratio	100% of ball interstices
Powder size (μm)	1–10	5–100	5–100	5–100	10–50

On a larger scale, the economic point of view prevails and the efficient use of the equipment and raw materials, as well as energy consumption, become important.

Coldstream process

In this process, a high-pressure air-stream (e.g. 7 MPa) containing the particulate material, enters a vacuum chamber through a venturi nozzle where it impacts a tungsten carbide target.⁹ The pressure drop at the exit of the nozzle induces a temperature drop thus chilling and embrittling the material inducing its fracture when it impacts the tungsten carbide target. The material is then transported to a first classifier, which allows oversized products to drop into a storage vessel for subsequent impact against the target. This process applies to many body-centred cubic metals that go through a ductile to brittle transition at low temperatures. It is used for hard, abrasive, relatively expensive materials such as tungsten carbide, tungsten alloys, molybdenum, tool steels, beryllium, and other alloys (Inconel, nickel and cobalt high temperature alloys). This process allows a rapid production (1 t/day) of irregular micron-sized particles.

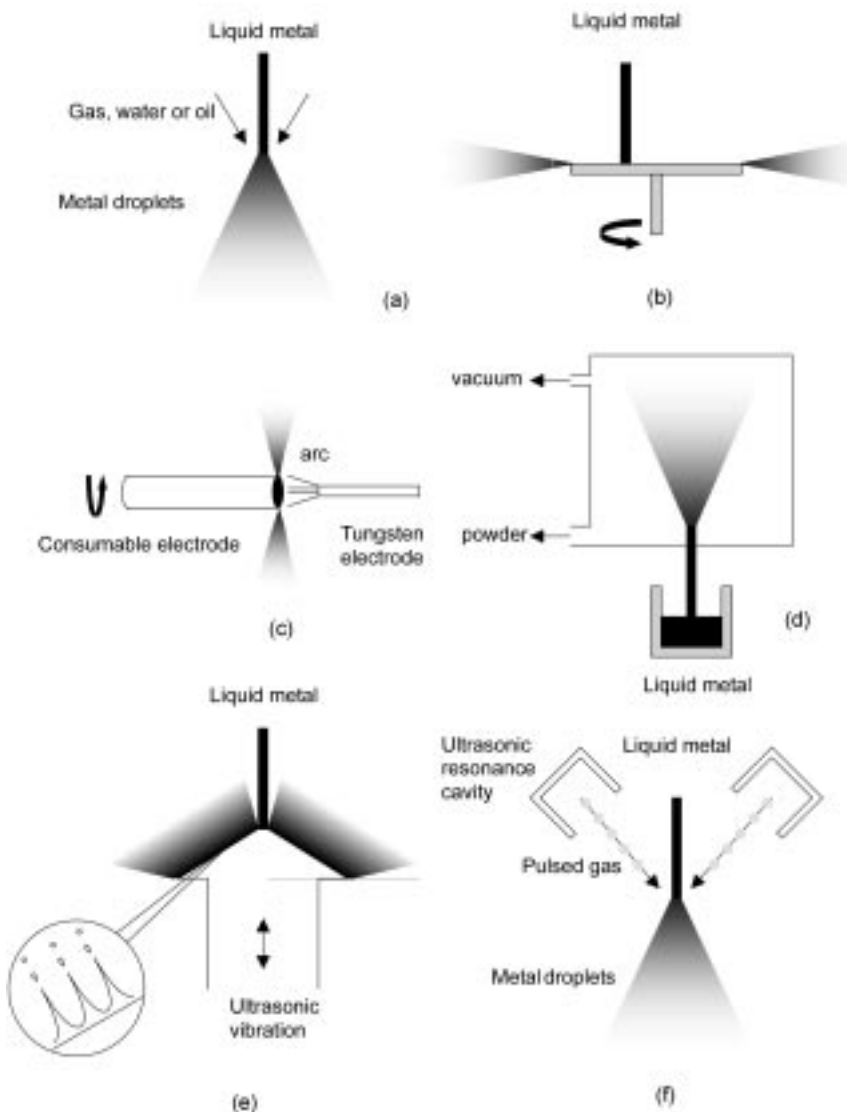
12.2.2 Atomisation route

Atomisation is often used to produce metal powders and especially pre-alloyed powders (brasses, stainless steels, superalloys, NiAl ...). Moreover its high cooling rates (10^2 to 10^7 K/s) allows producing alloys that cannot be obtained by casting. The flexibility of this method, coupled to its applicability to many alloys, easy process control and high production rate makes it a very interesting route.^{10,12} The world capacity of production is estimated to be higher than one million tons per year.¹¹

Atomisation occurs when a jet of liquid is converted to very small droplets. The different atomisation processes are (see Fig. 12.2):

- Two-fluid atomisation, where a molten metal is broken up into droplets by impingement of high-pressure jets of water, oil or gas (a).
- Centrifugal atomisation, where a liquid-stream is dispersed into droplets by the centrifugal force of a rotating electrode (c), disc or cup (b).
- Vacuum or soluble-gas atomisation, where a molten metal is supersaturated with a gas that causes atomisation of the metal in a vacuum chamber (d).
- Ultrasonic atomisation, where a film of liquid metal (e) or the atomising fluid (f) is agitated by ultrasonic vibration.

Atomised metal powders are generally found to follow a log normal distribution. The particles size distributions are generally from few μm up to $500 \mu\text{m}$ and the mean particle size from 10 to few $100 \mu\text{m}$. The geometric standard deviation σ_g measures the spread of particle size around the median mass diameter d_m and

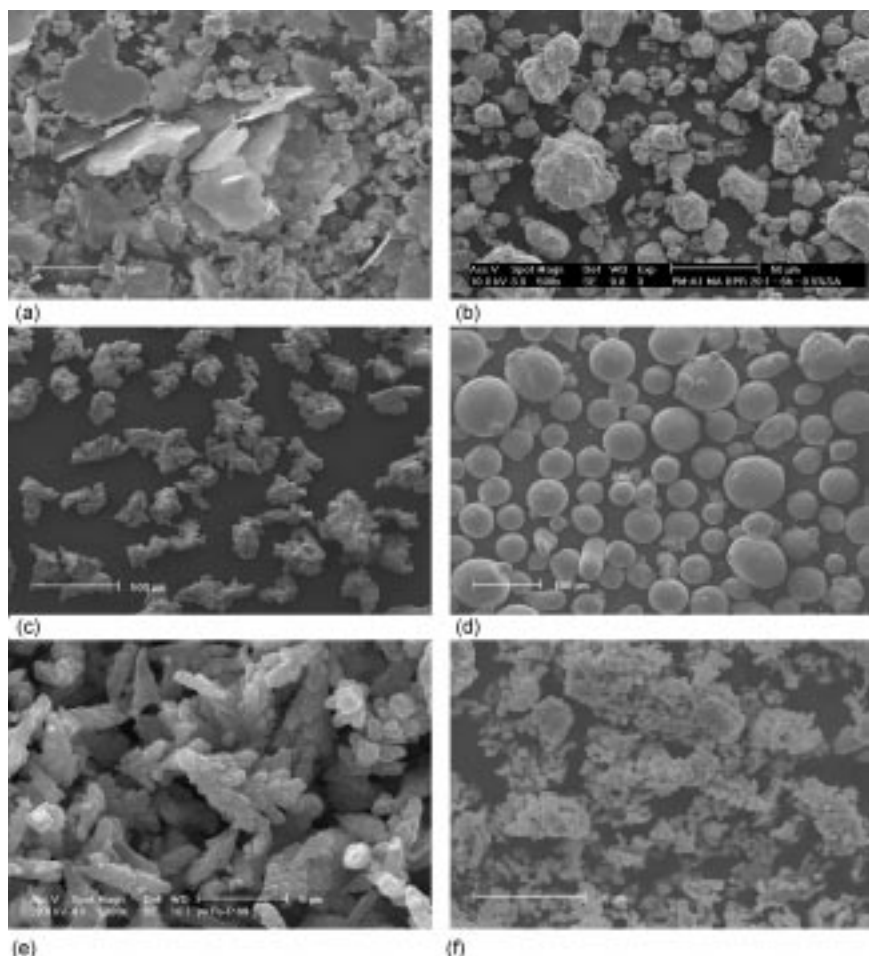


12.2 Atomisation processes. (a) gas, water or oil atomisation, (b and c) centrifugal atomisation, (d) vacuum atomisation, (e and f) ultrasonic atomisation.

typically varies from about 1.7 to 2.3 for water- and gas-atomised metal powders. Compared to other types of powders, the atomised powders are relatively compact (apparent density up to 65% of the theoretical density), with a high packing density and a low specific surface area. This induces good flow characteristics, good compressibility but low sintering activity. Particles shape varies from irregular to

spherical for respectively water and gas atomisation (Fig. 12.3c, d). The required particle shape depends on the following process used to obtain the final product. Spherical powders are used for thermal spraying loose sintering or hot consolidation (e.g. extrusion, isostatic pressing). But irregular powders are needed to guarantee a high enough green strength after cold pressing. The cleanliness of the powder is also a very important parameter. The possible contaminants are bulk dissolved impurities, surface impurities and inclusions (mainly from melt practice). Surface oxidation is often considered as the main purity index.

The process parameters controlling the powder characteristics (size, distribution, shape and oxygen content) are related to the atomiser design (nozzle defining



12.3 Morphology of powders obtained by (a) milling, (b) mechanical alloying, (c) water atomisation, (d) gas atomisation, (e) electrolysis (courtesy of Ye Xingpu) and (f) precipitation (courtesy of Rudy de Vos).

the geometry of the atomisation), the atomiser operating conditions (nature of the fluid, pressure, temperature, atmosphere) and the material (melting temperature, viscosity, surface tension, superheat). Some of these parameters have a great influence on the powder characteristics. For example, the production of fine powders is favoured by low metal viscosity, low metal surface tension, high superheat of the metal (difference between the temperature of the molten metal and its melting temperature), small nozzle diameter, high atomising pressure, high flow rate and high velocity of the atomising fluid, short metal stream and short jet length.¹³ Spherical atomised powders are obtained by increasing the superheating of the liquid metal (reduction of viscosity), increasing its surface tension by addition of deoxidisers, such as B, P and Si and increasing the solidification time of the particle (atomising with gas instead of water). More details about the atomising parameters can be found in references 1 and 3.

In the following, the different atomisation methods will be described in more detail.

Water atomisation – oil atomisation

Water atomisation, with its capacity of at least 700 000 tons per year and production rates up to 500 kg/min (8 kg/s), is the process mostly used for the commercial production of irregular (Fig. 12.3c) metal powders (iron, stainless steels, tool steels, soft magnetic alloys, nickel alloys and copper).¹¹ The production costs are lower than the other atomisation methods. However, limitations exist in relation to powder purity (relatively high oxygen content (1 wt%)), particularly with reactive metals and alloys. The median particle size decreases with increasing water pressure. Most industrial plants use a water pressure in the range of 5 to 20 MPa, that results in mass median particle sizes of 30 to 150 µm. Finer powders (median particle size from 5 to 20 µm) can be produced by using much higher water pressures (50 to 150 MPa).

Oil atomisation is similar to water atomisation. Oil is used as atomising medium in order to decrease the irregular character of the particle shape and to reduce oxidation, especially for molten metal containing elements such as Cr, Mn or Si, which are readily oxidised.^{12,14}

Gas atomisation

The production of gas atomised powders is lower than water-atomised ones because of its higher cost. It is about 300 000 tons per year for air atomisation and around 50 000 tons per year for inert gas (nitrogen, argon and helium) atomisation, the later ensuring a low oxygen content (100 ppm) of the spherical powders (ferrous and non-ferrous alloys) (Fig. 12.3d).^{11,12}

In gas atomisation the powder size distribution strongly depends on the nozzle design ('free-fall' configuration or 'confined'). Confined nozzle designs

increase the amount of fine powder particles ($<10\text{ }\mu\text{m}$) because of a higher velocity and density of the gas on contact with the metal.¹⁰ In practice, the mean particle size decreases with increasing gas pressure and decreasing melt flow rate. The pressures used in gas atomisation are generally in the range of 0.7 to 3 MPa. High-pressure gas atomisation (HPGA) allows the production of very fine particles, e.g. Sn-5Pb with a mean size of $5\text{ }\mu\text{m}$ was obtained at 12.5 MPa.¹⁵

New trends in gas atomisation concern the nozzle design.¹⁴ In conventional nozzles, the atomising medium impacts the molten stream in the turbulent region instead of the laminar region as for a Laval nozzle. The use of such a Laval nozzle reduces the particle size and spread. A moderate gas pressure (e.g. 2 MPa) is sufficient to produce powders with $d_{50} = 10\text{ }\mu\text{m}$ with Ar or N₂ as atomising gas or $5\text{ }\mu\text{m}$ with He.¹⁶

Another possibility is hot gas atomisation. As the hot gas exit velocity in the supersonic gas nozzle increases substantially with the temperature of the atomisation die, a higher kinetic energy is available to disrupt the melt stream into finer droplets and hence lower powder median size. But for each atomising temperature, the nozzle design has to be optimised in the area of expansion of the gas at supersonic velocity.

Vacuum atomisation – tandem atomisation

In the vacuum atomisation, a molten metal supersaturated with gas (noble gas or hydrogen) under pressure (1 to 3 MPa) is exposed to vacuum as a thin stream, resulting in melt disintegration into fine droplets, as the dissolved gas bursts out of the molten metal.^{11,14} This method is mainly used to produce spherical superalloy powders.¹²

The combination of vacuum and gas atomisation, known as tandem atomisation, allows the production of fine superalloy powder.¹⁷ After gas atomisation, the droplets begin to cool down and the retained dissolved gas is rejected from the solidifying metal dendrites. So the remaining liquid metal becomes more and more supersaturated until a gas bubble nucleates that grows explosively to produce a secondary atomisation event. The partially solidified droplets shatter into much finer droplets that subsequently solidify into ultra-fine powder particles.

Centrifugal atomisation (rotating electrode, rotating disc)

In centrifugal atomisation, centrifugal forces break up the molten metal as droplets that then solidify as powder particles.¹⁰

In the rotating electrode process (REP), a consumable electrode is rotated (1000 up to 50 000 rpm) while it is melted by an electric arc. The molten metal is ejected at the edge of the electrode under the influence of centrifugal forces in the form of droplets that solidify as spherical particles in an inert gas filled

chamber. There is no liquid metal–crucible contact, which prevents the contamination by ceramic particles. This is also an advantage for molten titanium alloys that are corrosive to nearly all container materials.

The median particle size (about $250\text{ }\mu\text{m}$) decreases with decreasing melt rates, increasing rotational speed and electrode diameter. Usually the spreading of the particle size is much less by centrifugal than by gas atomisation.

Special methods – ultrasonic atomisation

There are several ultrasonic atomisation techniques such as capillary-wave atomisation (no commercial application) (Fig. 12.2e), ultrasonic gas atomisation (USGA) (Fig. 12.2f) and double ultrasonic atomisation (still in development).

In the capillary-wave atomisation, the liquid metal meets a vibrating surface at ultrasonic frequencies and droplets ($<100\text{ }\mu\text{m}$) are ejected from the surface. In ultrasonic gas atomisation (USGA) the molten metal stream is disintegrated by impact with multiple high velocity gas pulses. The high-pressure gas (1.4 to 8.2 MPa) is accelerated by a shock wave tube (resonance cavities) to speeds of up to Mach 2 at frequencies ranging from 60 to 120 kHz. The particle size is usually less than $30\text{ }\mu\text{m}$. It is used commercially for production of low-melting alloys such as aluminium alloys and on a lab-scale for stainless steels, Cu-, Ni- and Co-based alloys.¹⁰

In double ultrasonic atomisation, the metal stream is guided towards the inner wall of a tubular resonator excited at ultrasonic frequencies. The molten metal wets this vibrating wall and disintegrates according to the capillary-wave atomisation process. Meanwhile, non-stationary shock waves are generated in an inert gas flowing into the same tube. The pressure pulses, like in ultrasonic gas atomisation (USGA), therefore further disintegrate the capillary-wave-atomised droplets. As the break-up of a molten metal occurs in two steps, the problem of stream diameter in USGA is cancelled.

12.2.3 Aerosol routes

In aerosol-based processing techniques a liquid precursor (nitrates, acetates, chlorides, alkoxides) is atomised into finely divided submicrometer liquid droplets (aerosol) that are distributed in a gas medium. This aerosol enters a heated reaction zone, where the solvent (methanol, ethanol, acetylacetone) is rapidly evaporated or combusted and the intimately mixed chemical precursors are decomposed and/or undergo chemical reaction to yield the desired products. The temperature, the composition of the chemical precursors, the flow rate of the aerosol and the atmosphere are the main parameters. The temperature should be high enough to allow the complete reaction, but low enough to prevent excessive grain growth.

These simple and inexpensive processes can be adapted for the production of ultrafine multicomponent powders with a well-controlled stoichiometry (ultrasonic

droplet generators and electrostatic atomisation).^{18,19} These powders have a narrow size distribution and tend to be spherical and unagglomerated. This technology is mainly applied to the fabrication of oxides. However, dense spherical palladium particles²⁰ or 70 wt% Ni–30 wt% Fe alloy powders of 10–80 nm²¹ were produced by spray pyrolyse.

12.2.4 Physical routes

The main physical route to produce powder is physical vapour deposition (PVD). Even if the PVD process is usually applied for coatings, some set-up (inert gas condensation, electrical explosion wire, laser ablation) allows the production of very fine (10 nm) powders with high purity (vacuum environment process). However, the production rate is very low and the costs are very high.

During the PVD process vapour phase species can be produced by evaporation of the bulk material, sputtering, or ion plating. These vapour phase species will collide with the inert-gas molecule and undergo homogeneous phase nucleation to form powder particles that will be then collected.²⁴ When the vapour phase species are produced by evaporation, this process is also called inert gas condensation (IGC). It is used to produce Zn²² and Ni²³ nano-powders. However, the synthesis of multicomponent powder is difficult because the different elements have different evaporation temperatures or sputtering rates. This can be solved by using the laser ablation method.

12.2.5 Chemical routes

The numerous chemical processes can be classified as a function of the type of chemical decomposition involved in the metallic powder production. These are decomposition of a solid by a gas (oxide reduction), precipitation from a solution (electrolysis, wet reduction, precipitation), condensation and thermal decomposition (carbonyl process, hydrid-dehydird process).

Decomposition of a solid by a gas (oxide reduction)

This process consists of the reduction of the oxides by gasses such as hydrogen, carbon monoxide.^{12,14,25} A typical reaction is: $\text{MO}(\text{s}) + \text{H}_2(\text{g}) \rightarrow \text{M}(\text{s}) + \text{H}_2\text{O}(\text{g})$. The process parameters are composition and flow rate of the reducing gas, reduction temperature (main parameter), temperature profile in the furnace and bed depth of the oxide if reduction is performed in a stationary system. Non-stationary reduction, such as in rotary kilns or fluidised bed reactors favours access of the reducing gas to the metal oxide particles and so improves the kinetics of reduction.

Oxide-reduced powders are very porous and thus are called sponge powders. They contain most of their residual oxides within the particles, instead of a

surface enrichment as for atomised powders. This process is commercially used for the production of iron, copper, tungsten and molybdenum powders, and on a smaller scale, for cobalt and nickel powders.

Precipitation from a solution (electrolysis, wet reduction, precipitation)

Metal precipitation from a solution (obtained by leaching an ore) can be accomplished directly by electrolysis or wet reduction (Sherritt Gordon process). Indirect precipitation from a salt solution is done by first precipitating a compound of the metal (hydroxide, carbonate, or oxalate) followed by heating, decomposition, and reduction.

Electrolysis or electrodeposition from an aqueous solution consists in depositing a pure metal on an electrode. The deposit can be a loose adhering powder or sponge that can be disintegrated mechanically into fine particles (Cu, Ag) or a coherent dense brittle layer of metal that can be ground into powder (Fe, Mn).²⁵ Powder-like deposits are favoured by low cation concentration (limits particle growth), low pH (favours conductivity), high current density and frequent removal of the deposit at the cathode (brush-down interval). This technique is mostly used to produce irregular shape (dendritic) powders such as Fe, Cu and Ag, but it has also been employed for Sn, Cr, Be, Sb, Cd, Pb, Pd and Zn. The main advantage of electrolytic powder is its high purity level after removal of impurities coming from the electrolyte. However, the high production cost of, for example, electrolytic iron powders, limits their use to niche applications such as catalyst or food additives (Fig. 12.3e).

The wet reduction (Sherritt Gordon process) is based on the separation and precipitation of Cu, Ni and Co from a salt solution, by reduction with hydrogen. High temperature and high hydrogen pressure are used to increase the reaction rates. The pH value is increased by adding ammonia in order to guarantee a complete reduction. Powders with a good compactibility and different particle shapes can be produced (e.g. Co with $d_{50} = 60 \mu\text{m}$). Moreover, co-precipitation or successive precipitation of different metals allows the production of alloyed or composite powders.

Many metal powders are produced by the precipitation of their soluble salts as insoluble hydroxide, carbonate or oxalate (indirect precipitation) (Fig. 12.3f). Subsequent heating decomposes these compounds into the respective metals or metal oxides and gaseous products.¹⁸ Different precipitation methods can be used: direct strike precipitation (addition of a precipitating agent), solvent removal (sol-gel), hydrophilic non-solvent addition or precipitation from homogeneous solution (PFHS) (use of a precursor whose decomposition kinetics controls the rate of release of precipitating agent).²⁶ The parameters governing the powder characteristics (morphology and agglomeration) are concentration, pH, temperature, anion associated to the soluble metal cation, choice of the precipitating reaction and aging conditions. This process is

employed for platinum, selenium, tellurium, silver, nickel and silver-cadmium oxide compounds through co-precipitation.²⁵

Condensation (precipitation from a gas)

The main processes are inert gas condensation (IGC) and chemical vapour decomposition (CVD). CVD implies thermal dissociation and/or chemical reaction of the gaseous reactants (halides, hydrides and halohydrides of metals and metalloids) on or near a heated surface to form stable solid products. The decomposition of the gaseous reactants can be homogeneous and/or heterogeneous reaction forming respectively powders or films. The different heating methods lead to a variety of CVD methods such as plasma-assisted CVD (PACVD), as well as different types of precursors, e.g. metalorganic CVD (MOCVD) etc. ... The CVD process parameters are deposition temperature, pressure, input gas ratio and flow rate.

The main drawbacks of CVD are the toxic, corrosive, flammable and/or explosive precursor gasses and the difficulty to deposit multicomponent materials with a well-controlled stoichiometry because the different precursors have different vaporisation rates. Ultra-fine powders (few nm up to few 10 nm) can be produced.²⁷

Thermal decomposition (carbonyl process, hydride-dehydride process)

The carbonyl process was first used for the production of nickel powders (in 1889). Other possible metal carbonyls include iron, cobalt and, in fact, all of the metals of the first, second and third transition metal series.^{25,28}

Thermal decomposition of gaseous cobalt, iron and nickel carbonyls occurs at temperatures about 200°C to have favourable reaction kinetics for acceptable powder production rates. Fine spherical iron powder (less than 10 µm) while fine irregular porous nickel powder is obtained with this process. However, the carbonyls are dangerous for the health even at very low concentrations (ppb-level).

Hydride decomposition (hydride/dehydride process) is used for metals that are too ductile to be milled into very fine particles. The metal is embrittled by hydrogenation during heating in hydrogen atmosphere at elevated temperatures. Absorption of only a few per cent of hydrogen makes most transition metals so brittle that they readily can be comminuted. After milling, the hydrogen can simply be removed by heating the powder in a dynamic vacuum. This process is used for Ti, Ta and Nb.^{25,28}

12.2.6 Plasma techniques

Gaseous plasma consists of a mixture of electrons, ions and neutral particles and is electrically neutral (negative and positive charges balances each other) even if it is electrically conducting due to the presence of free charge carriers.²⁹

There are two types of plasma, thermal plasma and cold plasma, depending on the respective temperature of the electrons (T_e) and the heavy particles (neutral particles and ions (T_h)). In thermal plasmas (pressure $> 10 \text{ kPa}$), the temperatures of the gas and the electrons are comparable and are of many thousands of degrees. Starting materials are typically atomised at these temperatures and the powder synthesis occurs during condensation outside the plasma when the gasses cool.³⁰ In contrast, in a low-pressure ($p < 200 \text{ Pa}$) low-temperature plasma (cold plasma) the electron temperature is much higher than the gas or ion temperature, which is close to room temperature because of the poor collisional coupling between electrons and heavy particles at reduced pressures.³¹ As the growth of particles may be completely determined by chemical kinetic factors, thermal and low-temperature plasmas may produce materials with different structures and properties.

Plasma methods are very popular as they enable the preparation of two-component compounds as well as multicomponent powders with a high purity. Besides ceramic powders (SiC, SiN, BN), metallic nanoparticles are produced. Nano-powders are used for their light emission properties (Si) or magnetic recording tapes. Nanostructured thin films, consisting of nanoparticles embedded in a metal matrix have also been produced.

12.3 Forming processes towards near-net shape

Near-net-shape components can be obtained by a conventional two-step process consisting in first giving the shape of the component (compaction) followed by its consolidation (sintering). Other processes allow the shaping and the consolidation of the component in one step (hot isostatic pressing, hot extrusion, hot forging, etc.). Because of its economical importance infiltration is also shortly described in this part, as well as the fast developing rapid prototyping processes.

12.3.1 Conventional route

Compaction

Compaction is a widely used method to form semi-finished or near-net-shape components from a powder. The quality of compaction (density gradients, micro-cracks) has a great influence on distortion of the product shape after sintering step as well as on the properties (defect-free components) of the final product.

Powder compacts can be obtained by uniaxial pressing, isostatic pressing, metal injection moulding (MIM) or by less used processes such as powder rolling, extrusion and dynamic or explosive compaction.

Uniaxial pressing

Uniaxial pressing (dry or die pressing) is the most common method of compaction to form PM components. This low-cost process is adapted to high-volume (up to few hundreds of parts per minute) production of ‘relatively simple’ geometry powder compacts.³²

It consists in compacting a dry powder (i.e. < 2 wt% water) in a die at a pressure ranging from 20 to 700 MPa by operating one or more rigid punches (higher numbers of punches are needed with increasing complexity of the component). A sufficiently high pressure is required to guarantee a sufficient strength of the green compact for subsequent handling and processing.

Compaction consists in the following three steps: filling the die with the powder, compacting the powder and ejecting the powder compact from the die. Die filling and compaction control the uniformity of the green density in the powder compact, which is a crucial parameter. Green density gradients have to be minimised in order to reduce differential shrinkage during sintering and shape distortion, as well as to avoid induced defects that limit the properties and reliability of the part. Ejection of the compact is also a critical step because macroscopic defects can be created.

Uniform and high packing density of a powder during die filling favours high green density with low green density gradients after compaction. This implies the use of good-flowing powders, which are also necessary to guarantee reproducible die filling. High-flowability powders have a relatively large particle size distribution lying between 40 and 400 µm and are usually spherical or equiaxial. Powders with a low flowability (fine (1–10 µm) irregular powders) have to be granulated before dry pressing (e.g. by spray drying) with 1 to 5 wt% organic additives such as binders, plasticisers and lubricants, which also improve the handling of the compact and/or the compactibility of the powder. Organic binders (wax, polyethylene glycol) allow the increase the green strength of the compact. Plasticisers (water, ethylene glycol) are used in combination with binders to improve the deformability of the powder during compaction. Lubricants (wax, magnesium stearate, stearic acid) reduce the interfacial frictional forces between individual particles favourable to powder compaction and/or between particles and die surfaces. They also reduce the required ejection pressure of the compact, thus avoiding macro-defect formation. Those additives will be eliminated by thermal decomposition before sintering or in a special zone of a continuous sintering furnace.

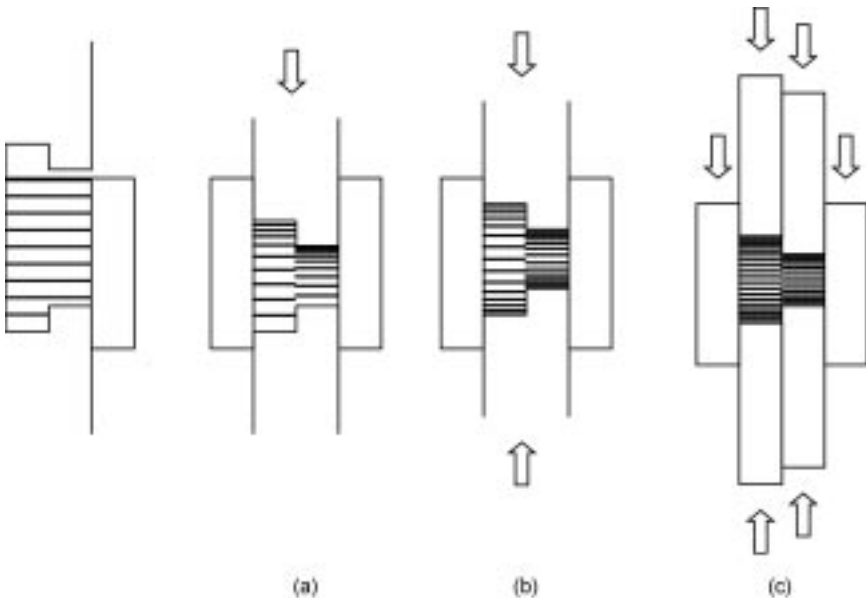
During powder compaction, the applied pressure induces particle rearrangement, deformation, in some cases fracturing, and finally consolidation of the particulate assembly. Green density and compact strength increase with increasing compaction pressure.¹² Two scales of green density gradients can occur during powder compaction: (i) macroscopic density gradient induced by non-uniform die filling and/or pressure gradients during compaction and (ii)

microscopic density gradient due to packing defects, hollow particles (granules), and/or insufficient particle (granule) deformation during compaction. Non-uniform pressure/stress gradient is due to the non-uniform pressure/stress transmission at particle-particle and particle-die (die wall friction) contacts. Green density gradients are minimised by using lubricants, smooth surface die, low compaction ratio, double-action or floating die pressing instead of single-action pressing and by adapting the numbers of punches to the number of different thickness areas in the part.

During ejection, the compact integrity is favoured by a sufficiently high green strength to withstand the applied forces on the compact required to eject it from the die, a low ejection pressure, favoured by the use of lubricant to reduce die wall friction and a low elastic springback (expansion of the powder compact after ejection from the forming die). The negative effect of a differential springback (the axial springback being higher than the radial one) can be reduced by maintaining a small axial pressure on the compact during ejection (punch hold-down ejection or withdrawal of the die).¹⁴

Uniaxial pressing can be performed with a single-action, double-action or floating die press (Fig. 12.4).

A single-action press uses only one moving punch. As it induces high green density gradients in the axial directions, it may be used for parts with a very low height to diameter aspect ratio and simple shape. A double action press has at least two independently moving punches that induce a more uniform compaction



12.4 Uniaxial pressing: (a) single action, (b) double action, (c) floating die and double action multiple punches.

especially for simple large and thick parts. In pressing of multi-level compacts, the several punches have to be operated independently so that the different areas in the die are equally compacted. In a floating die press, a similar effect can be obtained, the movement (floating) of the die corresponding to an upwards movement of the lower punch.¹⁴ In more sophisticated floating die press, the punches and the die can move independently in order to reduce the green density gradients. This allows the production of complex parts with tapers, holes and multiple steps. If higher working speeds and precise control of the movements are required, the die is directly moved by the press.

Isostatic pressing

Isostatic pressing (cold isostatic pressing) consists in compacting a powder in an elastomeric container submersed in a fluid at a pressure of 20 to 400 MPa. Cold isostatic pressing allows the production of simple-shaped small or large powder compacts (up to 2000 kg) with a uniform green density even for large height/diameter ratio part (impossible by uniaxial pressing), but with the sacrifice in pressing speed and dimensional control, requiring subsequent machining in the green compact. Cold isostatic pressing is used for powders that are difficult to press such as hard metals.

Metal injection moulding

Metal injection moulding (MIM) is adapted to the production of small complex near-net-shape compounds (wall thickness down to 0.3 mm) with very good tolerances (0.3 to 0.5%), especially for medium (thousands of parts/year) to high volume (millions of parts/year) production.³³ Because of the high raw-material costs, MIM is usually limited to the production of parts lighter than 100 g.

This process consists in filling a die cavity with a viscous mixture of powder and binder at around 130 to 200°C under a pressure up to 150 MPa.¹² Metal injection moulding parts are produced in four different steps: feedstock formulation, moulding, debinding and sintering.

The feedstock is a homogeneous pelletised (granulation to a special shape) mixture of fine spherical metal powder with a mean size ranging from 5 to 15 µm and 30 to 45 vol.% organic binder.³³ A binder system usually has three components, a backbone that provides green strength and that will stay after debinding, a filler phase that is easily extracted during initial stages of debinding and surfactant to control feedstock rheology. During moulding, the feedstock is introduced to the heated injection unit by, for example, a rotating screw, the mixture is then injected in the die by axial movement of the screw and finally the part is ejected from the die after quick cooling. The main parameters are injection temperature, pressure and speed, as well as thermal conductivity and viscosity of the feedstock and the mould temperature.

The debinding can be done by thermal decomposition, solvent extraction or a combination (also called catalytic decomposition). A typical binder removal rate is 2 to 3 mm wall thickness per hour. Finally, the part undergoes a densification up to 95% to 99% of the theoretical density as well as a shrinkage of 14% to 20% during the sintering step (see below).

The MIM process is applied to produce parts in stainless steels (304L, 316L), tool steels (M2), soft magnetic alloys (Fe-50 %Ni, Fe-3 %Si, 430L), alloys for glass-to-metal sealing applications (kovar), cobalt-, nickel- and titanium-based alloys used for wear medical, automotive and aerospace applications.

Powder rolling – extrusion – dynamic and explosive compaction

Powder rolling (roll compacting) consists in compacting a powder continuously passing between two turning rolls.¹⁴ A binder is usually added to the powder to favour densification. For a given thickness of the strip (defined by the distance between the two rolls), the density of the compacted strip can be increased by increasing the diameter of the roll and reducing the rolling speed (maximum speed lying about 0.5 m/s). The main advantage of powder rolling compared to conventional casting and rolling process is a low amount of rolling passes necessary to produce a thin strip. The main disadvantages are a high powder price and a low production rate.

Extrusion consists in forcing a viscous mixture of powder and binder through a die. The obtained, shaped product is sintered with a slow heating rate in order to remove the binder.

During dynamic and explosive compaction (high-energy rate compaction), that is only applied at lab-scale, powders are compacted at very high velocities (200 m/s) by the propagation of a high-pressure wave. One set-up uses the conventional die compaction with an upper punch moving at high velocity through the action of an explosive charge or compressed gas. Another one consists in encapsulating a powder in a mild steel tube and subjecting this tube to the action of sheet explosives taped to it.

The advantages are a high green density, a higher green and sintered strength and lower density gradient.^{13,14} Green density of 99% of theoretical density has been achieved for aluminium, stainless steel, amorphous powders,¹² even for tungsten compacts a relative density of 97.6% has been obtained.

Sintering

Sintering originally used to produce clay pots³⁵ is nowadays involved in the fabrication of net-shape components in ceramics, cermets, metals and composites. The application fields are automobile and aeronautic industries (valves, bearings, aircraft wings weight), electrical and electronic industries (tungsten wires, ultrasonic transducers), medical industries (dental or hip implants).

During sintering porosity and the microstructure change irreversibly from contacting particles to almost dense material. This induces improvement of many properties such as strength, ductility, conductivity, magnetic permeability, and corrosion resistance.

Sintering can be defined as a thermal treatment for bonding particles into a coherent, predominantly solid structure via mass transport events that often occur on the atomic scale.³⁴ The sintering induces the consolidation (increase of strength) of a loose or compacted powder and is usually accompanied by densification (shrinkage). During sintering the reduction of total surface energy (usual driving force for mass flow during sintering) is due to the decrease of surface area by formation of inter-particle bonds and the reduction of surface curvature. The path of the atomic motion occurring during the mass flow in response to the driving force is called the sintering mechanism.¹² For metal powders, the mechanisms are usually diffusion processes with surface, grain boundary or lattice paths. Sintering progresses in different stages; for each stage (i.e. for each driving force type corresponding to a particular particle-pore geometry), different ways of mass flow (i.e. sintering mechanism) are possible. The knowledge of the relations between the different sintering parameters and each sintering mechanism during the different stages allows modelling and thus optimising the sintering parameters.

The main sintering parameters are:

- particle size (reduction of particle size increases the surface energy per unit volume of the powder and so the driving force associated with sintering, thus the sintering rate);
- particle size distribution (large difference in curvature of the grains, due to grain size difference, will promote coalescence, i.e. the growth of the large grain at the expense of the smaller one);
- temperature (exponential influence on sintering because it is involved in the activation energy of the sintering mechanisms (e.g. diffusion processes));
- time (influences diffusion);
- green density (density gradients occurring during compaction will induce differential shrinkage during sintering and maybe distortion of the part because higher green density induces lower shrinkage);
- applied external pressure (to obtain fully dense material, HP or HIP processes);
- amount of liquid, if any;
- sintering aids (favouring diffusion in the solid or liquid state);
- atmosphere.

A particular sintering atmosphere can be used to protect the metal powder from oxidation (argon, vacuum), to remove the oxidation layer on the powder (reducing atmosphere such as hydrogen, carbon monoxide, dissociated ammonia or natural gas), to control the carbon content of the powder, to remove the

lubricants and binders introduced during compaction or even to react with the powder (formation of nitride). Sintering can be classified as solid state, liquid phase, reaction sintering and microwave sintering.

Solid state sintering

In solid state sintering the microstructure changes are divided into three different stages. The first stage corresponds to the growth of the bond, called neck, between two particles, independently of the growth of the neighbouring necks. The pores are interconnected with an irregular shape. The intermediate stage occurs as the merging necks shrink the pores to form interconnected pores with a more smooth usually cylindrical shape. Most of the densification and change in properties occurs in this intermediate stage. The final stage corresponds to pore closure, where the pores become spherical and isolated. By definition the driving force changes for each sintering stage. During the initial stage the driving force is the curvature gradient between the particle and the neck, during the intermediate stage it is the curvature around the cylindrical pore and during the final stage the curvature around the spherical pore. For every sintering stage, the mass transport process (sintering mechanism) can be described by a characteristic equation.

There are sintering mechanisms that induce shrinkage (i.e. densification) such as volume diffusion, grain boundary diffusion, plastic flow and viscous flow (for the amorphous solids) and some that do not such as surface diffusion, evaporation–condensation and volume diffusion from a surface source to a surface sink. Different sintering mechanisms are involved at different moments during the sintering process. For example, a finer particle size usually favours sintering by surface or grain boundary diffusion compared to volume diffusion.

During the initial stage, the different sintering mechanisms can be diffusion (surface-, volume- or grain boundary-diffusion), evaporation or dislocation motion. The sintering mechanism is usually described by the size of the growing neck between the particles but shrinkage or relative change in surface area can also be used.

The intermediate stage is characterised by densification usually coupled with grain growth during the latter phase of the intermediate stage. The smaller grains, having a higher curvature, are progressively incorporated to the neighbour grain by grain boundary motion. This grain boundary motion induces drag forces on the pores, which can move by volume, surface diffusion or evaporation–condensation mechanism across the pore. When the moving rate of the grain boundary is too high (e.g. favoured by high temperature), the pores cannot impinge the grain boundary any more and become isolated inside the grain (beginning of the third stage). In this case, the rate of densification is much smaller because volume diffusion is less fast than grain boundary diffusion.³⁵ Consequently, it is important to minimise pore–grain boundary separation by careful temperature control, the incorporation of second-phase inclusion such as

oxide particles into the microstructure to impinge the grain boundary, or the use of narrow initial particle size distribution.^{37,38} The usual parameter to follow the sintering is the rate of densification. The two sintering mechanisms involved in densification are grain boundary and volume diffusion. Surface diffusion or evaporation–condensation mechanisms, inducing no shrinkage, are also expected to be active in smoothing the pore structure and in pore migration with grain boundaries during grain growth. Long sintering times (compared to the first stage) are required to achieve significant property or density changes. Temperature has a complex effect on the sintering because diffusion, grain growth and pore motion are all thermally activated.

The third stage is characterised by the presence of isolated spherical pores. If the closed pores are mobile enough to stay coupled to the grain boundary, then continued shrinkage is expected. This is favoured by a homogeneous grain size, which lowers the curvature of the grain boundary and so decreases their motion rate. If not, after separation from the grain boundary, the pore must emit vacancies that move by volume diffusion, which is a slow process, towards the distant grain boundary. This leads to a drop of the densification rate. With prolonged sintering, the larger pores grow at the expense of the smaller ones (that emit more vacancies in the grain because of higher curvature). This is called pore coarsening or Ostwald ripening. In addition to pore coarsening, the pore size can increase by coalescence, due to grain growth by grain boundary motion dragging pores towards each other. If the pore has trapped gas, an internal pressure is induced inside the pore, which limits densification. If this gas is soluble in the matrix, the densification rate is controlled by the internal gas pressure and not by the limit of solubility.

The usual parameter to follow the sintering during the final stage is the rate of densification, but the rate of shrinkage, surface area change, or neck growth could also be used. The rate of densification depends on the pore amount, pore radius, volume diffusion, grain size distribution and stress effects (compressed trapped gas working against pore shrinkage).³⁹

Liquid phase sintering (HSS)

Liquid phase sintering is involved when powders of different composition are mixed. Usually the constituent, that remains solid during sintering, should have a relatively high solubility in the formed liquid and inversely the solubility of the liquid in the solid should be low to ensure that this liquid phase is not transient. Common systems are: WC-Co, Fe-Cu, Cu-Sn, etc.³⁶

The main advantage of liquid phase sintering is the lower sintering time required compared to solid state sintering. During heating, the mixture of powders first undergoes solid state sintering, which can induce significant densification, before the formation of the liquid at the sintering temperature. After the liquid is formed, the sintering depends on the amount of liquid and is

usually divided into three stages: rearrangement, solution–reprecipitation, and the third stage. If the amount of liquid is sufficient to fill all the interparticle spaces, the theoretical density can be obtained during the rearrangement stage. For lower liquid contents, the solid skeleton slows down the densification and the contribution of the last two sintering stages becomes significant. In fact, less than 15 vol.% of liquid is usually used to avoid distortion of the part during sintering.

During the first stage (rearrangement) and in case of a wetting liquid, the liquid spreads as soon as the liquid is formed between the solid particles under the influence of capillary forces. The rate of densification controlled by viscous flow is very high at the beginning and then continuously slows down. As the densification rate governed by rearrangement decreases, another mechanism called dissolution–diffusion–reprecipitation, characteristic for the second stage prevails. The solubility of a grain in its surrounding liquid increases with the curvature of the grain, i.e. with a decrease of the grain size. The difference of solubility as a function of grain size induces a concentration gradient of solute species in the liquid, that diffuse from the small grains to the large ones, on which the solute species precipitate (reprecipitation) when the solubility limit in the liquid is reached. So during this stage, grain coarsening occurs (Ostwald ripening). Simultaneously the elimination of the high-energy vapour interface is obtained by grain shape accommodation (flattening) during solution–reprecipitation events inducing densification by higher packing of the grains. The third stage corresponds to the densification of a rigid solid skeleton with a rate similar to the one obtained in solid state sintering.

Reaction sintering

Solid state reaction sintering of metal powder mixtures is a way to produce alloys such as carbon steel, Fe-Ni, Fe-Mn, Fe-Si, Fe-Cr, Fe-Mo and Cu-Ni. The principal phenomenon occurring during sintering is the solid state interdiffusion between the different compounds. The driving force is the chemical potential gradient due to concentration differences. This phenomenon superimposes the metal powder self-diffusion caused by surface and interfacial tension forces, occurring in solid state sintering of pure or pre-alloyed powders. Reaction sintering is favoured by fine particle size (smaller the diffusion distance) and high temperature (higher coefficient of diffusion).

Reaction sintering can also occur during liquid phase sintering ($\text{Mo} + 2\text{Si} \rightarrow \text{MoSi}_2$) or by reaction of the sintering atmosphere with the powder ($3\text{Si} + 2\text{N}_2 \rightarrow \text{Si}_3\text{N}_4$).

Microwave sintering

Sintering of metal powders is a surprising recent development in microwave applications because bulk metals reflect microwaves. However, compacted

metal powders at room temperature will absorb microwaves and will be heated very effectively and rapidly (above 100°C/min), inducing sintering. Metals such as iron, steel, copper, aluminium, tin, nickel, cobalt, tungsten have been sintered to high density by microwaves. Cylinders, rods, gears, and other automotive components with until now a maximum size of 10 cm have been produced in 30 to 90 min.⁴⁰

Contrary to the conventional heating where the transfer of thermal energy is done by conduction to the inside of the part, microwave heating is a volumetric heating consisting in an instantaneous conversion of electromagnetic energy into thermal energy. The mechanisms involved in microwave sintering are not completely understood at the moment. However, the sample size and shape, the distribution of microwave energy and the magnetic and electromagnetic field radiation are important parameters.

12.3.2 Other routes

This part is mainly dedicated to full density sintering processes such as hot pressing, hot isostatic pressing, hot extrusion, hot forging and field assisted sintering. However, other techniques such as infiltration and rapid prototyping techniques will also be presented.

Full density is required to improve product properties such as rupture and fatigue strength, toughness, thermal or electrical conductivity. This can only be achieved when stress and temperature are simultaneously applied during densification to close the pores.¹³ Because the powder usually has to be protected from reaction with air, this makes the hot compaction processes complex and costly. So these techniques are reserved for expensive materials with special properties such as beryllium and magnesium alloys (finer grain size), super-alloys (elimination of segregation), high speed steels and dispersion strengthened alloys (homogeneous distribution of the second phase). The main parameters are temperature, applied stress, strain rate and grain size.

'Near-net-shape' components, implying material saving, combined with higher properties can make these processes competitive compared to the conventional casting, forging, machining route.

Hot pressing

Hot pressing consists in applying pressure with a hot punch on the metal powder placed in a heated die usually under a protective atmosphere.¹⁴ The main problem with hot pressing is to find a suitable die material, which has to withstand the applied pressure without reaction with the metal powder. Although the total amount of deformation of the compact is relatively limited compared to hot extrusion or hot forging, complete densification is generally achieved.

Hot isostatic pressing

In hot isostatic pressing, a hydrostatic pressure is applied to the powder by the action of a gas (Argon, nitrogen) with a pressure up to 300 MPa simultaneously with a temperature up to 2000°C.¹⁴ Before HIPing, the powder is placed into a metallic or a glass container ('can') which is out-gassed and sealed. Spherical powders are the best suited for hot isostatic pressing, which is a long time process (around two cycles per day). The cycle duration can be reduced to a few hours for temperatures lower than 1250°C, which allow the opening of the isostatic press without requiring the cooling down of the furnace and so re-loading with a preheated can.

In spite of the high capital cost, hot isostatic pressing is used to produce large semi-finished components in hardmetals,⁴¹ high speed steels, superalloys (most common technique),⁴² titanium alloys and beryllium. Moreover a can with a complex form allows the production of near-net-shape components. This ability has been used for superalloys and titanium alloys.

Hot extrusion

There are three basic methods for the hot extrusion of powders. The first method consists in filling a heated extrusion container with a loose powder (magnesium alloys), which is heated during the 15 to 30 seconds before starting its extrusion. In the second method the powder has been compacted and sintered before extrusion (aluminium alloys)⁴³ and molybdenum, superalloys and high-speed steels. The third method, which is the mostly used (beryllium, stainless steel, aluminium, copper and nickel dispersion strengthened alloys), consists in filling a metallic capsule ('can') with the powder, to protect the powder from contamination by the atmosphere. The can is out-gassed and sealed before heating and extrusion. The material of the can (e.g. copper, low carbon steel) should have a stiffness similar to that of the powder at the extrusion temperature, should not react with the powder and should be removable by etching or mechanical stripping.

Circular, elliptical or rectangular cross-section parts can be obtained by hot extrusion. For a more complex cross-section shape the 'filled billet' technique was developed.⁴⁴ The mild steel filler contains a cavity with the shape of the desired cross-section, which is filled by the powder, the whole is placed in a carbon steel can and then extruded. Seamless tubing of stainless steel has been produced with this technique.⁴⁵

Hot forging

Metal powders that have been previously compacted and sometimes also sintered (preform) can be hot forged into parts of high density (elimination of

the residual porosity) and closely controlled dimensions.¹³ A height strain of 50% is at least needed for pore elimination and good interparticle bonding.¹² During hot forging the preform, which has a simpler shape than the final product, undergoes a lateral flow especially at the beginning of the deformation. This process allows subsequent quenching that makes it attractive for hardened steel. A production rate of 20 to 40 strokes per minute can be reached.

The main applications of this process concern the automotive industry (gears, connecting rods).

Electric field assisted sintering – ‘spark’ sintering

Electrical field assisted sintering is an emerging technology to densify powders with nanosize or nanostructure while avoiding the coarsening which accompanies standard densification routes thanks to its very short sintering time. However, it can also be used for coarser powders. This process is applicable to metals (Al, Fe, W, Mo, Be, Ti), metallic alloys (Al-Si-X, Fe-Co), intermetallics (Al-Ti, Al-Fe) and ceramics. It could be used to produce cutting tools, metal forming dies, gears, pump components, electric motors, household equipment.

Electrical field assisted sintering (FAST) consists in applying simultaneously a pressure with a punch and an electrical field to the powder that fills a conductive die. The electrical discharge induced by the electrical field at the contact of the particles and in the gaps between them is responsible for the physical activation of the powder particle surface (melting and vaporisation, inducing the cleaning of the particle surface) that favours sintering.

The main parameters are related to the powder characteristics, the compaction (e.g., uniformity of the packing of the die) and the characteristics linked to the electrical field (intensity, voltage, pulse pattern that induces the electrical discharge). The reached density is typically 98% to 99% of the theoretical density in very short time (10 min).⁴⁶

Infiltration

Infiltration consists in filling the pores of a sintered material with a liquid metal or alloy, having a (much) lower melting point.¹³ The driving force of infiltration is the reduction of surface free energy as in sintering. Infiltration is promoted by a low wetting angle of the liquid with the solid and by establishing a pressure gradient, e.g. putting the solid (porous skeleton) in a vacuum and applying pressure to the infiltrating liquid.

The infiltration parameters are the infiltration temperature (reduction of the viscosity of the infiltrating liquid) and the dwell time above the liquidus of the infiltrating liquid. Short times are preferred to limit eventually extensive reaction of the liquid with the skeleton (Fe-Cu). Infiltration can be advantageous

compared to liquid phase sintering when the liquid is insoluble in the skeleton material (W-Cu).

Rapid prototyping

Rapid prototyping (RP) concerns techniques that produce a complex part or a prototype to net or near-net shape by building the object layer by layer (additive processing) from a computer aided design (CAD) file without the need of specific expensive tooling (direct processes).⁴⁷ In many cases, a post-processing step such as, for example, co-firing, sintering or infiltration, etc., is needed to ensure sufficient strength of the part. Rapid prototyping techniques can be classified in direct, also referred as solid free-form fabrication (SFF), and indirect processes, the latter being the most widely used. Indirect processes use a pattern (model) or a mould made by a rapid prototyping technique to produce the final object, which can be metallic. The following concerns only the direct processes.

RP techniques mainly used for plastic products have been adapted for metals, ceramics or composites. The main advantages are the ability to produce complex parts and the absence of specific tooling that reduces the production time. However, the low dimensional accuracy and the high roughness of the part are the main drawbacks. The layer formation procedure is specific to each RP technique. The most common RP techniques are stereolithography (SL or SLA), fused deposition modelling (FDM or FDC and FDMet, respectively for ceramic and metal), ink jet printing (IJP) or three-dimensional printing (3DP) and selective laser sintering (SLS) or direct metal laser sintering (DMLS) or selective laser melting (SLM).

Laser technology is involved in more than a half of all the RP techniques: laser photo-polymerisation (stereo-lithography, ...), laser fusion or sintering (SLS), laser cladding (laser generating, controlled metal build-up (CMB), laser-aided powder solidification with powder jet (LAPS-J), LENS, ...), laser cutting (LOM, ...), laser-induced CVD (SALD, LCVD).

The applications of the metallic products are injection moulds, tools, dies, implants, etc.

Stereolithography (SL or SLA) consists in photo-polymerisation of a liquid monomer by an UV laser. The laser is scanned in selected areas of a liquid monomer layer, defined by a CAD file, to cure them.⁴⁷ After one layer has been processed another layer of resin is coated on the top of it (called re-coating) until the part is finished. This process has been adapted to produce metals.⁵⁰

Fused deposition modelling (FDM) consists in depositing a continuous hot extruded (low viscosity) thermoplastic filament with an elliptical cross section on a fixed substrate, following a path defined by a CAD-file.⁴⁷ In this case the not heated part of the filament acts as a punch. When one layer is completely cooled down the build platform indexes down and the deposition of the next

layer is performed. Adaptation of this process by using a particle-loaded thermoplastic filament followed by debinding and sintering allows the fabrication of ceramic (FDC) and metallic (stainless steel) components (FDMet).

Multiphase jet solidification (MJS) is similar to the fused deposition process of metals and ceramics.⁴⁷ The low melting metal or the powder-binder mixture is introduced in a patented extruder, melted (viscosity < 200 Pa s) and subsequently deposited on a substrate. Part of stainless steels, high speed steels, FeNi, Ti and SiC have been produced.

Three-dimensional printing (3DP or IJP) consists in printing with an ink jet printer a low viscosity binder, which forms a droplet, on a layer of deposited ceramic or metallic powder.⁴⁷ After drying of the binder (e.g. latex, wax emulsions, homogeneous solution phase binders), the next powder layer is deposited and so on until the part is finished. The part is then ultrasonically washed and its unprinted regions are removed through redispersion in the ultrasonic bath. The 3DP processes can be divided into dry powder processes and wet slurry processes, where the slurry of the powder is sprayed onto a substrate, dried, followed by the printing of the binder. The dry powder process has been used to produce injection moulds in stainless steel and tool steel parts (latex binder), which are subsequently sintered and infiltrated with Cu or Cu-alloys. The dimensional accuracy and the removal of the loose powder in the narrow regions are the main problems. The advantages of 3DP are its ability to produce very complex shapes with fine features (100 µm), its flexibility (many materials) and its well-controlled process.

Selective laser sintering (SLS) consists in scanning a thin layer (100–200 µm) of powder with a laser, that induces local sintering of powder particles corresponding to a path defined by a CAD-file.⁴⁷ The non-sintered particles act as support and so allow complex forms such as hollow sections, overhangs or undercuts, as for 3DP. After completion of the sintered layer, a new thin layer of powder is spread on top of it and then laser-scanned. The non-sintered particles are removed when the part is finished. SLS processes are mainly used for thermoplastics materials and less for metals and ceramics, because they require a higher energy input. Metals and ceramics can be produced by indirect or direct sintering approach. In the indirect sintering approach, a binder is used with the powder to be laser-sintered and a post-processing step is needed to obtain full density. For example, a polymer coated steel powder was processed by SLS and subsequently infiltrated with bronze or copper for tool making applications.⁴⁹ In the direct sintering approach, a high power laser (e.g. 1 kW, CO₂ laser) is used to sinter a preheated powder feed (reduction of thermal stresses) to reach the high temperature required for sintering. Liquid phase laser sintering was successfully performed for powder mixture such as Fe-Cu, stainless steel-Cu, WC-Co, TiB₂-Ni and Fe₃C-Fe. The SLS technique has a relatively fast building rate compared to the SLA or 3DP techniques for ceramics.

Direct metal laser sintering (DMLS) and selective laser melting (SLM) are similar to selective laser sintering (SLS). But in the case of DMLS most of the powder layer is melted whereas in SLM it is completely melted. As a consequence, there is a good metallurgical bonding between the layers and densities up to 100% can be reached.

Laser cladding (LC) includes processes such as laser engineered net shaping (LENS) and a variant of shape deposition manufacturing processes (SDM).⁴⁸ Laser engineered net shaping (LENS) and direct metal deposition (DMD) processes belong to laser powder deposition processes. They comprise focusing a laser beam (Nd:YAG) on a metallic substrate to create a weld pool while simultaneously injecting the metal powder directly into the laser beam, where it melts. The moving substrate along a defined path produces the component line-by-line and layer-by-layer. The high cooling rate allows the deposition of non-equilibrium phases (e.g. extended solubility alloys) and/or fine-grained microstructure, as full density and high mechanical properties can be achieved. The fabrication of multi-material graded and layered structures is possible.

12.4 Conclusions

Powder metallurgy is a mature industrial activity used to produce metallic and alloy components. There is a wide variety of powder production techniques, ranging from high output atomisation processes to high-value nano-powder production facilities. A broad spectrum of consolidation routes leads to simple or complex components. The high number of powder production techniques and consolidation methods allows enhancement of the relation between processing, microstructure and properties. Thanks to their high flexibility, PM processes find applications in the transport, energy, medical, machinery, and many other sectors.

12.5 References

1. Koch CC, ‘Milling of brittle and ductile materials’, *ASM Handbook: Powder metallurgy technologies and applications*, 1998, **7**, 53–66.
2. Hogg R and Cho H, ‘Grinding’, *Encyclopedia of Materials: Science and Technology*, 2001, 3652–58.
3. Lü L and Lai MO, *Mechanical alloying*, Boston/Dordrecht/London, Kluwer Academic Publishers, 1998.
4. Soni PR, *Mechanical alloying – Fundamentals and applications*, Cambridge International Science Publishing, 2000.
5. Suryanarayana C, ‘Mechanical alloying’, *ASM Handbook: Powder metallurgy technologies and applications*, 1998, **7**, 80–90.
6. Benjamin JS, ‘Mechanical alloying. A perspective’, *Met. Powder Rep.*, 1990, **45**(2), 122–27.
7. Suryanarayana C, *Bibliography on mechanical alloying and milling*, Cambridge

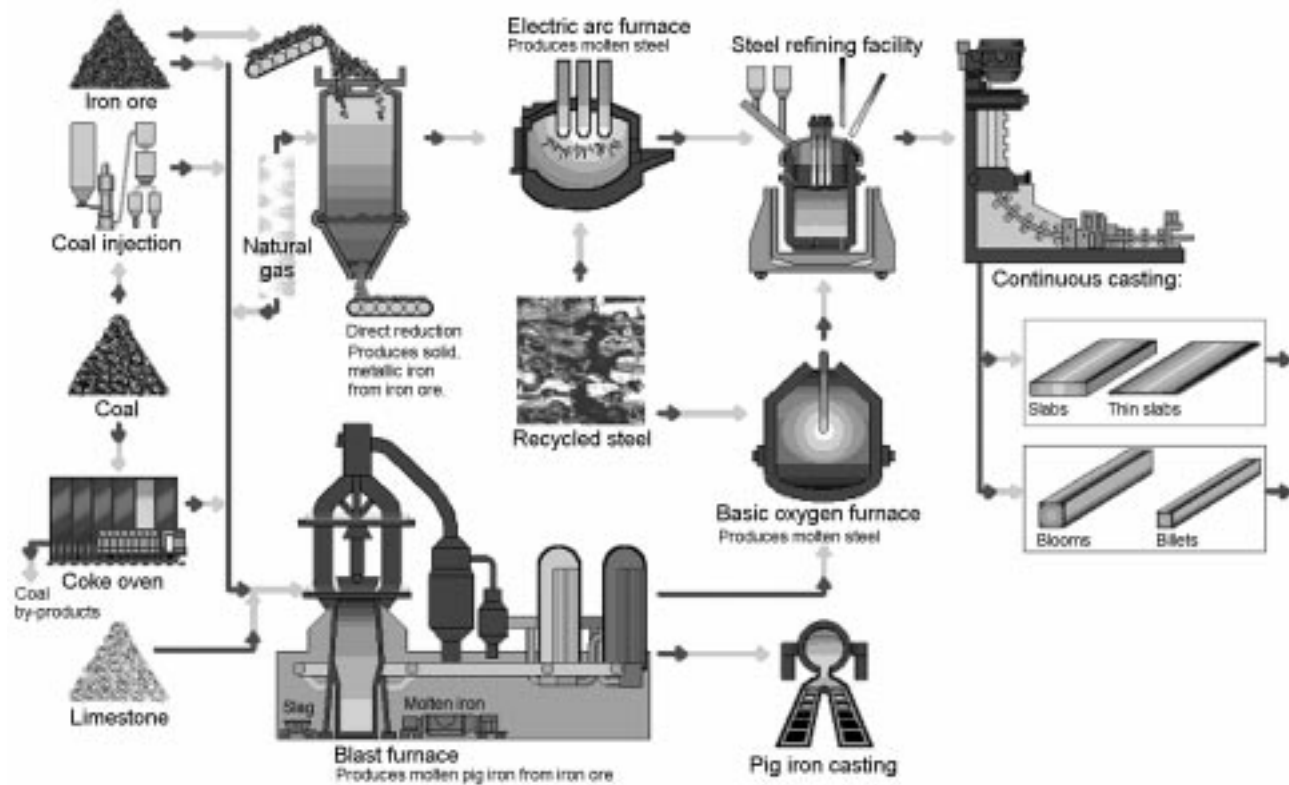
- International Science Publishing, 1995.
- 8. Bakker H, Zhou GF and Yang H, 'Mechanically driven disorder and phase transformations in alloys', *Progress in Mat. Sci.*, 1995, **39**(3), 159–41.
 - 9. Bradstedt SB, 'New powder making process may expand P/M's capabilities', *Precision Metal*, 1969, **27**, 52–55.
 - 10. Dunkley JJ, 'Atomization', *ASM Handbook: Powder metallurgy technologies and applications*, 1998, **7**, 35–52.
 - 11. Lawley A, 'Atomisation', *Encyclopedia of Materials: Science and Technology*, 2001, 387–393.
 - 12. German RM, *Powder Metallurgy Science*, Princeton, NJ, Metal Powder Industries Federation, 1984.
 - 13. Lenel FV, *Powder Metallurgy Principles and Applications*, Princeton, NJ, Metal Powder Industries Federation, 1980.
 - 14. Schatt W and Wieters KP, *Powder Metallurgy Processing and Materials*, EPMA, Shrewsbury, Liveseys Ltd, 1997.
 - 15. Anderson IE, 'Boost in atomiser pressure shaves powder – particle size', *Advanced materials and processes*, 1991, **140**(1), 30–32.
 - 16. Gerking L, 'Powder from metal and ceramic melts by laminar gas streams at supersonic speeds', *Powder Metallurgy International*, 1993, **25**(2), 59.
 - 17. Tornberg C, 'Gas efficiency in different atomization systems', *Advances in Powder Metallurgy and Particulate Materials, Volume 1: Powder production and spray forming*, Metal Powder Industries Federation, 1992, 127–35.
 - 18. Kerker M, 'Laboratory generation of aerosols', *Adv. Colloid Interface Sci.*, 1975, **5**, 105.
 - 19. Raabe OG, 'The generation of aerosols of fine particles', in *Fine Particle: aerosol generation, measurement, sampling and analysis*, symposium in Minneapolis, Minnesota, May 28–30 1975, Liu BYH. New York, Academic Press, 1976, 57–110.
 - 20. Plyum TC, Lyons SW, Powell QH, Gurav A, Kodas T and Wang LM, 'Palladium metal and palladium oxide particle production by spray pyrolysis', *Mater. Res. Bull.*, 1993, **28**(4), 369–76.
 - 21. Eroglu S, Zhang SC and Messing GL, 'Synthesis of nanocrystalline Ni-Fe alloy powders by spray pyrolysis', *J. of Materials Research*, 1996, **11**, 2131–34.
 - 22. Sasaki Y, Shiozawa K, Kita E, Tasaki A, Tanimoto H and Iwamoto Y, 'Fabrication of metal nanocrystalline films by gas-deposition method', *Mater. Sci. Eng. A*, 1996, **217**, 344–47.
 - 23. Daub O, Langel W, Reiner C and Kienle L, 'QSM-controlled production of nanocrystalline metals by inert gas condensation in q flow system', *Ber. Bunsen-Ges. Phys. Chem.*, 1997, **101**, 1753–56.
 - 24. Choy KL, 'Vapor processing of nanostructured materials', *Handbook of Nanostructured Materials and Nanotechnology, Volume 1: Synthesis and Processing*, Nalwa HS, Academic Press, 2000, 533–77.
 - 25. Klar E, reviewed by Taubenblat PW, 'Chemical and electrolytic methods of powder production', *ASM Handbook: Powder metallurgy technologies and applications*, 1998, **7**, 67–71.
 - 26. Rimann RE, 'Solution synthesis of powders', *Encyclopedia of Materials: Science and Technology*, 7800–10.
 - 27. Berger S, Schachter S and Tamir S, 'Photoluminescence as a surface-effect in nanostructures', *Nanostruct. Mater.*, 1997, **8**(2), 231–42.

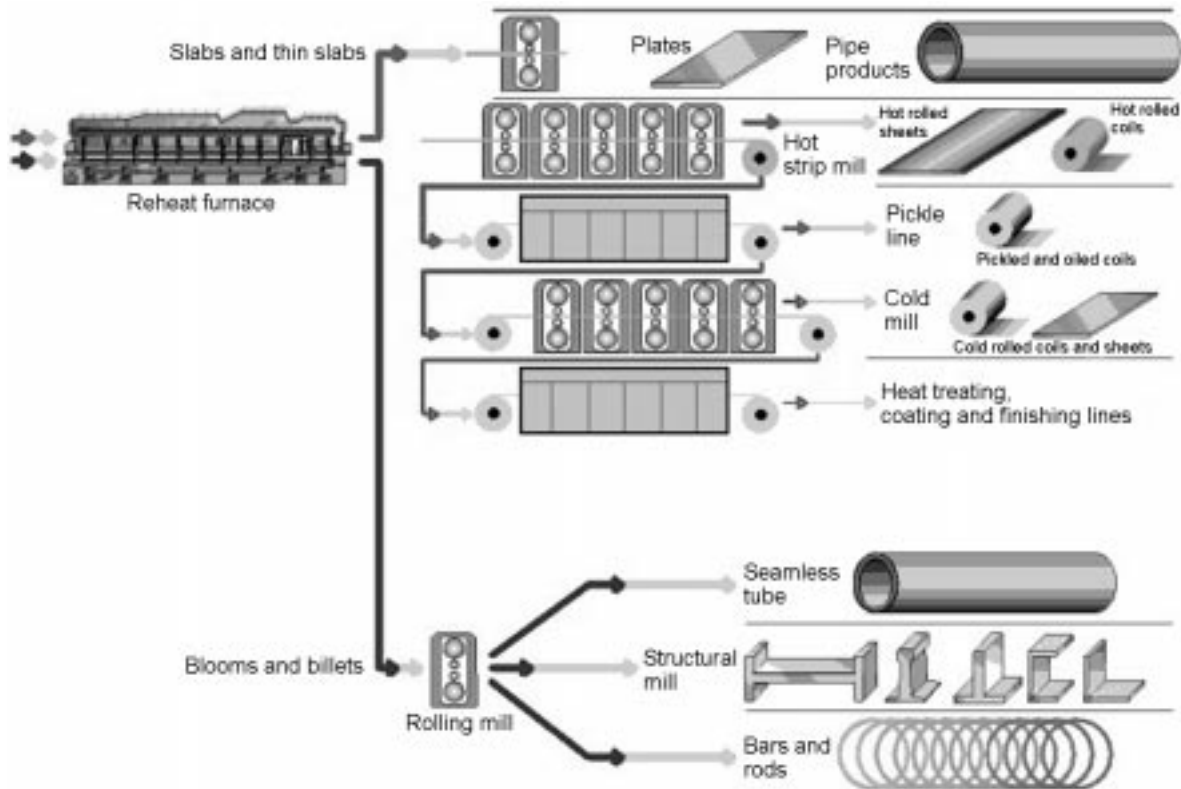
28. Ayers J D and Anderson I E, 'Very fine metal powders', *Journal of Metals*, 1985, **37**, 16–21.
29. Boulos MI, Fauchais P and Pfender E, *Thermal Plasmas – Fundamentals and Applications – vol. 1*, New York, Plenum Press, 1994.
30. Fauchais P and Vardelle A, 'Thermal Plasmas', *IEEE Transactions on Plasma Science*, 1997, **25**(6), 1258–80.
31. Costa J, 'Nanoparticles from low-pressure, low-temperature plasmas', *Handbook of Nanostructured Materials and Nanotechnology, Volume 1: Synthesis and Processing*, Nalwa HS, 2000, 57–158.
32. Ewsuk KG, 'Grinding', *Encyclopedia of Materials: Science and Technology*, 2001, 3652–58.
33. Tandon R, 'Metal injection moulding', *Encyclopedia of Materials: Science and Technology*, 2001, 5439–42.
34. German RM, 'Sintering', *Encyclopedia of Materials: Science and Technology*, 2001, 8640–43.
35. German RM, 'Sintering: modeling', *Encyclopedia of Materials: Science and Technology*, 2001, 8643–47.
36. German RM, 'Liquid phase sintering: metals', *Encyclopedia of Materials: Science and Technology*, 2001, 4601–03.
37. Brook RJ, 'Pores and grain growth kinetics', *J. Amer. Ceramic Soc.*, vol. 52, 1969, 339–40.
38. Hsueh CH, Evans AG and Coble RL, 'Microstructure development during final/intermediate stage sintering-1. Pore/grain boundary separation', *Acta Met.*, 1982, **30**, 1269–79.
39. Markworth AJ, 'On the volume-diffusion-controlled final-stage densification of a porous solid', *Scripta Met.*, 1972, **6**, 957–60.
40. Agrawal DD, 'Metal parts from microwaves', *Materials World*, 1999, **7**(11), 672–73.
41. Hodge ES, 'Elevated-temperature compaction of metals and ceramics by gas pressure', *Powder Metallurgy*, 1964, **7**(14), 168–201.
42. Fischmeister H, 'Isostatic hot compaction – a review', *Powder Metallurgy Int.*, 1978, **10**, 119–23.
43. Lyle JP Jr. and Cebulak WC, 'Fabrication of high strength aluminum products from powder', in *Powder Metallurgy for High-performance Applications*, Syracuse, Burke JJ and Weiss V, 1972, 231–54.
44. Bufferd AS, 'Complex superalloy shapes', *Powder metallurgy for high-performance applications*, Syracuse, Burke JJ and Weiss V, 1972, 303–16.
45. Aslund C, 'A new method for producing stainless steel seamless tubes from powder', *5th European symposium on powder metallurgy*, 1978, **1**, 278–83.
46. Groza JR, 'Field activated sintering', *ASM Handbook: Powder metallurgy technologies and applications*, 1998, **7**, 583–89.
47. Safari A, Danforth SC, Allahverdi M, Venkataraman N, 'Rapid prototyping', *Encyclopedia of Materials: Science and Technology*, 2001, 7991–03.
48. White D, 'Rapid prototyping processes', *Encyclopedia of Materials: Science and Technology*, 2001, 8003–09.
49. Kruth JP, Leu MC, Nakagawa T, 'Progress in additive manufacturing and rapid prototyping', *Annals of the CIRP*, 1999, **47**(2), 525–40.
50. www.dsmsomos.com

13.1 Introduction

Steel is the most popular metallic material and nearly 1,000 Mt of it was produced in 2003. This amount accounts for over 90% of annual total metals production in the world. Human life is greatly supported by steel due to its inherent advantages in production and properties compared with other materials. The production advantages include: (1) plentiful availability of raw materials (iron ore and steel scrap), reducing agents (coke and pulverized coal) and refining fluxes (mostly lime and dolomite), (2) high output rate per plant (10 Mt/year), and (3) relatively low total material demand (~ 5 t/t-steel) and ore reduction energy (22 GJ/t-steel). The advantages in properties encompass (1) high Young's modulus, (2) outstanding combination of high strength and ductility, and hence good formability, (3) good corrosion resistance on alloying, and (4) excellent magnetic properties. These properties have been significantly improved at competitive cost by alloying and controlling structure and texture, yet leaving more room for further improvement.

The production process and properties of steels have developed quite interactively as triggered by market demand. The key driver of the development in recent years has been, in many cases, market. In fact, assembly industries have required advanced steels with superior properties at shorter delivery times to produce better products at less cost for end users. The requirement has driven the steel industry to develop steels with improved or new properties. Such steels have prompted the emergence of new production processes in the steel industry. Conversely, the new steel production processes have sometimes unveiled avenues to produce more advanced steels with better properties at lower cost and/or better productivity. The advanced steels have prompted the assembly industry to refine their design and assembling process. Examples are plentiful and some representative ones will be discussed in this chapter.





13.1 Steel manufacturing processes from raw materials to semis (top) and semis to products (bottom) (courtesy of AISE Steel Foundation).¹

13.2 Developing processes and properties with reference to market, energy, and environment

An illustration of steel manufacturing processes is shown in Fig. 13.1,¹ the upper for upstream processing from raw materials to semis, and the lower for downstream processing from semis to products.

Major iron sources for steelmaking are hot metal and steel scrap. Hot metal is made in blast furnaces (BF) by reducing at high temperatures sintered or pelletized iron ore with CO gas, i.e., $\text{Fe}_2\text{O}_3 + 3\text{CO} \rightarrow 2\text{Fe} + 3\text{CO}_2$. CO gas is formed via the reaction of charged coke and hot blast blown into the blast furnace, i.e., $2\text{C} + \text{O}_2 \rightarrow 2\text{CO}$. Hot metal is saturated with C and contains some Si and impurity elements P arising from gangue in iron ore and S from coke. Hot metal is charged with steel scrap ($\leq 25\%$) into the basic oxygen furnace (BOF), desiliconized and decarburized by impinging pure oxygen gas jet from top lance and converted into steel. This is named the BF–BOF route. On the other hand, the majority of steel scrap, sometimes with a small fraction of hot metal and/or direct reduced iron (DRI), is charged into electric arc furnaces (EAF), melted and decarburized with injected oxygen gas and converted into steel. This is called the scrap–EAF route.

Decarburized and oxygen-bearing steel melt is tapped into a ladle with alloying elements and deoxidizing agents, Si-Mn, Fe-Si and/or Al, and then processed for final removal of H, S and deoxidation products, i.e. oxide inclusions like Al_2O_3 . The final removal and fine tuning of temperature and alloying element compositions for quality steels are done in various secondary refining furnaces (ladle furnace (LF) denoted Steel refining facility in Fig. 13.1). Refined melt is cast via tundish into the mold of a continuous casting machine (CCM), and withdrawn as semis. Semis are then reheated, hot rolled, pickled, cold rolled, heat treated, annealed and surface finished into products.

Major applications of steels are for construction, engineering works, automobile, ship, machinery, containers, etc. Automobiles consume a sizable fraction of total steel production. As the design, structure, manufacturing processes and fuel economy of automobiles advance, demands on steel materials have become more stringent and multifold, chasing extremes of properties at an affordable cost.

Recent moves to suppress global warming have emphasized the weight reduction of automobiles and hence thickness of steel for automobile parts. The thickness is to be determined by the strength and corrosion loss of steel sheet and the shape rigidity of steel parts. Strengthening steel helps reduce sheet thickness for auto body (panels, frame, reinforcements, members, pillars, side sills, seats, etc.) and traction system. However, strengthening must be made without impairing various formabilities (e.g. deep drawability, hole expansibility, stretch formability and bendability) that are specific to each part, and often inversely proportional to the strength. Thus, optimization of the balance between the

strength and formabilities has become a crucial issue for steels. More so for being challenged by competing materials, aluminum alloys and engineering plastics.

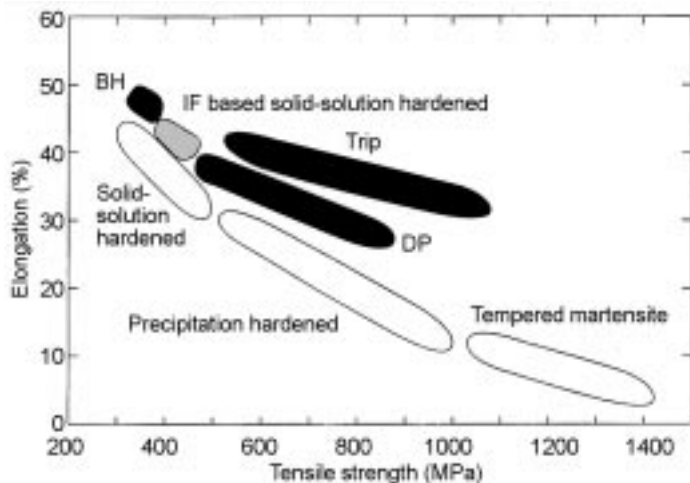
13.2.1 Properties driven by the market, environment and energy

Steels used in various parts of automobiles call for different properties depending on their applications, and hence best fit micro/nano-structure and texture have been developed for each part. Development has been in the following directions:

- Ultimate formability for exterior panels that are subject to transfer press forming (e.g. bake-hardenable, interstitial free steel (BH-IF)).
- Ultimate strength for seat frames and door impact beams (e.g. tempered martensitic steel).
- Intermediate but optimized strength and formability combination for various members and pillars (bainitic ferrite steel, dual-phase (DP) steel and transformation-induced plasticity (TRIP) steel).

These characteristics are shown on elongation-strength coordinates in Fig. 13.2.²

To meet the demands, innovative streamlining of the conventional sheet production process was mandatory for both upstream sectors of steelmaking/casting and downstream sectors of rolling/heat treatment. Exterior panels for door sides, engine hood, ceiling etc. are typical examples for which excellent formability and fine surface finish are of primary importance, since the panels determine the quality of autobody.



13.2 Elongation and strength of steels used for automobile (Komiya).²

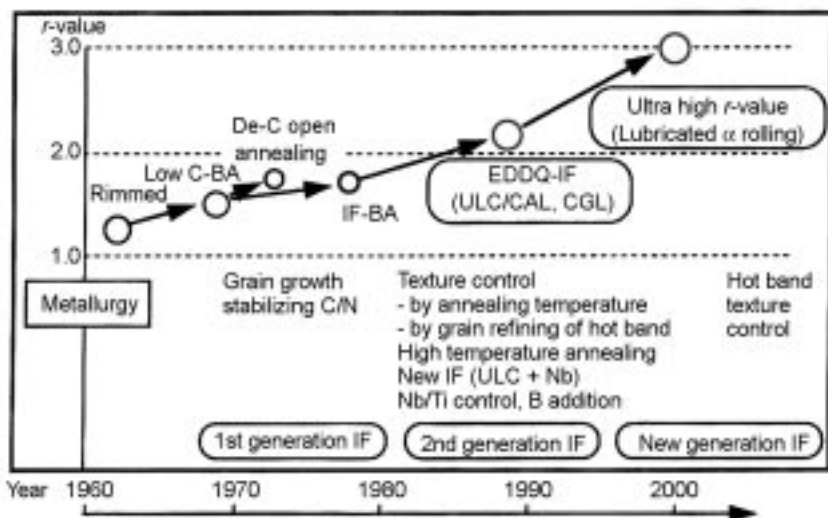
Among them, development of BH-IF steel is of particular interest in view of process vs product interaction. Process development for BH-IF steel includes preliminary removal of P and S in hot metal pretreatment and minimization of C, P, S and O in basic oxygen furnace blowing and secondary refining. It also includes heavy reduction in hot- and cold-rolling, high temperature continuous annealing and rapid cooling of cold rolled sheet to form fine grained <111//ND> texture (<111> axis of ferrite iron crystals aligned normal to rolling plane) for superior formability.

Properties required for BH-IF steel sheet

BH-IF steel for automobile body exterior panels is subject to press forming where deep drawability and stretch formability count most for the quality of the body. Deep drawability is expressed in terms of limiting drawing ratio (LDR), which is a ratio of the diameter of the blank before drawing to that of tube after drawing. LDR shows good correlation with plastic strain ratio (r) which is defined by a ratio of (the logarithmic ratio of sheet width before (w_i) to that after the deformation (w)) to (the logarithmic ratio of sheet thickness before (t_i) to that after the deformation (t)), i.e., $r = \ln(w/w_i)/\ln(t/t_i)$. Stretch formability is expressed in terms of limiting dome height (LDH) which is determined by uniform elongation (El) or work hardening coefficient. Good drawability securing sufficient metal flow without causing wrinkles is achieved at increased values of r and El .

Past development of steels for deep drawing application is shown in Fig. 13.3.³ For superior press formability, $r \geq 2.5$ and $El \geq 45\%$ are required that can be achieved when fine grained <111>//ND texture (called α -fiber) is developed in the matrix of steel sheet. For that, dissolved interstitial elements, C and N, are to be decreased and stabilized as precipitates of carbides and nitrides. An example of the chemical composition of such steel is C 20, Si 200, Mn 1500, P 100, S 30, Al 400, N 15, Ti 400 and Nb 150 all in mass ppm, for which $r \sim 2.5$, $El \sim 50\%$, yield strength (YS) ~ 140 MPa and tensile strength (TS) ~ 290 MPa have been materialized by controlling the texture and microstructure mentioned above.

These criteria were not met while decarburization of liquid steel below 0.04% (400 ppm) was impractical with BOF. Accordingly, box annealing (BA) of the low carbon Al-killed (LCAK) steel strip after hot rolling was practiced (low C-BA in Fig. 13.3) to reduce dissolved C, N and produce deep drawing quality (DDQ) steel. The BA makes N atoms precipitate as fine particles of aluminum nitride (AlN) to enhance the formation of <111>/ND texture. The BA also makes C atoms precipitate in coarse carbides and hence softens the steel matrix. Cooling after BA is slow due to the large thermal inertia of the process. Accordingly, only trace amounts of C remains as dissolved in the matrix, preventing age-hardening. However, BA is a very time- and energy-consuming,



13.3 History of the development of cold rolled deep drawing steel sheet (Obara and Sakata).³

costly process of low productivity. The heating/cooling rate has little allowance for control, limiting precipitation control. The values of r and EI thus achieved were about 1.6 and <50% and became inadequate to meet the increasing demands of press forming from automobile plants for more sophisticated shapes and better premium yield in the forming.

Thus, BA was replaced by continuous annealing (CA) of Al-killed (= Al-deoxidized) (AK) steel decarburized in the BOF to lower C to nearly 200 ppm (not shown in Fig. 13.3). The steel after cold rolling was heated to 800°C, rapidly quenched to 300°C, slightly reheated to 350°C, slow cooled to 300°C for over-aging and quenched. Insufficient decarburization was compensated for by the over-aging which served to decrease dissolved C and convert the resulting fine carbides into harmless coarse cementites. The decrease promoted grain growth and nucleation of <111>/ND recrystallization texture. This process could make steel with $r = 1.7$, while achieving bake hardening (BH) of about 40 MPa during paint baking, as a result of the anchoring of mobile dislocations by diffused C atoms that remained dissolved.

To solve the difficulty in decreasing C in BOF and downstream annealing, decarburization of liquid steel to 50 ppm C was made possible by implementing the Ruhr Stahl-Hausen (RH) vacuum degasser. The RH degasser circulates liquid steel in a ladle to a vacuum vessel where C and O in the liquid react to form CO that is removed in a vacuum (see the section on Process development to produce BH-1F SEDDOQ steel sheet, on page 512). Continuous annealing (CA) of the RH-degassed steel with Ti added to reduce dissolved C could make

an extra deep drawing quality (EDDQ) steel which exhibited $r = 1.9$. Yet the C concentration was still high, making the Ti addition too high for CA, calling for relatively long time high temperature annealing that was a heavy burden for CA line (CAL).

Accordingly, RH processing was further improved to produce an ultra low C (ULC) content in liquid steel of $C < 20$ ppm, followed by decreased and optimized addition of Ti and Nb to stabilize N and C, respectively. The ULC steel was hot rolled at a lower temperature with high reduction to make the grain size finer. Quick cooling of the hot coil was necessary to prevent the coarsening of crystal grains caused by such a low C content in hot coil. The hot rolled sheet was then pickled, cold rolled at heavy reduction, continuously annealed at a high temperature, and rapidly cooled to achieve intensive formation of fine grained $<111>/\text{ND}$ texture. This class of ULC-IF steel gives $r \sim 2.5$ and $EI > 50\%$, and is called super extra deep drawing quality (SEDDQ) steel. During the development of SEDDQ steel, it was recognized that impurity elements like P, S, and O need to be minimized. Metallurgical factors that have contributed to the advance of deep drawability are summarized in Table 13.1.

Recently, even better SEDDQ steel with $r = 3.0$ and $EI > 50\%$ has been developed with Ti and Nb added ULC-IF steel by incorporating lubricated rolling of the steel in the ferrite temperature range. The advantage of the ferrite

Table 13.1 Unit processes in an integrated system to produce BH-IF SEDDQ sheet

Unit process	Key operations and equipment
Steelmaking	<ul style="list-style-type: none"> • Removal of P and S by hot metal pretreatment • Decarburization by combined blowing BOF
Secondary refining	<ul style="list-style-type: none"> • Final decarb. C, $\text{N} < 20$ ppm, deoxidation by Al with Ti and/or Nb addition, alumina inclusion removal, fine tuning of Al, Ti and/or Nb, all by RH
Casting	<ul style="list-style-type: none"> • Melt transfer with special care to prevent the occurrence of macro inclusions caused by air reoxidation and slag entrainment • Continuous casting into slab with electromagnetic flow control in mold to avoid subsurface engulfment of inclusions and Ar bubbles
Hot rolling	<ul style="list-style-type: none"> • Roughing of low temperature heated slab into sheet bar • Rolling of sheet bar to strip by tandem mill with heavy reduction at final stand, finishing just above Ar_3 temperature (Continuous lubricated ferrite rolling)
Cold rolling	<ul style="list-style-type: none"> • Rapid cooling of strip on run-out table
Annealing	<ul style="list-style-type: none"> • Heavy reduction rolling of hot strip by tandem mill • Continuous annealing at high temperature followed by rapid cooling by CAL
Galvanizing	<ul style="list-style-type: none"> • Continuous hot dip galvanizing by CGL (with galvannealing), or • Continuous electrolytic galvanizing by EGL

rolling to achieve better drawability was reported earlier,⁴ but its industrialization has been made possible by the development of continuous hot rolling technology. Slabs are hot rolled to sheet bars that are coiled, stored in a thermally insulated box, paid off and welded hot, one after another on the fly, enabling whole length of the welded sheet bars to be low-temperature hot rolled in the ferrite temperature range under set tension with lubrication.⁵ Without the lubrication, considerable strain occurs in the surface layer of hot strip during rolling. The strain prevents uniform formation of <111>/ND texture in thickness direction during subsequent processing which is similar to that for SEDDQ.

The SEDDQ sheet is so soft that it cannot resist denting that may occur when dynamic pressure is locally applied during the use of the automobile. To prevent denting, BH has been employed. Baking (170°C) for curing polymer coatings on white body makes dissolved C atoms (a few mass ppm) diffuse and anchor the dislocations, giving a rise in YS of about 40 MPa. This has made BH-IF SEDDQ steel a functional material which is very soft (YS *circa* 240 MPa) for press forming without causing surface strain (wrinkles), while stiffening on baking to YS 280 MPa.

Another recent move is to increase the strength of SEDDQ sheet to meet ever increasing demands for weight reduction. SEDDQ sheet was solid solution hardened to a tensile strength (TS) of about 390–440 MPa by the addition of (largely) Mn and some P and Si, in this order. However, the quality of sheet surface and adhesion of Zn-alloy coating to the sheet on hot dipping were not ideal for press forming due to Mn, P and Si. These problems have been solved by a new species of grain refined (ASTM No. 11) and precipitation hardened SEDDQ sheet that utilizes C, increased threefold to 60 ppm, and Nb added in excess of atomic equivalent of C+N to let NbC and Nb(C,N) precipitate be finely dispersed. In the new species of SEDDQ, Si and P have been decreased, resulting in a smooth surface, good coating adhesion, and YS 290, TS 440 MPa, $r = 1.9$ and $El = 37\%$. Development of <111>/ND texture and a precipitate-free-zone at grain boundaries contribute to the high values of r and El at this TS level.⁶ This way, market- and energy-driven developments of properties have contributed to the progress of the manufacturing processes that will be mentioned in the following sections in more detail.

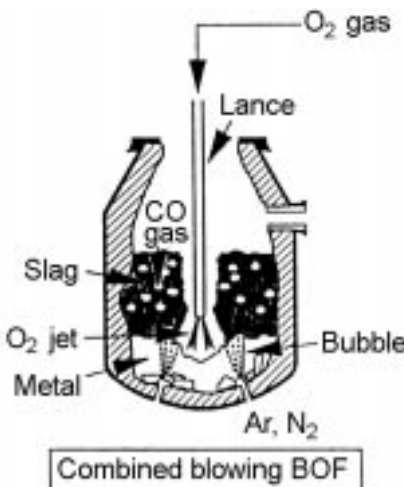
Process development to produce BH-IF SEDDQ steel sheet

A large amount of pretreated hot metal is utilized as iron source for BH-IF SEDDQ steel to minimize P, S, N and tramp elements that are known to adversely affect r and El . BOFs, that are usually employed to make steel melt from hot metal and scrap under atmospheric pressure, are able to decarburize the melt only to 300–400 ppm for economic reasons. Further decarburization causes excessive oxidation loss of iron into slag and corrosion of vessel refractory, even when melt bath stirring is done well with bottom injection of inert gas to

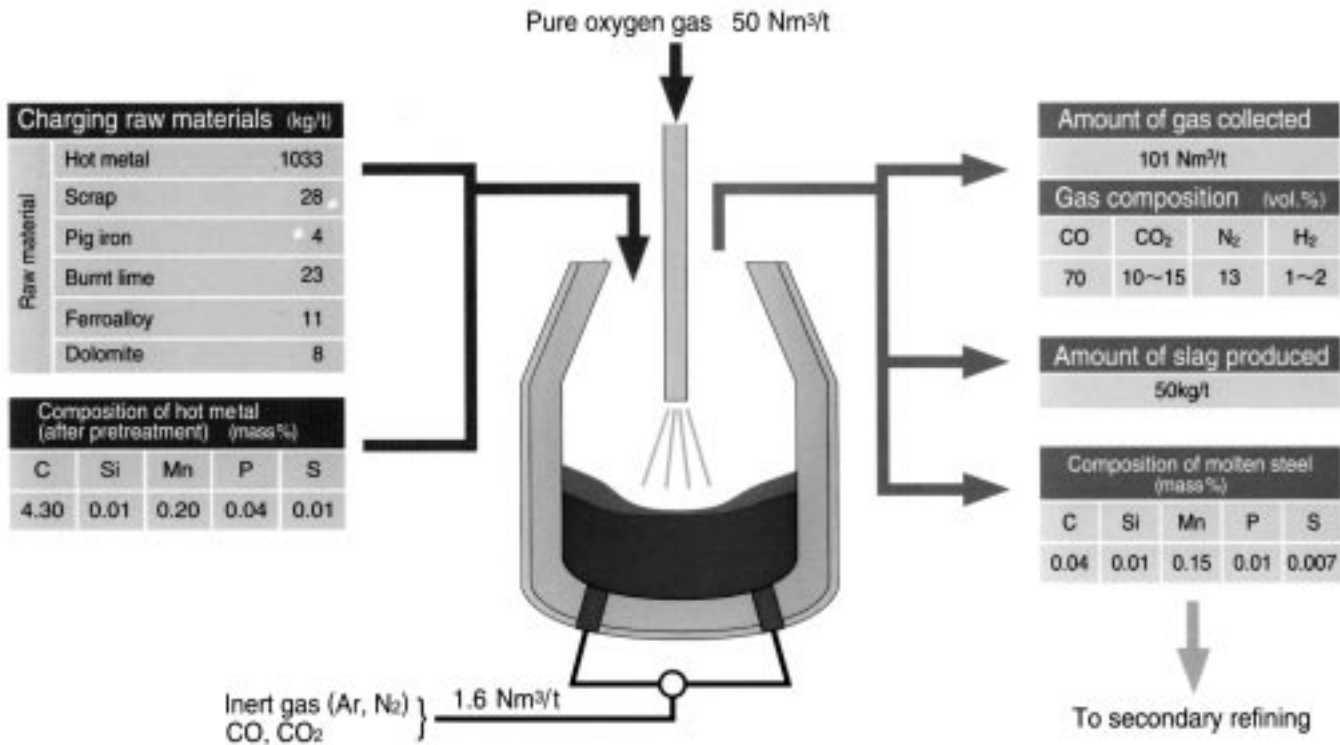
enhance mass transfer of C for decarburization. A typical operation and mass balance of BOF with bottom gas injection are shown in Fig. 13.4⁷ for pretreated hot metal (Si, P and S are fully or partly removed beforehand).

To promote decarburization reaction, $[C] + [O] = CO(g)$, to reduce C < 20 ppm, the exposure of steel melt to vacuum is required. The RH process shown in Fig. 13.5 circulates steel melt from the ladle through an up-snorkel into the vacuum vessel by air lift pump action of Ar injected into the up-snorkel, and back into the ladle through a down-snorkel, continually exposing the melt to a vacuum in the vessel. Detailed analysis of plant data has revealed that the following elements are the key to achieve extra-low C (< 20 ppm) at high productivity (600 t/hr) suited for producing BH-IF steel melt: (a) a high vacuum in the vessel, (b) a high rate of Ar gas injection into the up-snorkel, (c) large diameters of the up- and down-snorkels and vacuum vessel, and (d) proper melt bath depth in the vessel. These factors contribute to increase the rates of circulation and homogenization of the melt in the system, and hence increase the decarburization rate and decrease final C. Injection of oxygen gas through the top lance onto the melt surface in the RH vessel has often been practiced. It increases the decarburization rate in the early period of processing, making the BOF melt containing higher C negotiable by RH within a given cycle time. Steel splash sticking on the vessel wall is decreased by the injection, and hence productivity of the BOF-RH system increases at decreased oxidation loss of iron into BOF slag.

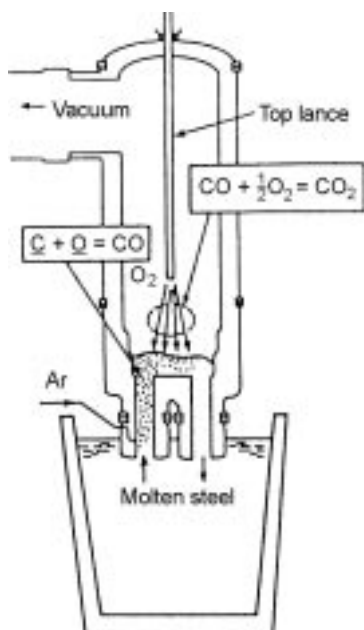
The melt is then deoxidized by the addition of Al in the RH vessel. The deoxidation products, mostly Al_2O_3 particles, formed in the melt are decreased by the circulation-stirring which enhances collision, agglomeration and flotation to the melt surface and dissolution into the top slag of the particles. The cleansed



13.4 Typical BOF operation for blowing pretreated hot metal to low carbon steel.⁷



13.4. Continued

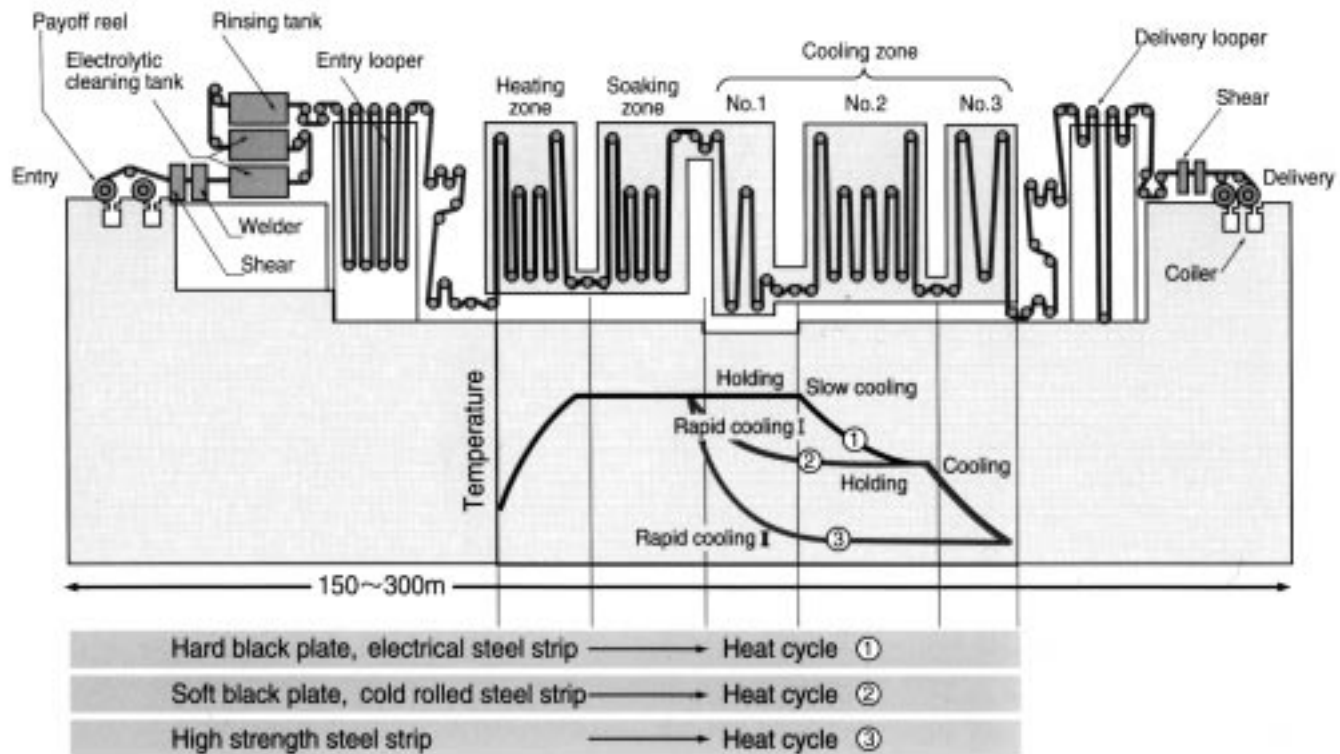


13.5 RH process for reducing H, C and O in steel by circulating steel melt from ladle to vacuum vessel.

melt is transferred from the ladle via tundish into the CC mold and cast into slabs. Insufficient removal of Al_2O_3 causes Al_2O_3 clusters that are entrapped in the slabs, resulting in surface defects on rolled and annealed sheet products from the slabs. Slabs are then processed to facilitate the formation of fine grained <111>/ND texture, as mentioned earlier.

Success in decarburizing steel melt to ultra low C by RH processing removed the heavy burden of decarburization by batch annealing (BA) of cold rolled coil. The IF steel strip can be annealed continuously at high speed by CAL for microstructure and texture control without any additional decarburization. The problems to be overcome in developing CAL were (a) high speed delivery of the strip through all rolls without causing meandering, and (b) high temperature annealing of the strip without causing strip breaks under applied tension. As partly shown in Fig. 13.6,⁷ CAL offers a wide process window for heating rate, soaking temperature, and cooling rate. The window enables a variety of microstructure/textural control which was not possible with BA, where the rates of heating and cooling were uncontrollable and the maximum heating temperature was lower than CAL. Thus, flexible manufacturing of diverse grades of steels has become possible with CAL. The annealed strip is coated either by hot dipping or electrolytic plating of Zn to form the final product.

BH-IF SEDDQ sheet is a typical case of market- and energy-driven property development. However, the property has been significantly advanced by the



13.6 Continuous annealing line (CAL) with some example of operating windows (Morita and Emi).⁷

process development. Thus, property and process are closely interlinked for mutual progress. The integrated manufacturing system of BH-IF SEDDQ steel sheet consists of unit processes listed in Table 13.1.

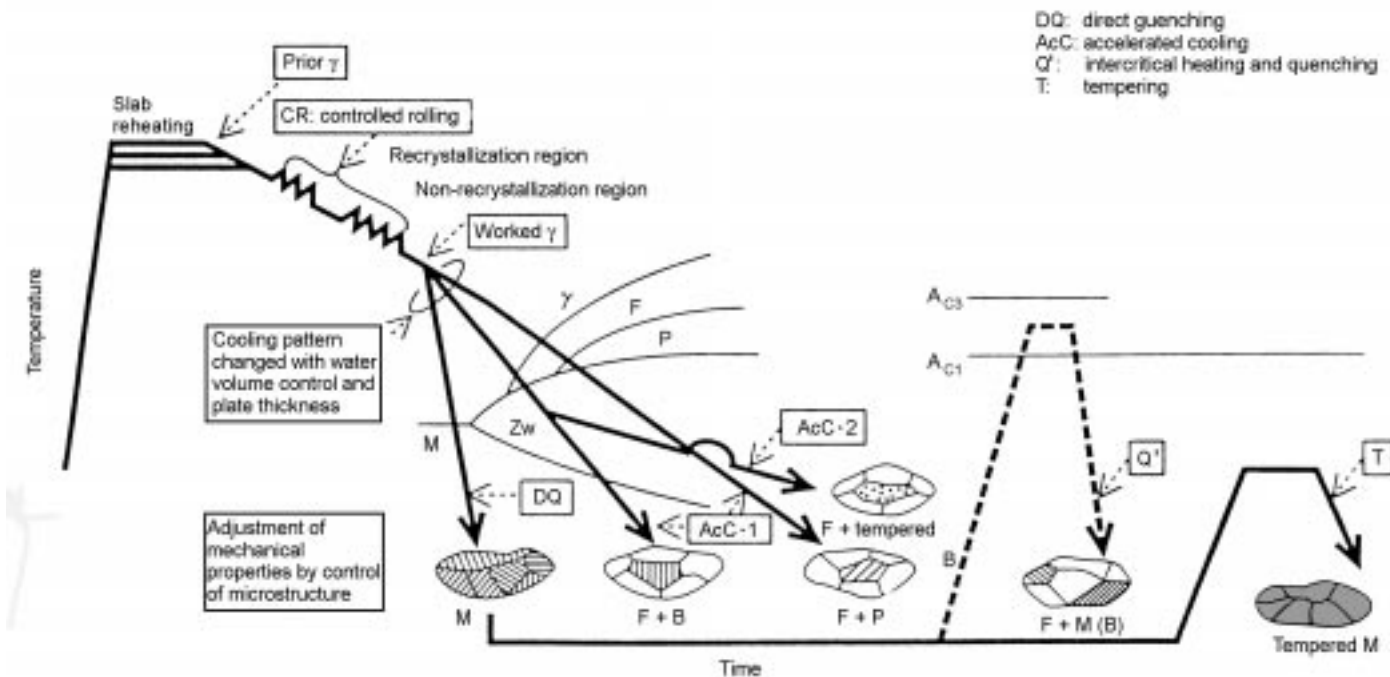
13.2.2 Processes driven by properties, environment and energy

Piping for gas transmission is usually produced in large tonnage, since pipelines need to transmit a large volume of gas over a long distance from well site to shipping port. High strength low alloy steel (HSLA) plate has been utilized for making the pipe. HSLA contains C, Mn, Cu, Ni and Cr each in a small amount depending on the mechanical and corrosion properties required. Also, some microalloying elements, Ti, Nb, V and/or Mo are commonly utilized. The plate is press formed into a U-channel, further pressed into an O-tube, and the seam is submerged arc welded in length direction, and finished into pipe. This is called UO pipe.

UO pipeline passing through Northern areas (e.g. the Trans-Alaska Pipeline System, TAPS) demands superior low temperature ductility for security reasons. Such ductility can be achieved by fine grain matrix of ferrite, α , that is obtained by recrystallizing fine grains of austenite, γ . Fine α grains of diameter d increase TS or decrease the fracture appearance transition temperature (FATT), according to the Hall–Petch relation or Cottrell–Petch relation, each predicting that YS/TS or FATT is positively or negatively proportional to $(d)^{-0.5}$.

Formerly, the grain refining was carried out by normalizing, i.e. heating hot rolled HSLA plate just above Ar_3 transformation temperature to form fine γ grains, and air cooling the plate to let the fine γ grains be transformed into fine ferrite and pearlite. The normalizing process is, however, costly and low in productivity. Elimination of the normalizing was trialed, and the thermo-mechanical control rolling process (TMCP), later followed by accelerated cooling, AcC, has been successfully industrialized.⁸ The success was due to lasting development efforts, progress of most modern plate rolling mills, online cooling facilities and advanced rolling and cooling schedules, combined with the use of the microalloying elements in HSLA steels.

TMCP utilizes low temperature hot rolling of γ grains near Ar_3 temperature to form fine recrystallized γ grains and non-recrystallized deformed γ grains as shown in Fig. 13.7.⁹ The deformed γ grains contribute more to refining α grains by providing a greater specific boundary area for the nucleation of an increased number of α grains. In addition, the deformed γ grains contain deformation bands within a grain that also serve as nucleation sites for α grains. Intensive AcC after rolling generates intra-grain transformation nuclei that contribute to refine α grains as well. The AcC converts pearlite (forming on air-cooling) into finely dispersed bainite that increases strength without impairing ductility (see AcC1 in Fig. 13.7). When the AcC is interrupted and taken over by air cooling



13.7 Thermomechanical control process with accelerated cooling for microstructure control of steel during hot rolling (γ : austenite, F: ferrite, P: pearlite, B: bainite, M: martensite), (Oosawa).⁹

(interrupted accelerated cooling, IAC), the bainite becomes tempered bainite (see AcC2 in Fig. 13.7). Strengthening by IAC includes refining of α grains and increase in precipitation hardening that make YS higher, and increase in volume fraction of bainite that increases TS.

Microalloying of Nb, Ti and V forms very fine precipitates of Nb (C N), TiN and VN that keep γ grains fine on reheating owing to their grain boundary pinning effect. Grain growth of recrystallized γ is inhibited particularly by the fine precipitates of TiN. Also, Nb and Ti dissolved in the γ matrix suppress recrystallization on deformation, and increase $A_{\text{r}3}$ in excess of 100K. This makes the advantages of TMCP available at higher temperatures. Also, Nb, Ti and V dissolved in γ matrix precipitate as fine carbonitride, carbide and nitride, respectively, during and/or after $\gamma \rightarrow \alpha$ transformation, and increase the strength of α matrix. In IAC, addition of Nb, Ti and V increases the quench sensitivity and volume fraction of bainite, and hence strength.

The pipe is connected by girth welding in the open field without pre- and post-heat treatment of the weld to save labor and cost. At such a weld, coarsening of grains in the heat affected zone (HAZ) occurs to impair low temperature ductility and strength, particularly for higher strength pipe grades. Usually, C increases strength but decreases both weldability and low temperature ductility. To assure low temperature ductility of the seam- and girth-weld, B-containing, low alloy steels bearing only low- to extra low-C have been developed for higher strength variants. Loss of strength by decreasing C has been compensated for by (a) further refining α grains with fine TiN precipitates, (b) hardening with Nb(CN) precipitates and (c) making texture converted from ferrite–pearlite to bainite with the addition of B. If C content is high, B is consumed as $\text{Fe}_{23}(\text{CB})_6$ which precipitates both at the boundaries and in the matrix of γ grains, and hence cannot serve to form bainite. Decreasing C to less than 0.04% by vacuum degassing of HSLA melt and combining excess C with Nb and Ti as NbC and TiC prevent the formation of $\text{Fe}_{23}(\text{CB})_6$.

API5LX-X60 and X65 UO pipe thus produced have found popular application to gas/oil transmission for their reliability and good balance between strength, low temperature ductility and weldability. However, higher tensile grades, up to API5LX-X80, are required to reduce total cost, and hence have found increasing use but yet in a limited amount. Recently, even API5LX-X100 (YS~700, TS~800 MPa) has been commercially utilized to cover some pipeline in Canada. For such high strength grades, TMCP-AcC, shown in Fig. 13.7, has been applied. The fine ferrite + bainite structure is preferred for low FATT values, and minimization of inclusions and precipitates are attempted for securing ductility. An example of the chemistry for X100 is C 0.06, Si 0.1, Mn 1.8, Nb 0.04, Ti 0.01, Mo 0.2% and some Cu and Ni. To assure ductility of the coarse grained heat affected zone (HAZ), control of Ti and N for γ refinement, utilization of TiO_2 for fine nucleation of α , and reduction of Si, Al and C-equivalent with B addition have been made.

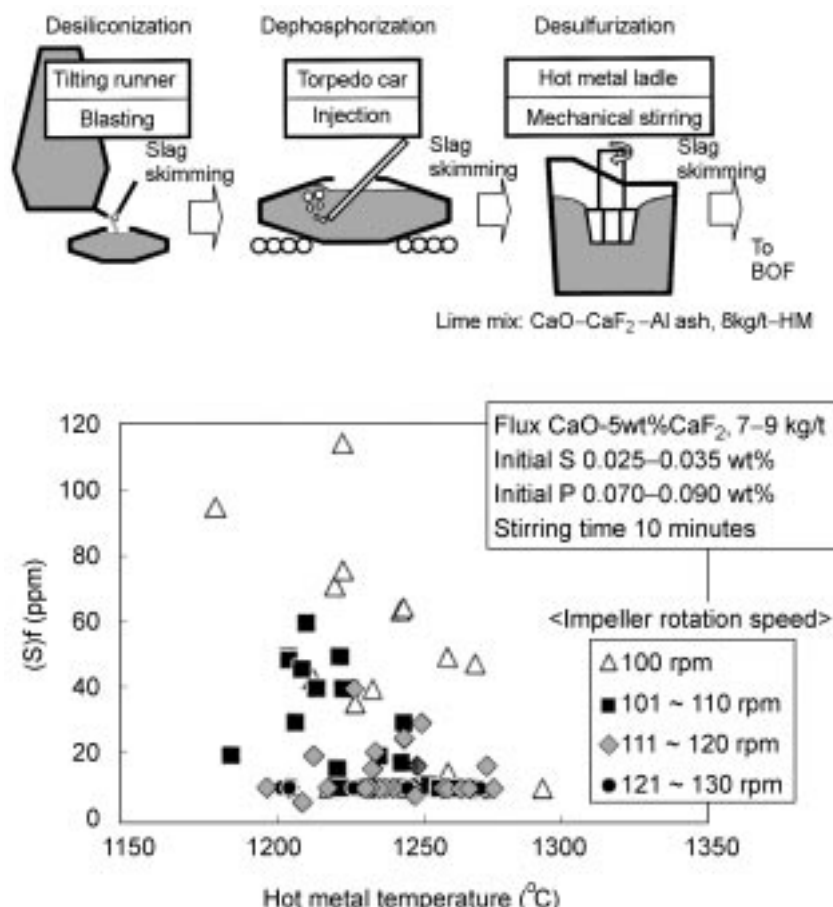
Gas and oil that contain H₂S (sour gas and oil) have been increasing in their production. H₂S reacts with moisture in pipes, forms H₂SO₄ which reacts with the inner surface of the pipe wall to form active hydrogen atoms. When desulfurization of steel melt is inadequate, MnS precipitates in steel slab during solidification. Deformability of the MnS precipitates relative to the steel matrix is high at plate rolling temperatures, and hence during cross-rolling they turn into thin, two-dimensional shape inclusions with sharp periphery in the plate. The hydrogen atoms diffuse into the pipe wall, and some of them recombine at the incoherent interface of MnS precipitates and steel matrix to form H₂ molecules, causing decohesion of the interface.

Stress arising from the increasing pressure of the recombined H₂ gas concentrates at the sharp peripheral edge of the deformed thin MnS where the steel matrix has been made brittle by accumulated atomic hydrogen. Cracks initiate there and propagate into the steel matrix around the periphery. If the number density (number per unit volume) of the elongated MnS precipitates is high, the crack connects the precipitates stepwise in the thickness direction of the pipe wall, finally causing a burst of gas/oil through the cracked pipe wall. This is called hydrogen induced cracking (HIC). It is not only S but also C and P in steel melt that can cause HIC. Both C and P segregate in the center-thickness of the CC slab and hence the plate during rolling, forming hard and brittle pearlite banding or martensite, causing brittle fracture there when extra stress is applied by the recombined hydrogen gas. The through-thickness crack can propagate in the length direction of the pipe over 10 m before the gas is decompressed during bursting. The burst can ignite the gas, causing fire and disaster in the area.

Measures that have been established to prevent the occurrence of HIC, and process developments to execute these measures are given in Table 13.2. Most

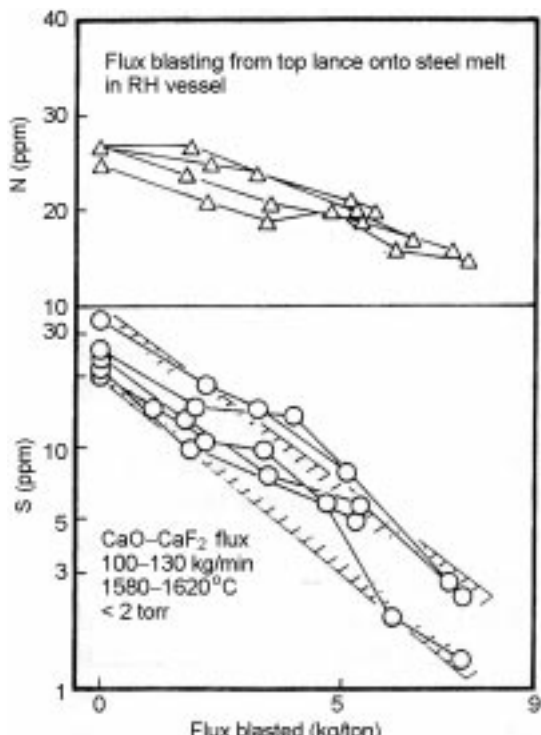
Table 13.2 Measures and processes to prevent the occurrence of HIC in API5LX-X60/65 pipeline for sour gas/oil transmission

Preventive measures	Process to execute the measures
1 Make C low or extra low	• Decarburization by BOF supplemented by RH
2 Minimize H, P, S (extra low), oxide inclusions	• HMPT followed by LF + RH refining
3 Convert S dissolved in melt into CaS	• Ca addition to steel melt in ladle/tundish
4 Minimize center- and grain boundary-segregation of C, P and S in slab	• Low superheat casting and electromagnetic flow control in mold to increase equiaxed crystal in pool end of CC-slab. • Electromagnetic stirring and soft reduction at pool end to disperse solute enriched melt in the boundaries of equiaxed crystals
5 Fine grain bainite structure with dispersed fine precipitates	• TMCP and Acc of low C or extra low C HSLA steel added with microalloying elements (Ti, Nb, Mo, V, B)



13.8 Desulfurization of hot metal with CaO-CaF₂ flux by impeller stirring (Ogawa *et al.*).¹⁰

important among them are (a) to desulfurize steel melt to extra low concentrations (single ppm range) by HMPT and RH/LF (or LF only) with a flux high in CaO (often CaO+CaF₂ for prompt melting) and (b) add Ca (often in Fe-clad wire) to the desulfurized melt to convert remaining dissolved S into solid CaS particles that do not deform in subsequent hot rolling. An example of HMPT to desulfurize hot metal to 10 ppm by mixing hot metal with CaO+CaF₂ flux with a mechanical stirrer in the hot metal transfer ladle is shown in Fig. 13.8.¹⁰ Another example of top injection of similar flux onto melt in RH vessel to desulfurize steel to < 5 ppm is shown in Fig. 13.9.¹¹ CaS particles formed are largely removed during the HMPT or RH processing. Center segregation of C and P that occurs during CC is reduced in two ways. One is to disperse solute enriched melt into the boundary area of sediment equiaxed dendrite crystals



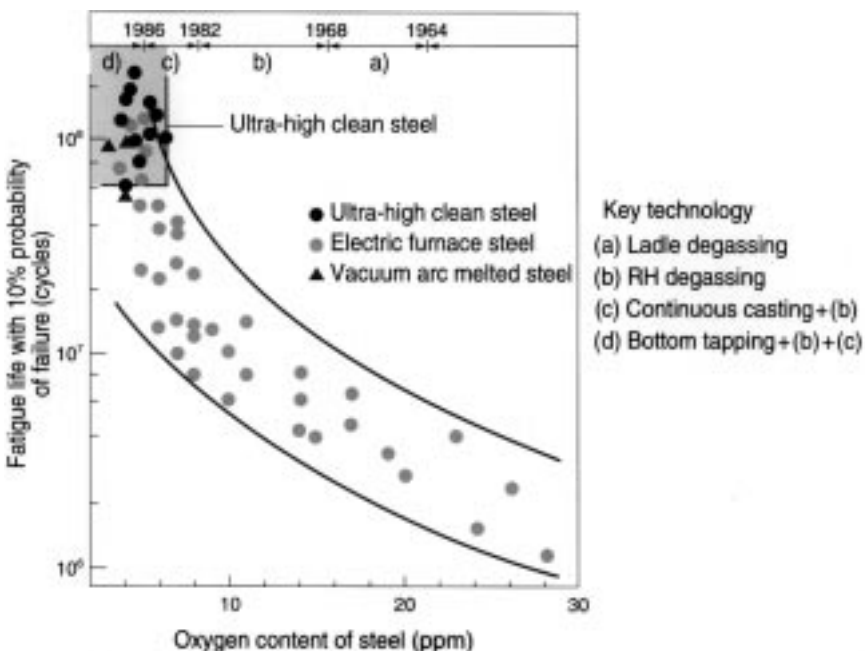
13.9 Desulfurization of steel in RH vessel with CaO-CaF₂ flux blasting through top lance (Okada *et al.*).¹¹

where the solutes are less segregated. The other is to prevent inflow of solute enriched interdendritic melt into the thin melt pool end of CC slab. The former can be done by a combination of low superheat casting and electromagnetic melt flow control in the mold that increases nucleation, growth and sedimentation of equiaxed crystals. The latter is practiced by soft reduction of the pool end with supporting roll pairs to prevent shrinkage-driven flow that is caused by solidification. Also, the decreased C-equivalent mentioned above effectively reduced the formation of the hard and brittle segregate zone.

In the pipeline case, the required properties demanded process developments in steelmaking, casting, rolling and heat treatment that in turn have made the production of HIC resistant pipe interactively possible up to X65 grade (X100 in the near future).

13.2.3 Properties driven by processes

The ball bearing is one of the most important parts for rotating machines including hard disc drives of PCs and engine and traction systems of automobiles. Resistance to wear and fatigue cracking on rolling contact must



13.10 Improvement of fatigue life of ball bearing with decreasing oxide inclusion content by process development of steelmaking and casting (Uesugi).¹²

be very high to assure durability of the machines, and hence surface hardness of the bearing must be high with ductile interiors. Accordingly, high carbon ($\sim 1\%$ C) Al deoxidized steel with Cr has been used. As shown in Fig. 13.10,¹² fatigue limit expressed in terms of 10% failure life, B_{10} , of typical ball bearings was of the order of 10^6 rotation under a given test condition. Here, the bearing was made of steel containing about 30 ppm of O that was mostly in the form of oxide inclusions. The root cause of the failure was identified to be large indigenous and exogenous oxide inclusions occurring during deoxidation and casting of steel melt. The critical size of the large inclusions was roughly $30 \mu\text{m}$ but it has become smaller, $< 15 \mu\text{m}$, as demands on fatigue life get more stringent. It may be smaller in future.

To reduce the harm of the inclusions, ladle degassing was introduced which effectively reduced total oxygen content, $[O]_t$ (sum of dissolved [O] in the melt and O in the deoxidation product, Al_2O_3 , suspending in the melt), in the high carbon melt to 15 ppm. Later, RH process for more effective deoxidation under vacuum has been implemented to make $[O]_t$ a low 8.3 ppm. The decrease of $[O]_t$ by ladle degassing and RH processing contributed greatly to reduce macro inclusions. They were formed by the collision and agglomeration of fine Al_2O_3 inclusions suspended in the melt during melt transfer, but not removed from the

melt. In addition, variation in the amount of exogenous macro inclusions occurring from reoxidation by air and slag entrainment, and formation of macro inclusion during solidification were much reduced by implementing continuous casting (CC). As a result, $[O]_t$ decreased to less than 6 ppm. Further implementation of bottom tapping (EBT) of EAF steel melt has effectively reduced macro inclusions arising from the reoxidation of the melt by oxidizing EAF slag and emulsification of the slag into the melt in the ladle. It is to be noted that the macro inclusions are detrimental to fatigue life but their number density is so small, and hence cannot be detected by total O analysis.

Later investigation on the critical size of inclusions that influences fatigue life has revealed that not only oxide inclusions but also Ti(C, N) inclusions, both in excess of $15\ \mu\text{m}$ in size as mentioned before, are harmful. Accordingly, thorough measures have been taken to minimize the number density of the two inclusions larger than the critical size by attending to every possible source of O and Ti. The sources of O were the reoxidation of Al-deoxidized melt by ladle refractory, ladle glaze, air and oxidizing slag and entrainment of slag during melt transfer into the CC-mold. The sources of Ti were inputs from ferroalloys added to the melt ($> 15\ \text{ppm}$). These measures reduced O and Ti to 3.8 ppm and $\sim 5\ \text{ppm}$ by 1996.

It must be noted that such a low total O only does not guarantee the absence of inclusions larger than the critical size, since they occur by chance. However, measures that consistently achieve total O of less than 4 ppm are more likely to assure fewer number densities of such macro oxide inclusions. As a consequence, the fatigue life has now exceeded 10^8 rotations, almost two orders of magnitude of fatigue life prolongation. A recent concern is to reduce the formation of large, hard octagonal spinel inclusions ($\text{MgO}\cdot\text{Al}_2\text{O}_3$). They probably arise from the reaction between the suspending deoxidation product, Al_2O_3 , and Mg produced by the reduction of MgO in slag and refractory by Al in the melt during intensive refining by stirring of the melt to remove the Al_2O_3 inclusions.

13.3 Optimization of processes to meet properties and productivity

To make steel, either the BF–BOF or scrap–EAF route combined with secondary refining and casting processes is utilized. Function and characteristics of these processes are summarized in Table 13.3 (see also Fig. 13.5). Depending on the requirements specific to each grade of steel, one or two-in-series of the secondary refining processes are chosen to bridge the primary steelmaking process, BOF or EAF to CC. Investment, productivity, availability of iron sources, cost of operation and versatility of operation to cover various steel grades, all determine the choice. Matching of the production rate and cycle time of processing among the BOF, EAF, secondary refining process and CC should be made consistent.

Table 13.3 Function of secondary refining processes to reduce impurity elements and inclusions, add alloys and control temperature

Process	H	C	N	O	S	P	Alloy	Temp	Other features
RH	S	S		S			Y		High speed mass processing
RH-KTB	S	SS	W	S	M		Y	W	RH with O ₂ top blow
RH-PB	S	SS	W	S	M		Y	W	RH with flux side blow
RH-PI	S	SS	W	S	S		Y	W	RH with flux top blow
ASEA-SKF	S			S	SS		Y + Red	S	Magnetic stirring + arc heating
LF	S			S	SS		Y + Red	S	Ar stirring + arc heating
AOD	S	S		S	S		Y + Red	S	Ar+O ₂ side blow, stainless
VAD	S			S			Y + Red	S	Ar bottom bubbling in vacuum
VOD	S	S	M	S			Y + Red		Same as above + O ₂ top blow
TN				M	S				Ca injection sulfide control
CAS				M	M		Y		Ar bottom bubbling + top slag
CAS-OB		W		M	M		Y	W	Same as above + O ₂ top blow
HMPT				S	S				See text

Note: Effectiveness of impurity removal or temperature control is qualitatively shown by SS (super strong removal to single ppm range), S (strong), M (modest) or W (weak). For alloying capability, Y (yes) and Y + Red (yes and reduction of alloy metal oxide possible)

13.3.1 Processes to optimize impurities and alloying elements

Typical impurities found in steel are H, N, O (including oxide inclusions) P, S, non-volatile tramp elements (Cu, Cr, Ni and Sn), and in some cases volatile tramp elements (Zn, Pb, Sb and As). The impurities occur from hot metal (P, S), scrap (P, S and tramp elements), ambient air (H, N and O) and refractory (O), and adversely influence steel properties and may cause process upsets. The impurities need to be removed below a critical concentration which is specific to a steel grade as roughly shown in Table 13.4. It depends often on subsequent processing to semis or final products. To minimize the cost of removing the impurities, the concentration of the impurities should be set somewhat lower (with tolerance given for concentration variation occurring from process fluctuation and segregation) but not excessively lower than the critical one for cost reasons. The tolerance depends much on the process itself and operational skill.

In the past, a combination of BOF or EAF with secondary refining was adequate to remove the impurities to fulfill properties requirements. BOF or EAF removed most of P and part of S into basic CaO-MgO-SiO₂-Fe_tO slag as 3CaO·P₂O₅ and CaS, and secondary refining removed the remainder of S. As the properties requirements increased, P and S had to be further reduced. Process optimization has been made first by improving secondary refining, and second by adding HMPT for desulfurization to achieve lower S at a reasonable cost. So

Table 13.4 Tolerable maximum inclusion sizes and impurity elements contents in high performance steels

Application	Key property	Critical inclusion size (μm)	Critical impurity content (ppm)
DI-can sheet	Flange crack	<40	
SEDDQ sheet	Average $r > 2.0$		C < 20, N < 30
Shadow mask	Blur in etching	<5	Low S
Lead frame	Punch crack	<5	
Sour gas pipe	HIC	Shape control	S < 5
LNG plate	Embrittlement		P < 30, S < 10
Lamellar tear	Z-crack	Shape control	ibid.
Bearing, race	Rolling fatigue	<10	O < 10, Ti < 15
Case hardening	Fatigue crack	<15	O < 15, Ti < 50
Tire cord	Rupture	Shape control < 20	Al < 10
Spring wire	Fatigue	Shape control < 20	ibid.

far, optimization has been proceeding toward splitting the original refining function of the BOF into HMPT and secondary refining, leaving the BOF as a decarburizer.

In Japan, BOFs operate at a higher hot metal ratio (roughly 90%) than in USA and Europe (~75%) owing to sufficient BF capacity with its cost efficient operation. HMPT for both dephosphorization and desulfurization has been extensively developed and industrialized in most of integrated steel plants at very high availability due to favorable thermal balance with the higher hot metal operation. In fact, some plants are processing near 100% of hot metal by the HMPT, making it possible to take advantages listed in Table 13.5. Strong demands for steels extra low in P and S are behind the choice of this type of HMPT which could as well be the case in industrially advanced countries in future if demands for extra low P steels increase.

HMPT in this case is carried out in the following sequence: the desiliconizing fluxes are blasted to hot metal with O_2 in the BF runner or tilting tundish which distributes hot metal into transfer ladles. Low Si (~0.3%) operation of the BF, followed by desiliconization to ~0.1%Si of hot metal during tapping into the transfer ladle is preferred to realize the above-mentioned advantages. The desulfurizing fluxes are either injected with N_2 into or mixed with hot metal by mechanical- or gas-stirring in the hot metal transfer/charging vessels. The dephosphorizing fluxes are mostly injected into the hot metal transfer vessels (torpedo- or ladle-type) with O_2 , with some top addition. Either pre-mixed or post-mixed fluxes are used, but post-mixing seems to have advantages in terms of cost and dynamic control of the process. For more efficient refining with less slag, many efforts have been paid to find fluxes with

Table 13.5 Advantages and disadvantages of HMPT process

Advantages	Disadvantages
1 Reduce BOF slag to a minimum	• Advanced sintering and BF iron making techniques required to get low Si hot metal consistently
2 Reduce eruption of slag and metal to near zero	• Hot metal de-Si required
3 Reduce iron loss in BOF slag	• Occurrence of HMPT slag
4 Reduce BOF blow time, increase productivity	• Decreased use of scrap for BOF
5 Increase hit rate at blow end of aim C and temperature	
6 Increase Mn yield from Mn ore added in BOF	
7 Reduce P, S to much lower concentrations with hot metal low in Si	

greater sulfide and phosphate capacities. After more than a decade of industrial campaign, the compositions of the fluxes seem to have converged into those given in Table 13.6 mostly for cost reasons. To promote flux utilization for removing P and S and minimizing heat loss, enhanced contact between the fluxes and hot metal has been worked out in various designs of injection device and vessel shape.

Utilization of a spare BOF for HMPT, where surplus BOF capacity exists, is getting popular. The BOF provides (a) better slag–metal mixing without using

Table 13.6 Characteristic operating parameters of HMPT process

Objective	Reactor	Flux addition	Flux composition
1 Desiliconization	BF runner Tilting tundish Transfer ladle	Blasting with O ₂ ibid.	Ore/sinter ibid.
2 Desulfurization	Transfer ladle	Injection with N ₂ Addition and Mechanical stirring	Lime + Mg, or Lime + CaF ₂ /soda ash ibid.
3 Dephosphorization and desulfurization	Torpedo Transfer ladle Torpedo Spare BOF	Injection with N ₂ Injection with O ₂ ibid. Addition and O ₂ top blowing	ibid. Lime + sinter/scale + CaF ₂ /soda ash ibid. Lime + ore/sinter/ scale, partly recycled

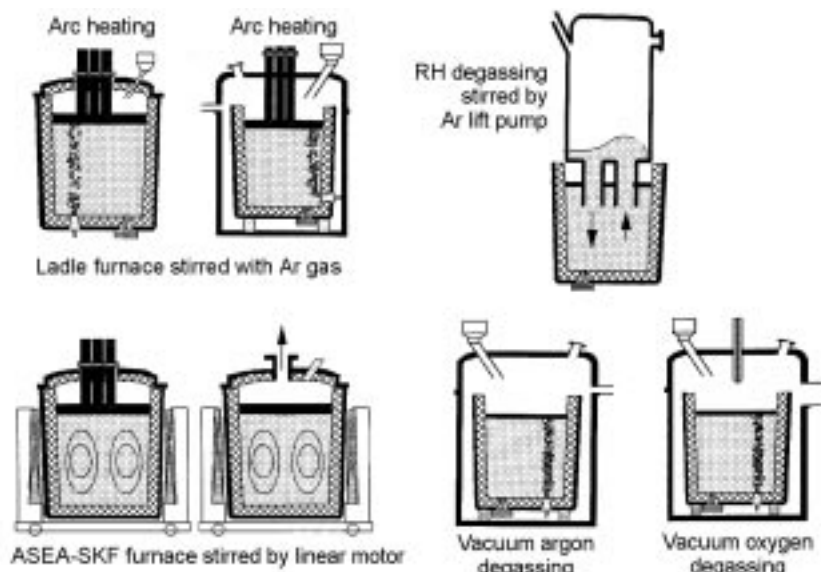
Note: Use of CaF₂ and soda ash as fluxing reagent is limited to its minimum for environmental aspect

environmentally unfavorable CaF_2 for fluxing CaO and (b) decreased heat loss due to shorter turnaround times and recycling of a part of HMPT slag as hot. An increase of scrap ratio up to some 15% has been estimated.¹³ However, green field installation of HMPT with the BOF is expensive. Thus, choice between the transfer vessel type and the BOF type for HMPT is a matter of compromise between the increased investment and decreased running cost at higher scrap rate with the environmental advantage.

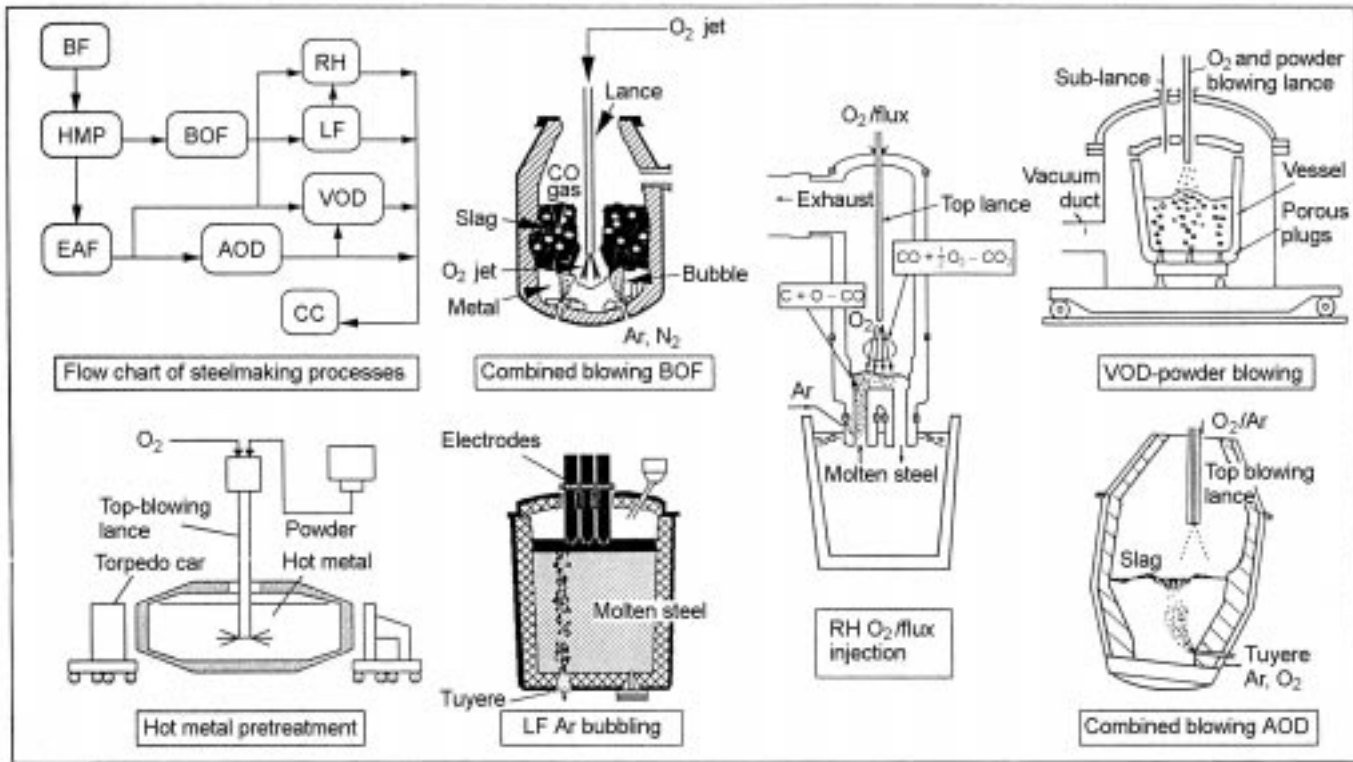
HMPT in USA and Europe is limited to desulfurization with $\text{CaO}-\text{Mg}$ injection and the like into the transfer/charging ladle in order to save heat and utilize more scrap in the BOF for cost reasons. Thus, choice of HMPT is also a trade-off between the above-mentioned advantages and disadvantages, depending on local conditions.

Optimization of HMPT will develop as the demand grows for increased mass processing of steel with improved properties and better lifecycle assessment. This will be met in one way by reducing impurities to lower concentrations during high speed refining. The obvious obstacle for implementing HMPT is the decrease in the use of scrap in the BOF when the scrap has cost advantage. One way to overcome the obstacle is to integrate the BOF, operating predominantly on hot metal, and EAF, based on scrap but with hot metal heeling, into a steel works.¹⁴

Regarding secondary refining, representative processes are shown in Figs 13.5 and 13.11.⁷ LFs utilize enhanced contact of steel melt with top slag by use of bottom Ar injection (and electromagnetic stirring) either under reduced pressure or mostly at ambient pressure and in some cases with electric arc heating as shown



13.11 Secondary refining vessels (Morita and Emi).⁷



13.12 A process integration for mass production of clean steel.

in Fig. 13.11. Top slag for Al-deoxidized steel melt is often CaO-Al₂O₃ base slag with high CaO activity that has low oxygen potential, high sulfide capacity and good capability to dissolve oxide inclusions. For Al-Si- and Si-deoxidized steel melt, it is CaO-SiO₂ base slag with low SiO₂ activity to decrease S, O, oxide inclusions and minimize the occurrence of Al₂O₃ rich inclusions. Simpler versions of the LF, such as the CAS and CAS-OB are also in operation.

The RH utilizes vacuum vessel to circulate steel melt as described in some detail in the section on Process development to produce BH-1F SEDDQ steel sheet, on page 511. Its major function is to decrease H, C, O and oxide inclusions. Powder flux injection is made through the top lance (RH-PI) or side tuyeres (RH-PB) of the vessel to reduce C and S to the order of single ppm as already shown in Fig. 13.9. VOD is for high Cr steels, mostly stainless steels low in C and N. Oxygen gas is soft blown on top of steel melt in the ladle placed in the evacuated chamber, and the melt is decarburized to a very low concentration without causing much oxidation loss of Cr.

In all processes, the intensive melt stirring function is implemented to enhance mass transfer of impurities to reaction sites, i.e., gas–metal and/or slag–metal interface, for efficient removal and homogenization of chemistry and temperature.

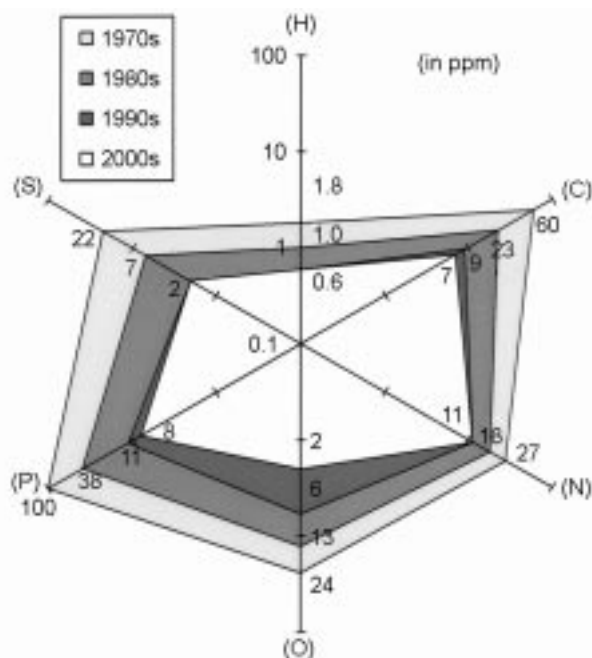
Process combinations effective in minimizing the majority of impurities are shown in Fig. 13.12 for integrated iron and steel plants. It consists of HMPT (for removing P and S or S), the BOF (C and some P), the LF (S, O and oxide inclusions) and/or the RH (H, C, O and oxide inclusions). Tolerable limits of impurities and non-metallic inclusions for typical high performance steels are listed in Table 13.4. Ultimate levels of impurities commercially attainable by best combinations of the above processes are given in Fig. 13.13.¹⁴ The figure shows that the level of each impurity is attainable if the process combination concentrates on minimizing that specific impurity. The requirement on impurity contents of high performance steels has become increasingly stringent. Measures to meet the requirement have been industrialized, but more effort is needed to make them more efficient, faster and economical.

13.2.2 Processes for controlling inclusions

Inclusions here include oxides and sulfides, carbides and nitrides. Control means reduction of the total amount and maximum size and modification of chemistry and morphology of the inclusions. Oxide inclusions occur indigenously and exogenously in steel melt whereas others occur mostly in solid steel indigenously during solidification and cooling.

Indigenous oxide inclusions

Indigenous oxide inclusions occur from deoxidation of steel melt with deoxidizing alloys, mostly Fe-Si and Al, which combine with O to form silicates and



* Numerals in this figure represent the average contents in the beginning year of each decade

13.13 Minimum impurity elements concentrations achieved on industrial steelmaking and refining operation (Emi and Seetharaman).¹⁴

alumina particles. In steel melt deoxidized with Al, dissolved O becomes very low (a few ppms with dissolved Al of a few hundred ppms), and deoxidation product, solid Al_2O_3 particles, is easy to remove by stirring the melt to let them collide, agglomerate and surface to the meniscus. In reducing the amount of oxide inclusions, inert atmosphere, and slag and refractory low in oxygen potential, need to be utilized together with sufficiently strong stirring of steel melt for the surfacing. Representative processes for this objective are the LF and the RH as mentioned earlier.

However, suspended fine Al_2O_3 particles tend to collide and agglomerate to form large Al_2O_3 clusters during melt transfer from ladle to mold even when their O content is very small (e.g. only 1 ppm of O as alumina particles of $2 \mu\text{m}$ in diameter is equivalent to about 10^6 particles/cm 3 steel melt). The clusters cause process upsets (i.e. break during deep drawing of sheet and drawing of wire) and are detrimental for properties, if they have been caught in the solidified steel shell. Also, clogging due to the deposition of the suspended Al_2O_3 on the inner wall of SEN during teeming for CC is not uncommon. The deposit inhibits smooth teeming, results in asymmetric melt flow out of SEN. Such flow causes meniscus turbulence to entrain mold slag and penetrates deep

into the strand crater to prevent flotation of inclusions and entrained mold slag.

For steels where the cluster formation is critical, and sometimes for avoiding the nozzle clogging, modification of inclusion chemistry from solid Al_2O_3 to liquid $\text{CaO}-\text{Al}_2\text{O}_3$ has been practiced by adding Ca-alloy into the steel melt. Dissolved Ca reacts with Al_2O_3 , converting solid Al_2O_3 into liquid lime aluminates. Liquid lime aluminate inclusions are less prone to agglomerate, do not form large clusters even when they agglomerate, merging into smaller spheres. The spheres elongate during hot rolling, being fragmented into less harmful fine pieces during cold rolling, and hence the process upsets and deterioration of properties can be avoided.¹⁵

In an extreme case where Al_2O_3 inclusion formation is strictly prohibited due to upset in downstream processing, deoxidation is carried out with (insufficient amount of Al) + Fe-Si or Fe-Si together with slag that is sufficiently low in silica activity. Tire cord steel and valve spring steel are sensitive to break up during cold drawing when Al_2O_3 inclusions are left in the rod to be drawn. Accordingly, they are deoxidized and inclusion controlled as mentioned above. Namely, dissolved O content in equilibrium with Si of given concentration (for mechanical properties) cannot be made low enough with Si-deoxidation. However, by the use of the insufficient amount of Al prior to Fe-Si addition or use of the above slag with Fe-Si, dissolved O can be decreased to reasonably low levels. Composition of the slag is so chosen as to bring the composition of resulting inclusions in the melt falling within the low temperature eutectic valley of pseudo-wollastonite and anorthite in the ternary $\text{CaO}-\text{SiO}_2-\text{Al}_2\text{O}_3$ system. Also, composition of inclusions occurring from solute segregation during solidification (without contacting the slag) should be made to fall in the low melting temperature range of spessartite composition in $\text{MnO}-\text{SiO}_2-\text{Al}_2\text{O}_3$ system.¹⁶

These measures make the two inclusions plastically deformable during hot rolling, and fragmented during the early stage of cold rolling, leaving only fine independent pieces of the fragment at sufficiently long intervals of separation in the steel for further cold working. This type of inclusion control is favorably applied to high C steels, like tire cord and valve spring, that contain inherently low equilibrium dissolved O in the melt before deoxidation, and hence suited for Si deoxidation.

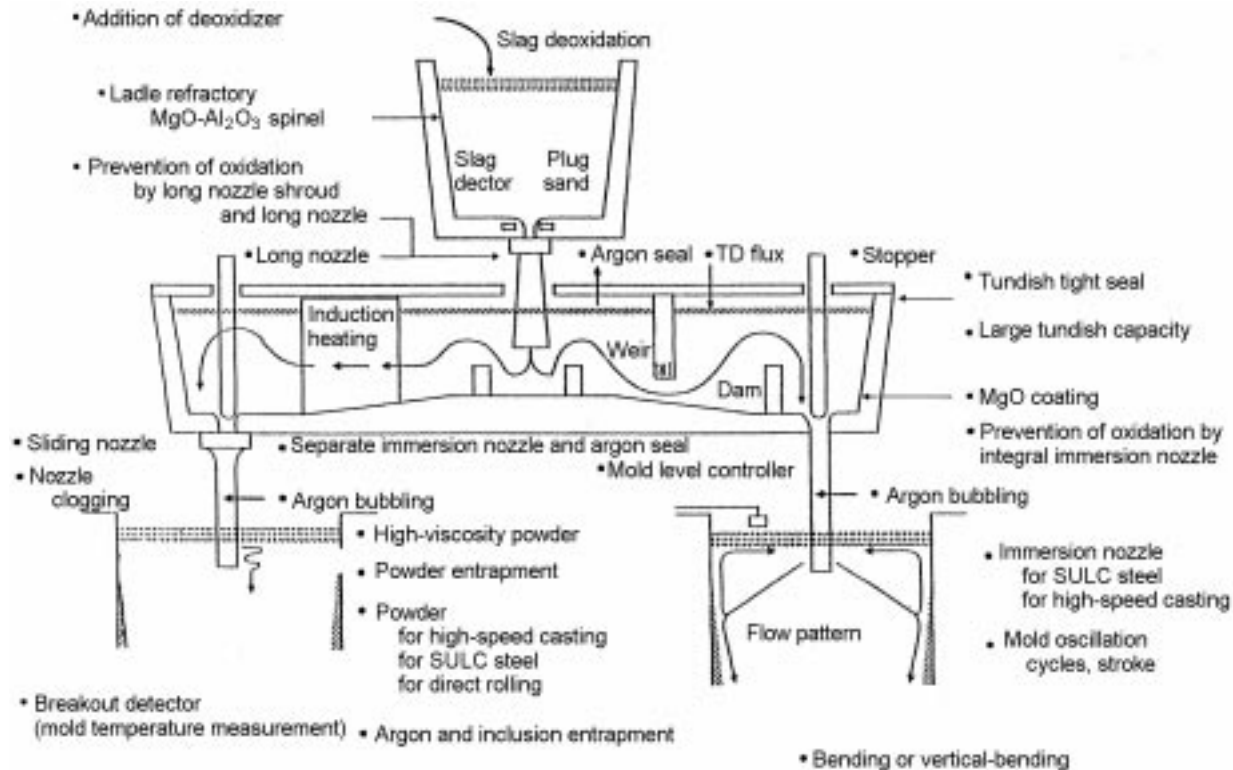
Exogenous oxide inclusions

Exogenous inclusions arise from (a) the reoxidation of deoxidized steel melt by air and oxidizing slag and (b) entrainment of slag and refractory/ladle glaze while the melt is carried over from ladle through tundish to mold. Exogenous inclusions can be macroscopic in size (up to several hundred μm), and hence detrimental to every property of steels. To prevent the formation of macro inclusions, measures have been taken to minimize the reoxidation and slag/refractory/glaze entrainment, starting from the ladle and ending up at the mold.

Table 13.7 summarizes origin, cause and preventative measures of exogenous macro inclusions. Typical examples of such system with the preventative measures for metal transfer from ladle through tundish to mold is shown in Fig. 13.14.¹⁷ Detailed discussion on this subject is available elsewhere.¹⁸

Table 13.7 Origin, cause and preventative measures for the occurrence of macro inclusions

Origin	Cause	Preventative measures
1 Oxidizing ladle slag	<ul style="list-style-type: none"> Slag entrainment in melt by vortex and drainage in later stage of teeming Reoxidation by top slag and emulsified slag 	<ul style="list-style-type: none"> Stiffening slag with MgO Leave some melt in ladle BOF tap hole slag stopper EAF-EBT Slag deoxidation with Al
2 Reoxidation by air	<ul style="list-style-type: none"> Air aspiration at loose joints (ladle/long nozzle, slide gate plates/tundish/SEN) Air in tundish at transient period 	<ul style="list-style-type: none"> Air tight packing with Ar seal Ar injection in tundish nozzle/SEN Inertization of tundish inlet with Ar flushing
3 Tundish slag	<ul style="list-style-type: none"> Slag entrainment by vortex/drainage while bath is shallow Same by turbulent melt flow at meniscus in transient period 	<ul style="list-style-type: none"> Large tundish with reasonable depth and residence time Tundish furniture
4 SEN	<ul style="list-style-type: none"> Clogging by alumina → asymmetric aggressive melt flow from SEN → penetration of inclusions deep into pool Dislodging of accretion 	<ul style="list-style-type: none"> Ar injection from tundish nozzle/SEN wall Fluid dynamic nozzle design (annular, swirl type) Ca addition to melt, all to reduce clogging
5 Mold slag	<ul style="list-style-type: none"> Slag entrainment by vortex Same by turbulent metal flow at meniscus 	<ul style="list-style-type: none"> Electromagnetic meniscus flow control Optimization of throughput rate and port angle of SEN Slag viscosity control
6 Indigenous, exogenous inclusions	<ul style="list-style-type: none"> Large cluster formation of suspending alumina inclusions during melt transfer into mold 	<ul style="list-style-type: none"> Large tundish, tundish furniture Electromagnetic damping of penetrating flow into melt pool in strand Vertical bending caster
7 All sources		<ul style="list-style-type: none"> Same as for no. 6



13.14 Tundish configuration effective to reduce macro inclusions and prevent air reoxidation and slag entrainment during transfer of steel melt from ladle to mold in continuous casting (Okimori).¹⁷

Sulfide, nitride and carbide inclusions

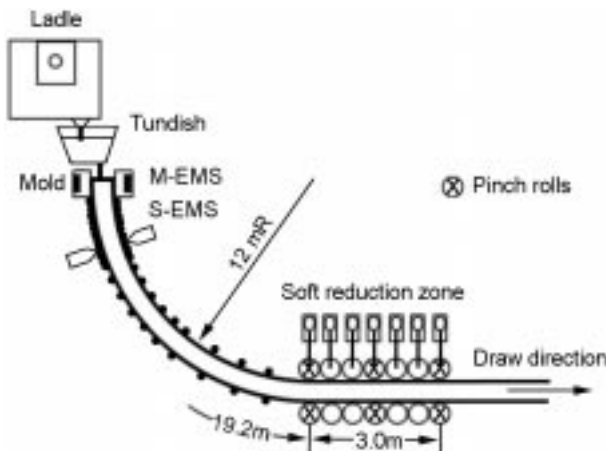
Formation of coarse inclusions of sulfides (MnS), nitrides (TiN, VN) and carbides (Cr_xC_y , TiC, NbC) can be reduced by refining S, N and C to a low concentration and avoiding the incorporation of compound-forming partner elements, Mn, Cr, Ti, Nb, and V to the melt whenever applicable. The limitation is that some of the above elements and compounds are used as beneficial components to improve properties. Thus, chemical composition of steel materials is to be optimized to avoid the occurrence of these compounds in harmful sizes and amounts.

When the melt is cast into CC strands, however, solute segregation takes place in the remaining melt as solid fraction in the strand increases with time. Finally, near the center thickness of the strands, the concentration of solutes in the melt, typically C, P and S, becomes excessively high or exceeds solubility products to form precipitates because the partition coefficient, C_s/C_l , for these elements is less than unity. The solute segregation, whether it is with or without the precipitates, is called center segregation for billets and blooms and centerline segregation for slabs.

The center/centerline segregations can be reduced, as mentioned in Section 13.2.2, by:

- Increasing the sedimentation of solute-lean equiaxed crystals of steel in the vicinity of the pool end in CC strand.
- Dispersing solute enriched melt between the sediment crystals.
- Preventing suction, that is caused by shrinkage on solidification and/or bulging of the strand shell, of the solute-enriched interdendritic melt in the columnar dendrite crystal zone into the thin layer of the pool end at center thickness.

To increase the sedimentation of equiaxed crystals, casting is made at reasonably low superheat temperatures with electromagnetic stirring (EMS) of melt in the mold. Low superheat and EMS enhance nucleus formation and growth of the equiaxed crystals to near the end of the melt pool. EMS near the pool end disperses the solutes enriched interdendritic melt among equiaxed crystal boundaries. To prevent the suction, bulging of strand is not tolerated, and hence alignment and profile of support rolls should be precisely maintained. In addition, squeezing of solute-enriched melt out of the pool end is performed by soft reduction of the strand near the pool end by support roll pairs to surpass solidification contraction. A bloom caster equipped with electromagnetic stirrer and soft reduction roll pairs is shown in Fig. 13.15¹⁹ that is effective to produce blooms without appreciable center segregation of solutes. This also applies to slab casters.



13.15 Bloom caster with electromagnetic stirrer in mold and soft reduction rolls at pool end to reduce segregation of solute elements in the center of bloom (Isobe *et al.*).¹⁹

13.3.3 Integrated optimization of refining, casting, rolling and heat treatment for better properties and productivity

In modern steel mills, processes are interconnected to make steel flow as continuous as possible to achieve maximum productivity and premium yield at minimum cost and delivery time. Optimization of properties vs productivity is pursued through all processes, from raw material preparation, ironmaking, to surface finishing. Only property-related subjects will be mentioned in the following listing.

In the ironmaking sector, major issues are to keep up stable production of hot metal with designated chemistry and temperature while pursuing reduction of energy consumption and CO₂ emission in spite of degrading ore and coal.

In the steelmaking and refining sector, the optimization measures include:

- (a) Separating refining function of P and S from the BOF/EAF to HMPT and the LF, making the BOF/EAF to be more or less a decarburizing furnace. When HMPT covers deposphorization and desulfurization of hot metal, Si in hot metal is decreased to its minimum. This minimizes lime addition and hence slag evolution, eruption and iron loss and maximizes Mn reduction from the Mn ore in the BOF as discussed in the previous section.
- (b) Development of the high speed blow and low slag process in the large size combined blown BOF (top O₂ blow + bottom Ar injection for stirring) with dynamic blow control followed by direct tapping. The objectives are to maximize productivity and metal yield and minimize over-oxidation of steel and slag melt and carry-over of slag into the ladle.

- (c) Development of high speed secondary refining systems (the RH and the LF) that implement intensive stirring of steel melt to enhance removal of impurities and inclusions.
- (d) Advance of the quality and installation of refractories for all metallurgical vessels. In fact, monolithics, advanced composite bricks and zone lining have cutback energy consumption and CO₂ emission of refractory origin considerably.²⁰

In the casting sector, the developments of the following are included:

- (e) The rationalized melt transfer system consisting of long nozzle on ladle, large tundish with flow control furniture and atmosphere inertization, and tundish nozzle and SEN with flow control device, and Ar injection to reduce nozzle clogging and air aspiration.
- (f) The multi-sequential high speed continuous casting with mold width change and vertical progressive bending (liquid core) type strands equipped with EM stirrer/EM flow controller in the mold, and EMS and soft reduction roll pairs at the pool end.
- (g) The thin slab caster to eliminate roughing of slabs for steel grades that do not require heavy reduction in hot rolling for microstructure and texture control.

In the rolling sector, the following have been developed:

- (h) Hot charge rolling (HCR) and hot direct rolling (HDR) of CC strands to save sensible heat.
- (i) Endless continuous hot rolling of CC slabs.
- (j) TMCP for plate mills and tandem hot strip mills. Both mills have a high mill constant, high speed roll gauge control system, and pair cross rolls or shift rolls in the final tandem stand for strip profile control.
- (k) The AcC and DQ system with devices for intensive rapid water cooling to prevent film boiling.
- (l) The highly rigid reverse or tandem cold strip mill with high accuracy to maintain size and profile and every precaution taken to monitor and keep good the surface finish.

In the heat treatment, annealing and surface coating sector, the measures are:

- (m) CAL with high speed degreasing, heating and cooling capability for a variety of microstructure and texture control to produce designed properties.
- (n) CGL to coat Zn by pickling, heat treating, hot dipping, jet wiping to control Zn thickness followed by galvannealing to form Fe-Zn alloy layers in between the Fe matrix and coated Zn (some Fe is even diffused on the surface of Zn for better paint adhesion), and EGL to coat Zn by electrolysis.

And last but not least:

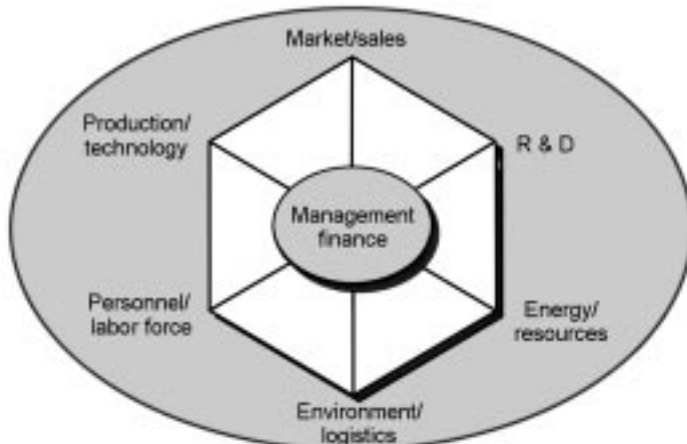
- (o) An advanced management system for total integration of these processes and equipment for production. The management system includes an order intake subsystem connected with subsystems for production and logistics control. All of these are built in hierarchical computer systems. The production subsystem is supported by numerous dispersed PC network systems installed with each sector of the production and control processes.

13.4 Economic optimization

To design a steel production system, optimization must be carried out for the many factors shown in Fig. 13.16. Among them, material properties and quality, productivity and cost are of major importance to meet market demands. Here, quality refers to consistency of product properties, i.e. limited variation from specifications of size, profile, chemistry, properties, and occurrence of surface- and internal-defects, as represented by premium yield at steel mills and users.

Compromise of material properties and quality with productivity and cost has always been a critical issue in the steel industry for commodity steels that are exposed to international competition. On the other hand, particular high performance steels of superior properties and quality (so-called ‘one and only’ steels, that are not available elsewhere since they cannot be produced by competitors) are exempt from such hardship at least when there is demand in the market and until competitors catch them up at comparable cost without infringing related intellectual properties. Quality steels fall in between the high performance steels and commodity steels.

Superiority in material properties and quality can be achieved by excellence in research and development of processes and products, combined with consistent production which is supported by modern equipment, operational



13.16 Factors influencing the design of steel production systems.

skill, maintenance and management. Cost competitiveness stems from the choice of raw materials and energy, scale of production, product mix which is optimized for the market, proper investment in modern equipment, processes and technologies that assure lower consumptions of energy, material and labor. Although profitability of the integrated steel industry is largely dependent on the market price of steels, optimization of the above-mentioned factors by management determines the fate of competing mills under otherwise similar conditions.

13.4.1 Raw materials and energy

In countries where domestic per capita steel stock is sufficient (e.g. 10 ton/capita), circulation of obsolete scrap would be a few percent (2.5% in Japan) of the domestic stock. In such countries, scrap recycles to the extent that total steel production is split into roughly 60% by the BF–BOF route and 40% by scrap–EAF route as long as total steel consumption in the world keeps increasing.

Hot metal vs scrap

If world steel production keeps increasing for at least the coming decade, the BF–BOF route will be the mainstay of steel production, supplemented to a small extent by direct reduced iron (DRI by Midrex, HyL, etc.) and hot metal by smelting reduction processes such as Corex. Even when world production has leveled off, BF–BOF will be the mainstay until the tramp elements issue has been resolved. Demands to reduce energy consumption (and hence cost) have caused considerable change in equipment and operation of iron and steelmaking processes. The changes include items listed in Tables 13.8 and 13.9 that have been developed and implemented directly or indirectly to meet the demands.

Among them, the BF sector consumes, including heats associated with raw materials, off-gases, slags, furnaces and equipment, over 70% of the energy required to produce steel in an integrated plant. Thus, attention has been focused on saving energy in the ironmaking sector as shown in Table 13.8. CDQ and TRT have been in place, and measures such as CMC, PCI, and use of waste plastics in coke ovens and the BF have been practiced. Continued efforts have been made to decrease the reducing agent rate (RAR) by improving reducibility of sintered ore, optimizing burden distribution, utilizing reactive coke, increasing blast temperature, decreasing moisture of blast, aiming at low Si and low tap temperature of metal and slag, and decreasing the heat loss of the BF.

As a consequence of these measures, RAR has decreased to about 514 kg/t-hot metal, energy consumption to 22.0 GJ/t-steel, cutting back CO₂ emission to 1.72 t-CO₂/t-steel in 2001 in the steel industry in Japan. The contribution of CDQ and TRT totaled about 0.87 GJ/t-steel.²¹ Combining favorable but critical operational measures, total C consumption (including C for sintering and coke

Table 13.8 Measures to reduce energy consumption in raw materials processing and ironmaking sector of an integrated iron and steelmaking plant

Coking and sintering	Ironmaking
<ul style="list-style-type: none"> • Coal moisture control (CMC) • Advanced mix charge coking (>50% semi soft coking coal) • Coke dry quenching (CDQ) • Waste plastics charging • Prolonging coke oven life (>50 yrs) • Advanced agglomeration (e.g. HPS) • Use of low grade ore high in alumina or water • Sinter plant waste heat recovery 	<ul style="list-style-type: none"> • Pulverized coal injection (PCI) • Waste plastics injection • BF top gas pressure recovery turbine (TRT) • Scale-up of BF (av. 3760 m³)* • Hot stove waste heat recovery • Prolonging BF life (>16 yrs) • AI optimized operation of BF with preferred center blasting

* Average in Japan

making but excluding that for oxygen generation) may decrease to about 500 kgC/t-hot metal at RAR of 455 kg/t-hot metal with CR 255, PCI 150, plastic injection 50 kg/t-hot metal.²²

On the other hand, scrap as iron source has a great advantage over hot metal since it does not require energy for reduction. In fact, the scrap–EAF route emits only about 30% of CO₂/per ton steel compared with the BF–BOF route. However, tramp elements in scrap deteriorate steel properties if critical concentrations listed in Table 13.10²³ are surpassed. Use of obsolete scrap in EAF for high quality steels, such as sheet for SEDDQ and plate and pipe for high tensile strength regimes, has been limited due to the tramp elements constraints. To avoid this, the recycling of scrap is attempted selectively on a tramp elements content basis, but there is a limitation. Accordingly, extensive use of obsolete scrap has been for commodity shapes and merchant bars. Thus, better utilization of obsolete scrap must be promoted for other grades, without increasing tramp elements, by the following measures:

Table 13.9 Measures taken to reduce energy consumption in the steelmaking and casting sector of an integrated iron and steelmaking plant

BOF-CC	EAF
<ul style="list-style-type: none"> • Off-gas recovery as fuel • Prolonging vessel lining life (>10 000 heats) • High speed high hit rate combined blowing with direct tapping • Reduced slag blowing with HMPT • Hot charge rolling and hot direct rolling of CC slabs 	<ul style="list-style-type: none"> • UHP-AC/DC EAF with high rate O₂ injection • Advanced scrap preheating system • Submerged short arc heating with foamy slag • Hot heel operation with hot metal • Eccentric bottom tapping (EBT)

Table 13.10 Tolerable maximum tramp element contents for various steels and processes

Grade/properties	Cu	Ni	CR	Mo	Sn	As	Sb
Drawing quality	0.06	0.10	0.07	0.02	0.01		
Commercial quality	0.10	0.10	0.07	0.03	0.015		
Tinplate	0.06	0.04	0.02	0.02	0.02		
Merchant bar	0.35	0.15	0.15	0.04	0.03		
Hot formability		0.4*					
Cold formability		0.1			0.02	0.025	
Hardenability							0.02
Notch impact strength					0.04	0.045	

Figures are in mass%, and give tolerable maximum concentrations

* for Cu + 8Sn

- (a) Organizing social systems that enhance efficient collection, transportation, processing and delivery of the scrap. The driver is economics, being assisted by legislation.
- (b) Dismantling of parts that contain metallic tramp elements from disposed assemblies in close cooperation with designers in assembly industries before shredding or pressing (e.g. Cu winding in numerous motors equipped on end-of-life vehicles (ELV)).
- (c) Not all the parts can, however, be dismantled in practice, and hence improved shredding machines or alternative new processes need to be developed to separate metallic tramp elements effectively from the shredded or processed scrap. This should enable the use of automobile shredder scrap as a pure iron source for diluting the tramp elements in EAF in preference to DRI which consumes C-containing reductant.
- (d) Developing steels that are insensitive to the adverse influences of tramp elements.

Attempts have been made, but economy and productivity have imposed insurmountable obstacles. Reducing the tramp elements from steel melt does not seem reasonable,²³ since it dilutes the tramp elements first by melting the scrap and trying to remove them later. At present, dilution of the tramp elements is made with hot metal or DRI for steels whose properties are sensitive to them. Energy saving measures practiced in steelmaking and casting sector are listed in Table 13.9.

New iron and steelmaking processes

The need for saving energy and processing degrading raw materials has enhanced the development of new iron and steelmaking processes as well. A comparison of energy consumption and greenhouse gas (GHG) emission was

made between various new processes on LCA basis.²⁴ Most of them are or will be operating with non-agglomerated ores and non-coking coal. Some of them appear to offer additional reduction in energy consumption and CO₂ emission. Natural-gas-based FINMET-EAF and MIDREX-EAF give about 1.95 t-CO₂/t-*cast* steel with the use of a large fraction of scrap. Coal-based ones like ITmk3, Hismelt and Tecnored are said to consume 20–25% less energy than average BF–BOFs, comparing favorably with the natural-gas-based ones. Many of them are, however, in the emerging stage, and hence the above figures need confirmation on a large-scale operation, taking into account the challenge by advancing BF–BOFs.

(Note: the definition of t-CO₂/t-steel would be better made on a LCA basis covering stages from the raw materials excavation to liquid steel. At present, the literature uses different definitions that make straightforward comparison among processes difficult.)

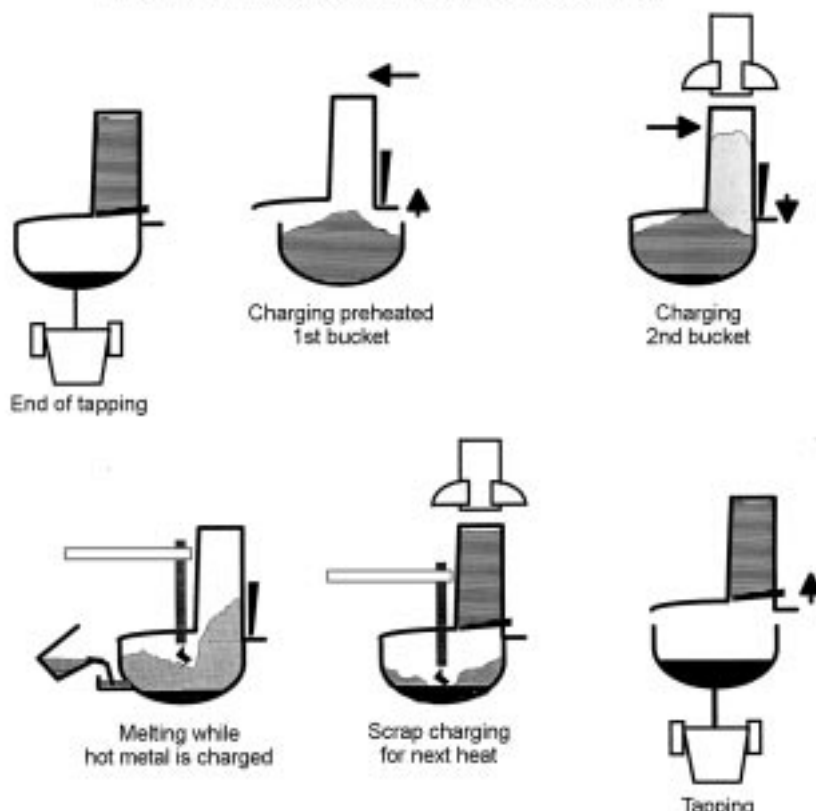
Among others, Corex, in commercial operation, has been said to emit less GHG than conventional average BF–BOF route provided that electricity credit and slag credit are fully utilized. The size of Corex furnaces is, however, too small to rationalize the construction of highly efficient, off-gas driven large power plants. Thus, further development to better utilize the credit is underway in Korea and South Africa, including the Finex process that utilizes off-gas of Corex for preliminary reduction of iron ore.²⁵ These new processes may find a better possibility for success in areas where the relatively small size of investment and limited amounts of scrap and electricity are available and small scale steel production meets local demand.

Combination of BF and EAF

Recently, EAFs have been made highly productive, even compatible with BOFs, by incorporating (a) various ways of preheating and charging scrap, (b) foamy slag practice, (c) hot heel operation, (d) extensive use of oxygen and/or fuel burners, and (e) eccentric bottom tapping. A variety of new species of EAFs have emerged in the last decade. Under the circumstances, combination of BFs in an integrated mill with modern EAFs for hot heel operation with 30–40% hot metal charge offers interesting flexibility of the choice of iron sources. Such a BF can be compact and operate on low quality coke and coal. The combination of a compact BF with modern EAFs can be a choice where scrap availability is not sufficient.

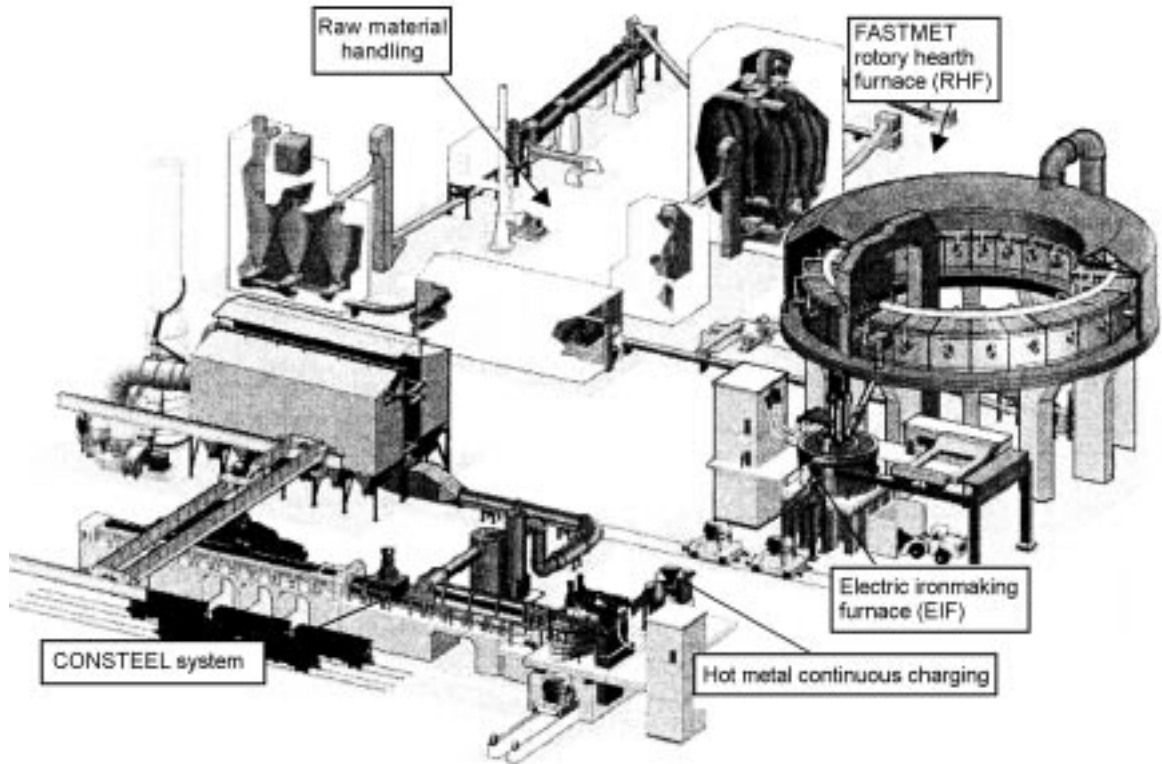
An example is shown in Fig. 13.17²⁶ where the stable operation of EAF with a Finger Shaft type scrap preheater is used with hot metal charging. There, 35% hot metal charging and extensive oxygen gas injection of near 30 m³/t-steel have shown a remarkably short power-on time of 30 minutes and a low electricity consumption of 210 kWh/t-steel to produce liquid steel of over 230 t/h (tapping weight 170 t, [N] is also low, 37 ppm) elsewhere in Europe and China. In the hot

Finger shaft furnace process (EAF) with hot metal charging

13.17 Combination of BF and EAF for energy efficient high rate production of steel with hot metal heeling operation (Denier *et al.*).²⁶

metal charging practice, use of obsolete scrap has also been made easier due to the dilution of tramp elements by hot metal. Also, effective use of home scrap and selected scrap has been promoted, substantially reducing energy consumption and CO₂ emission with less contamination by tramp elements for high quality bar and wire production.

New ironmaking processes have progressed toward this direction as well, as exemplified by Fasteel that is an integration of the Fastmelt process and Consteel process, as shown in Fig. 13.18.²⁷ Fastmelt takes DRI from the Fastmet process (that employs a rotary hearth reduction furnace to produce coal-based DRI) and converts the DRI to hot metal using the DC-arc Electric Ironmaking Furnace (EIF). In the Consteel process, scrap preheated by combusting EAF off-gas is continuously charged in the EAF. Hot metal from the EIF is also charged into the EAF to optimize the EAF steelmaking operation. Direct charging of hot DRI (1000°C) to the EIF and the EIF hot metal to the Consteel EAF together



13.18 Integration of new ironmaking process and EAF with continuous preheating and charging of scrap (Shoop *et al.*).²⁷

with preheated scrap (400–600°C) has shown a power-on time of 45 minutes at 235 kWh/t-steel. Also, the cost of the EIF hot metal is reportedly said to be 20% less than the BF hot metal in USA. Long-term industrial viability remains to be seen, but such challenge should be encouraged.

13.4.2 Production and investment

As mentioned earlier, the production of steel aims at the highest yield of premium products within the specifications, while keeping the highest productivity and the lowest cost with given facilities. To achieve these compromising aims, the basic design of the production amount and product mix, being supported by the installation of proper facilities for process equipment and logistics, have to be optimized from a long-term perspective.

Process design and corresponding equipment are usually so selected as to make each process interconnected virtually continuously, and to achieve a good balance among the processes without causing bottlenecks. The minimum cost is set to occur somewhat below the maximum production rate, allowing the best profit to arise when the plant is on the set availability, yet leaving some upward flexibility to produce more when demand increases. Production will increase in the future, and technology and equipment for production will also develop, calling for continual improvements and timely/occasional revamps. Plans for spare space and equipment installation should include such future expansion and revamps.

The steel industry is heavily equipment oriented, and hence investment becomes enormous. This is particularly so when the product mix is shifted toward high performance steels. The tramp element issues still require hot metal as a necessity. Control of microstructure and texture demands rather heavy rolling reduction of semis. Thus, integrated iron and steel plants that consist of ‘BF–BOF–LF/RH–conventional CC-Plate/Hot Strip Mill with TMCP-AcC and cold strip or reverse mill and CAL’ will remain necessary, preceded by raw materials processing units (sintering and coke making) and followed by surface coating lines (e.g. CGL and EGL) or outsourcing both of these. The production rate should be sufficiently high, above several Mt/year to remain competitive in terms of depreciation, yield, energy consumption and labor.

With regard to the production facility, one requires investment into the following to keep up low impurities, good cleanliness and low segregation in slabs for quality steels at high production rates:

- (a) Combined blown BOF with slag cut tapping device, sub-lance, and oxygen generator.
- (b) LF and RH with intensive melt stirring capacity, electrode heating unit, and vacuum system.
- (c) Ladle with bottom Ar injection, and large volume inertized tundish.

- (d) Vertical progressive liquid core bending type slab/bloom CC with electromagnetic flow control device on mold, width change mold, and soft reduction device at the pool end.

For a high production rate downstream processing, investment in the following is required:

- (e) A sizing mill to take care of different slab widths for sequential rolling without roll change.
- (f) A hot rolling mill with TMCP, AcC and devices to control the size and profile of plate, and sheet (e.g. AGC, crown rolls, roll shift, pair cross rolls, etc.).
- (g) CAL with post quenching facility.

Equipment for various sensors and activators, inspection, logistics, utilities, waste processing, data processors for operation and quality control system, and maintenance are all additional.

For plants aiming to produce commodity flat steels, the Scrap-EAF-thin slab CC-Hot Rolling Mill may be a choice when the supply of scrap and electricity is secured at affordable cost. Recent developments in the productivity of UHP-EAF with scrap preheating and high-rate oxygen injection and improvement in the quality of thin slab CC have made this avenue even more cost competitive for commodity steels as well as some quality steels. Total energy cost for this route is naturally much less, and total investment per ton-steel is also less than the integrated plant. Production rates can be up to several million tons per year depending on the number of units installed. Operation of advanced EAFs with partial supply of hot metal from BF and/or DRI has emerged as mentioned in the section Combination of BF and EAF, page 541. Dilution of tramp elements in this case will, to some extent, broaden the product mix for the EAF toward more quality steel with increased productivity, making the distinction from the BF-BOF route somewhat fuzzy.

13.4.3 Market and management

Steel, being a commodity material, faces international competition. When the market grows, the price soars, and production surpasses the set rate of production. Managerial efforts in terms of production and properties are to maintain the high rate of production at the highest premium yield without degrading properties and quality within the specification, to arrange necessary raw materials and labor at minimum costs, and to distribute material resources to the production of steel grades best fitted to the circumstances. When the market shrinks, price and production both decrease. The efforts are directed as above, but it is often necessary to cut back production costs by increasing total production to come closer to a cost minimum production rate for the steel plants

by shipping out semis. Compromise is required in this case between reduced cost and declining price which is caused by increased steel stock in the market resulting from the increased total production.

In either case, continuous research and development (R&D) are mandatory to create value added ‘one and only’ steels and processes ahead of competitors. It is common practice to set aside a proportion of the cash flow for such R&D as an indispensable investment. R&D are effectively carried out by the combined efforts of research and production divisions in close cooperation with customer industries. Knowledge and technologies gained in developing ‘one and only’ super performance steels are often fed back to upgrade quality steels to make them stay competitive.

13.5 Environmental optimization

Environmental issues have become a crucial factor for sustaining steel production. Minimization of CO₂, pollutants such as SO_x, NO_x, dioxins, dust, particulates, acid liquors and fumes, etc., must meet legislative requirements at any stage of steel production. Also, minimization, recycle and reuse of wastes must be pursued to save energy, materials and reduce environmental problems. In addition, design and production of steels need to be made on a lifecycle analysis (LCA) basis.

13.5.1 Abatement of hazardous wastes

The steel industry in Japan, like any industrially advanced country, took comprehensive measures and made a heavy investment to reduce SO_x, NO_x, toxic gases like dioxins, particulates and water pollution long ago. The level of these pollutants has been far below the threshold set by legislation since late 1970 to early 1980 (except for dioxins, for which the level cleared the threshold in 1990s). The pollutants emission thresholds can be met provided that appropriate investment, operation and maintenance have been made for corresponding equipment such as NO_x removal at sinter plants and SO_x removal at coke ovens. Advanced integrated steel plants in the world are at a similar level. In industrially developing countries, assistance is needed to upgrade the level of dealing with hazardous wastes.

13.5.2 Minimization, recycle and reuse of wastes

Internationally the steel industry utilizes (and produces) near neutral (CaO%/
SiO₂% ~ 1) to basic (CaO/SiO₂ ~ 4–6) silicate slags of the order of over 300 million tons per year. They come from BF, HMPT, BOF, EAF, LF and CC operation. The slags call for application-specific physical and chemical properties that have been changing to comply with (a) degrading raw materials,

Table 13.11 Amount, treatment and use of waste slag occurring in Japanese steel industry in 2002

Slag	Amount (kg/t-steel)	Treatment	Application
BF	290	<ul style="list-style-type: none"> • 76% water granulated • Balance, air cool • Rock wool 	Cement > 60% Concrete filler 10% Road 17% Balance, own use, civil engineering
HMPT + BOF	110	<ul style="list-style-type: none"> • Recycle to sinter + HMPT* • HMPT + zero slag • BOF blow* • Hydration/carbohydration* 	Asphalt filler Temporary road Civil engineering/ land reclaim
EAF	70	None	Same as above
LF	40	None	In house

*see text

(b) increasing productivity of ironmaking and steelmaking processes, (c) improving quality of steel products, and (d) progress of process modification. As an example, the occurrence of slags in steel industry in Japan is listed in Table 13.11. Measures taken so far to minimize the occurrence are detailed elsewhere.²⁹ Most of them, up to 99%, are utilized in the civil engineering sector. Better utilization is under development.

BF slag is near neutral, composition being quaternary 40–45%CaO–5%MgO–35–40%SiO₂–20%Al₂O₃. Utilization of BF slag for cement reduces energy, that is otherwise consumed for calcining limestone, resulting in a considerable decrease in CO₂ emission. Instability exists in this application, however, as challenged by less expensive replacements that are coal ash occurring from coal fired power plant for cement clinker and recycled concrete from demolished buildings and asphalt filler. The slag has also been industrially converted to rock wool and fertilizer, but on a small scale. The balance has found only low-end applications in civil engineering, road and port construction. Attempts to utilize the sensible heat of molten slag were made extensively, but without much industrial success.

Gangue materials in the ore and ash in the coke and coal, together with additives to sinter and pellet determine the chemistry of BF slag. Recent notable improvement under increasing PCI up to 230 kg/ton-hot metal is that the BF slag has been successfully decreased from 280–330 to 265–300 kg/ton-hot metal without impairing BF operation by reducing SiO₂ content in sinter from *circa* 5.1% to 4.6% (see refs 3, 4, and 5 in [30]).

Table 13.12 Reduction of waste slag in steelmaking sector by incorporating HMPT in BF–BOF route

Type of HMPT	BOF slag recycle process	Zero BOF slag process
Slag before implementation*	138 (BOF slag 92)	130
Slag after implementation*	121 (BOF slag 42)	60 (BOF slag 10)
Slag reduced**	59 + α (desiliconized slag)	70
Occurrence of waste slag***	79 - α	60~70

*For details, see text. **138 – [121 – 42(recycle) – α] = 59+ α , ***121 – (42 + α) = 79 – α

Figures are in kg/t-steel

For HMPT and BOF slag, two typical methods have been in operation to optimize the total production system for reducing P, S and waste BOF slag as briefly mentioned before.³⁰

One method is to recycle the BOF slag to sintering to recover iron and CaO in the slag in the BF. This naturally causes the increase of P in hot metal from the BF, beyond the deposphorizing capability of the BOF, and hence implementation of HMPT for deposphorization is mandatory. However, if 85% or more of hot metal was deposphorized at HMPT to 0.04%, P in hot metal could be kept below 0.14% even at 100% recycling of BOF slag. In this case, all hot metals are desiliconized at the runner and tilting tundish in the BF shop, deposphorized and desulfurized in sequence by injecting post-mixed fluxes into the desiliconized hot metal in torpedo cars at the pretreatment center, and blown in the BOF. As shown in Table 13.12, occurrence of waste slag in this case decreased to about 80 kg/ton-steel, about 60% of 138 kg/ton-steel for ordinary BOF operation (see ref. 6 in [30]).

The other method to minimize the BOF slag without such recycling is to reduce Si in hot metal to a minimum. Si in hot metal at tap from BFs is reduced to a low 0.2%. The hot metal is desiliconized (to $\leq 0.1\%$ Si), desulfurized and deposphorized in the transfer ladle. The pretreated hot metal is blown in the BOF without the addition of slag materials. Occurrence of slag (HMPT slag inclusive) in the steelmaking sector is much reduced from 130 kg/ton-steel for an ordinary BOF shop to 60 kg/ton-steel, less than 50%, by this method. BOF slag itself is reduced to only 10 kg/ton-steel (see ref. 7 in [30]).

In both cases, the slags after deposphorization ($\text{CaO}/\text{SiO}_2 \leq 2$, $\text{Fe} \cong 10\%$, P_2O_5 3–4%) and desulfurization ($\text{CaO}/\text{SiO}_2 > 3$, $\text{Fe} \leq 1\%$, some S and F, and/or Na) are not much recycled, considerable portions being disposed of for landfill at some expense. Only small fractions of BOF slag has been used as a supplemental raw material for cement. Otherwise, use is limited to landfill and gravel for temporary paths.

Recently, however, HMPT and BOF slag are finding possible applications to:

- (a) Improve the sea bed by capping, forming fishery ranches.
- (b) Protect the seashore from breaker waves or strengthen land foundations for heavy structures by forming the slags into large blocks with hydration or carbohydration.
- (c) Promote the growth of biomass of biofouling organisms (phytoplankton) on the block (as fertilizer) to fix CO₂ and feed fish.
- (d) Preform the mixture of HMPT waste slag with BF slag, fly ash and water into large blocks for a similar application to (b).

Although (a) to (c) are in the trial stage, (d) has been commercialized in large quantities.

EAFs have been operating largely for melting and oxidizing with single slag practice. Thus, properties and the use of EAF slag are similar to BOF slag. Secondary refining calls for a variety of slag compositions to meet product requirements as mentioned before. However, there are not many applications available for LF slag except for some internal use and civil engineering.

Sludge consisting of iron oxides, metallic iron, water and oil is usually separated from water, heated to 1200°C to remove oil, and returned to sinter plant. Dust is mostly sent to Wealtz kilns where iron is recovered; evaporated Zn and Pb are concentrated and sent to non-ferrous refiners for recovery. As a new development, the Fastmet process, with rotating hearth furnaces, has emerged to recover iron and Zn from dust pelletized with C. It also utilizes recycled waste oil as fuel.

13.5.3 Lifecycle analysis of steels

The process development referred to in previous sections contributes to the reduction of CO₂ emissions. Properties development does the same via product stewardship which has become popular through two-way interactions with the customers. High strength steels to reduce the weight of cars, trains and ships, electric steels to reduce transmission loss of electricity, pre-coated sheet steel for electric appliances that make oiling, degreasing and painting unnecessary,

Table 13.13 Reduction of CO₂ emission by use of high performance steel products

Application	Production (kt)	Energy saving (PJ)	CO ₂ reduction (Mt)
Automobile	631	89.5	6.4
Ship	1531	30.7	2.4
Electric train	8	3.5	0.1
Building	1529	14.0	1.1
Transformer	55	74.4	2.9
Power plant boiler	1.4	26.2	2.4
Total	3757	238.3	15.4

Note: Peta Joule (PJ) = 10¹⁵J

eliminating polluting organic solvents, all fall into this category. Here, the energy required to produce these steels must be kept reasonably lower than the energy saved by lifetime use of the steels. Detailed LCA indicates that the use of high performance steel products resulted in a total reduction of CO₂ emissions of 15.4 Mt for the year 2000 in Japan as shown in Table 13.13.²⁸

13.6 Future trends

13.6.1 General trend of future development of processes and properties

Needs for steels for various applications will be upgraded, driven largely by energy and environmental concern and international competition. Strength, fatigue strength, ductility, weld ductility, various formabilities, corrosion resistance, resistance to SSC, HIC, SOHIC, machinability, etc. will further be improved. Regarding mechanical properties, upgrading of the balance between strength and ductility/formability at a higher level without impairing weldability will remain a moving target to chase with continuous effort.

Obviously, not all of these properties are required simultaneously. In-depth cooperation with user industries from the planning stage to identify what properties are required under what conditions becomes essential to clarify real needs and enables the best specification to be developed, suited to and optimized for processing both in the user and steel industries. User needs have driven the progresses of steel materials and processes in the steel industry. Conversely, the progress in the steel industry has provided user industries with opportunities for new and advanced design and manufacturing processes and products of better performance. Such cooperation and interactive developments will continue more closely in future for the benefit of both parties.

The needs for steel materials will be met only by semis lower in impurities, inclusions, segregation, and internal and external defects with precise control of alloy components. The semis are to be processed for more advanced control of micro/nano-structure and texture with better size and profile accuracy to fulfill requirements. All these will be achieved in the presence of degrading raw materials and increasing demand to reduce energy consumption, GHGs and waste emission.

To comply with these circumstances, steel manufacturing processes have developed by:

- (a) Splitting the function of smelting reduction of iron ore and refining of hot metal into ‘pelletizing/sintering + coke making + BF ironmaking + HMPT + BOF steelmaking + secondary refining’, although it has been made in an integrated way to keep up smooth material flow through the unit processes.
- (b) Converting batch ingot casting to CC or thin slab CC + inline rolling.
- (c) Converting hot- and cold-rolling mills into tandem mills.

- (d) Integrating the function of hot rolling, microstructure control and texture control into TMCP + AcC + (DQ).
- (e) Converting batch annealing into CAL.

It is interesting to note that in the upstream processing, functions have been split, while in downstream processing they have been integrated, and in casting and annealing, they have been made continuous. Overall, optimization of the unit processes will continue in the future toward the two opposite directions but in integrated ways with emphasis always placed on continuous processing. The following is a perspective on possible future progress.

13.6.2 Future development of processes to reduce energy consumption/ CO_2 emission and deal with downgrading raw materials

In raw materials and ironmaking, utilization of downgraded raw materials will proceed. To deal with the unfavorable raw materials conditions, we foresee the progress in:

- (a) Advanced agglomeration for sintering of iron ores containing more water and gangues.
- (b) Increased rate of charging soft coal and waste plastics into coke ovens.
- (c) Injection of soft coal up to 300 kg/t-hot metal and waste plastics into BFs to reduce coke
- (d) Combined operational efforts to decrease RAR in BFs.
- (e) Industrialization of new ironmaking processes to supplement the mainstay BF–BOF/scrap–EAF route at reduced occurrence of CO_2 even by using downgraded materials.
- (f) Cooperation with customer industries to dismantle parts that contain tramp element metals and enhance the separation of tramp element metals from shredded scrap for recycling.

13.6.3 Future development of upstream processes to reduce impurities, inclusions and defects on semis for better material properties

- (a) Metallurgical reactors in the upstream of the steel manufacturing system will be developed toward better mixing of liquid metal with fluxes, aiming at shorter cycle time, lower heat loss and improved efficiency of flux utilization for decreased impurities and inclusions. The utilization ratio in units of the phosphate and sulfide capacities of the fluxes in current practice would be at best somewhere around 50% for a top slag operation, and much lower for an injection operation. In addition to process thermodynamic considerations, improvement of process kinetics is necessary to improve the

utilization ratio. Shorter cycle time and reduced flux amount by the enhanced utilization and improved kinetics will reduce heat loss and increase productivity of both HMPT and secondary refining. That will make implementation of HMPT economical for better integration of the refining system in countries other than Japan and Korea (where HMPT for dephosphorization and desulfurization has been practiced).

- (b) After the above has been achieved, the BOF will be shifted toward a high speed decarburizer with minimum occurrence of slag. Preliminary and finishing refining function is transferred to HMPT and secondary refining. It appears that better HMPT systems will emerge to allow increased use of scrap in BOFs.
- (c) A variety of combinations of iron sources (including hot metal) with high performance EAFs will continue to be industrialized, supplemented with efficient scrap heating systems.
- (d) Utilization of HMPT slag and BOF slag will be developed for better application.
- (e) Improved melt delivery system from ladle to tundish to mold will be developed to avoid exogenous macro inclusions caused by reoxidation and slag entrainment.
- (f) CC machines to cast high performance steels will be converted to those with vertical bending (progressive bending) profile. Optimization of electromagnetic flow control in mold will proceed to reduce subsurface inclusions, Ar bubbles, slag emulsions and enhance inclusion flotation.
- (g) Macroscopic center segregation of solutes in semis has been practically reduced by the combination of EMS and soft reduction of the pool end, but more effective ways to reduce semi macroscopic center segregation of solutes will be developed.

13.6.4 Future development of downstream processes for better material properties

- (a) TMCP-AcC-(DQ) with microalloying elements will proceed further in a continuous way toward microstructure control for higher strength and ductility for plate steels for buildings, ships, and bridges.
- (b) Fine control of oxides or nitride/carbonitride precipitation will develop more through precise composition control in steelmaking followed by TMCP-Acc-(DQ) for microstructure control of HAZ for better weldability.
- (c) Fine graining of IF-, DP- and TRIP-steel strip to lower single μm sizes will be pursued by intercritical rolling and precipitates control with microalloying elements.
- (d) Above all, better clarification is necessary of microstructure control for achieving extremes of materials properties, in particular, changes in microstructure and corresponding properties during working.

Some examples related to the above issues for specific steel grades that represent a part of super performing steels are:

- (a) Process to prevent delamination of 5 GPa tire cord wire.
- (b) More advanced reliable minimization and control of non-metallic inclusions for longer rolling fatigue life of ball bearing steel, thermal fatigue life of turbine rotor steel for large scale power plants and better premium yield of PET laminated stretcher draw can sheet steel.
- (c) More precise alignment of Goss texture toward rolling direction of grain oriented 3% Si steel.

Steel materials are often misunderstood to have matured in their properties and production processes. However, the processes and properties have been substantially improved by continuous efforts, yet leaving more room to advance in the future.

13.7 Further reading

Readers are recommended to refer to the following articles for their basic understanding of the subjects referred to in this chapter.

1. *For steel production processes*, (1) *Steel Manual*, (1992), Verlag Stahleisen, Dusseldorf; (2) *Making, Shaping and Treating of Steel, Steelmaking and Refining Volume*, 11th edn R. Fruehan (2001) AISE Steel Foundation, Washington, DC; (3) *Making, Shaping and Treating of Steel, Casting Volume*, 11th edn, A. Cramb (ed.), CD-ROM publication (2003) AISE Steel Foundation, Washington, DC; (4) B. Deo and R. Boom, *Fundamentals of Steelmaking Metallurgy*, 2nd edn (2005) Prentice Hall International, UK; (5) *Advanced Physical Chemistry for Process Metallurgy*, N. Sano, W.-K. Lu, P.V. Riboud (eds), Academic Press (1997).
2. *For steel product properties*, (1) T. Gladman, *The Physical Metallurgy of Microalloyed Steels*, The Institute of Metals, London, UK, 1996; (2) W.C. Leslie, *The Physical Metallurgy of Steels*, Hemisphere Publishing Co., Washington, USA, 1981.
3. *For more details of each section*, (1) *Proceedings Internat. Symp. for LC and ULC Sheet Steels* (1998); (2) *Proceedings Internat. Conf. TRIP aided High Strength Ferrous Alloys* (2002); (3) *Thermec 88*, Ed. I. Tamura, (1988, ISIJ, Tokyo); (4) *Accelerated Cooling of Steel*, Ed. P.D. Southwick, (1986, TMS-AIME, Warrendale).

13.8 References

1. AISI (Washington, DC), <http://www.steel.org>.
2. Y. Komiya, *R & D Kobe Steel Engineering Report*, 52(3), (Dec. 2002), 2.

3. T. Obara and K. Sakata, *Proceedings of 39th Mechanical Working and Steel Processing Congress*, Indianapolis, ISS, Warrendale, (1997), 307.
4. H. Senuma and K. Kawasaki, *ISIJ Internat.*, 34 (1994), 51.
5. K. Sakata, S. Matsuoka, T. Obara, K. Tsunoyama and S. Shiroishi, *Materia*, (JIM, Sendai), 36 (1997), 376.
6. F. Kitano, T. Urabe, T. Fujita, K. Nakajima and Y. Hosoya, *ISIJ Internat.*, 41 (2001), 1402.
7. Z. Morita and T. Emi (eds), *Introduction to Iron and Steel Processing*, Kawatetsu 21st Century Foundation, Text, Tape and Transparency Package, Tokyo (1998).
8. C. Ouchi, *ISIJ Internat.*, 41 (2001), 542. (Also, I. Kozasu, *Controlled Rolling and Controlled Cooling*, Chijin Shokan Co., Tokyo (1997).)
9. K. Oosawa, *Tetsu-to-Hagane*, ISIJ, Tokyo, 81 (1995), 449.
10. H. Ogawa, N. Kikuchi, T. Yamauchi and H. Nishikawa, *ISSTech 2003 Conf. Proceedings*, Pittsburgh, (2003), 335.
11. Y. Okada, K. Yada, T. Nagahata, K. Maya, H. Ikemiya, S. Fukagawa and K. Shinme, *Tetsu-to-Hagane*, ISIJ, Tokyo, 80 (1994), T9.
12. T. Uesugi, *Tetsu-to-Hagane*, ISIJ, Tokyo, 74 (1988), 1889.
13. K. Kume, K. Yonezawa, M. Yoshimi, H. Motowatari and M. Kumakura, *CAMP-ISIJ*, 16 (2003), 116.
14. T. Emi, T. and S. Seetharaman, *Scand. J. Metall.*, 29 (2000), 185.
15. K. Ahlborg, R.J. Fruehan, M.S. Potter, S.R. Badger and G.S. Casuccio, *ISSTech 2003 Conference Proceedings*, Pittsburgh, (2003), 177.
16. J. Lehman, P. Rocabois and H. Gaye, *J. Non-Cryst. Solids*, 282 (2001), 61.
17. M. Okimori, *Nippon Steel Technical Report*, No. 361 (1996), 67.
18. J. Schade, R.J. O'Malley, F.L. Kemeny, Y. Sahai and D.J. Zacharias, Chapter 13 'Tundish Operations', in *Making, Shaping and Treating of Steel, Casting Volume*, 11th edn, A. Cramb (ed.), CD-ROM publication (2003).
19. K. Isobe, H. Maede, K. Syukuri, S. Sato, T. Horie, M. Nikaidou and I. Suzuki, *Tetsu-to-Hagane*, 80 (1994), 42.
20. T. Emi, *J. Korean Ceram. Soc.*, 40 (2003), 1141.
21. I. Ogata and M. Sanui, *Ferrum*, ISIJ, Tokyo, 8 (2003), 818.
22. M. Naito and S. Matsuzaki, *CAMP-ISIJ*, 17 (2004), 2.
23. T. Emi and O. Wijk, *Steelmaking Conf. Proceedings*, ISS, Warrendale, 76 (1996), 551.
24. P. Scaife, J. Nunn, A. Cottrell and L. Wibberley, *ISIJ Internat.*, 42 (2002) S5. (Also, Report of ACARP Project C8049 Revision 2.00, February 29, (2000).)
25. N-S. Hur, *Proceedings Internat. Symp. Global Environment and Steel Industry*, CSM, Beijing, (2003), 50.
26. G. Denier, A. Kremer and J. L. Roth, *25th Symp. New Melting Technologies*, St Petersbourg, FL, ISS, Warrendale, May 11–14, (1997).
27. J.K. Shoop, J.C. Simmons and J.M. McClelland, *ISSTech 2003 Conf. Proceedings*, Pittsburgh, (2003), 379.
28. O. Iimura, *Proceedings Internat. Symp. Global Environment and Steel Industry*, CSM, Beijing, (2003), 38 (originally from Japan Iron and Steel Federation).
29. T. Emi and D.-J. Min, *Proceedings of 2nd Internat. Green Processing Conf.*, Freemantle, Australia, AIMM , May 11–14 (2004).
30. T. Emi, *High Temp. Materials and Processes*, 20(3-4), (2001), 167.

Index

- absorption coefficients 145–6
estimation 165–8
- absorptivity 212–14
- accelerated cooling (AcC) 516–18
- acid leaching 103–7
- activation area 458
- activation energy, falsification of 304–5
- activity 59, 60
- activity coefficients 61, 64, 65–6
- additive reaction times, law of 298–304
- additives 473
 uniaxial pressing 487
- adhesion, work of 134, 248, 249
- adhesional wetting 249
- adiabatic processes 44
- adsorption 246–8, 271–2, 391
- aerosol-based processing techniques 482–3
- alloying elements, processes to optimise 524–9
- alloys
 oxidation of 13
 reactive/high requirement 25–7
 thermal conductivity
 liquid alloys 162
 mushy phase alloys 163
 solid alloys 163
- alteration curve 91, 92, 100, 101
- alumina
 activity in slag models 76, 77, 379–80
 CaO-Al₂O₃-SiO₂ system 91–4
 inclusions 429–30, 431, 529–31
 spheroidised particles 430–1
- aluminium 13
 Al-Si binary system 102, 103
 deoxidation using 374, 382–4, 429–30, 512–14
- electrolytic production 317–18
- Ni-Al system 151
- annealing sector 536
- anode 315
- anode furnace (fire-refining furnace) 18–20
- API5LX pipeline 518–20
- Archimedean method 123
- area viscosity (surface dilatational viscosity) 247–8
- argon
 injection 395
 purging and dehydrogenation 386–7
- Arrhenius equation 147–8, 154, 189
- atomisation 28, 30–1, 477–82
- attrition 472
- attrition mills 474, 475, 476
- austenitic stainless steel 459, 460
- axial and radial flow methods 141
- backmixing, degree of 337–40
- Bain distortion 290
- bake-hardenable interstitial-free (BH-IF) steel 507, 508–16
 process development to produce BH-IF SEDDQ steel sheet 511–16
 properties required for BH-IF steel sheet 508–11
- Bakker equation 243–4
- ball bearings 521–3
- ball mills 474, 475, 476
- basic oxygen furnace (BOF) 371, 511–12, 513
- blast furnace-basic oxygen furnace (BF-BOF) route 504, 506, 538–9
- processes to optimise impurities and alloying elements 524–5, 526–7
- slag 547, 548–9
- batch casting processes 28
- Bauschinger effect 468
- bed porosity 234–5

- belt furnaces 385–6
 Bergström model 455
 binary systems 51, 52, 53
 binary diffusion couple 279
 diffusion in binary mixtures 272
 solidification 95
 binders 487
 black bodies 213
 blast furnace (BF) 4–5, 6, 178, 179, 370, 371
 blast furnace-basic oxygen furnace (BF-BOF) route 504, 506, 538–9
 combination of BF and EAF 541–4
 slag 76, 77, 378–80, 547
 blister copper (crude copper) 18
 bloom caster 534–5
 boiling point 251
 bond energies 62
 bottom-gas-injected solvent extraction process 331–40
 bottom tapping 522, 523
 boundary layer
 diffusion and vacuum degassing 25–6
 flow over a flat plate 227–32
 solidification of molten steel 266
 boundary lines 90–1, 92, 96, 97, 100, 101
 box annealing (BA) 508–9
 Bragg's law 113
 bridging oxygens 115, 116
 bubble flotation 391–3
 bubble injection 264
 bubbles
 foreign particles and bubble defects 266
 gas bubbles rising in metals 319–20
 buffer zone 225–6
 Burke-Plummer equation 235
- calcium 13
 Ca-S-O system 85–7
 solidification refining of silicon 104–7
 calcium oxide
 Ca-Al₂O₃-SiO₂ system 91–4
 Ca-SiO₂ system 152
 calorimetric analysis 362–3
 calorimetry 136–7
 CALPHAD approach 71–2
 capillary methods 144
 capillary reservoir method 148
 capillary viscometers 128
 capillary wave atomisation 478, 482
 carbide inclusions 534–5
 carbon
 Cr-C binary system 72
 injection 390
 reaction with oxygen on the surface of carbon 183–4
 reduction of metal oxides by 4–10, 306–8
 uphill diffusion 182
 carbon dioxide emissions 549–50, 551
 carbon monoxide, reduction of metal oxides by 4–10
 carbonyl process 485
 carburisation
 mass transfer 192–5
 reactions 7
 Carnot cycle 45
 casting 27–31, 370, 373, 428–49
 heat conduction in the mould controls heat transfer 29–30
 heat transport across the mould-solid metal controls the heat transfer 30–1
 integrated optimisation 536
 interactions between mould and steel shell 447–9
 precipitation of oxides 428–32
 solidification of mould slags 432–9
 surface of steel cast in an oscillating mould 439–42
 undercooling and initial solidification 443–7
 cathode 315
 cells 424, 426–7
 growth 427
 central atom model 68–9
 centrifugal atomisation 477, 478, 481–2
 ceramic moulds 29–30
 charcoal-water-gas system 392–3
 chemical diffusion 146
 chemical diffusion coefficient 279
 chemical driving force of the cell reaction 79
 chemical equilibrium 40, 44–8
 effect on gas-solid reaction kinetics 304–5
 chemical potentials 40, 59–60, 82
 potential diagrams 83–7
 chemical powder metallurgical processes 483–5
 chemical reaction fluxes 183–4
 chemical vapour decomposition (CVD) 485
 chemical vapour synthesis 15–17
 chill zone 439
 Chilton-Coburn j factors 276–7
 chlorides 15–16

- chlorination of rutile 326–30
 chromium 13
 Cr-C binary system 72
 Clapeyron equation 49–51
 Clausius-Clapeyron equation 50–1
 climb 455, 459
 closed systems 39
 ‘cloud’ solidification structure 433, 434,
 435
 CMn-steel 460, 461
 coal-based DRI processes 7–9
 coalescence 256–7
 coarsening 287, 407, 408, 429, 430, 493,
 494
 coking 13–14
 cold isostatic pressing 489
 cold plasmas 486
 cold rolling 464–7
 Coldstream process 477
 columnar structures 433, 434
 combined blowing converters 372
 commercial materials 120
 compaction 486–90
 compensation effect 148
 complete thermodynamic equilibrium 40
 complex gas-solid reactions 305–11
 components of a system 39
 composite wall 207–8
 compression 472
 computerised fluid dynamic (CFD)
 models 386, 393
 concentration gradient 182
 concentration profiles 191–8
 concentric cylinder method 124, 141
 condensation 485
 conduction 200–2, 273
 conservation equation 204–11
 steady state conduction 205–7
 heat conduction in the mould 29–30
 see also thermal conductivity
 configurational entropy 47
 congruent solidification 95
 conjugation line (tie-line) 88–91, 92
 conservation of heat 204–11
 heat loss through composite wall 207–8
 steady state conduction 205–7
 temperature distribution in a hollow
 cylinder 208–10
 temperature distribution in a spherical
 shell 210–11
 conservation of mass 190–8
 diffusion in solids 192–5
 evaporation of liquids 196–8
 conservation of momentum 221–32
 Consteel process 542, 543
 contact angle 133–4, 248–50
 container materials 121–2
 containerless methods 121
 contamination of powders 472, 475, 479
 continuous annealing (CA) 509–10
 continuous annealing line (CAL) 514,
 515
 continuous casting 28, 370, 373, 428,
 437–9, 522, 523
 surface of steel cast in an oscillating
 mould 428, 439–42
 continuous stirred tank reactor (CSTR)
 332–40
 controlling reactions 306–8
 convection 116, 117–19, 139, 200–1
 heat and mass transfer 275–8
 converter 370, 371–2
 converting
 copper 17–20
 sulphide 20, 321
 cooling rate 445–7
 copper 10
 smelting and converting 17–20
 Corex process 541
 corrosion
 local corrosion of refractories at
 interfaces 260–3, 314
 of zinc in a de-aerated environment
 315–17
 counter diffusion 186
 critical free energy 403–4
 critical nuclei, number of 256
 critical radius
 for droplet formation 408
 solidification 283, 403–4
 critical velocity 266, 388
 cross-slip 455, 459
 crude steel production 370, 371–2
 crystallisation curve 91, 92, 100, 101
 crystals, specific heat of 351–2, 353
 crystobollite 413, 414
 cuspidine 435–7
 cylindrical coordinate systems 182,
 191–2, 205, 222, 223
 evaporation of liquid 196–8
 flow through a pipe 221–7
 temperature distribution in a hollow
 cylinder 208–10
 Dalton’s law of partial pressures 54
 Debye characteristic temperature 351–2
 decarburisation 511–12
 decomposition reactions 14–15

- deep drawability 508–16
 defects
 in casting 110
 point defect formation and elimination
 278
 reducing on semis 551–2
 see also bubbles; impurities;
 inclusions
 deformation processing 32–4
 degassing, vacuum 25–6
 dehydrogenation 386–7
 dendritic fragmentation 434, 435
 dendrite morphology models 313
 dendrites 417, 419, 424, 426–7
 alumina 429, 430
 growth 427
 denitrogenation 391
 densification 491, 492, 493
 density 122–4, 126–7
 estimation 151–2
 models for calculating 152, 153
 deoxidation 374
 steel casting 428–32
 using aluminium 374, 382–4, 429–30,
 512–14
 dependent variables 40–1
 dephosphorisation 548
 de-polymerisation, degree of 116, 175–6
 desiliconisation 548
 desorption 271–2, 391
 desulphurisation 373, 520–1
 ladle treatment 381–2
 micro-modelling 393–6
 detachment method 132
 dew point detectors 364
 dicalcium silicate 435–7
 die casting 30–1
 die pressing 487–9
 differential power scanning calorimeter
 (DPSC) 137
 differential scanning calorimetry (DSC)
 137, 355, 360–1
 differential temperature scanning
 calorimetry (DTSC) 137
 differential thermal analysis (DTA) 355,
 356, 358–60
 calorimetric analysis 362–3
 DSC and 360–1
 diffraction 118
 diffuse interfaces 413
 diffusion
 in a binary mixture 272
 grain-pellet system with intra-grain
 diffusion effect 302–3
 homogenisation of compositional
 gradients 278–9
 multicomponent 272–3
 pore diffusion 274–5
 in solids 179, 192–5
 see also mass transfer
 diffusion coefficients 146–8
 estimating 168–9
 diffusion couple method 148
 diffusional transformations 281–2
 diffusivities 187–90, 272
 gases 187
 gases in porous solids 187–9
 liquids 189–90
 in solids 190
 dilatometry 123
 dilute solutions
 mass flux in 184
 multicomponent 66–70
 direct measurements for electrical
 resistivity 144
 direct metal deposition (DMD) 500
 direct metal laser sintering (DMLS) 500
 direct reduction (DR) technology 6–9
 direct strike precipitation 485
 direct thermal methods 353–4
 dislocations 454–7
 disorder 47
 dispersion 256–7, 258
 disregistry 412
 dividing surface, Gibbs' 238–9
 position of 240–1
 dolomite 14–15
 double-action die pressing 488–9
 double ultrasonic atomisation 482
 downstream processes 505, 506
 future development of 551, 552–3
 see also under individual processes
 drag force 232–5
 drainage 24–5
 draining crucible method 121, 123, 125,
 128
 driving energy 257, 258
 driving force 266
 drop calorimetry 137, 362
 drop weight method 132
 droplets
 experiments and superheating 443–7
 formation of 405–8
 dry pressing 487–9
 dry powder 3DP processes 499
 DTG curves 357
 dual-phase (DP) steel 507
 DP 600 468

- dynamic compaction 490
 dynamic interfacial tension 312–13
 dynamic strain ageing 459, 460
 dynamic techniques 119–20
- economic optimisation 537–46
 market and management 545–6
 production and investment 544–5
 raw materials and energy 538–44
- eddies 217–18
 effective diffusivity 187–9
 Einstein’s mass-energy relationship 42
 ejection pressure 447
 electromagnetic stirring (EMS) 534–5
 electric arc furnaces (EAFs) 6, 76, 77, 370, 371, 372
 combination of BF and EAF 541–4
 scrap-EAF route 504, 506, 539–40
 slag foaming 389–90
 slags 378–80, 384, 547, 549
 electric field assisted sintering (FAST) 497
 electric ironmaking furnace (EIF) 542–4
 electrical analogy for heat transfer 207, 216
 electrical conductivity 169
 electrical resistivity 126–7, 143–4
 estimation 160–2
 and thermal conductivity 138–9, 162
 electro slag remelting 26
 electrochemical method 148
 electrochemical reactions 314–18
 electrochemical thermodynamics 78, 79, 80
 electrodes 315
 electrolysis 479, 484
 electrolysis cells 315, 316
 electrolyte 315
 Ellingham diagrams 54–6, 83
 elongation 508
 emanation thermal analysis (ETA) 355, 365
 emissivity 126–7, 145, 212–14
 empirical slag models 75–6, 376
 emulsification 313
 of steel in slag 388–9
 energy
 developing steelmaking processes and properties 506–23
 processes driven by properties, environment and energy 516–21
 properties driven by market, environment and energy 507–16
 first law of thermodynamics 41–2
 raw materials and 538–44
 reducing energy consumption 551
 energy balance equation 204–11
 enthalpy 43, 47, 58, 59, 126–7
 DTA and 362
 estimation 149–51
 relative integral molar enthalpy 63
 enthalpy of fusion 119–20, 126–7, 149–50
 enthalpy interaction parameter 69
 entropy 45, 48, 58, 59
 and disorder 47
 entropy interaction parameter 69
 environment
 developing steelmaking processes and properties 506–23
 processes driven by properties, environment and energy 516–21
 properties driven by market, environment and energy 507–16
 environmental optimisation 546–9
 abatement of hazardous wastes 546
 minimisation, recycling and reuse of wastes 546–9
 equation of continuity 221–32
 equation of motion 221–32
 equiaxed crystals 433, 434
 equilibrium constant 59–60
 equilibrium partial pressure 406–7
 equimolar counter diffusion 183–4
 equivalent ionic fractions 73
 Ergun’s equation 235
 Eucken’s equation 203
 eutectic diagrams 51, 53
 eutectic point 91, 95, 96
 eutectoid transformations 281–2
 evaporation 447–8
 conservation of mass 196–8
 heat of evaporation 251
 melt 319
 evolved gas analysis (EGA) 355, 356, 363–5
 evolved gas detection (EGD) 355, 363–5
 excess properties 61–2
 excess stabilities 65–6
 exogenous oxide inclusions 531–3
 expendable moulds 28, 29–30
 exploding wire method 119, 121, 123, 137, 144
 explosive compaction 490
 extensive properties 40
 extinction coefficients 145–6
 extra deep drawing quality (EDDQ) steel 509–10
 SEDDQ steel 510–16

- extrusion 34, 490
 Eyring relation 169
- faceted crystals 433, 434–5
 falling ball method 124
 Fasteel process 542–4
 Fastmelt process 542
 Fastmet process 8, 542, 549
 ferrite 458–9
 ferritic perlitic steels 456
 ferritic steels 462
 Fick's laws of diffusion
 first law 146–7, 180, 182, 272, 278
 second law 146–7, 193, 278, 279
 filled billet technique 496
 film theory 198, 199
 fine powders 480
 fine superalloy powder 481
 Finex process 541
 FINMET-EAF 451
 fire-refining furnace 18–20
 first law of thermodynamics 41–4
 flame ionisation detectors 364
 flash smelting process 322–6
 flat grains 297
 flat interfaces 413
 flat plate, flow over 227–32
 floating die presses 488–9
 Flood *et al.*'s ion activity concept 73
 flotation coefficient 134, 392–3
 flow stress 456–7, 460, 461
 fluid flow 217–35
 conservation of momentum 221–32
 flow over a flat plate 227–32
 flow through a pipe 221–7
 friction factor and drag coefficient 232–5
 Newton's law of viscosity 218–20
 properties related to 113, 122–36
 viscosity of gases 220
 viscosity of liquids 221
 fluidised-bed processes 8, 9
 fluidised-bed reactors for gas-solid
 reactions 326–30
 foaming 264–5, 320–1, 389–90
 forced convection 201
 foreign particles 266–7
 forging 32, 33
 four-phase equilibria 95–101
 Fourier Transformed Infra Red (FTIR)
 method 365
 Fourier's law of heat conduction 201–2,
 273
 fraction solidified 437, 438
- free energy change 352
 and nucleation 402–4
 free oxygens 115
 Freundlich-Ostwald equation 252
 friction factor 232–5
 fugacity 54
 fused deposition modelling (FDM) 498–9
- galena 302
 galvanic cells 315, 316
 gas analysers 364
 gas atomisation 477, 478, 479, 480–1
 gas-based DRI processes 7–9
 gas chromatography 365
 gas-liquid reactions 318–21
 gas pipelines 516–20, 521
 gas purging 319–20
 gas-solid reactions
 high-temperature processes 4–17
 kinetics 290–311
 complex 305–11
 initially non-porous solid producing
 a porous product layer 291–4
 porous solids 294–311
 modelling fluidised-bed reactors
 326–30
 simultaneous 310
 successive 309–10
 gas tungsten arc (GTA) welding 109
 gases
 diffusion of binary mixtures 184–5
 diffusivity 187
 diffusivity in porous solids 187–9
 gas mixtures 54
 heat exchange by radiation and 217
 oxide reduction to produce powders
 483–4
 precipitation of powders from 485
 rate of heterogeneous reaction between
 gas and metal 263–4
 reaction of a porous solid with a gas
 accompanied by a volume change
 in the gas phase 303–4
 thermal conductivity 203
 viscosity of 220
 geometrical slip distance 455, 456–7
 Gibbs' adsorption equation 246–8
 Gibbs' dividing surface 238–9, 240–1
 Gibbs-Duhem equation 58
 Gibbs energy 45
 ideal mixing of silicates 74
 integral and partial molar 57–8
 relative integral and partial 58–9
 unary systems 49, 50

- variation with pressure and temperature 46
 Gibbs-Helmholtz equation 46
 Gibbs-Marangoni viscosity 248
 Gibbs phase rule 51–4
 Gibbs-Thompson effect 285, 406
 Gibbs triangle 87–8, 89
 Giddings equation for diffusivity of gases 187
 glass transition temperature 150, 410, 411
 glasses 122
 - structure 115–17
 - viscosity 125, 154, 157
 Good-Girafalco equation 134
 Graham's law 183
 grain-pellet system with intra-grain diffusion effect 302–3
 grain refined and precipitation hardened SEDDQ sheet 511
 grains
 - evolution of 280–1
 - grain model of porous solid 296–8
 grey bodies 213
 - heat exchange between 215–17
 grinding 472–3
 growth 284–6, 413–28
 - combining nucleation and growth kinetics 286, 287
 - gas-solid reactions 300–2
 - heat transfer dominated growth rates 415–25
 - interface dominated growth rates 413–15
 - mass transfer dominated growth rates 425–8
 - solidification of mould slags 435, 436
 Guggenheim's equation 403
 Gulliver Scheil equation 426
 haematite 4
 Hagen-Poiseuille law 224–5
 hazardous wastes, abatement of 546
 heat balance equation 204–11
 heat capacity 126–7, 136–8
 - estimation 149–51
 heat of evaporation 251
 heat flux
 - conduction 201–2
 - heat loss through composite wall 207–8
 - steady state heat conduction 205–7
 heat flux mode DSC 361
 heat generation 205
 heat transfer 40, 200–17, 290–1
 - casting moulds 28–31
 conduction *see* conduction
 conservation equation 204–11
 convection *see* convection
 growth rates dominated by 415–25
 heterogeneous kinetics 272–8
 properties related to 113, 136–46
 radiation 200–1, 212–17, 277–8
 resistance to 423–4, 437–8
 steelmaking process design 385–7
 thermal conductivity *see* thermal conductivity
 heat transfer coefficients 31, 211–12, 423
 heat treatment sector 536
 heating, phase transformation upon 286
 Helmholtz energy 45
 Henry's law 63–4, 66
 Hess's law of constant heat summation 42–3
 heterogeneous kinetics 270–8
 - adsorption and desorption 271–2
 - heat and mass transfer 272–8
 - rate of reaction between gas and metal or slag and metal 263–4*see also* kinetics of metallurgical reactions
 heterogeneous nucleation 255, 284, 402, 404–5
 - nucleation rate 411–12
 heterogeneous systems 39
 high-energy rate compaction 490
 high manganese steels 448
 high performance steel products 549–50
 high requirement/reactive alloys 25–7
 high strength low alloy (HSLA) steel 462, 516
 high-temperature processes 3–37
 - casting processes 27–31
 - heat conduction in the mould 29–30
 - heat transport across the mould 30–1
 - reactions involving gases and solids 4–17
 - chemical vapour synthesis of metallic and intermetallic powders 15–17
 - coking 13–14
 - decomposition reactions 14–15
 - oxidation 10–13
 - reduction of metal oxides 4–10
 - reactions involving liquid phases 17–27
 - processes for reactive/high-requirement alloys 25–7
 - slag refining 21–5
 - smelting and converting 17–20
 - thermomechanical processes 31–4

- deformation processing 32–4
 Hill yield criterion 465
 HIsmelt 541
 HMPT 520, 524–7, 552
 incorporation into BF–BOF route 548
 slag 547, 548–9
 hollow cylinder 208–10
 hollow spherical shell 210–11
 homogeneous nucleation 253–5, 282–4,
 402–4
 nucleation rate 408–11
 homogeneous systems 39
 homogenisation of compositional
 gradients 278–9
 horizontal casting 447
 horizontal mills 474, 475, 476
 attritor 474, 476
 ball mill 474, 476
 hot extrusion 496
 hot forging 496–7
 hot gas atomisation 481
 hot isostatic pressure (HIP) 496
 hot metal charging 541–2
 hot pressing 495
 hot rolling 463–4, 465, 510–11
 hydrated barium hydroxide 364
 hydraulic radius 232
 hydride-dehydride process 485
 hydrogen
 reduction of metal oxides by 4–10
 vapour-phase reduction of metal
 chlorides 15–16
 hydrogen induced cracking (HIC) 519–20
 hydrogen sulphide 519
 hydrophilic non-solvent addition 484
 hydrostatic probe 123
 HYL process 8, 9
 hypercooling 417
 hysteresis of wetting 250
- ice calorimetry 362
 ideal mixing 74, 376–7
 ideal-reactor-network model 332–40
 ideal solutions 60–1, 62
 immersional wetting 249
 impaction 472
 impurities 21–2
 future development of processes to
 reduce 551–2
 processes to optimise 524–9, 530
 removal for reactive/high requirement
 alloys 25–7
 slag refining 21–5
 impurity diffusion 146
- inclusions 22, 266–7
 critical inclusion sizes 525
 effect of interfacial energy on
 separation of inclusions by bubble
 flotation 391–3
 future development of processes to
 reduce 551–2
 oxide inclusions in ball bearings
 522–3
 precipitation of oxides in steel casting
 428–32
 processes for controlling 529–35
 removal 23–5
 incongruent solidification 95
 independent variables 40–1
 indigenous oxide inclusions 529–31
 indirect methods for electrical resistivity
 144–6
 indirect precipitation 484–5
 indirect rapid prototyping 498
 inert gas condensation (IGC) 483, 485
 inert gas purging 320, 386–7
 inert species, flux of 184
 infiltration 497–8
 ingot casting 370, 373, 428, 447
 ink jet printing (IJP) 499
 inner state variable 41, 42
 instantaneous plane method 148
 integral molar properties 57–8, 60
 relative 58–9, 61, 63
 integrated iron and steel plants 528, 529,
 539, 544
 integrated optimisation processes 535–7
 intensive properties 40
 interaction parameters 68–9
 estimations 69
 and solubility of oxides in metallic
 melts 70
 interdiffusivity 146, 190
 interface instability 426–7
 interface temperature 415–18
 interfacial phenomena 117, 237–69
 fundamentals of the interface 238–57
 mechanical aspects of surface
 tension 243–6
 physical chemistry 246–57
 thermodynamics 238–43
 interface dominated growth rates
 413–15
 mass transfer 198–200
 metallurgical melts system 257–60
 interfacial tension between slag and
 metal 259–60, 312–13
 surface tension 257–9

- wetting of ceramics by liquid metal and slag at high temperature 260
- metallurgical processing and 260–7
 - bubble injection 264
 - interaction of foreign particles with solid-liquid interface 266–7
 - local corrosion of refractories 260–3
 - penetration of slag or metal into refractory 265–6
 - rate of heterogeneous reaction 263–4
- optimisation of interfacial reactions in steelmaking 387–93
- slag foaming 264–5, 320–1, 389–90
- slag-metal mixing 388–9, 394–6
- interfacial tension 117, 129, 133–6, 248–50
 - estimation 163
 - slag-metal 259–60, 312–13
- intermediate zone 225–6
- intermetallic powders 15–17
- interrupted accelerated cooling (IAC) 516–18
- intra-grain diffusion effect 302–3
- intrinsic diffusivity 190
- inverse rate cooling 354
- inverse thermal methods 353–4
- investment 544–5
- investment casting 29–30
- ion activities 73
- ionic melts 72–9
 - KTH model 76, 77, 377–8, 384
 - Lumsden's description of silicates 75
 - Richardson's theory of ideal mixing of silicates 74
 - slag capacities 23, 76–9, 381–2
 - slag models 75–6, 77, 376–80
 - Temkin's and Flood *et al.*'s description 73
- iron
 - direct reduced iron (DRI) 6–9
 - removal from silicon by acid leakage 104–7
- iron oxides
 - phase diagrams 83, 84, 85
 - reduction 4–9
- iron silicide phase 104–7
- irregular powders 472, 479, 480
- irreversible processes 44–5
- IRSID model 76, 376
- isolated systems 39
- isostatic pressing 489
- isothermal cross-section 88–91, 92
- isothermal processes 44
- isothermal thermogravimetry 358
- isothermal transformations 352, 353
- isotropic materials 202
- ITmk3 process 8, 541
- Jacob-Alcock empirical equation 69
- Japanese steel industry 547, 549, 550
- Johnson-Mehl-Avrami equation 286, 414
- Kelvin equation 244, 251, 406–7, 408
- kinetics of metallurgical reactions 270–349
 - comprehensive process modelling 321–40
 - bottom-gas-injected solvent extraction process 331–40
 - flash smelting process 322–6
 - fluidised-bed reactors for gas–solid reactions 326–30
- gas–liquid reactions 318–21
- gas–solid reactions 290–311
 - initially non-porous solid producing a porous product layer 291–4
 - reaction of a porous solid 294–311
- heterogeneous kinetics 270–8
 - adsorption and desorption reactions 271–2
 - heat and mass transfer 272–8
- kinetic block in micro-modelling 394–5
- liquid–liquid reactions 311–13
- solid–liquid reactions 313–18
- solid-state reactions 278–90
 - multiphase reactions 281–90
 - single phase reactions 278–81
- steelmaking process design 385–7
- Kirchhoff's law 214
- Kirkendall shifts 279
- Knudsen diffusion 188–9
- Kolmogorov-Johnson-Mehl-Avrami (KJMA) equation 414
- Kozeny-Carman equation 235
- KTH model 76, 77, 377–8, 384
- ladle degassing 522
- ladle furnaces 76, 77, 527–9
 - slags 378–80, 547, 549
- ladle treatment 373–5
 - dehydrogenation 386–7
 - desulphurisation 381–2
 - micro-modelling of sulphur refining 393–6
 - thermodynamics and mass balance 382–4
- laminar flow 217–18

- in a pipe 221–7
- laminar sub-layer (viscous sub-layer) 225–6
- Langmuir-Hinshelwood rate equation 271, 294
- Laplace's equation 244–5
- large drop method 123, 131
- laser cladding (LC) 500
- laser engineered net shaping (LENS) 500
- laser powder deposition processes 498, 500
- laser pulse method 121, 141–2
- latent heat 352–3
- lattice disregistry 412
- Laval nozzle 481
- law of additive reaction times 298–304
- lead smelting 20, 375
- leakage rates 186
- ledge mechanism 285
- levelling 467–8
- levitated drop calorimetry 137
- levitated drop method 123
- levitation 121
- lifecycle analysis 549–50
- lime 308–10
- limestone, decomposition of 14
- limiting drawing ratio (LDR) 508
- liquid alloys, thermal conductivity of 162
- liquid-gas reactions 318–21
- liquid-liquid reactions 311–13
- liquid metal solution calorimetry 362–3
- liquid metals
 - interfacial properties of a metallurgical melts system 257–60
 - thermodynamic description for steelmaking 376, 380
- liquid phase sintering 493–4
- liquid-solid reactions *see* solid-liquid reactions
- liquids
 - diffusivity in 189–90
 - evaporation 196–8
 - high-temperature processes involving liquid reactions 17–27
 - nucleation at liquid-liquid interface 405
 - thermal conductivity 203
 - viscosity of 220
- local solidification time 110, 112
- logarithmic rate of oxidation 12
- lubricants 487
- Lumsden's description of silicates 75
- macro inclusions 531–3
- magnesite 14
- magnesium 10
 - reduction of metal chlorides 16–17
- magnesium carbonate 14–15
- magnesium oxide
 - erosion of refractories 314
 - reduction of 10
- magnesium sulphide 519
- management, market and 545–6
- management system for integrated processes 537
- manganese oxide 448
- Marangoni effect 245–6
- Marangoni flows 245–6, 261–3, 314
- Marangoni viscosity 248
- marginal stability criterion 426–8
- market
 - developing steelmaking processes and properties 506–23
 - properties driven by market, environment and energy 507–16
 - and management 545–6
- martensite formation 456, 457
- martensitic steel, tempered 507
- martensitic transformations 290
- mass balance 190–4
 - constraints and steelmaking 381–2
 - ladle treatment 382–4
 - sub-processes and 374
- mass flux 180–6
 - components of 182
 - relation between fluxes 183–6
- mass spectroscopy (MS) 365
- mass transfer 40, 178–200, 211–12
 - conservation of mass 190–8
 - diffusivity of gases, solids and liquids 187–90
 - gas purging 319–20
 - gas-solid reactions 290–1, 304
 - growth rate dominated by 425–8
 - heterogeneous kinetics 272–8
 - high temperature oxidation 11–12
 - interface mass transfer 198–200
 - mass flux 180–6
 - properties related to 113, 146–8
 - steelmaking process design 385–7
- mass transfer coefficient 198–9
 - correlations for 199–200
- matte smelting (mattemaking) 17–18
- maximum bubble pressure (MBP) method 123, 132
- maximum drop pressure (MDP) method 135–6
- Maxwell's relations 46
- mechanical alloying (MA) 472, 473–4, 479

- mechanical equilibrium 40
 mechanical milling 473
 mechanical powder production processes 472–7
 medium carbon steels 439, 440
 melt evaporation 319
 melt reoxidation 318–19
 melting point 252
 meniscus solidification 439–42
 metal injection moulding (MIM) 489–90
 metal working processes 453–70
 development trends 468–9
 examples of material behaviour during processing 463–8
 cold rolling 464–7
 hot rolling 463–4
 levelling 467–8
 skin-pass rolling 467
 interaction with phase transformations 462–3
 rate effects 457–61
 work hardening 32, 454–7
 metallic systems, thermodynamic modelling of 70–2
 metallurgical process modelling 321–40
 bottom-gas-injected solvent extraction processes 331–40
 flash smelting process 322–6
 fluidised-bed reactors for gas-solid reactions 326–30
 metals 122
 electrical resistivity 160–2
 surface tension 129–33
 thermal conductivity 162–3
 viscosity 125–8, 159, 160
 metastable phases 408–12, 474
 method of mixtures 362
 micro-gravity 121
 micro-modelling 393–6
 microporosity models 313
 microwave sintering 494–5
 MIDREX 8, 9
 MIDREX-EAF 541
 milling 479
 mechanical 473
 technologies 474–7
 mixer-settler systems 331, 340
 mixing 57
 Mizukami's technique 443, 444
 molar concentration 271–2
 molar heat capacity 43–4, 350
 molar rate of consumption of fluid
 reactant per unit area of reaction interface 271
 molar volume 151–2
 relation of diffusion constants to 168
 molecular dynamics (MD) 118
 molybdenum 10
 momentum, conservation of 221–32
 momentum flux 219–20
 Mond process 9
 mould slags, solidification of 432–9
 moulds 27–31
 cooling against a mould 419–25
 expendable ceramic 29–30
 heat transport across the mould-solid metal 30–1
 interactions between mould and steel shell 447–9
 oscillating 28, 428, 439–42
 rotating 26, 428
 see also casting
 multicomponent diffusion 272–3
 multicomponent systems 51–7
 multicomponent dilute solutions 66–70
 central atom description 68–9
 estimation of interaction parameters 69
 interaction parameters and solubility of oxides in metallic melts 70
 Wagner's equation 66–7
 multiparticle systems 310–11
 multiphase jet solidification (MJS) 499
 multiphase materials, work hardening of 455–7
 multiphase reactions 281–90
 coarsening 287
 combining nucleation and growth kinetics 286, 287
 diffusional transformations 281–2
 growth 284–6
 martensitic transformations 290
 nucleation 282–4
 ordering 289–90
 phase transformation upon heating 286–7
 precipitation of multiple phases 435–7
 spinodal decomposition 288–9
 mushy zone 120, 139, 163, 424
 mutual (inter) diffusivity 146, 190
 nanoparticles 486
 natural convection 201, 276
 Navier-Stokes equation 221, 222–3
 near-net shape forming processes 486–500
 compaction 486–90
 electric field assisted sintering 497

- hot extrusion 496
 hot forging 496–7
 hot isostatic processing 496
 hot pressing 495
 infiltration 497–8
 rapid prototyping 498–500
 sintering 490–5
 negative strip time 439–42
 Nernst-Einstein equation 169
 Nernst equation 79, 315
 new iron and steelmaking processes 540–1
 Newmann Kopp rule 48
 Newton's law 233
 Newton's law of viscosity 218–20
 nickel 9, 13
 Ni-Al system 151
 smelting 20
 nickel-based superalloys 119
 nickel carbonyl 15
 nickel sulphide 56, 57
 nitride inclusions 534–5
 nitrogen 263–4
 non-bridging oxygens (NBO) 115, 116
 NBO/T 116, 175
 non-equilibrium solidification 98–9, 100
 nucleation rate and 408–12
 non-isothermal transformations 352, 353, 354
 non-isotropic materials 202
 non-metallic inclusions *see* inclusions
 normal solidification 419–20
 normalising process 166
 nozzle clogging 266–7
 nozzle design 480–1
 nucleation 290, 402–5
 effects of size 405–8
 gas-solid reactions 300–2
 kinetics 256, 282–4
 combining with growth kinetics 286, 287
 rate 284
 alumina formation 429
 and formation of non-equilibrium
 solids 408–12
 subgrains and recrystallisation 460
 thermodynamics of 253–5
 Nusselt number 211–12
 oil atomisation 477, 478, 480
 open systems 39
 optical basicity 116, 175–6
 optical properties 145–6
 estimation 165–8
 optical thickness 140–1
 ordering 289–90
 oscillating drop method 128, 132
 oscillating plate method 125
 oscillating viscometers 128
 oscillation marks 439–42
 oscillation mould casters 28, 428
 surface of steel 428, 439–42
 Ostwald ripening 252, 253, 407, 493, 494
 overflow oscillation marks 439–42
 overpotentials 316
 oxidation 315
 high temperature 10–13
 of metal sulphides with lime in the
 presence of water vapour 308–9
 oxide-dispersion strengthened (ODS)
 materials 474
 oxide-graphite refractories 262–3
 oxide inclusions 529–33
 ball bearings 522–3
 exogenous 531–3
 indigenous 529–31
 oxide metallurgy 431–2
 oxide scale 11–13
 oxides
 Ellingham diagrams 54–6, 83
 precipitation in steel casting 428–32
 reduction of 4–10, 306–8
 and powder production 483–4
 representation of ternary oxide systems 91–4
 solubility in metallic melts 70
 oxygen 264
 bridging oxygens 115, 116
 Ca-S-O system 85–7
 free oxygens 115
 injection 390
 and measurement of surface tension 129–31
 non-bridging oxygens *see* non-bridging
 oxygens
 reaction with carbon on the surface of
 carbon 183–4
 packed bed 234–5
 pair distribution factor 113–15
 parabolic time dependence 11–12
 paraboloid 427, 428
 parallel plate method 141
 partial molar method 149, 150
 partial molar properties 57–8, 60
 relative 58–9
 partial pressure 271
 Dalton's law of partial pressures 54

- equilibrium partial pressure 406–7
- particle pushing models 313
- particle shape 471–2, 478–9
- particle size 234–5
- Peierls-Nabarro barrier 458
- pelletising 370, 371
- pendent drop method 121, 131–2
- peritectic diagrams 51, 53
- peritectic point 91
- peritectic steels 439, 440
- phase diagrams 51, 52, 53, 82–108
 - CALPHAD approach 71–2
 - and potential diagrams 83–7
 - solidification 95–107, 400–2, 408
 - examples of solidification behaviour from a phase diagram perspective 102–7
 - ternary systems and four-phase equilibria 95–101
 - ternary phase diagrams 87–94
- phase rule 252–3
- phase stability diagrams 56, 57
- phase transformations 281–90
 - coarsening 287
 - combining nucleation and growth kinetics 286, 287
 - diffusional 281–2
 - growth 284–6
 - upon heating 286
 - hot deformation and 462–3
 - martensitic 290
 - nucleation 282–4
 - ordering 289–90
 - specific heat of crystals and 351–2, 353
 - spinodal decomposition 288–9
 - in ternary systems 99–101
 - see also* phase diagrams
- phases 39
- phenomenon block of micro-modelling 394, 396
- phosphate capacity of a slag 23
- physical properties
 - at high temperatures *see* thermo-physical properties
 - physical property block in micro-modelling 394
- physical vapour deposition (PVD) 483
- Pilling-Bedworth ratio (PB ratio) 12–13
- pipe, flow through a 221–7
- pipelines 516–20, 521
- plane temperature wave (PTW) method 142–3
- planetary ball mills 474, 475, 476
- plasma techniques 485–6
- plastic strain ratio 508
- plasticisers 487
- point defects 278
- polymerisation, degree of 116
- polymers 365
- pores 22
 - solid state sintering 492–3
- porosity, bed 234–5
- porous pellets 273–4, 310
 - grain-pellet system with intra-grain diffusion effect 302–3
- porous product layer 291–4
- porous purging plugs 265–6
- porous solids 187–9
 - heat and mass transfer 273–5
 - kinetics of gas-solid reactions 294–311
 - complex gas-solid reactions 305–11
 - effect of chemical equilibrium on and falsification of activation energy 304–5
 - grain model 296–8
 - law of additive reaction times 298–304
 - nucleation-and-growth kinetics 300–2
 - potentials 40, 59–60, 82
 - potential diagrams 83–7
- powder metallurgy (PM) 471–502
 - chemical vapour synthesis of metallic and intermetallic powders 15–17
 - near-net shape forming processes 486–500
 - compaction 486–90
 - electric field assisted sintering 497
 - hot extrusion 496
 - hot forging 496–7
 - hot isostatic processing 496
 - hot pressing 495
 - infiltration 497–8
 - rapid prototyping 498–500
 - sintering 490–5
 - production processes for powders 471–86
 - aerosol routes 482–3
 - atomisation 28, 30–1, 477–82
 - chemical routes 483–5
 - mechanical routes 472–7
 - physical routes 483
 - plasma techniques 485–6
 - powder rolling 490
 - power compensation DSC 360–1
 - Prandtl number 211–12
 - precipitation 400, 401, 402, 462, 479

- of oxides in steel casting 428–32
- of powders from a gas 485
- of powders from a solution 478, 484–5
- precipitation from homogeneous solution (PFHS) 484
- precipitation hardened steel 507
- precipitation transformations 281–2
- predominance area diagrams (phase stability diagrams) 56, 57
- primary crystals 96, 98
- primary phase fields 96
- process control agents (PCAs) 473, 474
- process control systems 468–9
- process design 369–98
 - kinetics 385–7
 - mass balance constraints 381–2
 - micro-modelling 393–6
 - optimisation of interfacial reactions 387–93
 - denitrogenation 391
 - foaming 389–90
 - separation of inclusions by bubble flotation 391–3
 - slag-metal mixing 388–9
 - overview of 369–75
 - sub-process 373–5
 - whole process 369–73
- thermodynamic description 375–80
- thermodynamics and mass balance in ladle treatment 382–4
- process integration
 - integrated iron and steel plants 528, 529, 539, 544
 - integrated optimisation of processes 535–7
- processing routes 369, 370
- production, and investment 544–5
- production line 369–73
- protective oxide scale 12–13
- pseudo-binary phase diagram 89, 91
- pseudo-steady-state approximation 294
- pycnometry 123
- pyrometer 353
- quality 537
- radial distribution factor (rdf) 114, 115
- radial temperature wave (RTW) method 142
- radiation 200–1, 212–17, 277–8
 - emissivity and absorptivity 126–7, 145–6, 212–14
 - heat exchange between grey bodies 215–17
- view factors 214–15, 277
- radiation conductivity 139–41, 143
- radiosity 215
- radius
 - of droplets 405–8
 - and growth rate 418
- radius of curvature 241–2
 - influence of 250–3
- Ranz-Marshall correlation
 - heat transfer 211, 276
 - mass transfer 199–200, 276
- Raoult's law 60–1, 63
- rapid prototyping (RP) 498–500
- rate effects 457–61
 - low to ambient temperatures 458–9
 - warm to hot working temperatures 459–61
- raw materials 538–44
 - downgraded 551
- Rayleigh scattering 148
- reaction rates 375
- reaction sintering 494
- reactive/high-requirement alloys 25–7
- reactive wetting 133
- reactivity of sample 120–2
- rebound force 24
- reciprocity relation 215, 216, 277
- recrystallisation 459–61
- rectangular coordinate systems 182, 191–2, 205, 222
 - steady state heat conduction 205–7
- recycling of wastes 546–9
- reducing agent rate (RAR) 538–9
- reduction 314–15
 - of metal oxides 4–10, 306–8
- reference states for thermodynamic properties 47–8
- refining 535–6
 - slag 21–5
 - solidification refining 102–7
 - zone refining 26–7
 - reflectance methods 146
 - reforming reactions 7
 - refractive indices 168
 - refractories
 - local corrosion at slag-gas and slag–metal interfaces 260–3
 - metal-melt refractory reactions 314
 - penetration of slag or metal into 265–6
 - regular solution model 63, 377
 - relative integral molar properties 58–9, 61, 63
 - relative partial molar properties 58–9
 - reoxidation, melt 318–19

- research and development (R&D) 546
 residence-time distribution (RTD) 332–40
 resistances to heat transfer 423–4, 437–8
 reuse of wastes 546–9
 reversible processes 44–5
 Reynolds number 199, 225, 230, 232
 Richard's rule 47
 Richardson's theory of ideal mixing of silicates 74
 roll compacting 490
 rolling 32, 33, 536
 rotating bob method 124
 rotating crucible method 124
 rotating electrode process (REP) 481–2
 rotating magnetic field method 144
 rotating mould casters 28, 428
 roughness of cast surface 444, 445
 Ruhr Stahl-Hausen (RH) process 509–10, 512, 514, 527, 529
 desulphurisation of steel in RH vessel 520–1
 and oxide inclusions 522–3
 rupture 24–5
 rutile, chlorination of 326–30
- sand casting 29–30
 Schmidt number 199
 scrap
 hot metal vs in economic optimisation 538–40
 recycling 370, 372
 scrap-EAF route 504, 506, 539–40
 scrap-EAF-thin slab CC-Hot Rolling Mill 545
 second law of thermodynamics 44–5
 secondary dendrite arm spacing 445–6
 secondary refining furnaces 504, 506
 secondary refining processes 370, 372–3, 523, 524
 optimisation of impurities and 527–9
 secondary solidification 96, 98, 99
 segregation 426
 control of inclusions 534–5
 selective laser melting (SLM) 500
 selective laser sintering (SLS) 499
 self diffusion 146, 168
 semi-empirical slag models 75–6, 376
 sessile drop method 123, 131, 135
 shaft furnaces 8, 9
 shape casting 29–30, 31
 see also near-net shape forming processes
 shape changes: deformation processing 31, 32–4
 shear 472
 shear method 148
 shear stress 219
 shell, steel 28–9, 30–1
 heat-transfer dominated growth and mould-shell interface 419–24
 interactions between mould and 447–9
 Sherritt Gordon process 484
 Sherwood number 199–200
 shrinking-core reaction system 291–4
 Shuttleworth's equation 242–3
 Sievert's law 63–4
 silica
 CaO-Al₂O₃-SiO₂ system 91–4
 CaO-SiO₂ system 152
 silicates 73, 377
 indigenous oxide inclusions 529–31
 Lumsden's description of 75
 Richardson's theory of ideal mixing of 74
 see also ionic melts
 silicon 102–3
 Al-Si system 102, 103
 reduction to minimise BOF slag 548
 segregation coefficients of impurities in 103
 solidification behaviour of a ternary silicon-based alloy 103–7
 silicon oxide/metal oxide ratio 22
 similarity transform 194
 simultaneous gas-solid reactions 310
 single-action die pressing 488
 single pan calorimeter 137
 single phase materials, work hardening of 454–5
 single phase reactions 278–81
 sintering 370, 371, 490–5
 in a belt furnace 385–6
 mechanisms 491, 492, 493
 parameters 491
 size effects, and solidification 405–8
 skin-pass rolling 467
 slag 122
 compositions in different processes 378–80
 electro slag remelting 26
 interfacial tension between slag and metal 259–60, 312–13
 local corrosion of refractories at slag-gas and slag-metal interfaces 260–3
 minimisation, recycling and reuse of wastes 546–9
 penetration into refractory 265–6

- rate of heterogeneous reaction between slag and metal 263–4
- reactions between molten metals and slags 312–13
- refining 21–5
- solidification of mould slags 432–9
- structure 115–17
- surface tension 129–33, 165, 166–7
- thermal conductivity 163
- viscosity 124–5, 154, 155–7, 160
- wetting of ceramics at high temperature 260
- slag capacities 23, 76–9, 381–2
- slag foaming 264–5, 320–1, 389–90
- slag line attack 260–3, 314
- slag meniscus (slag film) 261–2
- slag-metal mixing 388–9
- micro-modelling 394–6
- slag models 75–6, 77, 376–80
- smelting 17–20
- of lead 20, 375
- modelling the flash smelting process 322–6
- sulphide smelting and converting reactions 321
- soda-iron smelting system 375
- SOHNEX process 331–40
- solid alloys, thermal conductivity of 163
- solid-gas reactions *see* gas-solid reactions
- solid-liquid reactions
- application of law of additive reaction times 302
- kinetics 313–18
- electrochemical reactions 314–18
- metal-melt refractory reactions 314
- solidification 313
- solid-solid reactions
- proceeding through gaseous intermediaries with a net production of gases 306–8
- proceeding through gaseous intermediaries with no net production of gases 308–9
- solid-solution hardened steel 507
- solid-state reactions 278–90
- multiphase 281–90
- single phase 278–81
- solid state sintering 492–3
- solidification 27–8, 313, 399–452
- casting of steels 428–49
- interactions between mould and steel shell 447–9
- precipitation of oxides 428–32
- solidification of mould slags 432–9
- surface of steel cast in an oscillating mould 428, 439–42
- undercooling and initial solidification 443–7
- experimental observations 399–400
- fundamentals 400–12
- conditions necessary 400–1, 402
- effects of size 405–8
- nucleation rate and formation of non-equilibrium solids 408–12
- thermodynamics 401–5
- growth of solids 413–28
- heat transfer dominated growth rates 415–25
- interface dominated growth rates 413–15
- mass transfer dominated growth rates 425–8
- heat transfer resistances 28–9
- phase diagrams *see* phase diagrams
- solidification refining 102–7
- solids
- diffusion in 179, 192–5
- diffusivities in 190
- thermal conductivity 203–4
- solubility 252, 253
- change during solidification for impurities 21
- soluble-gas atomisation (vacuum atomisation) 477, 478, 481
- solutions
- ideal 60–1, 62
- mass flux in dilute solutions 184
- precipitation of powders from 478, 484–5
- regular 63, 377
- solution models for liquid metals 376, 380
- see also* slag models
- thermodynamics of *see* thermodynamics
- solvent extraction 331–40
- solvent removal (sol-gel) precipitation 484
- Soret diffusion 146
- ‘spark’ sintering 497
- specific heat 350, 354
- of crystals and phase transition 351–2, 353
- DTA and 362–3
- spectral emissivity 145
- spectroscopy 118
- sphalerite 9
- sphere, flow around a 232–3

- spherical atomised powders 471–2, 479, 480
 spherical coordinate systems 182, 191–2, 205, 222, 223
 temperature distribution in a spherical shell 210–11
 spinel inclusions 523
 spinodal decomposition 288–9
 sponge iron 6–9
 sponge powders (oxide-reduced powders) 483–4
 spray column contactors 331
 spreading coefficient 134, 248, 249
 spreading wetting 249
 stabilities 65–6
 stability diagrams 56, 57, 79, 80
 stagnant film 198, 199
 standard electrode potentials 78, 79
 standard states 64
 state 39
 state properties 40–1
 steady state techniques 141
 steel casting *see* casting
 steelmaking processes and properties 503–54
 developing with reference to market, energy and environment 506–23
 processes driven by properties, environment and energy 516–21
 properties driven by market, environment and energy 507–16
 properties driven by processes 521–3
 economic optimisation 537–46
 market and management 545–6
 production and investment 544–5
 raw materials and energy 538–44
 environmental optimisation 546–50
 abatement of hazardous wastes 546
 lifetime analysis of steels 549–50
 minimisation, recycling and reuse of wastes 546–9
 future trends 550–3
 downstream processes for better material properties 552–3
 energy consumption, carbon dioxide emissions and downgrading raw materials 551
 general trend for processes and properties 550–1
 upstream processes to reduce impurities, inclusions and defects 551–2
 optimisation of processes to meet properties and productivity 523–37
 controlling inclusions 529–35
 integrated optimisation of refining, casting, rolling and heat treatment 535–7
 optimising impurities and alloying elements 524–9, 530
 overview of process 504–5
 process design *see* process design
 Stefan-Boltzmann equation 214, 277
 Stefan number 417
 Stefan's law 423
 stereolithography (SL or SLA) 498
 Stokes-Einstein equation 168–9
 Stokes law 233
 strain rates 453
 rate effects 457–61
 stretch formability 508
 strip casting 30–1
 strontium carbonate 15
 structural slag models 75–6, 376
 structure
 methods of determining 117, 118
 and physical properties 113–17, 118
 subgrains 460
 sub-processes 373–5
 successive gas-solid reactions 309–10
 sulphate decomposition 15
 sulphide capacity 23, 76–9, 381–2
 sulphides
 decomposition 15
 hydrogen reduction of in the presence of lime 309–10
 inclusions 534–5
 modelling the flash smelting process 322–6
 oxidation with lime in the presence of water vapour 308–9
 smelting and converting reactions 321
 sulphur
 Ca-S-O system 85–7
 effect on steel's surface tension 109–10, 111
 refining in ladle treatment 393–6
 in slag 22–3
see also desulphurisation
 sulphur partition ratio 381–2
 sulphurisation 389
 super extra deep drawing quality (SEDDQ) steel 510–11
 process development to produce BH-IF SEDDQ steel sheet 511–16
 super structures 289–90
 superalloys 150
 superheat 443–7

- supersaturation 400, 401, 402
 nucleation rate 409, 410
- surface
 roughness 444, 445
 of steel cast in an oscillating mould 428, 439–42
- surface activity 117
 solutes in liquid iron 258–9
- surface coating sector 536
- surface dilational viscosity (area viscosity) 247–8
- surface energy: solidification and 404, 405–8
- surface excess quantities 239
- surface laser light scattering method (SLLS) 121, 125, 128, 132
- surface of tension 241
- surface stress 242–3
- surface tension 126–7, 129–34, 239–42
 effect of sulphur on steel's 109–10, 111
 estimation 163–5, 166–7
 liquid metals 257–9
 mechanical aspects 243–6
 mechanical definition 243–4
 position of dividing surface 240–1
 radius of curvature 241–2
 slag 129–33, 165, 166–7
 and surface stress 242–3
 temperature 242
 thermodynamic interpretation 239–40
- systems, in thermodynamics 39
- Szegvari attrition mill 475
- tandem atomisation 481
- tangential pressure 243–4
- tarnishing (high temperature oxidation) 10–13
- Tecnored 541
- Temkin's ion activity concept 73
- temperature
 distribution in hollow cylinder 208–10
 distribution in spherical shell 210–11
 rate effects 457–61
 low to ambient temperatures 458–9
 warm to hot temperatures 459–61
 and surface tension 242
 typical values for metal working processes 453
- tempered martensitic steel 507
- terminal velocity 233–4
- ternary phase diagrams 87–94
 isothermal cross-section and tie-line 88–91, 92
- representation of composition and Gibbs triangle 87–8, 89
- representation of ternary oxide systems 91–4
- ternary systems
 solidification in and four-phase equilibria 95–101
 ternary oxide systems 91–4
- testing methods 453
- thermal conductivity 126–7, 138–43, 203–4
 estimation 162–3, 164
 gases 203
 liquids 203
 porous solids 273–4
 solids 203–4
- thermal diffusivity 138–43
 estimation 162–3
- thermal decomposition 485
- thermal effusivity 138–43
- thermal equilibrium 40
- thermal expansion coefficient 122–4, 126–7
- thermal plasmas 486
- thermoanalytical methods 350–66
 calorimetric analysis 362–3
 DSC 137, 355, 360–1
 DTA 355, 356, 358–60
 EGA and EGD 355, 356, 363–5
 estimation of thermal effects 352–5
 principal thermoanalytical methods 355–6
 specific heat 350–2, 353, 354
 thermogravimetry 355, 356–8, 364, 365
- Thermo-Calc system 70, 71, 72
- thermocouples 353, 432–3
- thermodilatometry (DA) 355
- thermodynamic modelling 118
- thermodynamically stable intermediate phases 310
- thermodynamics 38–81, 151
 basic concepts 39–44
 first law 41–4
 state and state functions 39–41
 chemical equilibrium 40, 44–8
 constraints and sub-processes 374
 description of steelmaking 375–80
 ladle treatment 382–4
 slag models 376–80
 solution models for liquid metal 380
 electrochemical thermodynamics 78, 79, 80
 of interfaces 238–43
 interpretation of surface tension 239–40

- of ionic melts 72–9
 modelling of metallic systems 70–2
 of multicomponent dilute solutions 66–70
 of nucleation 253–5
 reference states for thermodynamic properties 47–8
 second law 44–5
 and solidification 401–5
 of solutions 57–66
 thermodynamic block in micro-modelling 394
 thermodynamic compilations 48
 third law 46
 unary and multicomponent equilibria 49–56
 thermogravimetry (TG) 355, 356–8, 364, 365
 and DTG curves 357
 isothermal TG 358
 sources of error 357–8
 thermomagnetometry (TM) 355, 358
 thermomechanical control rolling process (TMCP) 516–18
 thermomechanical processes 31–4
 deformation processing 32–4
 thermo-physical properties 109–77
 estimating metal properties 148–69
 density and molar volume 151–2, 153
 diffusion constants 168–9
 electrical resistivity 160–2
 heat capacity and enthalpy 149–51
 optical properties 165–8
 surface tension 163–5, 166–7
 thermal conductivity and diffusivity 162–3, 164
 viscosity 152–60
 factors affecting physical properties
 and their measurement 113–20
 commercial materials 120
 convection 117–19
 dynamic methods 119–20
 measurements in the mushy zone 120
 structure 113–17, 118
 surface and interfacial properties 117
 fluid flow properties 113, 122–36
 density and thermal expansion
 coefficient 122–4, 126–7
 interfacial tension 129, 133–6
 surface tension 126–7, 129–34
 viscosity 124–9
 heat transfer properties 113, 136–46
 electrical resistivity 126–7, 143–4
 heat capacity and enthalpy 126–7, 136–8
 optical properties 126–7, 145–6
 thermal conductivity, thermal diffusivity and thermal effusivity 126–7, 138–43
 mass transfer properties 113, 146–8
 measurements and problems 120–2
 different methods for metals, slags and glasses 122
 reactivity of sample 120–2
 need for thermo-physical property data 109–13
 THERMOSLAG software 76, 79
 thin films semiconductor technology 365
 thin slab casting 30–1
 third law of thermodynamics 46
 Thompson-Gibbs relation 406
 Thompson's equation 407
 three-dimensional printing (3DP) 499
 three-phase triangle 89–91, 92, 93, 96
 tie-line 88–91, 92
 time-temperature-transformation (TTT) curves 286, 287, 409–10, 411
 mould slags 432–4, 435–7
 titanium inclusions 523
 titanium nitride 431, 432
 titanium treated steels 430–1
 Tolman's equation 241–2
 torpedo furnace 373
 total emissivity 145
 tracer diffusion 146
 tramp elements 539–40
 transformation-induced plasticity (TRIP) steel 456–7, 507
 transient hot wire (THW) method 142
 transient techniques 120, 141–3
 transition region 218
 transmission methods 146
 transport phenomena 178–236
 fluid flow *see* fluid flow
 heat transfer *see* heat transfer
 mass transfer *see* mass transfer
 transport block in micro-modelling 394
 Trouton's rule 47
 TTT diagrams *see* time-temperature-transformation (TTT) curves
 tumbler ball mills 474, 475, 476
 tungsten 10
 turbulent boundary layer 230, 231
 turbulent flow 217–18, 225–6
 twin roll casting 447, 449
 two-film theory 393–4

- two-fluid atomisation 477, 478, 480–1
 two-sublattice model 70–1, 376
- ultra low carbon (ULC) steels 439–42,
 462–3, 510
- ultrafine multicomponent powders 482–3
- ultrafine powder (UFP) 15–17
- ultrasonic atomisation 477, 478, 482
- ultrasonic gas atomisation (USGA) 478,
 482
- unary systems 49–51
- undercooling 400–1
 effect of lattice disregistry on 412
 heat transfer dominated growth rates
 415–19
 and initial solidification in steel casting
 443–7
 nucleation rate 409, 410
- uniaxial pressing 487–9
- Unified Interaction Parameter Model
 (UIPM) 380
- UO pipe 516–20, 521
- uphill diffusion 182
- upstream processes 504, 506
 future development of 551–2
see also under individual processes
- vacancy mechanism 179
- vacuum atomisation 477, 478, 481
- vacuum degassing 25–6
- VAI-Q 468–9
- vapour-phase reduction 15–17
- vapour phase species 483
- vapour pressure 251
- variable weld penetration 109–10, 112
- vertical attritor 476
- vibrating mills 474, 475, 476
- vibrational heat capacity 351
- vibrational specific heat 351
- view factors 214–15, 277
- viscosity 124–9
 estimations 152–60
 of gases 220
 of liquids 221
 models 154–60
 Newton's law of 218–20
 problems in measurement 128–9
- relationship of diffusion constants to
 168–9
- viscous sub-layer (laminar sub-layer)
 225–6
- Volmer's equation 402–3
- Wagner's equation 66–7, 380, 384
- wastes
 abatement of hazardous wastes 546
 minimisation, recycling and reuse 546–9
see also scrap
 water atomisation 477, 478, 479, 480
- weld penetration, variable 109–10, 112
- Wenzel equation 250
- wet reduction 484
- wet slurry 3DP processes 499
- wettability 449
- wetting 248–50
 of ceramics by liquid metal and slag at
 high temperature 260
- Weymann-Frenkel approach 152
- Weymann relation 152, 154
- Wiedemann-Franz-Lorenz (WFL) rule
 120, 138–9, 162
- Wilson-Frenkel relation 413
- wire casting 30–1
- wire drawing 33
- work 41–2
- work of adhesion 134, 248, 249
- work hardening 32, 454–7
 multiphase materials 455–7
 single phase materials 454–5
- wustite 5
- X-ray diffraction 113, 114
- X-ray pendent drop 135
- X-ray sessile drop method 134–5
- yield stress 32
- Young-Laplace equation 406
- Young's equation 249–50, 404
- zinc 9–10, 12
 corrosion of zinc in a de-aerated
 environment 315–17
- zirconium 12
- zone refining 26–7